VISIT…

LANZAROTE
Caliente.COM

Madeleine Durand-Charre

Microstructure of Steels and Cast Irons

Translated by
James H. Davidson B.Met. Ph.D. C.Eng. M.I.M.

With 289 illustrations

Springer

Prof. Dr ès Sciences Madeleine Durand-Charre
Institut National Polytechnique de Grenoble
e-mail: madeleine.durand@ltpcm.inpg.fr

Originally published in French as *La microstructure des aciers et des fontes. Genèse et interprétation*, Ed. SIRPE, Paris 2003

ISBN 3-540-20963-8 Springer-Verlag Berlin Heidelberg New York

Cataloging-in-Publication Data applied for

Bibliographic information published by Die Deutsche Bibliothek
Die Deutsche Bibliothek lists this publication in the Deutsche Nationalbibliografie;
detailed bibliographic data is available in the Internet at <http://dnb.ddb.de>.

This work is subject to copyright. All rights are reserved, whether the whole or part of the material is concerned, specifically the rights of translation, reprinting, reuse of illustrations, recitation, broadcasting, reproduction on microfilm or in other ways, and storage in data banks. Duplication of this publication or parts thereof is permitted only under the provisions of the German Copyright Law of September 9, 1965, in its current version, and permission for use must always be obtained from Springer-Verlag. Violations are liable for prosecution under German Copyright Law.

Springer-Verlag is a part of Springer Science+Business Media
© Springer-Verlag Berlin Heidelberg New York 2004
Printed in Germany
springeronline.com

The use of general descriptive names, registered names, trademarks, etc. in this publication does not imply, even in the absence of a specific statement, that such names are exempt from the relevant protective laws and regulations and therefore free for general use.
Product liability: The publisher cannot guarantee the accuracy of any information about dosage and application contained in this book. In every individual case the user must check such information by consulting the relevant literature.

Coverdesign: Erich Kirchner, Heidelberg
62/3020 uw Printed on acid-free paper - 5 4 3 2 1 0 -

Preface

How many times have I heard the question "Is there still anything to discover in steels ?", often with the conclusive comment "We know everything about steels - they've been studied for years !" On the contrary, in recent decades, the development of new grades, extended functions and novel applications has continued at an accelerating pace. More than half the steels used today did not even exist five years ago.

This simply demonstrates the vast potential of these materials. Starting from an iron base, numerous alloying elements can be added to modify the microstructure, the mechanical and physical properties and the surface characteristics of steels. A wide variety of metallurgical mechanisms, including solidification, solid state phase transformations, recrystallisation and precipitation can be used in steels to obtain a whole range of useful properties, by appropriate thermomechanical and heat treatments. More reliable and simpler manufacturing processes, together with modern on line non destructive inspection systems, enable increasingly closer control of microstructures, and consequently the attainment of higher and more reproducible performance levels. The melting and processing of steels and cast irons therefore continue to challenge metallurgists and remain an essential driving force for research and development. This can be illustrated by two noteworthy examples, which are mentioned in the present book.

The first concerns packaging steels, particularly those used for beverage cans. The increased strength of today's steels has enabled the strip thickness employed to be reduced to less than 150 µm. This has placed extreme demands on cleanness requirements, with the need to guarantee no more than one inclusion larger than a micron in size per kilometre of strip.

The second example is related to solid state phase transformations. Depending on the steel composition and the thermomechanical processing cycles employed, the equilibrium conditions at the interface can vary tremendously, leading to transformation rates that differ by several orders of magnitude. This can generate highly localised concentration peaks at the interface. The mechanisms involved can be understood and verified only by the use of highly sophisticated modern experimental techniques, such as high resolution transmission electron microscopy and the tomographic atom probe.

The large number of different microstructures observed in steels and cast irons intrigued early metallurgists. The properties of metals in general are closely related to their microstructures. For example, the attractive appearance of many old Damascus steel swords was also a sign of their quality. The scientific study of the nature, composition and geometry of the blade patterns provided modern metallurgists with valuable clues to the processes employed by ancient smiths to manufacture these swords. This historical example, discussed in detail by way of introduction, illustrates the underlying theme of the book, namely, the central role of microstructures in steels and cast irons.

The numerous structural transformations that can occur in steels during solidification and cooling complicate the identification and interpretation of the final microstructures obtai-

ned. However, their analysis has been significantly clarified by extensive research studies and modelling work, providing a scientific understanding of the mechanisms involved. Variations in microstructure then become local "markers" of the composition and thermomechanical history, conserving the memory of successive metallurgical changes and enabling evaluation of transformation rates.

Equilibrium phase diagrams form an essential basis for the interpretation of microstructures. Their experimental determination is refined by the precise analysis of equilibrium constituents. Recent progress in modelling now enables experimental diagrams to be completed and enriched by calculating phase equilibria. The great originality of the present book is a constant and rewarding confrontation between equilibrium aspects, microstructural observations and modelling predictions. This approach also enables the vast variety of steels to be treated by considering a series of typical examples, illustrating the major categories of metallurgical phenomena. A new angle is thus provided for interpreting certain phase diagrams that appear difficult to understand for the non specialist. Moreover, emphasis is placed in this way on the limitations associated with the experimental interpretation of microstructures, on the possibility of misleading artefacts, and on the risk of drawing too hasty conclusions without giving due consideration to kinetic factors.

The exhaustive treatment of metallurgical changes in steels and cast irons prepares the reader for the last part of the book, which describes the major families of steels in a deductive manner. Emphasis is placed on the scientific procedure underlying the design of new steel grades, enabling more rapid development, together with breakthrough innovations that would be impossible by a purely empirical approach.

The book should prove useful for a wide range of readers and should find a prominent place on office bookshelves and those of many microscope rooms. It will remind investigation and quality control specialists of the imperative need to base the interpretation of microstructures on a rigorous scientific understanding. It will help R & D engineers to design new steels to meet increasingly challenging user requirements. For metallurgy teachers, it will provide a large collection of practical examples to illustrate their lectures, based on the author's wide experience accumulated during numerous case studies. Finally, it will reveal to students the fascinating world of steels and cast irons, at the same time didactically guiding them through a vast field of metallurgical knowledge.

While satisfying the curiosity and thirst for knowledge of a wide range of readers, the book also provides food for thought and proves that, despite the excellent level of current understanding concerning steels and cast irons, much still remains to be achieved, by pushing metallurgical science to its furthermost limits.

Jean-Hubert SCHMITT
Director, Isbergues Research Centre
Ugine & ALZ - ARCELOR Group

Acknowledgements

Research metallurgists of my generation have witnessed profound changes due to the progress achieved in the last few decades in the field of metallography. Thanks to the immense contribution of electron microscopy, microstructures can now be explored in their finest details. However, the task of the metallurgist is still that of analysing and interpreting the observations in order to understand the origins of the microstructure. The interpretation of a micrograph requires an extensive metallurgical culture, since numerous transformations have often left traces on different scales of observation. The present book aims to provide the fundamental concepts necessary for this purpose. Emphasis is placed throughout on micrographic features, which are discussed and interpreted in detail. The microstructural characteristics are also used as a guideline for classifying the major families of ferrous alloys, enabling beginners to steer their way through the labyrinth of commercial grades. The objective of the book is to comprise a useful tool that is sufficiently compact to find its place next to a microscope.

An important aspect throughout the book is the role of phase equilibria. The latter part of the 20th century saw the development of the theoretical calculation of phase diagrams based on thermodynamic data for the constituent phases, backed by direct experimental determinations of phase boundaries and characteristic temperatures. The models now available are extremely powerful, quite representative, and increasingly easy to use. However, the excessive simplification of these tools and their use as simple "black boxes" can lead to a loss of scientific information, a sort of "data laundering", that must be avoided by a thorough understanding of the underlying principles. It is for this reason that frequent reference is made to ternary diagrams, using examples chosen among the iron base systems, which undoubtedly represent an excellent basis for reasoning.

The project of the present book was ambitious and I am extremely grateful for the support and encouragement received from numerous sources. First of all, Bernard Baroux is to be thanked for welcoming the idea and obtaining the backing of the Arcelor company. He provided the confidence necessary at a stage when the outlines of the book were still hazy, and proved a staunch ally in promoting the project. I am also indebted to my colleagues in Grenoble for the faith accorded to the success of this work, particularly Colette Allibert at the Institut National Polytechnique de Grenoble (INPG) and Claude Bernard at the Laboratoire de Thermodynamique et Physico-Chimie Métallurgique (LTPCM).

From a scientific standpoint, it appeared a daring and somewhat foolhardy idea to adventure into fields outside my own research areas. I was able to take up the challenge thanks to the kindness and availability of numerous industrial and university scientists, and the help of colleagues in my own laboratory. For example, incursions have been made into territories as dangerous as the bainite transformation, thanks to safety nets provided by Yves Bréchet and his team. In the field of phase equilibria, my environment in the LTPCM was extremely helpful, and my thanks are due particularly to Annie Antoni-Zdziobek who satisfied my unquenchable thirst for calculated phase diagram sections. My teaching and research col-

leagues, Claude Bernard, Yves Bréchet, Catherine Colinet, Patricia Donnadieu, François Louchet, Catherine Tassin-Arques, Muriel Véron (and Francis Durand, my husband) formed an exceptionally constructive reading committee. In industrial circles, I am particularly grateful to Laurent Antoni, Pierre Chemelle, James Davidson, André Grellier, Philippe Maugis, Daniel Nesa, André Pineau, David Quidort, Pierre-Emmanuel Richy, Sophie Roure, and Zinedine Zermout, for much precious information and advice. Special thanks are also due to the technical team at my laboratory, particularly Alain Domeyne, who helped to prepare the experiments used as a source of examples.

I am especially grateful to my translator, Dr. James Davidson, for his rigorous translation, combining his linguistic skills with his competence as an industrial research metallurgist. Indeed, his contribution went beyond a simple translation, since the detailed critical analysis necessary to reformulate the text in English proved an extremely efficient means of clarifying the original French version whenever it appeared inexact or not sufficiently explicit. Finally, James Davidson frequently provided precious complementary indications based on his experience of industrial problems.

Over the years, I have built up a library of high quality electron micrographs, thanks to the help and competence of the members of the Consortium des Moyens Technologiques Communs (CMTC) within the INP in Grenoble. I am particularly grateful to Jacques Garden, Laurent Maniguet, René Molins, Florence Robaut and Nicole Valignat.

In addition, numerous photographs have been kindly supplied by outside laboratories and museums. I always found a warm welcome and a positive response to my severe demands concerning the quality of photographs. These people and organisations are mentioned in the figure captions and I am extremely grateful to all those concerned for their invaluable contribution.

Madeleine Durand-Charre

Contents

Preface v

Acknowledgements vii

Part I. The History of Iron Steed Steel – of Swords and Ploughshares **1**

1. From Iron to Steel 3
   - 1.1 The Long History of Iron 3
   - 1.2 The Three Sources of Iron 4
   - 1.3 Early Ironmaking Technology 6
   - 1.4 The Spread of Ironmaking Technology 8
2. Of Swords and Sword Making 13
   - 2.1 Swordmaking, the Cutting Edge of Metallurgical History 13
   - 2.2 The Celtic Swordmaking Tradition 14
   - 2.3 Merovingian and Carolingian Swords 16
   - 2.4 True or Oriental Damascus Steel Swords Produced Using Wootz Steel 20
   - 2.5 Mechanical or Pattern Welded Damascene Swords 20
   - 2.6 In Search of a Lost Art 21
   - 2.7 Asiatic Swords 27
   - 2.8 Contemporary Damascene Structures 31

Part II. The Genesis of Microstructures **35**

3. The Principal Phases in Steels 37
   - 3.1 The Phases of Pure Iron 37
   - 3.2 Solid Solutions 39
   - 3.3 Order-Disorder Transformations 40
   - 3.4 Intermediate Phases 42
4. The Basic Phase Diagrams 47
   - 4.1 Equilibria between Condensed Phases 47
   - 4.2 Theoretically Calculated Phase Diagrams 53
   - 4.3 Experimentally Determined Phase Diagram 56
   - 4.4 The Fe-Cr-C System: Liquidus Surface 56
   - 4.5 The Fe-Cr-C System: Isothermal Sections and Isopleths 60
   - 4.6 The Fe-Cr-C System: Solidification Paths 62
   - 4.7 The Fe-Cr-C System: The Austenite Field 65
   - 4.8 The Fe-Cr-Ni System 69
   - 4.9 The Fe-Mn-S System 71
   - 4.10 The Fe-Cu-Co System 75
   - 4.11 The Fe-Mo-Cr System 78
   - 4.12 The Fe-C-V System 84
   - 4.13 Mixed Carbides 86
5. The Formation of Solidification Structures 91
   - 5.1 Solute Partitioning Phenomena during Solidification 91
   - 5.2 Local Solute Partitioning 94
   - 5.3 The Growing Solid Interface 95
   - 5.4 The Evolution of Dendritic Microstructures 101
   - 5.5 Secondary Dendrite Arm Spacings 106

This page has been reformatted by Knovel to provide easier navigation.

5.6 Eutectic Microstructures 108

5.7 Peritectic Microstructures 116

6. Liquid/Solid Structural Transformations 121

6.1 Experimental Techniques: Controlled Solidification 121

6.2 Experimental Techniques: Thermal Analysis 124

6.3 Solidification Paths 127

6.4 Metastable Solidification Paths 138

6.5 Peritectic Transformations 141

7. Grains, Grain Boundaries and Interfaces 151

7.1 General Aspects 151

7.2 Characteristics Associated with Grain Boundaries 157

8. Diffusion 163

8.1 Chemical Diffusion 163

8.2 Zones Affected by Diffusion 165

8.3 Case Hardening 168

8.4 Diffusion Couples 172

8.5 Galvanizing 173

9. The Decomposition of Austenite 179

9.1 The Different Types of Solid State Transformatione 179

9.2 The Representation of Solid State Phase Transformations 180

9.3 Growth Mechanisms 184

9.4 Diffusive Exchanges at Interfaces 187

9.5 The Formation of Pro-Eutectoid Ferrite and Cementite 191

10. The Pearlite Transformation 195
  10.1 The Eutectoid Transformation in the Fe-C System 195
  10.2 The Kinetics of Pearlite Transformation 199
  10.3 The Influence of Alloying Elements 200
  10.4 The Re-Dissolution of Pearlite 206
11. The Martensite Transformation 209
  11.1 Displacive Transformations in the Fe-C System 209
  11.2 Characteristics of the Martensite Transformation 211
  11.3 The Morphology of Martensite 215
  11.4 Softening and Tempering of Martensite 219
12. The Bainite Transformation 223
  12.1 Bainite Structures 223
  12.2 Upper Bainite 225
  12.3 Lower Bainite 232
13. Precipitation 239
  13.1 Continuous Precipitation 239
  13.2 Discontinuous Precipitation 245

Part III. Steels and Cast Irons 253

14. Steel Design 255
  14.1 Mechanical Properties 255
  14.2 The Effects of Alloying Elements 263
  14.3 The Common Alloying Additions 265
15. Solidification Macrostructures 269
  15.1 Solidification of Steels 269
  15.2 Solidification Structure of a Continuously Cast Steel 270

This page has been reformatted by Knovel to provide easier navigation.

15.3 Solidification Structures in Large Conventional Ingots 273

15.4 Quality of Solidification Structures 276

16. Macro- and Microstructures of Sintered Powder Products 281

16.1 Sintering 281

16.2 Steels Produced by Solid State Sintering 284

16.3 Steels Produced by Transient Liquid Phase Sintering 286

16.4 Sintered Fe-Cu-Co Composite Alloys 287

17. Plain Carbon and Low Alloy Steels 289

17.1 Mild Steels for Deep Drawing 289

17.2 Low Alloy Structural Steels 291

17.3 The TRIP Steels 295

18. Quench Hardening Steels 297

18.1 Hypoeutectoid Steels 297

18.2 Hypereutectoid Steels 300

18.3 Tool Steels and High Speed Steels 302

19. Stainless Steels 305

19.1 Martensitic Stainless Steels 305

19.2 Austenitic Stainless Steels 313

19.3 Nitrogen-Containing Stainless Steels 318

19.4 Manganese-Containing Austenitic Steels 320

19.5 Resulphurised Stainless Steels 321

19.6 Ferritic Stainless Steels 323

19.7 Duplex Stainless Steels 325

20. Heat Resisting Steels and Iron-Containing Superalloys 331

20.1 Ferritic Heat Resisting Steels 331

20.2 Austenitic Heat Resisting Steels 335

This page has been reformatted by Knovel to provide easier navigation.

20.3 Precipitation Hardened Alloys 338

21. Cast Irons 347

21.1 Phases and Microstructural Constituents in Cast Irons 347

21.2 White Cast Irons 347

21.3 Grey Cast Irons 349

21.4 Spheroidal Graphite (SG) Cast Irons 356

21.5 The Heat Treatment of Grey (SG) Cast Irons 363

22. Appendices 367

22.1 General Comments 367

22.2 Interface Energies 367

22.3 Chromium and Nickel Equivalents 367

22.4 Etching Reagents 368

22.5 Characteristic Diffusion Lengths 369

22.6 Empirical Formulae for Determining the Ms and Mf Temperatures 370

22.7 Effects of Alloying Elements in Steels 370

22.8 Typical Hardness Values of Various Constituents Found In Steels 373

23. References 375

Index 399

This page has been reformatted by Knovel to provide easier navigation.

First Part

The history of iron and steel - of swords and ploughshares

"To those craftsmen whose intuitive understanding provided the seed from which metallurgical science grew", C.S. Smith in "A History of Metallography" [Smi65].

"The smith created his artefacts by taming the divine element of fire; and it is significant that the only human craft which was found sufficiently worthy to be practised by one of the Olympian gods - Hephaistos/Vulcan - was that of the smith", H. Nickel in "Damascus Steel" by M. Sachse [Sac94].

1

From iron to steel

1-1 The long history of iron

Man's relationship with iron goes back deep into prehistoric times, and is presently believed to cover at least seven millennia. Fragments of iron and small iron objects such as beads, blades and decorative inlays have been found in archaeological sites dating to around 5000 BC, in Irak (Samarra), Iran (Tepe Sialk) and Egypt (El Gerseh). Later discoveries, corresponding to the early bronze age (3000–2000 BC) and middle bronze age (2000–1600 BC), are all situated in the east and south-east of the Mediterranean Basin, in Mesopotamia, Turkey, Egypt and Cyprus.

Written evidence of early iron-making activities exists in the form of mural hieroglyphic inscriptions and papyruses, for example in the *Book of the Dead*. However, the translation of ancient technical terms remains uncertain. Some early civilisations do not appear to have recognised iron as being distinct from copper and refer to it as black copper, in the same manner as unrefined copper. References to black metal or to metal from the sky could apply to iron or hematite ore, but also to other metals. Furthermore, the presence of objects made from iron does not necessarily imply the ability to extract the metal from its ores, since iron also exists in native and particularly meteoritic form, although the sources are by no means abundant.

Gold and copper were used extensively in ancient civilisations well before the mastery of the metallurgy of iron. The earliest evidence of iron smelting has been found at Hittite excavation sites in Asia Minor, dating from between 1700 and 1400 BC. However, this does not necessarily mean that iron-making originated in this region and then spread elsewhere. It is the aim of the present chapter to consider in more detail the dawn of iron metallurgy.

While the extraction of iron from its ores is closely related to the characteristics of the iron-carbon system, the practical exploitation of the remarkable properties of iron and steel provides a further illustration of how technical progress resulted from a combination of empirical observations and ingenuity. With rudimentary means and limited knowledge, early iron-smiths gradually developed their skills and know-how, succeeding in manufacturing a wide variety of high quality objects. This is nowhere more clearly evident than in the art of sword-making throughout the world. This subject is considered in Chapter 2, where the study of the microstructure of ancient damascened sword blades provides an appropriate transition to the major theme of the book.

1-2 The three sources of iron

The earliest iron used by man was generally *meteoritic* in origin, as shown by the presence of nickel in most prehistoric objects, as well as in those from the early and middle bronze ages. The microstructure of a typical metallic meteorite is shown in Figure 1-2-1. Note that another name for a metallic meteorite is *siderite*, although this term is also used for an iron carbonate ore. In prehistoric times, meteorites were worked in the same way as stone in order to obtain tools. In Greenland, three meteorites among the largest ever found (one weighed 36 tonnes) had been used for generations by Eskimos, until they were shipped to the American Museum of Natural History by Peary in 1895–7. In Central and South America, the Aztecs, Mayas and Incas used meteoritic iron without knowing its metallurgy. They considered it as extremely precious and restricted its use to jewellery and religious objects. In Egypt, the blade of a magnificent ceremonial dagger found in Tutankhamen's tomb (1350 BC) was identified as being made from meteoritic iron. It was one of a pair of objects, the other being gold. Meteoritic iron was often considered as divine [Eli77]. It was realized that meteorites were of celestial origin and they were often considered to be of a *divine nature* and were sometimes even worshipped, for instance in ancient Greece the stone of Elagabalos and the stone of Chronos.

Native iron is of terrestrial origin and is found in basalts and other rocks, generally in the form of small grains or nodules. It often contains considerable quantities of nickel, up to 70%. It is rarer than meteoritic iron, but has also been found in ancient precious objects.

However, most of the iron present at the Earth's surface is in the form of ores, mainly the oxides, particularly hematite (Fe_2O_3) and magnetite (Fe_3O_4), although carbonate (siderite), sulphide (pyrites) and mixed iron and titanium oxides (ilmenite) are also fairly common. *Iron extracted from ores is normally free from nickel*, and iron of this type has been found in objects dating from prehistoric times. Iron objects have been found in Egypt, in the Temple valley and Cheops' pyramid at Giza (2500 BC) and at Abydos (200 BC). However, the number of such objects is small and their authenticity is doubtful, due to their poor state of conservation (heavy rusting).

The oldest iron not of meteoritic or native origin is found as small decorative inlays in gold jewellery or tiny cult objects. It has been suggested that this iron is a by-product of the gold production process. Magnetite is frequently present in the gold-bearing sands in Nubia and could have been reduced during the smelting operation, pasty iron floating to the slag above the molten gold. Another possibility is that iron oxides were deliberately associated with other oxides used as fluxes for the manufacture of bronze.

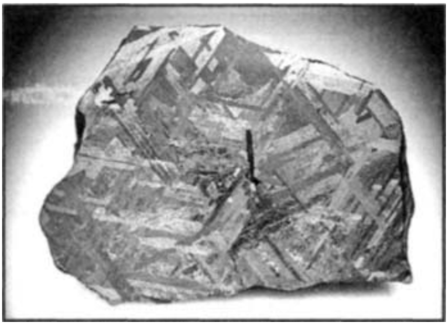

Figure 1-2-1:
Polished section of a metallic meteorite, from the Henbury crater in Australia, showing a coarse Widmanstätten structure (approximate sample width 8.5 cm). Meteoritic iron generally contains a few percent of nickel, with amounts typically ranging from 5 to 26 %, although much larger concentrations are sometimes found, together with small amounts of cobalt (up to 1%) and traces of sulphur, phosphorus and carbon. Metallic meteorites are relatively malleable. In fact, there are three major classes of meteorites, corresponding to metallic, stony and mixed structures. They are generally believed to be fragments of planets that have disintegrated, the metallic meteorites emanating from deep inner layers. The crystalline phases present in metallic meteorites have names specific to this field of study. For low nickel concentrations, the body-centred cubic crystal structure is known as kamacite (ferrite in steels), whereas the face-centred cubic structure found in high nickel meteorites is called tænite (austenite in steels). The structure shown in the photograph, consisting of plate-like ferrite in austenite, was first observed in 1808 by the Austrian metallurgist Aloys Beck von Widmanstätten (1754–1849) who sectioned, polished and etched a meteorite that had fallen in Croatia in 1751. The plates are oriented in directions which form an octahedron. The term "Widmanstätten structure" is now used to describe the preferred growth of a phase in the solid state with low index habit planes with respect to the matrix (for example $<110>\alpha$ // $<111>\gamma$), and will be frequently encountered in the main part of the book. However, Widmanstätten structures in steels are rarely as coarse as those found in meteorites, which can be seen without a microscope.
The origin of this structure in meteorites has been suggested to be associated with the existence of a eutectoid reaction between kamacite and taenite at high pressures. Thermodynamic calculations show that this would be possible at pressures above 50 kbar [Bér96b]. Such conditions could occur deep within a planet. However, the extreme coarseness of the structure, with plate widths of several millimetres, is such that some authors consider a solid state transformation to be unlikely. Another possibility proposed is that the plates formed by extremely slow solidification, under conditions of micro-gravity [Buc75], [Bud88].
Courtesy Mineralogical Research Company.

Several archaeologists are now convinced that the extraction of iron by the reduction of ores was discovered at an early stage, before 2000 BC, probably in several different places. However, the presence of non-meteoritic iron objects is not always associated with evidence of local mining activities. For example, in Egypt, where iron ore deposits are abundant, there is no sign of their exploitation. This is probably due to the absence of forests capable of supplying the charcoal necessary for reduction.

What is clear is that several millennia elapsed between the first reliable identifications of iron artefacts and the start of what can be genuinely termed the iron age. Several explanations can be suggested. The most obvious one is the inherent difficulty of extracting iron from its ores. The processes used for gold and copper are not applicable, and in particular, much higher temperatures are required. The iron dating from this period has been termed *accidental* [Bér96a]. Another possible reason is the fact that the iron obtained by the most primitive processes was of insufficient quality to be really useful. It was pure, with a low carbon content, and was consequently malleable and could be fashioned into ornaments, but was not hard enough for the manufacture of tools or weapons. It was rare and its value was probably several times that of gold, in spite of the fact that, unlike gold, *iron rusts*, being converted to red hydrated oxides on contact with air and moisture. Indeed, it is probably for the latter reason that iron was often the subject of adverse superstitions and religious beliefs, being considered to be impure. For example, like red hair, iron was despised by the Egyptians, who made it one of the attributes of the evil god Seth, murderer of his brother Osiris, and called it "Seth's bone". At the time of King David, the Israelites showed a similar aversion and forbade the use of iron tools for making altars. The classical Greeks even composed a prayer to prevent rust. In other times, it was considered ill-advised to use iron implements for cutting herbs or carving meat. In Africa, excessive drought was sometimes blamed on the use of iron tools to till the soil. Many such examples can be found in the literature.

Since the second half of the 20th century, metallurgical archaeology has made considerable progress, due to the discovery of new sites, more rigorous and methodical excavation procedures, and sophisticated modern techniques for the characterisation of metal artefacts. The subject is extremely vast and the following references will provide a useful starting point for readers wishing to pursue the question in more detail : [For64], [Smi65], [Tyl87], [Ple88], [Moh90], [And91].

1-3 Early ironmaking technology

Iron ores

After aluminium, iron is the second most abundant metal in the Earth's crust. The major iron ores are essentially oxides (magnetite, hematite and limonite), carbonates (siderite) and sulphides (pyrites). Ilmenite, another fairly common ore, is a mixed oxide of iron and titanium. Many ore deposits occur in the eastern Mediterranean basin and can often be readily recognised due to the associated rust-red coloration of the earth. Indeed, they were often exploited as pigments, giving the yellows, ochres, browns and reds used by the Egyptians. Evidence of early mining activities are visible in deposits in Syria and Cappadocia, which appear to have been the first to be exploited on a large scale. They include Germanicia in South-East Turkey, just north of the ancient city of Duluk, often considered as the cradle or ironmaking. Production sites at Tabriz and the plain of Persepolis in Iran are also associated with evidence of early ironmaking activities. Metallurgical culture is extremely ancient throughout the "fertile crescent" and the Assyrians appear to have practised the reduction of iron ore as early as the 19th century BC. The presence of numerous rich ore deposits facilitated the gradual expansion of ironmaking to central Europe, north Italy, Spain, France and Great Britain.

Some ores contained other elements that became incorporated in the iron, conferring particular properties. For example, ore from Siegerland in Germany contained manganese, while certain Greek and Corsican deposits contained nickel. The Lorraine deposits are rich in phosphorus, which causes strengthening, but reduces ductility [Sal57], [Ype81].

Ironmaking

In the earliest ironmaking processes, washed and crushed ore was heated with charcoal in a primitive furnace, often consisting of little more than a hole in the ground. The temperature attained was insufficient to achieve melting and the oxide ore was reduced by the carbon in the solid state, leading to a spongy agglomerate called a bloom. The slag envelope was removed and the bloom was repeatedly heated and hammered to expel residual slag inclusions, forming a more compact mass. The iron obtained in this way was fairly pure, with a low carbon content. It was therefore malleable, but relatively soft.

Furnace construction techniques evolved in such a way as to optimise natural draught, but the use of rudimentary bellows made from animal hide was probably adopted at an early stage. Traces of cast iron found amongst the slag in ancient smelting centres indicate that the temperatures attained were sufficiently high to induce melting. However, such cast iron was probably initially obtained accidentally and considered as a worthless by-product, since it was hard, brittle and unworkable.

The development of *iron smelting* was particularly facilitated in areas where ore deposits were associated with ready supplies of charcoal and refractory materials for furnace construction. However, the use of iron accelerated when ways were discovered to improve its mechanical properties. One technique consisted in heating soft iron in the presence of charcoal, whereby carbon diffused into the metal in what was essentially a cementation process. At the temperatures attained, the depth of carbon penetration was no more than about a millimetre. However, this was sufficient to achieve effective surface hardening, for example in the points and edges of sword blades. When applied to thin iron strip, a hard steel was obtained, which could be combined with soft iron strip by forge welding. Intense and repeated forging enabled the carbon level to be homogenised to a certain extent by diffusion, although exposure to air involved the risk of decarburisation. Objects produced in this way in the latter centuries of the pre-Christian era have very heterogeneous structures and relatively poor mechanical properties, with low toughness [Le_00]. A significant improvement was obtained when the method was modified to conserve a composite forge-welded structure, with appropriate combinations of soft iron and hard but brittle carburised steel [Wad02].

Empirical *carburising-nitriding treatments* were also performed by mixing nitrogen-rich organic wastes with the charcoal. Indeed, sophisticated proprietary case hardening mixtures were developed, containing ingredients considered to have a magical influence, such as dung and manure, which in fact provided sources of both carbon and nitrogen. However, the contribution of nitrogen to hardening is relatively small and the significance of such practices was more mystical than technical.

Quenching

When an iron object is rapidly cooled, for example by *quenching in water after forging,* its structure is transformed to martensite. This can induce great hardness, particularly when the carbon content has been increased by heating with charcoal. Evidence of such carburising treatments has been found as early as the second millennium BC. However, martensite is difficult to recognise in very old carburised artefacts, due to corrosion, since the presence of carbon significantly enhances the tendency for rusting. Nevertheless, a few rare objects dating from the 13th and 12th centuries BC clearly demonstrate a knowledge of both carburising and quenching treatments. For example, a miner's pick from this period found at Mount Adir in Galilee shows a structure containing lightly tempered martensite laths.

In iron with a very high carbon content, such as the wootz iron described below, transformation to martensite is only partial and is associated with brittle behaviour. It is therefore generally avoided. Cooling is then performed at moderate speeds, simply with the aim of obtaining a fine structure, which can be highly complex (*cf.* § 2-1). Indeed, quenching treatments *are not systematically associated with martensite formation.*

1-4 The spread of ironmaking technology

From Asia Minor to Europe

The manufacture of iron by solid state reduction with carbon was well established in north east Turkey around 1500 BC and the practice gradually spread westwards over a period of more than a thousand years, with a number of significant milestones.

- Around 1400–1200 BC, iron tools and weapons were used by the Hittites in Anatolia, to the south of the Black Sea, but remained much rarer than bronze artefacts, becoming commonplace only towards the end of this period. *The age of carbon-enhanced iron, or steel,* can thus be considered to have effectively begun in the Armenian mountains around 1200 BC.
- Around 1100 BC, iron was produced from abundant ore deposits in the Near East and southern Europe, particularly in Mycenaean Greece and Cyprus, where it was used for the manufacture of numerous small objects. Production had become widespread in this region by about 900 BC.
- Around 900 BC, ironmaking technology had reached central Europe. In particular, the Hallstatt civilisation knew how to harden iron by carburising. The Celtic people of La Tène subsequently greatly developed the use of iron and improved its quality.

> *Hallstatt is the name of a village in Austria where a rich iron age cemetery was discovered, with many objects dating from 1200 to 500 BC. The third level at this site, called Hallstatt C, extending from 800 to 600 BC, corresponds to the beginning of the iron age in this region.*

> *La Tène is another rich excavation site, situated to the north of Lake Neuchâtel in Switzerland, and dates to between 500 and 50 BC. It has given its name to an artistic style. In fact, the La Tène culture is derived from that of Hallstatt, but is more homogeneous and more typically Celtic. The gold and bronze artefacts are richly and imaginatively decorated, in a manner so uniform that some archaeologists believed they were due to a single artist, "the Waldalgesheim Master."*

- Around 600 BC, the metallurgy of iron spread to the Etruscans in central Italy and to Catalonia in north east Spain. The Etruscans and Catalonians developed a technology independent of that practised by the Celts, probably due to their commercial contacts throughout the Mediterranean basin.
- Between 500 and 300 BC, iron production spread throughout Europe. The Celtic culture, with its metallurgical know-how, reached northern Spain and Ireland, where it withstood the onslaught of the Roman empire.
- By the end of the La Tène period, in the 1st century BC, Celtic smiths had invented the technique of forge welding soft and carburised iron, and were able to produce simple composite sheets and rods.

The spread of wootz steel throughout the Arab world

A type of high carbon steel made in India and called wootz, whose origins go back to 500–200 BC, was of unequalled quality and became internationally famous, particularly for the manufacture of sword blades (*cf.* Chapter 2) [Fig91]. It was produced by a well established traditional technique similar to the much later crucible process. The high quality magnetite ore was carefully sorted, finely crushed and washed by panning to remove gangue and increase the iron content before smelting. The prepared ore was then mixed with bamboo charcoal and leaves of specific plants considered sacred, and hermetically sealed in chalk. The small charges were then inserted in clay crucibles, which were heated by a charcoal fire in batches of up to twenty. The prolonged heating process at temperatures up to 1200 °C led to significant carbon uptake, lowering the melting point and enabling at least partial melting, forming a spongy iron mass, called a cake, in the bottom of the crucible, typically weighing up to 2 kg [Pra95]. Wootz iron differed from other irons by its high carbon content, up to about 1.5%. Trace elements such as vanadium and titanium, possibly from the bamboo charcoal or other plants employed, probably contributed to the exceptional properties of wootz steel, which was widely appreciated. It was extensively exported from India, first of all to Asia and later to the Middle East, Iran, Turkey and Russia. Its success lasted more than 2000 years and its quality was acknowledged throughout the world.

Ironmaking in China

Iron produced by smelting appears to have been known in China about 1000 years before Christ. The production of cast (*i.e.* molten) iron was developed in China around the 6th and 5th centuries BC, leading to a different approach to iron metallurgy [Moh90], [Rub95]. Evidence for this includes cast iron cauldrons dating from 512 BC and cast iron moulds from the end of the 1st millennium BC. It has been suggested that these developments were facilitated by the presence of phosphorus-rich ores, since phosphorus lowers the melting point of iron (*cf.* Figure 2-3-4). Furthermore, technical know-how in other fields was further advanced in China than in other parts of the world. For example, in the case of pottery, the Chinese mastered the manufacture of both red pottery, baked in oxidising atmospheres, and black and egg-shell pottery baked in reducing environments. Their furnaces were ingeniously designed and made from high quality clay refractories, and bellows were in regular use in the 4th century BC. Their advance was maintained by improvements such as the introduction of piston bellows in the 2nd century BC, and the replacement of charcoal by coal in the 3rd century BC, nearly two thousand years before Europe.

Under the Han dynasty, in the 2nd century BC, cast iron was decarburised to render it malleable and slow cooling rates were imposed during solidification to obtain grey cast iron. Early in the 5th century AD, an original carburising technique was developed, consisting in immersing mild steel in cast iron and then subjecting the coated product to a series of forging and bending cycles [Rub95]. Even more surprising is the recent discovery of cast iron objects dating from the Han and Wei dynasties (206 BC to 225 AD) containing graphite nodules similar to modern SG iron, invented in 1948. Chemical analysis revealed none of the inoculants used today for spheroidisation. It has been suggested that an appropriate Mn/S ratio enables graphitisation of cementite to occur in the solid state with a nodular morphology [Hon83].

Ironmaking in Africa

In Equatorial Africa, neolithic practices were directly followed by an iron age, with no intermediate use of copper or bronze. The analysis and dating of many small artefacts indicates that the metallurgy of iron in this area goes back to at least the 3rd millennium BC, and possibly even to the 4th [Gré88]. In Gabon, furnaces dug into the soil have been carbon dated to the 7th century BC, based on charcoal residues found in the vicinity. However, the lack of spatial coincidence does not provide unambiguous proof. Furthermore, iron objects remain relatively rare, due to the difficulty of conservation in the prevailing moist climate and acid soils.

It has been suggested that liquid iron was obtained at an early stage in prehistoric furnaces found near Lake Victoria in Tanzania, high temperatures being attained by the injection of preheated air. However, what is probably more important is that, in the region concerned, the iron ore is extremely rich in phosphorus, while the local vegetable matter mixed with the ore is also rich in phosphorus, facilitating melting.

In Africa, more than anywhere else, ironmaking practice was closely tied to social structures. Africa is the only continent where iron continued to be produced and worked according to ancestral customs until the middle of the 20th century [Sch78]. Ethnologists have been able to directly question old-timers and even to reproduce melts complete with their social context (Figure 1-4-1). The smith was an important person, being both a

Figure 1-4-1:
Iron smelting furnace constructed during a reconstitution at Yatenga, Burkina Faso, in 1988. The furnace is one of the tallest of its type. The combustion level is at the base. The slag was removed via a channel. The furnace could produce 200 to 250 kg of iron from a tonne of ore. About 1 000 to 1 500 similar furnaces existed at the beginning of the 20th century, and worked two or three times per season. Two other bellows-blown furnaces were used to refine and preheat the iron before forging.
Numerous installations subsist in the region from Niger to the Atlantic Ocean. The furnaces have a wide variety of shapes and sizes, with cell, column or chamber designs, and heights ranging from 1.3 to 6 metres, based on tribal know-how passed down through generations [Mar93].
Courtesy Aix-Marseille University.

craftsman and a sorcerer. He supervised preparation of the furnace and the smelting operation, and was the grand master of a ceremony celebrating the "espousal of ore and the inferno" and "fecondation by fire", to give birth to iron. The great day of smelting was preceded by purification rites and abstinence, with collective sacrifices, which sometimes included humans or foetuses. The feast was accompanied by music and incantations. Indeed, the example of Africa highlights the almost liturgical symbolism that was associated with primitive iron smelting practice throughout the world [Eli77].

Steel in more recent times

The history of steel in the 2nd millennium AD is closely related to the improvement of ironmaking technology and mining practices [Maî96]. In the 12th century, the invention of the hydraulic tilt hammer greatly facilitated forging operations. In the 14th century, the Catalan furnace used compressed air produced by a blast pump driven by a waterfall, a technique invented in the north of Italy. The 16th century saw the widespread development of the crucible process, in which wrought iron bars were heated in charcoal to increase their carbon content. Deforestation, due to the consumption of wood for charcoal manufacture, eventually became a problem. In 1709, Abraham Darby replaced charcoal by coke, a carbon-rich residue obtained by the distillation of coal to drive off its volatile constituents, and particularly sulphur, which is incompatible with the steelmaking process. Finally, in the 19th century, steelmaking entered the industrial era, with mass-production processes such as the Bessemer converter and Siemens-Martin furnace.

Metallurgy became a science when traditional know-how was analysed and exposed in written form, greatly aided by the development of printing in the 16th century. In this respect, a major milestone was the publication of Agricola's richly illustrated *De Re Metallica* in Basle in 1556. In the late 18th century, the French Encyclopaedia included several articles on metallurgy, including subjects such as canon founding and the malleablising of cast irons. Finally, in keeping with the subject of the present book, the application of optical microscopy to the study of metallic microstructures in the second half of the 19th century made a major contribution to the development of the science and technology of metals.

2

Of swords and swordmaking

In her book La Ville Noire *(Levy, Paris, 1860), the French 19th century novelist George Sand describes her impressions of the metalworking profession, gained during a visit to cutlery workshops in Thiers, in the following terms : "There is nothing in the world more delightful than to see all those people, so sharp, so dexterous, so skilful, and so careful, each in his own domain... they (armourers, cutlers, locksmiths, men of fire) twist a bar of raw metal and pass it from hand to hand so fast and so expertly that in less than twenty minutes you see it change into a handy, light and sturdy tool, as bright and shiny as you could wish."*

2-1 Swordmaking, the cutting edge of metallurgical history

A mythical instrument

The history of metallurgy can be read from the evolution of many different objects commonly found in archaeological excavations, including axes, ploughshares and nails. However, weapons, from knives to canons, have always been the first to benefit from the most recent technological progress. In particular, knives and swords of many kinds have been used as combat weapons for more than three millennia. Moreover, a sword was often an attribute of social rank and could be a highly precious and luxurious object[1]. Indeed, because of this symbolic role, many richly decorated swords have been conserved, either passed on as family heirlooms, guarded as sacred relics, or buried alongside their warrior owners.

The best swordsmiths were considered as master craftsmen and were held in high esteem in all ancient civilisations. This was clearly apparent in graves excavated of at Hallstatt and La Tène period. The act of forging a sword went beyond a simple question of craftsmanship, since a sword was a mythical and sacred instrument. The smiths were likened to their divine counterpart Vulcan, who forged thunderbolts to arm the gods, and many popular legends concern magical swords, including Durandal in the Song of Roland, and Excalibur

---

1. The term sword is used in a generic sense throughout this chapter to refer to a wide variety of slashing and stabbing weapons, including daggers, sabres, glaives, etc.

in the tales of King Arthur and his Knights of the Round Table. The legend of Wieland, which inspired Wagnerian operas, is known to have existed in the 6th century, but had probably been passed down from much earlier times. The mythical aspect of swords was often reflected in special inscriptions and decorations, and in rituals that accompanied manufacture. It was a common superstitious belief that the swordsmith and his environment transferred a mystical force to the weapon during the forging process.

> *In this respect, it is interesting to quote a comment on the work of Zschokke [Zsc24] : "One of his conclusions, indicating that the composition of Damascus steel prevented the use of severe quenching, in order to avoid excessive brittleness, recalls a curious oriental tradition, concerning the air cooling of certain Damascus blades. As soon as forging was finished, while the blades were still red hot, they were given to a horseman, who galloped away furiously holding the blade in the air. This method of forced air cooling was probably more suitable than quenching in cold water for these high carbon and phosphorus steel blades."*
>
> *Mild cooling also appears to be confirmed by the description of the Indian process whereby the red hot blades were thrust into the hollow trunk of a banana tree [Pra95].*

In Muslim countries, the religious aspect of swords is clearly clearly illustrated by decorative inlays representing verses and extracts from the Koran on the blades, as well as by the symbolic ladder pattern, representing Mahomet's 40-step ladder, recalling how Allah will welcome the brave warrior killed during a holy war. In Catholic countries, during the middle ages, swords were blessed during the knighting ceremony. In Japan, samurai swords were decorated with Buddhist or Shinto inscriptions, and were both a symbol of honour and a sort of talisman.

Sword design has varied greatly, both across the ages and in different civilisations, depending on contemporary know-how and fighting techniques. Although an abundant literature is available on the subject, considerable uncertainty remains concerning the dates and places of manufacture of the oldest swords. Those that are described in the present chapter have been chosen because of their typical metallurgical structures. They include Celtic and Merovingian weapons, oriental swords forged from wootz steel, Japanese and Indonesian swords, and contemporary reproductions of damascened blades.

2-2 The Celtic swordmaking tradition

The earliest iron swords in Europe

A strong impetus was given to the spread of ironmaking practice by the expansion of the Celtic civilisation throughout Europe from about the 6th century BC (Figure 2-2-1). The Celts originally corresponded to numerous tribes inhabiting the region of Central Europe between the Rhine and the Danube. They were extremely warlike and had a large weapon consumption, particularly since it was their tradition to bury warriors killed in battle,

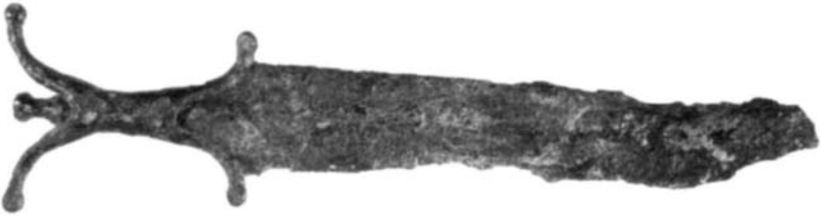

Figure 2-2-1:
Short Celtic sword from the La Tène II period (length 37 cm, maximum width 9.6 cm, maximum thickness 1.6 cm). The anthropomorphic hilt shows a certain degree of forging skill. The ability to carburise iron and to forge weld different metallic materials is demonstrated by certain Gaulish artefacts dating from the 3rd and 2nd centuries BC [Ype 81].
Courtesy Annecy Museum, France.

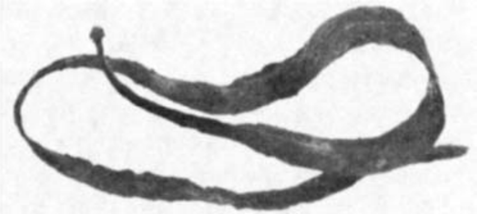

Figure 2-2-2:
Bent iron sword, 91 cm long, found with burnt bones in a Gaulish cemetery dating from the middle La Tène period, around 200 BC. Numerous twisted swords have been found in the tombs of Celtic warriors and appear to have been rendered deliberately unusable. Courtesy Dauphinois Museum, Grenoble, France.

including enemies, with their arms (Figure 2-2-2). It is difficult to determine whether the progress observed in swordmaking practice was due to the ingenuity of Celtic smiths alone or whether it was the result of wars, invasions or commercial exchanges.

The most recent Celtic swords were made with a core of soft iron and carburised iron blade edges, combining stiffness and toughness, welded together by forging. It was possible in this way to produce longer and thinner blades of moderate strength.

The majority of Celtic blades are found to have ferrite-pearlite microstructures corresponding to hypo-eutectoid steels, with Vickers microhardness values ranging from 70 to 250 for the ferrite and 150 to 250 for the pearlite [Bér96a]. Harder constituents, such as martensite or bainite have rarely been observed, even for the highest carbon contents. The grain size varies widely [Flu83]. The study of many other Celtic steel artefacts dating from between the Hallstatt period and the Roman Empire also reveals mainly ferrite-pearlite structures with hardnesses between 100 and 200 H_V [Tyl87]. In the case of swords, quenching was certainly employed, but the formation of martensite probably affected only a narrow zone along the edge, which had the highest carbon content and was thinnest, cooling most rapidly. Unfortunately, this region is generally eaten away by corrosion. For the compositions concerned, with very small amounts of alloying elements, the pearlite transformation is rapid, and martensite forms only for very high cooling rates (*cf.* § 10-3).

For several centuries, both iron and bronze were used for swords. The Romans, who had conquered territories in Spain containing rich deposits of copper ores, used bronze swords. They did not see the advantage of changing to iron until the Punic Wars against the Carthaginians, in the 3rd and 2nd centuries BC [Reh92]. Indeed, several Roman authors ironically criticise the poor quality of the Gaulish swords, considered to be "insufficiently wrought", which tended to bend and have to be straightened, provided that the enemy left them enough time !

2-3 Merovingian and Carolingian swords

Swords with a damascene structure eventually appeared as a natural consequence of a more sophisticated forge-welded composite manufacturing process. They have been found throughout Europe, from Yugoslavia to Scandinavia. Swords from the 2nd and 3rd centuries AD were discovered in a Danish bog, buried in conditions where they were protected against corrosion. However, stratified Celtic blades have been dated to as early as 500 BC. The technique developed into an art, which culminated in the 8th to 10th centuries AD, during the Frankish Merovingian and Carolingian dynasties. Numerous such swords have been found in Scandinavia, but their place of manufacture remains uncertain. It is known that important manufacturing centres existed in the Rhineland and there are a number of indications, including written texts, that the Vikings obtained their swords through trade, smuggling or plunder. The Frankish king Charlemagne and his successor Charles the Bald issued decrees forbidding, on pain of death, the sale of arms to the "Norsemen", suggesting that arms trading was rife at the time. Arab chroniclers called these weapons Cologne glaives and reveal that they were highly prized in Muslim countries as spoils of war [Sal57]. In Europe, the manufacture of Carolingian type swords ceased towards the end of the 10th century, probably because swordsmiths learnt ways to make better weapons than by imitating the *wavy* structures of the famous damascus swords (§ 2-4 and Figure 2-4-1).

Whether Merovingian or Scandinavian in origin, the swords dating from the 5th to 10th centuries AD, between the "barbarian" and Viking invasions, usually had straight double-edged blades. In some cases, the alternation of different materials produces a pattern. Swords found in the north of France and Germany have been classified into 17 types, depending on the arrangement of chevron and wave markings. The various patterns probably correspond to different swordsmiths or periods, since the same general process was used for nearly a thousand years. A high degree of skill had been achieved to produce harmonious patterns. Forging had to be performed rapidly and efficiently, since prolonged heating would tend to homogenise the layers and attenuate the pattern. Some swords were not decorated in depth, consisting of a laminated surface structure on a soft iron core, a sort of metallic marquetry, different on each side of the blade. This is illustrated by the Merovingian sword shown in Figure 2-3-1 (but probably not by the Carolingian one in Figure 2-3-2). Like in modern composites, the longitudinal configuration of the welds

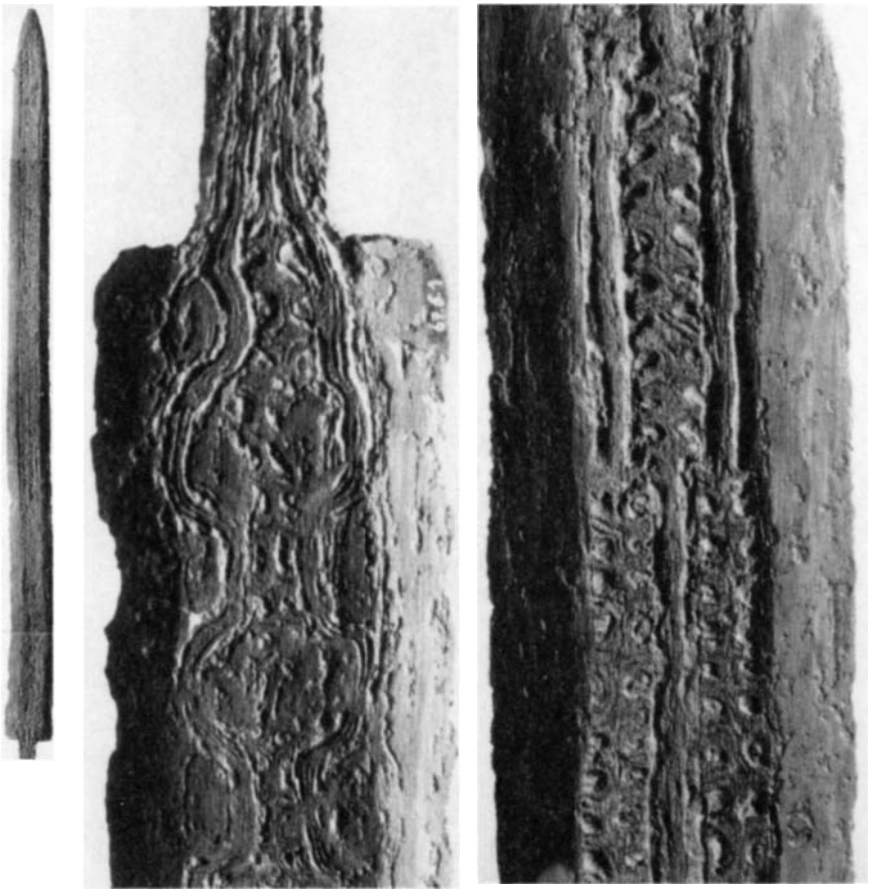

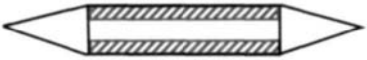

Figure 2-3-1:
92.5 cm long Merovingian sword of unknown date. The pattern is different on each side of the blade, as is often the case for the common five-part configuration shown schematically in the accompanying diagram. The centre of the blade is composed of two composite steel plates (hatched) on a soft iron core, with separate hard carburised steel edges. The photographs of the two sides are not directly opposite one another, being chosen where corrosion was least and the pattern most clearly visible.

The composite facings were prepared from seven superimposed plates, consisting alternately of soft and carburised iron, forge welded together by repeated heating and hammering, to obtain a laminated bar of roughly square section. The bar was then further hot worked, bent like an accordeon or twisted, then flattened to strip. Several such strips (probably three) were then forge welded together. The resulting pattern depends on the forging process employed and is rendered visible either by etching the polished blade in acid, or simply by corrosion.

Courtesy Musée de L'Histoire du Fer, Nancy Jarville, France.

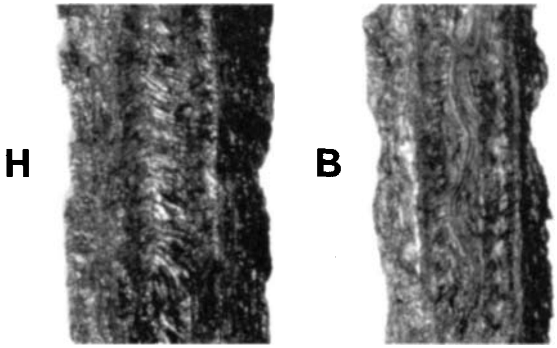

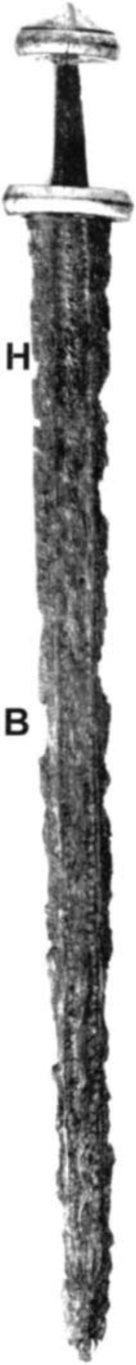

Figure 2-3-2:
94.5 cm long Carolingian sword found in the rue de Vaux, in Strasbourg in 1899 and dated to between 780 and 950 AD [Ehr88].
The upper part, H, shows a chevron pattern at the centre of the blade, obtained by welding together two bars twisted in opposite directions.
The lower part, B, shows a series of waves parallel to the axis.
Courtesy Strasbourg Archaeological Museum.

ensured good strength, reducing the risk of transverse fracture [Sal57], [Fra52], [Mar58].

The typical compositions of Merovingian swords and the range of possible working temperatures are positioned on the Fe-C phase diagram in Figure 2-3-3. The differences in composition between the materials used in the laminated surface layers are usually relatively small (*e.g.* Table 2-3-5, [Fra52]). A ratio of 1.5 to 2 has been found between the nitrogen content of the cutting edge and the core, probably indicating deliberate heat treatment of the former in contact with nitrogen-rich organic wastes.

This recalls the legend of Wayland (German Wieland), smith, artificer and king of the elves in ancient European folklore, who was dissatisfied with the first forging of his sword Mimung and broke it into thin fragments which he mixed with flour and fed to ducks and geese. Regretting his act, he recovered the metal in the birds' excrements and found the oxides to have been cleaned away. He then forged the metal, together with the dung, repeating the operation several times, and obtained a sword of incomparable quality.

Scientific experiments in 1930 showed that heat treatment in nitrogen-rich bird droppings can effectively slightly increase the nitrogen content of iron [Ype81].

Figure 2-3-3:
Fe-Fe$_3$C phase diagram showing the typical compositions and forging ranges of Merovingian steels and Indian wootz steel used for damascened swords. The higher carbon wootz steel had to be forged at lower temperatures due to the greater risk of melting.

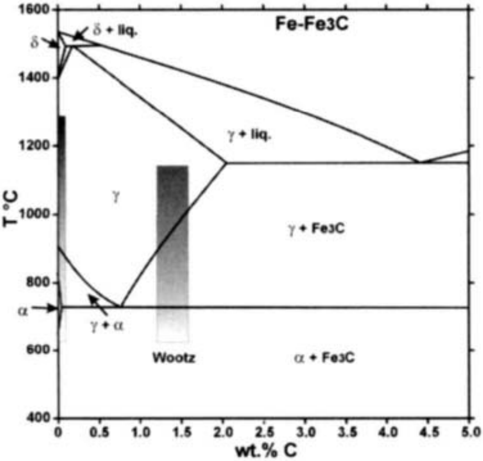

Figure 2-3-4:
Fe-Fe$_3$C diagram with a superimposed 0.3 % P isopleth from the Fe-Fe$_3$C-P diagram. The grey area represents the γ+Fe$_3$C+liquid region in the ternary system, the temperature of the γ/Fe$_3$C/Fe$_3$P ternary eutectic being 955 °C. In the ternary system with graphite rather than cementite, the ternary eutectic temperature is 977 °C [Rag88a].

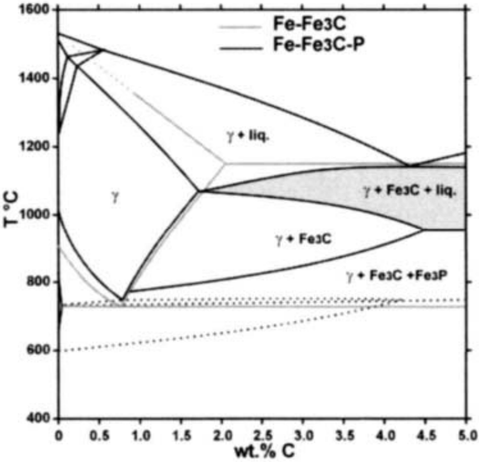

The presence of phosphorus probably played an important role. At phosphorus levels from 0.1 to 0.3 %, a small amount of liquid is present above about 950 °C (Figure 2-3-4) and could facilitate welding in carburised surface layers with sufficiently high carbon concentrations. Unfortunately, the highly corroded nature of many ancient artefacts makes precise metallurgical analysis difficult. Like nitrogen, phosphorus has a powerful solid solution strengthening effect in ferrite, even at low concentrations, but tends to reduce ductility. However, this problem can be overcome by the use of composite structures, where ductility is provided by layers of relatively pure iron. The presence of phosphorus could have helped to inhibit carbon diffusion between the different layers during the complex forging operations.

Table 2-3-5: Range of compositions found in different layers of Merovingian swords by France-Lanord [Fra52].

Element	C	Mn	S	P	N
Concentration (at.%)	0.08-0.15	0-0.05	0.016-0.03	0.14-0.35	0.004-0.01

2-4 True or oriental Damascus steel swords produced using wootz steel

The swords produced in Damascus were reputed for their exceptional quality and were said to be so sharp that they could cut in two a silk handkerchief thrown into the air. They were light, extremely strong and flexible, with magnificent wavy *moiré*-type patterns on the blades, often termed damask or watering (Figure 2-4-1). They were unknown in the West until discovered by the crusaders in the Middle Ages. Their reputation was enhanced by the fact that western smiths were unable to reproduce them. Unlike their pattern welded imitations (§ 2-5), they were forged in a single piece, from high carbon Indian wootz steel (~1.5% C). Because of their composition, forging was difficult and required great skill. The art of their manufacture spread slowly from India and the Middle East at the beginning of the 1st millennium AD, eventually reaching China and Russia in the Middle Ages. It propagated principally throughout the Arab world, where it later became part of Islamic culture (*cf.* § 1-4).

The pattern has been called pulad or bulat, from the Indian name, due to the ripply appearance [Le_03]. It is caused by the presence of coarse cementite particles revealed by polishing and light etching (the metallurgical aspects will be discussed later in § 2-6). Bands of cementite particles generally appear silvery, against a black matrix background. Different features were obtained by carefully chosen forging sequences, which aligned the metal grains and their cementite precipitates, forming concentric rose-like features or the pattern variously known as "Kirk Narduban", "Mahomet's ladder", the "Ladder of the Prophet", "Jacob's ladder" or the "Forty Steps" (Figure 2-4-1 C).

2-5 Mechanical or pattern welded damascene swords

The damask or damascene structure characteristic of Damascus steel blades, with a multitude of wavy lines, was considered to be a guarantee of high quality and many attempts were made to imitate it using composite forging techniques derived from those described in § 2-3. The result is often referred to as mechanical or pattern welded Damascus steel (but this is unfortunate[2]). Several sheets or bars were forge welded together by hammering between 1000 and 1200 °C, alternating soft iron and carburised steel, producing a flat strip. The strip was then folded in two and re-forged, the process being repeated several times, each fold doubling the number of layers and reducing their thickness after further forging. The hammering process could be carefully performed in such a way as to curve the successive layers, producing an undulating *moiré* pattern on the surface after polishing and etching. The art was developed to the extent where even experts had difficulty in distinguishing pattern welded blades from true wootz Damascus structures. Indeed, many swordsmiths firmly believed they had rediscovered the technique used for genuine Damascus swords. However, a true Damascus steel gives a clear crystalline ring when struck, contrary to the dull sound produced by composite blades.

Because of the nature of wootz steel and the associated forging techniques (described below), the variety of designs is limited to *wave, ladder and rose patterns, with finely spaced bands.* Nevertheless, surface irregularities can be introduced by the use of hammers or dies, while notches and grooves can be produced by cutting and grinding. This modifies the metal flow during the final forging steps and leads to specific local patterns. In contrast, in the mechanical welding process, many different patterns can be produced, for example, by combining laminated layers of various types and thickness, by twisting bars, or by forging in small objects such as nails. The "onion ring" design shown in Figure 2-5-1 is an example. Indeed, blades of this sort were essentially works of art, and were a fairly late development, being typical of the 18th and 19th centuries. Gun barrels were produced by wrapping alternate layers, followed by forge welding.

The metallurgical structure of pattern welded objects is quite different to that of ones made from wootz steel, the average carbon content in the composite materials being much lower, typically around 0.5 %, compared to 1.5 %. After heavy forging, the carbon content tends to become more uniform. Pattern welded swords had higher strength and much greater toughness than composite weapons made in the Merovingian and Carolingian periods, due to their very fine structure and the absence of a separate core and edges. All objects showing the typical wavy damascene pattern, which has become synonymous with high quality, tend to be indiscriminately described as Damascus steel. Indeed, until the late 19th century, the different structures were not clearly defined and were poorly understood, leading to considerable confusion [Fig91].

2-6 In search of a lost art

The secret of wootz steel

European smiths inherited the composite forge welding techniques developed by the Celts in the early Christian era. While pattern welding was a natural extension of these practices,

---

2. Translator's note : True Damascus steel is a single material and it is the microstructural constituents and forging sequence that produce the pattern. It is preferable not to use the term Damascus steel when referring to composite structures. However the derived adjectives "damascene" or "damascened" can be employed to describe the pattern or product, whatever the manufacturing process, provided that the latter is otherwise made clear. The French text employs the adjective *damassé* in this sense, whereas true Damascus steel is Damas or wootz Damas

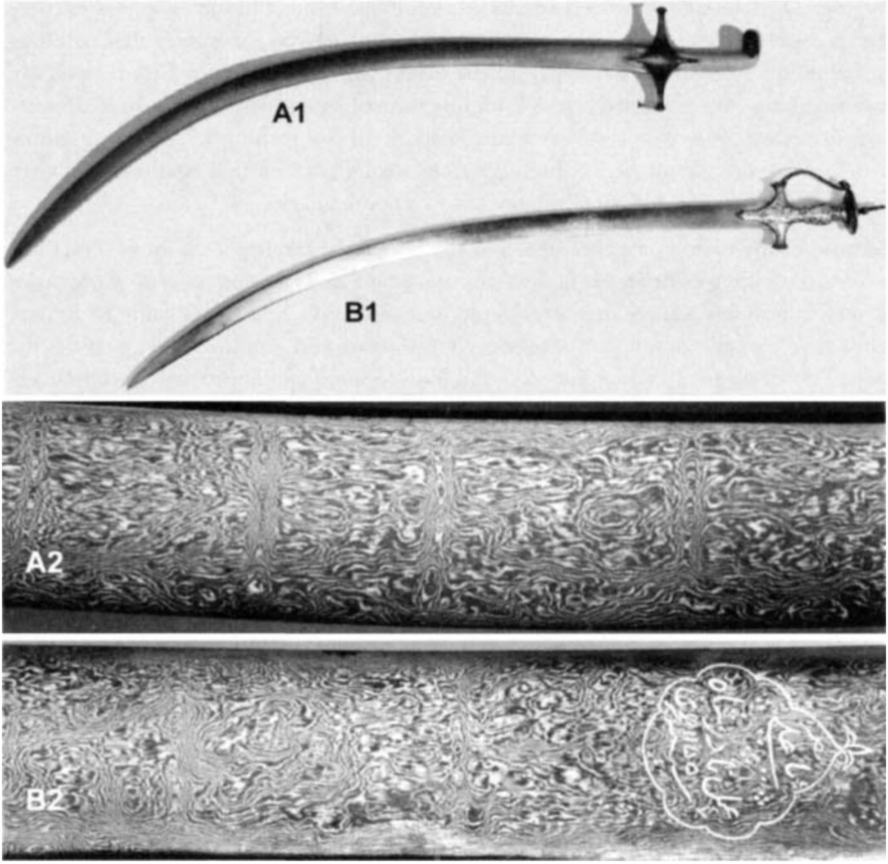

Figure 2-4-1:
A1) 98 cm long Iranian "shamshir" sabre (1820–1860 AD) with a walrus ivory handle. A2) Detail of the wootz steel blade.
B1) 93 cm long Indian-Persian "shamshir" sabre bearing the inscription "By the order of King Naser", dated 1 165 in the Arabian calendar (*i.e.* 1738). The handle is steel decorated with gold and enamel. B2) Detail of the wootz steel blade.
Document from the Henri Moser Charlottenfels collection.
Courtesy Bern Historical Museum, Switzerland [Bal92].
C) Close-up of a blade from the Moser collection studied by Zschokke [Zsc24], showing a local transverse ladder pattern. The decoration was revealed by etching in boiling picric acid, which has reversed the usual contrast, the cementite appearing dark and the pearlite matrix light.
Courtesy University of Iowa, USA [Ver98a].

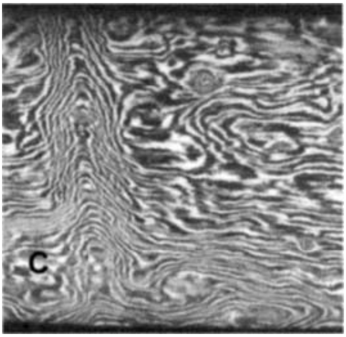

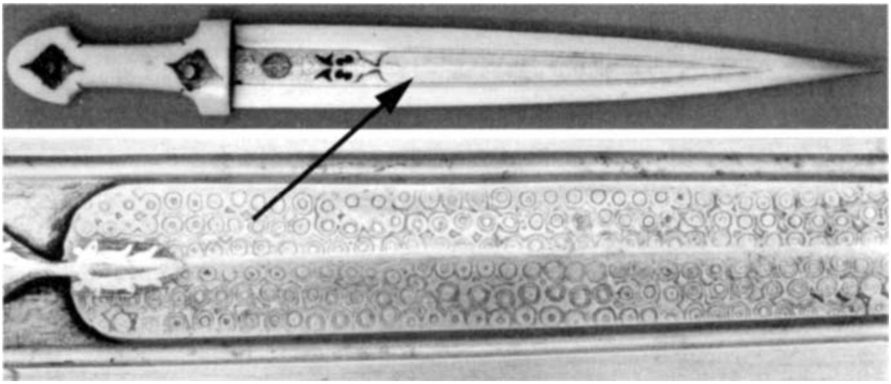

Figure 2-5-1:
Short (51 cm) pattern welded sword from Iran or Azerbaijan (1820–1860 AD), showing an onion ring design. Courtesy Bern Historical Museum, Switzerland.

for many centuries, western smiths were unable to forge wootz steel. It was hot short when worked at very high temperatures and brittle when forged too cold. Furthermore, even in the right temperature range, when forging was performed too slowly, the cementite was converted to graphite and the properties were lost. The technique began to be mastered only towards the 18th century AD, when there was a strong demand. The last swords were manufactured in the early 19th century, when they were replaced by high performance modern steels. In fact, by the end of the 19th century, swords were no longer considered as major weapons and had lost their symbolic aura, becoming simple decorative objects. The practice of Damascus sword making died out and the techniques were lost, the finest specimens surviving merely as collector's items. Indeed, it is thanks to collectors such as Moser (Figure 2-4-1) that recent work has been able to be performed in an attempt to elucidate the ancient traditions [Bal92]. The book by Figiel [Fig91] includes many photographs of specimens dispersed among private collectors and museums throughout the world.

The scientific study of wootz steel and damascened structures was begun by Pearson in England in 1795. Another Englishman, Michael Faraday, whose father worked in a forge, became interested in the subject in 1819 before concentrating on electricity. In 1823–4, Jean Robert Bréant in France published the first description of the microstructure of Damascus steel and confirmed that its essential characteristic was a high carbon content (Table 2-6-1). In Russia, Pavel Anossoff devoted his life to breaking the secret of its manufacture. He tried using various clays and graphites and, like Bréant, studied numerous additions, including diamond.

Table 2-6-1: Range of composition determined on various samples of wootz steel [Ver96].

	C	Mn	Si	S	P	Cu	Cr	Ni
minimum	1.34	0.005	0.005	0.007	0.05	0.04	trace	0.008
maximum	1.87	0.14	0.11	0.038	0.206	0.06		0.016

In the early 20^{th} century, optical microscopy revealed that the patterns in Damascus steel are associated with periodic alignments of *cementite particles* [Zsc24], [Smi65] (Figure 2-4-1). However, the forging technique necessary to obtain these patterns was only understood almost fifty years later. Two independent American teams, those of Wadsworth, Sherby *et al.* in Stanford University [Wad80] and Verhoeven *et al.* at the University of Iowa, assisted by a skilled forging practitioner Pendray [Ver98a], succeeded in reproducing damascene patterns in wootz steel forgings. The underlying metallurgical mechanisms, together with the complex thermomechanical processing sequences and "tricks of the trade", now appear to have been clearly explained, thanks to modern laboratory techniques and patient experimentation.

First hypothesis :
break-up and redistribution of pro-eutectoid intergranular cementite

The first metallurgists who attempted to reproduce a damascene structure in wootz-type steel all emphasized that the cake had to be slowly cooled and not reheated above bright red heat during forging. By respecting these recommendations, an experimental technique was established by Wadsworth and Sherby in the 1980s, leading to structures apparently similar to those in genuine Damascus blades [She85a], [She92a]. The first step involved subjecting the "wootz" ingot to a high temperature homogenising treatment, followed by hot working to obtain a uniform billet of the required size. The billet was then held for 48 hours at 1093 °C, to completely dissolve all the cementite and obtain a fully homogeneous coarse-grained austenite structure (see the Fe-Fe_3C phase diagram in Figure 2-3-3). Subsequent slow cooling induced the *precipitation of coarse pro-eutectoid cementite at the austenite grain boundaries.* Finally, in a fourth step, the billet was worked at dull red heat, just above the eutectoid (A1) temperature. The heavy deformation involved in manual hammering was simulated by a series of large hot rolling reductions. This procedure broke down the coarse intergranular carbide particles into more or less angular fragments, a few microns in size, strung out in rows parallel to the rolling direction. It is these coarse carbide alignments that produce the pattern observed in Damascus steel blades. During final cooling, the austenite matrix transformed to a distribution of very fine cementite particles in ferrite.

Second hypothesis :
selective precipitation of cementite in the interdendritic spaces

After a detailed examination of the published literature, Verhoeven, Pendray *et al.* [Ver98a] carefully studied a series of ancient Damascus steel blades and pointed out a number of microstructural features that can be considered as criteria for distinguishing genuine Damascus steels. They essentially concern the distribution, morphology and size of the cementite particles.

> *In authentic Damascus steels, the cementite particles have sizes ranging from about 3 to 20 µm and have a rounded, non-facetted, morphology. They are arranged in parallel planes, appearing in section as rows, about 4 to 6 particles wide, that are*

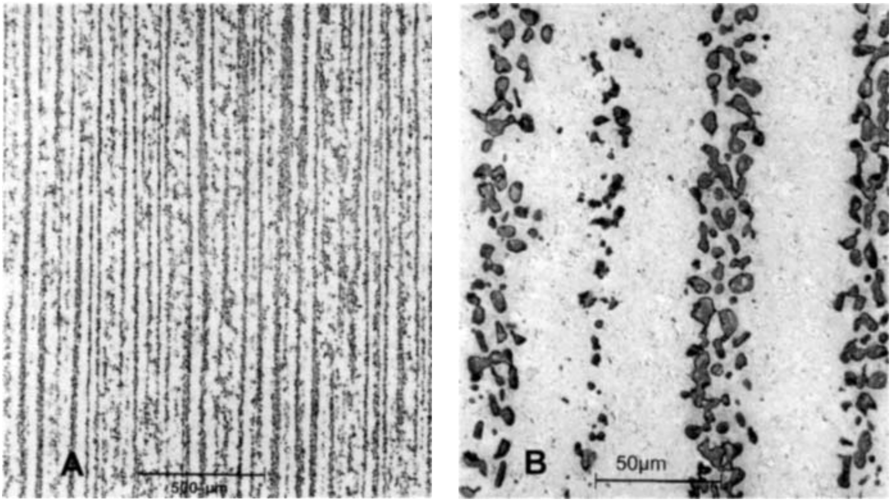

Figure 2-6-2:
Microstructure of a blade produced by Pendray [Ver98a]. A) Longitudinal section showing the alignments of dark cementite particles.
B) Close-up of the carbide rows, with very fine pearlite colonies just visible in the intervening matrix. Courtesy University of Iowa, USA.

> *rarely interconnected, with an inter-row spacing of between 30 and 100 µm. There is no significant difference between transverse and longitudinal sections.*

Figures 2-6-2 and 2-6-3 show blade forgings reproduced by Pendray, in which these criteria are fulfilled. In comparison, the carbides obtained by slow cooling according to the Wadsworth-Sherby process are considerably coarser and conserve angular facets after working, despite a certain degree of spheroidisation during hot working. Furthermore, their size distribution covers a wider range, representing a clear difference with respect to real ancient Damascus blades.

The essential point demonstrated by the Iowa University team is that the rows of carbides can be generated by heat treatment cycles, *without the need for plastic deformation*, either by hammering or rolling. Experiments were performed both on authentic wootz steel and on synthetic materials of similar composition. The important factor is that the initial coarse interdendritic or intergranular carbides must be completely redissolved in order to precipitate new cementite particles in a controlled manner. *Precipitation occurs selectively in regions where impurities have segregated.* The principal impurities concerned were found to be silicon, phosphorus and vanadium, and play a key role in spite of their relatively low concentrations [Ver98a]. There is a correlation between the spacing of the carbide rows and that of the primary dendrite network in the initial alloy, proving the influence of residual segregation. Small but significant differences in composition were effectively detected between the centres and edges of the carbide rows. Contrary to the situation in

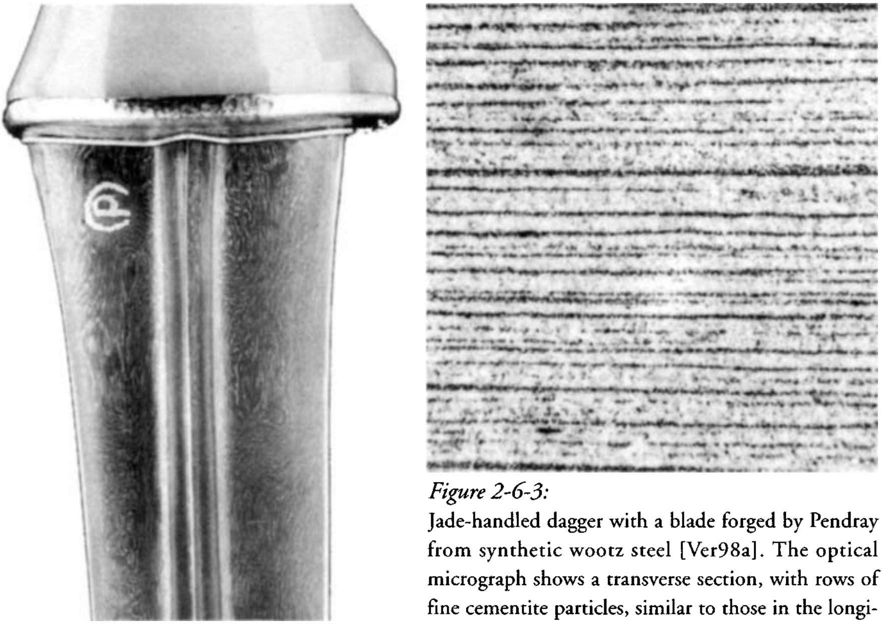

Figure 2-6-3:
Jade-handled dagger with a blade forged by Pendray from synthetic wootz steel [Ver98a]. The optical micrograph shows a transverse section, with rows of fine cementite particles, similar to those in the longitudinal section visible in Figure 2-6-2.
Courtesy University of Iowa, USA.

the Wadsworth-Sherby process, the resulting structure does not contain coarse intergranular carbides.

> *The heat treatment cycles must be carefully controlled in order to achieve the required result. Firstly, solution annealing must be performed above 1050 °C, in order to exceed the Ac1 point and completely redissolve the existing cementite particles. Secondly, the dissolution temperature should not exceed about 1200 °C and the holding time should not be too long, in order to avoid homogenisation of the segregated impurities. Thirdly, at least one cycle must fall below the eutectoid temperature A1 (723 °C), probably to facilitate nucleation of new cementite particles.*

However, hot working is obviously necessary to produce the blade, and must therefore be performed within a carefully controlled temperature range. The final carbide row spacing is consequently smaller than that of the primary dendrite structure.

Another essential feature observed in real Damascus steel blades is the presence of a decarburised line of virtually pure ferrite along the dorsal ridge of the blade. It is thought to provide evidence of the swordsmiths' technological skill. Wootz steel often contains amounts of phosphorus and sulphur sufficient to lower the incipient melting temperature to around 960°C (Figure 2-3-4). The resulting hot shortness causes delamination during forging. In order to overcome this problem, a prior decarburising treatment was performed, consisting in holding for about five hours at 1200 °C, followed by water quenching. A thin decarburised layer was formed at the surface, with a much higher melting point, and created a malleable ferritic envelope through which forging could be performed without cracking. The dorsal ridge is the only remaining evidence of this process and is due to a single initial folding operation.

Great dexterity was required during forging, since the temperature and time had to be limited to prevent graphitisation of the cementite. Observations on unfinished blades suggest that the rose and ladder patterns were probably produced by introducing local humps or ridges at intermediate stages of forging, or on the contrary, by creating grooves or hollows with punches. Subsequent metal flow evens out the thickness and produces local irregularities in the general pattern.

> *The conclusions of Verhoeven's team agree closely with those of Zschokke 70 years earlier [Zsc24], who stated that : "Firstly, it is clear that genuine ancient Indian Damascus steel, called* pulat, *is not produced by welding... On the contrary, it is a uniform steel produced by crucible melting, whose particular structure is due to crystallisation and segregation phenomena...*
> *By repeated forging of Damascus steel, the ancient Indian and Persian swordsmiths aimed not so much to produce a decorative pattern, but rather to enhance the toughness of the metal. This assumption agrees with Belaïev's observation that the astonishing beauty of Indian steel was merely a secondary goal and an accidental consequence."*

The method described by Verhoeven *et al.* effectively produces a result closer to genuine Damascus steel structures. However, it is probable that techniques closer to that proposed by Wadsworth and Sherby were also employed in practice, since they seem less sensitive to the hot working temperature and consequently easier to perform.

Finally, a third manner of working high carbon steels was employed by Japanese swordmakers. During each heating and forging cycle, a thin decarburised layer was formed at the surface and was partially transferred to the centre by folding. Repetition of this procedure led to alternate bands of soft ferrite and high carbon steel, or to an almost uniform steel of lower average carbon content when the number of cycles was large (greater than about 8).

2-7 Asiatic swords

Chinese swords

The oldest non-meteoritic iron object found in China is a short sword dating from the 8th century BC. Other more richly decorated iron objects have been dated to the 6th and 5th centuries BC. Like all other very early irons, they were low carbon materials produced by reduction of ore. Later swords from the 2nd and 1st centuries BC have been discovered at several sites, often with gold inserts giving the date of manufacture, together with the indication "under favourable auspices", followed by "30, 50 or 100 refinements". Metallographic examination reveals rows of small inclusion particles distributed in layers, whose numbers are close to 32, 64 or 128. This is clear evidence of a folding process, which leads to a number of layers that is a power of 2. In this case, the aim of the refinement procedure was to improve the quality of the metal, rather than to obtain a patterned structure [Rub95].

China was the first country to employ cast iron, and in particular, used it to carburise soft iron. The latter was immersed in a bath of molten cast iron, forming a welded coating. The composite was then repeatedly hot forged and folded to produce a homogeneous medium carbon metal.

Japanese swords

The oldest swords discovered in Japan date from the 4th and 5th centuries AD and were probably imported from China, via Korea. In particular, the technique of hot dip coating soft iron with cast iron was borrowed from China. It was during the Heian period (794–1185 AD), when the capital was at Kyoto, that the Japanese developed their own traditional swordmaking technique. The blades had a ductile low carbon core and a harder, more carbon rich, outer envelope, including both the faces and edges (Figure 2-7-1). The art of producing swords and daggers reached a high degree of sophistication, culminating in the 16th and 17th centuries AD. It is still alive today, after having gone through numerous difficult periods, particularly that immediately following the Second World War (1945-53), when the manufacture and possession of weapons was banned. Most of the craftsmen converted to other activities, but some, such as Yoshindo Yoshihara in Kyoto, a worthy descendent of ten generations of swordsmiths, subsequently revived the traditional techniques [Kap87].

The traditional starting material was usually what was known as *tamahagane*, a strongly hypereutectoid steel (1.2–1.7 % C) obtained from soft iron by carburising with charcoal, sometimes replaced by imported Indian wootz steel. It was hot worked in a series of folding and forging operations, which expelled inclusions and gradually removed carbon by oxidation at the surface.

The *core* structure, known as *shingane* (Figure 2-7-1 B), is obtained by a large number of repeated forging and folding cycles, leading to a practically uniform carbon content of about 0.2%, which ensures the required ductility.

The *outer envelope*, called *kawagane* (Figure 2-7-1 A), has a higher carbon content. The repeated forging and folding cycles are less numerous in this case and the loss of carbon is limited, with a final average level of about 0.5%. Since full homogenisation is not achieved, the local variations in carbon content can give rise to a damascene type pattern on etching. However, in the earliest swords, the layers were fairly thick and the pattern was not apparent, and it was not until later periods that the decorative potential was exploited.

One of the particular features of Japanese swords is the martensitic structure of the *cutting edge*, known as the *hamon* (Figure 2-7-1 E, F and G), which was obtained by a special treatment. Various clays, in different thicknesses, were coated on the blade before austeni-

Figure 2-7-1:

Long modern *katana* sword (opposite) made by Yoshindo Yoshihara in Kyoto, using the traditional Japanese process. The *hira-tsukuri* style blade is 75 cm long. The cutting edge, or *hamon* appears light, with a wave and loop pattern called *choji midare*. The blade also shows traditional *horimono* engravings.

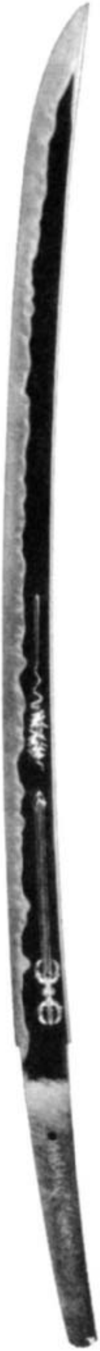

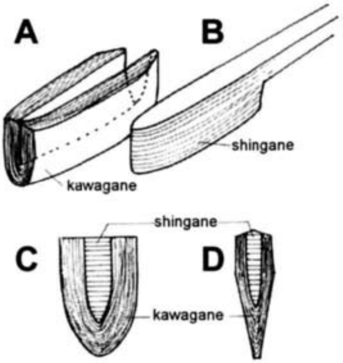

A to D) Japanese sword fabrication process, according to [Kap87].

A) Preparation of the outer envelope, made from *kawagane* steel.

B) Preparation of the core, made from *shingane* steel.

C) Forge welding of the two parts.

D) Forging of the blade.

E to G) Details of the cutting edge or *hamon.* E) Schematic transverse section, showing the region of martensitic structure at the cutting edge. The intermediate region, or *habuchi,* shows patterns such as *nie* or *nioi.*

F) Longitudinal close-up of a 14th century sword from Bizen (Okayama). The hamon design is called *gunomi-midare.* Zone “a” is martensite, zone “b” (nioi) is a mixture of fine pearlite and bainite, while the main blade surface (“c” and “d”) is composed of ferrite and pearlite. The granite-like appearance of this part of the blade is due to the variations in carbon content in the different layers produced by the folding and hammering process. The lighter zone “d” is called *utsuri,* meaning “mirror image of the hamon”, and is characteristic of swords of this period, probably being caused by non-uniform heating of the blade.

G) “Choji-midari” hamon pattern on a modern sword. The white line corresponds to a change in slope on the blade surface.

All photographs courtesy Yoshindo Yoshihara, Kyoto

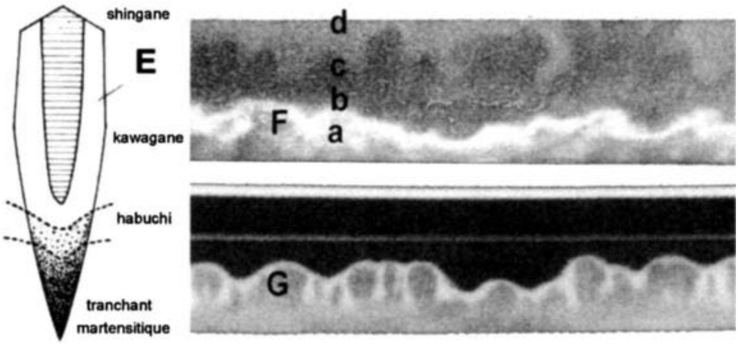

tising and quenching, only the edge being left bare, and thus exposed directly to the water. The cooling rate in this region was sufficient to locally induce martensite transformation. The clay coatings were applied in such a way that the transitions in microstructure either occurred along straight lines, or in the form of patterns or silhouettes, which were revealed by polishing and etching. Many different codified polishing and etching procedures were developed to obtain various effects, often involving complex sequences of operations, defined in great detail. Numerous western authors have admired the immense skill involved, pointing out the almost *ritual respect of tradition* [Bai62], [Smi65], [Tan80], [Ino97], [Ino99]. Indeed, a poetic vocabulary was coined to describe the appearance of blades, with expressions such as *nie,* a fine dispersion of silvery sand, and *nioi,* a multitude of cherry blossoms palely lit by the rising sun [Tan80].

Malaysian swords

The Malaysian kris is a relatively short stabbing and slashing weapon typical of South East Asia, including Malaya and Indonesia. The blade was produced by the assembly of different materials, which were worked by forge-welding and folding. Because of the relatively small number of folds, the layers are fairly thick, leading to a coarse, clearly visible pattern (Figure 2-7-2). A characteristic feature of these swords is the sinuous geometry of the blade, which takes advantage of a natural flow pattern associated with the layered structure. Early kris swords used a combination of soft iron and nickel-rich meteoritic iron, making the different layers stand out sharply. In more recent times, meteoritic iron has been replaced by imported stainless steels. A wide variety of patterns can be found,

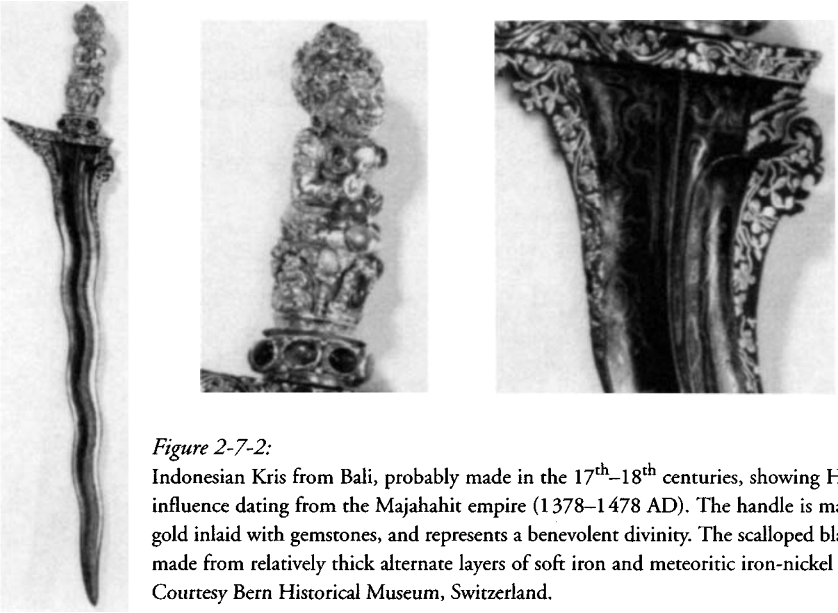

Figure 2-7-2:
Indonesian Kris from Bali, probably made in the 17th–18th centuries, showing Hindu influence dating from the Majahahit empire (1378–1478 AD). The handle is massive gold inlaid with gemstones, and represents a benevolent divinity. The scalloped blade is made from relatively thick alternate layers of soft iron and meteoritic iron-nickel alloy. Courtesy Bern Historical Museum, Switzerland.

since many ancient techniques have been employed, including twisting during forging, to produce undulations, and indentation to obtain rose effects.

2-8 Contemporary damascene structures

Damascene structures produced by forge-welding different materials

Contemporary craftsmen, such as Sachse in Germany [Sac94], rediscovered damascene structures after the Second World War and successfully re-launched this art form. However, the objects proposed are sometimes only poor imitations of the old techniques. Craftsmen can either manufacture the iron strips themselves using ancestral methods or directly purchase sheets of numerous metals readily available in various thicknesses, associating them in different combinations. Nickel is often chosen for its silvery sheen, contrasting with the darker colour of high carbon steel. The composition of the steel and the thickness of the sheet must be such as to facilitate transformation to martensite (*cf.* Figures 2-8-1 A and B). Diffusion of carbon between the different layers during forging can lead to homogenisation and excessive loss of this element [Ver98c]. Three pattern-welding processes are commonly employed

- High temperature bundle forging of coarse wires of different grades, or sometimes recovered cables. The result obtained is an irregular interlaced design. In the case of cables of only one type of metal, it is the surface oxides that reveal the pattern.
- Hot forging of sheet stacks. A simple block forging process produces a wavy *moiré*-like pattern (Figure 2-8-1 A). If the blocks are drawn to bars and twisted, the pattern is

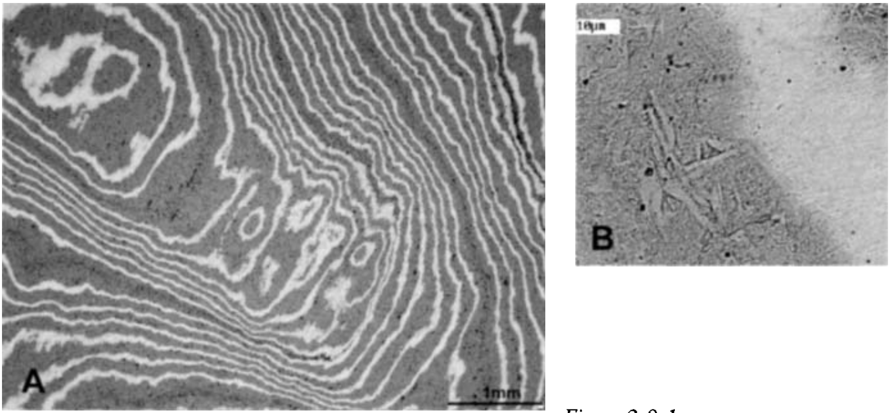

Figure 2-8-1:

A) Scanning electron micrograph of a pattern produced by forge welding a steel and nickel composite bar.
B) High magnification view showing the martensitic structure of the steel and the austenitic structure of the nickel.
Sample courtesy H. Viallon, Thiers, France. (1995)

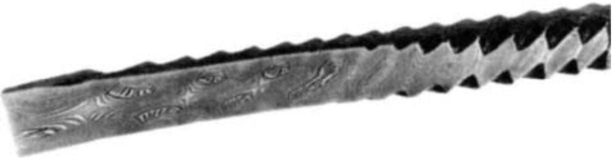

Figure 2-8-2: Example showing pattern deformation due to hot twisting.
Sample courtesy H. Viallon, Thiers, France. (1995)

changed. Several such bars can be forge welded together to produce an even more complex design, in a manner similar to that employed for Merovingian swords

- Forge welding of blocks containing profiled inserts of another type of steel (Figure 2-8-2 A). A prismatic profile is machined from a block of one grade and is inserted in a bore of equivalent profile machined in a block of the other steel. The composite blocks are hot drawn to obtain a rod of the required section. In this case sixteen rods were forge welded forming a small bar which was cut into slices (Figure 2-8-3). The latter can be placed side by side between sheet stacks to form a new bar, which is then forge welded. The pattern is obtained by machining down to the centre of the bar and is revealed by etching (Fig. 2-8-2 and 2-8-3 D). Composite patterns can be built up by combining numerous blocks or sections. In order for the pattern contour to remain sharp, care must be taken *to limit interdiffusion of alloying elements during forging.*

Damascene structures produced by powder metallurgy techniques

A method was developed in the 1990s to produce stratified structures with the aid of powder metallurgy techniques [Pat98]. Sheets of ductile high melting point steel are first of all stacked inside a steel container to form an array with a predetermined separation. Pre-alloyed metal powder (*cf.* Chapter 16) of appropriate composition is then poured into the spaces between sheets and the container is evacuated and hermetically sealed. The container is then heated in an autoclave under a pressure of about 1 000 bars. This so-called hot isostatic pressing treatment leads to creep deformation of the powder particles, sintering them together, eliminating porosity, and inducing diffusion welding to the sheets. The resulting compact is then used as a forging billet.

Although the technique is expensive, it enables the choice of powder materials, such as high carbon or chromium-rich steel, that would be impossible to work in conventional form. For example, the combination of medium carbon martensitic stainless steel sheets and high carbon stainless steel powders produces a visible contrast between layers while combining the strength of martensite with the hardness of micron-sized mixed iron-chromium carbides of the $M_{23}C_6$ type (Figure 2-8-5). If necessary, the stratified pattern can be modified during the forging process, for example by twisting.

It is thus possible to obtain a high cutting power similar to that conferred by the "micro-tooth" effect of cementite particles in genuine Damascus steel blades, while at the same time ensuring corrosion resistance by the presence of chromium.

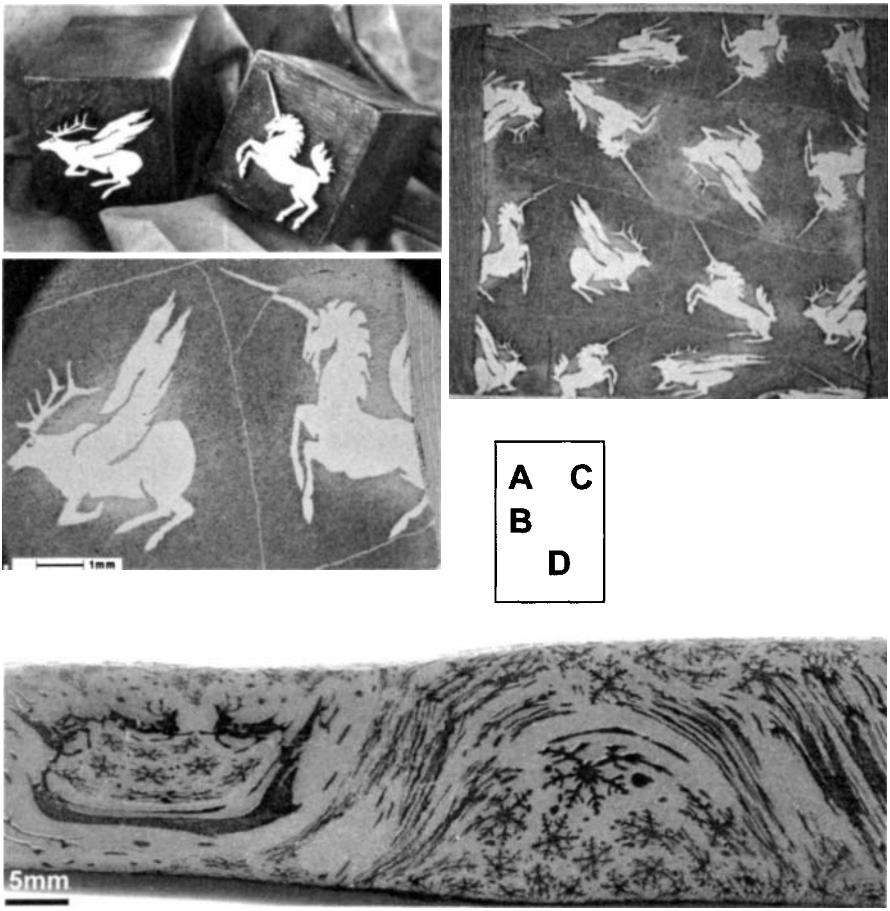

Figure 2-8-3:
Production of a pattern welded steel blade.
A) Unicorn and winged stag profiles machined from blocks of 203E 3.5 % Ni steel and inserted in bores of identical profile machined in 70 x 70 x 100 mm blocks of Fe-0.9C-2 Mn-0.3Cr-0.1V steel.
B) Section of the bar after forge welding, which has reduced the size of the patterns (scanning electron micrograph, back-scattered electron image). Fracture and slipping of one of the blocks has produced an offset in the unicorn's horn. The white border between blocks is ferrite formed by decarburisation during forging. The pattern has been revealed by etching in ferric chloride.
C) Low magnification view showing the block stacking arrangement between layered plates (visible at the sides and on the right in B), after forge welding to a bar. The central part containing the pattern is removed, then polished and etched.
D) Optical micrograph in which the contrast is reversed, showing a blade made by this technique, with stag and snowflake patterns, and which has been twisted during forging.
Courtesy P. Reverdy, Romans, France. (1993)

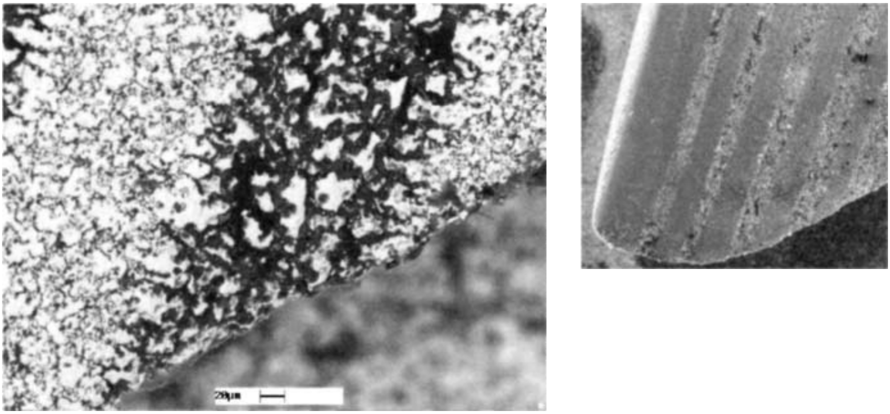

Figure 2-8-5:
Scanning electron micrographs of a damascened knife blade obtained by forging a hot isostatically pressed billet made from stainless steel sheets and powder of different compositions. Etching has revealed the mixed iron-chromium carbides present at grain boundaries in both materials.
Courtesy INPG, Grenoble.

These methods are today employed by craftsmen and professional artists for whom the metallurgical aspects are simply part of their many skills. The value of damascened objects today available on the market varies greatly according to the technique employed and the degree of skill involved. However, cheap imitations are sometimes proposed, made by processes such as chemical etching, whereby a pattern is engraved on exposed regions of the surface after prior coating with a protective mask.

Part 2

The Genesis of Microstructures

The concept of microstructure would never have existed were it not for the optical microscope, whose invention is attributed to the English scientist Robert Hooke (1635-1702) and which was further improved by the Dutchman Anton van Leeuwenhoek (1632-1723) for examining textiles. The new instrument quickly became popular, to the extent that the humorist Georg C. Lichtenberg wrote in his notebook of Collected Thoughts (1793-1796) "The only path to innovation is to find the appropriate microscope for each situation, in order to see everything enlarged."

It was not until the second half of the 19th century that the optical microscope was used to examine the structure of metals. The first work concerning photomicrography (The constitution of carbon steels) was published by Floris Osmond in 1894 (Encyclopedia Universalis).

3

The principal phases in steels

3-1 The phases of pure iron

The concept of a phase

From a thermodynamic standpoint, the concept of a "phase" is related to the structure of matter on the atomic scale, and involves both the physical and chemical arrangements of the atoms. A phase transformation corresponds to a change in atomic structure. The idea of what is a phase becomes intuitive when the macroscopic properties change, as for example when a liquid freezes to a solid. It is also apparent in the case of miscible or immiscible liquids or in the ability of a liquid to dissolve other substances. In a crystalline solid, a phase is characterized by the geometry of a regularly repeated pattern of atoms and by their chemical nature and relative positions within the basic unit. An important feature of a phase is the range of temperature over which it is stable. The exact chemical composition of a phase may vary to a certain extent, and for a crystalline structure, will induce parallel variations in the lattice parameters. An abundant literature is available on the principles of crystallography and general outlines are usually given in most textbooks on physical and structural metallurgy.

Face-centred cubic iron

Between 912 and 1394 °C, pure iron has a face-centred cubic "fcc" crystal structure. This phase is called gamma iron (γ-Fe), and in steels is known as *austenite* (named after the eminent English metallurgist W.C. Roberts-Austen). If the iron atoms, with a radius of 0.126 nm, are considered to be hard incompressible spheres, the γ-Fe structure is that in which each iron atom is *in contact* with a maximum number of neighbours. In fact, the distance between the centre of each iron atom and that of each of its 12 nearest neighbours (the atomic diameter) is $a\sqrt{2}/2$, where a is the side of the cubic unit cell (Fig. 3-1-1). The number of nearest neighbours in a structure is also called the coordination number Nc. The large value in the fcc structure (12) indicates a high degree of symmetry. The ratio between the atomic volume and the unit cell volume a^3 is 0.74, a high value which reflects the compact nature of the structure. However, the interstices between the iron atoms can accept certain small solute atoms, provided that their size is compatible with the radius r_i of the sphere capable of being contained within the interstice. There are two types of

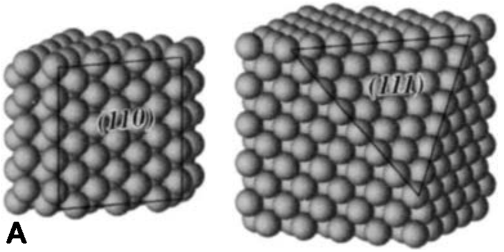

A

Figure 3-1-1:
A) Atomic packing in the bcc (left) and fcc (right) structures. The sectioned planes are those of densest packing, i.e. (110) in the bcc structure (twofold symmetry) and (111) in the fcc system (threefold symmetry).

B

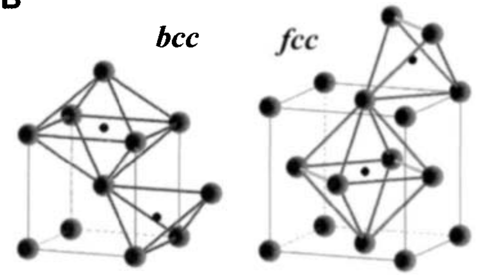

B) Octahedral and tetrahedral interstices in the body-centred cubic and face-centred cubic crystal structures. The scale of the lattice parameters has been respected.

interstitial sites, called octahedral and tetrahedral, according to the number of atoms within which they are enclosed (see Fig. 3-1-1 and Table 3-2-2).

The fcc structure can be described by the *stacking of close-packed planes.* Thus, in any one plane, the most compact stacking arrangement corresponds to a series of equilateral triangles, leading to a hexagonal symmetry. If a first plane of this type is designated A and a second plane B is fitted closely on top of it, then the B atoms will be lodged in every second hollow between the atoms of plane A. If now a third such plane, C, is placed on top of plane B, the C atoms can be situated either in the hollows of plane B above those in plane A not occupied by B atoms, or in the hollows of plane B directly above the atoms of plane A. The first choice for plane C leads to the stacking sequence ABCABC...(fcc), while the second choice leads to the so-called close-packed hexagonal (cph) stacking sequence ABABAB..., with the same coordination number and the same compactness.

Body-centred cubic iron

Pure iron has a body-centred cubic "bcc" structure, both between 1394°C and the melting point at 1538 °C, and below 912 °C. In the high temperature range, the phase is known as delta iron (δ-Fe), while the low temperature form is designated alpha iron (α-Fe). In steels, the corresponding phase is called *ferrite* (delta ferrite at high temperatures). In the bcc structure, each atom has 8 first nearest neighbours, at a distance $a\sqrt{3}/2$ and 6 second nearest neighbours at a distance a. The ratio between the atomic volume and that of the unit cell is 0.68, *i.e.* lower than for the fcc structure, reflecting its less compact nature. The bcc lattice also contains octahedral and tetrahedral interstices (*cf.* Fig. 3-1-1 and Table 3-2-2).

However, there are no close-packed planes, the contact between atoms being limited to one-dimensional rows.

3-2 Solid solutions

Substitutional solid solutions

In any particular solid phase, atoms of several different types may occupy certain lattice sites. When solute atoms replace the solvent atoms on normal lattice sites, the phase is called a substitutional solid solution. For example, in the Fe-Ni system, the fcc structure, known as austenite, which occurs over a particular temperature range, contains nickel atoms substituting for iron, distributed in a perfectly random manner on normal lattice sites. Above 912 °C, the proportion of nickel atoms can vary from 0 to 100%, since nickel and iron are then totally miscible (Fig. 3-3-3). The lattice parameter varies continuously between these two extremes. No difference can be seen in the microstructure, unless local gradients in composition cause variations in the response to etchants. The principal solid solution phases in steels are summarized in Table 3-2-1.

Table 3-2-1: Important stable and metastable terminal phases (martensites are shaded grey).

Phase	Pearson symbol [Hub81]	Strukturbericht	Space group	Prototype
δFe, δMn	cI2	A2	$Im\bar{3}m$	W
γFe, γNi	cF4	A1	$F\bar{3}m$	Cu
βMn	cP20	A13	$P4_132$	βMn
αMn	cI58	A12	$I\bar{4}3m$	αMn
α'martensite	tI2	L'2	I4/mmm	Fe-C martensite
εmartensite	hP2	Bh	$P\bar{6}m2$	WC

Interstitial solid solutions

The sizes of the interstices in the different crystal structures, represented by r_i, are proportional to the size of the solvent atoms. Only the smallest solute atoms can be accepted in these positions. Indeed, for iron, only hydrogen has a radius smaller than the size of the interstices, leading to a large solubility and a high mobility, the latter being enhanced by the small atomic weight. The other interstitial solute elements, oxygen, nitrogen, carbon and boron, are all larger than the interstices and therefore create lattice distortions when they are present in solution (compare the values in Tables 3-2-2 and 3-2-3).

In the face centred cubic structure, the two types of interstitial sites have quite different sizes. Only the octahedral sites ($r_i = 0.052$ nm) are sufficiently large to accept carbon atoms, and even then their solution is accompanied by significant lattice distortion.

In the bcc structure, it is again the octahedral sites that are occupied by carbon atoms, but their irregular size in different directions leads to asymmetrical distortion. These simple

Table 3-2-2:
Radius r_i of interstitial sites as a function of the atomic radius r. Nc is the number of nearest neighbours and N is the number of sites per atom. The atomic radius of iron is 0.126 nm.

Structure	Site	Nc	N	r_i nm
Close-packed structures	tetrahedral	4	2	0.225 r
fcc and cph	octahedral	6	1	0.414 r
Bcc	tetrahedral	4	6	0.291 r
	octahedral, <100> et <110>	6	3	0.154 r and 0.633 r respectively

Table 3-2-3:
Atomic radii of the light elements capable of occupying interstitial sites, compared to that of iron.

Element	Hydrogen	Oxygen	Nitrogen	Carbon	Boron	Iron
r nm	0.03	0.071	0.071	0.077	0.087	0.126

considerations explain why the solubility limit of carbon in steels is much greater in the fcc structure (austenite) than in the bcc phase (ferrite).

These volume considerations only partially explain the fact that nitrogen has a greater solubility in austenite than carbon and cannot account for its greater strengthening effect. In fact, nitrogen enhances interatomic bonding, increasing the concentration of free electrons, whereas the valency electrons of carbon are added to the 3d band of iron. The higher intermetallic bonding induced by nitrogen in austenite facilitates the creation of short range order, a precursor for the Fe_4N structure, whereas the more covalent nature of the bonding in Fe-C solutions promotes the formation of clusters [Gav98].

3-3 Order-disorder transformations

For certain compositions, particularly at relatively moderate temperatures, the different elements in a solid solution may occupy specific sites in the crystal structure, to form interwoven sub-lattices corresponding to each atomic species. The solid solution is then said to be *ordered*, and in fact, corresponds to a new crystal structure, with a lower degree of symmetry than for a fully disordered distribution. Table 3-3-1 gives the correspondence between disordered solid solutions and the derived ordered structures.

For example, in the Fe-Co system (Fig. 3-3-2), at around 50 at.% Co, below 1 000 K the random bcc A2 α phase transforms to the ordered simple cubic B2 structure of identical overall composition, the cobalt atoms simply moving preferentially to the cube centres and the iron atoms to the cube corners. The reaction involves a relatively small amount of energy and is said to be of second order in the classification of phase transformations. The effect of ordering is not visible in the optical microscope, but can be revealed in transmission electron microscopy by the appearance of weak superlattice spots in diffraction patterns. Similarly, small superlattice peaks are observed in X-ray diffraction spectra.

Table 3-3-1: Ordered crystal structures derived from simple random structures.

Random solid solution	Ordered solid solution Pearson's notation [Hub81]	Ordered solid solution Strukturbericht notation	Type
Body centred cubic, A2	cP2	B2	CsCl
	cF16	$D0_3$	Fe_3Al ord
Face centred cubic, A1	tP2	$L1_0$	HgMn
	cP4	$L1_2$	$AuCu_3$
	hP8	$L1_1$	CuPt
Close packed hexagonal	hP8	$D0_{19}$	Ni_3Sn

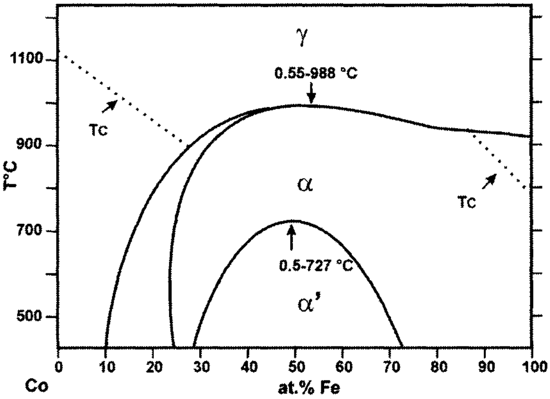

Figure 3-3-2:
Calculated Fe-Co phase diagram. T_C is the Curie point. The arrows indicate the maximum temperatures for the α and α' phases, with the corresponding atomic concentrations. From [Col00]

Ordering of the crystal lattice may be completely uniform or may involve the formation of small local domains of perfectly ordered structure surrounded by a disordered matrix. In this case, the domains become visible in the transmission electron microscope, since their interfaces represent antiphase boundaries with a change in stacking sequence.

Ordering is accompanied by an increase in hardness compared to the disordered structure. In the Fe-Co system, the order-disorder transformation on heating occurs well below the melting point, but this is not always the case. For example, in the Fe-Al system, the two ordered phases, with $D0_3$ and B_2 structures, are stable right up to their melting points, in agreement with thermodynamic calculations which predict that melting occurs at a lower temperature than the loss of order. .

In the Fe-Ni system, at exactly 75 at.% Ni (Fig. 3-3-3), the ordered phase $FeNi_3$ forms with an $L1_2$ structure, without change in composition. To either side of the stoechiometric ratio, the order transformation involves local changes in composition. For example, an alloy containing 60 at.% Ni undergoes phase separation on cooling, with the formation of local regions of ordered and disordered phases, with different compositions. There is a transfer of matter between the two phases and consequently the process is thermodynamically a first order reaction. In terms of the microstructure, although the transformation products are fine, they are visible in the optical microscope.

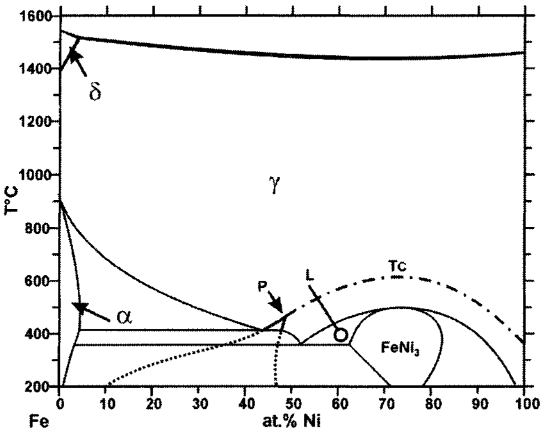

Figure 3-3-3: Calculated Fe-Ni phase diagram adapted from [Ans96] (see also [Yan96]). The magnifying glass indicates the order transformation involving mass transfer. The dashed line represents the paramagnetic-stable ferromagnetic transformation in the fcc phase, while the dotted lines indicate the separation of γ into the paramagnetic and metastable ferromagnetic fcc phases. Although this system is of great practical importance, the diagram cannot be considered to be fully reliable below 400 °C.

According to the calculated diagram, the variation in Curie point with composition ends at point P (Fig. 3-3-3), beyond which the ferromagnetic/paramagnetic transition (dot-dashed line) induces separation into a nickel-rich ferromagnetic phase and an iron-rich paramagnetic phase (dotted lines).

3-4 Intermediate phases

The principal intermediate phases in steels

An intermediate phase is one in which the elements combine to form a structure different from those that they adopt when they are pure. The thermodynamic stability of a particular association depends on several factors, but the three major parameters are the *electronegativity*, the *electron concentration* and *atomic size* effects. Two categories particularly important in steels will be distinguished below :

- semi-metallic compounds based on a difference in electronegativity, such as carbides, nitrides, carbonitrides, sulphides, phosphides and oxides.
- A_xB_y compounds in which the A elements include the transition metals (*e.g.* iron) and the B elements are other metals. These compounds are governed principally by the atomic size factor and the electron density. The size factor is dominant in the case of the so-called Laves phases, while electron density considerations are more important in numerous other phases, such as μ, χ, σ, δ, P, etc

Carbides, nitrides, etc..

Some of the alloying elements used in steels are strong carbide formers, with a higher affinity for carbon than iron. These elements are situated in groups IV to VIII of the periodic table. Indeed, the group to which an element belongs has been used by Goldschmidt to classify carbide crystal structures, and these in turn determine the characteristics of the corresponding phase diagrams.

- The metals in groups *IV (Ti, Zr, Hf)* and *V (V, Nb, Ta)* form MC type carbides with a simple cubic crystal structure of the NaCl type, while those of group V also form M_2C carbides with an orthorhombic structure.
- The transition metals at the head of groups *VI (Cr, Mo, W)* and *VII (Mn)* each form carbides of the $M_{23}C_6$ and M_7C_3 types (M = Cr or Mn), while the heavy metals, W and Mo, form hexagonal MC and M_2C carbides. According to Goldschmidt (quoted in [Hab66]), the behaviour of chromium is similar in certain ways both to those of tungsten and molybdenum and to those of the last of the transition series elements, nickel and cobalt.
- The transition metals in group *VIII (Fe, Co, Ni)* all form M_3C type carbides, but only Fe_3C is stable under the conditions of temperature and pressure normally encountered. Three metastable carbides are known, χ or Hägg's carbide (Fe_5C_2), Fe_7C_3 (similar to the stable Cr_7C_3), and ε carbide. Nickel has little tendency to interact with carbon.

> *A review article on carbides by Yakel [Yak85] includes two interesting approaches. Firstly, cementite,* Fe_3C*, is considered as a hexagonal structure, consisting of an ABAB... stacking sequence of rumpled densely packed planes of iron atoms, with the carbon atoms located between the layers along the fold lines. The size of the interstitial atom is assumed to affect the type of structure, large atoms such as boron promoting the formation of rumpled structures similar to* Fe_3C*, whereas smaller atoms such as nitrogen favour flat structures similar to* ε Fe_3N*. Since carbon atoms are intermediate in size, both the* Fe_3C *and* ε Fe_3N *forms can occur. The second approach is to consider the folds as microtwins. In both cases, the basic crystal lattice is composed solely of iron atoms, with carbon relegated to the role of an interstitial. These considerations facilitate understanding of the orientation relationships observed between the carbides and the ferrite or austenite matrix.*

Some nitrides are quite similar to the corresponding carbides, in particular the cubic MC and MN phases and the M_2N and M_2C compounds. The principal nitrides encountered in steels are summarized in Table 3-4-1.

Intermetallic compounds

The metallic nature of the bonding in these compounds is determined mainly by the number of unpaired electrons. In terms of their electronic structure, the atoms of group VIIIa transition elements, which include iron, nickel and cobalt, have a *d* electron shell that is nearly full and can potentially accept electrons to complete it. Conversely, the atoms of the *refractory* metals in groups IVa, Va and VIa (Ti, V, Zr, Nb, Mo, W, Ta) act as electron donors, since their *d* shells contain several unpaired electrons. Numerous intermetallic phases are therefore formed between the group VIII transition elements and the metals of groups IV, V and VI. Most intermetallic phases can be classified by reference to binary compounds with stoechiometric ratios A_3B, A_2B, A_5B_3, A_7B_6, and AB, where the B elements include Sc, Ti, V, Cr, Y, Zr, Nb, Mo, La, Hf, Ta, W and Ac, and the A

Table 3-4-1: The carbides, sulphides and nitrides most frequently encountered in steels.

Phase	Pearson symbol	Struktur-bericht	Space group	Prototype
Fe_3C	oP16	$D0_{11}$	Pnma	Fe_3C
χ Hägg, (Fe_5C_2)	mC28		C2/c	Mn_5C_2
ε, Fe_2C-Fe_3C	hP*	D_3^2	$P\bar{3}ml$	
Fe_2C	oP6		Pnnm	CFe_2
Cr_7C_3, Mn_7C_3	hP80	$D10_1$		Cr_7C_3
τ, $Cr_{23}C_6$ $Fe_{21}Mo_2C_6$	cF116	$D8_4$	Fm3m	C_6Cr_{23}
MoC, WC	hP2	Bh	$P\bar{6}m2$	WC
Mo_2C, W_2C, Fe_2C	hP3	L'3	$P6_3/mmc$	W_2C
κ , W_3(Fe, Mn)C			$P6_3/mmc$	$W_9Co_3C_4$
η M_6C η, $(NiCoFe)_3(MoWTa)_3C$	cF112	$E9_3$	F d3m	cFe_3W_3
ξ, Fe_2MoC	oP*		$P222_1$	Fe_3C mod
VC(V_4C_3), VN, CrN	cF8	B1	Fm3m	NaCl
γ', Fe_4N	cP5		Pm3m	CaO_3Ti
ζ, Fe_2N	hP3	L'3	$P6_3/mmc$	W_2C
γFeS, CrS	hP4	$B8_1$	$P6_3/mmc$	NiAs
αMnS	cF8	B1	Fm3m	NaCl
Z, NbMoN, TaMoN, NbCrN	tP6	D^7_{4h}	P4/nmm	CaGaN
AlN	cP2	B4	Pm3m	ZnS
β, Cr_2N (X=N, C)	hP9		$P\bar{3}1m$	ε Fe_2N

elements include Mn, Fe, Co, Ni, Cu, Tc, Ru, Rh, Pd, Ag, Re, Os, Ir, and Au. The most important intermetallic compounds encountered in steels are listed in Table 3-4-2.

Topologically close packed phases

In 1927, Friauf introduced the idea of considering the crystal structures of compounds as being made up of polyhedra formed by groups of 16 atoms and arranged together as equal-sized hard spheres in a cubic array of maximum compactness. The polyhedra concerned were in fact tetrahedra with the four corners truncated. In 1934, Laves was one of the first to examine real structures in terms of Friauf's reference polyhedron. Laves found that certain structures could indeed be described by the stacking of polyhedra with 16-fold coordination (CN16), and these compact structures are now known as the Laves phases.

Using a similar approach, Frank and Kasper, whose work was published in 1958–1959, showed that the structure of compounds in multicomponent systems could be broken down into an assembly of polyhedra derived from the icosahedron, one of which is Friauf's polyhedron. According to Frank and Kasper, compounds are built up from antiprisms that are either pentagonal (Laves phases), hexagonal (σ phase and similar structures) or mixed (P phase). A review of this approach can be found in [Sin72].

Table 3-4-2: Nominal composition and crystal structure of the intermetallic compounds most frequently encountered in steels [Cam81].

	Phase	Formula	Pearson symbol	Struktur-bericht	Space group	Prototype
Close-packed phases	Laves phases	Fe_2Mo (λ), Fe_2Ti, Fe_2W, Fe_2Ta, Fe_2Nb	hP12	C14	$P6_3/mmm$	$MgZn_2$
		Fe_2Zr	hP24 cF24	C36 C15	$P6_3/mmc$ $Fd\bar{3}m$	$MgNi_2$ Cu_2Mg
		Fe_2Hf	hP12, hP24 cF24	C14, C36 C15	$P6_3/mmm$ $P6_3/mmc$ $Fd\bar{3}m$	$MgZn_2$ $MgNi_2$ Cu_2Mg
	μ	$(Fe,Co,Ni)_7(Cr,Mo,W)_6$	hR13	$D8_5$	$R\bar{3}m$	Fe_7W_6
	σ	(Fe,Co,Ni)(Cr,Mo,W)	tP30	$D8_b$	$P4_2/mnm$	$Cr_{46}Fe_{54}$
	π	$Fe_7Mo_{13}N_4$	cP20	A13		βMn
	ν,		oI186	$D2h^{25}$	Immm	Mn_4Si
	χ	$Fe_{18}Cr_6Mo_5$ $Fe_{36}Cr_{18}Mo_{10}$, $M_{18}C$	cI58	A12	$I\bar{4}3m$	αMn
	P2	Cr(12-x)Fe13Mo(2+x)Ni3	mP30	monoclinic	P2	type CrFe distorted
	G	$Ni_{16}Ti_6Si_7$ $Ni1_6Nb_6Si_7$	cfc			
	R	(Fe,Co,Ni)CrMo	HR53	$A12/C3i^2$	$R\bar{3}$	$Cr_{18}Mo_{31}Co_{51}$
	P	$Cr_{18}Mo_{42}Ni_{40}$	oP56	$A12/D2h^{16}$	Pbnm	$Cr_9Mo_{21}Ni_{20}$
		TiS	hP4		$P6_3/mmc$	NiAs
	H, Y, τ	$Ti_4C_2S_2$ ou TiSC	hP16	$D0_{24}$	$P6_3/mmc$	Ni_3Ti/AlN_3Ti_4
A_3B compounds	γ'	Ni_3Al	cP4	$L1_2$	$Pm\bar{3}m$	Cu_3Au
	γ"	$(NiCrFe)_3(NbMoTiAlTa)$	tI8	$D0_{22}$	14/mmm	Al_3Ti
	η	Ni_3Ti	hP16	$D0_{24}$	$P6_3/mmc$	AlN_3Ti_4, Ni_3Ti
	β	Ni_3Nb	oP8	B2/B31 /D0a	Pnma	BFe MnP
	ε	(NiFeCo)3(NbTi)	hP8	$D0_{19}$	$P6_3/mmc$	Ni_3Sn
	β	NiAl	cP2	B2	Pm3m	CsCl

The most common intermetallic compounds in steels are those of the A_2B type, since iron forms phases of this sort with all the elements in groups IV, V and VI except vanadium. These compounds include the three types of Laves phases, whose structures are designated C14, C15 and C36. In several of these compounds, the A_2B stoechiometry is rigorously observed, A being the transition element. It is the Laves phases that are the most compact, *i.e.* that have the highest atomic packing density. However, even for the Laves phases, the compactness is not the only important factor. A correlation has also been found between the type of structure, C14 or C15, the ratio of the atomic radii (r_B/r_A) and the valency electron concentration (VEC). Thus, the stability of the C15 structure is enhanced by an increase in both r_B/r_A and VEC [Kei98].

In numerous compounds other than the Laves phases, such as the σ, χ, δ, G, R and P phases, the electron density, and to a lesser extent the atomic size ratio, also influence the crystal structure adopted. The σ phase in the Fe-Cr system can be ranked among the A_2B phases, even though the stoechiometry is poorly defined, ranging from A_4B to AB_4. Certain complex intermetallic compounds, such as the χ, G and R phases, occur in multicomponent alloys. Their range of existence in terms of composition and temperature is poorly established.

The A_7B_6 type compounds represent the so-called μ phases that are observed in many different systems. In complex alloys, only certain elements can be taken into solution in these phases, on specific sites. The general formula for μ phase can thus be summarized as $(Fe,Ni,Co)_7(Cr,Mo,W,Ta,Nb)_6$.

A common feature of all these compounds is their dense atomic packing, and for this reason they are described as *topologically close packed* (TCP) phases. Their crystallography is well described, but the physical parameters that determine their stability are still poorly understood. Thermodynamic modelling is difficult and requires a very detailed description (see § 4-11). For a long time, it was not possible to reliably predict the formation of TCP phases, such as σ, using a thermodynamic approach. A semi-empirical technique was therefore developed for alloy design requirements, based on consideration of the number of unpaired electrons, or "electron vacancies", in the *d* shell, designated N_V. Each element is assigned a more or less empirical N_V value, based on its electronic structure, and an average value is then determined for the alloy as a whole (or for the composition of the residual matrix after the formation of certain other phases). A critical value of N_V beyond which TCP phases are liable to form is determined experimentally. The *Phacomp* (Phase Computation) model and its derivatives have been extensively used for optimizing the composition of nickel base superalloys [Dur97b], but much less in the case of steels.

A_3B compounds

The A_3B compounds are extremely common in nickel-base and nickel-rich alloys of the superalloy family. They are considered as geometrically close packed phases, since their crystal structures can be considered as being composed of a stack of flat planes containing "hard sphere" atoms closely packed in both dimensions. Alternate rows in these planes contain either only A atoms or an ABAB... sequence. The B atoms in every second row may be opposite one-another or in intermediate positions, leading to either a triangular (T) or rectangular (R) symmetry (see examples Figure 20-3-2 and Table 20-3-3). The close-packed planes are thus either of type T or of type R. Different stacking sequences of R and T planes lead to a variety of crystal structures, the most common ones being designated $L1_2$, $D0_{22}$ and $D0_{24}$. For example, the pseudo binary or pseudo ternary sections Ni_3Ti-Ni_3Nb, Ni_3Ti-Ni_3Ta and Ni_3Al-Ni_3Ti-Ni_3Nb [Dur97b], [Tom02] include several different phases whose stabilities are closely related to the electron/atom ratio.

4

The basic phase diagrams

The reader is assumed to be familiar with the interpretation of binary phase diagrams and the chapter begins with a brief description of the specific features involved in the graphical representation of ternary and even higher order systems. Six ternary systems are analysed in detail by way of example : Fe-Cr-C, Fe-Ni-Cr, Fe-Mn-S, Fe-Co-Cu, Fe-Mo-Cr and Fe-C-V. They have been chosen because they include all the typical phase reaction configurations encountered in iron-base alloys, and especially in steels.
Calculated phase diagrams[3] *are extensively employed in this section, since they enable large numbers of isothermal sections and isopleths to be plotted, facilitating the detailed study of their variation with temperature or composition.*

4-1 Equilibria between condensed phases

Basic rules

Our knowledge of the metallurgy of steels, particularly as regards the effects of composition and temperature on microstructure, is largely based on experimental data obtained using a wide range of physical and chemical techniques. The thermodynamics of phase equilibria provides the only unifying framework that enables these data to be compared and validated.

When considering a particular system, a given quantity of matter is treated, that is a fixed total number of molecules (usually gram molecules or moles). The nature of the molecules is determined by the composition, *i.e.* by the concentrations of the different constituents, either elements or compounds. If a system comprises N constituents, the composition will be fully defined when N-1 concentrations are fixed. The concentrations may be given in terms of atom or mole fractions or atomic or weight percentages. In practice, metallurgical phase diagrams are usually represented in terms of weight percentages. This approach will be applied in most of the diagrams considered, atomic percentages being used only when it is necessary to emphasize stoechiometric proportions.

---

[3] The majority of the calculations were performed using the Thermocalc or Pandat softwares, with data available in the SGTE bank in 2002.

The equilibrium conditions to which the system is subjected are described based on the first and second laws of chemical thermodynamics. In particular, at equilibrium, the *chemical potential* of each constituent is identical in each of the phases present. *The equilibrium state is unique*, that is, the number of phases, their proportions and their compositions are fixed.

The phase rule was formulated by J.W. Gibbs in 1876. It stipulates the number of degrees of freedom F, or variance, in a system at equilibrium, *i.e.* the number of parameters that can vary independently, the variables in question being the temperature, the pressure and the concentrations of each of the constituents. For an alloy :

$$P + F = C + 2 \tag{4-1-1}$$

where P is the number of phases, C is the number of components and 2 represents the two variables pressure and temperature. In condensed metallic systems, pressure generally has very little influence in the rage of temperatures normally considered and is usually neglected, in which case the relation becomes $P + F = C + 1$.

The phase transformations considered conserve the number of atoms of each species, and involve only their redistribution among the different phases. This forms the basis for the so-called "lever rule" in binary equilibria (*cf.* § 5-1), which is a particular form of the barycentre rule for multicomponent systems.

Representations of phase equilibria

The graphical representations of phase equilibria are governed by the phase rule mentioned above. Thus, in a binary system (two constituents), an equilibrium between two phases will have only a single degree of freedom. If the temperature is fixed, the compositions and proportions of the two phases are automatically also defined. For example, in a temperature/composition diagram, the equilibrium between the solid and liquid phases is described by two points at the same temperature. The line joining the two points is known as a *tie-line*. When the temperature varies, the points representing the corresponding solid and liquid compositions describe curves called the *solidus* and *liquidus* respectively. For a given alloy composition, the liquidus temperature T_L is the temperature at which the first solid forms on cooling from the liquid field, while T_S is that at which the last liquid disappears. T_S will subsequently be called T_{Sth}, since it is the theoretical solidus temperature when equilibrium is maintained throughout solidification, a condition rarely fulfilled in practice (*cf.* § 4-6). In a binary system, an equilibrium between three phases is represented by three points and has zero degrees of freedom. It can occur only at one temperature and the compositions and proportions of the three phases are fixed.

Since it is assumed that readers are familiar with the interpretation of binary phase diagrams, the remainder of the discussion will concern the particular features of ternary and even higher order systems. Exhaustive treatments can be found in basic text books on phase diagrams [Pri66], [Wes82], while short introductions are also given in certain collections of phase diagrams [ASM92].

Consideration of multicomponent systems is essential in order to understand the microstructures of steels, which generally contain a large number of alloying elements. For a system containing N constituents, graphical representations are limited to two or at most three spatial dimensions, so that for high values of N they are restricted to particular projections or sections to reduce the number of variables appropriately. However, in practice, this limitation is not as restrictive as it might appear. The essential requirement is to be able to represent all the phases liable to occur, particularly the intermetallic compounds. Although many of these do not exist in binary systems, they can generally be found in at least one of the constituent ternary systems. It is for this reason that the present chapter emphasises the importance of ternary systems, which provide an extremely useful guide and are often quite sufficient to understand the microstructures of commercial steels. An attractive feature of ternary systems is that they can be represented graphically in several different ways.

The addition of an extra element to a system increases the number of degrees of freedom by one. For example, in a ternary, equilibrium between three phases is represented by a set of three lines that vary with temperature, instead of three points at a single temperature in a binary system. The lines are said to be *monovariant.* In a quaternary system, the lines become surfaces. Similarly, the liquidus line in a binary diagram becomes a liquidus surface in a ternary. In the latter case, it is divided into a number of distinct regions representing equilibrium between the liquid and each of the *primary* solid phase fields.

The barycentre rule

A ternary system can conveniently be represented using triangular coordinates. An isothermal section can then be plotted in two dimensions, the complete section being a triangle with the three pure constituents at the corners (*cf.* Fig. 4-1-4). In two-phase fields, the compositions in equilibrium are connected by tie-lines, which can never intersect one another (otherwise the composition at the crossover point would have two possible equilibria, in contradiction with the phase rule). The proportion of the two phases for any composition can be calculated by applying the inverse segment (lever) rule to the corresponding tie-line. For example, in Figure 4-1-4, an alloy of overall composition p will consist of two phases of compositions h and k, whose percentages *(h)* and *(k)* are given by :

$$(h) = kp/kh \text{ and } (k) = ph/kh \qquad (4\text{-}1\text{-}2)$$

In the three-phase field, the compositions of the phases are fixed (a, b and c) and their proportions in an alloy of overall composition m are determined by applying the lever rule to the points of intersection of the lines drawn from a, b and c through m to the opposite tie-line. For example, referring to Figure 4-1-4:

$$(a)=rm/ar;\ (b)=sm/bs;\ (c)=tm/ct \qquad (4\text{-}1\text{-}3)$$

(Note that the proportions are also given by ($(a)=cs/ac;\ (a)=bt/ab$ etc).

The proportions defined in this way are in the units used to construct the phase diagram, usually atomic or weight percent or mole fractions. Values determined by micrographic

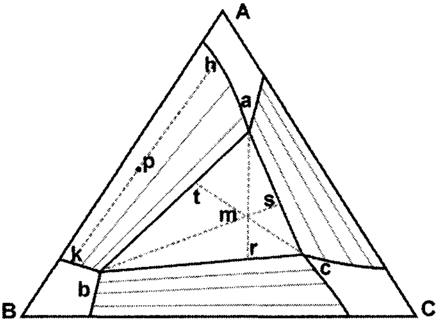

Figure 4-1-4:
Representation of the barycentre rule on a ternary diagram. Three types of phase field can be distinguished :
those corresponding to the single phase regions A, B and C,
the intervening two-phase fields where a number of tie-lines are shown,
and the three-phase field enclosed by the tie-line triangle abc.
The proportions of the different phases at any point are given by the relations 4-1-2 and 4-1-3.
When two equilibrium curves intersect (a, b and c for example) their metastable extensions in the neighbourhood of the points of intersections lie inside, either outside of the corresponding three-phase triangle.

measurements or image analysis are volume fractions, so that density corrections must be made to establish the equivalence.

A number of geometrical rules govern the possible nature of the junctions between adjacent phase fields (number of phases, angles of junction and tangents), [Pri66]. Thus, a single phase field cannot be adjacent to a three-phase field and can only join it at a point (in an isothermal section), and similarly cannot be adjacent to another single phase field. An exception to this rule is the case of second order reactions such as disorder-order transformations. A single phase field is thus always bounded on the sides by two-phase fields and by three-phase fields at the apexes. However, single phase fields may sometimes appear as a line when they are very narrow. These rules are the natural consequences of the properties of the thermodynamic functions governing phase equilibria, especially with regard to their continuity as a function of temperature.

Phase reactions

Since each state of equilibrium is unique, the change from one equilibrium at temperature T_1 to another at temperature T_2 is considered to be reversible. The state attained at *T2* is the result of a reaction that occurs *on cooling* from T_1 to T_2. In a binary system, three-phase equilibria are invariant, *i.e.* they occur at only one temperature. Cooling or heating from this temperature therefore requires that one or more of the phases must disappear. For example, if the liquid in equilibrium with two solid phases a and b disappears on cooling, the reaction will be written $L \rightarrow a + b$ and is said to be eutectic in nature. Indeed, a name has been given to all the reactions that occur during cooling from an invariant three-phase equilibrium, depending on the products formed. These names have the suffix "ic" for the reactions between a liquid and two solids and the suffix "oid" for those involving three solid phases. Thus, if L, L_1 and L_2 are liquids and a, b and c are solids :

$L \rightarrow a + b$, eutectic reaction
$c \rightarrow a + b$, eutectoid reaction

$L + a \rightarrow b$, peritectic reaction
$a + b \rightarrow c$, peritectoid reaction
$a \rightarrow b + L$, metatectic reaction
$L_1 \rightarrow a + L_2$, monotectic reaction
$L_1 + L_2 \rightarrow a$, syntectic reaction

By extension, the same reaction names are used in ternary systems when the initial equilibrium is not invariant but monovariant. Ternary reactions can also occur starting from invariant four-phase equilibria. Those that will be most frequently encountered in the present book are the following:

$L \rightarrow a + b + c$, ternary eutectic reaction
$L + a + b \rightarrow c$, ternary peritectic reaction
$L + a \rightarrow b + c$, pseudo-peritectic reaction sometimes termed quasi-peritectic

> *The expression "three-phase eutectic" will be used for multicomponent systems when a non-invariant equilibrium involves three solid phases and the liquid.*
> *The liquid phase is often forgotten, since it is absent in room temperature microstructures.*

Hillert's criterion

The feature that determines the *type of reaction* is the variation in the proportions of the different phases. Consider a reaction between two solid phases *a* and *b* and a liquid phase *L*, present at a temperature *T* in respective proportions m_a, m_b and m_L and with concentrations in element *i*, X^a_i, X^b_i, X^L_i. A small temperature drop ΔT causes changes Δm_a, Δm_b and Δm_L respectively in these proportions (Relation 4-1-5). The alloy contains three elements, two of whose concentrations are independent. For the element *i*, the principle of conservation leads to Relation 4-1-6, known as Hillert's criterion [Pri66], [Hil79].

$$\Delta m_a + \Delta m_b + \Delta m_l = 0 \tag{4-1-5}$$

$$m_a \Delta X^a_i + X^a_i \Delta m_a + m_b \Delta X^b_i + X^b_i \Delta m_b + m_l \Delta X^L_i + X^L_i \Delta m_l = 0 \tag{4-1-6}$$

According to Relation 4-1-5, the Δm values for *a*, *b* and *L* cannot all be positive. We will therefore assume that Δm_L is negative, *i.e.* that the proportion of liquid decreases. The reaction is eutectic if both Δm_a and Δm_b are positive, and peritectic if either Δm_a or Δm_b is negative. The reaction is thus considered to be of peritectic nature when the proportion of one of the two solid phases decreases and the other increases as the temperature falls.

Starting from a three-phase equilibrium *at a given temperature*, the nature of the reaction depends on the relative proportions of the phases present, that is on the position of the alloy composition in the tie-line triangle. According to relation 4-1-6, the reaction may be eutectic in certain zones and peritectic in others.

The tangent rule for a ternary system

The distinction between peritectic and eutectic reactions is simplified in the particular case where no solid has yet been formed and where the overall composition of the liquid lies on the monovariant line at temperature *T*. This is illustrated by the ternary system shown in

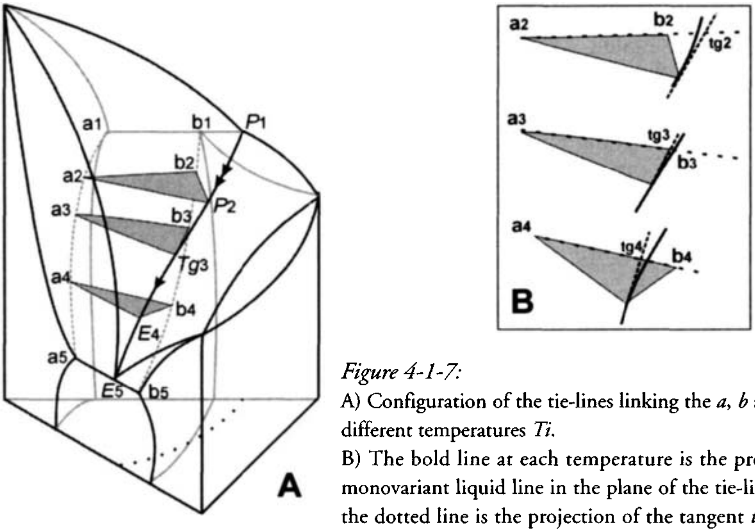

Figure 4-1-7:
A) Configuration of the tie-lines linking the *a*, *b* and *L* phases at different temperatures *Ti*.
B) The bold line at each temperature is the projection of the monovariant liquid line in the plane of the tie-line triangle and the dotted line is the projection of the tangent t_{gi} to the liquid line in this plane. At temperature T_2, t_{gi} cuts the solid tie-line outside the segment a_2b_2, indicating a peritectic reaction
$a_2 + L \rightarrow b_2$, whereas at temperature T_4, the intersection lies within the segment a_4b_4, indicating a eutectic reaction $L \rightarrow a_4 + b_4$. T_3 lies at the transition between the two types of reaction.

Figure 4-1-7, which comprises a binary peritectic at temperature T_1 on one side and a binary eutectic at temperature T_5 on the opposite side. Three different tie-line triangles are shown for temperatures T_2, T_3 and T_4. On the right hand side of the diagram, the projection of the monovariant line and its tangent are shown on these isothermal sections. The nature of the reaction is determined by the relative movements of the liquid, *a* and *b* compositions as the temperature falls. A useful guide is the so-called tangent rule which states that :

- when the projection of the tangent to the monovariant line lies outside the tie-line triangle (*i.e.* it intersects *ab* beyond *b*), then the reaction is peritectic, as at T_2.
- when it lies inside the triangle (*i.e.* it intersects *ab* between *a* and *b*), then the reaction is eutectic, as at T_4. T_3 is an intermediate case and represents the temperature where the tangent intersects *ab* at *b*.

The monovariant lines where the reaction is peritectic in nature are conventionally indicated by a double arrow, and those where it is of eutectic type by a single arrow.
The fact that the lines corresponding to the variation of the liquid and *b* compositions with temperature cross in a low temperature plane of projection is an indication that the configuration of the tie-line triangles has changed with respect to the monovariant line (Fig. 4-1-7). Similarly, configurations exist in which the projections of the solid solution lines *a* and *b* cross one-another. In this case there is a transition between a peritectic and a metatectic reaction.

4-2 Theoretically calculated phase diagrams

Basic principles

In a system at equilibrium, there is no excess free energy and consequently no driving force to induce a change. The equilibrium state is that with minimum free energy, and for a given pressure and temperature, in a system involving several constituents and several possible phases, it is necessary to consider the free energy of each constituent in each phase. The formulation of the free energy of each phase as a function of composition, together with the imposed overall composition, enables calculation of the compositions and proportions of the individual phases corresponding to a *minimum total free energy.* The concept of *chemical potential* or *activity* is a consequence of this relationship, since by definition, the chemical potential of each constituent is identical in each of the phases in equilibrium. The problem has a simple geometrical solution in the case of a binary system, where the compositions and proportions of the phases at equilibrium at a given temperature are defined by the common tangents to the free energy-composition curves for the different possible phases and the overall compositions considered. In a ternary system, the equilibrium is defined by tangent planes common to free energy-composition surfaces.

The calculation of equilibrium diagrams thus requires a knowledge of the free energy-composition relations as a function of temperature for all the phases liable to exist in the system considered. In fact, the intrinsic free energies are not known and it is the differences in free energy with respect to a known common reference state that are employed. These differences are estimated or determined experimentally.

The enthalpy of mixing ΔH involved in the formation of a compound or solution AB is the difference in enthalpy between the two pure components and that of the compound. A useful common practice is to refer to an *ideal* mixture in which the chemical potential of the constituent considered is given by a function $RTln(x_j)$, where R is the perfect gas constant, T is the absolute temperature and x_j is the concentration of element j.
The deviation from ideality is expressed by an excess free energy of mixing ΔG^{xs} :

$$\Delta G^{xs} = \Delta H - T\Delta S^{xs} \qquad (4\text{-}2\text{-}1)$$

where ΔG^{xs} is the change in excess entropy.

The sign of the excess free energy of mixing ΔG^{xs} gives an indication concerning the type of bonding between the elements A and B. A positive value indicates repulsive forces, while a negative sign signifies attraction. The excess free energy is often employed to qualify the behaviour of different systems. Thus, a large negative value implies a tendency to form intermetallic compounds, as in the Fe-Mo-Cr system (§ 4-11), while a positive value indicates a tendency for decomposition, as in the Fe-Co-Cu system (§ 4-10). It is because of these characteristics that these two systems were chosen among the examples considered in the present book. Various methods exist for expressing the free energy and the interactions between atoms, including techniques based on first principles and ones involving the optimisation of thermodynamic parameters.

"Ab initio" methods

The *ab initio* methods for calculating phase diagrams are based on a quantum mechanics and statistical analysis approach. The total energies for the formation of perfectly ordered structures at $T = 0K$ are obtained from local approximation electron density functions. Statistical calculations using the cluster variation method (CVM) or Monte Carlo simulations enable the thermodynamic parameters to be determined at finite temperatures [Col02]. Such first principle calculations are generally extremely demanding in terms of computer time and cannot be employed for systems containing more than two or three elements at most. Nevertheless, their use has extended rapidly since 1990. The only input data required are the atomic numbers of the elements considered and the crystal structures of all the phases involved. The data obtained can then be used for other phase diagram computation techniques employing an optimisation approach [Col01].

Methods involving the optimisation of thermodynamic parameters

In these methods, the variation of ΔG (or $\Delta G x_s$) as a function of temperature and composition must be expressed for each phase with a minimum number of phenomenological parameters. A simplified description of the thermodynamic model employed is given in the review article [Kat97].

Sets of parameters for the phases of different systems are optimised to obtain the best fit with observed equilibria and the optimised values are collected in data banks such as SGTE [SGTE]. A general library is accessible to users of different calculation softwares. Specific data bases also exist for particular types of alloys (steels, superalloys, aluminium alloys, etc) and are marketed independently. New results are continually collected and critically analysed before making them available for future calculations [Ans97], [Sau98].

Numerous calculation codes are now available and are becoming increasingly sophisticated to more precisely describe phase interactions. Noteworthy examples, in alphabetical order, are ChemCAD®, FactSage®, MTDATA®, Pandat®, Thermocalc®, and Thermodata®[4]. They can be used for binary, ternary and multicomponent systems. However, the number of parameters increases faster than the number of combinations of the elements two by two. Calculation rapidly becomes extremely difficult, even for powerful computers.

In particular, the following five points must be checked :

Experimental data contained in the data bank

Modern calculation softwares give the references that have been used to establish the data base concerned. It is strongly recommended to consult them to check which experimental data have been used in the parameter optimisations. Calculated optimisations generally *depend entirely on existing experimental data.* Thus, if the data bank contains no data on a compound that was unknown when the base was compiled, the calculation will be unable to consider its existence. Some calculated diagrams have not been verified and updated using modern techniques, while certain experimental results can be more than sixty years old. Many old results, published several decades ago, are still used as basic data. Even though the experimental facts may remain valid, their interpretation must be critically analysed in the light of the accuracy of the measurement techniques used at the time.

---

[4] web sites :
ChemCAD http ://www.chemcad.fr
FactSage http ://www.Factsage.com;
MTDATA http ://www.npl.co.uk;
Pandat http ://www.computherm.com;
Thermocalc http ://www.thermocalc.se;
Thermodata http ://online.fr.

Date of revision

There may be a considerable delay between the publication of new experimental results and their inclusion in the data bank. The correction and updating of a data bank is a lengthy procedure and can take several years, since *it is not possible to modify only the data for a single phase in isolation.* Some of the basic systems have been revised many times.

Phase models

Some phases are difficult to model. For example, many different attempts have been made to model the σ phase in steels [Ans97], [Wat01]. The unit cell of the σ crystal structure contains 30 atoms distributed on five independent sub-lattices. Ideally, the model should also consider five sub-lattices, but would then probably comprise a large number of adjustable parameters depending on the approach employed. Consequently, σ phase is described with only three sub-lattices, using models of the types $(A,B)_{18}(A)_{14}(B)_8$ or $(A,B)_{10}(A)_4(B)_{16}$, where iron is represented by the B atoms. Energy of mixing parameters (excess Gibbs free energy) are used to adjust the possibilities of substitution of A and B atoms. However, the same parameters can also be involved in other equilibria (*e.g.* α/γ) and in other systems. In order to take into account all the systems concerned, their adjustment is extremely laborious.

Simplifications

Steels can contain a large number of alloying elements. The rigorous calculation of phase equilibria then becomes so complex that it is impossible to allow for all the potential interactions between the different types of atoms. The simplification required to calculate phase diagrams in this case usually involves neglecting certain parameters.

Scope of use

Even when the majority of the equilibria involved have been optimised, calculated phase diagrams can give erroneous results for equilibria other than those considered. Data extracted from banks intended for purposes other than the determination of phase diagrams may prove unusable, due to the experimental values having been obtained outside the ranges of temperature and composition of interest. A good example is the extrapolation to lower temperatures of solid state phase transformation data.

4-3 Experimentally determined phase diagram

The role of carbon associated with iron to make steels was understood only towards the middle of the 19th century. The first proposals for the Fe-C phase diagram date from 1895–1899 (quoted in [LeC99], see also [Wad02]). The determination of many other phase diagrams began in the first half of the 20th century. Then, as is still the case today, the experimental techniques employed were essentially optical micrography, X-ray diffraction, chemical analysis, dilatometry and thermal analysis. The amount of work involved in determining even a fairly simple diagram is enormous. Phase compositions were originally determined by extraction and wet chemical analysis. Consequently, inorganic chemistry played an extremely important part in these basic studies. Many of the very old experimental results remain perfectly valid today, due to the meticulous quality of the work performed.

Transmission electron microscopy subsequently provided a better understanding of precipitation reactions and age hardening phenomena, originally studied using X-ray diffraction techniques (*e.g.* Guinier-Preston zones in Al-Cu alloys). Great progress was made when electron microprobe analysis became available in the 1960s and the scanning electron microscope in the 1970s. The ability to investigate structures at the micron scale led to the discovery of many new phases, giving rise to a continuous process of correction and refinement of phase diagrams.

The literature on phase diagrams has become extremely voluminous, making periodic reviews and critical comparative examinations of data essential. A noteworthy example is Hansen's Handbook [Han58], which is one of the earliest collections of binary diagrams based on the compilation of experimental results. For the reasons outlined above, even the oldest compilations merit attention, since they contain references not included in modern computer-based libraries. Since the 1980s, updated handbooks and compilations of critically reviewed phase diagrams have been regularly published (by the ASM, the Indian Institute of Metals, *etc.*). Phase diagram collections of this type are specifically identified in the list of references.

4-4 The Fe-Cr-C system : liquidus surface

The limiting binary systems : Fe-C, Fe-Cr and Cr-C

The Fe-C system has two variants, the *stable* version, where undissolved carbon is in the form of graphite, and the *metastable* version with the formation of cementite (Fe_3C). The diagram published in 1948 and quoted in [Han58] was for a long time considered as the reference. Since then, the major correction concerns the extension of the austenite field. For example, the carbon solubility limit in austenite at the eutectic temperature in the

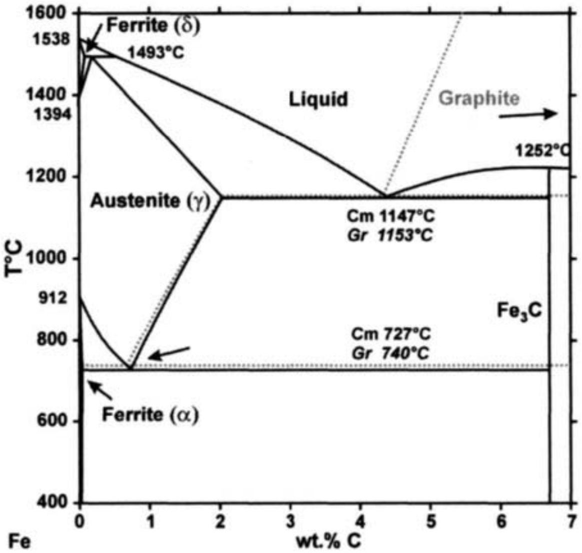

Figure 4-4-1:
Calculated Fe-graphite (grey) and Fe-cementite (black) systems.

Phase compositions for invariant reactions (in order of increasing carbon content)	Iron-cementite		Iron-graphite	
	wt %C and (at%)C	T°C	wt %C and (at%)C	T°C
Peritectic	0.09(0.4)-0.16(0.74)-0.53(2.43)	1493	**0.09(0.4)-0.16(0.74)-0.53(2.43)**	**1493**
Eutectic	2.14(9.23)-4.3(17.3)-6.69(25)	1147	**2.1(9.06)-4.2(17.1)-100(100)**	**1153**
Eutectoid	0.022(0.104)-0.76(3.46)-6.69(25)	727	**0.02(0.096)-0.65(2.97)-100(100)**	**740**

presence of Fe_3C is now recognized to be 2.14 % instead of 1.7[5]. The modern version of the diagram is illustrated in Figure 4-4-1 [Mas90].

The Fe-Cr system shows three important features (Fig. 4-4-2) :

- the existence of a two-phase region called the *gamma loop* separating the ferrite and austenite fields;
- the formation of the intermetallic σ phase below 812 °C;
- the separation of the ferrite field at low temperatures into the α and α' forms (decomposition reaction described in § 13-1).

---

[5] In practice, metallurgical phase diagrams are usually represented in terms of weight percentages

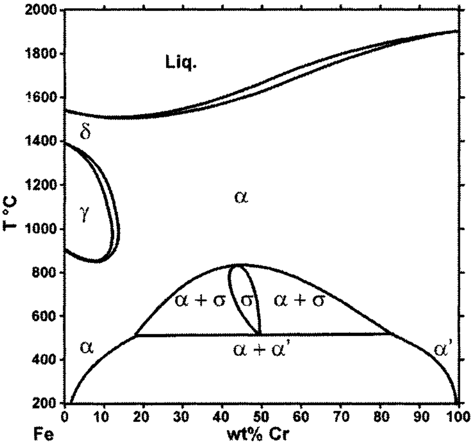

Figure 4-4-2:
Calculated Fe-Cr phase diagram.

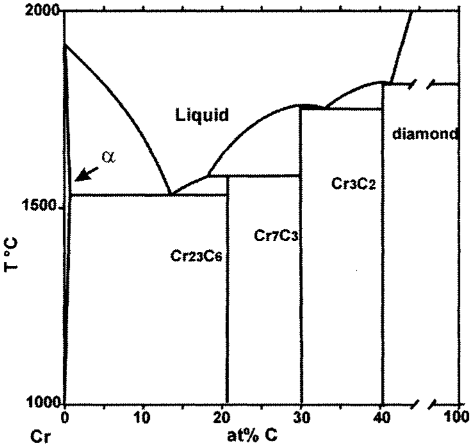

Figure 4-4-3:
Calculated Cr-diamond phase diagram.

Several versions of this diagram can be found in the literature. The most recent modifications concern the σ phase region and the α/α' decomposition.

The Cr-C system also has two stable and metastable variants, in which pure carbon is in the form of either diamond (Fig. 4-4-3) or graphite. This difference does not affect the region of interest for steels.

The Fe-Cr-C system

As in the Fe-C system, two possibilities must be considered, corresponding to stable and metastable variants. In fact, chromium has a strong affinity for carbon and stabilises all the carbides, including cementite. It is the metastable version of the diagram that is the reference for steels, since graphite is never observed in the range of compositions and processing conditions concerned in practice. The situation is different in the case of chromium-

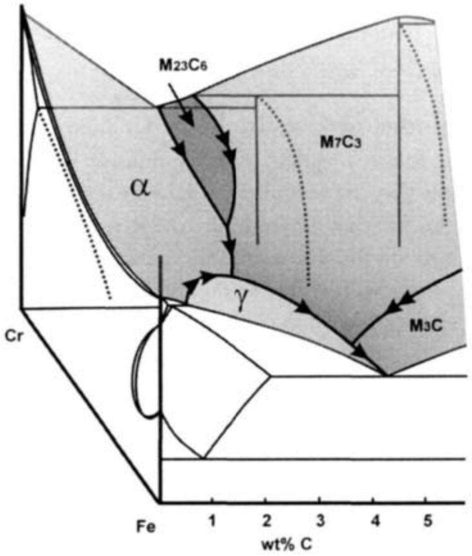

Figure 4-4-4:
Metastable Fe-Cr-C phase diagram for carbon contents less than 5%. Simplified perspective view adapted from [Jac70]. The bold black lines are the monovariant lines separating the primary solidification fields. Conventionally, eutectic type equilibria are indicated by a single arrow and those of peritectic type by a double arrow. The dotted lines represent the limiting solid compositions in equilibrium with the liquid on the corresponding monovariant line. There are three four-phase invariant equilibria:
Liquid + α + $M_{23}C_6$ + M_7C_3
Liquid + α + γ + M_7C_3
Liquid + γ + M_7C_3 + M_3C

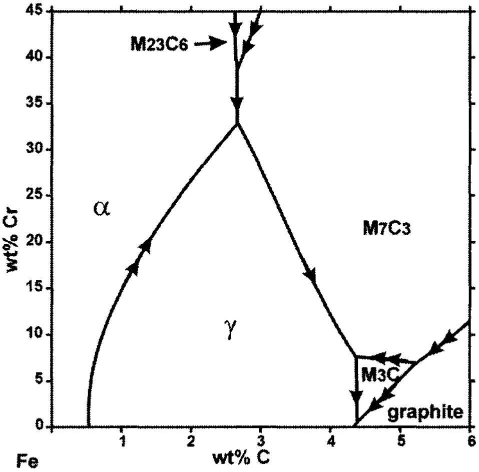

Figure 4-4-5:
Calculated liquidus projection in the iron-rich corner of the stable Fe-Cr-C system (with graphite). In the metastable diagram, the graphite field does not exist.

containing cast irons, where the composition and processing conditions can sometimes promote the appearance of graphite.

Several versions of the stable and metastable diagrams have been published, including [Bun58], [Gri62], [Jac70], [For73], [Riv84] (compilation), [Tho85], [And88]. The modifications mainly concern the extent of the $Cr_{23}C_6$ phase field, which has long been a subject of debate. The field was originally joined to the primary austenite field at about 20 %Cr. The disagreement is probably due to the fact that the primary M_7C_3 carbides are unstable on cooling and readily transform to $M_{23}C_6$ at temperatures that are still quite high. Both experimental and calculated versions published since the late 1990s show relatively good agreement.

Liquidus surfaces in the Fe-Cr-C system

The different regions of the liquidus surface are illustrated schematically in Figure 4-4-4, where they are bounded by those of the Fe-C and metastable Cr-C systems. A projection of the liquidus surface of the stable version is shown in Figure 4-4-5, while an equivalent projection for the metastable system is given in Chapter 6, Figure 6-3-3. Each region of the liquidus surface corresponds to the primary solidification of one of the five phases already present in the binary systems, namely Fe_3C, Cr_7C_3, $Cr_{23}C_6$, ferrite α and austenite γ. In fact, the ferrite is usually designated α-Cr on the Cr-rich side and δ-Fe on the Fe-rich side, but in this temperature range, the two elements are fully miscible in the same body-centred cubic phase. The difference between the stable and metastable versions is due to the existence of an extra region in the stable diagram, corresponding to the primary solidification of graphite. The different primary solidification regions are separated by eutectic or peritectic monovariant lines.

4-5 The Fe-Cr-C system : isothermal sections and isopleths

Isotherms

In a ternary diagram, the *isotherm* T_i is a section through the diagram in the plane of the temperature T_i (*cf.* Fig. 4-5-1A). Two sorts of line can be shown on an isothermal section. They correspond to the curved boundaries of the single phase fields in the temperature plane considered and to the straight tie-lines joining the phases in equilibria. The barycentre rule is applicable to these tie-lines. For a given overall composition, it is thus possible to determine the proportions of the different phases present (*e.g.* the fractions of $M_{23}C_6$, α and liquid for a composition situated in the corresponding tie-line triangle).

Isopleths

The isopleth C_i is a section through a ternary diagram on a plane corresponding to a fixed concentration of one of the constituents (*cf.* Fig. 4-5-1 B). The lines that appear represent the boundaries between the different phase fields. This representation only indicates which phases will be present for a particular composition at a given temperature. The tie-lines are not usually contained in this section, except in the particular case of a so-called *quasi-binary* section. *The lever rule cannot therefore be applied.*

The two sections shown in Figure 4-5-1 are mutually perpendicular and have a common intercept, corresponding to a chromium concentration of 80 % for the isotherm and a temperature of 1 427 °C for the isopleth. These unusual sections for steels were chosen

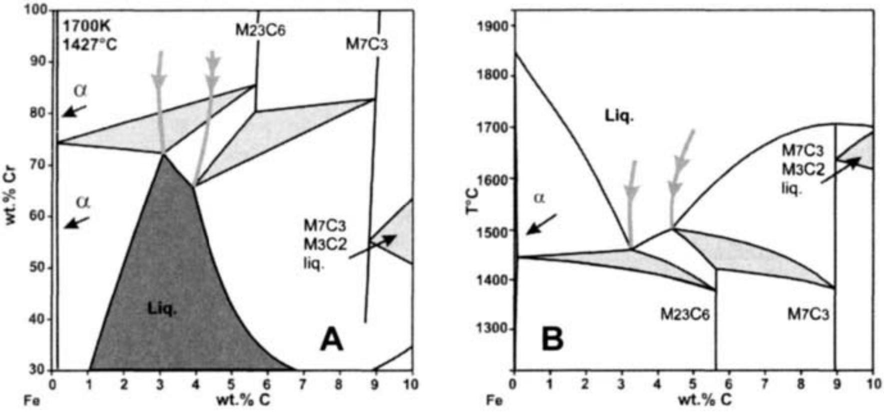

Figure 4-5-1: Fe-Cr-C system; (A) 1427 °C isotherm, (B) 80 % Cr isopleth.
The grey lines represent the eutectic and peritectic monovariant lines situated outside the plane considered. The three-phase regions concerned by these reactions (α-liquid-$M_{23}C_6$, liquid-$M_{23}C_6$-M_7C_3, liquid-$M_{23}C_6$-M_3C_2) are shaded light grey.

because of the exemplary configuration of the phase fields. The polythermal monovariant lines shown in grey lie outside the plane of the section in each case, intersecting it at a single point. During cooling, there is a *eutectic* reaction $L \rightarrow \alpha + M_{23}C_6$, where the liquid is gradually replaced by the two solid phases. The tangent to the monovariant line cuts the α-$M_{23}C_6$ tie-line inside the triangle (*cf.* § 4-1). There is also a *peritectic* reaction $L + M_7C_3 \rightarrow M_{23}C_6$ where the liquid reacts with a solid phase already present to form a second solid phase. The tangent to the monovariant line cuts the $M_{23}C_6/M_7C_3$ tie-line outside the triangle.

Invariant equilibrium

At the point of intersection of two invariant lines in a ternary system, four phases are present, so that there are zero degrees of freedom and *the reaction is invariant* (Fig. 4-5-2). In this figure, three isotherms are shown for the same range of compositions, two for temperatures slightly above the invariant point at *Ti* and one just below it. On cooling, the two tie-line triangles merge together at T_i to form a quadrilateral, which splits again into two new triangles below T_i.

Multicomponent systems

In a system containing more than three elements, the tie-lines are no longer contained in an isothermal section, so that the barycentre rule cannot be applied geometrically. An exception is the case of a pseudo-ternary section, where the composition of one element is fixed, for example, between three stoechiometrically similar compounds $A_3B/A_3C/A_3D$. Isotherms and isopleths indicate only the number and nature of the phases present as a function of temperature but not their compositions.

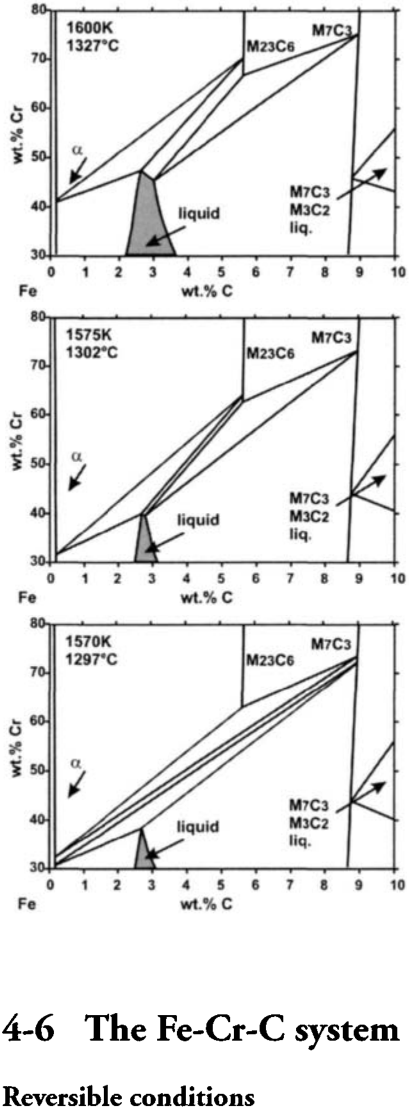

Figure 4-5-2:
Series of 3 isothermal sections through the Fe-Cr-C diagram showing the variation of the equilibria above and below the four-phase (liquid-α-$M_{23}C_6$-M_7C_3) invariant equilibrium point (1 299 °C). The liquid field is shaded in grey, while the α phase field is a narrow band along the Fe-Cr axis and the carbides are represented by lines, since they are considered to be perfectly stoechiometric.

At 1 327 °C, there are two 3-phase equilibria :
liquid-$M_{23}C_6$-M_7C_3.
liquid-$M_{23}C_6$-α

At 1 302 °C, the equilibria are still the same, but the compositions of the common phases are almost, but not quite, identical.

At 1 299 °C, the tie-line triangles merge to form a quadrilateral.

At 1 297 °C, two new three-phase equilibria appear : $M_{23}C_6$-M_7C_3-α and liquid-M_7C_3-α.

4-6 The Fe-Cr-C system : solidification paths

Reversible conditions

When a liquid alloy is cooled under so-called reversible conditions, it is assumed to go through a series of equilibrium states between the liquid and the homogeneous solid phases. The principle of conservation of mass dictates that *all the tie-lines* must pass through the composition of the initial liquid (*i.e.* that of the alloy as a whole).

The solidification path is the locus of the liquid composition as the temperature falls. The two solidification paths analysed in Figure 44-6-1 A and B have been chosen for two different alloy compositions, respectively m and p, with two solid phases designated *a*

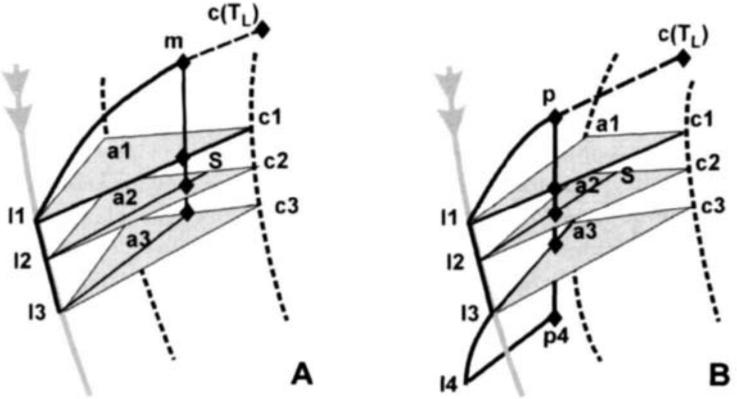

Figure 4-6-1:
Solidification paths under reversible conditions for two alloy compositions, m (diagram A) and p (diagram B), showing the variation in phase equilibria between the liquidus temperature T_L and a series of decreasing temperatures, T_1, T_2, T_3 and T_4. T_3 is the solidus temperature for composition m and T_4 that for composition p. The dotted lines a_i and c_i represent the compositions of the solid phases in equilibrium with the monovariant peritectic liquid, whose composition at temperatures T_i is given by the grey lines l_i.

In A, mc_{TL} is the first tie-line and only *c* phase forms down to temperature *T1*, below which a phase first begins to form. At T_2, the proportions of a_2 and c_2 in equilibrium with l_2 are respectively c_2S/a_2c_2 and a_2S/a_2c_2. At T_3, m lies on the tie-line a_3c_3 and the liquid is completely consumed.

In B, the solidification stages at T_1 and T_2 are the same as in A, but the liquid is not exhausted at T_3, so that below this temperature it is in equilibrium only with the *a* phase. The liquid is exhausted at T_4.

and *c*. By comparison with the two previous figures, the solid phases could be $M_{23}C_6$ and M_7C_3.

In diagram A, the liquidus surface is reached at temperature T_L where the only solid to form is *c*, with composition c_{TL}, mc_{TL} being the first tie-line. The liquidus composition then moves down to meet the monovariant peritectic line *l* at temperature T_1, below which the second solid phase a begins to form by reaction between the liquid and *c*. Since there is not yet any *a* phase, the alloy composition m lies on the tie-line between l_1 and c_1. At the lower temperature T_2, the line l_2m cuts the tie-line a_2c_2 at point S, the lever rule defining the relative proportions of the two solid phases (and also of liquid and solid along l_2mS). At the temperature T_3, the alloy composition m lies on the tie-line a_3c_3 and the liquid is completely exhausted.

In diagram B, for alloy composition p, the major difference is that at temperature T_3, p lies on the tie-line l_3a_3, so that the *c* phase has now been completely consumed before the liquid is fully exhausted. During further solidification down to the solidus temperature T_4, only the *a* phase continues to form.

Solidification without diffusion in the solid phase

Permanent equilibrium between the liquid and solid can rarely be maintained during practical solidification conditions, due to the slow rates of diffusion in the solid phases. It is therefore useful to consider another extreme situation, where the liquid remains effectively fully homogeneous, but is in equilibrium with the solid only at the interface, *no diffusion* occurring within the solid phase. This situation corresponds to what are known in solidification theory as the Scheil-Gulliver conditions (§ 5-1 and 5-2). The solidification path is still defined by the locus of the liquid compositions during cooling. *As under reversible conditions, it begins at the liquidus point in the direction defined by the corresponding liquid-solid tie-line in the plane of compositions.* The liquid is enriched or depleted in solute elements due to the formation of solid in which their concentrations are lower or higher respectively. On further cooling, the process is repeated, with the new liquid composition as the starting point at each temperature (Fig. 4-6-2). The solidification path comes to an end when the liquid is exhausted, at a temperature still termed the solidus.

In Figure 4-6-2, the two types of solidification path are illustrated for an alloy composition situated in the primary M_7C_3 carbide liquidus surface. In the absence of diffusion in the solid, the phases formed are successively, primary M_7C, peritectic $M_{23}C_6$, eutectic $M_{23}C_6$ and α, eutectic M_7C_3 and α, then (not illustrated) eutectic M_7C_3 and γ and eutectic M_3C and γ. The last liquid to solidify has the composition of the eutectic with the lowest melting point.

To avoid confusion, the end of the solidification path is denoted T_{Sth} for the case of full equilibrium and total homogeneity in the solid phases and T_{Sp} for the case of only partial or no diffusion. It should be noted that, under non-equilibrium conditions, the solidification path always crosses peritectic lines, as illustrated in this example.

In practice, some diffusion occurs in the solid, and solidification paths closer to real conditions are analysed in § 6-3.

> *In a binary diagram, the solidification path follows the liquidus line, whereas in a ternary it follows the liquidus surface. An exception to this rule is the case of a quasi-binary section, i.e. a section through a ternary system represented as a binary, for example Fe-WC, Fe-VC or Fe-NbC. The XC carbides have a precise stoechiometric ratio between carbon and the element X, so that the liquidus-XC tie-lines all lie in the Fe-XC/T plane. A "binary" reasoning of this sort is valid only when the tie-lines are coplanar. However, the eutectic Fe/XC is not invariant (since the amounts of C and X dissolved in the iron in equilibrium with XC can vary).*
>
> *The term "pseudo-binary" will be reserved for the representation of a section between two compounds in a system of n elements, without implications concerning the positions of the tie-lines. An example is the Fe_3C-V_4C_3 system [Rag84]. The principles applicable to binary systems (lever rule, solidification paths) are not valid in this case.*

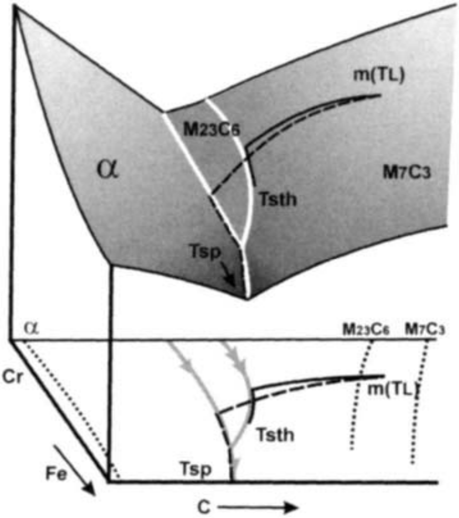

Figure 4-6-2:
Examples of solidification paths in the Fe-Cr-C system, in both reversible conditions (full lines) and without diffusion in the solid (dashed lines). Perspective view and projection in the composition plane.
The grey arrowed lines are the projections of the peritectic and eutectic monovariant lines in the composition plane, while the dotted lines are the projections of the α, $M_{23}C_6$ and M_7C_3 compositions associated with the monovariant equilibria.
The path m_{TL}-T_{Sth} corresponding to reversible equilibrium conditions stops at the point where the liquid is exhausted. The path m_{TL}-T_{Sp} corresponding to the absence of diffusion in the solid crosses the peritectic line, then follows the eutectic line down to what in this case is the binary invariant eutectic point γ/M_3C (not shown), where solidification is completed at constant temperature.

4-7 The Fe-Cr-C system : the austenite field

Perspective views, isothermal sections and isopleths

A precise knowledge of the limits of the austenite field and of the associated equilibria is of vital importance for steels based on this system.

- In particular, for compositions lying outside the austenite field at all temperatures, it is impossible to obtain a martensitic structure by quenching.
- Furthermore, the type of carbides in equilibrium can have a marked influence on properties, especially the corrosion resistance.

Figure 4-7-1 shows two perspective views illustrating the three-dimensional shape of the austenite phase field and its relationship with the adjacent phases with which it is in equilibrium, together with the associated invariant lines and points. the connection between the different maps, lines and invariants points in equilibrium with austenite.

The fields of existence of the various carbides at 880 °C can be seen in the isothermal section shown in Figure 4-7-2. The carbon axis has been extended to 10 wt.% to completely include the three-phase triangles. The carbides M_3C, M_7C_3 and $M_{23}C_6$ are represented by straight lines, corresponding to precise stoechiometry, and although the diagram is calculated on this assumption, it is very nearly the case in reality. The proportion of $M_{23}C_6$ carbide at 880 °C can be evaluated by applying the barycentre rule to the tie-line triangle $\alpha/\gamma/M_{23}C_6$. The amount is very small in the composition range

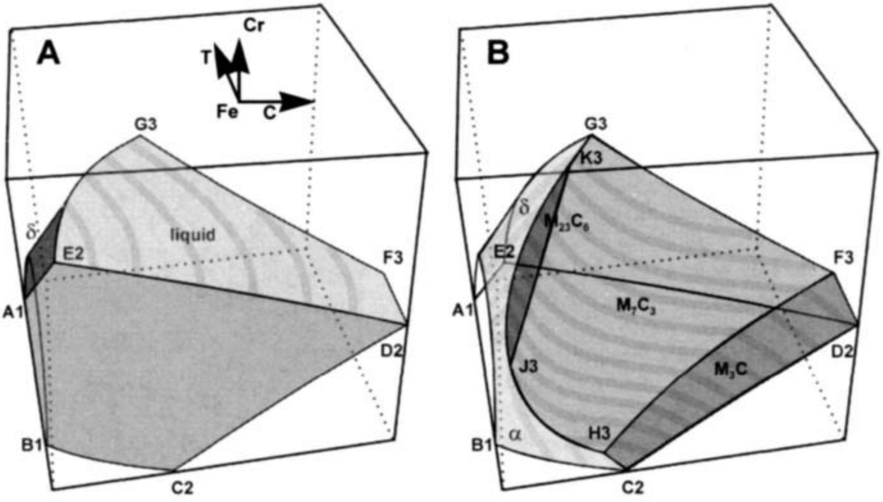

Figure 4-7-1:
Perspective view of the austenite phase field in the metastable Fe-Cr-C system.
A) Phase field boundaries corresponding to the γ/liquid (*solidus*) and γ/δ-ferrite (*solvus*) equilibria. The phases in equilibrium with the austenite are indicated on the corresponding boundary surfaces.
B) Solvus surfaces bounding the austenite field. The invariant points are labelled with a figure representing the number of phases in equilibrium with austenite. The characteristics of the invariant equilibria are given in the table below.

Invariant reactions	Austenite composition C and Cr wt.%	Temperature °C	Phases in equilibrium with austenite
A1	0C-0Cr	1394	δ-ferrite
B1	0C-0Cr	912	α-ferrite
C2	0.76C-0Cr	727	α-ferrite/M_3C
D2	2.14C-0Cr	1147	liquid/M_3C
E2	0.16C-0Cr	1493	δ-ferrite/liquid
F3	2C-4.35Cr	1178	liquid/M_7C_3/M_3C
G3	0.77C-19.8Cr	1284	liquid/M_7C_3/δ-ferrite
H3	0.59C-1.28Cr	749	α-ferrite/M_7C_3/M_3C
J3	0.10C-7.9Cr	814	α-ferrite/$M_{23}C_6$/M_7C_3
K3	0.61C-18.8Cr	1209	δ-ferrite/$M_{23}C_6$/M_7C_3

corresponding to 14 %Cr steels. The 14 %Cr isopleth is shown in Figure 4-7-3 and is limited to 1 %C to focus essentially on the austenite field.

The addition of chromium markedly changes the extent of the austenite field, which disappears completely at about 20 % Cr. This is illustrated in Figure 4-7-4 in which a

Figure 4-7-2:
Calculated 880 °C section of the Fe-Cr-C system. The phases present are indicated only for the single and three-phase fields. The "magnifying glass" indicates the $\alpha/\gamma/M_{23}C_6$ field, also shown in the 14 % Cr isopleth below.

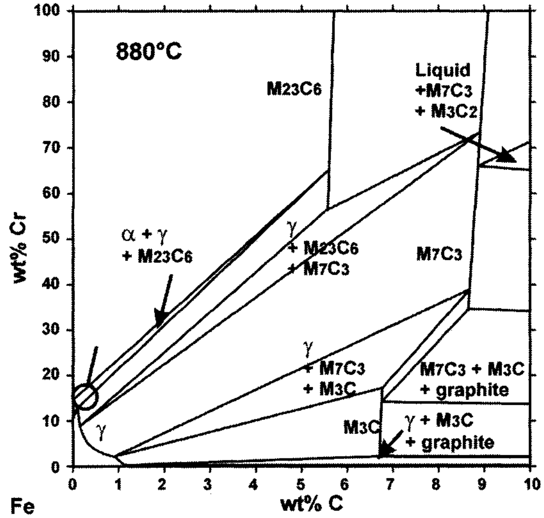

Figure 4-7-3:
Calculated 14 % Cr isopleth for the Fe-Cr-C system. This diagram indicates the phases present under equilibrium conditions. The "magnifying glass" indicates the $\alpha/\gamma/M_{23}C_6$ field, also shown in the 800 °C isotherm above.

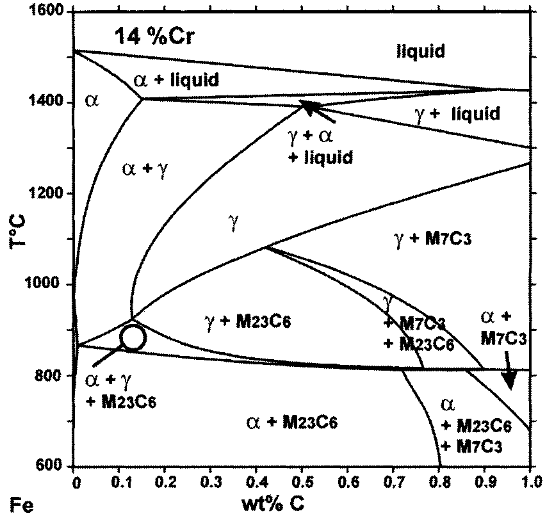

series of isopleths from 0 to 19 % Cr are superimposed. This simplified diagram was first published in 1962 [Rob62] and has since been reproduced in many textbooks on the metallurgy of stainless steels. The version shown in Figure 4-7-4 is an updated form, based on isopleths calculated using the recently optimised Fe-Cr-C diagram. It indicates the transition between the M_7C_3/γ and $M_{23}C_6/\gamma$ fields, materialised by the position of the three-phase field. From a practical standpoint, it should be noticed that, the higher the

Next Page

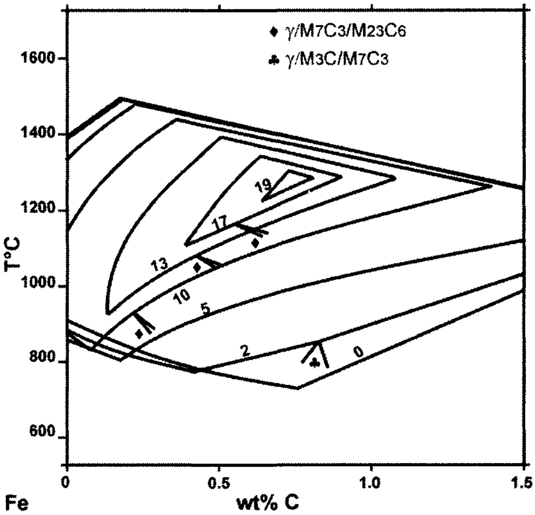

Figure 4-7-4:
Calculated isopleths for different Cr contents in the Fe-Cr-C system. Only the limits of the austenite field are shown, together with indications of the junction with the $\gamma/M_3C/M_7C_3$ and $\gamma/M_7C_3/M_{23}C_6$ three-phase fields.

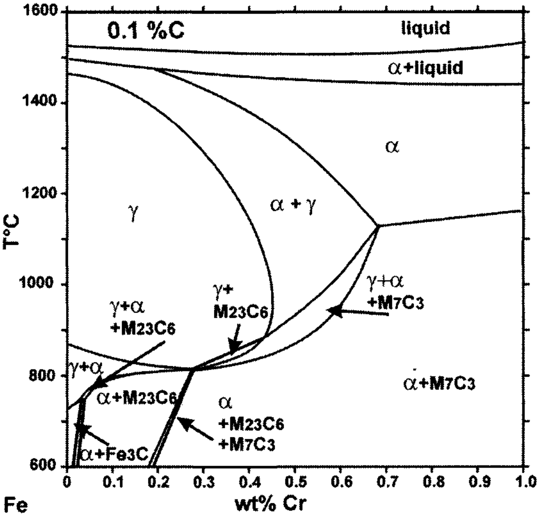

Figure 4-7-5:
Calculated 0.1% C isopleth for the Fe-Cr-C system.

chromium content, the more the range of stability of M_7C_3 is pushed to higher temperatures.

Constant carbon isopleths are also frequently employed, since they reveal the modifications induced by carbon in the Fe-Cr system. Figure 4-7-5 shows a calculated isopleth for 0.1 % C and is little different to the experimental version published in 1958 [Bun58].

Previous Page

4-8 The Fe-Cr-Ni system

The limiting binary systems, Cr-Fe, Cr-Ni and Fe-Ni

In the Fe-Ni system (*cf.* Fig. 3-3-3), the austenite field extends from pure iron to pure nickel at high temperatures.

In contrast, in the Fe-Cr system (*cf.* Fig. 4-4-2), there is an extensive ferrite solid solution field, together with two solid state transformations.

The Cr-Ni system (*cf.* Fig. 5-1-5) includes two fairly extended terminal solid solutions, corresponding to ferrite (α-Cr) on the chromium side and austenite on the nickel side, which form a eutectic.

The Fe-Cr-Ni system

The liquidus surface is shown in Figure 4-8-1 and contains only two primary solidification regions, corresponding to ferrite and austenite, separated by a monovariant line. For the compositions close to this line, the reaction is peritectic on the iron-rich side and eutectic on the Ni-Cr side. This important basic system has been extensively studied experimentally [Ray88] and the calculated diagrams are in good agreement with practical observations.

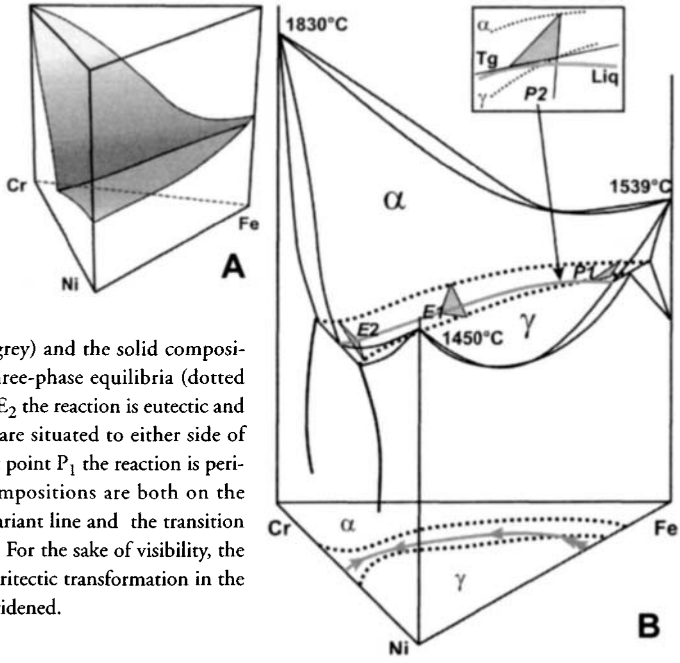

Figure 4-8-1: Perspective views of the liquidus surface in the Fe-Cr-Ni system : A) calculated, B) showing schematically projections of the monovariant line (grey) and the solid compositions involved in the three-phase equilibria (dotted lines). At points E_1 and E_2 the reaction is eutectic and the solid compositions are situated to either side of the monovariant line. At point P_1 the reaction is peritectic and the solid compositions are both on the same side of the monovariant line and the transition is at point P_2 (close up). For the sake of visibility, the zone surrounding the peritectic transformation in the Fe-Ni system has been widened. See also Figure 4-1-7.

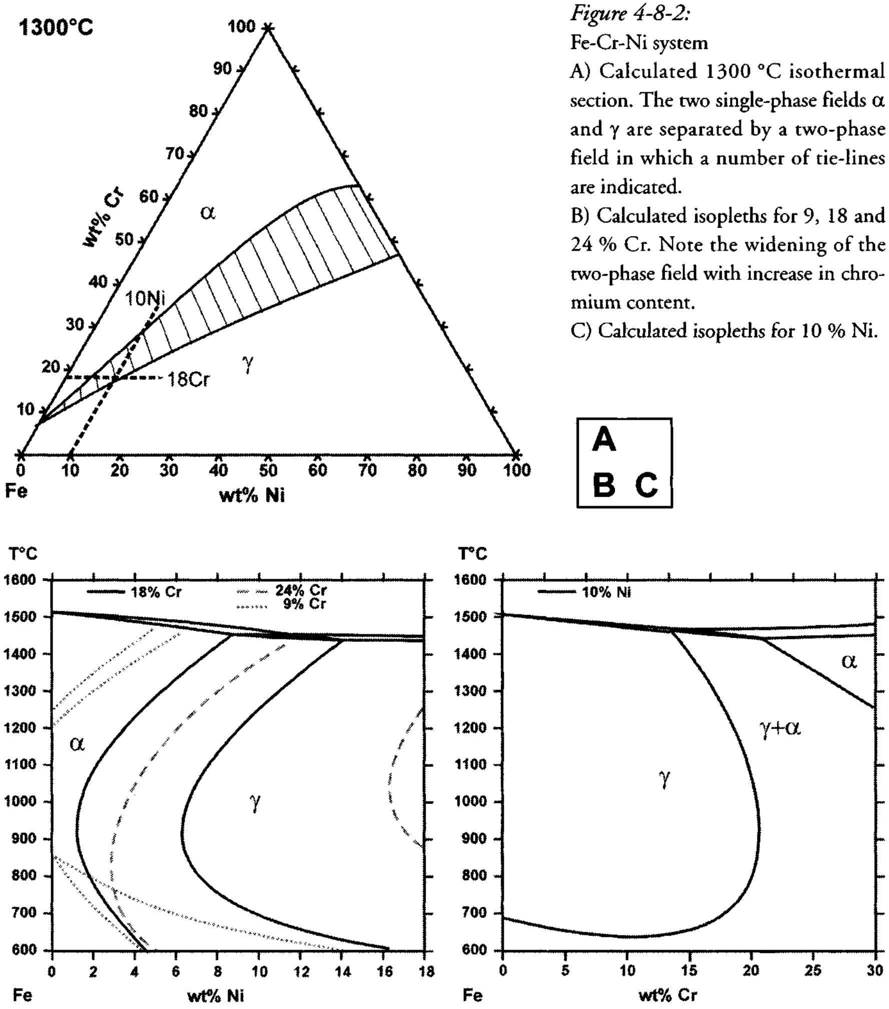

Figure 4-8-2:
Fe-Cr-Ni system
A) Calculated 1300 °C isothermal section. The two single-phase fields α and γ are separated by a two-phase field in which a number of tie-lines are indicated.
B) Calculated isopleths for 9, 18 and 24 % Cr. Note the widening of the two-phase field with increase in chromium content.
C) Calculated isopleths for 10 % Ni.

The Fe-Cr-Ni phase diagram clearly shows that nickel stabilises the austenite phase, whereas chromium stabilises the ferrite, the two elements thus having antagonistic effects. All the phases in the ternary system already exist in the limiting binaries. The σ phase in the Fe-Cr system extends well into the ternary, where it exists up to higher temperatures and is involved in both two- and three-phase equilibria.

In the solid state, the respective extents of the austenite and ferrite fields vary with temperature and composition in the gamma loop region. The limits of the these two solid solution phases at high temperature are illustrated by the 1300 °C isothermal section shown in Figure 4-8-2 A. The shape of the gamma loop can be seen in the calculated

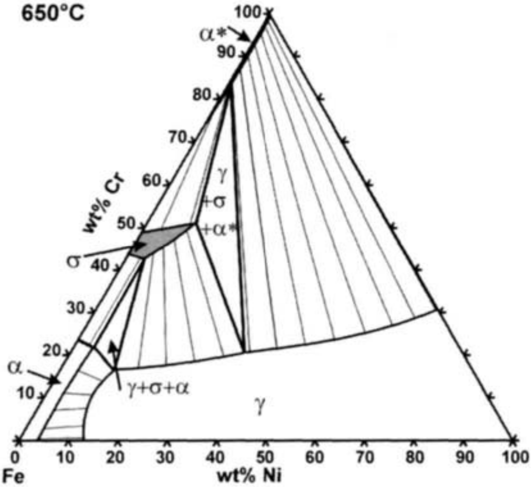

Figure 4-8-3:
650 °C isothermal section of the Fe-Cr-Ni system, comprising four single-phase fields, α, α*, γ and σ (grey), two three-phase fields and five two-phase fields, in which some tie-lines are indicated.
It can be seen that σ phase is liable to appear for compositions containing somewhat less than 20 % Cr. The highest temperature at which it occurs in the calculated ternary system is 964 °C, compared to 818 °C in the Fe-Cr binary.

isopleths of Figure 4-8-2 B and C. The corresponding positions of the 18 % Cr and 10 % Ni compositions are indicated on the 1300 °C isotherm. The isopleths for constant chromium or nickel contents can be used as a general guide for the heat treatment of stainless steels. However, since the tie-lines are generally not in the plane of the isopleth, this type of diagram gives no indication of the compositions of the phases in equilibrium. Similar isopleths were determined experimentally in 1930 by Bain, whose work still serves as the reference in textbooks on stainless steels.

The 650°C isothermal section in Figure 4-8-3 is designed to show the extent of the σ phase in the ternary system, where it is stabilised to higher temperatures than in the Fe-Cr binary. This is important for alloy design purposes, since the s phase is intrinsically brittle and frequently adopts a coarse plate-like morphology that can induce severe loss of ductility.

4-9 The Fe-Mn-S system

The limiting binary systems : Fe-Mn, Fe-S, Mn-S

The Fe-Mn system contains relatively few phases, corresponding to α, δ and γ for iron and α, β and γ for manganese (Fig. 4-9-1 and Table 3-2-1), [Mas90].

The Fe-S system is of particular importance for steels, since sulphur is a common residual impurity introduced from the ore. The part of interest for steels is limited to the region between iron and iron sulphide. A eutectic γ-Fe/FeS occurs at 988 °C, at a concentration of 44.6 at.% S (Figs. 4-9-2 B and 4-9-3), [Mas90]. Furthermore, the system includes a fairly

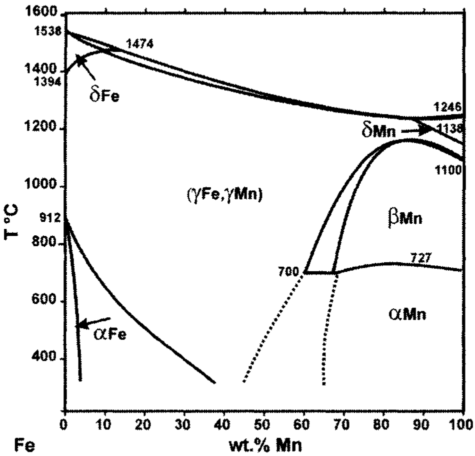

Figure 4-9-1:
Fe-Mn phase diagram according to [Mas90].

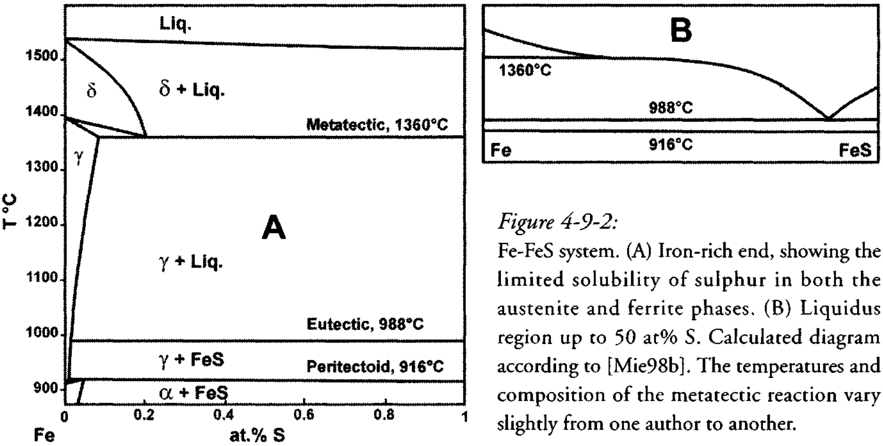

Figure 4-9-2:
Fe-FeS system. (A) Iron-rich end, showing the limited solubility of sulphur in both the austenite and ferrite phases. (B) Liquidus region up to 50 at% S. Calculated diagram according to [Mie98b]. The temperatures and composition of the metatectic reaction vary slightly from one author to another.

uncommon type of transition, called a metatectic (or sometimes catatectic) reaction [Wag74]. Thus, an alloy completely solidified to δ phase transforms on cooling below 1360 °C to a mixture of γ and liquid (Fig. 4-9-2 A). In this case, the *metatectic reaction* is thus : $\delta \rightarrow \gamma + Liq$

The Mn-S system (Fig. 4-9-3 C) includes the sulphide MnS, and the important part as regards steels is limited to the region between pure manganese and MnS. At the manganese-rich end, there is a eutectic δ-Mn/α-MnS at 1 at.% S, whose temperature (1242 °C) is only 4 °C below the melting point of pure manganese. To facilitate the interpretation of these diagrams referred to compounds, the concentrations are given in atomic or molar percentages. This system includes a region of non-miscibility in the liquid phase. The decomposition of a homogeneous liquid on cooling to form two separate liquid phases is

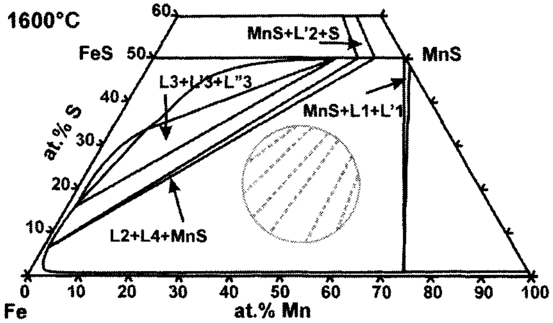

Figure 4-9-4:
Isothermal section of the Fe-Mn-S system at 1600 °C. The three-phase fields are indicated by the triangles. The grey circle shows the directions of the tie-lines in the MnS-liquid two-phase field, where the compositions vary respectively from (Mn,Fe)S to MnS and from L_4 to L_2.

called a *monotectic reaction*, $L_l \rightarrow a + L_2$. The bell-shaped region where it occurs is called the miscibility gap. This term is sometimes also used improperly to designate simple two-phase regions in the solid state.

The Fe-S system does not contain a miscibility gap of this sort, but a tendency for decomposition is revealed by certain ternary additions. A similar situation is observed in the Fe-Cu (*cf.* Fig. 4-10-1) and Co-Cu systems.

The Fe-Mn-S system

The most characteristic feature of this system is the liquid miscibility gap that affects a wide range of compositions in the Fe-Mn-MnS portion of the diagram (Fig. 4-9-3 A to D). The perspective view was drawn using both experimental results [Rag88}, [Mas90] and calculations based on retroactively optimised thermodynamic data available in data banks [Mie98].

The most interesting region for steels is the part limited by Fe, Mn, FeS and MnS. On the Mn-MnS binary side, there is a liquid miscibility gap, corresponding to a Mn-rich liquid L_1 and a MnS-rich liquid L'_1. In the ternary system, the miscibility gap extends almost up to the Fe-FeS binary side.

The Fe-MnS isopleth is often used to explain the liquid decomposition reaction and is presented as a quasi-binary section. This is a reasonable approximation, since the tie-lines, and particularly those representing the equilibrium between the two liquids, are almost in the plane of the section. The calculated Fe-MnS isopleth (Fig. 4-9-3 A and B) is slightly shifted with respect to the true quasi-binary section (that which includes the tie-lines and the extremities of the monovariant lines). It contains a small three-phase region $\delta/L_1/MnS$ in place of the eutectic point. On the quasi-binary section, the eutectic line attains a maximum at the point S_1 (Fig. 4-9-3 D), to either side of which the solidification paths diverge. This configuration is often referred to as a saddle point. The monotectic line shows two maxima, at S_2 and S_3. These are not invariant points, but simply points where the tie-line triangle is reduced to a line.

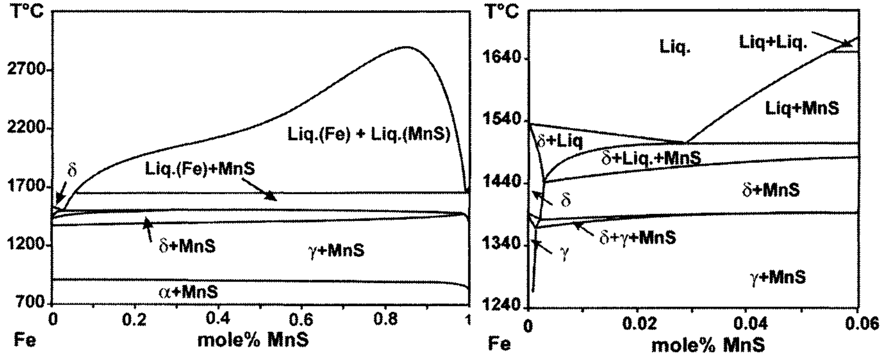

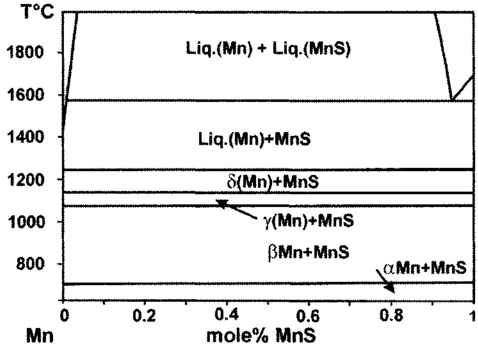

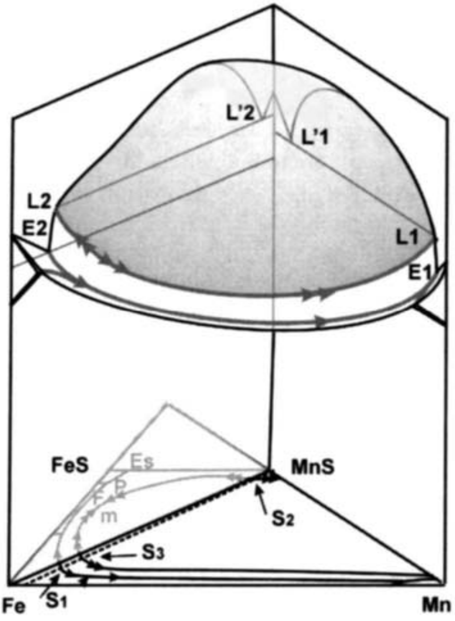

Figure 4-9-3:
Fe-Mn and Fe-Mn-S systems.
(A) Calculated Fe-MnS section.
(B) Magnified view of the iron-rich side. In a true quasi-binary section, the three-phase field δ/liquid/MnS is reduced to a point.
(C) Mn-MnS system. The configuration differs from the experimental situation close to the pure manganese side, where there is a eutectic [Rag88].
(D) Perspective view and projection in the composition plane. Adapted from the published liquidus projection [Rag88] and calculated isothermal sections [Mie98b]. For the sake of visibility, the zone surrounding the miscibility gap has been widened. The locus of the quasi-binary section close to the line Fe-MnS is shown on the projection as a dashed line. The points S belong to this section.
Some characteristic temperatures are as follows
L_1-L'_1 1571 °C
L_2-L'_2 1654 °C
S_1 1512 °C
S_2-S_3 1671 °C
E_1 1242 °C
E_2 1506 °C
E_s 1182°C
P 1006°C ((pseudo-peritectic FeS-Fe-MnS)
F 988°C (eutectic Fe-FeS)

This representation explains the formation of manganese sulphide precipitates in iron-rich alloys. Thus, for any composition containing a sufficient amount of sulphur, there is a separation into two liquids, one rich in iron and the other rich in sulphur and manganese. The line representing the extreme compositions defines two possibilities.

- If the Mn/S ratio in the overall composition is greater than one, the sulphur-rich liquid formed solidifies mainly as MnS at the eutectic temperature (1571 °C). Depending on the steel composition, MnS may even form as a primary solidification product.

- If the Mn/S ratio in the overall composition is less than one, the solidification path lies on the sulphur-rich side and the liquid is depleted in manganese. If there is no diffusion in the solid phase, the path falls down to a eutectic, FeS/(Mn,Fe)S (point E_S in Fig. 4-9-3 D), followed by a ternary pseudo-peritectic (point P) and finally the Fe-FeS eutectic (point F at 988 °C). The sulphur-rich phase thus remains liquid down to much lower temperatures.

The presence of other alloying elements modifies the solidification temperatures and the effect of Mn/S ratio may even be reversed. Consequently, the solidification structures can vary considerably, depending on whether the sulphides are formed as primary solidification products or at the end of the solidification path.

The Fe-Mn-O diagram is similar to that for the Fe-Mn-S system, with a wide liquid miscibility gap. The simultaneous presence of traces of sulphur and oxygen in commercial steels makes the situation extremely complicated to interpret in terms of phase diagrams.

4-10 The Fe-Cu-Co system

The limiting binary systems : Fe-Cu, Co-Cu, Fe-Co

The only phases in the Fe-Cu system are the terminal solid solutions δ-Fe, α-Fe, γ-Fe and γ-Cu. The complete diagram shown in Figure 4-10-1 is the result of recent data optimisation and calculation using Thermocalc [Ans93]. Under equilibrium conditions, the liquid is a single phase, but some authors report a tendency to form a metastable miscibility gap. Indeed, this can be predicted by calculation and is shown by the dotted line in Figure 4-10-1 A. The more detailed representation of the Fe-rich side in Figure 4-10-1 B was also determined by data optimisation, followed by a CVM-based calculation [Bei00], [Ant01]. The solubility of copper in iron is very small at low temperatures.

The Co-Cu system is quite similar to Fe-Cu, with the terminal phases γ-Co, ε-Co and γ-Cu. It also shows a tendency for liquid immiscibility. The solubility of copper in cobalt is very small, like in iron.

The Fe-Co system has already been mentioned when considering the order-disorder reaction (Fig. 3-3-2). At high temperatures, the terminal phases γ-Fe and γ-Co are fully miscible, except close to the iron-rich side in the temperature region where δ-Fe is stable.

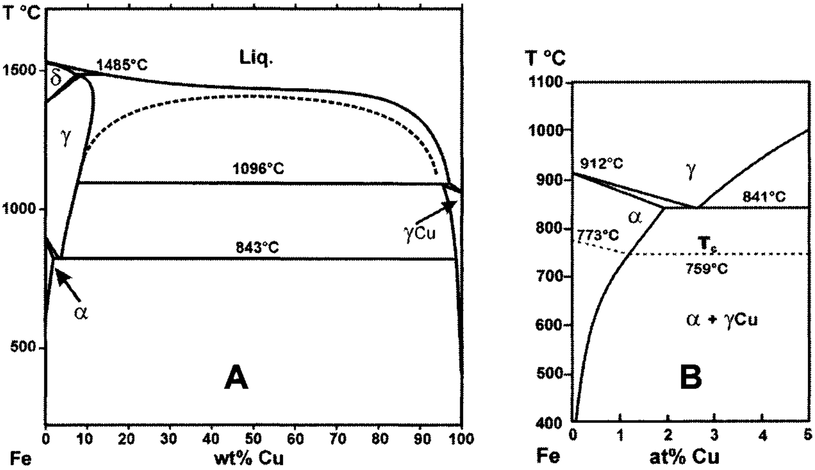

Figure 4-10-1:
Fe-Cu system. (A) Complete calculated phase diagram [Ans93]. The dotted line represents the liquidus for a metastable miscibility gap.
(B) Detail of the iron-rich side, based on a CVM calculation [Ant01]. Note the slightly different eutectoid temperature compared to (A). The compositions are expressed in atomic % to facilitate comparison with the calculated Fe-Co and Fe-Cu-Co diagrams.

The Fe-Co-Cu system

The Fe-Co-Cu ternary system has been relatively little studied, apart from an experimental investigation by Jellinghaus in 1936 [Jel36]. In his review of 1992, Raghavan [Rag92a] uses these data together with the limiting binary diagrams to describe the system. In fact, it appears to be very simple, with no other phases than those already present in the binaries, namely α–Fe, γ–Fe, δ–Fe, γ–Co, ε–Co and γ–Cu The respective solubility limits of iron and cobalt in copper and of copper in the γ-(Co,Fe) and α-(Fe,Co) solid solutions remain very small. Recent experimental work, together with CVM calculations, have been used to obtain a more refined description [Ant01], [Bei00].

Liquid immiscibility becomes effective in the ternary, with the formation of two liquids, with high and low copper contents. The question remains as to whether the miscibility gap is stable or metastable [Kim00]. In the solid state, most of the diagram is occupied by two- and three-phase fields, as can be seen in the experimental 900 °C isothermal section shown in Figure 4-10-2. In the narrow band corresponding to the existence of the γ-(Fe,Co) solid solution, this section has been completed by calculated phase boundaries. The detailed configuration of this region can be understood with the aid of Figure 4.10.4, based on CVM calculations. The isothermal section at 800 °C, with a single three-phase field towards the cobalt-rich side, is illustrated in Figure 4-10-3. The different lines compare calculated and experimental results. The CVM calculation gives excellent agreement when the magnetic contribution is taken into account.

Figure 4-10-2:
900 °C isothermal section of the Fe-Co-Cu system. The points represent experimental results obtained for alloys sintered from elemental powders and annealed for one month. From [Ant01].

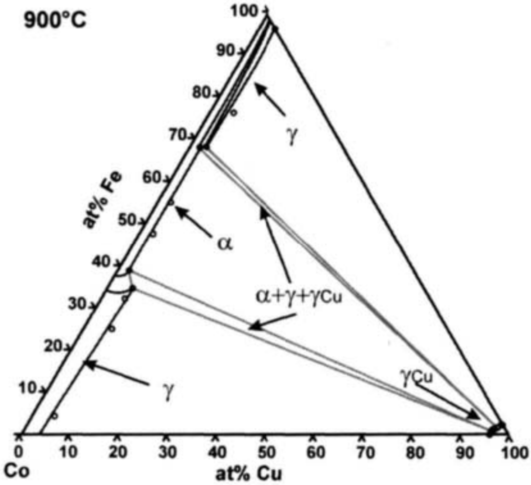

Figure 4-10-3:
800 °C isothermal section of the Fe-Co-Cu system, showing details of the α–γ–γ_{Cu} three-phase field. The full lines represent the experimental boundaries, while the light grey triangle corresponds to simple CVM calculations. The dark grey triangle is the result of CVM calculations allowing for the magnetic contribution. From [Bei00] and [Ant01].

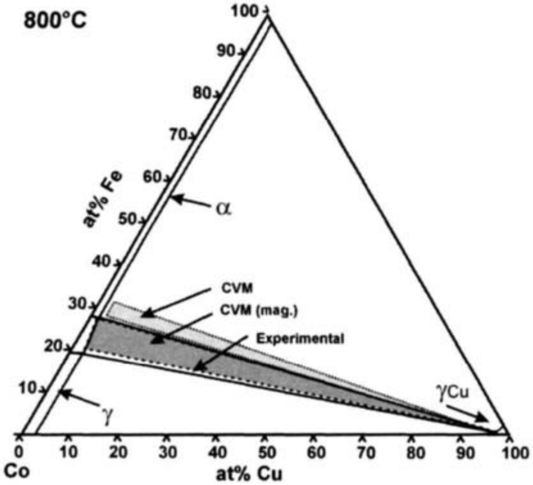

A recent experimental study of this system [Mal99] emphasized two difficulties that can arise in the determination of phase equilibria. When alloys are prepared by melting, the γ-(Co,Fe) and γ-(Fe,Co) solid solutions remain supersaturated, even after long annealing times between 700 and 1000 °C, and the nucleation of copper precipitates does not occur. This problem is not encountered with alloys produced by the solid state sintering of elemental powders, where the specimens are held below the solvus temperature. However, sintered samples can contain oxygen, due to the finely divided form of the starting materials, and this can modify the equilibria. According to the Fe-Cu-O phase diagram [Rag89], a very small amount of oxygen

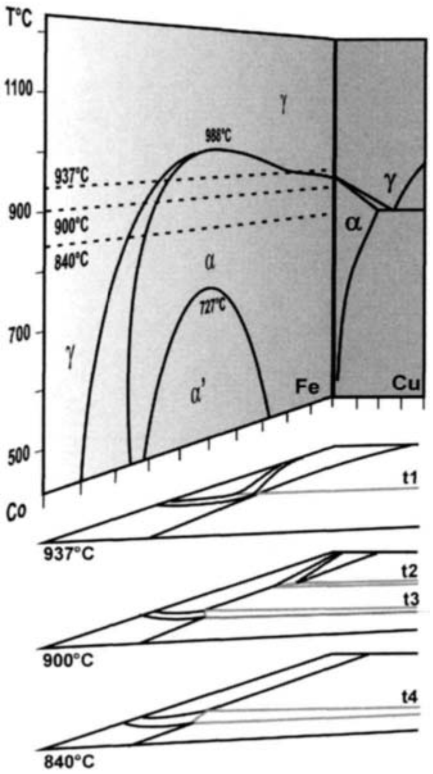

Figure 4-10-4:
Schematic representation of the low-copper region of the Fe-Co-Cu system. The limiting binaries are shown in Figures 3-3-2 and 4-10-1. The α phase field has a flattened cone shape, culminating on the Fe-Cu binary side at 988 °C. The temperature of 937 °C corresponds to the appearance of the first three-phase field, t_1, reduced to a line. The section at 900 °C includes two three-phase fields, t_2 and t_3, with the same phases, but different compositions. Below 841 °C (or 843 °C, depending on the version), no austenite remains on the iron-rich side, and there is only one three-phase field, t_4. Constructed from the calculated isotherms, [Bei00] and [Ant01].

> *can be sufficient to effectively reduce the solubility of iron in copper and to produce a small quantity of iron oxide.*

4-11 The Fe-Mo-Cr system

The limiting binary systems, Cr-Mo and Fe-Mo

The Cr-Mo system is very simple, with complete miscibility between the terminal phases at high temperatures and a miscibility gap below 880 °C, Figure 4-11-1.

The most interesting feature of the Fe-Mo system is the fact that it contains the four major intermetallic phases frequently encountered in steels, corresponding to the σ, R, μ-(Fe_7Mo_6) and λ-(Fe_2Mo) phases, Figure 4-11-2, whose crystal structures are indicated in Table 3-4-2.

The calculated equivalent system Fe-W includes only two corresponding phases, namely μ-(Fe_7W_6) and λ-(Fe_2W), Figure 4-11-3. Several versions of the experimental diagram exist, the principal differences concerning the extent of the μ phase field and the existence

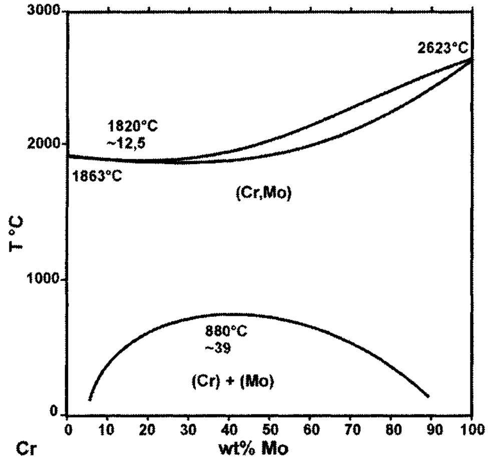

Figure 4-11-1:
Calculated Cr-Mo phase diagram, according to [Ven87].

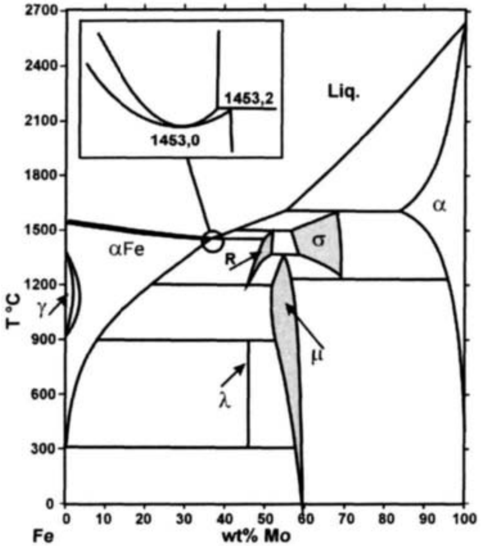

Figure 4-11-2:
Calculated Fe-Mo phase diagram. The insert shows an enlargement of the liquidus minimum and peritectic reaction.

of the Laves phase, λ. According to Nagender *et al.* [Nag91], above about 1200 °C, μ decomposes to α-Fe and δ-(Fe,W). The disagreements are hardly surprising considering the long exposure times often necessary for these phases to form, particularly in the case of λ. The similarity between the two systems is such that the μ and λ phase fields extend into the Fe-Mo-W ternary.

The Fe-Mo-Cr system

Consideration of the Fe-Mo-Cr system explains the powerful sigma-stabilizing effect of molybdenum in steels. Indeed, the isothermal sections in Figures 4-11-4 and 4-11-5 show

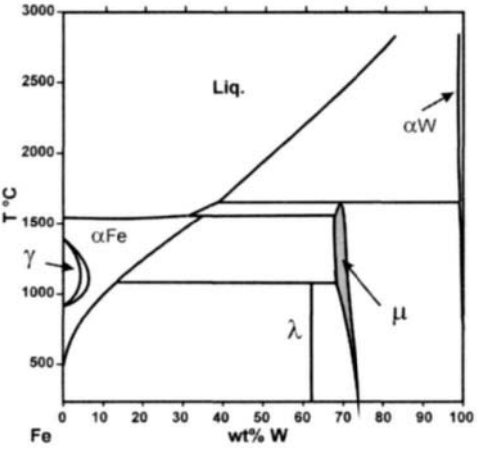

Figure 4-11-3:
Calculated Fe-W phase diagram.

that sigma phase is still stable in the ternary system at 1500 and 1600 °C, over a wide composition range. It is stabilised by numerous A type elements (*cf.* § 3.4) frequently encountered in steels (V, W, Nb, Ta, Si, Mo). Although these elements are also ferrite stabilisers, this is not necessarily true for all sigma-promoting elements.

The isothermal sections, liquidus projection and corresponding isopleth in Figures 4-11-4 A to D show the liquid/solid equilibria. The aim is to give an example of the interpretation of monovariant lines in terms of the tie-lines in an isothermal section and to illustrate the analysis of a fairly complex isopleth with the aid of the associated isotherms.

The 800 °C and 1000 °C isotherms shown in Figure 4-11-5 include the intermetallic phases present in the Fe-Cr system and reveal the occurrence of an additional purely ternary phase χ. It should be noted that the Laves phase, λ-(Fe_2Mo), has a strictly stoechiometric composition. In contrast, the χ, R and σ phases occupy wide compositional ranges, without a clearly defined stoechiometry.

Figure 4-11-6 shows a quaternary isopleth corresponding to Fe-26Cr-5Ni as a function of molybdenum content. These chromium and nickel contents are close to those in duplex stainless steels, which generally also contain variable additions of molybdenum. In practice, duplex grades often also have high nitrogen contents. Since nitrogen is a strong austenite stabiliser, it shifts the phase boundaries and allows the use of higher molybdenum contents without increasing the risk of forming embrittling intermetallic phases. Comparison between calculated and experimental results

The Fe-Mo-Cr and Fe-Mo-Cr-Ni systems provide a good opportunity to compare calculated phase diagrams with those determined experimentally. The Fe-Mo-Cr system was calculated from the constitutive binary systems, for which abundant experimental data are available. Although much less work has been performed on the ternary, measurements of the liquidus surface were published in 1957 [Tak57]. The experimental results differ significantly from the calculations, since they include an additional primary phase, χ, with

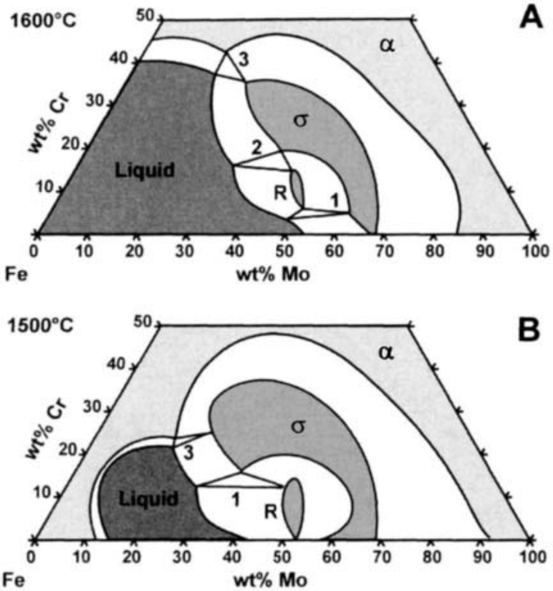
1600°C
A
α
3
σ
2
Liquid
R
1
wt% Cr
0
10
20
30
40
50
wt% Mo
Fe
60
70
80
90
100
1500°C
B
α
σ
3
Liquid
1
R

Figure 4-11-4:
Liquid/solid equilibria in the Fe-Mo-Cr system. Calculated isothermal sections at (A) 1600 °C, (B) 1500 °C. The single-phase fields are shown in grey. The tie-line triangles correspond to the three-phase fields; 1 and 2 between R, σ and liquid; 3 between α, σ and liquid. The other white areas are two-phase fields.

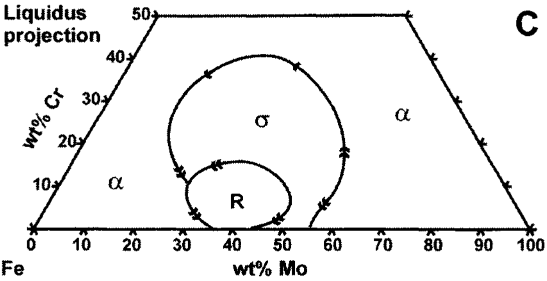
Liquidus projection
C
σ
α
α
R
wt% Cr
wt% Mo
Fe

(C) Liquidus projection showing the monovariant lines separating the σ, α and R primary solidification fields. A single arrow indicates that the reaction is eutectic in nature and a double arrow that it is peritectic. The distinction is made based on the configuration of the corresponding tie-line triangles with respect to the tangent to the monovariant line (*cf.* Fig. 4-8-1).

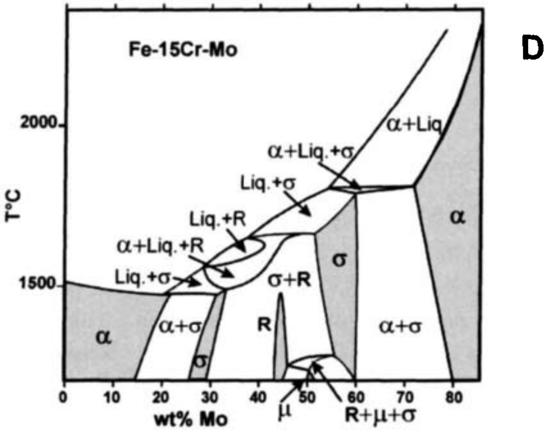
Fe-15Cr-Mo
D
2000
1500
T°C
α+Liq
α+Liq.+σ
Liq.+σ
Liq.+R
α+Liq.+R
Liq.+σ
α
σ
σ+R
α
α+σ
σ
R
α+σ
μ
R+μ+σ
wt% Mo

(D) Isopleth for 15 wt.% Cr.

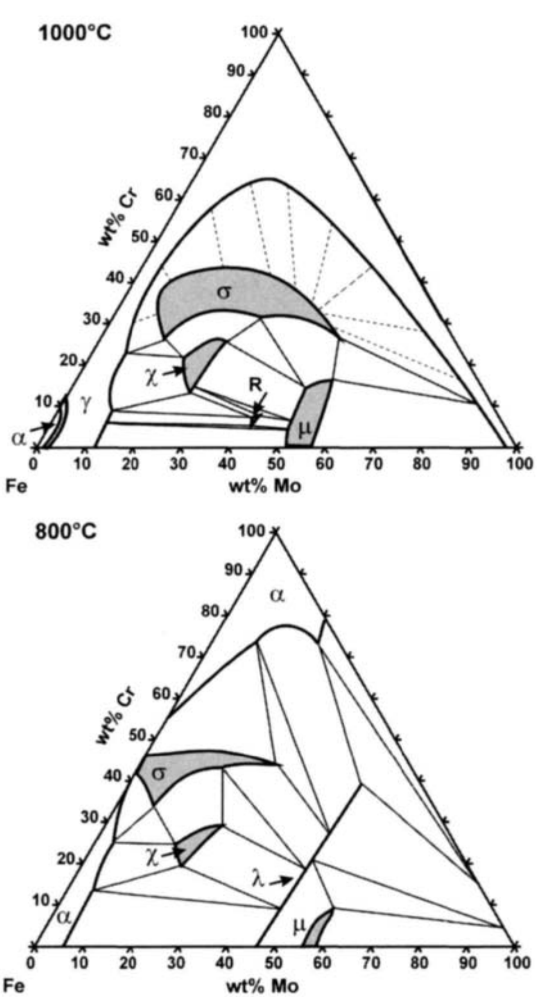
1000°C
100
90
80
70
60
50
40
30
20
10
wt% Cr
σ
χ
R
γ
α
μ
0
10
20
30
40
50
60
70
80
90
100
Fe
wt% Mo
800°C
100
90
80
70
60
50
40
30
20
10
wt% Cr
α
σ
χ
λ
α
μ
0
10
20
30
40
50
60
70
80
90
100
Fe
wt% Mo

Figure 4-11-5:
Calculated isothermal sections of the Fe-Mo-Cr system at 1000 and 800 °C. The single-phase fields shaded in grey are those corresponding to the intermetallic phases. The R phase is no longer present at 800 °C. The Laves phase λ is represented by a line, since the calculation considers a strictly stoechiometric composition *(cf.* § 3-4). Some tie-lines between the σ and α phases are indicated by the dotted lines.

a ternary eutectic between χ, R and σ at 1345 °C, *i.e.* 150 °C lower than the calculated liquidus temperature at the corresponding composition. Which version is to be believed ? The following discussion indicates the points to be considered.

Possible criticisms of the experimental results

In the case of the Fe-Mo-Cr system, the use of simple thermal analysis to measure the liquidus temperatures can be considered to be not sufficiently accurate. In particular, it is known that the solidification of intermetallic phases frequently involves marked undercooling and that stable phases can be replaced by metastable ones that nucleate more readily. It is thus possible that the authors of the experimental work in fact observed a metastable eutectic.

Figure 4-11-6:
Calculated isopleth from the Fe-Cr-Ni-Mo system. A five-phase invariant reaction leads to the disappearance of χ phase below 725 °C :
$\gamma + \sigma + \chi \rightarrow \alpha + \gamma + \sigma +$ Laves.
The table below indicates the compositions of the five phases concerned.

α	71.7Fe-21.6Cr-3.3Ni-3.3Mo
γ	73.7Fe-15.5Cr-8.5Ni-2.2Mo
χ	54.9Fe-25.7Cr-0Ni-19.4Mo
σ	51.3Fe-38.2Cr-3Ni-7.4Mo
Laves	40Fe-13.4Cr-0Ni-46.6Mo

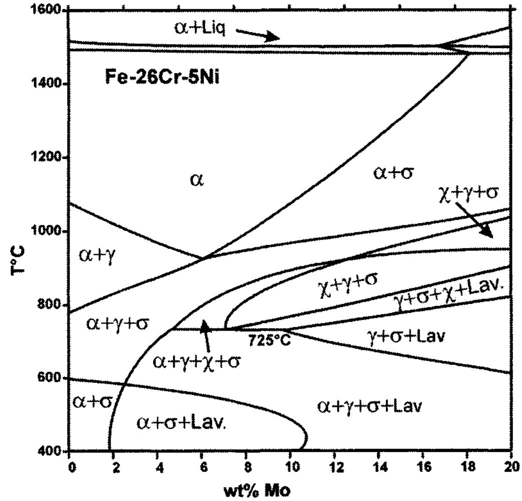

Metastable phases are quite common and often persist during long time high temperature exposures. Conversely, certain phases assumed to be stable only appear after extremely long holding times, well beyond those commonly used in the laboratory. Observations of components withdrawn from service after very long times (*e.g.* in a thermal power station, *cf.* § 20-2) often shed new light on what is the real equilibrium structure.

In the system considered here, another possible cause of error is the risk of confusion when interpreting the microstructure. In particular, a solid state transformation product of the pearlite type could readily be mistaken as being produced by a eutectic reaction. The sigma phase forms in the solid state with several different morphologies, including platelets that look like needles in cross section and lamellar cells corresponding to a discontinuous precipitation reaction. The latter can be quite coarse when formed at high temperature (*cf.* Fig. 19-7-4).

Critical aspects of the calculated phase diagrams

Although the calculated Fe-Mo-Cr phase diagram appears credible, it will probably undergo modifications in the future due to the difficulty in correctly representing the numerous intermetallic phases. The distribution in the crystal lattice of the type A elements and the transition elements of type B is performed by assigning them to sub-lattices (indicated by brackets in the formulae below). The models employed may consider three, four or five sub-lattices, depending on the accuracy required. A very detailed description is not always necessary and renders computing more difficult. The following examples taken from [Ans97] illustrate the complexity of the problem. The transition elements are named B here after [Ans97] instead of A in § 3-4.

- The Laves phase, λ-Fe_2Mo (B_2A) has a strictly stoechiometric composition in the binary system, where it is represented by a line. The situation is more complicated in ternary systems, and the structure is represented in the form $(A,B)_2(A,B)$. However, other models can be adopted, depending on whether the Laves phase is of the C14, C15 or C36 type.

- The μ-phase, Fe_7Mo_6 (B_7A_6), can be described by the formula $(A,B)_1(A)_2(A)_2(A,B)_6$, simplified to $(B)_7(A)_2(A,B)_4$ in the case of the Fe-Mo-Cr system.
- The σ phase is represented geometrically by a field that extends in all directions (Fig. 4-11-5), proving that the substitution elements are not limited to two selective sub-lattices. It is described by the formula $(A,B)_{16}(A)_4(A,B)_{10}$, simplified to $(A,B)_{16}(A)_4(B)_{10}$.
- The χ phase is the most complicated in terms of crystal structure, with 58 atoms per unit cell. There have been only a limited number of attempts to model it, since it occurs less frequently than σ phase in common systems. An appropriate formula is $(B)_{24}(A)_{10}(A,B)_{24}$.

For example, to represent the phase equilibria in duplex stainless steels (Fig. 4-11-6), it is necessary to consider the Fe-Mo-Cr-Ni quaternary system, with certain simplifications. For most of these intermetallic compounds, their nickel content is assumed to be zero. However, experimental analyses show them to contain small amounts of this element (4 to 5 % in χ phase and 4 to 6 % in Laves phase for types 316 and 317* stainless steel [Pec77]). The consequence of neglecting nickel in the calculations is an inaccuracy in the phase boundaries. Another example for a duplex stainless steel showed a difference of 100 °C between the experimental and calculated values of the temperature below which σ phase appears [Nil00].

4-12 The Fe-C-V system

The limiting binary systems, Fe-V and V-C

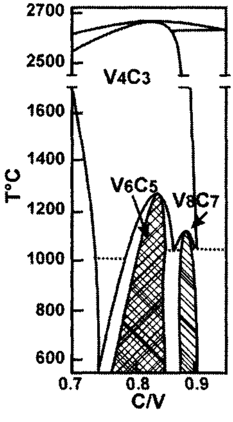

Figure 4-12-1:
Part of the V-C phase diagram, from [Bil72].

The Fe-V phase diagram is similar to that for the Fe-Cr system, with complete miscibility between the terminal phases at high temperature. On the iron-rich side, the gamma loop is very narrow, the associated two-phase region extending to less than 2 % V. A sigma type phase, FeV, forms in the solid state below 1219°C (*cf.* compilation [Rag84]).

The V-C system includes two carbides, VC and V_2C. The VC carbide is always sub-stoechiometric, and at high temperature, the composition in equilibrium with austenite is typically V_4C_3. This phase transforms at lower temperatures to produce two ordered compounds with compositions V_8C_7 or V_6C_5. (Figure 4-12-1). The carbon sub-lattice loses its cubic arrangement. The V_6C_5 carbide has been identified as having either a monoclinic or orthorhombic structure [Bil72], [Kes88b]. In fact, the commonly cited composition V_4C_3 is not found in the eutectic constituents of vanadium-containing steels and cast irons, but rather V_6C_5, or V_8C_7 for hypereutectic compositions.

The Fe-V-C system

The phases present in the Fe-V-C ternary system are those of the binaries, and possibly a ternary carbide η–Fe_3V_3C. The existence of the η and V_2C phases is limited to the part of the diagram where the atomic V/C ratio is greater than one. The Fe-VC section has been extensively studied and presented as a quasi-binary (Fig. 4-12-2 A). However, this is not really true, since the monovariant line UE (Fig. 4-12-2 B) shows no minimum or maximum corresponding to a quasi-binary eutectic. In addition, the monovariant line separating δ and γ crosses the section. However, in the solid state, the α-VC_{1-x} tie-lines are close to the quasi-binary plane. The system includes a ternary eutectic γ-Fe/M_3C/MC. The 0.5 % V isopleth shown in Figure 4-12-2 C is of interest for steels and reveals an extensive range where VC carbide is in equilibrium with either austenite or ferrite, indicating that secondary precipitation hardening is possible throughout this region. Similar isopleths for larger vanadium contents show that the vanadium carbide becomes stable up

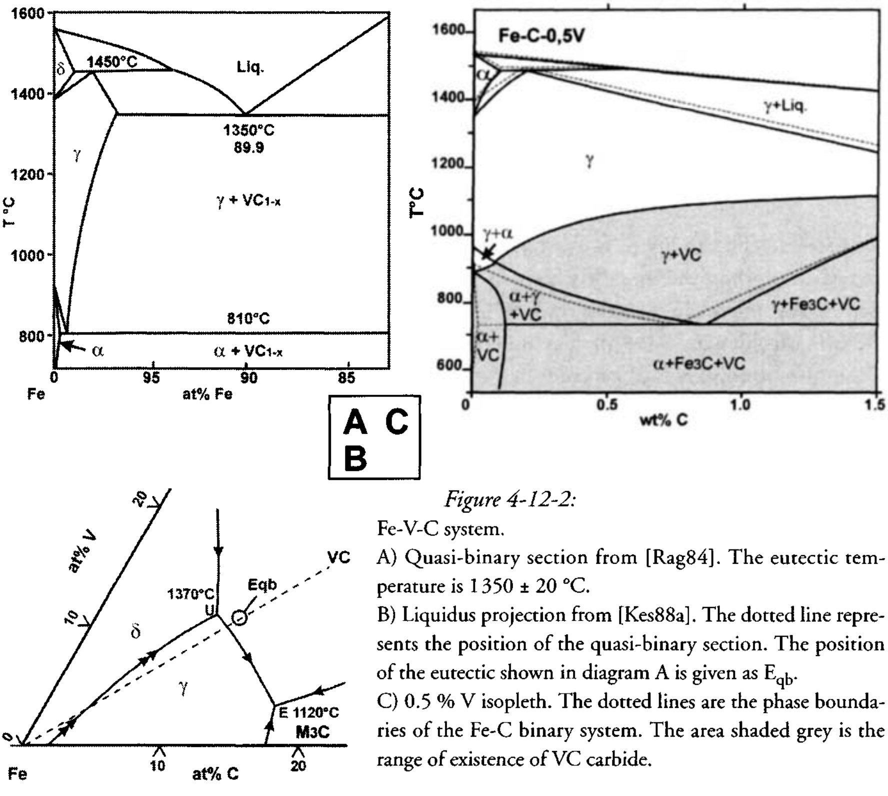

Figure 4-12-2:
Fe-V-C system.
A) Quasi-binary section from [Rag84]. The eutectic temperature is 1350 ± 20 °C.
B) Liquidus projection from [Kes88a]. The dotted line represents the position of the quasi-binary section. The position of the eutectic shown in diagram A is given as E_{qb}.
C) 0.5 % V isopleth. The dotted lines are the phase boundaries of the Fe-C binary system. The area shaded grey is the range of existence of VC carbide.

to even higher temperatures. In practice, it is impossible to dissolve these carbides with conventional austenitizing treatments.

Other Fe-C-X systems, where X is an element of groups IV or V

The Fe-C-X ternary systems, where X is an element belonging to either group IV (Ti, Zr, Hf) or group V (V, Nb, Ta), have many similar features. They form cubic carbides of the M_2C or MC types. At high temperatures, niobium carbide adopts the stoechiometric composition Nb_8C_7. All these elements form quasi-binary eutectics γ/MC with Fe, Co and Ni. Hollek has compiled 18 Fe-MC quasi-binary sections, all similar to Fe-VC (Figure 4-12-2 A). In the ternary systems, the eutectic γ-Fe/M_3C/MC is known to exist for titanium, tantalum and niobium [Kes88a], [Kes87].

The presence of groups IV and V metals markedly reduces the activity of carbon in solution in the austenite and ferrite, leading to solubility products that are already low at 900 °C and become increasingly small as the temperature falls. Among the MC carbides formed by the group V elements, vanadium carbide is the least refractory in nature, with a melting point around 2500–2600 °C, compared to the extreme value of about 4000°C for TaC. It also has the highest solubility product, several orders of magnitude greater than those of the other MC carbides. Consequently, austenite can contain a greater amount of carbon in the presence of vanadium than for the other MC formers. This is important for many low alloy steels, since the ability to form martensite generally requires a certain amount of carbon in solution in the austenite. The ability to form stable carbides, as well as nitrides and carbonitrides, is used to strengthen the so-called high strength low alloy (HSLA) steels, sometimes also referred to as microalloyed steels (*cf.* § 17-2).

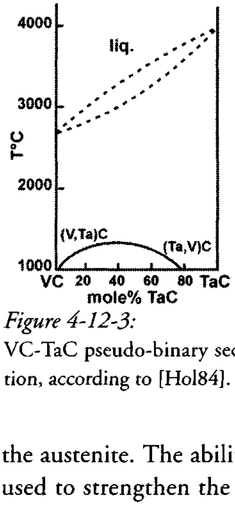

Figure 4-12-3:
VC-TaC pseudo-binary section, according to [Hol84].

The MC carbides and MN nitrides are completely miscible at high temperatures, leading to the formation of mixed carbides or carbonitrides, which decompose at temperatures below about 1200 °C. An example is shown in Figure 4-12-3 for the VC-TaC system, the VC-NbC diagram being almost identical [Hol84]. At lower temperatures (*e.g.* 600 °C), the decomposition is extremely sluggish, [Ino01] (*cf.* § 20-1).

4-13 Mixed carbides

Little detailed information is available for quaternary phase diagrams and higher order systems, so that the experimental basis for calculations is very poor. For the design of new steels, the choice of alloying elements is usually based on known qualitative effects, such as their tendency to form carbides, or to stabilise ferrite or austenite. It is necessary to predict whether a new alloying element will be liable to participate in the carbides or other phases

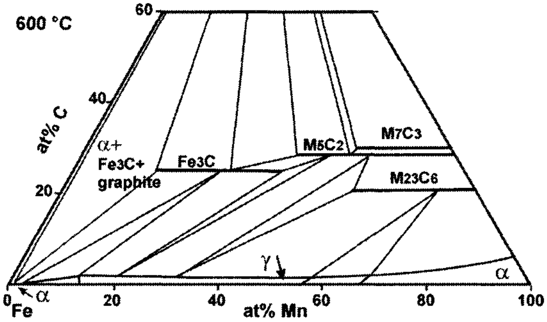

Figure 4-13-1:
600 °C section of the Fe-Mn-C system, calculated for stable equilibrium with graphite. In the metastable system, the cementite field extends up to the Fe-C binary. Manganese appears to stabilise cementite.

already present. A first indication is provided by consideration of the crystal structures. Elements that form phases of similar crystal structure often show significant mutual solubility. If an element Y is not soluble in a carbide XC in the system X-Y-C, it will be unlikely to be so in a system containing a larger number of elements. The behaviour in systems not containing iron often reveal interactions that can be transposed (with precaution !) to iron-based alloys. From this standpoint, the extensive compilation of carbon and nitrogen-based ternary phase diagrams published by Holleck [Hol84] proves extremely useful. A number of examples of calculated isothermal sections are given below. When the phase equilibria remain valid at lower temperatures, the solubility ranges tend to become smaller, and never to increase.

The transition metals at the top of groups VI (Cr, Mo, W) and VII (Mn) form two similar carbides, $Cr_{23}C_6$/$Mn_{23}C_6$ and Cr_7C_3/Mn_7C_3. These phases can form as primary solidification products in the Cr-C and Mn-C systems. The corresponding liquidus surfaces in the Fe-Cr-C and Fe-Mn-C systems cover a wide range of compositions. The stability of M_7C_3 decreases with falling temperature and it tends to be replaced by $M_{23}C_6$. Both these carbides can accept considerable amounts of iron in substitution for chromium, as illustrated by the 600 °C isotherms for the Fe-Cr-C and Fe-Mn-C systems in Figures 4-13-1 and 4-13-2 A and B. They can also dissolve significant proportions of cobalt, and to a lesser extent, nickel, niobium, vanadium, molybdenum and tungsten. The latter two elements have greater solubilities in $M_{23}C_6$ than in M_7C_3, contrary to the situation for iron (Figures 4-13-1 and 4-13-2 A and B) [Cha72]. In $Cr_{23}C_6$, only 8 of the 92 chromium atoms in the unit cell can be replaced by tungsten or molybdenum [Hab66].

The heavy metals from group VI, W and Mo, form both M_2C carbides and hexagonal MC carbides (not to be confused with the cubic MC carbides). The carbides MoC and WC show complete mutual solubility. The stoechiometric ratio (Mo,W)C is strictly respected and they accept practically no other element in solid solution.

The Mo_2C and W_2C carbides also show total miscibility. The carbon content can deviate slightly from the nominal composition, varying by 2 to 3 %. They can dissolve a considerable amount of chromium (Fig. 4-13-2 C), together with limited amounts of titanium, tantalum, vanadium and niobium, but do not accept iron, cobalt or nickel.

Figure 4-13-2:

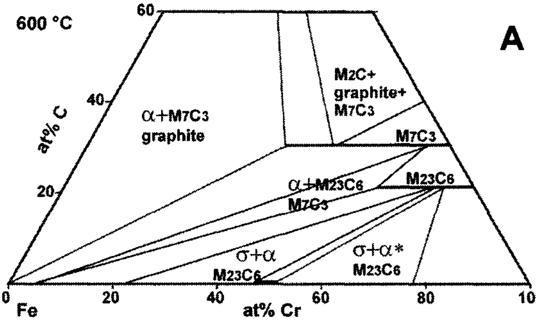
600 °C
A
60
40
20
at% C
α+M7C3
graphite
M2C+
graphite+
M7C3
M7C3
M23C6
α+M23C6
M7C3
σ+α
M23C6
σ+α*
M23C6
0
Fe
20
40
at% Cr
60
80
100

(A) Calculated 600 °C isothermal section of the stable Fe-Cr-C (graphite) system.

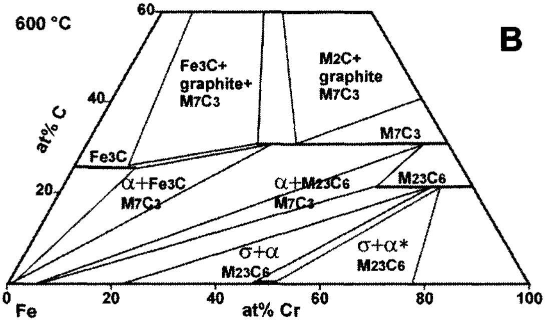
600 °C
B
60
40
20
at% C
Fe3C+
graphite+
M7C3
M2C+
graphite
M7C3
M7C3
Fe3C
α+Fe3C
M7C3
α+M23C6
M7C3
M23C6
σ+α
M23C6
σ+α*
M23C6
0
Fe
20
40
at% Cr
60
80
100

(B) Calculated 600 °C isothermal section of the metastable Fe-Cr-C (cementite) system. The cementite field extends up to the Fe-C binary.

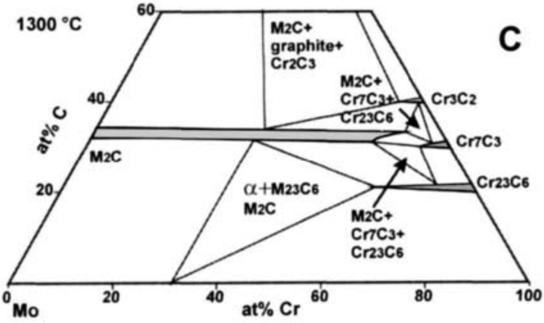
1300 °C
C
60
40
20
at% C
M2C+
graphite+
Cr2C3
M2C+
Cr7C3+
Cr23C6
Cr3C2
Cr7C3
M2C
α+M23C6
M2C
Cr23C6
M2C+
Cr7C3+
Cr23C6
0
Mo
20
40
at% Cr
60
80
100

C) 1300°C isotherm of the Cr-C-Mo system, based on the experimental plot of [Cha72].

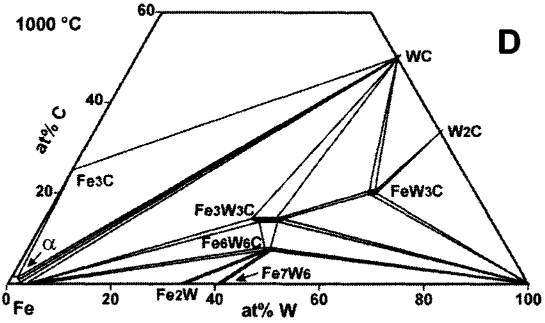
1000 °C
D
60
40
20
at% C
WC
W2C
Fe3C
FeW3C
Fe3W3C
Fe6W6C
α
Fe7W6
Fe2W
0
Fe
20
40
at% W
60
80
100

(D) 1000 °C section of the Fe-W-C system, based on the experimental plot of [Pol70].

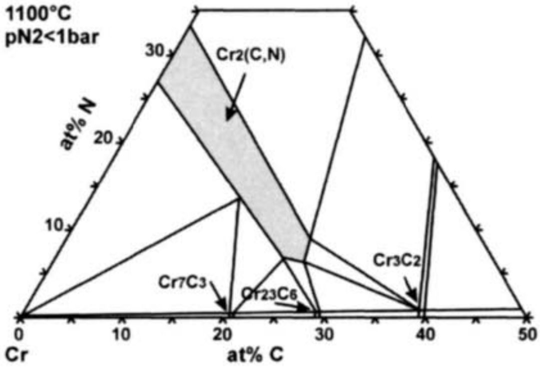

Figure 4-13-3: Chromium-rich region of the Cr-N-C system. 1100 °C isothermal section.

The η-carbides are two ternary carbides of the type Mo_3Fe_3C and W_6Fe_6C, in which iron can be replaced by another transition metal and molybdenum by another heavy element, giving the general formula $(Mo,W,Nb,Ta)_x(Mn,Fe,Co,Ni)_xC$, with x equal to either 3 or 6. The Fe-W-C diagram shown in Figure 4-13-2 D is an experimentally determined version in which the two η-carbides are distinct [Pol70]. Whether or not they are really two different species or a single phase with a wide range of composition is still the subject of debate. The calculated diagrams consider only a single phase.

Among the group VIII metals (Fe, Co and Ni), only iron forms a carbide (M_3C type) that is stable under normal conditions. In fact, the tendency for iron to form carbides is similar to those of Cr in group VI and Mn in group VII. However, Fe_7C_3 is only metastable. Cementite, Fe_3C, can accept a large amount of manganese (Fig. 4-13-1). Although the solubility of chromium in cementite is also relatively large, high chromium contents lead rather to the formation of the chromium-rich carbides $(Fe,Cr)_7C_3$ and $(Fe,Cr)_{23}C_6$. In contrast, the solubility of silicon and nickel in M_3C appears to be negligibly small, a fact that is probably related to their retarding effect on the pearlite transformation (*cf.* § 10-3). Molybdenum and tungsten can dissolve in M_3C in amounts up to about 5 %. Higher contents lead to a specific carbide, designated ζ, with stoechiometry $Fe_2(Mo,W)C$. The crystal structure is close to that of cementite and the two phases are often confused. Indeed, ζ carbide is sometimes referred to as molybdenum cementite.

The principal nitrides encountered in steels are VN, AlN, TiN, BN and Cr_2N. VN is fully miscible with the nitrides of the group IV elements : Ti, Zr and Hf, while Cr_2N accepts significant amounts of Mo. Nitrogen has very limited solubility in the M_7C_3, $M_{23}C_6$ and M_6C carbides (Fig. 4-13-3). In fact, the only two carbides in which the solubility of nitrogen is sufficient for them to be considered as carbonitrides are cubic MC (VC type) and M_2C (Mo_2C type).

Although the phase diagrams for complex iron-based systems corresponding to steels are often not available, the systems containing N, B and C and the metallic elements provide a useful guide [Hol84], [Rog98]. $M_{23}C_6$ carbide is known to be able to accept significant amounts of boron.

5

The formation of solidification structures

Metals and alloys are almost always processed in the liquid state at some stage during their manufacture. Subsequent solidification leads to characteristic microstructures, whose examination enables identification of the mechanisms involved. The effects may sometimes persist even after lengthy hot and cold working sequences, so that it is important to closely control the solidification conditions.

5-1 Solute partitioning phenomena during solidification

Equilibrium state and kinetic effects

During solidification of a liquid containing several elements, the first solid which forms generally has a composition different to that of the liquid. For example, ice formed on salty water contains less salt. The composition of the remaining liquid changes and that of the solid in equilibrium with it also. As the temperature falls, if diffusion is unable to ensure homogeneity, composition gradients will appear in the solid. When solidification is complete, the average composition must obviously be the same as that of the initial liquid.

For the sake of simplicity, the description given below considers a system of only two constituents, designated *solvent* and *solute*. The same reasoning can be generalized to multi-component systems. The approach followed is to consider the equilibrium state corresponding to the imposed conditions and then to analyse kinetic effects, involving diffusion or other transient phenomena.

Reversible solidification - the lever rule

The concept of reversible solidification implies several assumptions :

- the liquid and solid phases are at the same temperature
- each phase has a unique (uniform) composition, X_S for the solid and X_L for the liquid
- the two phases are at equilibrium at the interface.

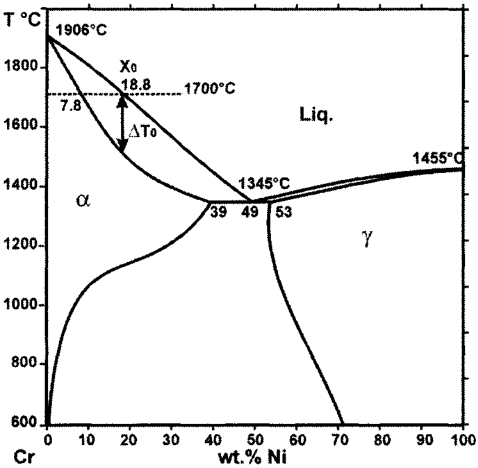

Figure 5-1-5:
Calculated Cr-Ni phase diagram. The figures represent the solubility limits at the eutectic temperature and the 1700 °C tie-line used to calculate the partition coefficient and the slope of the liquidus.
$X_0 = 18.8$ %
$X_S = 7.8$ % at 1700 °C
$X_L = 18.8$ % at 1700 °C
k=7.8/18.8=0.4
k>1

Application of the conservation of atoms to the second condition leads to the *lever rule* or *inverse segment rule* (§ 4-1). For a system of n atoms this can be written :

$$\text{Lever rule} \quad n\,X_0 = n\,f X_S + n\,(1-f)\,X_L \tag{5-1-1}$$

It can be used to calculate the solid fraction f when the initial concentration and those of the solid and liquid phases are known :

$$f = \frac{X_L - X_0}{X_L - X_S} \tag{5-1-2}$$

The condition of *equilibrium at the interface* implies that the liquid and solid compositions at this location are determined by a single variable, the temperature. The fraction of solid f represents the extent of the liquid/solid transformation and increases as the temperature falls. A similar reasoning can be applied when the temperature rises, and f then decreases. This is the concept of reversible transformation. The successive equilibria are represented by the phase diagram, and can often be simplified by the consideration of only two parameters, the equilibrium partition coefficient k, given by $k = X_S/X_L$, and the slope of the liquidus m, given by:

$$T = T_{Sth} - m \cdot X_L \tag{5-1-3}$$

A third parameter, the *solidification range*, $\Delta T_0 = T_L - T_{Sth}$ where T_L and T_{Sth} are the liquidus and solidus temperatures, can be derived from them (*cf.* Fig. 5-1-5), and is extremely useful for characterising the solidification behaviour.

$$\Delta T_0 = -\,mX_0 \cdot \left(\frac{1}{k} - 1\right) \tag{5-1-4}$$

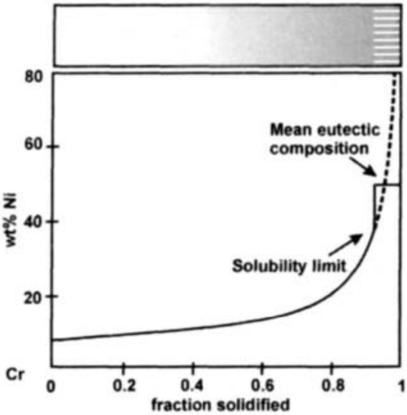

Figure 5-1-7:
Solute distribution in the solid during solidification of a Cr-7.8 %Ni alloy, plotted using the Scheil-Gulliver (S-G) relation, with the approximation k=0.4 (Fig. 5-1-5).
For the sake of simplicity, solidification is assumed to occur unidirectionally along the length of a bar. The shading represents the resulting concentration gradient. The full lines represent local phase equilibrium, while the dashed line is the extrapolation of the S-G relation.

Non-reversible conditions - the Scheil-Gulliver model

The condition of reversibility implies that the whole of the solid remains in equilibrium by complete diffusion. This situation is rarely observed in practice and a better representation of real behaviour is given by the Scheil-Gulliver model, which makes the following assumptions

- equilibrium is maintained at the interface
- the liquid is perfectly homogeneous
- there is no diffusion in the solid.

The third of these assumptions means that the lever rule no longer applies in the same way. The composition of the solid formed at a particular temperature remains fixed, with no exchange of solute, either with the liquid or with the solid formed at higher temperatures. However, as for the lever rule, the solid/liquid system is assumed to be confined, that is, the total number of atoms remains unchanged after the transformation. For a small solidification increment $f \rightarrow f + df$, this gives :

$$(X_L - X_S)\, df = (1-f)\, dX_L \qquad \text{(5-1-6)}$$

where X_S is the concentration of solid corresponding to the fraction f.

The first condition imposes $X_S = kX_L$. When k can be considered to be constant over the whole of the solidification range, integration of the above relation from X_0, the initial liquid concentration, gives the Scheil-Gulliver relation :

$$X_S = kX_0\,(1-f)^{-(1-k)} \qquad \text{(5-1-8)}$$

Figures 5-1-5 and 5-1-7 show an example application in the Cr-Ni system. When $k<1$ (as in this case), the solute is rejected into the liquid, which becomes gradually enriched as solidification proceeds. The integrated relation predicts infinite enrichment at the end of solidification, when f tends to one. In reality, the composition of the solid cannot exceed the solubility limit given by the phase diagram. The liquid corresponding to this limit is at the eutectic composition and solidifies to two phases, whose average composition is that of the eutectic.

The total area beneath the X_S *vs.* f curve represents the mean composition, that is the initial composition of the liquid. The local area beneath the curve is larger at the end of the bar, indicating that the rejected solute has accumulated in this region. The lower the partition coefficient k, the greater the solute rejection.

If $k > 1$, the opposite situation occurs, and pure solvent is formed at the end of solidification.

Limitations of the simplified formalism

The Scheil-Gulliver (S-G) relation was initially proposed by Gulliver in 1922 and independently reformulated by Scheil in 1942. It is still used as the basis for the analysis of segregation phenomena, but has numerous shortcomings. Thus, to consider the partition coefficient *k* and liquidus slope *m* as being constant is to take the liquidus and solidus as being straight lines. Although this approximation can be generalised to multi-component systems at the beginning of solidification, later parts of the solidification path require a more appropriate model. A more accurate approach is to use a stepwise analysis, introducing representative data for the phase equilibria at each stage.

Furthermore, the hypotheses of the S-G model are extremely restrictive. In particular, the assumption that the liquid is perfectly homogeneous is plausible only in the case of vigorous stirring, since natural convection is not sufficient. Even so, a boundary layer exists near the interface that is not affected by stirring. The assumption of no diffusion whatsoever in the solid is also unrealistic, and solute elements will tend to diffuse at different rates, depending on their nature, to reduce concentration gradients (see § 6-3). Interstitial elements such as carbon, nitrogen and oxygen have high diffusivities, whereas those of the substitutional elements can effectively be considered to be negligible to a first approximation.

5-2 Local solute partitioning

The diffusion layer at the solid-liquid interface

If we focus attention on the liquid-solid interface I and its immediate vicinity, the solid composition C_S^I is different to that of the liquid C_L^I from which it forms. If the interface advances at a velocity V, solute transfer creates fluxes in both the liquid and solid. The latter flux is usually neglected, so that the solute balance per unit time becomes :

$$V(C_L^I - C_S^I) = -D_L \left(\frac{\partial C_L}{\partial C_z}\right)_I \qquad \text{(5-2-1)}$$

The compositions are represented here by the *volume* concentrations C_L^I and C_S^I to take into account the fact that the equation involves fluxes. If equilibrium is assumed to exist between the solid and liquid at the interface and if the solidifying bar is considered to have

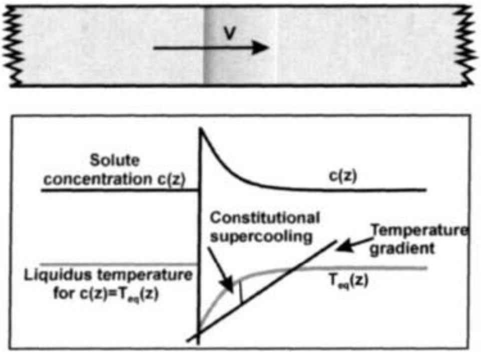
V
Solute concentration c(z)
c(z)
Constitutional supercooling
Temperature gradient
Liquidus temperature for c(z)=T$_{eq}$(z)
T$_{eq}$(z)

Figure 5-3-1:
Planar front steady state solidification, showing the diffusion layer and constitutional supercooling. The bold curve C(*z*) represents the solute distribution in the liquid ahead of the interface, expressed by relation 5-2-3. The grey curve represents the variation of the equilibrium liquidus temperature for the corresponding liquid composition. The bold straight line is the imposed temperature gradient.

infinite length and to move continuously through a temperature gradient, then $C_S^I = C_0$ (the overall composition of the alloy) and $C_L^I = C_0/k$. The steady state chemical gradient G_C at the interface is given by :

$$G_C = -\frac{V}{D_L} C_0 \left(1 - \frac{1}{k}\right) \tag{5-2-2}$$

where D_L is the diffusivity in the liquid. This equation can be integrated, starting from the position $z=0$ at the interface, to obtain the solute distribution in the liquid ahead of the interface (Figure 5-3-1) :

$$C(z) = C_0 + C_0 \frac{1-k}{k} exp\left(-z \cdot \frac{V}{D}\right) \tag{5-2-3}$$

Solute elements for which k is less than one are rejected into the liquid and the concentration decreases with distance from the interface $(G_C < 0)$. Conversely, solute elements for which k is greater than one are absorbed by the solid and their concentration increases with distance from the interface $(G_C > 0)$. The excess or deficiency is spread over a region called the *diffusion layer*, whose thickness can be assimilated to $\delta = D_L/V$.

5-3 The growing solid interface

Stability of a planar interface

A first approach is to consider the stability of the diffusion layer (Fig. 5-3-1). For each value $C(zi)$ there is a single equilibrium liquidus temperature $T_{eq}(zi)$. These values must be compared to the effective temperature gradient $T(z)$ imposed by the furnace. In the case shown in Figure 5-3-1, in a zone immediately adjacent to the interface, the liquid has an effective temperature that is lower than the local equilibrium liquidus point. This is a region of *constitutional supercooling* :

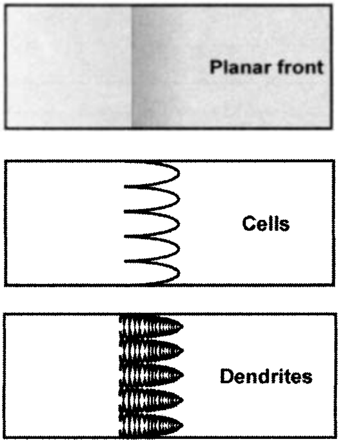

Figure 5-3-5:
Variation of the solid-liquid interface geometry as a function of the relative values of G and V.
Planar front : $V \leq V_{PC}$

Cells : $V > V_{PC}$

Dendr*ites* : $V \gg V_{PC}$

$$\Delta T = T_{eq(z)} - T_{(z)} \tag{5-3-2}$$

The supercooled layer disappears in the limiting situation where the imposed temperature gradient $T(z)$ becomes tangent to $T_{eq}(z)$. This condition is formulated by the following criterion for constitutional supercooling [Til53], where the suffix I indicates the equilibrium value at the interface :

$$\left(\frac{G}{V}\right)_{critique} = -\frac{1}{D_L}\frac{\partial T_{eq}}{\partial C_L^I}\cdot\left(C_L^I - C_S^I\right) \tag{5-3-3}$$

Assuming for simplicity that the temperature gradient G is fixed, there is found to exist a critical growth velocity, designated V_{PC}, beyond which the planar solidification front takes on a cellular morphology :

$$V_{PC} = \frac{D_L \cdot G}{\Delta T_0} \tag{5-3-4}$$

When there is no constitutional supercooling, the interface is planar, and follows an isotherm close to the liquidus, the difference being due to normal growth related supercooling. If a steady state regime is attained, it is given by ΔT_0 in relation 5-1-4. Ahead of the interface, the temperature is everywhere above the local equilibrium liquidus, so that solidification is thermodynamically impossible. The composition of the solid is uniform in all planes or surfaces parallel to the interface.

In the presence of constitutional supercooling, a planar front becomes unstable. Experience shows that a network of local depressions forms, deepening to grooves, delimiting central dome-shaped protuberances, the morphology being described as cellular Fig. 5-3-5, middle). For higher degrees of constitutional supercooling, the extent of local undercooling increases rapidly with distance from the interface, and the protuberances become

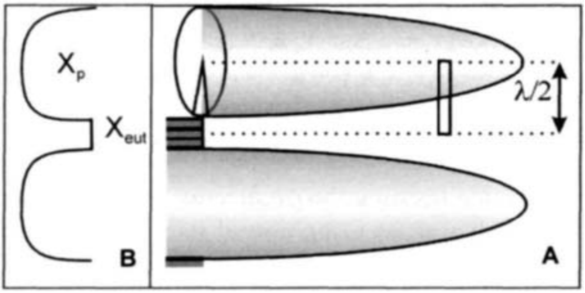

Figure 5-3-6:
A) Schematic illustration of cellular growth with rejection of solute into the separating grooves.
B) Concentration profile across the cell diameters. X_p is the solute concentration at the cell centres, while the maximum value in the bottom of the grooves is here represented as being that for the formation of a eutectic, X_{eut}.

sharper and develop secondary arms, and sometimes even tertiary ones. These branched structures are known as dendrites (Fig. 5-3-5, bottom).

Consequences of cellular and dendritic solidification

The propagation of a solidification front leaves traces that are subsequently visible as the solidification structure, and which vary depending on whether the front was planar, cellular or dendritic.

In the case of a *planar front*, solidification takes place at a single temperature and the composition is uniform in all planes parallel to the interface. When conditions of steady state solidification are not achieved, the composition varies in the growth direction, for example, according to the S-G law. This leads to classical macrosegregation.

When the solidification front is *cellular or dendritic*, a frequent simplification is to consider it as a set of adjacent protuberances, as illustrated schematically in Figure 5-3-6 A.

Consider a section perpendicular to the protuberance axes, fixed with respect to the material. The movement relative to the furnace displaces the temperature gradient and the uniform temperature in the section falls. The first points to solidify as the front moves are the tips of the cells or dendrites, where the composition is X_p. As the front advances further, the proportion of solid increases laterally around the tips until the section is completely solidified (Figure 5-3-6). The region surrounding the protuberances is called the intercellular or interdendritic space or groove. For the sake of simplicity, Brody and Flemings assumed the liquid in this zone to be homogeneous and confined, with no exchanges with other sections [Bro66], [Bow66]. Exchanges of solute occur only laterally, perpendicular to the direction of displacement of the front. In these conditions, the S-G law applies in the transverse growth direction. All that is required is to establish a relation between the fraction solidified and the local geometry of the protuberances (see § 6-3).

The result is a modulation in the solute concentration in the directions transverse to the overall movement of the solidification front. If k is less than one, the concentration is a minimum X_p at the protuberance axes and increases with distance from the axes up to the solubility limit. Beyond this level, a second phase appears, perhaps in the form of a eutectic, as indicated in Figures 5-1-7 and 5-3-6. If k is greater than one, the concentration decreases from a maximum X_p at the axis to zero (pure solvent). In all cases, the periodicity of the transverse modulation in solute concentration is equal to the cell size or the primary dendrite arm spacing λ_p. It corresponds to the *phenomenon of microsegregation* (Fig. 5-3-6 B).

Factors determining the occurrence of planar front, cellular or dendritic growth and the formation of stable and metastable phases

The kinetic phenomena associated with the growth of a solid/liquid front can be described theoretically in at least three simple cases [Kur89] :

- destabilisation of a planar front by the formation of periodic disturbances (Mullins, Sekerka school)·
- the growth of isolated protuberances (Kurz, Glicksman, Trivedi school)
- periodic sets of protuberances considered as a growing array (Hunt).

The driving force for solidification is the degree of supercooling $\Delta T = T_{eq} - T$, the difference between the liquidus temperature of the alloy and the local temperature of the interface. The supercooling can be considered to have four origins [Kur89] :

$$\Delta T = \Delta T_t + \Delta T_c + \Delta T_r + \Delta T_k \qquad (5\text{-}3\text{-}7)$$

where ΔT_t is the thermal supercooling due to the temperature gradient G, ΔT_c is the chemical supercooling related to the concentration gradient G_c (Relation 5-2-2), ΔT_r is the supercooling due to curvature of the interface, which modifies the local state of equilibrium, and ΔT_k is the kinetic supercooling associated with bonding of the atoms at the interface, often taken as being negligible.

The different contributions to ΔT are in fact interdependent. For example, the distribution of rejected solute affects the radius of the dendrite tip, which in turn influences the radial diffusion flux.

For a given alloy, if steady state growth occurs with a planar front, the supercooling is ΔT_0. However, under real conditions, the degree of supercooling depends on G and V. For the sake of simplicity, we will consider G to be fixed, as is usually the case in unidirectional solidification experiments. The periodic disturbance and protuberance set models show that planar front growth cannot occur between two limiting values of V. It is possible for either low rates $(V < V_{PC})$ or very high rates $(V > V_{AC})$.

V_{PC} is the planar/cellular transition related to constitutional supercooling (Relation 5-3-3). A positive effective temperature gradient stabilises planar front growth.

V_{AC} is the absolute chemical rate, which depends on the interface energy via the Gibbs-Thompson parameter Γ:

$$V_{AC} = \frac{\Delta T_0 \, D_L}{k\Gamma} \qquad (5\text{-}3\text{-}8)$$

The value of Γ is about 10^{-7} m.K for the majority of liquids in equilibrium with their solid. The physical interpretation of this limit is that when V increases, the periodicity of

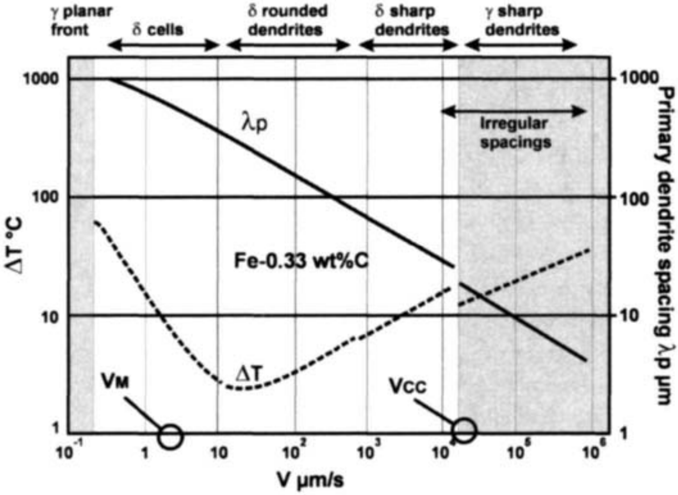

Figure 5-3-9:
Steady state solidification of an Fe-C alloy at different growth rates V in a temperature gradient of 5 °C/cm. The solid line represents the primary dendrite arm spacings λ_p, while the dashed line is the overall supercooling ΔT. There is a discontinuity due to a transition from ferrite (grey areas) to austenite as the primary solidification product. The morphologies corresponding to each regime are indicated. To give an idea of the solidification rates concerned, the magnifying glasses show the typical rates used for single crystal growth (V_M) and the continuous casting of steel (V_{CC}).
The graph was obtained using Oxford University's "*Alloy*" software [Hun97a].

the protuberances diminishes. The distance over which significant diffusion can occur becomes very small, and the limit corresponds to the value for which segregation becomes negligible.

The results are exploited in the form of diagrams in which ΔT, λ or R are plotted against V, where λ is the periodicity of the solidification structure and R the dendrite tip radius [Tri94]. In situ observations on transparent "alloy" materials have demonstrated the trend for protuberances to form lateral branches and the relation between secondary arm spacings and the dendrite tip radius [Esa85].

An example is shown using a numerical code based on Hunt's approach [Hun96]. The overall supercooling is calculated as a function of the temperature gradient G and the growth rate V, with the choice of three cooling modes. The results have been calculated for an Fe-0.33 wt.%C alloy (1.5 at.% C), close to the peritectic transformation point (Fig. 5-3-9). This composition was chosen because it allows competition between austenite and ferrite as the primary solidification phase. For each combination of G and V, the solid phase formed, considered as the *stable phase*, is that for which the interface temperature T_I is the highest :

$$T_I = T_{eq}^{ph} - \Delta T^{ph} \text{ where ph = austenite } \gamma \text{ or ferrite } \delta. \qquad (5\text{-}3\text{-}10)$$

Because of this condition, the primary solid phase changes as a function of V for the alloy considered. The phase diagram predicts a liquidus temperature of 1512 °C for δ ferrite and 1506 °C by extrapolation for austenite.

The composition of the solid formed locally is that for the equilibrium at $T = T_I$. In the case of planar front growth, the supercooling is equal to ΔT_0 and the composition of the solid is that of the alloy as a whole (*cf.* phase diagram, Fig. 5-1-5). For the low value of *G* and the relatively high solute concentration chosen in this example, the calculations predict planar front solidification only for unrealistic growth rates. The use of higher growth rates would shift the curves to the right. At intermediate growth rates, it is the protuberances on the front that are at the temperature T_I. The tips of the cells or dendrites have the composition corresponding to equilibrium at this temperature, the difference with respect to the overall alloy composition being greater the larger the degree of supercooling. In the grooves between the protuberances, the local composition and temperature vary periodically, up to the values for eutectic growth. In the same way that the supercooling goes through a minimum at intermediate solidification rates, the composition at the dendrite tips goes through a maximum, *which is the closest approach to the tie-line on the phase diagram.*

As it advances, the solidification front sweeps through a solute-enriched layer whose thickness δ decreases with increasing growth rate. Whether δ is larger or smaller than half the dendrite or cell spacing affects the morphology and determines the transitions between cells and dendrites and between round- and sharp-tipped dendrites. The calculations predict two dendritic growth regimes, one in which the regular dendrite spacing is stabilised by mutual interactions and another in which such stabilisation is not possible [Wan97b].

> *In a range of compositions close to a peritectic transformation, the system is highly sensitive to the solidification conditions. Another example of such a critical composition, where the growth rate can favour one phase rather than another, is that of the 18 %Cr-10 %Ni stainless steels, which lie close to the L/α/γ monovariant line in the Fe-Ni-Cr phase diagram. These alloys have been studied experimentally by directional solidification and differential thermal analysis, the latter technique clearly revealing the occurrence of supercooling [Bob88], [Fre72]. The primary phase can change from austenite to ferrite as a function of the solidification rate. It is the austenite that can show the largest extent of supercooling.*

Primary dendrite arm spacings

The array model effectively confirms the observed changes in solidification structure with *G* and *V* and predicts their variation with a constant based on the thermodynamic properties of the system at the temperature considered [Hun77] :

$$\lambda_p = const \cdot V^{-1/4} \cdot G^{-1/2} \qquad (5\text{-}3\text{-}11)$$

The previous reasoning assumes that G and V are controlled and that a steady state solidification regime prevails. This is true in particular for unidirectional solidification experiments. However, the practical conditions under which steel solidifies in an ingot or a continuously cast bloom or slab are such that both G and V change locally. Moreover, comparison is possible only in the region of columnar solidification (see § 15-1). This generally concerns only a relatively narrow zone close to the skin. Even in this case, micrographs are difficult to interpret, since measurements of primary dendrite spacings must be made in a plane perpendicular to the solidification front, and this is usually difficult to achieve in a fully solidified part. Consequently, primary dendrite spacings are scarcely used.

The high growth rates corresponding to the right hand side of Figure 5-3-9 are only attained in exceptional cases, either during the solidification of thin ribbons or fine droplets, with dimensions in the range 10 to 100 μm, or in regions rapidly resolidified on a substrate after local laser or electron beam melting. In all cases, G and V vary locally. G can reach very high values. In the most rapidly solidified zones, the microstructure is extremely fine with spacings of only a few microns, the structure consisting of regular cells, with the absence of well-defined secondary branches.

5-4 The evolution of dendritic microstructures

Dendrite growth

The secondary dendrite arms form from protuberances that grow laterally behind the tip of the primary arm, due to the radial concentration gradient in the liquid (Fig. 5-4-1). Tertiary arms can form from the secondary arms in the same way, leading to a highly branched structure in the early stages of growth. There is a high area of liquid/solid interface per unit volume. This situation is a source of instability, since it involves a large amount of energy. As solidification proceeds, two distinct but related phenomena occur; the fraction of solid increases at the expense of the liquid, and the shape of the dendrites evolves to reduce the area of interface. Various mechanisms contribute to these changes in morphology.

Reconstruction of the geometry at constant solid volume fraction

Consider the general case of a two-phase system with a large area of interface, for example, dendrites in contact with their parent liquid, equiaxed grains suspended in a liquid, or even precipitate particles in a solid matrix. Let us assume also that each of the two phases has a uniform composition corresponding to the equilibrium phase diagram. At high temperature, the system will nevertheless evolve continuously, since complete thermodynamic equilibrium is not attained. The driving force for the change is the decrease in interfacial energy, the phases tending to become more rounded, with larger radii of curvature.

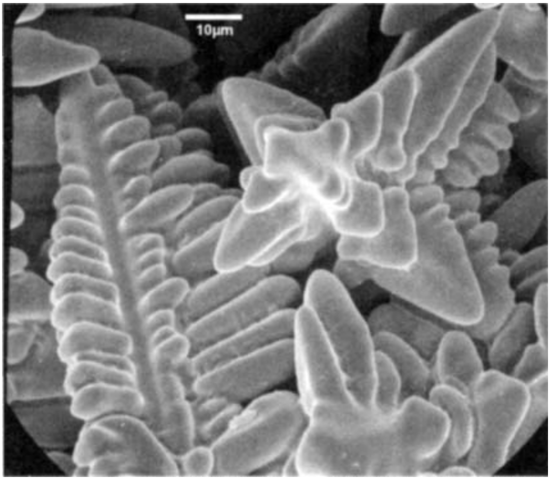

Figure 5-4-1:
Dendrites made visible by draining away of the liquid in the shrinkage pipe of a small steel ingot (scanning electron micrograph). The secondary arms grow out symmetrically from the primary arms. Tertiary arms can also be seen, particularly towards the right hand side of the micrograph. The angles between the arms depend on the crystal structure of the solid. In cubic systems, the preferred growth direction is [100], with an angle of 90 °.
Courtesy INPG, Grenoble

Indeed, the total free energy of the system is composed of both volume and surface contributions. The volume terms are those that determine the phase diagram and no longer change in the present case, since the compositions and proportions of the phases are those corresponding to equilibrium. Only the surface contributions remain, their orders of magnitude being much smaller. Thus, the chemical potential of each solute species includes a term related *to the local curvature of the interface.* The latter is often expressed by a mean value $<R>$, representing the combination of the two principal radii R_1 and R_2. The variation in chemical potential with curvature is given by the Gibbs-Thompson relation :

$$\Delta\mu_{vol} = \frac{\sigma}{\Delta s_f}\left(\frac{1}{R_1}+\frac{1}{R_2}\right) \tag{5-4-2}$$

where σ is the solid/liquid interface energy in Jm^{-2}, μ is the chemical potential in $J\,mole^{-1}$, and Δs_f is the entropy of melting per unit volume in $Jm^{-3}K^{-1}$.

The difference in chemical potential in the vicinity of a curved interface induces solute transport, which occurs essentially by diffusion and is therefore thermally activated. The transport occurs from high curvatures (low $<R>$) to lower ones (higher $<R>$). In the case of isolated spherical particles, the larger ones will grow at the expense of the smaller ones. For dendritic structures, this rearrangement begins right from the start of the growth process. Over longer periods of time, the mean radius $<R>$ is found to increase approximately according to a relation of the type :

$$<R>^3(t) - <R>^3(t=0) = Kt \quad \text{where } K \text{ is a constant} \tag{5-4-3}$$

Another formulation considers a specific surface area S_V, corresponding to the area of interface per unit volume in a multi-phase system. The parameter S_V is independent of the shape of the interface and decreases continuously as the microstructure coarsens. In the case of a diffusion-based mechanism, the decrease in S_V is given by [Mar96] :

Figure 5-4-5:
Fe-1.3C-12.7Mo alloy quenched during unidirectional solidification at a rate of 6.6 cm/h (scanning electron micrograph). The first stages of dendrite ripening can be seen, with the coalescence of secondary arms at A and liquid entrapment at B. Some branches dissolve and their neighbours thicken to fill in the gap.The light-coloured zones represent the quenched liquid and consist of a fine eutectic.
Courtesy INPG, Grenoble.

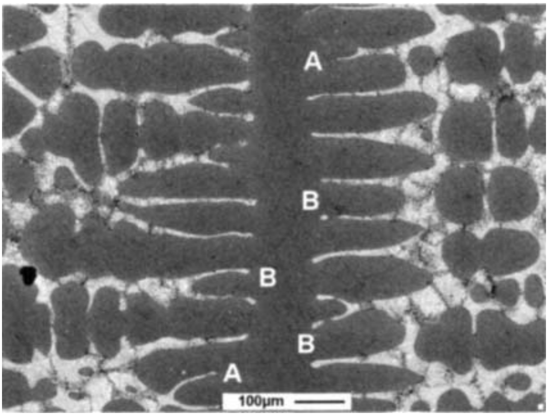

$$S_V^{-3}(t) - S_V^{-3}(t=0) = K_S\, t \qquad (5\text{-}4\text{-}4)$$

The relation 5-4-3 describing the variation of <*R*> with time is similar to the Lifshitz-Slyozov-Wagner (LSW) law, which describes the *ripening* of dispersed particles with a relatively small volume fraction, a situation quite different to the evolution of dendrites in the mushy zone. The common feature is the reduction in interfacial energy. In the case of dendrites, there is a large proportion of solid phase and a small distance between regions of different curvature, with a wide range of positive and negative curvatures, leading to steep solute gradients and high fluxes. The diffusive transport of matter thus involves mechanisms different from those proposed for dispersed particles. Nevertheless, experimental results show that the coarsening kinetics for particles, grains or dendrites can all be described approximately by laws similar to the LSW relation.

First stage : dendrite evolution during solidification

Arm coalescence

Dendrites have a complex shape with a large surface area of continuously variable curvature. The latter is positive at the arm tips and negative at their junctions (Fig. 5-4-1). The difference in chemical potential between the roots and the stems of the arms causes them to thicken and dissolution at the root may lead to breakaway of the arm concerned. Some fine branches dissolve and their neighbours fill in the vacant space. Others coalesce to form a single arm and liquid becomes trapped at the base (Fig. 5-4-5). It should be remembered that each dendrite is a single crystal, so that all the branches have the same crystallographic orientation, greatly facilitating the joining of adjacent arms.

The complex overall process of coarsening and morphological evolution is called ripening, and is sometimes mistakenly referred to as coalescence. In certain compound phases, dendrite ripening can involve the formation of crystal facets, corresponding to easy growth planes (Fig. 5-4-6).

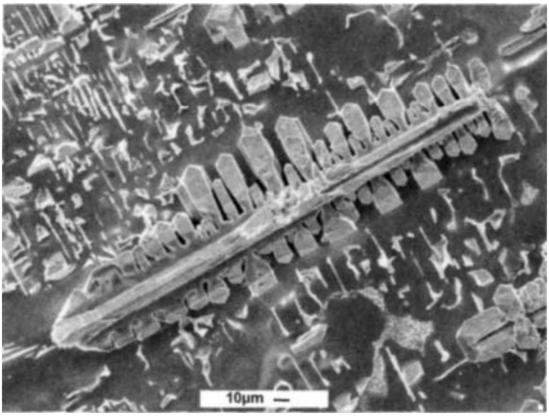

Figure 5-4-6:
Scanning electron micrograph showing a dendritic primary NbC carbide in an austenite matrix. The secondary arms are rounded when they first begin to grow, and later develop crystal facets, particularly visible at the ends of the largest ones (see also Figs. 5-6-14 B and 7-1-3, representing the same sample).
Courtesy INPG, Grenoble.

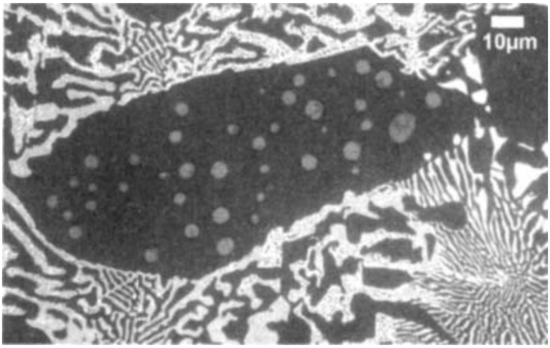

Figure 5-4-7:
Scanning electron micrograph of a Fe-2.2C-20.5Mo alloy cooled from the liquid at 5°C/mn in a DTA furnace. In atom %, the composition is 10.4C-12Mo (cf. phase diagram in Fig. 6-5-1). Nodules representing spheroidised liquid are visible in the dark austenite dendrites, which are surrounded by two carbide eutectics. The light coloured carbides are M_6C (coarse) and Mo_2C (fine). The M_6C carbides appear porous, since they become unstable on cooling and begin to dissolve.
Courtesy INPG, Grenoble.

Spheroidisation of the entrapped liquid

When the entrapped liquid is present in only small amounts, it becomes spheroidised. This is well known in the case of the interdendritic liquid trapped at the end of solidification. Micropores may be generated due to shrinkage on cooling.

The formation of coarse polyphased nodules such as those visible in Fig. 5-4-7 is less common, and has been observed in the austenitic matrix of alloys containing ferrite-stabilising elements (Mo, W, V, Nb).

Second stage : grain coarsening

Once the dendrite skeleton has disappeared due to ripening, the microstructure continues to evolve by grain and particle coarsening (§ 13-3). This complex process is illustrated by the example of a Fe-1.3C-11Mo-4Cr-1V alloy produced by the sintering of prealloyed powders with initially very fine dendritic microstructures obtained by water atomisation. The specimens were prepared by presintering the powder for a short time, just sufficient to

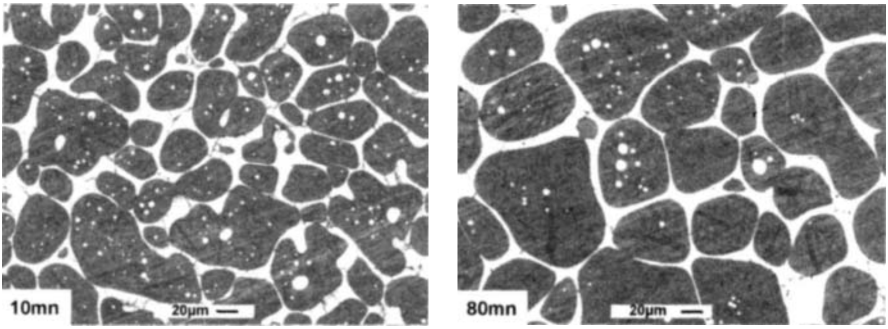

Figure 5-4-8:
Scanning electron micrographs of a Fe-1.3C-11Mo-4Cr-1V alloy produced by the sintering of prealloyed powders with initially very fine microstructures. The two images are at the same magnification and show the coarsening that has occurred between 10 and 80 mn at 1242 °C. The grains are surrounded by a very fine eutectic constituent (light).
Courtesy INPG, Grenoble.

compact it and weld the grains together. Exposures were then performed for various times at a temperature chosen so as to obtain a certain amount of liquid phase in equilibrium with the solid grains. The composition of the alloy concerned is different from those of the usual powder metallurgy grades (§ 16) and the amount of liquid phase is higher than that normally employed.

The microstructure resulting from the presintering process remained fine with a grain size of a few microns. Subsequent holding for only 10 mn at 1242 °C was sufficient to achieve equilibrium and the proportion of phases can be assumed to be stabilised. However, ripening has already begun and the grains have relatively smooth, rounded surfaces quite different from the initial dendritic structure (Fig. 5-4-8 left). The small light-coloured intragranular nodules represent liquid trapped between the growing dendrite arms. Their alignment reveals the original network of secondary dendrite arms. After 80 mn holding time, the microstructure is significantly coarser, both the grains and the nodules are larger and rounder (Fig. 5-4-8 right). Size measurements confirm the relation 5-4-3.

Coarsening in a multiphase structure

The presintered alloy described above was held for 40 mn at a temperature slightly below that for the formation of the γ/M_6C eutectic (determined by DTA). Three phases are in equilibrium, austenite, the liquid and the eutectic carbide M_6C. The austenite grains are bounded by a eutectic constituent, while the carbides can be divided into different populations, varying in size and location (Fig. 5-4-9) :

- The eutectic constituents, with very fine carbides formed by solidification of the intergranular liquid during quenching at the end of the holding period.
- Coarse intergranular carbides, situated close to the eutectic, which probably remained in contact with the liquid at high temperature. They have coarsened rapidly at a rate almost

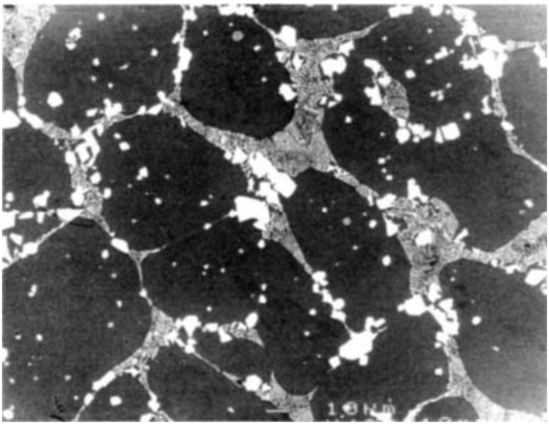

Figure 5-4-9:
Scanning electron micrograph of a Fe-1.3C-12.7Mo alloy (*cf.* Fig. 6-5-1) produced by the presintering of alloyed powders. The specimen was quenched after holding for 40 mn at a temperature in the three phase γ/M_6C/liquid field. Note;
1) the very fine intergranular eutectic carbides;
2) the coarse intergranular carbides;
3) the isolated carbides within the austenite grains.
Courtesy INPG, Grenoble.

as high as if they had been completely surrounded by liquid, the only limitation being the narrowness of the liquid *corridors* through which diffusional transport occurred.

- Intragranular carbides, originally fine eutectic carbides, that have been trapped by grain growth. Once incorporated in the solid, their growth rate is greatly reduced, so that their size is intermediate between those resulting from diffusion in the completely solid or liquid states.

Holding just above and just below the temperature at which the third phase appears shows that coarsening of the austenite grains is considerably restricted by the presence of the carbide particles [Dur97a].

5-5 Secondary dendrite arm spacings

Phenomenological behaviour

The secondary dendrite arms initially form from periodic lateral disturbances on the primary arms. In situ observations on transparent "alloys" show that they are immediately subjected to the ripening process [Esa85]. Their spacing λ_s is the mean value measured between secondary arms whose attachment to the primary arm is clearly visible. Experimental measurements show good agreement with particle coarsening laws (§ 5-4), the time considered being that during which the arms are in contact with the liquid. This is represented by the *local solidification time* θ_S, defined as the time spent between the liquidus temperature T_L and the solidus T_S. An example is shown in Figure 5-5-2.

Most measurements of λ_s have been performed on small directionally solidified (chill cast) ingots equipped with thermocouples. The value of θ_S can then be read directly from the temperature/time recording. More rarely, λ_s has been measured in unidirectional solidification experiments, in which the conditions are defined by three parameters; V, the rate of advance of the liquidus isotherm T_L at a particular point, G_L, the temperature gradient in

Figure 5-5-2:
Variation of secondary dendrite arm spacing with local solidification time θ_S for different tool steels containing about 1 % C (solid line). The dotted line is for a steel with only 0.5 % C, for which the spacings are larger. Adapted from [Jay92].

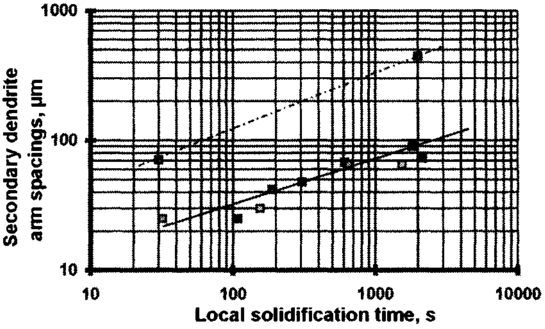

the liquid ahead of the interface, and the cooling rate *p*. Only two of these parameters are independent, since $p = G_L * V$. The local solidification time is given by :

$$\theta_S = \frac{T_L - T_S}{G_L \cdot V} \tag{5-5-1}$$

θ_S is difficult to determine accurately, due to the fact that there are different interpretations of how to evaluate the temperature T_S at which solidification is complete. For low carbon alloys, T_S is close to the thermodynamic solidus and the solidification range $(T_L\text{-}T_S)$ is then equal to ΔT_0 (*cf.* Fig. 5-1-5). In high carbon alloys, which form eutectics, T_S can be assimilated to the temperature of the last eutectic. In this case, coarsening of the secondary dendrite arms is slowed by the appearance of the first eutectic and finally stops when the quantity of liquid becomes too small and the grains are partially blocked. In the example shown in Figure 5-4-5, the grains are blocked by the second eutectic at 1200 °C and the proportion of the third eutectic is extremely small. It is generally found that λ_s is related to p and θ_S by power laws, such as :

$$\lambda_S = \mathrm{B}\ \theta_S^{\mathrm{n}} \tag{5-5-3}$$

The exponent *n* varies from 0.2 to 0.45. It should be noted that, when *n* is taken as 0.33, relation 5-4-3 gives a $t^{1/3}$ law :

$$\lambda_S^3(\theta_S) - \lambda_S^3(0) = \mathrm{B}\theta_S \tag{5-5-4}$$

The regularity of these laws is sufficiently reliable to make λ_s the best indicator of the local cooling rates in industrial ingots and castings. Experimentally determined laws for both the primary and secondary dendrite arm spacings are given in [Jac76], [Jer77], [Oka78], [Tah82], [Fis89].

Primary dendrite arm spacings λ_p can be determined only on transverse sections of quench-interrupted unidirectional solidification specimens corresponding to a given temperature. The observation of longitudinal sections gives information on ripening, enabling the measurement of secondary arm spacings λ_s along the primary arms. Each

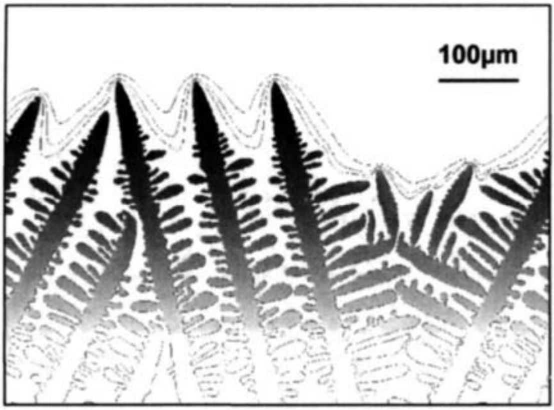

Figure 5-5-5:
Solidification front for a Fe-0.15C alloy predicted by a multi-phase field model for G = 150 °C/cm and p = −1.5 °C/s. The simulation shows how the dendrites with lower angles to the temperature gradient dominate the others. In the spaces between two grains (represented by parallel dendrite arms), the tertiary arms develop into new primary arms.
Courtesy Access, Aachen, G. (see also [Tia98]).

stage in solidification is represented by a different section through the same specimen (Figs. 6-1-1 6-3-1, 6-3-8).

Phase field modelling

A recent approach gives a realistic idea of the microstructural changes associated with ripening phenomena, diffusion in the solid and even crystal orientation selection [Dan00], [Tia98]. The liquid/solid interface is not considered as an abrupt threshold, but rather as a narrow diffuse zone in which all the coupled heat and diffusion transport processes occur. This method demands a very fine calculation mesh in the liquid/solid region. An example of predicted dendrite growth and ripening is shown in Figure 5-5-5.

5-6 Eutectic microstructures

Eutectic solidification in a binary alloy

Eutectic solidification is the transformation of a liquid into a solid composite comprising two separate phases (binary eutectic), which will be designated α and β. In a binary system, the corresponding equilibrium is invariant (*i.e.* it occurs at a single temperature). Compared to the system previously considered, where a single solid phase is formed, the solidification range ΔT_0 is zero, as for the solidification of a pure substance.

The areas in which the α and β phases have formed by eutectic transformation are usually easy to distinguish in a microstructure, due to their particular geometrical configurations, which will be described below. Moreover, the constituents are generally much finer than cells or dendrites formed under similar conditions. Since the associated properties are also specific, *eutectic* is often considered as a single microstructural constituent.

The fact that the liquid transforms to two solid phases simultaneously imposes particular conditions that determine the growth morphology. In general, the simultaneous formation

Figure 5-6-1:
Schematic representation of the solidification front for a regular eutectic where the liquid forms two solid phases, α (grey) and β (white), showing the curvature of the α/liquid and β/liquid interfaces. The β phase regresses behind the front. Along the front, there is equilibrium at the liquid/α/β triple junctions.

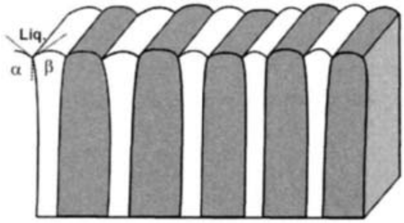

of α and β phases implies :

- The existence of triple junctions, where the three phases α, β and liquid are in contact and in equilibrium (Fig. 5-6-1 and § 7-2). Each interface contributes its own energy to the junction line, leading to curvature of the lamellae in its vicinity.
- Solute transfer, principally by diffusion, in a direction globally tangent to the liquid/solid interface.

The growth of each phase is governed by physical-chemical factors related to its specific composition and crystal structure. This leads to different morphologies, which are experimentally divided into two categories : *regular eutectics* and *irregular eutectics.*

Regular eutectics

When both phases are metallic in nature, the eutectic is regular, with a morphology that obeys simple geometrical rules. It is composed of regularly spaced lamellae or fibres, the choice between the two depending on the relative proportions of the two phases. When one phase represents less than a third, it forms fibres, in order to minimise the interface energy per unit volume. The lamellae or fibres grow perpendicularly to the interface, with a spacing λ. The growth front follows an isotherm T_I and is practically planar, except for grooves corresponding to the triple junctions between the liquid and the two solids.

As in the case of dendrites, eutectic growth occurs with a certain degree of undercooling, due to the formation of a diffusion layer and the effect of curvature. For medium solidification rates, the main effect of supercooling is the accumulation or depletion of solute at the growth front, due to rejection or absorption as it advances. The relation linking supercooling to the growth rate V is [Mag88], [Kur90] :

$$T_I - T_E = \mathrm{K}\sqrt{V} \tag{5-6-2}$$

The interlamellar spacing λ depends essentially on the growth rate and obeys the relation :

$$\lambda = \frac{\mathrm{K}'}{\sqrt{V}} \tag{5-6-3}$$

where K and K' are system-dependent constants.

Even under steady state experimental conditions, the measured λ value is the resultant of local fluctuations. The mechanism is relatively well identified for both lamellar and fibrous structures [Jac66]. A local extra lamella (λ too small) is eliminated by overgrowth of its neighbours, while a local deficiency (λ too large) induces higher undercooling, leading to the formation of a new lamella by lateral branching. Experimental measurements of λ show a fairly narrow scatter (<20 %) for regular eutectics. The relation 5-6-3 is usually applied to the mean measured value $<\lambda>$.

$$V\langle\lambda\rangle^2 = constant \tag{5-6-4}$$

The relation 5-6-3 has been theoretically justified by considering the supercooling due to both diffusion and curvature [Jac66], giving two relations involving three variables, the supercooling $(T_I - T_E)$, the growth rate V and the spacing λ. This leads to the relation 5-6-5 between ΔT_{total} and λ, for which the representative curve goes through a maximum :

$$\Delta T_{total} = K_3 \lambda V + K_4 \frac{1}{\lambda} \tag{5-6-5}$$

The question is to decide which solution the system will adopt. It has been demonstrated that spacings smaller than λ_m (value at the maximum) are unstable in the event of fluctuations. Furthermore, spacings that are too large (*e.g.* $\lambda > 2\lambda_m$) cause liquid "furrows" at the growth front, which are a source of instability [Fis80].

This formulation was originally developed for eutectoid growth, with the same indeterminacy [Hil71]. In this case it was proposed that growth occurred in the conditions corresponding to the maximum ΔT_{total}. In fact, measurements on regular eutectics show that :

$$\lambda \approx 1.20\,\lambda_m \tag{5-6-6}$$

Two-phase eutectic structures can also be formed in alloys containing more than two elements. However, in this case, the liquid composition at the eutectic is no longer the mean of the compositions of the two solids, since the eutectic reaction is not invariant but takes place over a range of temperature. The difference between the liquid composition and the mean solid composition leads to segregation effects. Supercooling at the interface is changed due to the chemical gradient associated with solute redistribution. The effect of this segregation on the solidification front is to produce cells and dendrites instead of a globally planar morphology. The modulation of the front is larger than the eutectic spacing, leading to the formation of cellular eutectic colonies.

Irregular eutectics

Among the many examples of irregular eutectics, two are particularly important in commercial materials, corresponding to Al-Si and Fe-graphite alloys, both of which are widely used for castings. According to the criterion for irregular eutectics, at least one of the solid phases is non-metallic in nature (silicon and graphite respectively). In each case, this phase shows a *facetted growth morphology*, with elongated faces corresponding to densely packed crystal planes (Fig. 5-6-7). A single facetted phase is sufficient to create an irregular microstructure.

Growth of the facetted phase is oriented by crystallographic factors, and the plates are not necessarily perpendicular to the overall growth direction. In fact, growth does not occur

Figure 5-6-7:
Schematic representation of the interface of an irregular eutectic. Note that the solidification front is not isothermal and that the plates of the facetted phase (grey) are not parallel, leading to the formation of intermediate plates by lateral branching when the spacing becomes sufficiently large (λ_{br}). Growth of a plate stops when the spacing reaches a certain minimum value (λ_0). The magnifying glass indicates a liquid furrow between two lamellae whose spacing has become too large.
Adapted from [Fis80].

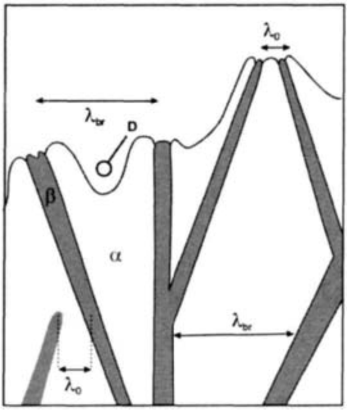

under steady state conditions. It is dominated by the nucleation of lateral branches, which more or less periodically correct the local spacing, with a lag and a degree of supercooling characteristic of nucleation phenomena. Consequently, the growth of irregular eutectics involves large supercooling and a non-isothermal solidification front. Significant temperature differences can occur between the tips of facetted particles and the bottom of the intervening liquid gullies (*cf.* Fig. 5-6-7), [Mag87], [Fis80], [Jon81].

Regular periodicity is not satisfied locally, but only on average ($<\lambda>$), with a wide scatter. However, the mean value approximately follows the kinetic law described for regular eutectics. Some authors include an effect of the temperature gradient.

The eutectics in the Fe-graphite and Fe-cementite systems

The Fe-C system shows two different eutectic equilibria, Fe-graphite (γ/gr.) and Fe-cementite (γ/Fe_3C), respectively at 1153 and 1147 °C (see Fig. 4-4-1). The Fe-graphite eutectic is considered to be *grey,* due to the dark colour of the graphite, whether etched or unetched, Figs. 5-6-8 and 5-6-9 (whence grey cast irons), while unetched cementite appears *bright,* Figs. 5-6-10 A and B (whence white cast irons). In straight Fe-C cast irons, the cementite and austenite have similar contrasts in the electron microscope and light etching is necessary to distinguish them. Other micrographs of grey and white cast irons can be found in § 21.

Three solid constituents are in *competition* during solidification ; austenite dendrites, eutectic graphite and eutectic cementite. The degree of supercooling required for solid growth is different for each phase or constituent, depending on the overall solidification rate. For a given alloy composition, the choice of solid phases can be determined with the aid of a temperature/solidification rate diagram (Fig. 5-6-11), [Jon80]. *The solid constituent formed is the one with the highest interface temperature.* For several reasons, the degree of supercooling necessary for the graphite eutectic is greater than that for the cementite eutectic. In particular, the difference in composition between the two phases in the eutectic is greater for graphite, and therefore requires a larger carbon flux.

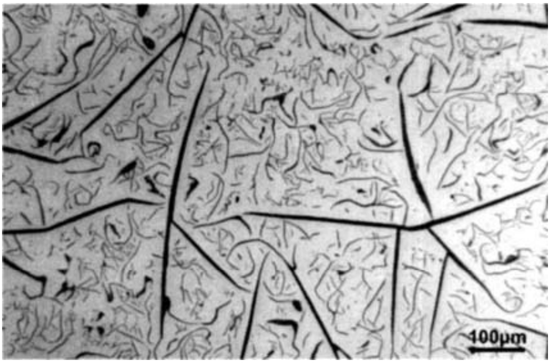

Figure 5-6-8:
Electron micrograph of a hypereutectic grey cast iron. The coarse flakes are primary graphite.
Courtesy CTIF, Paris.

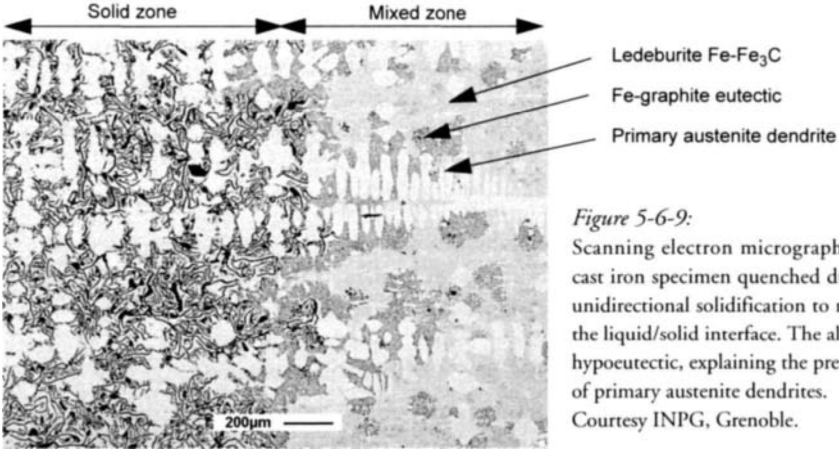

Figure 5-6-9:
Scanning electron micrograph of a cast iron specimen quenched during unidirectional solidification to reveal the liquid/solid interface. The alloy is hypoeutectic, explaining the presence of primary austenite dendrites.
Courtesy INPG, Grenoble.

The transition between the two forms ought to be observed when the two growth temperatures are equal. However, experimentally, it has been found that the transition temperature between the two types of eutectic is not the same depending on whether growth began with graphite or with cementite [Hil68], [Jon81], [Ma88]. The combination of solidification rate and transition temperature is different in each case. The graphite/cementite transition is poorly defined and less reproducible than the cementite/graphite transition. The graphite eutectic tends to persist at supercooling levels where the cementite eutectic would be expected to predominate.

The graphite/cementite transition is illustrated in Fig. 5-6-9, for a hypoeutectic cast iron specimen quenched during unidirectional solidification. The slowly solidified zone shows only a coarse graphite eutectic, while the quenched regions contain both cementite eutectic and scattered areas of very fine graphite eutectic. The latter occur close to the secondary arms of the austenite dendrites, probably due to rejection of silicon into the confined spaces, facilitating the formation of the graphite eutectic. Indeed, the solidification rates

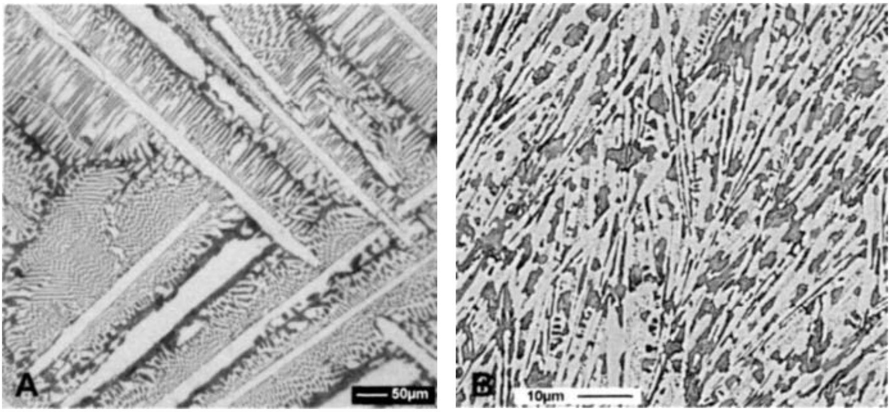

Figure 5-6-10:
A) Scanning electron micrograph of the Fe-Fe$_3$C eutectic produced at a slow solidification rate.
B) Scanning electron micrograph of a rapidly solidified slightly hypoeutectic cast iron. The microstructure is finer and secondary branching has been virtually eliminated. The cementite plate clusters show a fan-like morphology.
Nital etch.
Courtesy INPG, Grenoble.

Figure 5-6-11:
Solidification (growth) temperature as a function of solidification rate for the Fe-4.28C eutectic composition, with a constant temperature gradient.
Three possible solid constituents are in competition, the γ/graphite eutectic (Gr. eut.), the γ/cementite eutectic (Cem. eut.) and primary austenite dendrites (γ dend.).
The bold line represents the phase for which the interface (growth) temperature is highest. At low solidification rates, the γ/graphite eutectic forms, then the γ/cementite eutectic at higher rates, followed by austenite dendrites, and then the γ/cementite eutectic again at the highest solidification rates. From [Jon80].

for the cementite/graphite and graphite/cementite transitions are also affected by the presence of other alloying elements. Thus, chromium, phosphorus and manganese facilitate the nucleation of cementite, while, beyond a certain concentration, silicon, aluminium, titanium and sulphur increase supercooling and promote the graphite eutectic. Commercial cast irons generally contain elements with opposing effects, such as silicon and manganese [Wol85], [Kag80], (*cf.* § 23).

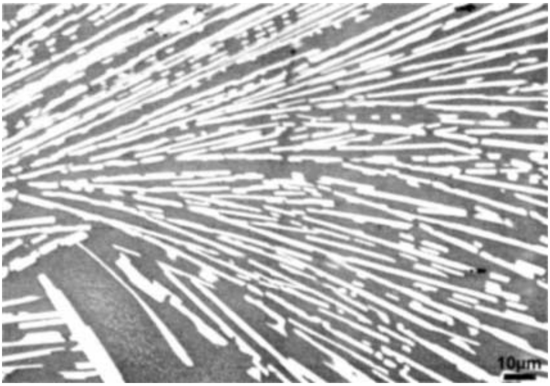

Figure 5-6-12:
Scanning electron micrograph of a Fe-C-Mo alloy, showing the γ/Mo_2C eutectic.
Courtesy INPG, Grenoble.

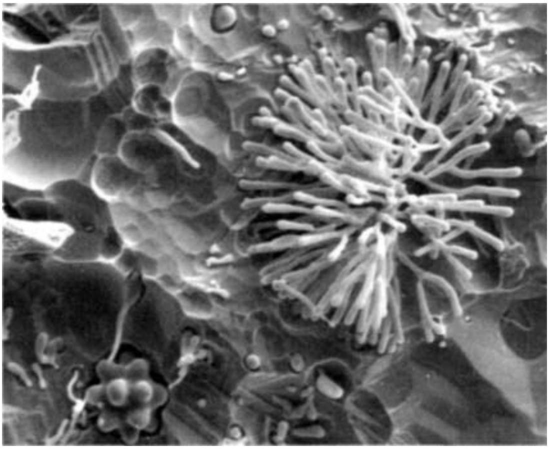

Figure 5-6-13:
Scanning electron micrograph showing γ/MnS eutectic in a deeply etched AISI 303 stainless steel. The sulphides form coral-like colonies of interconnected rods.
Courtesy Ugine-Savoie-Imphy, Arcelor Group, France.

Eutectic carbide morphologies

It is always tempting to try to identify carbides from their solidification morphology. Some eutectic carbides effectively have characteristic morphologies, such as lanceolate (spear-shaped) M_7C_3 (Figs. 6-3-6, 6-3-7, 6-3-9), fibrous VC, Chinese script NbC, fishbone M_6C (Figs. 5-6-14 A, B and C), feather-like Mo_2C (Fig. 5-6-12), and coral-formed MnS (Fig. 5-6-13). The Fe-Fe_3C eutectic is so typical that the name ledeburite has been commonly accepted (Fig. 5-6-10). Carbides generally grow along preferred crystallographic axes, so that their morphology often reflects the crystal symmetry. For example, NbC shows 90 ° junctions due to its cubic symmetry.

However, the eutectic morphology is not an intrinsic characteristic and depends on the solidification rate. All eutectics become more regular at high solidification speeds, plates and fibres becoming less branched and more lamellar (Fig. 5-6-10).

Figure 5-6-14:
Scanning electron micrographs of specimens deeply etched to expose the eutectic phases. Courtesy INPG, Grenoble.

A) Fe-V-C system. The fibrous VC particles in the γ/VC eutectic radiate outwards from the centre of the cellular colony. The γ matrix has partially transformed to pearlite (fine eutectoid colonies in which the cementite lamellae are at least an order of magnitude smaller than the VC fibres.

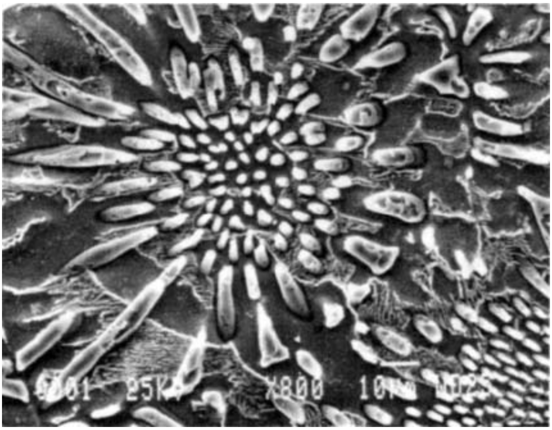

A

B) Fe-Nb-C system. The NbC particles in the γ/NbC eutectic are in the form of orthogonally branched lamellae. Martensite needles are faintly visible in the matrix. In a polished section, the NbC particles have a so-called Chinese script morphology.

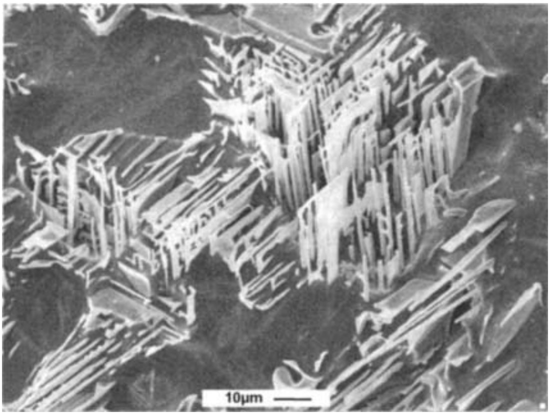

B

C) Fe-Mo-C system. The M_6C particles in the γ/M_6C eutectic are lamellar and some have branches at 120 °. In a polished section, the carbides show a fishbone morphology.
Courtesy INPG, Grenoble.

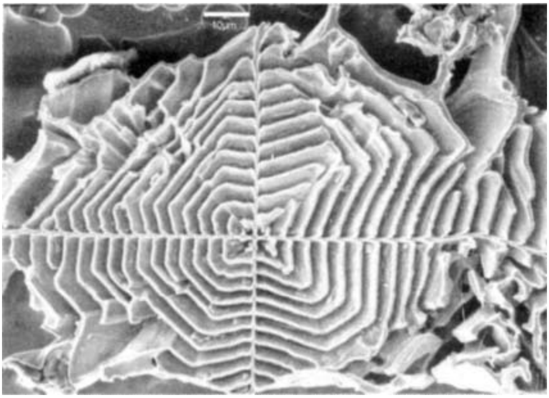

C

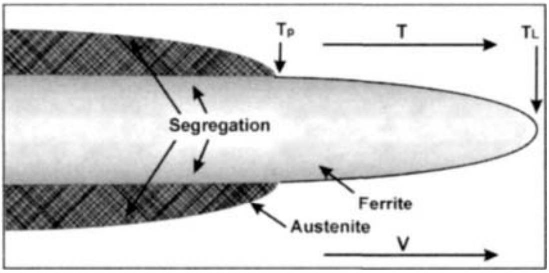

Figure 5-7-1:
Schematic representation of peritectic growth in a temperature gradient in the S-G conditions, with no diffusion in the solid. The primary dendrite is δ ferrite and segregation is indicated by graded shading. Austenite (γ) develops in contact with the ferrite at the peritectic temperature *Tp*.

The different constituent phases may also change their morphology in the presence of other elements. For example, VC carbide, which generally adopts a fibrous form, becomes facetted when small amounts of tungsten are added. Cementite also becomes more facetted when it contains manganese. Finally, ledeburite is lamellar and almost regular in simple iron-carbon alloys.

5-7 Peritectic microstructures

The peritectic transformation in iron-base alloys

In the Fe-C binary system (at a fixed pressure), there is an invariant reaction of the peritectic type at 1393 °C : δ ferrite + liquid → γ austenite. On cooling below the peritectic temperature T_p, the δ ferrite disappears and is replaced by austenite. Since there is only a single solid phase, there is no peritectic constituent equivalent to that formed in a eutectic reaction. Nevertheless, the transformation leaves visible traces in the microstructure. In order to analyse the transformation mechanism, two situations will be considered ; complete absence of diffusion in the solid (S-G conditions), and a certain degree of diffusion without attaining the equilibrium corresponding to the lever rule.

Transformation in the S-G conditions

The steps in the solidification of an Fe-C alloy are shown in Fig. 5-7-1, assuming a cellular front. Between the liquidus temperature T_L and the peritectic temperature T_p, δ ferrite forms, with the segregation of carbon, the solid becoming increasingly enriched in solute as the cell develops. The liquid is also enriched until it attains the peritectic composition, at the temperature T_p. The second stage then commences, with the formation of peritectic austenite around the primary δ phase. The resulting microstructure is quite characteristic. Indeed, the Greek prefix peri- signifies "around, enclosing, encircling". The solidification path finally ends with the formation of a eutectic, not shown in the figure, whose quantity calculated using relation 5-1-8 is negligibly small.

Transformation with supercooling and some diffusion in the solid

In practice, a certain amount of diffusion always occurs in the solid. This is particularly true in the case of carbon and other interstitial solute elements, which diffuse rapidly at

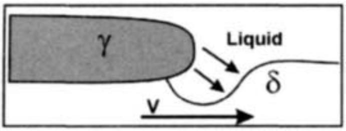

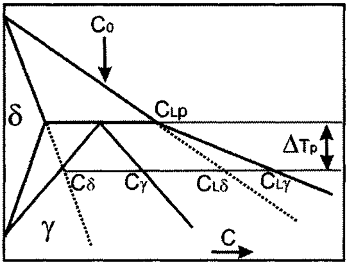

Figure 5-7-2:
Schematic representation of peritectic growth, with partial diffusion in the solid phase, for a phase diagram of the Fe-C type and an initial composition C_0. At the temperature $T_P - \Delta T_P$, the liquid is locally in equilibrium with both the δ and γ phases, its carbon content being different in each case.
Adapted from [Hil79] and [Ker96].

such high temperatures. Moreover, even under steady state solidification conditions, each phase forms with a specific degree of supercooling, modifying the actual transformation temperature. Nevertheless, diffusion remains limited and the solid phases are not uniform and are globally out of equilibrium, *although phase equilibria are respected locally at the interfaces.* In the presence of an imposed temperature gradient, interfacial equilibrium is thus established at each temperature level. The schematic diagram in Fig. 5-7-2 can be used to analyse the mechanisms that determine the microstructure due to the different solute exchanges; liquid-δ, liquid-γ and δ-γ.

Exchanges via the liquid have been analysed by Hillert [Hil79] and Kerr [Ker96] (Fig. 5-7-2). The austenite grows just below the peritectic temperature, at $T_p - \Delta T_p$, the degree of supercooling ΔT depending on the solidification rate and temperature gradient and on the physical chemistry of each phase. Because of the supercooling, the primary δ ferrite continues to form in a metastable fashion between T_p and $T_p - \Delta T_p$. In order to respect the interfacial equilibria, a diffusion layer forms along the whole of the solid/liquid interface. The compositions of the solid phases formed at $T_p - \Delta T_p$ are respectively C_δ and C_γ and are in contact with liquids of composition $C_{L\delta}$ and $C_{L\gamma}$. Because of these differences in composition, the exchange of solute occurs via the liquid, which is richer in carbon at the interface with the austenite. The excess carbon diffuses through the liquid towards the ferrite. The increase in carbon content causes the ferrite to remelt locally, the extent of the remelted zone depending on the solidification conditions and the alloy chemistry. A wide range of different microstructures can be formed. If the remelted zone spreads laterally, pockets of liquid can become trapped and may even form transverse bands, completely cutting through the primary phase [Tri95], [Boe00], [Lo_01].

Further back in the solidification zone, at lower temperatures, the austenite grows in contact with the liquid, and it is this stage that is called here *peritectic solidification.* For initial alloy compositions near to the peritectic point, T_L is close to T_p and the primary dendrites have little time to project far beyond the overall solidification front. Because of the presence of the liquid zone between them, the two solid phases appear to advance in a staggered manner. The two phases alternate as in a eutectic, but their growth is completely independent.

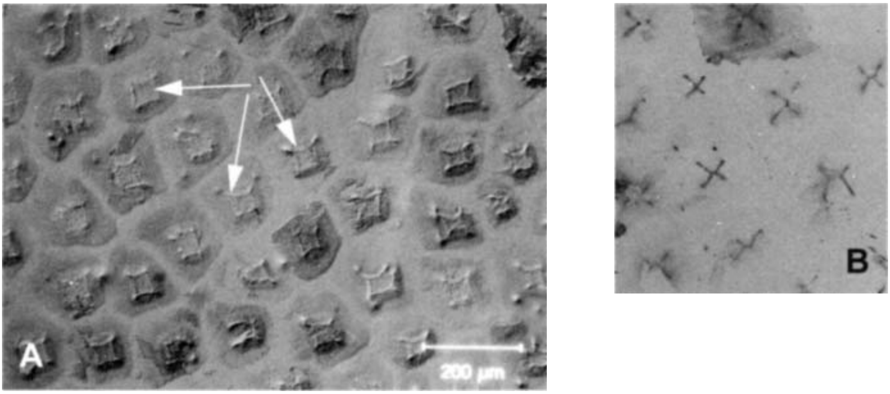

Figure 5-7-3:
Optical micrograph using interference contrast of an Fe-4.7Ni alloy quenched during unidirectional solidification ($V = 41.7\ \mu m/s$, $GV = 4*10^8\ Ks/m^2$).
A) Transverse section 0.9 mm behind the primary dendrite tips. The arrows indicate the position of the δ/γ interface at the moment of quenching.
B) Transverse section 1.3 mm behind the primary dendrite tips. Solidification was complete at the moment of quenching. The δ ferrite is reduced to a thin skeleton at the centre of the former dendrites.
Courtesy Ecole Polytechnique, Lausanne, Switzerland.

In sections at a temperature below $T_p - \Delta T_p$, the austenite forms in the solid phase at the expense of the ferrite with which it is in contact, by peritectic transformation. It is sometimes called *regression austenite*. In Fe-C alloys, equilibrium is attained rapidly and the austenite develops by both processes. However the regression phenomenon does not occur in all systems and depends on the configuration of the phase diagram.

A good example is provided by the Fe-Ni system (Fig. 5-7-3). The primary δ ferrite phase is followed by peritectic austenite. In the solid state, the proportions of ferrite and austenite change with temperature (§ 4-8). The evolution of the microstructure has been studied on transverse sections of a bar quenched during slow unidirectional solidification. Quenching *freezes* the transformation that was occurring at the interface (Fig. 5-7-3 A). As the bar slowly cools, the ferrite regresses, and after complete solidification, only a thin iron-rich skeleton remains at the centres of the former dendrites (Fig. 5-7-3 B), [Hun98], [Boe00].

Most commercial steels contain other elements in addition to carbon. In this case, as the peritectic transformation proceeds at the δ/γ interface, various excess solutes are rejected into the ferrite, *forming a diffusion layer*. Except for the interstitials, for most of these elements, equilibrium is attained only locally, since the exchanges between the unstable primary ferrite and the liquid must take place through the austenite, which forms a diffusion barrier (Fig. 5-7-4). The formation of a diffusion layer is particularly pronounced in the presence of ferrite stabilising elements, which are rejected on formation of the

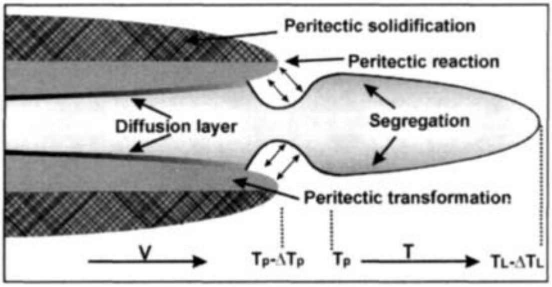

Figure 5-7-4:
Schematic representation of the peritectic growth process in a steel. The light phase is primary ferrite, shaded to indicate segregation. The outer hatched zone is austenite formed by peritectic solidification, while the darker grey layer is austenite formed in the solid state by peritectic transformation at the δ/γ interface. The diffusion layer formed along the latter interface by solute rejection is shown in black.

austenite. Temperature dependent supersaturation in this layer gives rise to various transformations, which leave traces in the subsequent microstructure (see § 6-5) [Fre76], [Rie90], [Ker96].

The variation of the microstructure during the peritectic transformation in an Fe-C-Mn alloy has been simulated using the phase field method, together with phase equilibrium data for this system (SSOL-SGTE Solution Data Bank) and the diffusion coefficients of carbon and manganese in δ ferrite and austenite, Fig. 5-7-5. The carbon concentration appears uniform in each phase (Fig. 5-7-5 B). However, segregation of manganese can be seen in the austenite, formed both from the liquid and by regression of the δ phase, and is particularly marked ahead of the γ/δ interface, where the diffusion layer has the darkest contrast (Figs. 5-7-5 C and D).

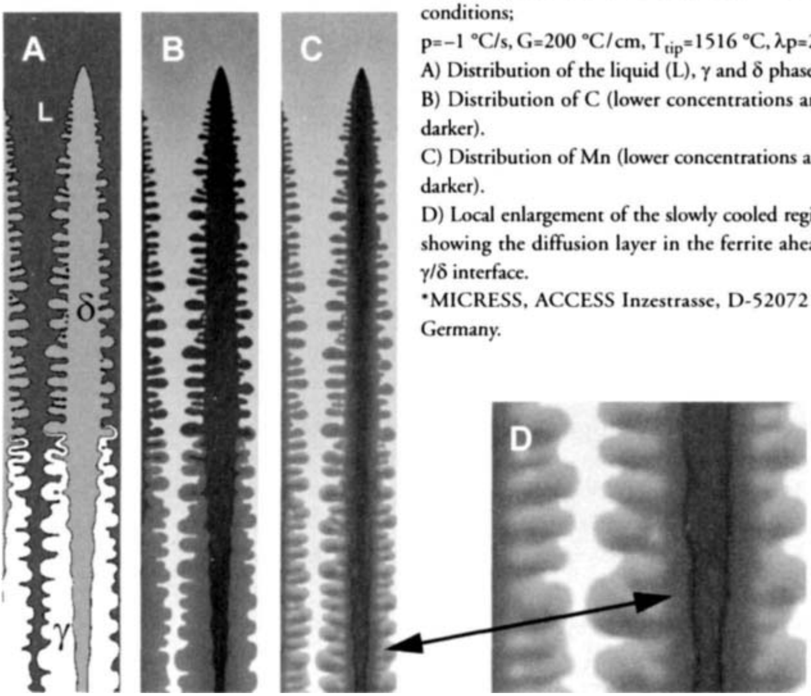

Figure 5-7-5:
Peritectic growth front in an Fe-0.2C-1Mn alloy, simulated using the MICRESS* phase field model. Growth conditions;
p=−1 °C/s, G=200 °C/cm, T_{tip}=1516 °C, λp=200 µm.
A) Distribution of the liquid (L), γ and δ phases.
B) Distribution of C (lower concentrations are shown darker).
C) Distribution of Mn (lower concentrations are shown darker).
D) Local enlargement of the slowly cooled region in C, showing the diffusion layer in the ferrite ahead of the γ/δ interface.
*MICRESS, ACCESS Inzestrasse, D-52072 Aachen, Germany.

6

Liquid/solid structural transformations

It is difficult to interpret the origins of final microstructures when one or more intermediate transformations have occurred since the start of solidification, each leaving traces but partly obliterating those of previous ones. The present chapter considers a number of different examples, chosen both to illustrate the possibilities and limits of determining transformation mechanisms from the analysis of microstructures and to describe the typical morphologies of a wide variety of constituents

6-1 Experimental techniques : controlled solidification

The Bridgman(-Stodebarger) technique

Experiments in which the overall solidification front is made to move unidrectionally along the length of a bar were mentioned several times in the previous chapter. Techniques of this sort have been used since the 1950s. In the Bridgman technique, the specimen is in the form of a long thin bar held inside a tubular crucible and is displaced at a constant speed *V*, either horizontally, or more often, vertically, through a furnace, which imposes a controlled constant temperature gradient *G*. Except for one extremity, which acts as a seed, *the bar is melted completely.*

Depending on the imposed values of *G* and *V*, various solidification regimes can be obtained (cellular, dendritic, etc.). However, transitions that occur at high solidification speeds cannot generally be attained using this method. The heat cannot be extracted sufficiently rapidly and the isotherms are deformed. Very slow withdrawal speeds require sophisticated equipment, since the slightest instability creates growth irregularities resulting in unwanted transverse banding. The range of solidification rates accessible using the Bridgman technique normally lies between 1 and 50 cm/h. This is higher than the speeds corresponding to planar front growth in most alloys. One or more thermocouples attached to the tube (withdrawn with the bar) enable the temperature gradient to be measured. Typical values are from a few degrees to several hundred degrees per centimetre.

This method can be employed to produce single crystals, for example, halides for optical applications. In this case, planar front growth conditions are achieved. Single crystal superalloy turbine blades are also produced by a variant of this technique, but the growth regime is dendritic. To obtain a single crystal, all grain boundaries must be excluded, and this is achieved by the use of seed crystals or chicanes in the mould.

Quench-interrupted directional solidification

Quench-interrupted directional solidification experiments are used to study the variation of the microstructure during dendritic growth. The specimen tube/crucible (or the furnace) are displaced at a controlled constant speed, with a fixed temperature gradient imposed by the furnace. If the crucible and specimen are sufficiently long, the heat transfer conditions are not affected by the withdrawal and *a steady state can be achieved.* The growth rate of the solidification front can then be assimilated to the withdrawal speed *V.* The chemical composition remains constant along the specimen, except in the vicinity of the liquid/solid interface. Each level is at equilibrium at the corresponding temperature. Quenching freezes the liquid as it was during controlled solidification. The examination of transverse sections, associated with *in situ* temperature measurements, gives a precise indication of the state of solidification at the moment of quenching. The quenched liquid can be readily distinguished by its very fine microstructure, clearly revealing the position of the solid/liquid interface. The use of lower temperature gradients spreads the transformation over a longer length of bar.

It is thus possible to determine the fraction of liquid and the geometry of the interface as a function of temperature. The analysis and identification of the different phases formed enables determination of the solidification path. Strictly speaking, solidification takes place neither in a reversible manner nor under the Scheil-Gulliver conditions, due to the existence of supercooling and *a certain amount of diffusion in the solid.* Consequently, the solidification path corresponds to neither of the cases described in § 4-6, but represents an intermediate situation. The method is not appropriate for all systems. For example, when one of the solid phases has a density significantly different from that of the liquid, it may tend either to settle (WC, NbC, TaC) or to float (VC, TiC, graphite) at slow solidification rates, and may be absent in the zone where it formed. Interpretation of the microstructure is then extremely difficult.

The following example clearly illustrates the evolution of the microstructure in the liquid/solid zone (Fig. 6-1-1). It corresponds to a steel with a wide solidification range (146 °C), between the liquidus at 1396 °C and the experimental solidus at 1250 °C. For a withdrawal rate of 7 cm/hr and a mean gradient of around 70 °C/cm, the local solidification time will be about 30 mn. During this time, the microstructure undergoes pronounced modifications, that can be clearly seen on a longitudinal section of the quenched bar. The secondary dendrite arms thicken and coalesce as the fraction of solid increases. Some also redissolve locally, and in the extreme stage of this process, certain dendrite branches break off and become completely surrounded by liquid. They can give

Figure 6-1-1:
Schematic representation (right) and optical micrographs (left) of an X200Cr12 steel quenched during directional solidification at a withdrawal rate of 7 cm/h. The specimen was a 40cm long bar 0.8 cm in diameter.
The fraction that was still liquid at the moment of quenching has a very fine microstructure, enabling it to be clearly distinguished from the solid already formed. In the early stages, the dendritic structure evolves in a manner similar to that shown in Fig. 5-4-5. In the present case, the wide solidification range and consequent long liquid/solid contact time cause fragmentation of the dendrites, whose arms become disconnected.
Courtesy INPG, Grenoble, adapted from [Dur80b].

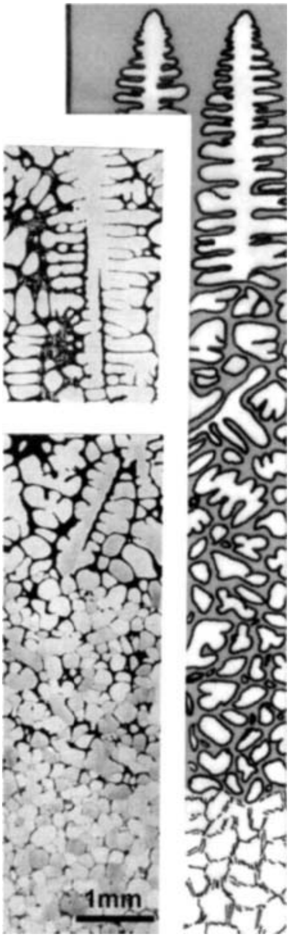

rise to *grains* whose orientation is different from that of the original dendrite to which they were attached. This stage is attained when the solid remains in contact with the liquid for long times. In zones quenched earlier in the solidification process, the secondary dendrite arms remain firmly attached to the primary trunks, and it is possible to measure their spacings. The primary dendrite arm spacing can be determined only on transverse sections.

Chill casting

Numerous studies of dendritic solidification have been performed by casting into a mould with a cooled base. Solidification occurs with almost planar isotherms, but in a transient regime, that is, under planar front conditions, but with V and G variable. Sensitive thermocouples are closely spaced at various points. Temperature recordings as a function of

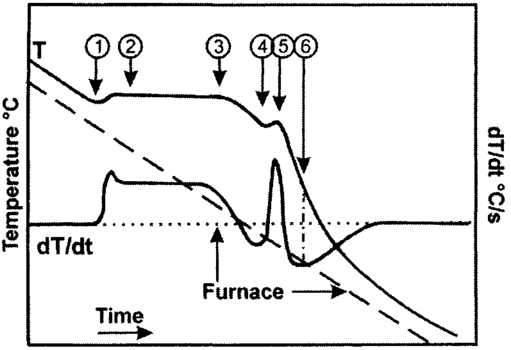

Figure 6-2-1:
Example of simple thermal analysis during cooling, for an initially molten 35 g steel specimen, showing the imposed furnace temperature (dashed line), the specimen temperature T as a function of time t, and the derived curve dT/dt = f(t). The labelled events are :
1 Start of growth of the primary phase.
2 Temperature of dendrite growth, considered as the liquidus temperature.
3 The dendrite tips reach the thermocouple at the centre of the specimen. The heat transfer regime changes.
4 Start of formation of the secondary phase.
5 Maximum of the secondary phase solidification reaction, the peak temperature being considered as that for secondary phase formation.
6 End of solidification, the temperature being considered as that of the solidus.
Courtesy from Jernkontoret, "*A guide for solidification of steels*", [Jer77]

time during solidification indicate the local cooling rates and may detect supercooling. This technique is useful for studying columnar solidification.

6-2 Experimental techniques : thermal analysis

Thermal analysis

Simple thermal analysis *(TA)* and differential thermal analysis *(DTA)* are extremely sensitive methods for detecting thermal events during heating or cooling of a specimen. The associated problems of calibration and the choice of reference specimens for *DTA* are well understood and have been extensively treated elsewhere [Mil84], [Wen64]. For steels, a collection of thermal analysis curves has been published with corresponding micrographs [Jer77]. Except for pure substances, where reactions are invariant, the interpretation of thermal analysis recordings can be difficult [Fre79a]. An example of a simple thermal analysis curve and its derivative is given in Figure 6-2-1, corresponding to the imposed cooling of an initially molten 35 g steel specimen, with a thermocouple placed in the crucible. Theoretically, in the course of cooling, temperature gradients will appear in the specimen, so that the temperature recorded by the thermocouple must be interpreted by considering the sample as a small ingot.

In differential thermal analysis, at least two thermocouples are employed, one in the specimen under study and the other in an *inert* reference sample. Both the imposed temperature (which may be that of the reference) and the temperature difference between the specimen and the reference sample are recorded. Small specimens are employed,

usually weighing between 200 mg and 2 g, depending on the apparatus.
The thermocouples are usually not directly in contact with the specimens. An example of a recording and the associated final microstructure are shown in Figure 6-5-1.

Supercooling associated with solidification

The measured solidification temperature is always lower than that predicted by the equilibrium phase diagram, due to supercooling. Supercooling can have several origins (§ 5-3), associated either with growth effects, such as solute redistribution in the liquid at the interface, or with nucleation problems, *not encountered in steady state directional solidification.* The degree of supercooling depends on the experimental conditions.

> *Nucleation supercooling can be evaluated from the temperature recorded on a thermocouple in contact with the specimen, since the temperature rises again once solidification is under way. To avoid supercooling, it is recommended not to heat the specimen too far above the liquidus (not more than 20-30 °C for steels). The reason why excessive overheating retards nucleation may be the destruction of potential precursors in the liquid, or the dissolution of rare solid phases such as carbonitrides (e.g. Nb(C,N)), which are known to act as nucleants. Very small specimens (<300 mg) are more prone to supercooling.*

In order to correct for the supercooling associated with growth, the liquidus can be measured at different cooling rates [Old62]. The measured liquidus temperature is found to decrease as cooling becomes slower and the true liquidus is taken as the value obtained by extrapolating the T_L *vs.* V curve to V=0. Experimentally, several melting and solidification cycles are performed on the same *DTA* specimen with different cooling rates. This extrapolation method is valid only for transformations involving a homogeneous phase such as a liquid. It cannot be transposed to solid phase transformations when the solid contains concentration gradients. The difference between measured liquidus temperatures and extrapolated values is small for slow cooling rates of the order of 2 to 5 °C/mn. In the example given by Old [Old62], the deviation is 5 °C for rapid cooling at 100 °C/mn.

Interpretation of thermal analysis curves

Unfortunately, DTA provides only the temperatures corresponding to thermal events. *There is no direct indication of the transformations that occur* in the specimen and errors of interpretation can be easily made. It is essential to complete the recorded curves by micrographic or crystallographic observations. Interpretation based on a phase diagram may be erroneous if the diagram is incomplete, inexact, or used wrongly, in a manner not adapted to the experimental conditions. The most common error is to assimilate thermal events during cooling with the crossing of a phase field read from an isopleth through the initial alloy composition. This implies global equilibrium at all temperatures, that is, conditions corresponding to the lever rule (§ 4-6). Such practice may be acceptable for sintered or nanocrystalline samples that conserve their very fine structures, enabling equilibrium to be attained rapidly due to small diffusion distances, but *certainly not after melting,* in coarse segregated solidification structures. Each point in the sample behaves according to its local composition and structure, confusing the overall picture.

Another frequent error is to assume that sufficiently slow heating or cooling enables overall chemical equilibrium to be maintained. Although the rate of 5 °C/mn often chosen for DTA experiments is a good compromise in order to obtain an exploitable curve, the resulting *solidification structure* is heterogeneous and coarse, like most as-solidified structures. Equilibrium is not attained at all temperatures and the measured thermal events do not correspond to the transformations predicted at equilibrium. Consequently, to measure solid state transformation temperatures, it is always preferable to choose a specimen with an initially very fine microstructure, on a scale comparable to the diffusion distances at the temperature considered. Specimens produced by quenching from the liquid or by thermomechanical processing can be employed and the analysis must be performed without melting.

Finally, it is recommended always to examine the microstructure on a vertical section after the DTA experiment, in order to verify the uniformity of the specimen and the absence of spurious effects such as oxidation, settling of heavy phases or flotation of light ones.

The areas beneath the peaks are proportional to the heat liberated and therefore to the quantity of constituent concerned. However, they can rarely be used quantitatively, since the latent heat varies with the composition of the phases. The DTA signals obtained for minority phases are very weak.

Quench interrupted solidification during thermal analysis

In order to ***unambiguously*** associate a thermal event with a particular transformation in the solidification path, it is useful to be able to quench the specimen at the moment when the event is observed. The transformation is then frozen in and can be identified by micrographic examination. For example, for the Fe-17.2 at.%C-8.8 at.%Mo alloy (*cf.* phase diagram in Figure 6-5-1), the DTA curve obtained with continuous cooling down to ambient temperature shows three events, at 1 107, 1 080 and 1 065 °C. Another cycle was performed and the specimen was quenched from just below the second event at 1 080 °C. In the micrograph in Figure 6-2-2, the liquid can be distinguished by its very fine microstructure, providing useful indications concerning the solidification path. The primary phase is austenite (γ), a portion of dendrite appearing black in the micrograph. The next constituent to form is a two-phase eutectic γ/ξ (Fe_2MoC), immediately adjacent to the primary dendrite, with a coarse structure (finer round the edges, where it has continued to grow during quenching). The morphology of this γ/ξ eutectic is quite similar to that of γ/Fe_3C ledeburite. Solidification was not complete at the moment of quenching, so that the thermal event at 1 080 °C can be identified as corresponding to the γ/ξ eutectic. The third constituent to form, in this case during quenching, is a three-phase eutectic $\gamma/\xi/Fe_3C$. In spite of the coarse dark-coloured cementite plates, which are a characteristic feature of this eutectic (see also Fig. 6-4-2), the other two phases are fine, [Gir95].

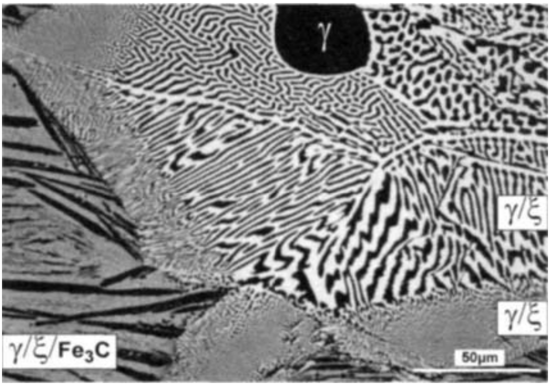

Figure 6-2-2:
Scanning electron micrograph of a Fe-4C-16.2Mo alloy (17.2C-8.8Mo in at.%) cooled at 5 °C/mn in a DTA furnace then quenched from 1075 °C. Three constituents are visible; primary γ dendrites (black), γ/ξ (Fe_2MoC) eutectic, and a three-phase eutectic $\gamma/\xi/Fe_3C$ with coarse dark-coloured cementite plates. The regions of finer structure, apparently also γ/ξ eutectic, correspond to solidification of the liquid during quenching.
Courtesy INPG, Grenoble, [Gir95].

6-3 Solidification paths

Effect of diffusion in the solid on solidification paths

During the solidification of commercial steel products, neither the reversible model nor the Scheil-Gulliver conditions are valid. Significant solute redistribution can occur between the solid and liquid phases, particularly considering the high temperatures concerned in the case of steels. However, the S-G model can be used to determine the maximum degree of segregation. The latter is often represented in practice by the ratio between the maximum and minimum concentrations measured in the matrix.

The problem is to evaluate the extent of solute diffusion in the solid during the time it is in contact with the liquid. In the case of carbon and other interstitial elements, diffusion is rapid and is not limited to the surface region of the solid. Indeed, it is commonly assumed that interstitial solutes behave in a reversible manner. In contrast, the depth of penetration of substitutional solute elements is much more limited. Like in all diffusion problems, the essential parameters are the temperature, the time, and the size of the structure. The first attempt to model this situation [Bow66] introduced these parameters in the S-G model as a correction coefficient in the form of a dimensionless Fourier number $\alpha = 4D_S\theta_S/\lambda^2$, where D_S is the temperature-dependent diffusion coefficient in the solid, θ_S is the fractional local solidification time concerned and λ is the primary dendrite arm spacing. In fact, the correction for diffusion in the solid turns out to be small, and its variation with solidification rate can often be neglected for substitutional elements, because of two mutually compensating effects. Thus, in the Fourier coefficient, when solidification is rapid, both θ_S and λ are small, while at low speeds, they are both large.

Segregation in the solid phase is illustrated by the microstructure of a chromium and carbon rich tool steel shown in Figures 6-3-1 and 6-3-2. The specimens were taken from a

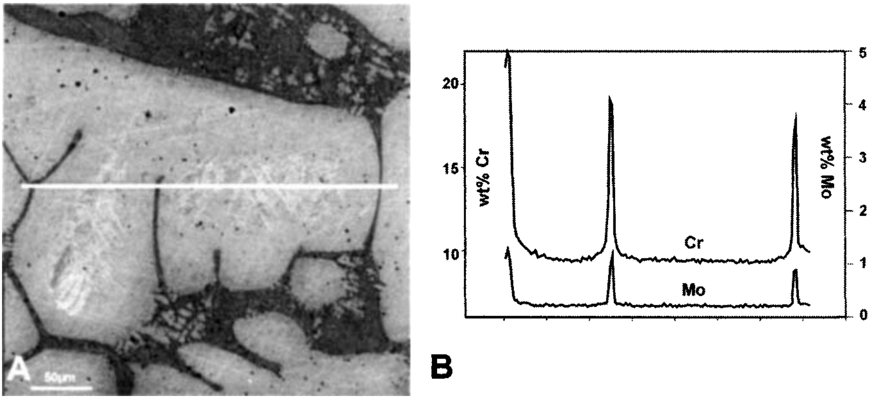

Figure 6-3-1:
Segregation during solidification of an Fe-12Cr-1.65C-0.5Mo-0.5W-0.25V tool steel (ASTM A681-89a, UNS T30402). Specimen quenched during unidirectional solidification.
A) Scanning electron micrograph of a section that was at 1300 °C at the time of quenching, *i.e.* 93 °C below the experimental liquidus temperature. The light-coloured needles in the centre of the dendrites are martensite. Absorbed electron image#, in which the heavier molybdenum-containing carbides appear dark.
B) Chromium and molybdenum concentration profiles determined by point analyses every 2 µm along the white line in A. Specimen supplied by Aubert et Duval, Les Ancizes, France.
# The operating conditions in an electron microprobe enable measurement of the specimen current or absorbed electron signal, which is complementary to the back-scattered and secondary electron signals. The contrast is consequently reversed and the carbides containing molybdenum appear dark.

bar quenched during unidirectional solidification. For the one in Figure 6-3-1, solidification has occurred slowly through about 100 °C, while in Figure 6-3-2, it has occurred rapidly during quenching (note the difference in scale). The amount of segregation determined experimentally is quite similar for the coarse slowly-cooled dendrites and for the small ones formed during quenching.

Recent more sophisticated models take into account structural ripening [Vol99]. The major difficulty in modelling diffusion stems from the fact that the dendrites have a complicated morphology, which is neither axial nor spherical, and which changes in time. It is therefore hard to accurately predict the transverse segregation in a dendrite as a function of the solidified fraction. From the experimental standpoint, it is difficult to precisely locate the centre of a dendrite (minimum segregation for $k<1$) in a section that is not transverse. Several measurements must be made to obtain a significant value.

Apart from diffusion into the solid, another phenomenon that affects measured segregation is supercooling ΔT_L at the dendrite tips. The solid composition C_p at these points is defined by the equilibrium at $T_L - \Delta T_L$ (Fig. 5-3-9), and is enriched in solute for $k<1$. The degree of supercooling increases with solidification rate. The relation $C_p = k.C_0$ is approached only when the rate is not too high, as in the solidification of industrial ingots.

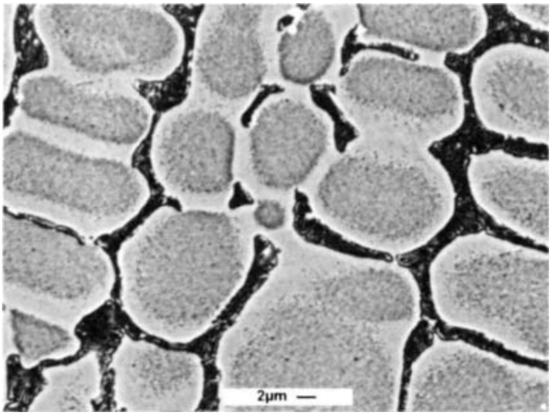

Figure 6-3-2:
Microprobe absorbed electron micrograph of the same bar as in Fig. 6-3-1, in a section that was still fully liquid at the moment of quenching, leading to a very fine microstructure. Point analyses revealed segregation of the same order as in the coarse dendrites in Fig. 6-3-1. The lighter-coloured dendrite edges are richer in chromium and have reacted less to the etchant employed.
Specimen supplied by Aubert et Duval, Les Ancizes, France.

In summary, it is practically impossible to avoid a certain amount of segregation at the end of solidification. The extent does not vary greatly for the solidification rates normally encountered in practice. The significant heterogeneity resulting from this microsegregation can have important repercussions on subsequent solid state transformations, such as localised precipitation and non-uniform martensite formation. The mechanical properties and corrosion resistance can be adversely affected (*cf.* variable etching response visible in Fig 6-3-2). It is generally necessary to perform homogenising heat treatments to eliminate or attenuate the segregation. The ease of homogenisation depends greatly on the fineness of the solidification structure. To a first approximation, the time necessary to achieve a given degree of homogenisation varies with the square of the "wavelength" of the fluctuations in composition.

Since the first attempts to take diffusion into account, many models have been proposed over the last thirty years [Kra97], the most recent ones incorporating the calculation of multi-component phase equilibria. The thermodynamic calculation codes determine the liquid and solid compositions in equilibrium in a step-by-step manner as a function of temperature, assuming either reversibility or S-G conditions. A major difficulty is the insufficient accuracy of existing thermodynamic phase diagram data. Data specifically adjusted for the particular range of compositions have been optimised (*e.g.* for 18Cr–10Ni stainless steels [Mie98c]).

> *The solidification path is calculated step-by-step, based on the tie-lines at each temperature considered. If the calculated partition coefficient is too small, for example, the liquid will be too rich in solute. The error becomes amplified at each step in the calculation. It is for this reason that these models require precise values for the partition coefficients, otherwise the predicted end of the solidification path can be totally false.*

Some codes incorporate partial diffusion according to a defined space scale [Hil99a]. The example shown in Figure 6-3-3 was calculated using the DICTRA software, associated

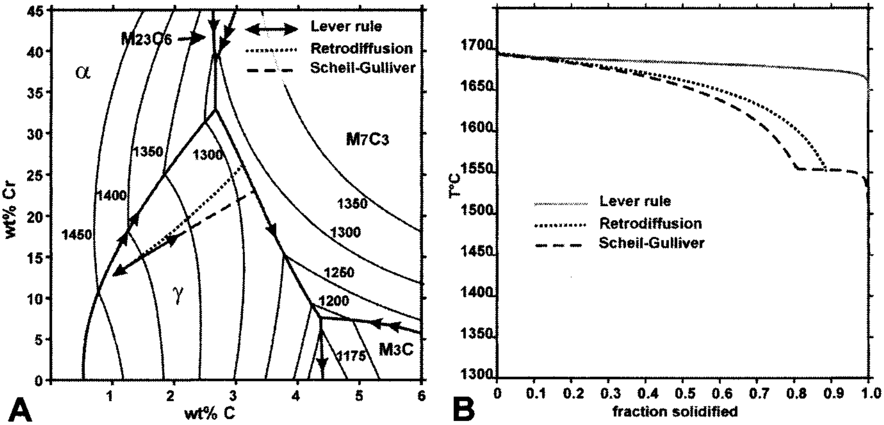

Figure 6-3-3:
Solidification of an Fe-14Cr-1.1 C alloy.
A) Solidification paths on the liquidus projection in the metastable Fe-Cr-Fe_3C system (*cf.* § 4-6), for three different conditions :

- with diffusion into the solid (reversible, lever-rule, conditions); the path stops at the equilibrium solidus, where the composition of the final liquid is equal to the overall composition of the alloy (grey line ending in an arrow);
- with no solid diffusion (Scheil-Gulliver model); the path continues down to the Fe/Fe_3C eutectic, which is the end-point of the eutectic valleys;
- with partial diffusion, a cooling rate of 0.5 °C/s and a secondary dendrite arm spacing of 50 μm.

B) Variation of the solid fraction as a function of temperature in each of the cases considered (the calculation has not been continued beyond the eutectic for the conditions with diffusion).
Courtesy INPG, Grenoble

with Thermocalc, for a simple Fe-Cr-C ternary alloy. In the case of the Fe-Cr-C-Mo-W-V alloy in Figure 6-3-1, the experimental concentration profile is relatively close to that calculated for the fraction of solid concerned, assimilating the dendrite to a sphere. In fact, the essential point in this case is that the agreement between calculation and experiment is good for the extreme values at the centre and edges of the dendrites.

Solidification paths with segregation in carbides

Segregation in the metal matrix is perfectly common. In contrast, segregation within carbides or other compounds is more rarely envisaged. The first example to be considered is the case of cubic MC-type carbides. In the Fe-V-Ta-C system, a eutectic consisting of austenite and mixed (V,Ta)C carbide can form. In this iron-based system, the mixed carbide appears to exist at high temperature over the whole range of compositions from VC to TaC. The eutectic solidification begins with the formation of a tantalum-rich carbide, practically pure TaC, and continues with continuous depletion in tantalum, ending with a vanadium-rich carbide. The carbide phase appears physically continuous (Figure 6-3-4 A), but there is a strong contrast in the scanning electron micrograph, the

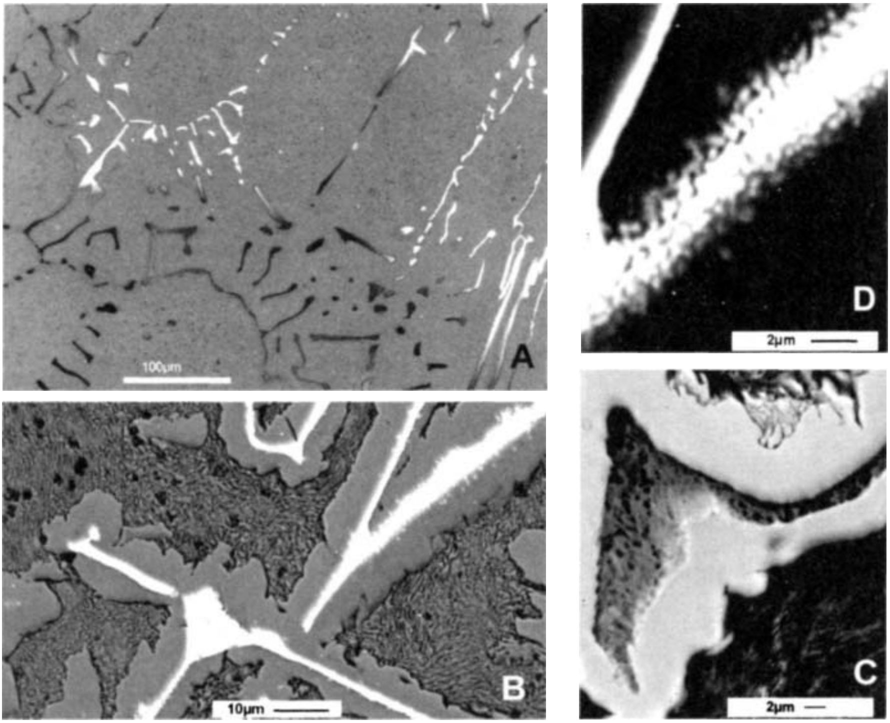

Figure 6-3-4:
Scanning electron micrographs of an Fe-V-Ta-C alloy slowly cooled from the liquid at 5 °C/mn.
A) Austenite dendrites (γ) surrounded by γ/(V,Ta)C eutectic. The dark areas of the carbides are rich in vanadium and the light areas rich in tantalum.
B) After deep etching, the (V,Ta)C carbides appear to be surrounded by cementite formed in the solid state (smooth grey borders). The matrix is pearlitic with a few secondary VC precipitates that do not contain tantalum (black spots).
C) Enlargement of the dark MC carbides. The light grey border is cementite, while the dark grey centre is a mixture of the two dissociated MC carbides.D) Enlargement of the light MC carbides. The contrast has been enhanced to reveal the dissociation, making it impossible to distinguish the cementite, also present in this case.
Courtesy INPG, Grenoble

gradient in concentration being revealed by the large difference in atomic weight between vanadium and tantalum. According to the phase diagrams, or to be more exact, the pseudo-binary sections between carbides, or between carbides and certain nitrides, there is effectively a high miscibility at temperatures above 1000-1300 °C (Fig. 4-12-3) [Hol84].

Carbide decomposition

Mixed compounds are often unstable and decomposition is observed in several systems at temperatures below about 1000 °C [Adn92]. For example, the mixed carbonitride (V,Nb)(C,N) decomposes to NbC and VN, the proportion of the latter phases increasing

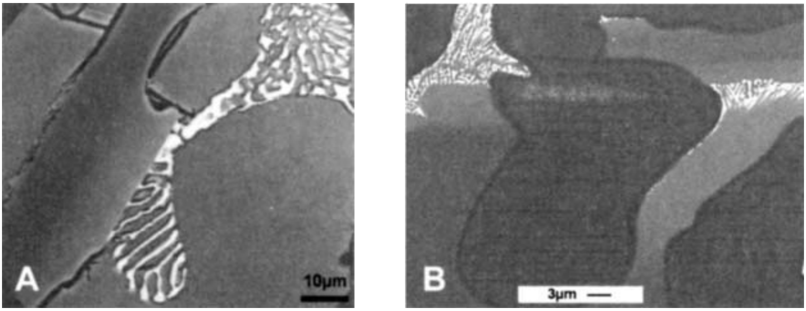

Figure 6-3-5:
Scanning electron micrographs of as-solidified alloys (back-scattered electron images) :
A) Eutectic carbides in an Fe-3.3C-16Cr-3Mo-1Mn-0.5Si alloy. Mo_2C appears white, while M_7C_3 has a dual grey contrast, corresponding to two different Mo concentrations, respectively 1.3 and 5 at%, [De-83].
B) Eutectic carbides in an Fe-3.8C-4.6Mo alloy. The black background is the austenite matrix, while the white constituent is the $\gamma/\xi/M_3C$ eutectic and the grey carbides are M_3C with respectively 1.7, 3.4 and 5.1 at% Mo [Gir95].
Courtesy INPG, Grenoble

with time. In the example shown in Figures 6-3-4 C and D, the initial mixed carbides appear to have decomposed into two vanadium and tantalum rich carbides :
$(V,Ta)C \rightarrow (\underline{V},Ta)C+(V,\underline{Ta})C$. However, in steels, mixed carbides can persist for long times at temperatures where they are only metastable. For example, in thermal power station steels (*cf.* § 20), the decomposition reaction at 500 °C occurs over a period of many years.

Discontinuous changes in composition

The second example concerns eutectic carbides of the M_7C_3 and M_3C types containing more than one metallic element, such as $(Fe,Cr,Mo)_7C_3$ or $(Fe,Cr,Mo)_3C$. These carbides are heterogeneous in as-solidified alloys. The phenomenon is clearly visible in the scanning electron microscope for heavy substitutional elements, such as molybdenum or tungsten. The concentration of the substitutional element does not vary continuously within the carbide as would be the case with an ordinary segregation process, but appears to change in distinct steps (Fig. 6-3-5). The transition zone has been studied by transmission electron microscopy, and no change in crystal structure was apparent. In the case of $(Fe,Cr,Mo)_3C$ carbide, the molybdenum contents in the different zones were found to be in a ratio of 1, 2 or 3. It is as though each zone corresponds to the occupation of specific sites in the carbide lattice in a defined order.

Solidification paths including a series of eutectics

The Fe-C-X ternary systems, where X is a carbide-forming element, include various eutectics. In the phase diagrams, numerous pseudo-peritectic transformations often occur along the monovariant eutectic line. Under normal cooling conditions (greater than a few degrees per minute), a typical eutectic morphology of the constituents is observed.

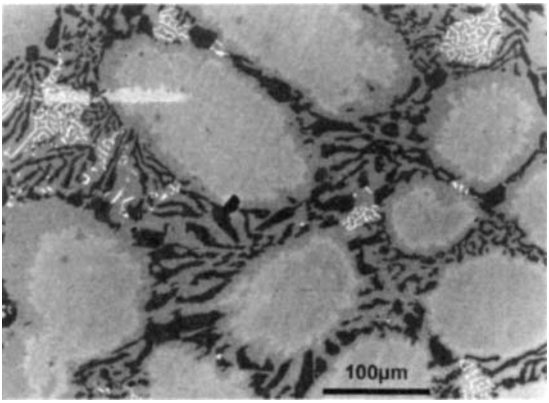

Figure 6-3-6:
Scanning electron micrograph of an Fe-2.1C-14.7Cr-1Nb alloy cooled from the liquid at 2.5 °C/mn. The centres of the primary austenite dendrites have transformed to martensite (light contrast). Between the dendrites, the coarse M_7C_3 eutectic carbides appear black, while the finer NbC eutectic carbides are white.
Courtesy INPG, Grenoble [Kes87].

The first example is an alloy cast iron containing niobium, slowly cooled during a DTA experiment (Fig. 6-3-6) [Kes87]. Three steps in the solidification path can be deduced from the micrograph :

1 the formation of primary austenite dendrites
2 the formation of γ/M_7C_3 eutectic
3 the formation of γ/NbC eutectic

The γ/M_7C_3 eutectic surrounding the austenite has a characteristic fairly coarse morphology. The γ/NbC eutectic forms in the interdendritic spaces, at triple points, in the last regions to solidify. The solidification structure corresponding to the last liquid is often fine, probably because the latent heat can be easily dissipated to the surrounding solid, due to the small volume and large surface area of the regions concerned.

The second example is a vanadium-containing alloy cast iron (Fig. 6-3-7). In this case also, the micrograph reveals a three-step solidification process :

1 the formation of primary austenite dendrites
2 the formation of γ/VC eutectic
3 the formation of γ/M_7C_3 eutectic

Both eutectics are coarse and present in large amounts. The order in which they form is difficult to deduce from the microstructure. However, it can be readily determined by means of directional solidification experiments, which show that it is the γ/M_7C_3 eutectic that appears last, at a temperature quite distinct from that for the γ/VC eutectic.

> *Comparison of Figures 6-3-6 and 6-3-7 A reveals a difference in the propensity of the two alloys to form martensite on cooling. In the presence of niobium, the amount of carbon in solution in the austenite remains small at all temperatures during solidification, and particularly at the eutectic temperature (see solubility products in Table 17-2-5). Consequently, the austenite transforms readily to martensite. In contrast, in the presence of vanadium, the carbon solubility in the austenite is significantly higher during solidification, but decreases on further cooling,*

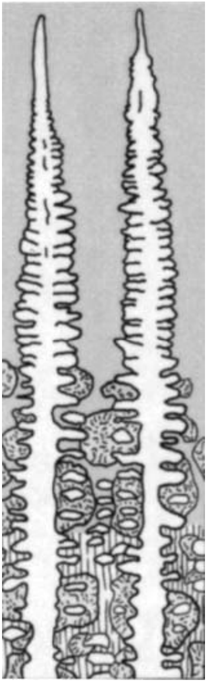

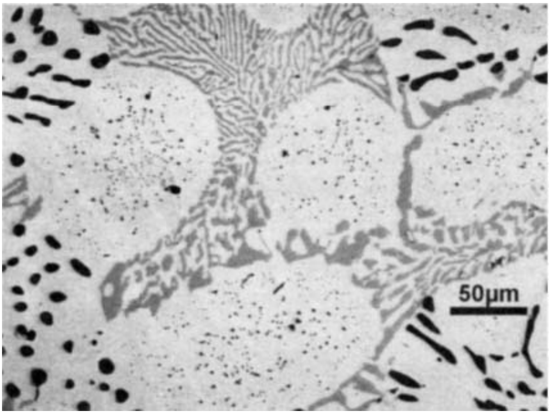

Figure 6-3-7: A:
A) Scanning electron micrograph of an Fe-2.4C-5.4Cr-6V alloy cooled from the liquid at 5 °C/mn. The volume fraction of carbides measured over a large area is 5.2 %VC and 12.8 % M_7C_3.
B) Schematic representation of the corresponding microstructure observed by quench-interrupted unidirectional solidification. The VC carbides, solidified first, form globular cells, while the M_7C_3 carbides have an oriented lanceolate morphology.
Courtesy INPG, Grenoble (see also [De-84]).

causing the precipitation of secondary vanadium carbides. Nevertheless, the residual carbon and vanadium contents in solution are too high to allow martensite transformation. For the latter to occur, it is necessary to heat treat the alloy at about 900 °C in order to enhance the carbide precipitation and so lower the carbon and vanadium contents in the austenite.

This is of considerable practical importance, since the alloy concerned has much better abrasion resistance when the hard VC carbides (Vickers hardness about 2400) are embedded in a fine martensite matrix.

The third example has been chosen to illustrate the identification on a micrograph of the beginning of solidification of the γ/VC eutectic. The material is a vanadium-containing alloy cast iron (1.7C-1.2Si-1.1Mn-0.8Ni-3.6Cr-1.7Mo-4.7V), in which the first two stages of solidification are similar to the previous example [Jay92]. The specimen was quenched during unidirectional solidification. The first two constituents to form (γ and γ/VC) can be clearly distinguished by their coarse morphologies (Figs. 6-3-8 A and B). The proportion of γ/VC eutectic is large, and detection of the point of initial appearance requires detailed examination of transverse sections. At the end of solidification, molybdenum and chromium become concentrated in the interdendritic spaces and induce the formation of a small amount of another eutectic.

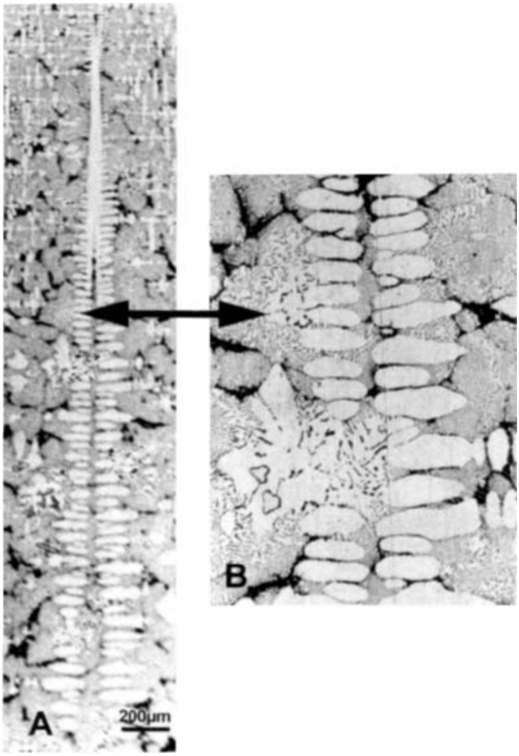

Figure 6-3-8:
Solidification structure observed in an Fe-2.4C-0.9Si-0.9Mn-0.1Ni-2.9Cr-3.4Mo-5.9V alloy quenched during unidirectional solidification at a rate of 9 cm/h, with an average temperature gradient (non-linear) of 95 °C/cm.

A) Scanning electron micrograph of a longitudinal section. The light coloured primary phase is austenite, while the dark nodular or fibrous phase is eutectic VC carbide. The fine regions corresponding to the quenched liquid contain cells of γ/VC eutectic and dark zones where the final liquid has transformed to other eutectic constituents.

B) Enlargement enabling identification of the initial solidification of fibrous γ/VC eutectic, distinguished by its coarser morphology. The double arrow indicates the position of the enlarged zone in micrograph A.
Courtesy INPG, Grenoble.

Unusual morphologies

The eutectic constituents in the three previous examples are quite distinct and can be differentiated by their characteristic morphologies, but this is not always the case. For various reasons, particularly the difficulty of nucleation, metastable transformations can occur instead of the expected stable ones. For alloy compositions close to a transition between different reactions, a change in solidification rate can modify the amount of supercooling required for solidification and can lead to significant variations in microstructure.

A fairly common case is that of a ternary eutectic in which the proportion of one of the phases is small. The morphology remains typical of a two-phase eutectic. A good example is the $\gamma/M_3C/VC$ eutectic in the Fe-V-C system. This eutectic is clearly identified as a ternary, due to its temperature of formation and the configuration of the tie-lines. However, high magnification examination of microstructures obtained by quenching from just below the eutectic temperature reveal no signs of the expected small proportion of cementite, whereas this phase is clearly visible in specimens held at the eutectic temperature.

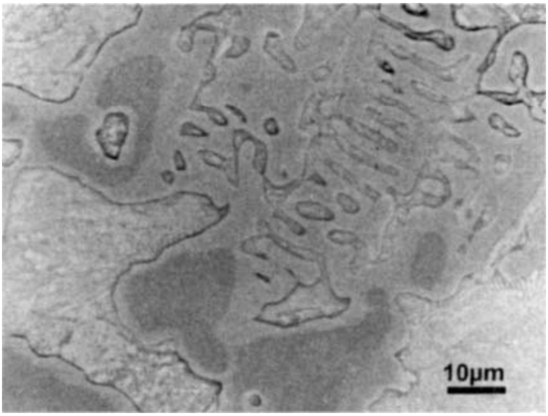

Figure 6-3-9:
Scanning electron micrograph of an Fe-1C-4.4Cr-1.6V alloy cooled from the liquid at 5 °C/mn. The contrast has been enhanced, enabling two carbides to be distinguished in the eutectic constituent, M_7C_3 (dark) and M_3C (lighter). The matrix is austenite that has transformed to fine pearlite. The approximate compositions of the carbides are :
$M_7C_3 = (Fe_{3,5}Cr_{2.5}V_1)C_3$
$M_3C = (Fe_{1,5}Cr_1V_{0.5})C$
Courtesy INPG, Grenoble (see also [De-84]).

Another example is shown in Figure 6-3-9, where agglomerates can be seen in the interdendritic regions of an as-solidified Fe-C-Cr-V alloy. In these materials, the addition of small amounts of vanadium or niobium changes the pseudo-peritectic reaction $\gamma + M_7C_3 \rightarrow M_3C$ in the Fe-Cr-C system to a eutectic reaction $\gamma \rightarrow M_3C + M_7C_3 + \gamma$ [De-84], [Lai91]. M_7C_3 and M_3C carbides are effectively identified, but with an interwoven configuration, not very typical of a ternary eutectic morphology. It is not possible to conclude from the microstructure whether it is the result of a eutectic or peritectic reaction. Reasoning must be based on tie-lines determined at several temperatures.

> *Discrimination between M_7C_3, M_3C and $M_{23}C_6$ carbides is sometimes difficult in Fe-Cr-C alloys in the absence of other elements, since the difference in contrast in the scanning electron microscope is practically negligible. These phases also react similarly to chemical etchants. Furthermore, they tend to grow in epitaxy on one another, so that their detection often requires careful observation.*

Disappearance of non-equilibrium carbides in a pseudo-peritectic reaction

The above examples have shown that carbides formed during solidification remain present, in spite of the pseudo-peritectic reaction that ought to have caused them to disappear, at least partially. In multi-component alloys, according to the phase rule, it is quite normal for numerous phases to co-exist. However, the persistence of phases that are no longer in equilibrium is due to kinetic factors that make many reactions very sluggish.

When carbides redissolve, the process is not the reverse of that involved in their growth, that is, gradual thinning. When epitaxial relationships exist between carbides (*e.g.* M_7C_3 and M_3C, M_7C_3 and $M_{23}C_6$), the peritectic carbide nucleates on the phase that has become metastable and grows at its expense. Alloying elements are transferred from one carbide to the other. Some carbides, such as M_6C, dissolve in another manner, disintegrating and becoming porous. Inside carbide particles, in regions where the carbon

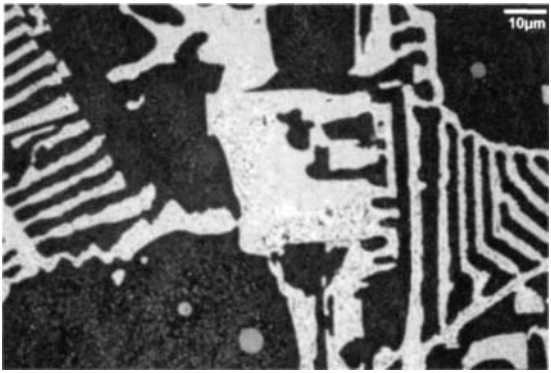

Figure 6-3-10:
Scanning electron micrograph of an Fe-Mo-C alloy with M_6C carbides in the course of dissolution.
Courtesy INPG, Grenoble.

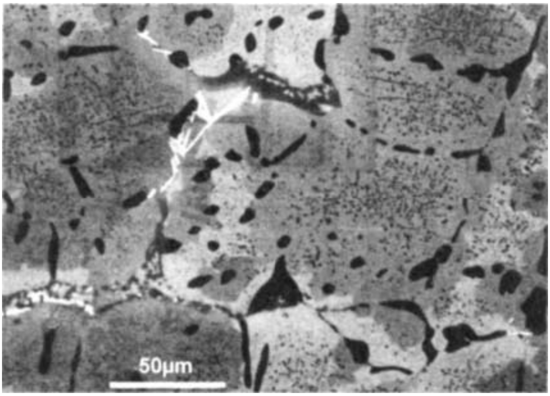

Figure 6-3-11:
Scanning electron micrograph of an Fe-1.7C-1.2Si-1.1Mn-0.8Ni-3.6Cr-1.7Mo-4.7V alloy slowly cooled in the form of a large casting.
Enhanced contrast reveals molybdenum-enriched zones due to the dissolution of eutectic carbides. The small white acicular carbides are Mo_2C. The coarse black carbides are eutectic VC, while the abundant fine dark spots are secondary VC precipitates.
Courtesy INPG, Grenoble.

has left, transient phases may form, such as ferrite. Figure 6-3-10 shows the resulting "moth-eaten" appearance of M_6C carbides in the course of dissolution in an Fe-Mo-C alloy.

Another example, shown in Figure 6-3-11, is a white cast iron similar to that illustrated in Figure 6-3-8. The specimen was cut from a large, slowly cooled casting. The M_6C carbides formed during solidification have completely decomposed and the molybdenum released into the matrix has re-precipitated in the form of $(MoCr)_2C$ platelets. However, the conventional heat treatment has not fully homogenised the composition and the molybdenum remains concentrated in regions around the prior eutectic constituents. The lighter-coloured zones affected by the dissolution are clearly visible in Figure 6-3-11. Although only slight, the differences in local composition affect the transformation behaviour to martensite or bainite and subsequent tempering reactions. The presence of unwanted Mo_2C and the general heterogeneous structure can significantly impair the mechanical properties.

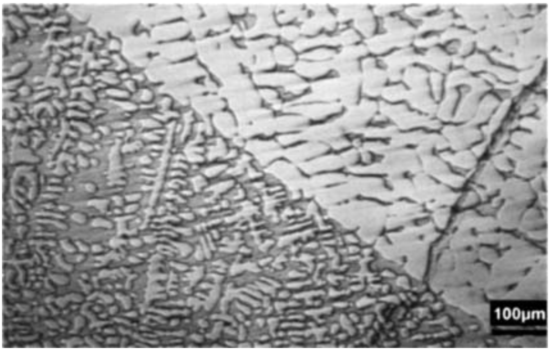

Figure 6-3-12:
Scanning electron micrograph of an as-solidified Fe-20Co-52Cu alloy, showing the region of separation between the two liquids.
Courtesy INPG, Grenoble.

Solidification paths with separation into two or more liquids

In some systems, the liquid can separate into two or more immiscible phases. There is therefore a range of compositions for which it is impossible to prepare alloys by melting. Such liquid immiscibility is observed in several Fe-Cu-X systems, particularly where X=Co or Cr. When the two liquids separate, droplets of the minor phase are formed, which in the absence of stirring forces, tend to coalesce to coarse homogeneous islands.

If the first liquid to solidify is the majority phase, it tends to surround the other one with a solid shell that acts as a "mould", through which the exchanges necessary to maintain equilibrium are severely limited. The consequence is the formation of two large zones where solidification has proceeded independently. The microstructure must be interpreted as being due to two different alloys (Fig. 6-3-12). However, this phenomenon may occur *on a fine scale,* for example, in the liquid regions formed during the sintering of Fe-Cu-X alloys.

6-4 Metastable solidification paths

The Fe-W-C system

Settling and flotation effects

The Fe-W-C system can be quite puzzling, and the experimental determination of liquid/solid equilibria encounters several difficulties. The most readily visible effect is the tendency for tungsten carbide WC to settle out at the bottom of the crucible. Similar gravitation-driven segregation of tungsten in the liquid is less easy to detect. Another major problem is the formation of highly stable intermetallic compounds which solidify with a high degree of supercooling. The solidification paths are therefore extremely difficult to interpret. Several phases can show primary solidification morphologies, due to the fact that their growth has not been stopped by that of another phase.

Figure 6-4-1 shows the microstructures of two slowly solidified specimens. In the micrograph W13, the austenite appears in the form of primary dendrites. The same is true for

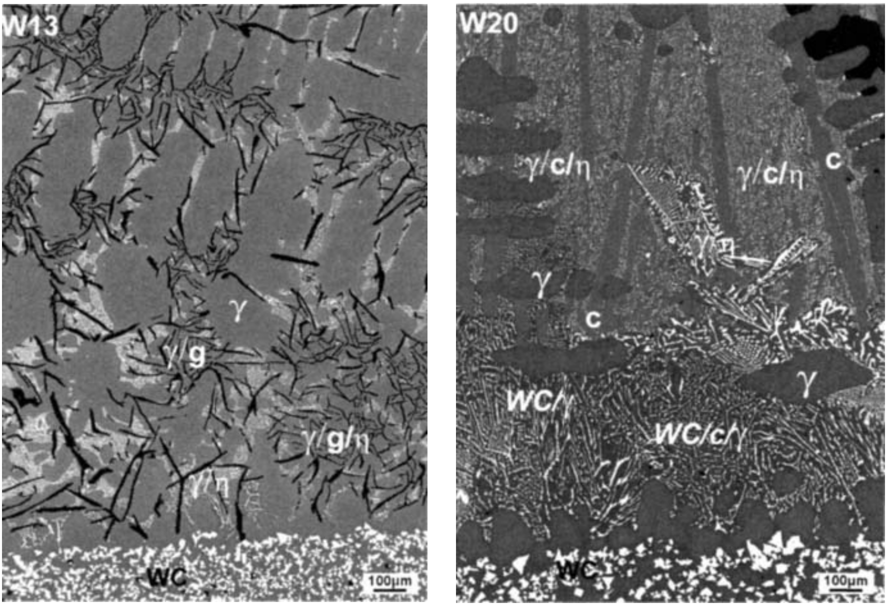

Figure 6-4-1:
Scanning electron micrographs on vertical sections of DTA specimens quenched during solidification.
W13) Fe-12.6W-3.96C alloy cooled at 5 °C/h.
W20) Fe-19.8W-3.1C alloy cooled at 2 °C/h.
γ = austenite, c = cementite, η = M_6C, g = graphite.
Courtesy INPG, Grenoble.

the large graphite flakes and for the white tungsten carbides (WC) that have settled to the bottom of the crucible in the form of coarse facetted particles. Three phases can be distinguished in the interdendritic regions; austenite (γ), fine graphite filaments and white M_6C carbides. Austenite and M_6C appear to be combined in a eutectic. A ternary eutectic, γ/M_6C/graphite also appears to exist. The microstructure resembles that of a grey cast iron in which segregation has caused the formation of local regions of white cast iron.

The structure is even more complicated in micrograph W20, where at least four phases can be identified, γ, Fe_3C, WC and M_6C. Several of them have primary solidification morphologies (the austenite dendrites, the settled-out WC carbides and the large cementite needles). The γ/Fe_3C/M_6C ternary eutectic is present in large amounts in the upper part of the specimen, while the ternary eutectic γ/Fe_3C/WC can also be seen in a band about a millimetre wide above the settled-out WC carbides.

In the micrograph W30 (Fig. 6-4-2 A), austenite dendrites are visible next to large M_3C carbide plates. In fact, the austenite dendrites required a large degree of supercooling to be able to form, and the necessary conditions were fulfilled only when the liquid depleted in carbon by the solidification of primary cementite had reached a clearly hypoeutectic composition.

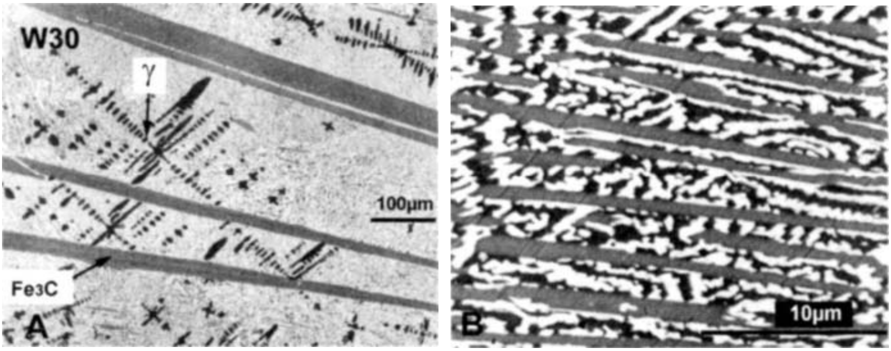

Figure 6-4-2:
Scanning electron micrographs of a slowly cooled Fe-30W-4.3C alloy.
A) In the top part, above the settled-out carbides, the composition is macroscopically homogeneous, with three uniformly distributed constituents; large dark grey cementite plates, black austenite dendrites and light grey "matrix".
B) At higher magnification, the "matrix" is seen to be a eutectic constituent, composed of three intermingled phases; austenite (black), cementite (grey) and Fe_3W_3C carbide (white) [She92].
Courtesy INPG, Grenoble.

In practice, the observation of several phases apparently formed by a primary solidification process is quite common, and occurs in several other systems. The compositions concerned are frequently hypereutectic and are associated with a highly refractory intermetallic compound.

The ternary eutectic

In both specimens W20 (Fig. 6-4-1) and W30 (Fig. 6-4-2), there is a large proportion of ternary eutectic $\gamma/M_6C/Fe_3C$. This constituent is found to occur systematically in the as-solidified alloys, even after slow cooling. The three phases have a characteristic closely intermingled morphology, clearly indicating stable coupled growth (Fig. 6-4-2 B). The corresponding eutectic temperature (1085 °C) is perfectly reproducible. The morphology is quite similar to that of the $\gamma/Fe_3C/Fe_2MoC$ ternary eutectic in the Fe-Mo-C system.

Altogether, three ternary eutectics have been identified in the Fe-W-C system; $\gamma/M_6C/Fe_3C$, $\gamma/WC/Fe_3C$ and $\gamma/M_6C/$graphite. Several quite different versions of the Fe-W-C phase diagram exist in the literature, but none is compatible with the above experimental observations. The most significant discrepancy is the ternary eutectic. In fact, seven different proposals have been made for this eutectic (Table 6-4-3). They include five distinct phases ; austenite, cementite, WC, M_6C and graphite. All combinations appear possible, provided that one of the phases is austenite.

From an experimental standpoint, the micrographic observations in some of the studies cited (Table 6-4-3) appear to have been limited to identification of the most readily visible phases, without considering certain constituents that are only revealed at high magnification and with carefully adjusted conditions of contrast.

Table 6-4-3: Compositions and temperatures of ternary eutectics proposed for the Fe-W-C system.

Constituents	Composition (wt.%)	Temperature (°C)	References
$\gamma/WC/graphite$	4.2C-4.9W	1140	Calculated, data from [Gus87]
$\gamma/\xi/Fe_3C$	3.9C-12.8W	1122	Calculated, excluding WC, data from [Gus87]
$\gamma/M_6C/Fe_3C$	3.9C-13.2W	1121	Calculated, excluding WC and ξ, data from [Gus87]
$\gamma/M_6C/Fe_3C$	3.9C-19.8W	1085	Experimental (Fig. 6-4-2A) [She92]
$\gamma/M_6C/graphite$	4.2C-12.6W	1121	[Uhr80]
$\gamma/WC/graphite$	4.2C-5.1W	1143	[Uhr80]
$\gamma/WC/Fe_3C$	3.6C-15W	1085	[Jel68]

The calculated Fe-W-C phase diagram

The calculated phase diagram is not very satisfactory. One failing is that it does not allow for the existence of the κ carbide Fe_3WC, which features in the isothermal sections determined experimentally by Hollek [Hol84], particularly at 1250 °C. The major problem stems from the fact that the predicted range of existence of WC is too wide, both on the liquidus surface and in the solid state. The calculated ternary eutectic is $\gamma/WC/Fe_3C$. If WC is excluded from the calculations, the liquidus surface obtained then explains some of the microstructures actually observed.

Although the modelling is not perfect, it is not the only reason for the disagreement, and other possibilities can be envisaged. For example, it may be a problem of specimen preparation. Thus, transient WC formed during melt-down of the charge could be difficult to redissolve completely, leading to the settling out of these heavy tungsten carbides. The facetted morphology of the WC particles is a characteristic often associated with high supercooling, which in this case may be very high. Marked chemical supersaturation is thus necessary for WC to form from the liquid, otherwise metastable phases will tend to replace it. The solidification paths can then be interpreted in the absence of WC, and when the primary WC particles settle to the bottom of the crucible, *the remaining microstructure effectively corresponds to this situation.*

6-5 Peritectic transformations

Solidification paths including the δ/γ peritectic

Like Fe-W-C, the Fe-Mo-C system is important for tool steels and there are many similarities, particularly as regards the types of phases formed. However, in this case, the calculated and experimental phase diagrams agree closely. The discrepancies remain acceptable and concern essentially the extents of the liquidus surfaces and the transformation temperatures, but not the fundamental configuration of the diagram.

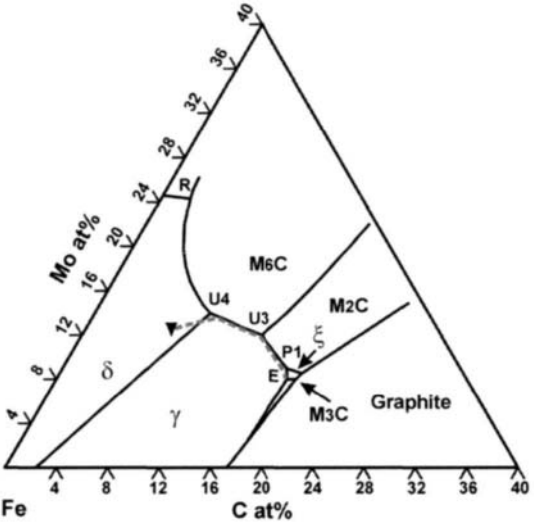

Figure 6-5-1:
A) Liquidus projection of the Fe-Mo-C system. The salient features are :
two pseudo-peritectics;
U4 at 1276 °C : $L+\delta \rightarrow M_6C+\gamma$ and
U3 at 1157 °C : $L+M_6C \rightarrow M_2C+\gamma$;
a ternary peritectic
P1 at 1080 °C : $L+M_2C+\gamma \rightarrow \xi$;
and a ternary eutectic
E at 1065 °C : $Liq \rightarrow \gamma+M_3C+\xi$.
The dashed line represents the solidification path for an Fe-23.3Mo-1.1C alloy (Fe-14.4Mo-5.3C in atom %). Adapted from [Gir95].

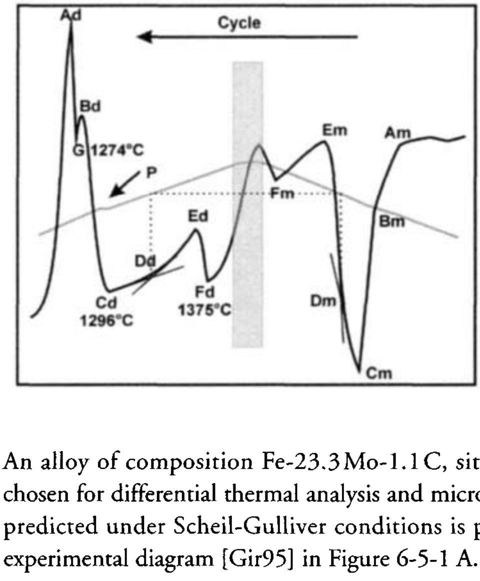

B) DTA recording for the Fe-23.3Mo-1.1C alloy heated and cooled at 5 °C/mn. The grey line is the imposed temperature, while the black line is the difference in temperature between the specimen and an inert reference sample. The small plateau P on the temperature curve is due to the marked dissipation of latent heat beyond Cd, that has been detected by the measurement thermocouple, placed close to the specimen. The grey region represents the change from heating to cooling. Adapted from [Gir95].

An alloy of composition Fe-23.3Mo-1.1C, situated in the primary δ-ferrite field, was chosen for differential thermal analysis and microstructural studies. The solidification path predicted under Scheil-Gulliver conditions is plotted on the liquidus projection of the experimental diagram [Gir95] in Figure 6-5-1 A. Six steps can be identified :

1 formation of primary δ-ferrite;
2 formation of austenite, γ;
3 formation of γ/M_6C eutectic;
4 formation of γ/M_2C eutectic;
5 formation of γ/ξ eutectic;
6 formation of the ternary eutectic $\gamma/\xi/M_3C$.

> *The morphologies of the various eutectic constituents have already been described for other alloys ;* γ/M_6C *in Fig. 6-3-3,* γ/M_6C *and* γ/M_2C *in Fig. 5-4-7,* γ/ξ *in Fig. 6-2-2, and a microstructure similar to* $\gamma/\xi/M_3C$ *in Fig. 6-4-2.*

Interpretation of the DTA curve

The differential thermal analysis (DTA) curve obtained for the above alloy is shown in Figure 6-5-1 B and is described in detail below. There are three major thermal events on cooling, corresponding to the first three transformations along the solidification path. The others are not visible, because the liquid is either already exhausted or in too small a proportion by the time the corresponding temperatures are reached. Contrary to those for pure metals, DTA recordings for alloys are often difficult to interpret, since solidification occurs continuously and the different signals cover a range of temperatures and can overlap. A clear understanding of the solidification path is necessary to identify the thermal events. The appearance of a new phase changes the specific heat, while latent heat is liberated, associated with undercooling. The beginning and end of a transformation are indicated by a change in slope. Thus, the points Am, Bm and Em represent the start of melting of three constituents on heating, while Ad, Bd and Ed correspond to the end of solidification of the same constituents on cooling. The point Fm is the end of melting, and corresponds to Fd, which is the start of solidification, that is, the liquidus. The point Cd indicates the appearance of the peritectic γ phase and point G represents the formation of the γ/M_6C eutectic. The peaks Cm, Ed, Bd and Ad indicate the approximate end of the absorption or dissipation of latent heat associated with the corresponding transformations. The inflection points Dm and Dd, situated at the same temperature on heating and cooling, represent the return to a normal regime for one of the constituents.

Marking of the peritectic transformation by precipitates

The various transformation processes often leave visible traces in the microstructure. In § 5-7, it was shown how primary δ-ferrite becomes unstable below the peritectic temperature and transforms to austenite. Thus, below the peritectic temperature, the liquid solidifies to primary austenite, which surrounds the ferrite dendrites. Peritectic reaction between the liquid and the ferrite to produce austenite can occur only near the points where the three phases are in contact. At the interface between the ferrite and austenite, the ferrite transforms to austenite in the solid state and thus regresses towards the centre of the dendrite. This process is accompanied by diffusion of carbon from the liquid through the austenite and by the rejection of ferrite-stabilising elements (Mo, W, V, Si, Nb, Cr, etc.) into the ferrite. These elements accumulate in a narrow diffusion layer (Fig. 6-5-2). This phenomenon is quite common in steels that contain elements that are both ferrite stabilisers and

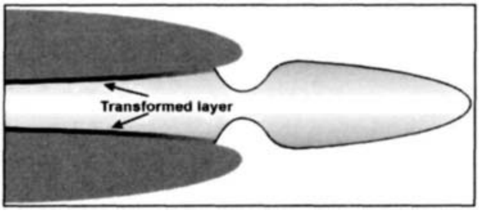

Figure 6-5-2:
Simplified version of Fig. 5-7-4, representing a primary ferrite dendrite (light), primary austenite (grey) and the diffusion layer rich in rejected solute elements associated with the peritectic δ/γ transformation (black).

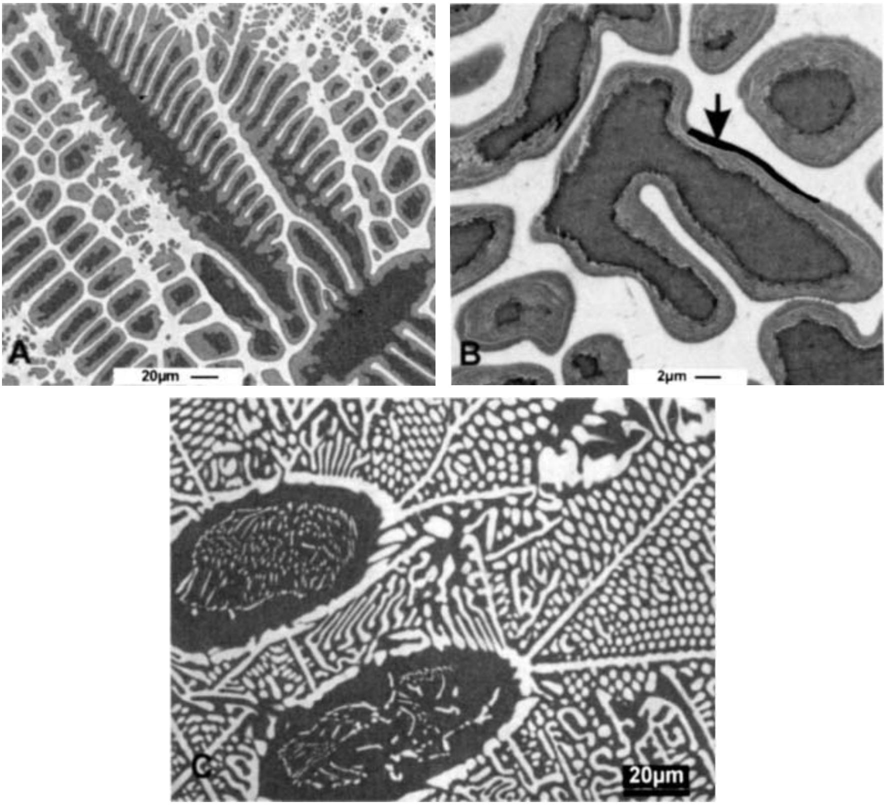

Figure 6-5-3:
Scanning electron micrographs of an Fe-23.3Mo-1.1C alloy cooled from the liquid at 5 °C/mn until the appearance of the first DTA peak, then quenched.
A) The primary δ-ferrite dendrites appear almost black, with their transformed boundaries grey. The eutectic constituents, composed of γ and various molybdenum-rich carbides, appear white.
B) Enlargement showing the presence of peritectic austenite (black, arrow) along the border, the stratified border being transformed austenite.
C) The same alloy cooled from the liquid at 5 °C/mn down to room temperature. The dark phase is austenite and the light phase is M_6C carbide. The carbides formed in the centres of the dendrites mark the contours of the original δ-ferrite.
Courtesy INPG, Grenoble (see also [Gir95]).

> *carbide formers. The diffusion layer can subsequently undergo various transformations that mark the peritectic transformation.*

The micrographs shown in Figures 6-5-3 A and B, corresponding to an Fe-23.3Mo-1.1C specimen cooled from the liquid at 5 °C/mn until the appearance of the first DTA peak, then quenched, confirm the peritectic transformation. The micrograph in Figure 6-5-4 C represents the same alloy cooled at 5 °C/mn right down to room temperature. The microstructure in this case is completely different.

In Figures 6-5-3 A and B, the microstructure has been frozen by quenching from the first DTA peak corresponding to the formation of primary δ-ferrite. During the rapid cooling, the solidification path can be interpreted in terms of Scheil-Gulliver conditions (Fig. 6-5-1 A). The δ-ferrite dendrites are surrounded by a narrow border of austenite, while the remaining structure is composed of an extremely fine eutectic constituent. The higher magnification image in Fig. 6-5-3 B reveals that the austenite has developed at the expense of the ferrite, depositing layers of carbides parallel to the interface. The morphology suggests a curved interphase boundary precipitation mechanism.

When cooling at 5 °C/mn is continued down to room temperature (Fig. 6-5-3 C), the ferrite has completely disappeared and only two phases remain, γ and M_6C. The precipitate-free periphery of the dendrites corresponds to primary austenite. In the centre of the dendrites, the carbide precipitates have transformed and coarsened. The transition between the prior ferrite dendrites and the primary austenite is marked by strings of these precipitates.

Marking of the δ/γ peritectic transformation by cellular precipitation

The second example is a carbon-rich alloy containing nearly 24 % of chromium, in which primary δ-ferrite remains stable. The solidification sequence involves three stages ; δ, γ, and

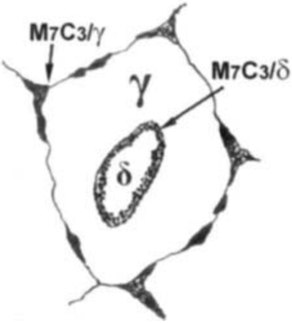

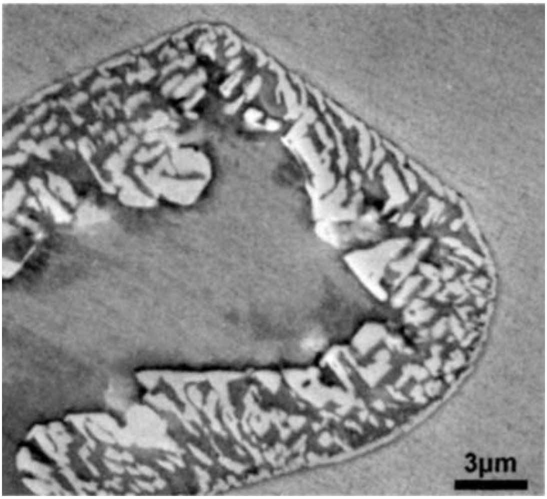

Figure 6-5-4:
Scanning electron micrograph of an Fe-0.86C-23.8Cr-1.9Si-2.1Ni alloy cooled from the liquid at 150 °C/h. The schematic diagram on the right shows the position of the phases within a dendritic grain. The primary δ-ferrite dendrite in the centre is surrounded by austenite γ formed below the peritectic temperature. Cellular precipitation of M_7C_3 has occurred inwards from the δ/γ interface. Solidification has ended by the formation of a γ/M_7C_3 eutectic at the grain boundaries. The micrograph represents the central part of the diagram. Courtesy INPG, Grenoble (see also [De-85]).

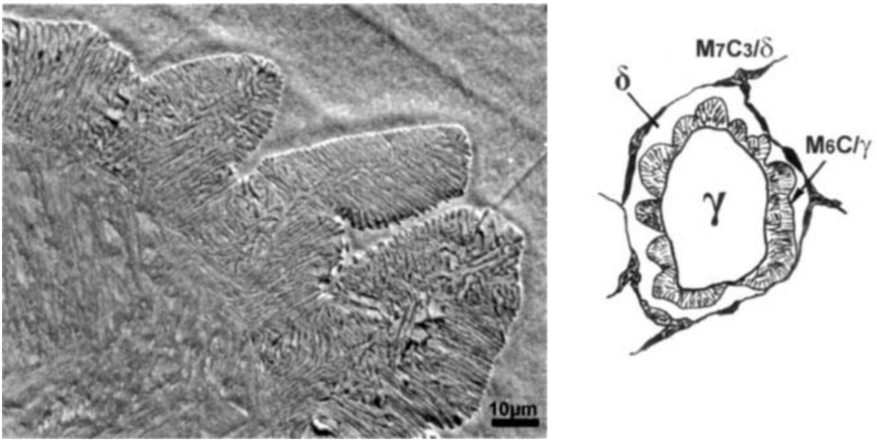

Figure 6-5-5:
Scanning electron micrograph of an Fe-0.87C-16 Cr-0.7Mn-2.8Mo-0.31 Si alloy cooled from the liquid at 5 °C/mn. The schematic diagram on the right shows the position of the phases within a dendritic grain. Courtesy INPG, Grenoble.

M_7C_3/γ eutectic (Fig. 6-5-4). During cooling, the δ-ferrite becomes supersaturated, leading to the discontinuous (cellular) precipitation of M_7C_3 carbides at the δ/γ interface, the latter being marked by an almost continuous layer of particles. The precipitate colonies have grown into the ferrite, carbon being supplied also by diffusion along the interface from the supersaturated austenite [De-85]. Because of the high temperature at which this transformation occurs, the carbon activity can be considered to be uniform throughout the material. The precipitation stops when the solubility product between the carbon and the carbide-forming elements has been reached. In this case, the peritectic reaction is marked by the precipitates, but there is no austenite formed by regression of the ferrite.

Marking of the γ/δ peritectic transformation by eutectoid transformation

Like the previous case, this example concerns a chromium-rich alloy (~16 % Cr) with a similar carbon content. The lower chromium level is such that the composition is situated this time in the primary austenite solidification field. The first three steps in the solidification sequence are γ, δ, M_7C_3/δ eutectic (Fig. 6-5-5). During cooling, a eutectoid transformation reaction $\delta \rightarrow \gamma + M_6C$ begins at the γ/δ interface, cellular colonies growing outwards into the δ phase [Kuo54], [Kuo55], [De-85].]. This eutectoid constituent is sometimes referred to as *δ pearlite*. The prior austenite in the centre of the dendrite has transformed to lath martensite during subsequent cooling. The segregation of ferrite-stabilising elements has created an accumulation zone in the ferrite at the γ/δ interface, facilitating formation of the γ/M_6C eutectoid, with carbon from both the ferrite and the austenite.

Figure 6-5-6:
Liquidus projection in the Fe-Ni-Cr system and approximate solidification path (LS) for an Fe-17 Cr-8 Ni-1.5 Mn-0.04 C-0.2 Mo-0.3 S alloy.

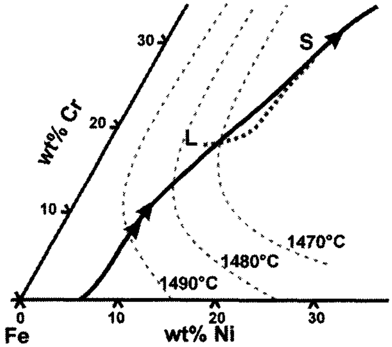

Marking by remelting due to δ/γ metatectic transformation

Several sulphides are known to form in steels and are classified according to their morphologies as types I, II and III (§ 19-5). The example of resulphurised 18 %Cr–8 %Ni austenitic stainless steel (AISI 303) has been chosen to illustrate the extremely complicated solidification process. A *cascade of transformations* takes place in the diffusion zone created by the δ/γ peritectic transformation, within a fairly narrow range of temperature. The solidification path is suggested in Figure 6-5-6 on the liquidus projection of the Fe-Ni-Cr phase diagram, based on the experiment described below (Fig. 6-5-7 D). The first two stages are the formation of δ-ferrite, followed by austenite, and correspond to those predicted by the model ternary system. However, things then become complicated in the presence of sulphur. The development of the final microstructure can be described step-by-step with the aid of the schematic diagrams A, B and C in Figure 6-5-7 and the micrographs D and E for a quenched specimen.

Solidification structure

The diagram of Figure 6-5-8 A represents the situation at the peritectic temperature, where only δ-ferrite is solid (grey). In diagram B, all is solid, and the microstructure is the result of both solidification and solid state transformations. Consider first of all the zone that was still liquid in A. Below the peritectic temperature, austenite solidifies around the ferrite, with a composition that varies during cooling. Since the rejected solute elements are ferrite stabilisers, the enriched liquid in the interdendritic spaces again forms ferrite. The composition of the latter is about 22 %Cr-11.5 %Ni, compared to 16.8 %Cr-9.3 %Ni for the primary ferrite. For the sake of distinction, it will be called *α*-ferrite, although it is really the same phase. It appears slightly lighter in Figure 6-5-7 D. The remaining liquid eventually becomes sufficiently enriched in sulphur to form (Mn,Cr)S sulphide via a monotectic reaction, followed by a (Mn,Cr)S/α eutectic. The latter often has a cellular morphology with interconnected sulphide fibres, resembling a coral (Fig. 5-6-13). However, the eutectic liquid is sometimes a thin film that solidifies to a string of precipitates.

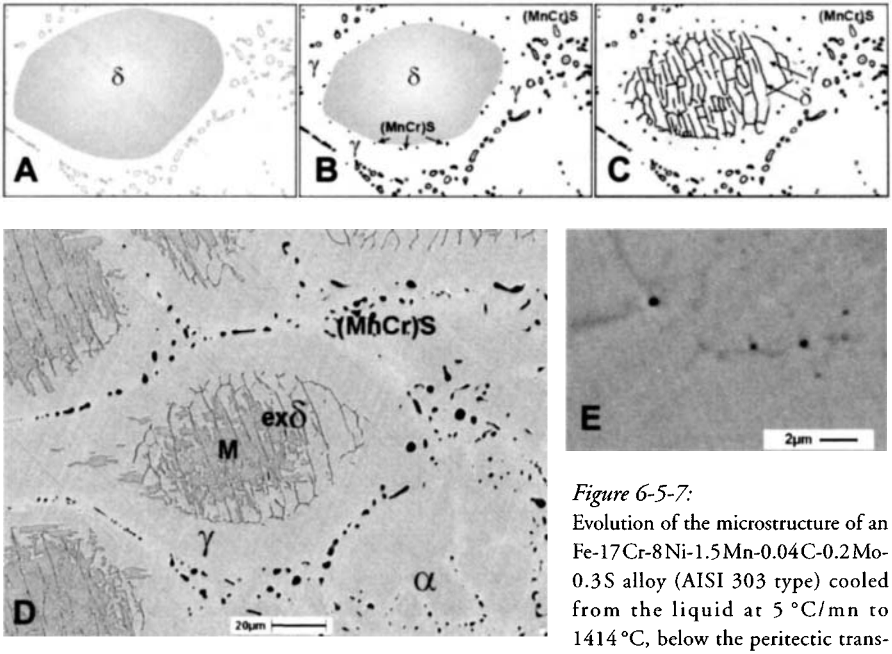

Figure 6-5-7:
Evolution of the microstructure of an Fe-17Cr-8Ni-1.5Mn-0.04C-0.2Mo-0.3S alloy (AISI 303 type) cooled from the liquid at 5 °C/mn to 1414 °C, below the peritectic transformation, then quenched.
A, B and C) : schematic representation of the microstructure at different stages before quenching (A and B) and after quenching (C).
D) Scanning electron micrograph after nital etching. M = martensite.
E) Enlargement of an unetched sample showing three phases; austenite (light grey), ferrite (medium grey) and (Mn,Cr)S nodules (black). Courtesy INPG, Grenoble (see also [Tas02].

Austenite formed by peritectic transformation

The region of primary δ-ferrite in diagram B transforms to austenite in the solid state. The reaction occurs from the outside inwards, ferrite-stabilising elements and sulphur being rejected from the growing austenite, creating a diffusion layer. When the sulphur concentration reaches a critical level, the δ/γ transformation becomes a metatectic reaction, in which liquid is created ($\delta \rightarrow \gamma + Liq$). The mechanisms proposed are based on the Fe-S and Fe-Mn-S phase diagrams (§ 4-9). The diffusion layer becomes a thin continuous film of liquid which spreads along the interface and drains the rejected solute elements. As this metatectic liquid becomes increasingly enriched in sulphur, it eventually reaches a point where it separates into two immiscible liquids, one rich in sulphur and the other rich in iron. On cooling, the iron-rich liquid gives rise to a monotectic reaction, increasing the proportion of sulphur-rich liquid ($L_l \rightarrow \alpha + L_2$). Nevertheless, the quantity of L_2 is small and in order to minimise interfacial energy, it adopts a spherical morphology. The droplets finally solidify to a γ/(Mn,Cr)S eutectic. The position of the δ/γ transformation front at this point is marked by sub-micron sized *metatectic-monotectic sulphides* [Tas02]. During further cooling at 5 °C/mn, the δ/γ transformation continues inwards until all of the original ferrite dendrite is consumed.

Transformation of δ-ferrite during quenching

When the specimen is quenched (Fig. 6-5-7C), the δ-ferrite regression process is interrupted and the ferrite in the centre of the grain becomes highly unstable. Large austenite laths are formed (Fig. 6-5-7D). The rejection of ferrite-stabilising solutes and sulphur again produces a diffusion layer that undergoes a metatectic reaction, with the formation of a liquid, separation into two liquids and final solidification to a γ/sulphide eutectic. The *metatectic-monotectic* process thus remains the same, but in this case, the (Mn,Cr)S sulphides are much smaller, since the reactions occur at lower temperatures and the diffusion layer is much narrower. In the high magnification scanning electron micrograph of Figure 6-5-7E, the untransformed ferrite appears in the form of darker elongated zones, with scattered sub-micron sized globular particles identified as sulphides. The austenite in the grain centres transforms to martensite on cooling (M in Fig. 6-5-7 D), further complicating the final microstructure, whereas that around the grain edges does not transform, because of its lower Ms temperature, due to segregation. The final structure thus contains four phases, ferrite, austenite, martensite and sulphides of various sizes.

The largest sulphides are formed by monotectic or eutectic reactions in the interdendritic regions, while two populations of finer ones result from metatectic-monotectic transformation processes. *All fall in the category of type II sulphides* (§ 19-5). The sulphides generated in the diffusion layer are generally not distinguished. Nevertheless, several sizes of sulphides are often clearly visible, even in industrial products (*cf.* Fig. 19-5-1).

Marking by segregation-induced remelting

The formation of liquid from a fully solid condition does not always imply a metatectic reaction, but can also be caused by local segregation. The example illustrated in Figure 6-5-8 concerns an alloy rich in vanadium and carbon, whose solidification path (*cf.* phase diagram in § 4-12) involves three stages; δ (1411 °C), γ (1373 °C) and γ/VC eutectic (1364 °C).

The growth of austenite by peritectic transformation of the primary δ-ferrite concentrates vanadium in the ferrite ahead of the front. An increase in vanadium level of 1-2 % is sufficient for the local composition to reach the monovariant eutectic line. The arrangement of the vanadium carbides in concentric rings suggests remelting due to the repeated attainment of a eutectic composition, followed by resolidification.

Marking due to dendritic segregation

The last example concerns a common T-type (tungsten-rich) tool steel. The first three steps on the solidification path are δ, γ and γ/M_6C eutectic. The microstructure is illustrated in Figure 6-5-9 and is quite typical. The eutectic carbides are coarse and brittle and the mechanical properties are consequently poor in the as-solidified condition. In practice,

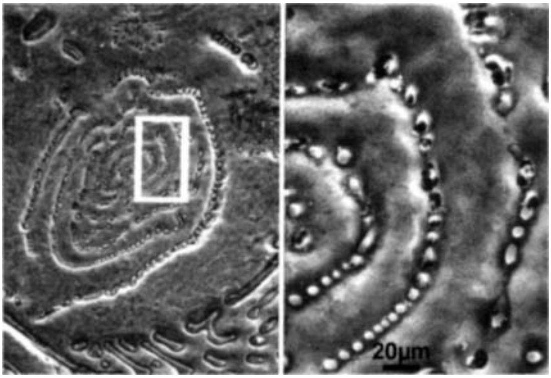

Figure 6-5-8:
Scanning electron micrograph of an Fe-1.47C-9V alloy cooled from the liquid at 5 °C/mn. The specimen has been deeply etched (Appendix 22-4). Courtesy INPG, Grenoble [Kes88a].

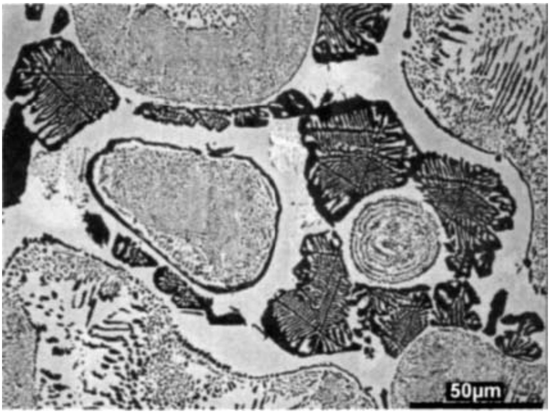

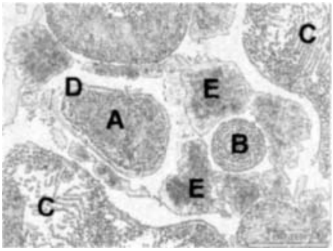

Figure 6-5-9:
Absorbed electron microprobe image of a tungsten tool steel Fe-0.52C-3.8Cr-0.5Mo-1V-18.8W cooled at 5 °C/mn from the liquidus (1476 °C).
Various morphologies are visible (compare the micrograph (right) with the key (left) :
A) continuous distribution of precipitates;
B) concentric rings of precipitates formed along a regression interface;
C) cells;
D) string of carbides at the δ/γ peritectic transformation interface;
E) γ/M_6C eutectic with a fishbone structure. Courtesy INPG, Grenoble.

thermomechanical processing is essential to completely modify the microstructure and obtain acceptable strength and ductility (*cf.* § 18-3).

The as-solidified structure illustrated in Figure 6-5-9 reveals several types of marking, including γ/M_6C eutectoid cells (δ pearlite), concentric precipitate rings, and continuously distributed precipitates. The rings seem to occur only in small dendrite arms, which are probably secondary ones. Secondary arms have a different composition to the primary ones, due to the fact that they form at a later stage in a more solute-enriched liquid. The morphology thus appears to be highly sensitive to small variations in the local composition.

7

Grains, grain boundaries and interfaces

The topic of grains and grain boundaries is extremely vast and covers many different concepts, involving not only the associated microstructural features, but also the effects on material characteristics such as corrosion resistance and mechanical properties. It is therefore essential to clearly define the relevant terminology in order to avoid all risk of confusion.

7-1 General aspects

Grains and their boundaries

In order to interpret the behaviour of metallic materials it is necessary to understand the structure of grains and their boundaries. This subject is treated in a variable extent of detail in numerous publications, including both general metallurgy textbooks [Cah83], [Por92] and more specialized works [Kau89], [Sut96].

A grain is a single crystal, within which the atomic lattice and its orientation are continuous. Adjacent grains of the same phase with different orientations are separated by an immaterial surface called a grain boundary. The two crystal lattices extend regularly right up to the boundary.

In most metals, the change in orientation across a boundary is abrupt and affects only a few atomic layers, typical boundary widths being of the order of 0.1 to 1 nm. The spatial configuration of a grain boundary is defined in terms of the difference in orientation between the two crystal lattices concerned and the orientation of the interface with respect to one of them. In the vicinity of the boundary, the atoms are displaced from their normal lattice positions to minimise the excess energy associated with the discontinuity. Nevertheless, the transition from one grain to the other introduces a large number of defects, which can be considered essentially as vacancies and dislocations, so that a boundary represents a region of high local energy.

The properties of a grain boundary are strongly affected by the change in orientation involved. If the angles of misorientation are small, less than about 3 °, they can be readily accommodated by the formation of a two-dimensional network of dislocations.

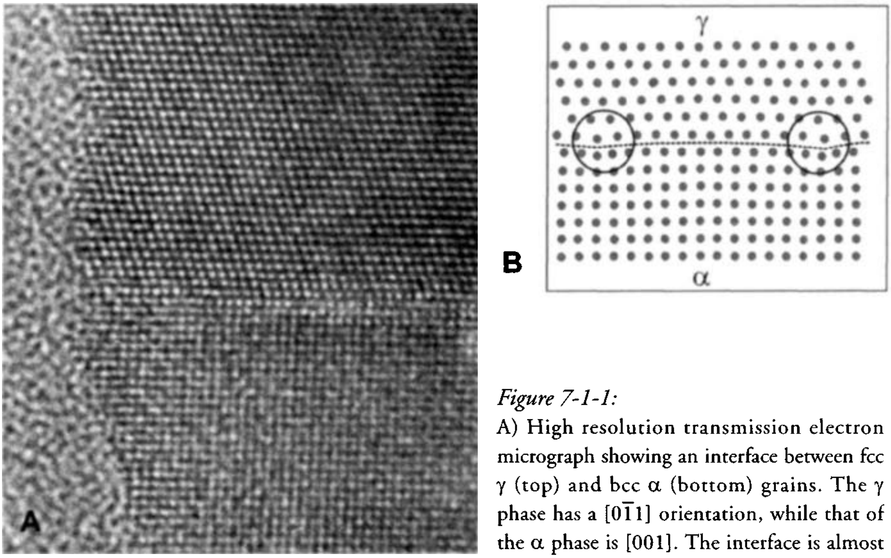

Figure 7-1-1:
A) High resolution transmission electron micrograph showing an interface between fcc γ (top) and bcc α (bottom) grains. The γ phase has a $[0\bar{1}1]$ orientation, while that of the α phase is $[001]$. The interface is almost parallel to the incident beam and corresponds to a $\{\bar{1}11\}\gamma$ plane. The circles show misfit dislocations, with a spacing of 2.6 nm.
Courtesy CEA, Grenoble (see also [Pen89]).
B) Schematic representation of the zone in the centre of micrograph A, each dot corresponding to a column of atoms perpendicular to the plane of the diagram. The dotted line is the interphase boundary, also perpendicular to the plane of the diagram. The diagram is the result of a simulation based on the experimentally observed orientations.
Courtesy INPG, Grenoble (see [Bon94]).

A boundary of this type is called a sub-boundary and its behaviour with respect to corrosion or mechanical loading corresponds to that of the dislocations concerned. For larger misorientations, the defects are more numerous, but remain concentrated within a layer only a few atomic diameters in width. This zone interacts with defects from the two crystals, and can act as both a source and a sink for mobile dislocations and vacancies generated during thermal and mechanical treatments. The excess energy associated with most high angle boundaries is of a similar order of magnitude, typically about 500–600 J/m^2 (erg/cm^2). This is the value to be considered in the case of random high angle boundaries.

The energy of a grain boundary can be divided into two components, corresponding to the mechanical energy associated with the local lattice distortions and the chemical energy associated with broken bonds. In fact, the majority of boundaries have a high chemical energy, due to a large density of broken bonds, and relatively low elastic distortion energy. Twin boundaries represent a special case, where the two crystal lattices are symmetrical across the boundary plane, with perfect matching, the only change being the stacking sequence. The associated energy is thus very small, since there are no broken bonds and no lattice distortion.

Phase interfaces (interphase boundaries)

When two adjacent grains have different crystal structures and lattice parameters, their common boundary represents a phase interface. Interphase boundaries often involve special orientations, where the lattice transition is either coherent or semi-coherent. In a coherent boundary, the atomic spacings on either side closely match one another. In a semi-coherent boundary, a slight difference in atomic spacing can be accommodated by relatively few regularly spaced edge dislocations (*cf.* Fig. 7-1-1).

Perfectly coherent boundaries are rare, since they require exactly identical atomic spacings in certain planes for each phase. However, good coherency and semi-coherency between two phases are commonly observed, since nucleation is significantly easier, due to the lower interface energy when such orientation relationships are adopted. Indeed, the system often adapts by forming a metastable phase that can nucleate coherently or semi-coherently (*cf.* § 13-1). A coherent interface can involve a high elastic energy, when the two lattices must be distorted to make them match, but the chemical energy is negligible in metallic systems, since there are no broken bonds.

The particular crystal planes that provide the lowest mismatch between the two phases are called the *habit planes*. They can be irrational, with no simple crystallographic orientation on a macroscopic scale. However, on the atomic scale, they may correspond to a series of terraces, for each of which the crystallographic relationships for good coherency are simple (*cf.* Fig. 9-3-1).

Close-packed planes, facetted and rough interfaces

Particularly in close-packed crystal structures, such as face-centred cubic and close-packed hexagonal, the planes of closest atomic packing often play an important role in interfaces. In these planes, the distance between atoms is smaller than on any other planes, although it may not necessarily correspond to the theoretical minimum value. The number of bonds between the atoms in other planes will consequently be smaller. During plastic deformation, the cohesion is strongest between the atoms in the close-packed planes, so that shear will tend to occur preferentially parallel to them. Moreover, any stacking faults caused by shear along these planes will have a lower energy. The close-packed planes generally have low Miller indices. Their distribution leads to an anisotropic response to plastic strain and phase transformations.

In body-centred cubic structures, such as ferrite, although there are no close-packed planes, some have a higher atomic density than others, and close-packed rows (*i.e.* directions) exist. Thus, the atoms are in contact with one another in the [111]bcc directions (*cf.* Fig. 3-1-1). There are still preferred slip systems, and anisotropic plastic deformation behaviour is still observed.

The difference in behaviour between ferrite and austenite can be illustrated by considering a duplex stainless steel. The steel shown in Figure 7-1-2 A has been water quenched to conserve the two-phase structure formed by annealing for six hours at 1 120 °C. Subsequent holding for 1 000 h at 400 °C has caused the ferrite to decompose to α and α', two

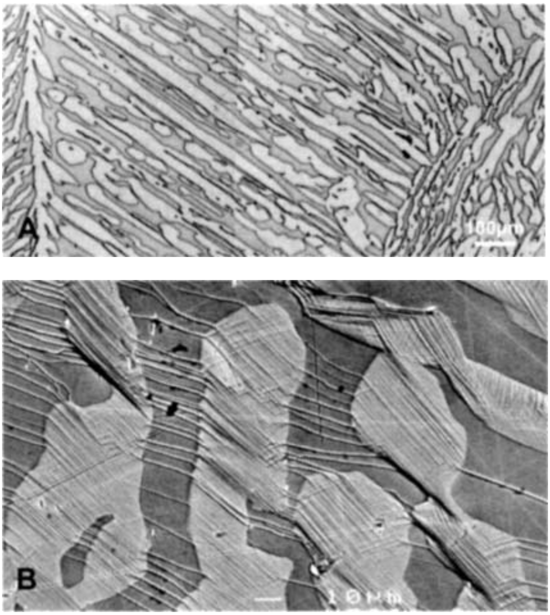

Figure 7-1-2:
Optical micrograph (A) and scanning electron micrograph (B) of a 0.038C-22.1Cr-10.4Ni-1.2Si-0.7Mn duplex stainless steel after 10.5 % plastic strain. The dark phase is ferrite (α) and the light phase austenite (γ).

In the austenite, the dislocations are dissociated and tend to remain in the same slip plane, since cross-slip is difficult, leading to straight or sharply angled slip lines.

In the ferrite, the dislocations are not dissociated and the screw segments can readily change slip planes, leading to wavy slip lines ("pencil glide"). Courtesy INPG, Grenoble, adapted from [Ver97], (see also [Bér97]).

virtually identical bcc phases, one rich in iron (α) and the other in chromium (α'). The precipitate particles are too fine (< 1 µm) to be visible in the micrographs and have formed by a spinodal decomposition mechanism involving spatial fluctuations in composition (*cf.* § 13-1). The specimen has been given 10.5 % plastic strain, leading to the formation of numerous slip lines, which can be seen to be continuous through the two phases (Fig. 7-1-2 B). This requires continuity of the most densely packed planes in the two structures, corresponding to an orientation relationship of the type {111}γ//{110}α.

Facetted interfaces are ones in which large areas are planar on the atomic scale, and are a result of the growth process. For example, in the case of a growing terraced solid/liquid interface, an atom from the liquid can join the solid in several different positions. In particular, it can take up a position either in the middle of a planar surface, against a step, or in a corner (*i.e.* a "jog" on a laterally growing step). The choice of site is governed by energy considerations. The number of "loose bonds" decreases from the planar surface to the step to the corner, so that corner and step positions will be preferred, extending the planar surface.

High index planes possess a large number of sites where atoms can attach themselves easily, and form *rough interfaces*, where growth is more or less isotropic, with no strongly preferred plane. On the contrary, densely packed low index planes tend to form facetted interfaces. Their growth is more difficult and requires a greater driving force, for example, higher chemical supersaturation or larger supercooling. The facet planes are those whose

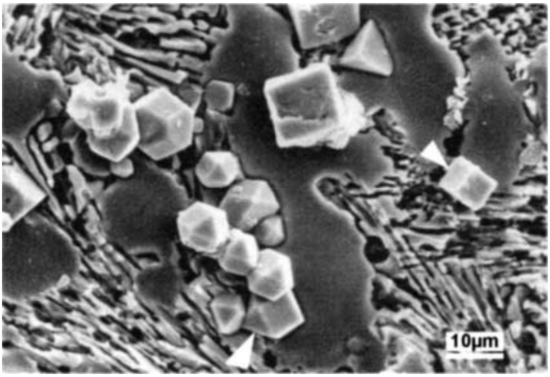

Figure 7-1-3:
Scanning electron micrograph of a slowly solidified Fe-Nb-C alloy. The facetted primary niobium carbides revealed by deep etching have formed from the liquid and have become trapped by the solidification of the austenite dendrites. The white arrow on the right shows a perfect cube that has grown on {100} planes, while that at the bottom of the picture indicates a {111} plane.Courtesy INPG, Grenoble, (see also [Kes88a]).

growth is most difficult and therefore slowest. Figure 7-1-3 shows the facetted growth of primary niobium carbides.

Crystal structure is an important factor, a high anisotropy promoting the formation of terraces due to the large differences in the energies and rates of attachment of atoms depending on the planes concerned. Impurity elements can either inhibit growth by poisoning potential sites, or on the contrary, facilitate it by providing new sites [Kur89].

Grain formation in alloys

In steels, and alloys in general, a grain is rarely formed as a compact homogeneous crystal, and in particular, is often the result of dendritic solidification. A dendrite has a complex geometry and forms *from a single nucleus.* It has a main trunk or primary arm and branches to form secondary and tertiary arms. It is a rigid structure and gives rise to a grain. The secondary and tertiary branches grow in preferred crystal directions, but the lattice is continuous throughout : it is a single crystal (Fig. 7-1-4). However, the resulting grain can have a non-uniform chemical composition, due to the segregation inherent to dendritic growth (Fig. 7-1-5).

The difference in orientation between grains has a marked influence on deformation behaviour, since the easy slip or cleavage planes and directions change across boundaries, while the latter can sometimes themselves represent planes of weakness. Figure 7-1-6 shows a brittle fracture surface in a X2CrMoTi29-4 (1.4592) ferritic stainless steel, where the individual grains are revealed by both transgranular cleavage facets and regions of intergranular decohesion.

The concept of a grain is also often extended to the case of multi-phase constituents such as eutectics and eutectoids, where the different phases grow together with well-defined interrelated crystallographic orientations (*e.g.* Fig. 6-4-2). These composite grains involve several rigidly interconnected phases. In this case, the continuity of the multi-phase structure is expressed by terms such as "colonies", "cells" or "nodules"

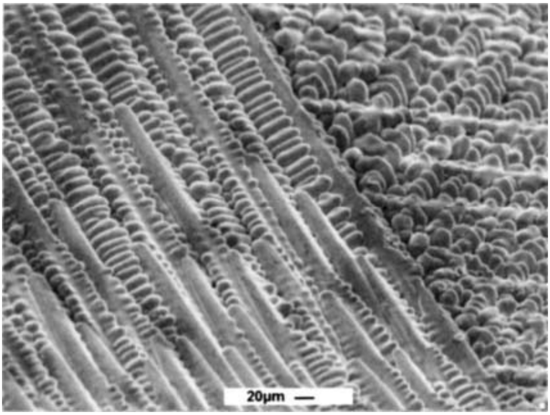

Figure 7-1-4:
Scanning electron micrograph showing two dendritic grains observed in the shrinkage cavity of an as-cast 100Cr6 steel bar. The dendrite arms are parallel inside each grain, since they have formed from the same nucleus (see Fig. 5-5-5). Each grain contains a large number of such branches.
Courtesy INPG, Grenoble

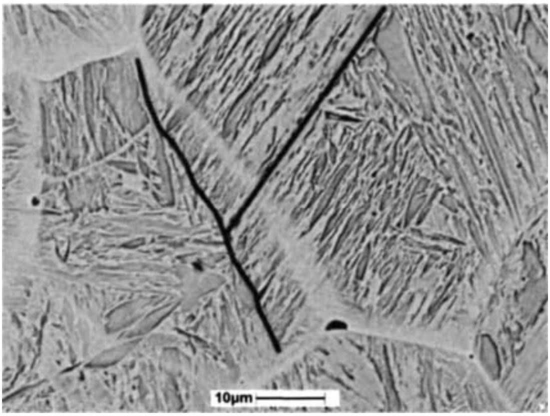

Figure 7-1-5:
Scanning electron micrograph (BSE image) showing the structure of an as-solidified 36NiCrMo16 steel (NE EN 10027). The lighter contrast reveals segregation of molybdenum in the interdendritic spaces. Martensite laths oriented parallel to the straight black line cross an interdendritic space and reach the position indicated by the wavy black line, demonstrating the continuity of the crystal lattice from one dendrite arm to another.
Courtesy INPG, Grenoble.

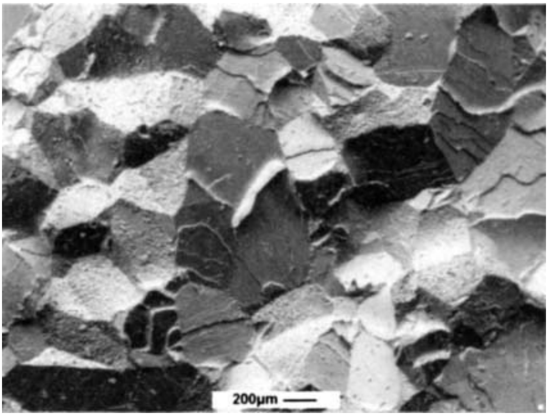

Figure 7-1-6:
Mixed transgranular and intergranular brittle fracture in a X2CrMoTi29-4 (1.4592) ferritic stainless steel.
Specimen contributed by CRU, Ugine Savoie Imphy, Arcelor Group.

However, in alloys containing a large volume fraction of a eutectic constituent, such as cast irons, the original primary grains, and particularly their boundaries, lose their identity. Thus, the primary single crystal dendrite initially in contact with the liquid degenerates due to ripening phenomena and is broken up into small single crystal fragments, surrounded by the eutectic aggregate formed in the interdendritic spaces (Fig. 6-1-1).

7-2 Characteristics associated with grain boundaries

Intergranular diffusion and segregation

Grain boundaries represent heavily disturbed regions of the crystal lattices with a high local concentration of defects (vacancies and dislocations). Consequently, atomic transport occurs more easily and they thus offer preferred paths for diffusion. The ratio *Di/Dv* between the intergranular and volume diffusion coefficients is very high, often several orders of magnitude. It depends on the temperature, approximately according to the relation :

$$D_i/D_v = D_{0,i}/D_{0,v} \cdot \exp(\Delta H_v)/(kT) \qquad (7\text{-}2\text{-}1)$$

where T is the temperature in kelvins, ΔH_v is the difference in the activation energies for diffusion, and $D_{0,i}/D_{0,v}$ is the ratio of the values extrapolated to $T = 0$. The difference becomes much more pronounced at lower temperatures, where preferential diffusion along grain boundaries is extremely marked.

Grain boundaries are also preferred sites for nucleation, since the excess energy of the defects can be reduced, while growth processes are facilitated by the enhanced diffusion rates. The excess energy of boundaries can also be diminished by the segregation of solute atoms from the crystal lattice. Local enrichment factors of 100, 1000, or even higher can be attained [Bér96a]. This phenomenon is termed equilibrium segregation. The elements with the greatest tendency to segregate to grain boundaries in this manner are the interstitial solutes, such as C, N, B and P, which may reach concentrations sufficient to form precipitate phases. The solute concentration in the boundary c_s^{joint} is given by :

$$c_s^{joint} = \frac{c_s^0 \cdot exp(Q_s/(RT))}{1 + c_s^0 \cdot exp(Q_s/(RT))} \qquad (7\text{-}2\text{-}2)$$

where c_s^0 is the concentration in solid solution in the grains, T is the temperature in kelvins, and Q_s is the interaction energy between the solute atoms and the grain boundary, corresponding to the difference in energy between an atom in the boundary and one in a normal lattice site. This difference increases with decreasing temperature, while the rate controlling process is the diffusion rate within the grains, so that in practice, the segregation phenomenon can be greatest at intermediate temperatures.

The thermodynamic equilibrium can be modelled by taking into account the particular structure of grain boundaries. The simplest way to describe them is to consider the interface as a region of finite thickness and to assimilate it to a specific phase [Hil99b]. In fact, this is not far from reality, since in some cases the boundary is a layer about one atom thick in which the atomic bonding is different. For example, phosphorous is known to segregate to boundaries in steel, where it can attain a coverage of up to 20 %, compared to a few tens of ppm in the bulk alloy. The concentration ratio can thus represent several orders of magnitude. In this case, the single layer of phosphorus corresponds to the formation of Fe_3P molecules, with specific bonding. The boundary is severely embrittled [Bri90]. In steels, the problem is complicated by the interaction between phosphorus and carbon, which also segregates to boundaries. The segregation rates depend on temperature, and a rapidly diffusing species may occupy boundaries initially in preference to a more sluggish one with a higher Q_s value. Thus carbon can segregate to boundaries in preference to phosphorus [Gut77], [Gut82], [Cow98].

Because of the change in crystal orientation across a grain boundary, the easy slip directions rarely coincide. Consequently, grain boundaries act as obstacles to dislocations and high stresses can be generated locally at the head of pile-ups. Thus, while grain boundaries can provide useful strengthening, care must be taken to ensure that they conserve sufficient ductility to withstand the high stress concentrations. In particular, the use of intergranular segregation or precipitation mechanisms to prevent grain growth after recrystallisation and ensure a fine grain size must not lead to excessive embrittlement. For example, aluminium nitride particles strengthen microalloyed steels due to grain refinement, but must be used under carefully controlled conditions [Pic78]. In carbon steel castings, excessive carbide precipitation at grain boundaries can lead to brittle rock candy intergranular fracture.

When grain boundaries move, for example during a phase transformation, segregated solute atoms can be dragged along and can also be picked up from the grains as they are intercepted by the boundary.

Equilibrium geometry of a grain boundary in contact with a liquid

When a grain boundary emerges at a surface in contact with liquid metal, the geometry of the triple junction is determined by the equilibrium between the three interface tensions involved at the temperature concerned (Fig. 7-2-3 A). The result is generally a groove at the triple point, corresponding to slight local penetration of the liquid into the solid surface. When the two solid grains correspond to the same phase, the energy γ_{SL} of their interfaces with the liquid can be considered to be equal (*i.e.* little dependent on orientation), so that the equilibrium between the interface tensions can be expressed in terms of the corresponding energies γ_{SL} and γ_{GB}, the grain boundary energy as :

$$\gamma_{GB} = 2\gamma_{SL} \cdot \cos\Phi/2 \qquad (7\text{-}2\text{-}4)$$

where γ_{GB} is the grain boundary energy. When only a small amount of liquid metal is present between the grains of a solid, it will adopt a geometry such as to minimise the total

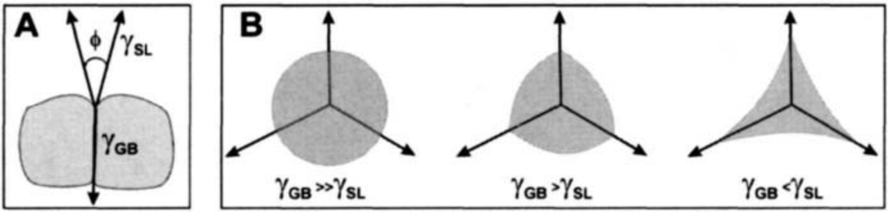

Figure 7-2-3:
A) Equilibrium geometry of a grain boundary in contact with a liquid.
B) Influence of relative interfacial energy on the shape of a liquid zone between three solid grains.

interface energy. Depending on the values of γ_{SL} and γ_{GB}, it will form either a thin continuous film or ellipsoidal droplets along boundaries and compact "tetrahedra" at triple junctions (Figure 7-2-3 B). Figure 7-2-5 shows an example of the penetration of liquid copper between iron powder grains.

An associated concept is that of *wettability*, which in practice indicates the propensity of a liquid to spread over the surface of a solid with which it is in contact. This property is related to the potential interactions between the two phases and the tendency to form bonds at the solid/liquid interface. Good (*i.e.* high) wettability corresponds to a low interfacial energy. When phase diagrams indicate the absence of reaction between two phases, low wettability can be expected. Thus, the majority of liquid metals wet oxidised surfaces, whereas the noble metals do not. Other important factors are the cleanness of interfaces and their orientation [Ger85], [Eus83], [Smi48]. In the case of iron, the interfacial energies vary widely, depending on the liquid metal concerned, while even trace amounts of certain third elements can profoundly modify their values (*cf.* Appendix 22-2). Wettability is important in numerous practical applications, including welding and liquid phase sintering. It plays an important role in liquid metal corrosion and embrittlement phenomena (*e.g.* by lead and sodium) and can have a decisive influence on inclusion morphologies.

Grain size

Strictly speaking, the mean grain size of a material is inversely related to the number of grains per unit volume. It is usually expressed as a length, whose exact meaning depends on the method of measurement (intercepts along a random line, *etc*). Grain size often has a marked influence on properties, especially mechanical strength and ductility (*cf.* § 14-1). Grains are commonly revealed by chemical, electrochemical or thermal etching treatments. In some cases, grain boundaries may be attacked preferentially, due to their specific structure or to the presence of solute segregation or precipitate phases. In others, differential reaction or dissolution, depending on the crystal orientation, may cause variations in colour or create steps at boundaries. Chemical etching is the technique most commonly employed, but the compositions of reagents and the conditions of application are still largely a matter of experience. Numerous books and publications give *recipes* for chemical

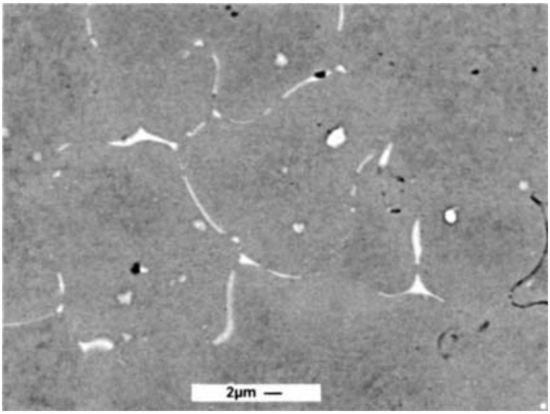

Figure 7-2-5:
Scanning electron micrograph of an Fe-Cu alloy produced from elemental powders (3 % Cu), compacted, then heated at 3 °C/mn to 1 100 °C and immediately cooled at 40 °C/mn. The liquid copper has spread along the boundaries between the iron particles. Holding at 1 100 °C leads to diffusion of copper into the iron and disappearance of the liquid.
Courtesy INPG, Grenoble (see also [Dub00].

and electrochemical etching techniques appropriate for revealing particular structures in different metals and alloys [Dav94], [Hab66], [Pec77], [Lac93], [Van99], [Van89]. A selection of etchants is also given in Appendix 24-1. Thermal etching can sometimes be used for steels, but the heat treatment involved can modify the microstructure it is wished to reveal [Kra80]. The use of automatic image analysis has considerably simplified the measurement of grain and particle sizes on polished surfaces, enabling both larger sample sizes and more detailed analysis of the results.

Grain orientation

The different grains in a metal or alloy frequently have orientations that are not random, with respect either to one another or to the geometry of the component concerned. In particular, the existence of preferred planes and directions of slip causes grains to rotate relative to the loading axes during deformation, resulting in particular orientation distributions or textures. For example, in a cold rolled ferritic steel sheet, the ferrite grains tend to adopt two major orientations relative to the plane of the sheet, designated α and γ (not to be confused with ferrite and austenite !). This is important, since the mechanical and physical properties of the individual grains, and hence the aggregates, are anisotropic. When the γ orientation predominates, good formability is obtained (*e.g.* a good aptitude for deep drawing). It is therefore important to be able to determine the proportions of grains with each type of orientation, together with their variation as a function of rolling reduction or the influence of precipitates formed during hot rolling, *etc.* A high volume fraction of γ-oriented grains can be obtained by appropriate control of the cold rolling reduction and subsequent recrystallisation treatment.

A statistical analysis of grain orientations can be achieved by the use of X-ray diffraction and the determination of pole figures, and this method is commonly employed for evaluating rolling textures. Grain orientations can also be determined by electron microscopy, using techniques such as Kikuchi electron back scattering diffraction (EBSD). The Kikuchi method, initially limited to transmission microscopy, has been greatly simplified,

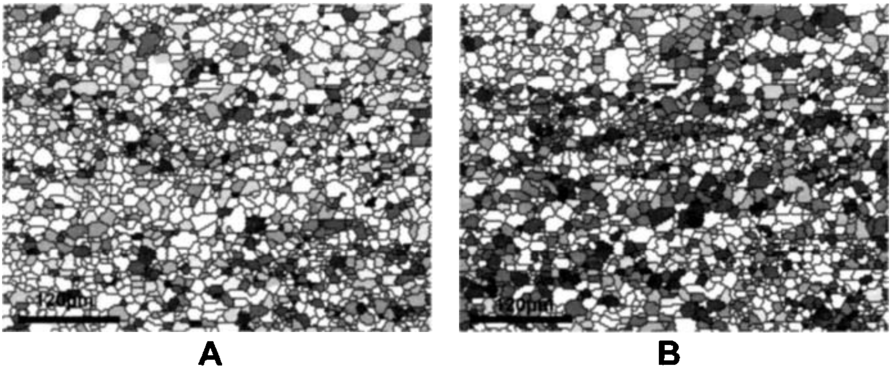

Figure 7-2-6:
Grain orientation maps for the same region of a 17 % Cr ferritic stainless steel (AISI 430), annealed at 900 °C after cold rolling. The grey level indicates the proximity to the reference orientation, ranging from very near (black) to outside a 20 ° cone (white).
A) <110> direction parallel to the rolling axis (α fibre).
B) <111> direction perpendicular to the plane of the sheet (γ fibre). Some grains appear white in both images, indicating that they belong to neither of the two orientations considered.
Courtesy Ugine SA, CRI, Isbergues, Arcelor group, and INPG, Grenoble

while at the same time significantly increasing the area analysed, by its recent application to back scattered electrons in the field emission scanning electron microscope (see the review article [Hum01]). An example is shown in Figure 7-2-6, where the two images correspond to the same region in a cold rolled ferritic steel. The image A shows the distribution of orientations with respect to the α fibre (<110> direction parallel to the rolling axis) and the image B that with respect to the γ fibre (<111> direction perpendicular to the plane of the sheet).

8

Diffusion

Diffusion phenomena are widely involved in many metallurgical transformations and processes and are frequently mentioned throughout the present work. This chapter treats the basic laws of diffusion before going on to describe three typical cases where its effects are clearly visible in the microstructure, corresponding to atomic transfer at an interface between (1) two solids (depleted zone formation); (2) a solid and a gas (case hardening); (3) a solid and a liquid (galvanising). These three examples all have important practical consequences.

8-1 Chemical diffusion

General aspects

Diffusion is a phenomenon whereby atoms move with respect to their neighbours. In a crystalline solid, the displacement involves jumps onto empty adjacent sites, which may either be lattice interstices or vacancies. It is often facilitated by the presence of crystal defects, such as dislocations, grain boundaries and phase interfaces, which represent continuous accumulations of potential sites. In general, only small solute elements, such as hydrogen, carbon, nitrogen and oxygen, can diffuse via interstitial sites. Larger atoms require the presence of vacancies, with which they exchange positions. An atom must acquire sufficient energy to make a successful jump. The frequency depends on the element concerned and varies strongly with temperature. At high temperatures, extremely high values can be attained, of the order of several billion jumps per second. For each individual atom, the displacement direction is completely random and for macroscopic diffusion to be observed, a gradient in chemical potential is necessary.

Chemical diffusion phenomena are important in metallurgy, since they enable a system to evolve towards an equilibrium state. However, they are inherently sluggish, being much slower than thermal diffusion (heat conduction), so that true equilibrium is rarely achieved. It is therefore important to consider the transient situation prior to the possible establishment of a steady state regime.

The fundamental laws governing macroscopic diffusion were derived by Fick, inspired by Fourier's work on heat conduction. Fick's first mathematical study was published in 1855.

His first law expresses the fact that the flux density J is proportional to the concentration gradient *c/x* :

$$J = -D \times \frac{\partial c}{\partial x} \tag{8-1-1}$$

J is the quantity of matter flowing through unit area in unit time. It is expressed in units of kg/m^2/s or atoms/m^2/s, depending on whether a mass flux or an atom flux is considered. D is the proportionality constant called the diffusion coefficient, expressed in m^2/s, c is the volume concentration in kg/m^3 or atoms/m^3, and x is the distance, in metres. It should be noted that, in the customary scientific approach, c is generally given as a weight or atom fraction rather than as a percentage. The minus sign in Equation 8-1-1 signifies that the flux occurs down the concentration gradient (or more rigorously, down the chemical potential or activity gradient). Any chemical potential gradient will therefore tend to decrease and eventually disappear.

Fick's first law is only strictly valid for diffusion along the x axis, in a binary system containing a single isotropic phase, at constant temperature and pressure. It is analogous to the heat conduction equation, where the heat flux is proportional to the temperature gradient. It is also similar in form to Ohm's law, where the current is proportional to the difference in electrical potential. More generally, a flux is commonly assumed to be proportional to its thermodynamic driving force.

The diffusion coefficient

The most simple cases of diffusion are those where it can be considered that the diffusion causes practically no modification in the composition. The diffusion coefficient D can then be taken as being independent of the local concentration. This is true for self-diffusion and for hetero-diffusion in dilute alloys.

However, the diffusion coefficient is strongly dependent on temperature, and in simple situations, it is found experimentally to obey an Arrhenius relation :

$$\ln D = \ln D_0 - \frac{Q}{RT} \tag{8-1-2}$$

where the activation energy Q is typically in the range from 50 to 250 kJ/mole. In the case of self-diffusion, elements with lower melting points (T_M) generally diffuse faster at a given temperature. The following relations give approximate orders of magnitude

$Q/T_M \approx 0.0147$ kJK^{-1}, $Q \approx 15L_M$ and $D_{L(TM)} \approx 10^{-5}$ cm^{2}s^{-1}

where L_M is the latent heat of melting and $D_{L(TM)}$ is the diffusion coefficient in the liquid at the melting point. Some diffusion coefficient values are reported in Appendix 22-5. The data are often difficult to compare since they refer to particular temperature ranges. The experimental technique used to measure them (*e.g.* diffusion couples or radioactive tracers) can introduce systematic errors [Alb74]. Thus, values slightly different to those given in the table are indicated elsewhere for the same elements [Hon95]. Nevertheless, there is a difference of several orders of magnitude in the values observed for interstitial and substitutional solute elements. The diffusivity of substitutional elements is partly related to their atomic number, heavier atoms usually diffusing more slowly. However, the relationship is not simple and, for example, nickel, cobalt and copper diffuse more slowly in ferrite than heavier elements such as x and y.

A simple practical parameter often used in metallurgy is *the diffusion length*, given by $l = \sqrt{Dt}$, where t is the time in seconds. For example, the depth of penetration of an element diffusing in from the surface will be proportional to l. It provides a useful first approximation, particularly for the interpretation of microstructures. A table is given in Appendix 24-3 and includes the following figures for the α/γ transition temperature in iron (910 °C). Thus, after cementation for one hour, the carbon penetration depth in ferrite is 1080 µm, compared to 192 µm in austenite. If carbon is replaced by nickel, the penetration depth in austenite is only 0.2 µm. Although this may seem small, it is large compared to the atomic radius of iron (0.167 nm) or the jump distance (0.26 nm = $a/\sqrt{2}$, where a is the lattice parameter of γ-Fe, equal to 0.37 nm).

In solid solutions that can no longer be considered to be dilute, the intrinsic diffusion coefficients can be very different from the self-diffusion values. For carbon, a relation due to Kaufman *et al.* [Zac62], predicts the variation of the diffusivity with concentration, x_C in austenite. In fact, in the case of a binary system A-B, the problem should strictly be treated as involving the ternary system A-B-vacancies. More extensive treatments of diffusion theory can be found in various physical metallurgy textbooks [Cah83], [Por92], [Bér96a] and in specialized treatises [Phi91].

8-2 Zones affected by diffusion

Chromium-depleted layers

In high alloy austenitic steels, the precipitation of chromium-rich carbides leads to depletion of this element in the surrounding matrix. The phenomenon most commonly occurs at grain boundaries and is particularly dangerous when the local chromium content falls below about 12 %, considered as the threshold value necessary to form a protective passive film. Materials in this condition are said to be *sensitised*, since they become prone to localized intergranular corrosion [Sta69], [Ted71], [Tho83], [Lac93]. The remedy is to equalize the chromium content in the matrix by a desensitising heat treatment at a temperature where diffusion can occur rapidly.

Consider the case of an Fe-Cr-C alloy slowly cooled from the liquid state. The alloy composition is such that solidification involves the formation of primary austenite dendrites, followed by a eutectic containing chromium carbides. Figure 8-2-1 schematically represents the distribution of chromium at four successive stages during cooling. Note that stages C and D could also represent subsequent annealing after cooling to ambient temperature.

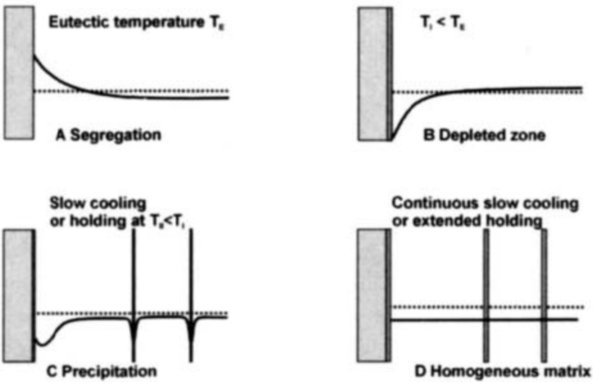

Figure 8-2-1:
Chromium concentration profiles in the vicinity of carbides (grey) in an Fe-Cr-C alloy at four successive stages of cooling from the liquid. The dotted line is the average chromium concentration, not including the eutectic carbides.
A) Solidification-induced segregation at a eutectic carbide.
B) Thickening of the eutectic carbide and formation of a chromium depleted zone.
C) Precipitation in the matrix, whose carbon content decreases.
D) The chromium content in the matrix has become uniform, at a level higher than the minimum in the depleted zone, but less than that in A and B.

A) *Solidification-induced dendritic segregation.* This stage is considered to represent the end of solidification, where the chromium concentration in the matrix next to the eutectic carbide corresponds to equilibrium between the matrix and the carbide at the eutectic temperature T_E.

B) *Formation of a depleted zone.* During slow cooling to temperature T_I, the chromium solubility in the matrix decreases, but the supersaturation remains insufficient for separate carbide nucleation. However, the existing eutectic carbide represents a nucleus for further carbide deposition and equilibrium can be approached at the interface by diffusion from the matrix. The supersaturation is reduced over a distance approximately equal to the diffusion length.

C) *Precipitation in the matrix.* Further slow cooling or holding at a lower temperature T_{II} enables carbide precipitation to occur in the matrix (which includes grain boundaries in this example). Equilibrium is established in contact with each precipitate, while the surrounding matrix is depleted in chromium over the corresponding diffusion distance. Due to its high diffusivity, the chemical potential of carbon can be considered to be uniform throughout the matrix, even around the eutectic carbides. The carbon concentration in the matrix decreases progressively as the volume fraction of carbides increases. A new equilibrium is imposed at the interface with the eutectic carbides. According to the Fe-Cr-C phase diagram (Figs. 4-7-2 and 19-1-2), the chromium content can increase in the depleted zone around these carbides, the diffusion flux being from the carbide to the

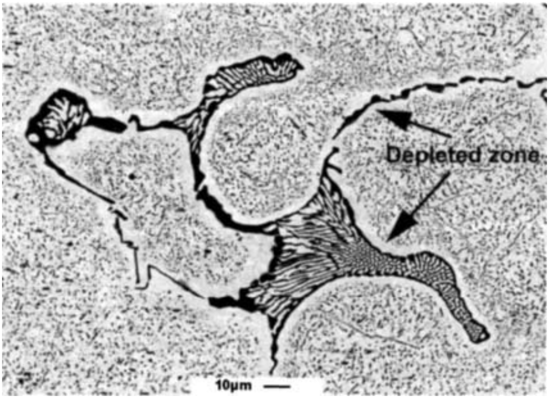

Figure 8-2-2:
Scanning electron micrograph of an experimental cast heat resisting alloy (0.5C-25Cr-24.5Ni-1.8W-1.9Si-1.9Mn), slowly solidified and cooled to simulate the conditions in an industrial casting. The solidification structure consisted of primary austenite dendrites and an M_7C_3/γ eutectic. Subsequent annealing for 90 h at 750 °C has caused the precipitation of secondary $M_{23}C_6$ carbides. Courtesy INPG, Grenoble.

matrix. The width of the chromium expulsion zone is small, since the temperature is now lower than for the initial depletion. The profile shown is typical of that observed in an as-solidified structure obtained by slow cooling.

D) *Desensitisation.* After continued very slow cooling or prolonged holding, the matrix becomes homogeneous, with a chromium content lower than the mean value in A and B, but higher than the minimum in the depleted zones. The latter difference, although small, is extremely important, since it is sufficient to bring the chromium concentration everywhere above the threshold for passive film formation. The alloy is no longer sensitive to localized corrosion around chromium carbides.

In more complex alloy steels, the approach to equilibrium can involve exchanges of several elements with highly different diffusion rates (*e.g.* carbon, chromium, nickel, molybdenum, etc.). As long as the matrix remains supersaturated, the growth of carbides is governed by diffusion near the interface, that of the element with the lowest diffusivity being the rate controlling parameter. However, as regards sensitisation to corrosion, only the chromium distribution has a significant influence.

Depleted zones around primary carbides are often made visible by the fact that they remain free from secondary precipitates. This is illustrated in Figure 8-2-2, corresponding to a cast heat-resisting alloy, in which secondary $M_{23}C_6$ carbides are absent in the region surrounding the eutectic M_7C_3 carbides, which have thickened at the edge of the depleted zone. This phenomenon is frequently encountered in the coarse microstructures of as-cast high carbon steels [Dur80a]. The depleted zones often undergo localized corrosion, as shown in Figure 8-2-3. Another example is shown in Figure 12-3-2, corresponding to a typical white cast iron microstructure, where the depleted zone is revealed by a difference in the tendency of the austenite matrix to transform to bainite.

However, the majority of steels have low carbon contents and therefore do not contain eutectic carbides. Furthermore, they are hot and cold worked and heat treated, breaking down the coarse solidification structure, to the extent where an almost fully homogeneous

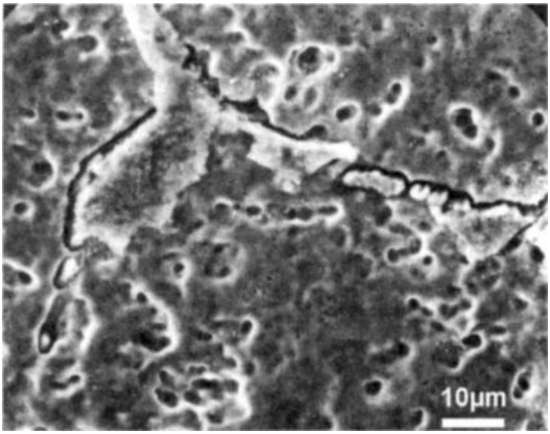

Figure 8-2-3:
Scanning electron micrograph of the same (0.5C-25Cr-24.5Ni-1.8W-1.9Si-1.9 Mn) steel shown in Figure 8-2-2, corroded by contact with a mixture of clinker and Na_2SO_4 in air for 140 h at 750 °C. The deep groove around the eutectic carbides corresponds to the chromium-depleted zone.
Courtesy INPG, Grenoble.

condition can be obtained. Localised corrosion can occur around secondary carbides, particularly in grain boundaries [Tho83]. Indeed, grain boundaries represent preferred sites for secondary precipitation and the depleted zones spread along the interface. Sensitisation is a problem particularly in austenitic alloys (*cf.* § 19-2). In ferritic materials, the diffusion rates for all elements are much higher, so that the chromium-depleted zones around carbides are much more readily eliminated by homogenisation.

8-3 Case hardening

Surface diffusion phenomena

The interstitial solute elements, including carbon and nitrogen, diffuse rapidly in austenite at high temperatures. When a steel is placed in contact with a medium of high carbon or nitrogen activity, they can penetrate to depths of several millimetres in a few hours. The surface zone enriched in this way will form harder martensite during subsequent quenching. It is thus possible to preferentially strengthen the surface layers by heat treatment in an active medium. In particular, case hardening treatments of this type are performed for applications demanding high abrasion resistance combined with a tough and ductile core.

The active medium providing the source of carbon and/or nitrogen can be a solid, a liquid or a gas. A commonly used cementation process involves placing the steel in a chamber where graphite is exposed to oxygen, the carbon activity being determined by the equilibrium CO/CO_2 ratio at the pressure and temperature concerned (Boudouard reaction). With a continual supply of oxygen in contact with the graphite, the carbon activity of the external medium can be considered to remain constant throughout the treatment. The carbon concentration at the steel surface is such that the chemical potential or activity is identical to that in the gas phase. The carbon diffuses into the steel down the concentration (activity) gradient, which is given by the analytical solution of the Fick equations :

$$\frac{c - c_{eq}}{c_0 - c_{eq}} = erf\left(\frac{z}{2\sqrt{Dt}}\right) \tag{8-3-1}$$

where c_{eq} is the equilibrium solute concentration at the interface, c_0 is the initial concentration in the steel and c is the value at a distance z from the interface after a time t. The penetration depth is of the order of a millimetre after two hours at 900 °C (Appendix 22-5). Beyond the carbon solubility limit in the austenite, cementite is formed. The presence of other alloying elements in the steel can significantly modify the carbon activity gradient beneath the interface and generally retards the penetration rate. Indeed, case carburising is rarely used for highly alloyed steels.

Mixed diffusion of carbon and nitrogen is complex, since the two elements have different diffusivities. However, both elements occupy the same interstitial sites in the austenite lattice. The first precipitate phase to form in practice is always cementite, although a nitride might often be expected. This is because nitrogen absorption at the interface is slow in the initial stages of reaction. Subsequently, equilibrium phases form, either in contact with the cementite, namely ε-$Fe_2(N,C)_{1-z}$, and γ'-Fe_4N_{1-x} between ε and the iron matrix [Du_00].

Microstructure in the case hardened layer

Consider the case of a plain carbon steel containing 0.2 % C, carburised for ten hours at 1000 °C to produce a case depth of about 4 mm (Fig. 8-3-2 left). Subsequent holding for four hours at 870 °C, still in contact with the carburising medium, slightly modifies the carbon distribution, since the equilibrium activity at the interface is lowered, leading to a maximum carbon concentration about half a millimetre below the surface. The final profile is shown in grey. The 870 °C treatment was followed by three cooling modes; slow furnace cooling, air cooling and quenching in liquid nitrogen. Figure 8-3-2 (right) shows the resulting hardness profiles, the labels A, B and C indicating the position of the micrographs in Figure 8-3-3. The intrinsic hardness of the martensite increases with the carbon content of the parent austenite, although at very high concentrations the opposite effect is observed, due to incomplete transformation associated with depression of the Ms and Mf temperatures (*cf.* § 11-2).

The micrograph corresponding to a depth of 1500 µm in the air cooled sample (Fig. 8-3-3 B) shows that transformation is almost complete in this position, whereas nearer the surface (Fig. 8-3-3 A) a considerable amount of untransformed austenite remains. Quenching in liquid nitrogen completes the transformation and significantly increases the hardness. Finally, the microstructure near the surface of the slowly cooled sample (Fig. 8-3-3 C) is characteristic of a hypereutectoid steel, with cementite at the prior austenite grain boundaries, surrounding colonies of pearlite.

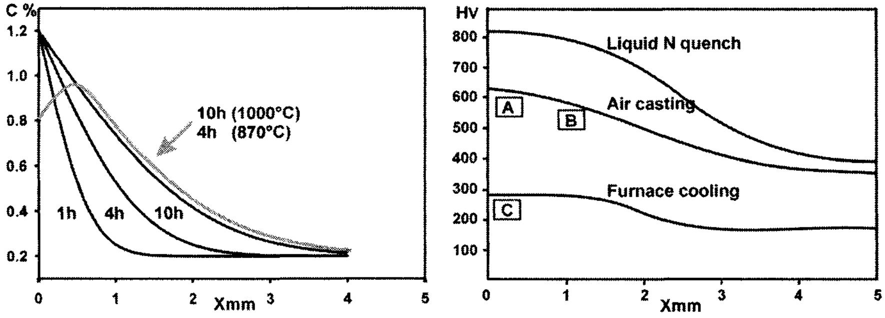

Figure 8-3-2:
Carbon and hardness profiles in a case carburised 0.2 % C steel.
Left) calculated carbon profiles after holding in a carburising atmosphere for 1, 4 and 10 h at 1000 °C. The grey curve represents the predicted carbon distribution after 10 h at 1 000 °C followed by 4 h at 870 °C in the same atmosphere.
Right) microhardness profiles obtained when the latter two-stage treatment is followed by three different cooling sequences. The labels A, B and C indicate the positions corresponding to the micrographs shown in Figure 8-3-3.

Carburising and nitriding processes

In order to achieve diffusion depths of the order of a millimetre, it is necessary to carry out the surface treatments at a temperature where the stable phase is austenite. Several processes are employed, depending on the type of component to be treated. In all cases, the aim is to harden the surface while maintaining good ductility in the underlying metal. The treatments can be divided into three categories; carburising, nitriding and carbonitriding [Ash92]. Separate austenitising is generally performed, because of both the difference in temperature and the need for quenching to obtain martensite.

In *carburising treatments*, the carbon can be introduced from a solid, liquid or gaseous source. In pack carburising, which is a very old process, the steel is embedded in a solid mixture of powdered charcoal or coke and alkali carbonates. Liquid sources involve molten salt baths containing sodium cyanide. Although carburising can be readily controlled, the salts and their vapours are highly toxic. Finally, in gas carburising, the carbon source is generally a hydrocarbon, particularly natural gas (methane). The typical treatment temperature is around 925 °C.

In *nitriding processes*, the nitrogen source is either a liquid or a gas. Molten salt baths at about 550 °C can be used, in which cyanide ions have been converted to cyanate by aging. Gaseous nitriding is often performed in partially cracked ammonia. Catalytic cracking in contact with the steel produces atomic nitrogen which can readily penetrate the surface. A cleaner, though more expensive process is plasma nitriding. These gaseous treatments are typically performed at temperatures from 450 to 570 °C.

Figure 8-3-3:
Scanning electron micrographs of the carburised 0.2 % C steel in Figure 8-3-2, corresponding to the positions A, B and C.

A) Structure at about 200 μm below the surface of the air cooled sample. The martensite is accompanied by a large amount of retained austenite (light contrast).

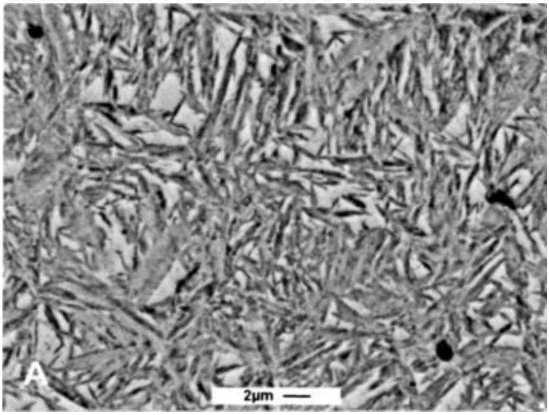

B) Structure at about 1500 μm below the surface of the air cooled sample. The martensite is accompanied by only a small amount of retained austenite.

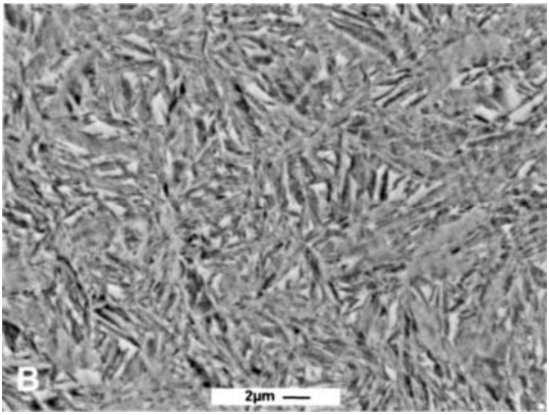

C) Structure at about 200 μm below the surface of the furnace cooled sample. It is characteristic of a hypereutectoid steel, with cementite at the prior austenite grain boundaries, surrounding colonies of pearlite. The presence of the carbides slightly enhances the hardness over a depth of about 2 to 3 mm.
Courtesy INPG, Grenoble.

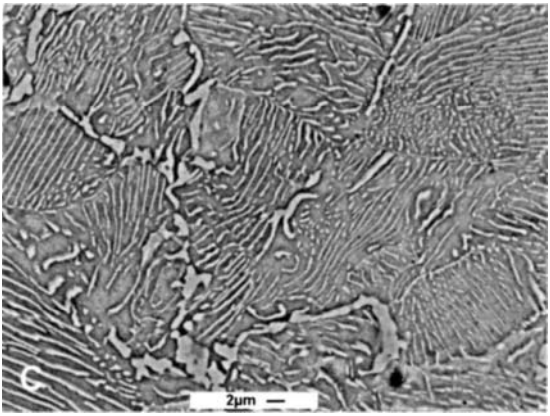

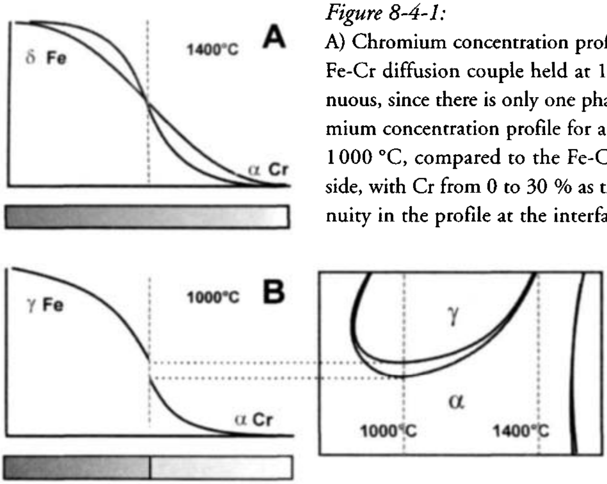

Figure 8-4-1:
A) Chromium concentration profiles at two different times for an Fe-Cr diffusion couple held at 1 400 °C. The profiles are continuous, since there is only one phase at all compositions. B) Chromium concentration profile for an Fe-Cr diffusion couple held at 1 000 °C, compared to the Fe-Cr phase diagram (turned on its side, with Cr from 0 to 30 % as the ordinate). There is a discontinuity in the profile at the interface between γ-Fe and α-Cr. The complete Fe-Cr phase diagram is given in Figure 4-4-2.

Finally, *carbonitriding* can be carried out either by immersion in cyanide salt baths, by exposure in a mixture of ammonia and hydrocarbon gas, or by plasma treatment.

8-4 Diffusion couples

A diffusion couple is an experimental configuration in which two metal samples are pressed tightly together at a planar junction and heated to a temperature where diffusion can occur across the interface. Thermodynamic equilibrium is first of all established at the interface and progressively extends to greater distances by the development of diffusion fluxes. Given sufficient time, uniform activities (but not necessarily chemical composition) will eventually be attained throughout the specimen.

Consider the case of a couple consisting of pure iron and pure chromium held at 1 400 °C. The two phases in contact, namely δ-Fe and α-Cr, have the same crystal structure and are fully miscible in one another. The instantaneous concentration profile at any time can be calculated for each element from Fick's equations and is found to have a sigmoidal shape. The zone where both elements are present widens with time, its thickness varying with $t^{1/2}$ (Fig. 8-4-1 A).

If the same diffusion couple is heated at 1 000 °C, two different phases are in contact, corresponding to fcc γ-Fe and bcc α-Cr. Equilibrium is established at the interface, but the Fe-Cr phase diagram shows that there is a range of compositions between the terminal solid solutions where no single phase can exist alone. Since the two diffusion fluxes are not necessarily identical, the interface advances towards the side where the flux is greatest. The composition changes suddenly on passing from one phase to the other, with no two-phase transition zone. Figure 8-4-1 B shows the correspondence between the successive layers predicted and the phase diagram. However, a representation of this sort can be confusing, since the profile obtained in systems where several phases can exist across the diagram is in no way related to the thicknesses of the successive layers. The latter depend only on the relative diffusivities of the elements in each phase. Some intermetallic compounds can act as veritable diffusion barriers, with very low diffusivities, and can be deliberately used for this purpose. When the opposing fluxes compensate one another exactly, it is also possible that a phase expected from the phase diagram does not in fact appear.

8-5 Galvanising

Fe-Zn diffusion couples

When pure iron is immersed in liquid zinc at 450 °C, the diffusion of iron and zinc in opposite directions gives rise to the formation of the whole series of phases predicted by the Fe-Zn phase diagram, namely α-Fe, Γ1, Γ2, δ1, ζ and η-Zn (Table 8-5-1 and Fig. 8-5-2). The fact that the zinc is liquid simply changes the reaction kinetics, and it is for this reason that the process is sometimes referred to as reactive diffusion. When the initial iron surface is perfectly planar and the fluxes are unidirectional, the different phases form parallel layers. A transition from one phase to another occurs at each interphase boundary (or phase interface), where the adjoining phases are in equilibrium with one another (*i.e.* the activities of Fe and Zn are identical). Figure 8-5-3A shows a schematic representation of the microstructure observed experimentally after 1 hour of immersion at 450 °C.

Table 8-5-1:
Structure of the phases in the Fe-Zn system and the principal phase in the Fe-Zn-Al system, Fe_2Al_5.

Phase	At% Zn	Pearson symbol	Space group
αFe	0-3	cI2	Im$\bar{3}$m
Γ1	68-74	cI52	I$\bar{4}$3m
Γ2	78.6-81	cF408	F$\bar{4}$3m
δ1	86.5-92	hP555	P6$_3$/mc
ζ, $FeZn_{13}$	92.5-94	mC28	C2m
η Zn	100	hP2	P6$_3$/mc
Fe_2Al_5		oC*	Cmcm

In this case, the experimental observations differ from what might have been expected. In fact, liquid zinc is highly reactive towards steel and several events occur in the first few seconds of contact. The phase seen to form first is ζ, followed by the other more iron-rich phases. The ζ phase has an energetically favourable epitaxial relationship with α-Fe, so that the orientations of the α-Fe grains influence the microstructure. When the bulk thermodynamic stabilities of the different phases are fairly similar, the relative ease of nucleation can become the overriding factor. Thus, the Γ1 phase has difficulty in nucleating when the temperature is close to that of the peritectic reaction by which it normally forms on cooling and it may sometimes not be observed at all. In general, a gain in chemical energy of 400 J/cm^3 is considered to be necessary for a phase to form.

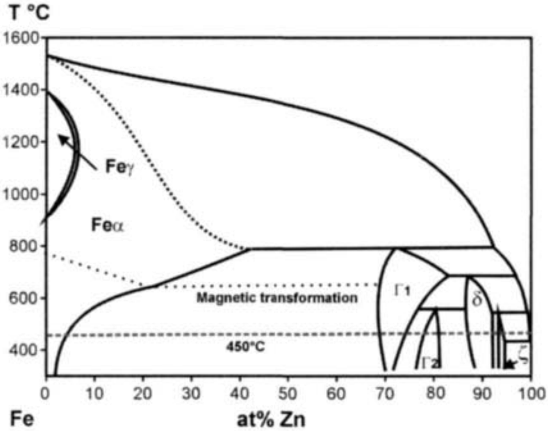

Figure 8-5-2:
Fe-Zn phase diagram. The line at 450 °C represents the usual conditions for galvanising.
From [Mas90].

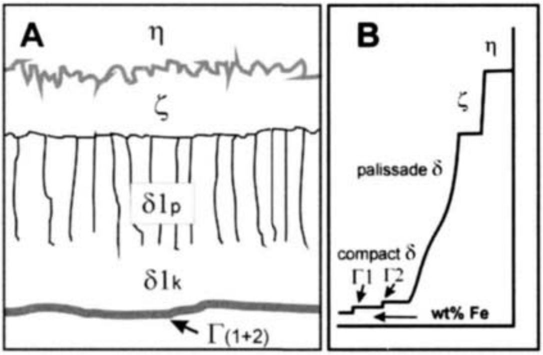

Figure 8-5-3:
A) Schematic representation of the stratified structure observed when iron is immersed in liquid zinc for one hour at 450 °C. The interaction layer is about 100-200 μm thick.
B) Corresponding iron concentration profile. The δ1 phase adopts two different morphologies, corresponding to two composition ranges. The compact δ1 phase grows towards the iron whereas the palissade δ1 phase advances towards the liquid zinc.
Adapted from [Gra80] and [Fer76].

Diffusion can occur both through the grains and along grain boundaries. It is generally more rapid at grain boundaries, although there are exceptions for certain intermetallic compounds. The relative distribution of the diffusion modes can have a significant influence on the morphology of the various layers formed. Finally, transgranular diffusion can be anisotropic in some phases, leading to a non-planar interface.

The δ1 phase occurs with two different morphologies, referred to as *compact* (δ1k) and palissade or *pillar-like* (δ1p) and for a long time they were taken to be two different phases (Fig. 8-5-3B). In fact, the difference is simply due to the formation mechanism, depending on whether growth occurs in contact with ζ or Γ2. The anisotropic columnar morphology of the δ1p phase could also be related to preferential diffusion along the [h00] directions.

After the first few seconds of reaction, once the different layers have begun to form, a purely diffusive regime is established and thickening proceeds according to parabolic (t^n) kinetics. The value of the exponent n determined experimentally for each phase includes the different diffusion modes. It is low, less than the truly parabolic value of 0.5, for the Γ1 and ζ ($FeZn_{13}$) phases, and high for the δ1 phase (from 0.5 to 0.68). This means that δ1 grows faster than the two phases with which it is in contact (Γ1 and ζ). In fact, the layer of δ1 acts as the principal diffusion barrier between the iron and the zinc. It inhibits the formation of the other intermetallic compounds and exerts a stabilising effect, maintaining the regular arrangement of the strata.

Effect of ternary additions - phase equilibria and diffusion paths

The addition of a third element in the Fe-Zn system, even in only small amounts, can modify the phase equilibria and induce the formation of new phases. In particular, the effect of aluminium is well documented, and the formation of the compound Fe_2Al_5 is considered to be beneficial (Table 8-5-1). The influence of ternary additions on coating constitution can be interpreted with the aid of the corresponding Fe-Zn-X ternary diagrams. Although the Fe-Zn-Al system has been most extensively studied, it remains the most controversial. However, there appears to be reasonable agreement on the 450 °C isothermal section, which can be used to explain industrial galvanising treatments [Che90b], [Per92], [Tan95a]. The Fe-Zn-Ni diagram is also fairly well established [Per94], [Tan95b], [Per95a], [Reu98]. The diagrams have been determined based on the phases observed in diffusion couples, usually after relatively short holding times. It is acknowledged that diagrams determined in this way must be considered with precaution, since they do not necessarily represent true thermodynamic equilibrium. As already mentioned, some expected phases do not actually form and the neighbouring phases then appear to cover an excessively wide range (*e.g.* δ1 in the Fe-Zn-Al system [Per95b] and Γ2 in the Fe-Zn-Ti system). The relatively low temperature range concerned by these processes, related to the high reactivity of the liquid, *makes the attainment of equilibrium difficult* in the solid state, with extremely slow diffusion rates in certain intermetallic compounds.

In a ternary system, each element diffuses across the initial interface at its own rate, which depends on the local composition. The locus of points in the ternary diagram representative of the overall compositions in successive sections ahead of the original interface is called the diffusion path. There is an extra degree of freedom compared to a binary system and several paths are possible, and in particular, they can cross three-phase regions [Ure73], [Lep98a]. The fact that a phase does not form can be explained thermodynamically by considering the diffusion paths. In contrast, the apparent excessive extension of a phase field, encroaching on those of its neighbours, remains a metastability phenomenon. The practical conclusions for multi-component systems are as follows :

- the microstructure is no longer forced to grow in parallel layers, but can include multi-phase regions;
- anomalies can occur due to the difficulty of nucleation of the thermodynamically most stable phase;
- the alloying elements present in the steel go into solution in the zinc bath, and even at low concentrations can cause the formation of new phases, both in the coating and in the bath.

Industrial hot dip galvanising processes

Hot dip galvanising has been used since the 18^{th} century to produce protective corrosion-resistant coatings on iron and steel. It can be performed as either a batch process, when the products are finished components, such as crash barriers, etc., or continuously, on coiled strip.

In the *batch process*, the component to be coated is immersed in a bath of liquid zinc saturated in iron, generally at about 450 °C. The two metals interact rapidly to form the various stratified phases illustrated schematically in Figure 8-5-3. The hardness of the intermetallic compounds is such that subsequent forming operations are virtually impossible without damaging the coating. Furthermore, some alloying elements present in the steel can have deleterious effects on coating quality. For example, silicon induces excessive thickening of the interaction layer and prevents the formation of a stable and regular morphology. Silicon in solution is rejected as the coating thickens, since it has very low solubility in the ζ phase. It diffuses towards the liquid and interactively modifies the other diffusion fluxes. It precipitates out in the bath and tends to form a crust at the liquid/solid interface (Sandelin effect [Bér96a], [Lep98b]).

In *continuous galvanising*, steel strip is fed through a molten zinc bath and excess liquid zinc is wiped off at the exit. The aim is to produce a thin uniform coating able to withstand subsequent forming operations without damage. For this purpose, aluminium is added to the bath to regulate the reactions between the steel and the zinc. Thus, the presence of about 0.2 % Al causes the very rapid formation of a thin uniformly distributed film of Fe_2Al_5, a few hundreds of nanometres thick, which acts as an inhibiting layer. As it solidifies, it traps zinc, and is often represented as Fe_2Al_5,Zn. On leaving the bath, the coating is composed of solid Fe_2Al_5 containing zinc, together with entrained liquid zinc. Wiping to remove excess liquid and control the final coating thickness is followed by solidification. The resulting coating, usually of the order of 10 µm thick, is thus composed essentially of zinc and is sufficiently ductile to allow subsequent forming operations, such as deep drawing. The zinc bath gradually picks up alloying elements present in the steel. Among these, phosphorus has a favourable effect, enhancing the inhibiting action of the Fe_2Al_5 layer. Titanium from interstitial-free steels is considered to be detrimental, probably because it ties up phosphorus, whereas manganese and niobium have little effect. Nickel is beneficial and helps to regularise the coating.

The efficiency of the Fe_2Al_5 diffusion barrier depends on the compositions of the steel and the bath and on the other process conditions employed [Gut95]. Its effect is temporary, lasting only a few minutes, beyond which protuberances start to appear on the surface, developing laterally in the form of *outbursts*, which eventually cover the whole surface with unwanted Fe-Zn compounds. This phenomenon, for which various mechanisms have been proposed [Zer02], occurs even when the bath composition is correctly chosen to obtain equilibrium with Fe_2Al_5. It has been shown that the substrate grain boundaries represent weak points (*cf.* Fig. 8-5-4).

Figure 8-5-4:
Outbursts of Fe-Zn compounds above the Fe_2Al_5 layer of a galvanised coating formed on pure iron iron treated for 20 minutes at 460 °C in a bath containing 0.18% Al, revealed by chemical dissolution of the overlying zinc. The outburst has formed above a ferrite triple grain boundary junction. The scale marker represents 10 µm.
Courtesy Sollac and IRSID, [Lep98a]

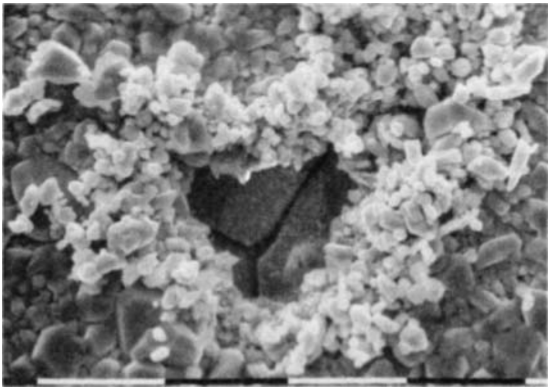

In contrast, when intergranular diffusion is attenuated, the inhibiting effect of the Fe_2Al_5 layer is stabilised. This is probably the mechanism by which phosphorus prevents outburst formation. Since free titanium (*i.e.* not tied up in sulphides, carbides or nitrides) can form phosphides, the titanium/phosphorus ratio in the steel is important and must be adjusted to leave sufficient active phosphorus [Bér96a], [Jor97]. Furthermore, titanium can cause the formation of unwanted $TiZn_{15}$ matte in the bath.

9

The decomposition of austenite

The final microstructures of steels, and consequently their service properties, are determined principally by solid state transformations. The present chapter discusses the essential features of the mechanisms involved.

9-1 The different types of solid state transformatione

Various characteristics are considered in classifications of solid state phase transformations, based on the mechanisms involved. For example, in the classification proposed by Christian (cited in [Cah83]), the transformations can be homogeneous or heterogeneous, thermally activated or athermal, diffusive or military, and can have an interface that is either coherent or incoherent. In the case of austenite decomposition during cooling, it is the *diffusive* or *military* nature that is the major criterion. In diffusive processes, the atoms move individually, whereas in military transformations they are displaced together, in a block.

As their name implies, diffusive transformations involve atomic diffusion. Since the movement is thermally activated, diffusion effects can become significant over large distances when the temperature is sufficiently high. The ultimate consequence of a diffusive transformation is the attainment of thermodynamic equilibrium. Examples of diffusive transformations are precipitation reactions and the eutectoid decomposition in Fe-C alloys at 727 °C (pearlite transformation) :
Austenite γ (fcc) $\rightarrow$ Ferrite α (bcc) + Cementite Fe_3C

Military transformations involve the collaborative displacement of atoms, essentially by shear. The displacement is less than the interatomic spacing and causes a change in crystal structure compared to that of the parent phase, the chemical composition remaining identical. The new phase is thermodynamically metastable. The best known example is the martensite transformation in steels :
Austenite γ (fcc)$\rightarrow$ Martensite α' (bct).

Martensite was named after the German metallographer Martens, who was one of the first to reveal it in steels. Military transformations of this type are often termed martensitic, even in systems other than steels. They occur in numerous other alloys, in intermetallic compounds, in ceramics and minerals, in polymers and solidified gases.

Some transformations involve *both* a military displacement and limited diffusion. The complexity of the mechanisms makes them more difficult to analyse. A typical example is the bainite transformation in steels.

9-2 The representation of solid state phase transformations

Effect of composition on the transformation products

In the case of steels, the products or constituents formed during the decomposition of austenite depend both on the composition of the parent phase and on the temperature for isothermal transformations or the cooling rate under anisothermal conditions. In all cases, the reaction products involve a ferrite-type phase and possibly carbides, with a wide variety of microstructures. Dubé's classification, established in the 1950s, rigorously describes the distinctive morphological characteristics of these different structures. They can be represented graphically in the Fe-C diagram, as shown in Figure 9-2-1. This temperature-composition-product (TCP) diagram shows the approximate ranges where the different constituents are liable to form first during isothermal treatment of an initially fully austenitic structure.

In the light of the vast amount of experimental results now available for steels, more modern interpretations have been proposed [Zha92], [Zha95]. Thus, in the version of the TCP diagram shown in Figure 9-2-1, the field boundaries are more accurate and new sub-divisions appear, distinguishing for example between upper and lower bainite. The

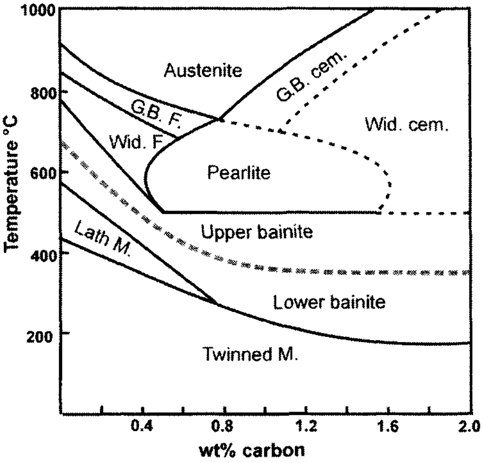

Figure 9-2-1:
TCP (Temperature-Composition-Product) diagram for Fe-C alloys, according to [Zha92], showing the metastable phases liable to form during the isothermal transformation of austenite. The different abbreviations used are GBF for grain boundary ferrite, Wid. F for Widmanstätten ferrite, cem. for cementite and M for martensite.(§ 9-5).

diagram takes into account the fact that twinned martensite can be obtained even at low carbon contents when the cooling rate is high. However, contrary to TTT and CCT diagrams which will be described below, this representation gives no direct information concerning the transformation kinetics.

Isothermal transformations

The transformations considered here involve nucleation and growth phenomena and are conventionally represented on time-temperature-transformation (TTT) diagrams. Such diagrams are determined for a particular steel composition, with an initial state corresponding to an austenitising treatment at a specific temperature T, for a time *t* sufficient to ensure a fully austenitic structure of given grain size.

To determine TTT diagrams, specimens are given the appropriate austenitising treatment and are then *rapidly* cooled to the temperature of the isothermal treatment. The progress of transformation at different temperatures is studied by various metallographic and physical techniques, particularly dilatometry. The times to attain a certain degree of transformation (*e.g.* 5 %, 50 %, 95 %) are plotted, forming curves that represent the transformation kinetics. The diagrams must be interpreted exclusively at constant temperatures (*cf.* Figures 9-2-2 and § 10-2).

The various isothermal transformation products observed are ferrite, cementite, pearlite and upper and lower bainites. Each of these constituents can be related to a distinct transformation, with a maximum rate at a specific temperature, corresponding to the *nose* on its C-shaped TTT curve. Examination of the large number of published TTT diagams reveals the frequent presence of several such noses, suggesting that each transformation has its own mechanism. In fact, many TTT curves have two principal noses, corresponding to the pearlite and bainite transformations. However, in plain carbon steels, the transformations occur almost immediately and their starting point is poorly defined. This is particularly true for old curves, determined with relatively slow experimental techniques. The different curves then overlap and are difficult to deconvolute (assuming that there is effectively more than one transformation).

Figures 9-2-2 and 9-2-3 show TTT curves for two steels of fairly similar composition and reveal the importance of the experimental conditions employed. In fact, the example illustrated in Figure 9-2-2 is quite exceptional and is extremely interesting, since the individual C-curves for the different transformations are clearly distinguished [Zha95]. Most TTT curves available in the literature are much less well defined. Figure 9-2-2 was determined with a large number of specimens treated at closely spaced temperatures. Furthermore, the steel contains molybdenum, nickel and chromium additions. As will be seen later for pearlite (§ 10-3), alloying elements can modify the different transformation mechanisms, helping to separate the transformations.

The diagram in Figure 9-2-3 [Qui01] is for a simple Fe-C-Mn steel and the separation between upper and lower bainite is not emphasised, since independent measurements of the transformation kinetics as a function of temperature revealed little indication of a

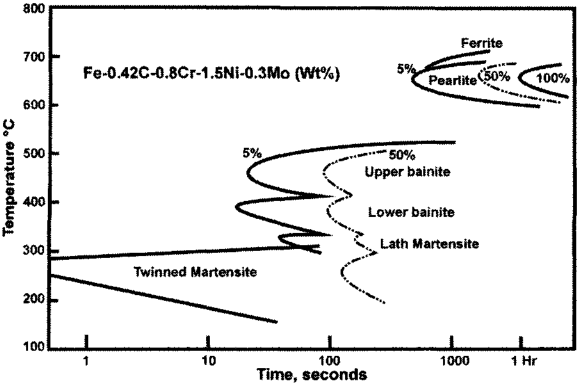

Figure 9-2-2:
Isothermal transformation diagram for a 0.42 % C low alloy steel, homogenised for 2 hours at 1000 °C, then hot rolled and austenitised for 2 minutes at 1000 °C. Curves plotted by Zhao *et al.* [Zha95], based on magnetometry measurements and metallographic observations by Morozov *et al.*

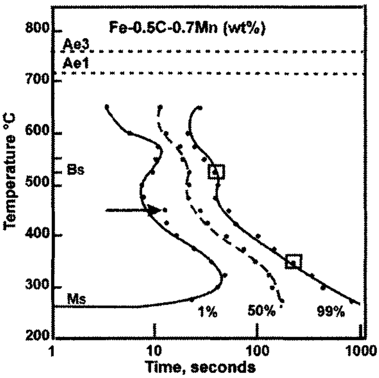

Figure 9-2-3:
Isothermal transformation diagram for a 0.5 % C-0.7 % Mn steel austenitised for 15 minutes at 1 100 °C, based on dilatometry measurements. The values Ae1 and Ae3 represent respectively the equilibrium temperatures for the eutectoid transformation and the the $\alpha+\gamma/\gamma$ phase boundary. The small rectangles indicate the points corresponding to the microstructures shown in Figures 12-2-2 and 12-3-1.
Courtesy IRSID, Arcelor Group, Maizières-les-Metz.

change in regime. Nevertheless, the curve could be plotted in a different manner if it were made to follow the experimental points more closely in the region of the arrow, where two noses could then be distinguished. In fact, the discontinuity in isothermal transformation rates is often not sufficient to reveal the change in mechanism. The conclusion is that the transformation mechanisms can not always be deduced by the simple examination of TTT curves.

The sudden increase in transformation rate on approaching the martensite start temperature Ms in Figure 9-2-3 is frequently observed. This phenomenon is known as *swing back* and is considered to be entirely due to isothermal transformation of martensite. The martensite then becomes tempered and convert into a structure similar to lower bainite.

Continuous cooling diagrams

Isothermal transformations have generally little relevance to industrial heat treatment conditions and the most practical representation is the use of continuous cooling transformation (CCT) diagrams. The transformation start and finish points are plotted in temperature-time diagrams along curves representing different cooling profiles, which generally

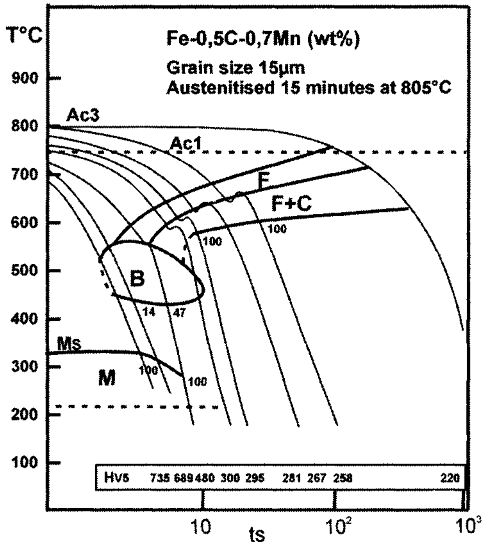

Figure 9-2-4:
CCT diagram for Fe-0.5C-0.7Mn steel for which the TTT diagram is shown in Figure 9-2-3. The diagram was determined experimentally by dilatometry. The curves read along the cooling lines from the austenitising temperature intersect the fields corresponding to formation of the different phases : F = ferrite, F+C = pearlite, B = bainite (also indicated F+C) and M = martensite. The figures on the curves indicate the percentage of austenite transformed on leaving the field concerned.
Courtesy IRSID, Arcelor Group, Maizières-les-Metz

show a classical *t½* form. These diagrams must be read exclusively along the cooling curves. CCT curves cannot and *must not be deduced* from TTT curves for the same steel [Zha92]. Figure 9-2-4 shows a CCT diagram for the same steel as the TTT diagram in Figure 9-2-3.

CCT diagrams serve a mainly technical purpose and are established under standard experimental conditions, with specified specimen dimensions and cooling fluids, usually air, oil and water. Heat losses are determined by the thermal characteristics of the specimen and the cooling fluid, together with those of the boundary layer, which is often a gas formed by vaporisation, or sometimes even a solid layer produced by precipitation. The effective conductivity of the cooling medium is inversely proportional to the thickness of the gaseous boundary layer, while heat dissipation by natural convection can be more than doubled by vigorous agitation. Table 9-2-5 gives an idea of the range of cooling rates that can be achieved with different fluids. The low cooling rate obtained by quenching in liquid air, compared to simple water quenching, is due essentially to the gas film produced by vigorous boiling in contact with the hot metal (recalescence). In spite of this, liquid air and liquid nitrogen quenching are often employed due to the fact that the final temperature attained is below the sub-ambient martensite finish temperature Mf [Kra80].

Table 9-2-5: Comparative cooling rates obtained in different media. The reference is a 4 mm diameter Ni-Cr steel ball cooled at 1810 °C/s between 717 and 550 °C.
Adapted from values given in [Kra80].

Water + 10% NaCl	Water at 18°C (Reference)	Oil	Hydrogen	Liquid air	Air	Vacuum
~ 2	1	~ 0.2	0.05	0.04	0.028	0.011

A relatively little used representation of transformation kinetics is in the form of temperature-cooling rate curves ($T(\dot{T})$). These diagrams show shelves at the bainite and martensite start temperatures Bs and Ms. They demonstrate that the Bs and Ms temperatures are specific and independent of cooling rate [Zha93]. However, numerous other factors can affect the start of transformation in fully austenitised structures. In particular, the austenite grain size, residual segregation, the presence of precipitates and internal stresses can influence the time necessary to form the first nuclei (the incubation time). Nucleation is thus facilitated by local heterogeneities, but the major effect remains that of alloying additions (see also Figures 10-3-1 and 18-1-2).

It should be noted that the eutectoid transformation temperature is often denoted A1 and the austenite solvus, (ferrite + austenite)/austenite phase boundary, A3, being originally determined as arrest points on dilatometer curves. These designations are sometimes completed by a suffix, either c or r, indicating that the value is measured on heating (c for *chauffage* in French) or on cooling (r for *refroidissement* in French). In fact, the values depend on the heating or cooling rate, due to the time necessary to attain equilibrium, and show a certain hysteresis.

9-3 Growth mechanisms

Interface movement

It is clear that several distinct transformation mechanisms exist, each in a specific temperature range. Temperature chiefly influences the approach to phase equilibrium and the movement of interfaces. This section briefly outlines the reasoning followed in order to interpret the different mechanisms

In the range of temperature and composition compatible with the formation of pro-eutectoid ferrite, a ferrite nucleus grows by movement of the α/γ interface at the expense of the austenite. The atoms diffuse across the interface and change their crystallographic arrangement. When they become attached to the ferrite surface in a random manner, with no preferred sites or directions, the interface is said to be "rough". The interface can then propagate readily in all directions. The movement of the interface is a thermally activated process and is rapid at high temperatures. A reduction in temperature lowers the mobility of the transformation front.

Certain preferred orientation relationships between the ferrite and austenite imply either perfect matching of the two crystal lattices (coherent interface) or almost perfect matching (semi-coherent interface). The crystal planes for which matching is good are generally the ones with densest packing (*cf.* § 7-1), for example $\{111\}\gamma$ and $\{110\}\alpha$. Interfaces of this sort can no longer move in an isotropic manner and are inhibited by the need to conserve coherency or semi-coherency with the parent phase. Mismatch dislocations that accommodate semi-coherency exert a pinning effect. In order to move, they must be able to climb,

Figure 9-3-1:
Schematic representation of an interface comprising terraces and ledges. The arrow D indicates the edgewise growth of the terraces, while the arrow P shows the macroscopic growth direction of the interface.

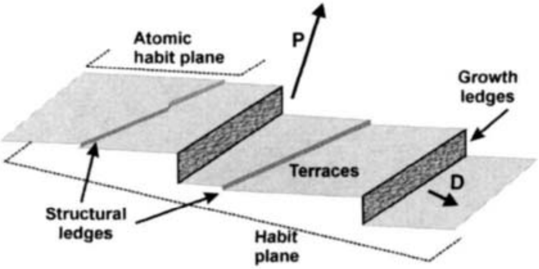

and this requires a certain activation energy, with a probability that becomes significant only above a critical temperature. Below this temperature threshold, the interface will prefer to move by the lateral displacement of growth ledges. The microstructure then reveals facetted interfaces oriented along specific crystal planes.

Interface structures

On an atomic scale, the ferrite/austenite interface generated by lateral growth shows different types of ledges with variable spacings and heights (Fig. 9-3-1). The growth ledges separating terraces are the largest steps, with typical heights of about 10 atom layers, depending on the transformation temperature. The terraces include smaller steps, called structural ledges, only one or two atom layers high, that accomodate lattice misfit.

The terraces and structural ledges are pinned by their mismatch dislocations. Although the growth ledges also contain partially coherent planes, it is energetically more favourable for atoms to become attached there, so that the transformation proceeds by lateral extension of the terraces, that is, by displacement of the growth ledges [Pur78], [Aar90].

The habit plane identified by conventional electron microscopy is the mean plane joining the terrace edges, and therefore has a high probability of being irrational (*i.e.* not corresponding to a simple relationship between low Miller index lattice planes). Some authors have described it as the TapHP (for TEM apparent Habit Plane) to distinguish it from the plane of the terraces on the atomic scale AHP (for Atomic Habit Plane). The difference between the two can be significant, and depends on the number and height of the growth ledges. For example, in the case of bainitic ferrite, the TapHP can deviate by up to 20° from the most common AHP, the close packed $\{111\}\gamma$ plane. The difference is greater the higher the carbon content and the lower the transformation temperature.

The synchronised movement of arrays of ledges has been observed during *in situ* TEM treatments at 800 °C [Pur78]. In Figure 9-3-2, regularly spaced ledges can be seen along the α/γ interface. Although the relevance of thin foil experiments is debatable, the results are consistent with conventional observations on macroscopically facetted phase interfaces. On an atomic scale, the interfaces consist of a series of terraces separated by ledges about 10 atoms high (~3 nm) [Pur78].

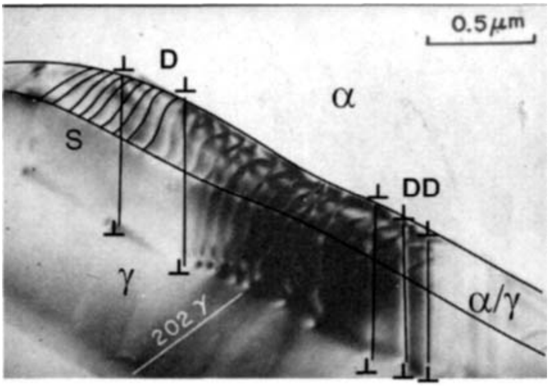

Figure 9-3-2:
Reverse contrast TEM micrograph of an Fe-Mo-C steel, showing the presence of ledges along an α/γ interface. Some of the ledges are marked by lines at S, while dislocations are indicated at D and DD.
Courtesy McMaster University, Hamilton, Canada, [Pur78].

Cementite/austenite interfaces show similar features. In the optical microscope, pro-eutectoid cementite platelets are seen to have a wide variety of habit planes. However, observations at higher magnification in the electron microscope reveal the presence of arrays of terraces, suggesting interface growth by the lateral displacement of ledges, as in the case of ferrite [Cow87], [Spa90], [Man99a].

Crystallographic considerations suggest the possibility that cementite could be formed by a mechanism involving the military displacement of the iron atoms in the austenite lattice, combined with random diffusion of the carbon atoms. Martensite formation could be an intermediate step, since the change to cementite then requires only limited ordering. This mechanism has been proposed by several authors (cited by [Cow87]) and has the merit of explaining the ease with which cementite grows, even at relatively low temperatures. It could also account for the fact that cementite often forms as a metastable phase in alloy steels, being subsequently replaced by the equilibrium carbides.

At sufficiently high temperatures, interface propagation becomes isotropic. In contrast, below about 800 °C, it can only occur by lateral growth at ledges. The macroscopic interface moves in a direction perpendicular to ledge growth by the stacking of successive terraces. *Exchanges of solute occur at the terrace edges*, along the growth ledges. The presence of alloying elements influences interface mobility by modifying the lattice parameters of the habit planes.

Growth determined by the direction of the invariant plane

At lower temperatures, around 300 °C, the driving force for the transformation of austenite is sufficiently large to overcome the lack of mobility of certain planes by inducing a shear mechanism. However, growth is then subjected to other conditions, and must take place in a plane corresponding to minimum strain. The martensite transformation involves invariant plane strain. In order to satisfy the interface relationships while conserving the crystal lattice intact, a combination of slip and rotation is necessary (lattice invariant deformation). On the atomic scale, terraces and ledges are formed at the interface to ensure coherency, but play no part in growth. Interface movement is again anisotropic, but involves completely different mechanisms (*cf.* § 11-1). Growth rates are extremely high since they are not limited by diffusion.

9-4 Diffusive exchanges at interfaces

Equilibrium at interfaces - concept of restricted equilibrium

When the two phases present, for example austenite and ferrite, have the compositions defined by thermodynamic equilibrium and are fully homogeneous, the situation is described as *equilibrium*. This ideal state is rarely observed in practice and various cases must be considered depending on the variation of the different atomic diffusivities with temperature. As early as 1947, Hultgren showed that in Fe-C-X alloys, the solute element X is not always redistributed between the γ and α phases in accordance with equilibrium predictions. As pointed out by Hillert [Hil80], it is therefore necessary to consider a partial equilibrium restricted to the highly mobile interstitial elements. Three principal situations are distinguished, depending on the distribution of carbon and substitutional elements at the interface (Figure 9-4-1). The aim is to correctly model the transformation kinetics associated with growth of the interface and redistribution of the alloying elements, assuming thermodynamic equilibrium to be maintained locally at the interface. The essential parameters are the concentrations of the different elements at the moving interface, designated C for the interstitials and X for the substitutional species. It is convenient to represent the reasoning graphically in the form of ternary diagrams. For local equilibrium between two phases, the phase rule allows many different solutions at a given temperature, corresponding to the various tie-lines in the isothermal section of the phase diagram. Only one of these tie-lines passes through the point corresponding to the overall alloy composition (X_0, C_0) and represents the ultimate true equilibrium state. The intermediate stages will satisfy conditions of restricted equilibrium at the interface, taking into account the diffusion fluxes. In the present case, equilibrium is assumed to be maintained at the interface. The application of a conservation of mass criterion to the diffusion rates enables the choice of the tie-line representing the local equilibrium. It is called the active tie-line and differs, depending on the solute partitioning mode considered.

Local thermodynamic equilibrium : the LE or PLE mode

It is considered that thermodynamic equilibrium is established *only at the interface*, by partitioning of all the elements between the two phases, including both interstitial and substitutional species. For substitutional elements, the concentration remains at the initial level beyond a diffusion distance of approximately $2(DT)^{1/2}$. Interstitial elements are assumed to have a constant chemical potential or activity at all points. In the schematic phase diagram shown in Figure 9-4-1 A, the initial composition is $(X_0$, $C_0)$. A carbon iso-activity line is drawn whose extension in the two phase field passes through this point. It intersects the austenite field boundary at a point having the same carbon activity, which can therefore be considered to belong to the active tie-line K_{LE}. Only one tie-line in the

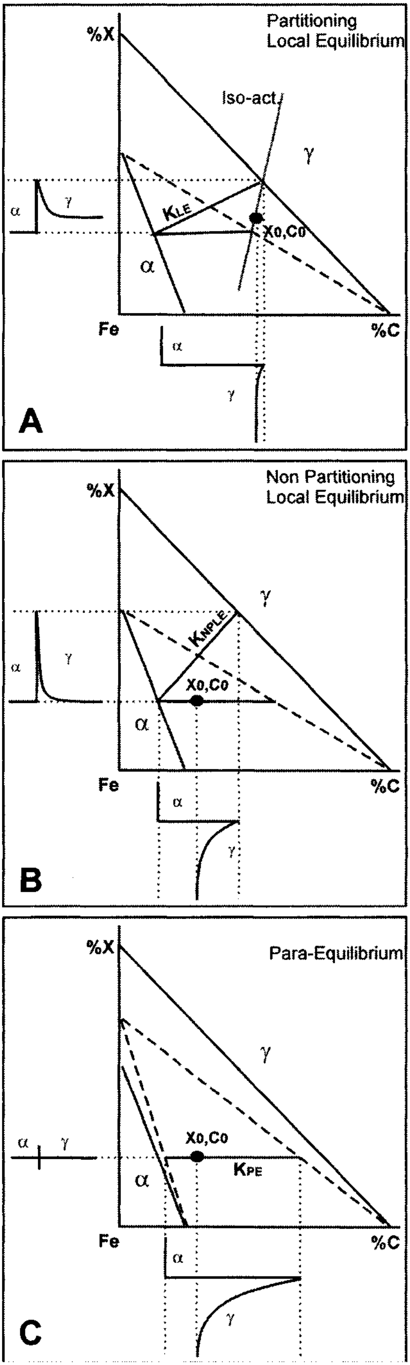
Partitioning
Local Equilibrium
%X
Iso-act
γ
α
γ
KLE
X0,C0
α
Fe
%C
α
γ
A
Non Partitioning
Local Equilibrium
%X
γ
KNPLE
α
γ
X0,C0
α
Fe
%C
α
γ
B
%X
Para-Equilibrium
γ
α
γ
X0,C0
KPE
α
Fe
%C
α
γ
C

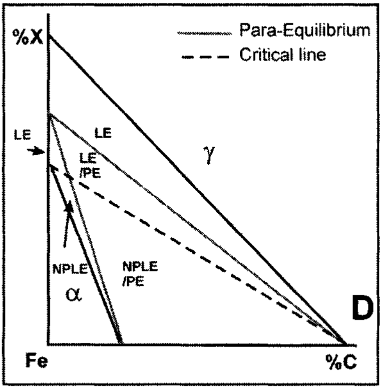
%X
Para-Equilibrium
Critical line
LE
LE
LE
/PE
γ
NPLE
NPLE
/PE
α
D
Fe
%C

Figure 9-4-1:
Schematic isothermal sections of an Fe-C-X ternary diagram illustrating the partitioning of iron, carbon and a substitutional solute element X in three different situations, during the transformation of austenite to ferrite, the initial composition of the austenite being the overall alloy composition Fe-C_0-X_0. In each case, the concentration profiles of C and X across the α/γ interface are shown adjacent to the corresponding axis.

A) Local equilibrium with partitioning (PLE). The dashed line is the zero partitioning envelope.

B) Local equilibrium without partitioning (NPLE).

C) Para-equilibrium (PE).

D) Summary of the composition regions thermodynamically possible for each situation. A fourth situation not shown is perfect meta-equilibrium. The four different situations cannot co-exist. Their occurrence depends on the diffusion rates and therefore on the temperature considered.
Courtesy INPG, Grenoble. Adapted from [Bré02].

phase diagram passes through this point. The other end of the tie-line indicates the composition of the ferrite. This tie-line determines the conditions of local equilibrium with partitioning compatible with the conservation of mass for both carbon and the solute X, which have highly different diffusion rates. This situation is designated PLE (for partitioning local equilibrium) or simply LE. The geometrical construction shown in Figure 9-4-1 A defines a *critical line,* which is the locus of the points of intersection of the carbon isoactivity line with the horizontal line corresponding to the concentration X in the ferrite determined by the active tie-line. This critical line is the zero partitioning envelope and represents the boundary of the region within which the conditions for partitioning can be achieved. Beyond it, the construction leads to a configuration where there is insufficient driving force for the reaction to occur [Hil80].

Equilibrium without solute partitioning : the NPLE mode

Beyond the critical line defined above, another construction is used, with different assumptions (Figure 9-4-1 B). In this case, there is no partitioning of the solute X, whose composition therefore remains almost constant (X_0) except at the interface. Its value is nearly the same in both the austenite and the ferrite. The carbon activity is again constant, but its concentration varies. The point where the $X = X_0$ line intersects the ferrite phase field boundary approximately defines one end of the active tie-line that determines the two compositions in equilibrium at the interface. This situation is called the no (negligible) *partitioning local equilibrium* (NPLE) mode.

Para-equilibrium : the PE mode

The NPLE model predicts solute accumulation and depletion in the immediate vicinity of the interface. As the temperature decreases, the width of this zone diminishes, and when it reaches atomic dimensions, the concept of local equilibrium loses all physical meaning. Another approach is then to consider that the interface composition is determined by a pseudo local equilibrium allowing for the fact that the concentration of X remains the same in the two phases. A new phase diagram is considered with the equilibria calculated as usual to minimise the free energy, but assuming that the solute concentration X is the same in both phases. The chemical potential (activity) of carbon is again taken to be uniform everywhere. The new equilibrium conditions are termed para-equilibrium and this situation is called the *para-equilibrium* (PE) mode. The new phase boundaries are represented by the dashed lines in Figure 9-4-1 C, the active tie-lines being horizontal by definition. Only one tie-line can pass through the initial (alloy) composition.

Effect of temperature and alloy composition

The different possible conditions can be compared by plotting them on the same isothermal section (Figure 9-4-1 D). This neglects the effect of temperature, which modifies both the equilibrium phase boundaries and the diffusivities of the elements. Furthermore, these parameters also depend on the nature of the substitutional element X considered. Each of the situations or modes described above *is possible only within a limited range of temperature,* depending on the diffusion rates involved.

In the PLE mode, for the activity of carbon to be effectively uniform requires a relatively high temperature, above 600°C. The diffusion controlled mechanism requires a fairly slow interface displacement velocity in order to maintain local equilibrium at the interface. This mode is generally observed for low supersaturations and the kinetics are determined by the most slowly diffusing substitution elements.

In the NPLE mode, only the carbon partitions effectively between the two phases, with local enrichment in the austenite near the interface. The interface displacement is theoretically much faster, since it essentially involves only carbon diffusion. However, certain authors believe that the diffusion of substitutional solutes is not restricted solely to the rough moving interface, and consider that bulk diffusion also occurs over very short distances.

At low temperatures, the diffusion of Fe and X atoms becomes difficult and it can be considered that partitioning between the phases is essentially limited to carbon. The situation then corresponds to *the PE mode* and the transformation is said to be reconstructive. The incoherent interface moves past the Fe and X atoms, which simply change their positions slightly to fit into the new crystal lattice. The interface displacement velocity is controlled solely by the diffusion of carbon (or other interstitials) and can be very rapid, although less than for a military type mechanism such as the martensite transformation. In the PE mode, the ferrite contains a small amount of carbon, more than predicted for thermodynamic equilibrium, but less than for a martensite transformation.

In summary, the order of the transformation modes with decreasing temperature is equilibrium, PLE, NPLE and PE. They must be considered above all as models on which to base reasoning.

For example, they are extremely useful for interpreting the effect of alloying elements on the pearlite transformation. They are also employed as arguments in the heated debate concerning the bainite reaction, where the existence of partial diffusive modes is supported by indirect experimental observations. Thus, lattice parameter measurements show that retained austenite becomes enriched in carbon during the transformation, which is consequently often incomplete. The change in composition demonstrates that carbon redistribution occurs in a range of temperature corresponding to the NPLE or PE modes, with no partitioning of the substitutional elements. Atom probe analyses at α/γ interfaces, with atomic scale resolution, have revealed that Mn, Ni, Mo and Cr do not partition during the growth of bainite. Another approach is to compare the chemical analysis of the carbides formed during the pearlite and bainite transformations in the same steel. The carbides in pearlite contain larger concentrations of substitutional alloying elements than carbides of the same type in bainite. The carbides in pearlite are in fact closer to the thermodynamic equilibrium composition than in the case of bainite.

The change from one mode to another (*e.g.* LE/PE) with temperature for a given alloy is not gradual, but occurs suddenly at a specific transition temperature. This temperature depends on the solute diffusivities, and therefore on alloy composition.

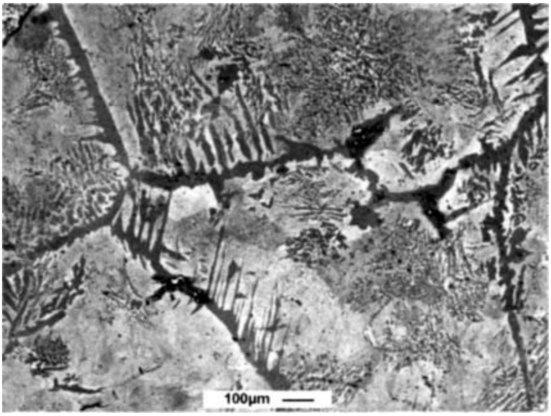

Figure 9-5-1:
Scanning electron micrograph of a C35E4 (XC38) steel slowly cooled at 5 °C/mn, nital etchant. Ferrite has precipitated in the prior austenite grain boundaries as both coarse allotriomorphs and Widmanstätten plates growing out into the grains. Finer ferrite "ideomorphs" have formed within the grains at lower temperatures. Their shape is poorly defined and is sometimes dendritic.
Courtesy INPG, Grenoble.

In the NPLE mode, a so-called *drainage* effect can occur at the reconstructively moving interface. The substitutional elements are trapped and pulled along by the interface, whose displacement is slowed by the associated solute drag phenomenon. Several theoretical models describe this process [Hil99b].

Because of the difficulty of experimentally evaluating interface mobility and the interactive diffusivity of carbon in the vicinity of the interface, a modelling approach now tends to be preferred, based on the combination of thermodynamic phase equilibria and diffusion data. For example, the DICTRA software incorporates sub-programs from Thermocalc [Bor00]. It is probable that a data bank for predicting TTT diagrams will become available in the near future.

9-5 The formation of pro-eutectoid ferrite and cementite

Ferrite

Pro-eutectoid ferrite forms during the cooling of hypo-eutectoid Fe-C alloys. It occurs with various morphologies, as indicated in the TCP diagram in Figure 9-2-1, [Zac62] :

- grain boundary *allotriomorphs* (GBAs) - particles of the same type distributed randomly within the grains are called *idiomorphs* ;
- Widmanstätten plates, which appear as needles in cross section, aligned along preferred crystallographic planes in the austenite ;
- acicular ferrite, consisting of fine lenticular platelets inside the grains.

Figure 9-5-1, corresponding to a slowly cooled C35E4 steel, shows a wide variety of morphologies, with necklaces of coarse GBAs along the prior austenite boundaries, parallel Widmanstätten plates growing out from the boundaries, and much smaller intragranular

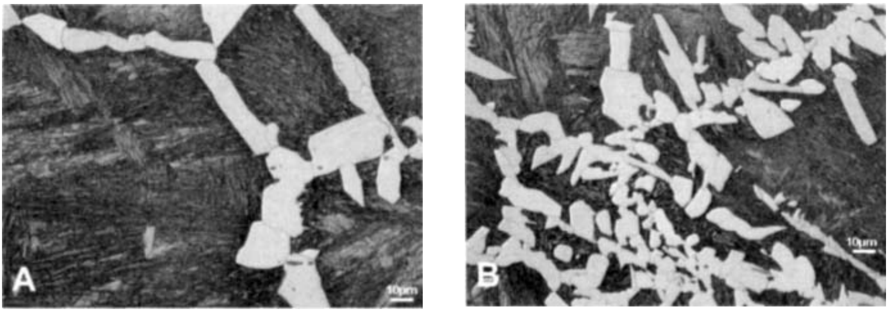

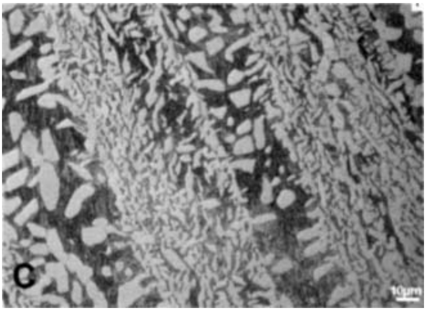

Figure 9-5-2:
Optical micrographs of an Fe-0.16C-1.4Mn steel austenitised for 15 mn at 1250°C and then cooled at about 20°C/s down to 840°C, followed by hot torsion testing and cooling at 50°C/s to 700°C, holding for 1 mn and water quenching. After nital and sodium metabisulphite etching, the ferrite appears light and the martensite matrix dark.
A) No torsion strain.
B) Torsion strain of 0.4 at a strain rate of 3.6 s^{-1}.
C) Torsion strain of 0.8 at a strain rate of 3.6 s^{-1}.
Courtesy INPG, Grenoble and IRSID, Arcelor Group. See also [Lac03]

ideomorphs dispersed in the martensite matrix. The GBAs nucleate at austenite grain boundaries and show a classical Kurdjumov-Sachs type orientation relationship with one of the grains and grow at the expense of the other one. Their nucleation is facilitated by thermomechanical treatments, leading to finer particle sizes. The GBA ferrite in the non-deformed sample shown in Figure 9-5-2 A is coarse, whereas increasing amounts of strain introduced by hot torsion testing refine the particle size (Figures 9-5-2 B and C).

When the $\gamma \rightarrow \alpha$ transformation is rapid, the ferrite can form elongated grains, with a high density of dislocations, similar to Widmanstätten plates. The dislocations accommodate the transformation strain [Sak84]. This situation is encountered when ferrite precipitation occurs in the temperature region close to the corresponding nose of the TTT diagram.

For very low carbon contents, the ferrite formed at high degrees of supercooling has a compact, relatively featureless appearance, and is described as massive ferrite. However, some authors believe that it is simply bainite containing very few carbides.

Cementite

Like ferrite, pro-eutectoid cementite initially forms at the austenite grain boundaries, this time in hyper-eutectoid steels, in the form of coarse precipitates, Widmanstätten plates, or laths at lower temperatures and higher carbon contents (Fig. 9-5-3).

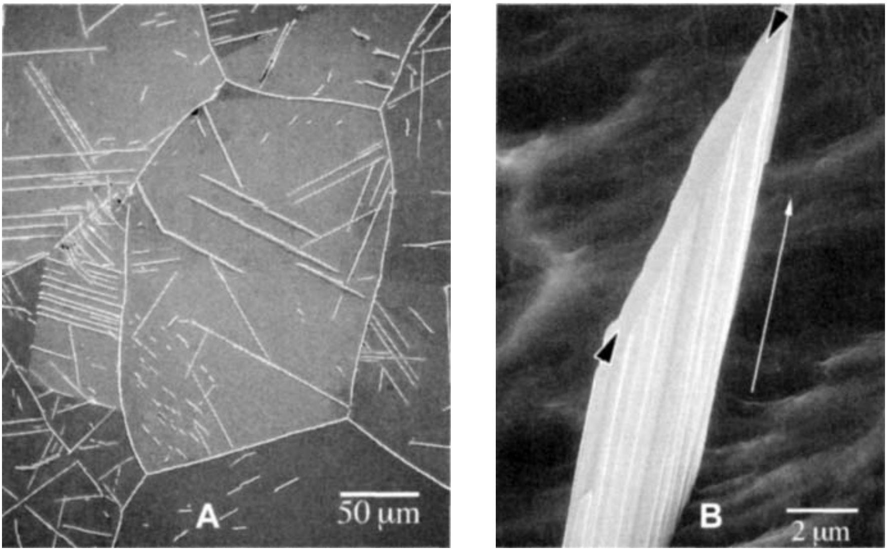

Figure 9-5-3:
Scanning electron micrographs of a Fe-1.34 C-13.1 Mn steel after different isothermal heat treatments.
A) Polished section of a specimen treated for 50 s at 650 °C then water quenched. Two morphologies of Widmanstätten cementite can be seen, corresponding to smooth plates and bundles of laths of apparently variable thickness ;
B) Specimen treated for 500 s at 750 °C then water quenched. Widmanstätten cementite lath with striations parallel to its longitudinal axis (white arrow), exposed by deep etching. The black arrows indicate the original polished surface.
Courtesy Naval Research Laboratory, Washington DC, USA (see also [Man99a]).

However, the properties of cementite are quite different to those of ferrite. Ferrite is soft and ductile, while cementite is stiff and relatively brittle (*cf.* typical hardness values in Appendix 22-8). These differences are reflected in the respective properties of hypo- and hyper-eutectoid steels.

High manganese steels have often been chosen in studies of pro-eutectoid cementite formation, due to the lower martensite start temperature which enables investigations over a wider temperature range. Moreover, cementite formation does not cause segregation, since the carbides have a high solubility for manganese. Two types of Widmanstätten structure are observed (Fig. 9-5-3 A), corresponding to smooth monolithic plates and lath bundles in the form of striated blocks (Fig. 9-5-3 B). On the atomic scale, good lattice matching is observed between the close-packed planes of the cementite and austenite, according to a Pitsch type relationship (*cf.* Table 10-1-4) for monoliths and a Farooque-Edmonds relationship for lath bundles [Man99a]. Coincidence occurs at arrays of terraces rather than on continuous planes.

10

The pearlite transformation

In the days before microscopy had become common practice, the iridescent appearance of the surfaces of certain steels under close observation led the structures concerned to be called pearlite.

10-1 The eutectoid transformation in the Fe-C system

Nucleation and growth of pearlite

A eutectoid reaction is very similar to a eutectic transformation, since one original phase gives rise to two new ones. However, while the parent phase is a liquid in a eutectic reaction, it is a solid in the case of a eutectoid. The eutectoid transformation in the Fe-C system is a typical example. Below the temperature of the invariant equilibrium (727 °C), austenite transforms to a mixture of ferrite and cementite ; $\gamma \rightarrow \alpha + Fe_3C$. The two reaction products form according to a cooperative process, with a characteristic structure called pearlite, consisting of alternate ferrite and cementite lamellae (Figure 10-1-1). The eutectoid reaction is therefore often referred to as the pearlite transformation. The term pearlite should not be applied to other constituents consisting of ferrite and cementite mixtures formed by other mechanisms (*e.g.* during tempering).

Pearlite nucleates only at grain boundaries, either austenite, or pro-eutectoid ferrite or cementite. When pearlite nucleates at an austenite grain boundary and the ferrite constituent forms first, the latter adopts a classical Kurdjumov-Sachs type orientation relationship with the parent phase (*cf.* Table 10-1-4). When the cementite constituent forms first, it also shows a preferred habit plane in contact with the austenite. In both cases, the pearlite colony grows into the austenite grain with which it has no special orientation relationship, the interface remaining macroscopically incoherent (Figure 10-1-2).

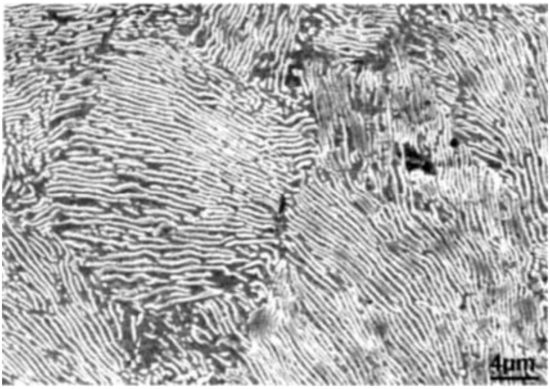

Figure 10-1-1:
Scanning electron micrograph showing the typical microstructure of pearlite, composed of alternate lamellae of ferrite and cementite, in an Fe-0.5C-0.7Mn steel. The individual cells or colonies are clearly visible due to their differences in orientation, in spite of the fact that they have formed in the same parent austenite grain. The interlamellar spacing is difficult to evaluate, since it depends on the angle of sectioning, and requires the statistical analysis of a large number of measurements.Courtesy IRSID, Arcelor Group, Maizières-les-Metz.

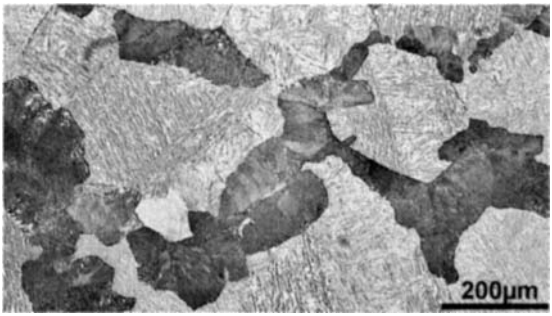

Figure 10-1-2:
Optical micrograph after nital etching of an Fe-0.55C-5.4Mn steel austenitised 20 minutes at 1 200 °C then annealed for 16 days at 625 °C. The pearlite colonies appear dark, the lighter areas being martensite formed during final cooling to room temperature.
Courtesy University of Virginia, USA (see [Hut01])

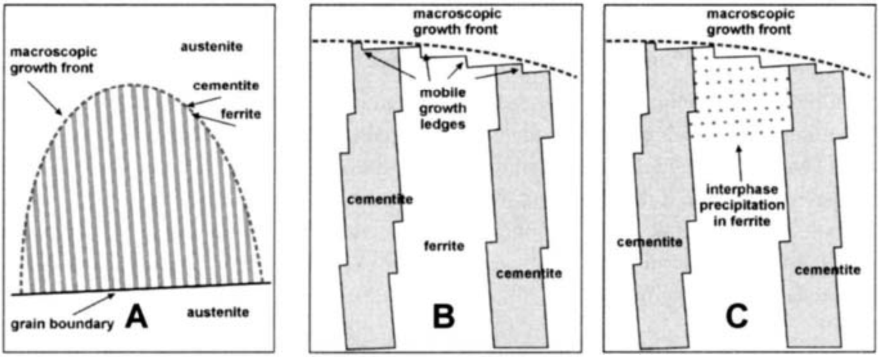
macroscopic growth front
austenite
cementite
ferrite
grain boundary
A
austenite
macroscopic growth front
mobile growth ledges
cementite
ferrite
cementite
B
macroscopic growth front
interphase precipitation in ferrite
cementite
cementite
C

Figure 10-1-3:
Schematic representation of pearlite growth.
A) Pearlite cell growing from a grain boundary.
B) Close-up of the growth interface showing mobile ledges.
C) Particle distribution in the case of interphase precipitation (VC carbides for example).

Pearlite forms by a discontinuous mechanism, starting at a grain boundary and growing outwards into a parent austenite grain in a macroscopically isotropic manner. Each nucleus gives rise to a cell or colony (Fig. 10-1-3 A). Within a cell, the individual ferrite and cementite lamellae are single crystals, with a well-defined orientation relationship, so that the colony as a whole could be considered as a sort of two-phased single crystal.

The preferred orientation relationships between ferrite and cementite in pearlite have been extensively studied, sometimes with conflicting results. Table 10-1-4 gives the three principal orientation relationships found for pearlite, together with those for pro-eutectoid cementite and austenite. No really convincing correlation has been established between the orientation relationships in pearlite and either the steel composition or the degree of undercooling. However, it is quite possible that the chosen orientation depends on the nature of the phase on which the cell embryo nucleated. Detailed observations have shown that nucleation on pro-eutectoid cementite produces pearlite with a Pitsch/Petch type orientation relationship [Man99b]. Consequently, pearlite cells with different orientation relationships can form within a same austenite grain, depending on the nature of the phase at the boundary nucleation site. Thus, in a hypereutectoid steel, the prior austenite boundaries are rarely completely covered with cementite, so that zones of γ/cementite interface co-exist with regions of γ/γ interface.

Table 10-1-4: Principal orientation relationships between cementite and austenite and between cementite and ferrite in pearlite. The habit planes are also indicated.

Type	Orientation relationship	Habit plane
Farooque/Edmonds Cementite/austenite	3° deviation from $[100]c//[112]\gamma$; $[010]c//[02\bar{1}]\gamma$; $[001]c//[\bar{5}12]\gamma$	
Pitsch/Petch Cementite/austenite	$(100)c//(5\bar{5}4)\gamma$; $(010)c//(110)\gamma$; $(001)c//(\bar{2}25)\gamma$	
Pitsch/Petch Pearlite	$(001)c//(\bar{5}2\bar{1})\alpha$; $(010)c$ 2-3° deviation from $[11\bar{3}]\alpha$ $(100)c$ 2-3° deviation from $[131]\alpha$	$(001)c//(\bar{2}\,\bar{1}5)\alpha$
Bararyatsk: Pearlite	$(100)c//(0\bar{1}1)\alpha$; $(010)c//(1\bar{1}\bar{1})\alpha$; $(001)c//(211)\alpha$	$(001)c//(11\bar{2})\alpha$
Isaichev: Pearlite	$[010]c//[111]\alpha$; $(101)c//(11\bar{2})\alpha$	$(101)c//(11\bar{2})\alpha$

Pearlite structure and interlamellar spacing

Depending on the alloy and heat treatment concerned, pearlite colonies can consist of regular parallel lamellae or fan-shaped bundles of lamellae with a certain degree of curvature. Detailed observations in the electron microscope provide a better understanding of the microstructural relationships on the atomic scale. The cementite/ferrite interface is thus seen to contain steps or ledges a few nanometers high, which accommodate variations in the direction or thickness of the lamellae, allowing macroscopic curvature (Figs. 10-1-3 B and C and 10-1-5). In the temperature range concerned, various growth modes are possible, and particularly the displacement of ledges (§ 9-3). Each phase thus grows by the lateral displacement of mobile ledges, while the overall transformation front

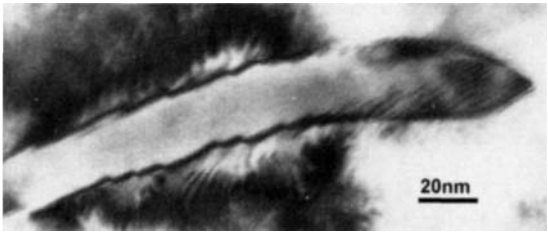

Figure 10-1-5:
Transmission electron micrograph of a thin foil showing a pearlitic cementite lamella in a XC50 steel treated at 550 °C.
Courtesy IRSID, Arcelor group, Maizières-les-Metz, Fr

advances perpendicular to ledge movement by accumulation of the terraces formed (Fig. 10-1-3 B). The growth mechanism takes into account the orientation relationships between the two crystal structures and the diffusivities of the elements involved. Growth of the two phases is synchronised and the relative rate of ledge displacement in each of them determines the interlamellar spacing, which is adapted by the formation of steps on the ferrite/cementite interfaces. The experimental observation of ledges (Fig. 10-1-5) provides proof for this mechanism and perhaps also the occurrence of interphase carbide precipitation in the ferrite (Fig. 10-1-3 C and § 13-2). The precipitates form preferentially on the wide faces of the immobile terraces rather than on the top edges of the mobile ledges [Hac87a], [Hac87b], [Zho91], [Zho92], [Fou95b].

Contrary to classical precipitate growth, the development of pearlite cells occurs by diffusion at the pearlite/austenite interface, the interlamellar spacing being continually adapted as a function of the degree of undercooling with respect to the equilibrium eutectoid decomposition temperature [Zac62]. The interlamellar spacing can vary widely, from a few microns to a few hundredths of a micron. Both models and experimental observations show that it depends on the difference between the effective transformation temperature T and the equilibrium eutectoid temperature T_E for the composition concerned. The spacing S is inversely proportional to the undercooling, which can sometimes attain several hundreds of °C. Indeed, pearlite can form at temperatures as low as 35°C in coarse-grained steels. The interlamellar spacing is given by :

$$S = \frac{\mathrm{A}}{(T_E - T)} \qquad (10\text{-}1\text{-}6)$$

where A is a constant determined by the thermodynamic parameters of the system.

Degeneration of pearlite

When pearlite is held at a sufficiently high temperature, the lamellar structure tends to evolve towards an energetically more favourable configuration, with a reduction in the interface/volume ratio. The cementite takes on a globular or spheroidal form in a continuous ferrite matrix, and the preferred orientation relationships are lost. So-called spheroidising treatments are often performed deliberately to achieve softening and improved ductility.

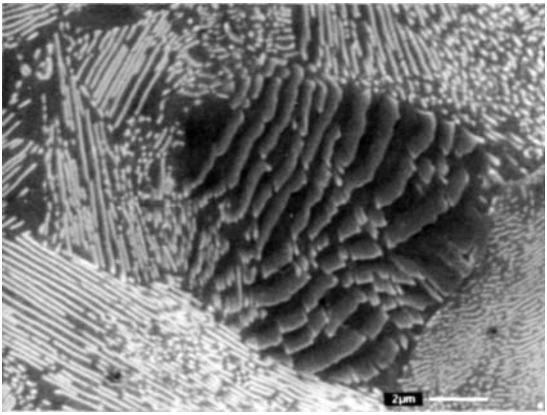

Figure 10-1-7:
Scanning electron micrograph of deeply etched pearlite in an Fe-0.5C-0.7Mn steel, showing a colony with a significantly larger intermetallic spacing that has grown from a triple grain boundary junction.
Courtesy INPG, Grenoble and IRSID, Arcelor Group.

Regions of coarser lamellae are sometimes observed between finer pearlite cells. Although this phenomenon is not rare, it is not always easy to detect, since a random section will cut most colonies obliquely, leading to an apparently irregular spacing (Figure 10-1-7). A possible mechanism for this local coarsening is discontinuous coalescence, whereby new coarser cells nucleate at grain boundaries, in zones already consisting of fine pearlite, and grow by diffusion at the new cell interface. The structure is completely reorganised, with an interlamellar spacing two to three times larger than in the pearlite it replaces. The interface energy released may possibly induce local heating, enhancing diffusion.

Divorced eutectoid transformation

When the cooling rate below the eutectoid temperature is sufficiently slow, the cementite is sometimes found to grow in a non-collaborative, "divorced", manner with respect to the ferrite [Ver98b]. The austenite with eutectoid composition transforms directly to a dispersion of ultra-fine spheroidal cementite particles in a fine-grained ferrite matrix. This type of reaction is called a divorced eutectoid transformation (DET) and leads directly to a spheroidised structure.

10-2 The kinetics of pearlite transformation

Cell growth

The pearlite transformation is an example of a discontinuous decomposition reaction, in which a cell consisting of the stable phases nucleates and grows at the expense of the untransformed supersaturated matrix phase (Figs. 10-1-2 and 10-1-3 A). For a given temperature, the transformation kinetics can be described by a classical Johnson-Mehl-Avrami type law :

$$y = 1 - exp(-\mathrm{k}t^{\mathrm{n}}) \qquad (10\text{-}2\text{-}1)$$

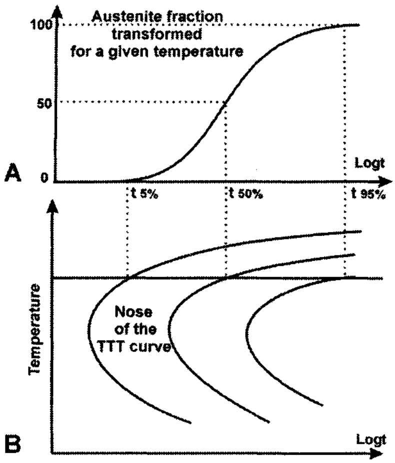

Figure 10-2-2:
A) Transformation kinetics according to relation 10-2-1 for a given temperature.
B) Times for 5 %, 50 % and 95 % transformation for different temperatures, plotted in the form of TTT curves.

where *y* is the fraction transformed in time *t* and k and n are system constants.

A plot of *y* against log(*t*) has a sigmoidal shape. The time to a constant degree of transformation can then be plotted as a function of temperature to produce TTT curves (Figure 10-2-2, *cf.* § 9-1). It is common practice to consider the time to the start of transformation (corresponding to $y = 1$ to 5 %), the time for 50 % transformation, and the time to the end of transformation ($y = 95$ to 99 %).

The TTT curves for the pearlite transformation have a typical "C" shape, with a nose corresponding to a maximum rate. This is caused by the conflicting effects of temperature on the activation energy and activation frequency for nucleation. At temperatures above the nose, the degree of supercooling, and hence the driving force for nucleation, decreases. The critical sizes that embryos must attain to remain stable are therefore greater, leading to fewer viable nuclei and longer incubation times, in spite of faster diffusion. Below the nose, the critical embryo sizes are smaller, with a greater probability of being attained. A larger number of viable nuclei are therefore formed, but after longer incubation times, since slower diffusion reduces the activation frequency.

10-3 The influence of alloying elements

Phenomenological aspects - modification of TTT curves

The large number of TTT curves available in the literature, covering the majority of commercial steels, show that the kinetics of the pearlite transformation are highly sensitive to alloy composition. Three typical examples are shown in Figure 10-3-1. The fraction transformed is plotted on temperature/log time coordinates. The initial austenite grain size is indicated, since it has an important bearing on the number of available nucleation sites, pearlite colonies forming almost exclusively from grain boundaries. The steels chosen have similar carbon contents and relatively small differences in the levels of alloying additions. Their TTT curves are nevertheless markedly different. The TTT curve for the C35E4 steel has a general C shape, but the nose occurs at such short times that it is impossible to accurately measure the transformation kinetics, and the pearlite and bainite reactions cannot be distinguished. The same is true for the 37Cr4 grade, although the curve is shifted to longer times, due to the presence of 0.9 % Cr (for a nominal content of 1 %). In the case of the 36NiCrMo16 alloy, the pearlite and bainite domains form two distinct C curves, and the transformations are much slower, the pearlite nose in particular being shifted to significantly longer times, due to the presence of a higher chromium content, together with nickel and molybdenum additions.

In fact, except for cobalt, all alloying additions to steel, including carbon, modify the TTT curves. *They retard nucleation, slow growth and modify the phase equilibria.* Some elements, such as manganese, silicon, sulphur, phosphorus and aluminium, are almost always present in steels in small amounts, as a consequence of the raw materials and refining processes employed, and their effects at the levels concerned are generally considered to be negligible to a first approximation. Larger additions of ferrite-stabilising elements, such as chromium and silicon, limit the range of stability of the austenite field, while austenite-stabilising elements, including nickel and manganese, extend it. Consequently, the eutectoid transformation temperature A1 is raised by ferrite stabilisers and lowered by austenite stabilisers (see § 4-4 and 14-3).

Retardation of nucleation

All alloying additions except cobalt are found to increase the incubation time for pearlite nucleation, shifting the TTT curves to the right. The mechanisms involved are complex. Like in most nucleation phenomena, diffusion plays a significant role [Rus90]. Furthermore, it is well known that a coarse grain size also retards nucleation, for which defect-rich grain boundaries represent preferred sites, as well as offering easy diffusion paths.

Pearlite often nucleates initially as a divorced eutectoid, an embryo of either ferrite or cementite forming individually and then acting as a site for the other. In this case, any inhibition of the first phase to form will retard transformation. Alloying elements that segregate to grain boundaries can change the chemical driving force for nucleation. This mechanism has been proposed to explain the influence of nickel, but perhaps the most pronounced effect is that of boron, which is known to strongly segregate to grain boundaries and markedly retards the nucleation of ferrite [Sak84].

> *A great deal of attention was focussed on boron in the 1960s. This element strongly inhibits the pearlite transformation, facilitating the formation of martensite. Only very small amounts are required, since the ratio between the grain boundary concentration and that in the bulk can be extremely high, increasing with decrease in temperature, due to equilibrium segregation. However, boron tends to combine with other elements to form phases such as carbo-borides and boro-nitrides (e.g.*

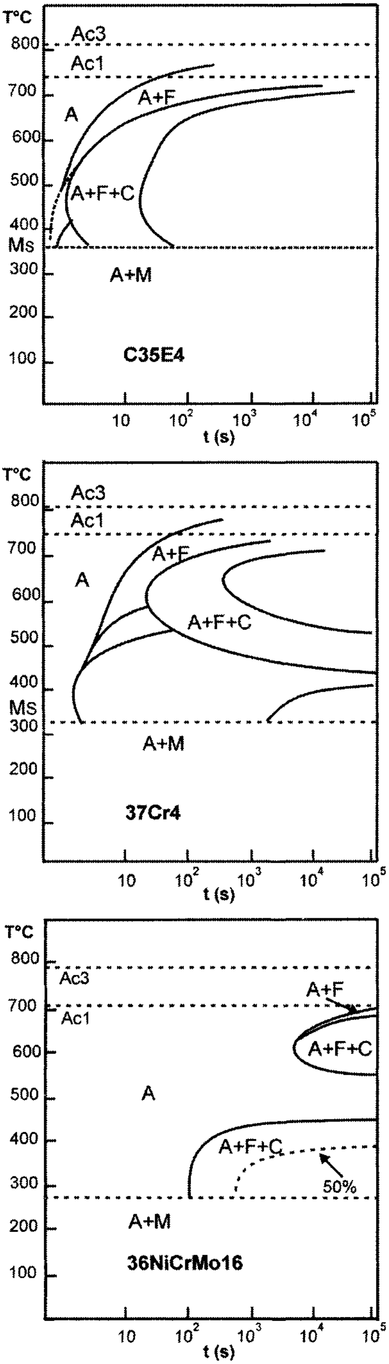

Figure 10-3-1:

TTT diagrams for three steels with similar carbon contents, C35E4 (1.1035), 37Cr4 (1.5135) and 36NiCrMo16 (1.6773). The compositions in weight % are given in the table below, the elements considered responsible for the differences in the diagrams being indicated in italic underlined font. The other elements and impurities not given are present in small amounts typical of these types of steel (*e.g.* -0.6% Mn, -0.3% Si).

	C	Ni	Cr	Mo
C35E4	0.36	0.02	0.21	0.02
37Cr4	0.38	0.023	*0.90*	0.04
36NiCrMo16	0.36	*3.70*	*1.66*	*0.23*

The prior austenite grain sizes are fairly similar (10-12 ASTM). The steels were austenitised for 30 minutes at 850°C. This temperature was chosen to be above both the Ac1 and Ac3 points (dotted lines), corresponding respectively to the pearlite → austenite transformation and the austenite solvus on heating.

The specimens were rapidly cooled to different temperatures for isothermal holding periods during which the structural transformations were monitored. The curves for the start and end of the transformations are shown by solid lines.

The phases present are labelled;

A for austenite,

F for ferrite,

C for cementite and

M for martensite.

F + C can represent both pearlite and bainite (the two regions are clearly distinguished in the case of 36NiCrMo16).

Taken from the IRSID Atlas of TTT diagrams, [Atlas].

> *CrBN), which can sometimes cause embrittlement. When boron is used for this purpose, care must therefore be taken to avoid its harmful effects, for example, by adding small amounts of titanium to tie up nitrogen and carbon in the form of insoluble titanium carbo-nitride.*

In general, strong carbide forming elements (*e.g.* Cr, Mo, W, V, Ti, Nb) are known to selectively retard the formation of pearlite.

Retardation of growth

The effect of alloying elements on TTT curves was established in the first half of the 20th century, when an extensive atlas of diagrams was compiled for steel optimisation purposes. This was followed by the study of transformation mechanisms throughout the second half of the century and the subject remains highly topical to this day, due to progress in the modelling of complex diffusion-based phenomena. The fundamental references include [Zen46], [Cah62], [Hil71], [Hon76], [Hil81], [Hil98], while studies of the interface behaviour were performed by [Raz76], [Fri77], [Tew85], [Lac99b].

During growth of a pearlite colony, the diffusive exchanges occur mainly along the α/γ interface, which is considered to be incoherent and therefore an effective short circuit path. Since carbon diffuses extremely rapidly, thermodynamic equilibrium at the growth interface is established easily for straight Fe-C alloys, where the rate is controlled essentially by carbon diffusion. However, the exchange of substitutional elements, whose diffusion rates are several orders of magnitude slower than for carbon, will be much more difficult, even across the boundary. It must then be considered that local equilibria are established on the atomic scale, over the several tens of atomic layers representing the thickness of each lamella. These equilibria occur between austenite and ferrite and austenite and cementite respectively, the chemical potential (activity) of carbon being identical throughout the interface. Depending on the assumptions made, various types of equilibria have been defined (see § 9-4) and have now become the general reference [Hil98]. The different types of equilibrium below are encountered in the order of decreasing temperature. Variations in solute diffusivity affect the growth modes adopted.
Total thermodynamic equilibrium requires long range diffusion of all elements, which is only possible at the highest temperatures. However, the necessary conditions are never achieved in industrial practice.

The *local equilibrium (LE) mode* gives rise to "ortho-pearlite", with two morphologies depending on the conditions :

- Local equilibrium is achieved at the interface for both carbon and substitutional solute atoms. Furthermore, global equilibrium is attained for carbon, whose chemical potential is identical everywhere, even over long distances. It has been shown that these conditions promote decelerating growth and increasing interlamellar spacings during isothermal transformation. The conditions required correspond to a low supersaturation and a slow growth rate. The pearlite formed is divergent (Fig. 10-3-2), [Hut01].
- Local equilibrium with respect to carbon and substitutional solute elements is

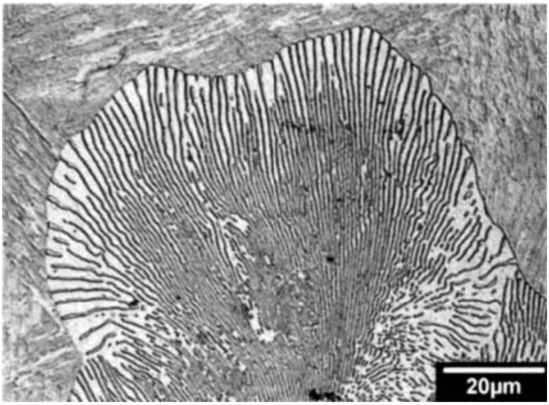

Figure 10-3-2:
Optical micrograph after nital etching of an Fe-0.55C-5.4Mn steel austenitised for 20 min at 1200 °C then annealed for 16 days at 625 °C. The darker matrix surrounding the pearlite colonies is martensite. Courtesy University of Virginia, USA (see [Hut01]).

established only at the interface (NPLE mode). There is no longer a long range flux of substitutional solute and the interlamellar spacing remains constant. The pearlite is said to be constant (Fig. 10-1-1).

At sufficiently low temperatures, either the *para-equilibrium (PE) mode* is established, in which only carbon diffuses at the interface, or else *an intermediate mode of the NPLE type*, with local equilibrium with respect to carbon and partial partitioning of substitutional solutes, without attaining equilibrium (*cf.* § 9-4). In these conditions, the compositions of the ferrite and cementite constituents of the pearlite do not comply with phase equilibria. For example, the cementite may be too rich in nickel and copper or too poor in chromium. The return to equilibrium is established by diffusion between the lamellae behind the transformation front, and may give rise to the rejection of a particular alloying element, as illustrated by the observation of copper precipitates at the γ/cementite interface [Kha93].

The behaviour of alloying elements

Each alloying element has a behaviour which differs according to its diffusivity and its tendency to partition preferentially to either the ferrite or the cementite. Thus, silicon is readily soluble in ferrite and diffuses rapidly, but has negligible or extremely low solubility in cementite. Consequently, the diffusion of silicon is often the controlling process for the pearlite transformation in steels. Silicon thus has a significant retarding effect, even when present in the steel only in trace amounts [Ind97], [Ind02]. Indeed, it appears to be the presence of silicon rather than its concentration that is important. For example, pearlite forms in a similar manner in steels containing 0.4–0.7 % Si and in grey cast irons with from 2 to 3.4 % Si [Lac99b].

The effect of small quantities of other elements is less marked, particularly when they can dissolve in both the ferrite and cementite, as is the case for manganese, chromium and cobalt. In Fe-C-Ni alloys, nickel shows quite different behaviour. It shows no tendency for preferential partitioning between the austenite and either the ferrite or the cementite and pearlite growth is possible only in the para-equilibrium (PE) mode. This is probably due to the combination of very low solubility in cementite and low diffusivity in ferrite.

The assumptions concerning local diffusion behaviour are based on both experimental observations and modelling. The transition between the LE and PE modes is sharp and occurs at a temperature determined by the alloy composition, depending on the diffusivities of the elements present [Tew85].

Formation of other pearlite-type structures

Many eutectoid reactions are described as being pearlitic in nature. In particular, they occur in steels containing strong carbide-forming elements, where carbides other than cementite can form. For example, in chromium-containing steels, two other lamellar eutectoid reactions of the type $\gamma \rightarrow \alpha$ + carbide can be observed in the same range of temperature as for classical pearlite, corresponding to :
$\gamma \rightarrow \alpha + M_{23}C_6$ (10–12 %Cr steels) et $\gamma \rightarrow \alpha + M_7C_3$ (5 %Cr steels) [Kay98].
Compared to straight Fe-C alloys, the pearlite structure can be somewhat finer for a given transformation temperature, if the undercooling with respect to the equilibrium temperature is greater. However, this effect is limited and has no significant consequences on the mechanical properties.

In steels rich in tungsten or molybdenum, delta ferrite undergoes a high temperature eutectoid decomposition, at around 800–1 100°C [Kuo54], [Kuo55], [Fri77], forming what is sometimes called *δ pearlite* : $\delta \rightarrow \gamma + M_6C$

Figure 10-3-3 shows the example of a tungsten-rich tool steel, where δ pearlite has formed during continuous cooling in a bar solidified unidirectionally in a controlled temperature gradient. The transformation has been frozen by quenching. The core of the dendrite formed at the beginning of solidification is composed of δ ferrite surrounded by austenite. The δ/γ nterface is revealed in the micrograph by a necklace of precipitates, corresponding to a marking phenomenon similar to the cases described in § 6-5 for the peritectic transformation. The δ pearlite transformation has started from this interface and has

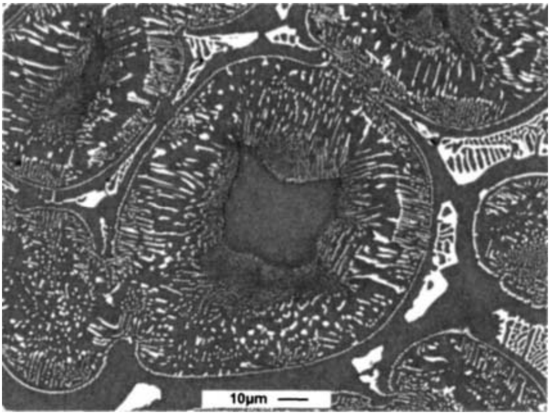

Figure 10-3-3:
Scanning electron micrograph of a type T tool steel (Fe-0.52C-3.8Cr-0.5Mo-1V-18.8W) quenched during unidirectional solidification. The coarse, fish-bone shaped interdendritic particles are eutectic M_6C carbides.
Courtesy INPG, Grenoble

grown inwards towards the centres of the dendrite arms. The temperature range between the start of the transformation and the moment of quenching is several hundred degrees. The interlamellar spacing thus changes to compensate for variations in diffusion behaviour, related both to the temperature and probably also to segregation effects.

Pearlite-type morphologies can also be formed by discontinuous (cellular) precipitation reactions, which do not correspond to eutectoid decomposition phenomena. In steels, in the temperature range corresponding to the austenite phase field, numerous precipitation processes lead to a two phase cellular reaction product. Typical examples include the precipitation of $M_{23}C_6$, σ phase (Fig. 19-7-4), Cr_2N ([Van95], [Kik90]), and Ni_3Ti (Fig. 20-3-4).

10-4 The re-dissolution of pearlite

Austenitising

In general, the transformation of pearlite, bainite and martensite to austenite on heating occurs relatively quickly. For most steels, the duration of austenitising treatments is typically about 30 minutes, which is quite sufficient for complete re-dissolution at temperatures above 800 °C. However, although the dissolution of pearlite is not a problem, care must be taken to ensure homogenisation of the austenite, which may prove difficult due to segregation resulting from initial solidification, or the presence of coarse eutectic phases or proeutectoid carbides.

In plain carbon steels, austenite nucleates almost instantaneously, but longer incubation times are often observed in the presence of alloying additions. The growth stage is governed by diffusion and can be retarded by slowly diffusing solute elements [Sht99b]. Because the temperature range is higher than for the formation of pearlite on cooling, diffusion is much more active, and can occur at grain boundaries, at phase interfaces and in the bulk. The difference between grain boundary and bulk diffusion rates is smaller than at lower temperatures, but remains significant, since the temperatures concerned are still well below the melting point. Two cases must be considered, depending on the pearlite morphology.

Spheroidised pearlite

Detailed analysis reveals that the austenite formation mechanism is quite complex and involves a sequence of steps that are described schematically in Figure 10-4-1, based on the behaviour observed during the continuous rapid heating of a eutectoid steel [Kal98]. The first austenite to form is usually located at prior austenite grain boundaries or at the original pearlite cell boundaries, in epitaxy with the ferrite in one of the neighbouring grains. The solubility of carbon in austenite is higher than in ferrite and its activity is maintained by dissolution of cementite and diffusion along the grain boundary. The first stage of austenite growth occurs in the temperature range from about 740 to 780 °C, with the formation of Widmanstätten type laths (Figure 10-4-2), by a mechanism involving the

Figure 10-4-1:
Initial stages of austenite formation during the rapid continuous heating of a spheroidised eutectoid steel.
A) Carbon diffuses mainly at grain boundaries.
B) Nucleation and growth of austenite laths.
C) Coalescence of laths behind the growth front.
D) At higher temperatures (or longer holding times), growth of an austenite grain by interface and grain boundary diffusion, fed by the dissolution of the cementite particles.
Adapted from [Kal98].

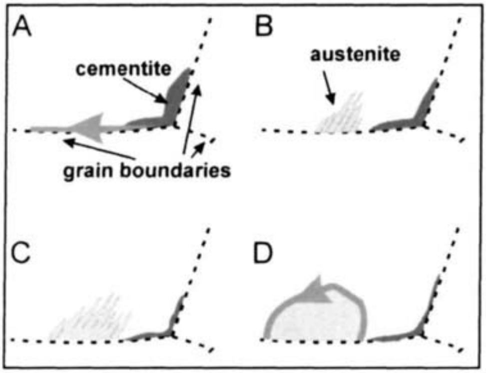

lateral extension of terraces. The laths appear to develop in groups by a coordinated process, leading to the formation of bundles. The morphology resembles that of bainite, but it is preferred to use the name Widmanstätten austenite and to reserve the term bainite for the eutectoid transformation product (*cf.* Hillert [Hil00]). Because of the relatively high temperature, laths of similar orientation coalesce rapidly behind the growth front. At still higher temperatures, the austenite nucleus can grow isotropically out from the boundary, with a morphology of the GBA type (grain boundary allotriomorph), particularly since the oriented growth of laths is impeded by remaining cementite particles, while intergranular carbide particles dissolve more rapidly.

Lamellar pearlite

The dissolution of lamellar pearlite on heating has been studied by Shtansky *et al.* [Sht99b]. In plain carbon steels, austenite nucleates principally at the pearlite cell boundaries and also at interfaces between ferrite and cementite lamellae. Nucleation is practically instantaneous and growth is rapid, since it is controlled only by the diffusion of carbon. The austenite grows inside ferrite lamellae and at the same time the adjoining cementite platelets thin by lateral dissolution at ledges and terraces. Carbide particles can be pinched off and become temporarily isolated behind the transformation front. The presence of alloying elements can retard the transformation and become the rate controlling factor, since austenite growth no longer involves only carbon redistribution, but also that of the solute element (chromium in the case considered). However, the lack of experimental evidence concerning the detailed mechanism makes it necessary to base models essentially on the different diffusivities of the various alloying elements.

Dissolution of alloy carbides

The inhibiting effect of chromium on dissolution is more marked at high chromium contents, of around 10 %, where the pearlite is composed of ferrite and a chromium-rich $(Fe,Cr)_7C_3$ carbide. The first stage of dissolution is always the expulsion of carbon, and carbon-depleted zones are seen in the immediate vicinity of the carbides [Sht99a]. Apart

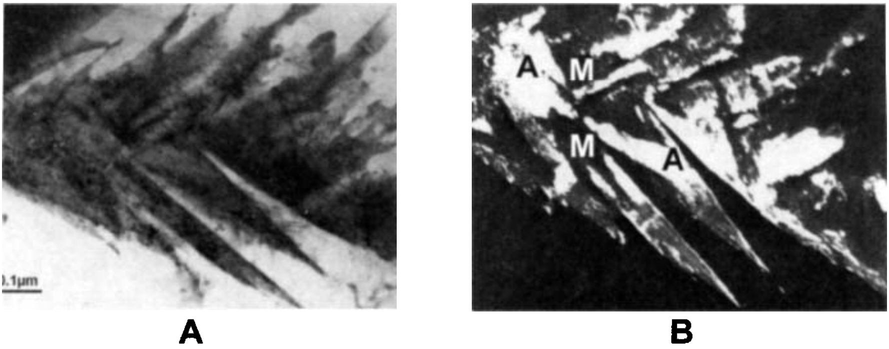

Figure 10-4-2:
Transmission electron micrograph of an Fe-0.68C-0.67Mn-0.24Si steel, spheroidised then heated at 1200 °C/s to 785 °C and finally quenched. Austenite laths have formed on both sides of a ferrite grain boundary.
A) Bright field image in which the laths appear dark.
B) Dark field image using a (220)γ reflection. The austenite laths show two different contrasts, the darker ones having transformed to martensite on quenching. The lighter untransformed laths are presumably richer in carbon, with a lower Ms temperature. They are situated closer to the boundary, which is the source of carbon.Courtesy University of Lille (see also [Kal98]).

from carbon, the composition in these regions is the same as in the carbide, so that they transform to the corresponding equilibrium phase, in this case to chromium-rich ferrite. Subsequent conversion to austenite requires significant outward diffusion of chromium.

Some strong carbide-forming elements can lead to a more complex situation, where transient phases having preferred epitaxial relationships with the matrix can form during the dissolution process. Thus, in the case of certain $M_{23}C_6$ carbides, decomposition during heating leads to local regions of chromium-rich ferrite, together with M_6C carbides. The process is discontinuous and leads to the formation of a fibrous two-phase structure that grows into the austenite : $M_{23}C_6 \rightarrow M_6C + \alpha$. The ferrite subsequently transforms to austenite [Sht97]. Diffusion of the metallic elements present in the carbides is thus the essential parameter in dissolution. A micrograph showing the dissolution of carbides can be seen in Figure 6-3-10.

11

The martensite transformation

Martensite is named after the German metallographer Adolph Martens who, in about 1890, was the first to describe its structure and formation.

11-1 Displacive transformations in the Fe-C system

In Fe-C alloys, the stable phase at high temperatures is austenite, with a face-centred cubic crystal structure in which the carbon atoms occupy interstitial sites. When cooled at a sufficiently slow rate, the austenite transforms to the phases in equilibrium at low temperatures, namely body-centred cubic ferrite and graphite. However, practical slow cooling rates lead to a metastable structure consisting of ferrite and cementite. In both cases, the reaction involves diffusion of carbon, which has a low solubility in ferrite. If, on the contrary, cooling is performed at an extremely ***high speed***, the resulting structure consists of martensite, ***a single thermodynamically metastable phase***. The martensite has the same composition, and therefore the same carbon content, as the original austenite. The transformation occurs by a so-called "military" mechanism, whereby the atoms move in a cooperative manner, like soldiers on parade, to convert the crystal structure, the displacement involved being less than the interatomic spacing. By analogy, transformations involving diffusion are sometimes termed "civil".

> *As regards terminology, Christian [Chr65] wrote "(the term MILITARY)... conveys an immediate picture of the basic postulate of the theory of martensite; and it is used here as a convenient sustained metaphor." Honeycombe and Bhadeshia [Hon95] state that "there are a number of transformations which possess the geometric and crystallographic features of martensitic transformations, but which involve the diffusion of interstitial atoms. Consequently, the broader term of SHEAR transformation is perhaps best used to describe the whole range of possible transformations." Bhadeshia [Bha92] summarises the transformations in steels as either "DISPLACIVE (Invariant-plane strain shape deformation with large shear component)" or "RECONSTRUCTIVE (Diffusion of all atoms during nucleation and growth)."*

Martensite can be considered as ferrite that is supersaturated in carbon. The carbon atoms occupy interstitial lattice sites situated on the [001]α axes. The fact that only one of the three possible sets of sites is occupied selectively leads to a tetragonal distortion of the body-centred cubic lattice. The question arises as to whether the selective occupation and resulting tetragonality is caused by the military transformation itself or by subsequent ordering of the carbon atoms. Considering the relatively high mobility of carbon atoms at ambient temperature, subsequent ordering seems the most plausible explanation [Kur72].

For binary Fe-C (and also Fe-N) alloys, the as-quenched structure is body-centred tetragonal, with lattice parameters a and c which vary linearly with carbon (nitrogen) content :

$$c = 0.28664 - 0.00027X_C \text{ et } a = 0.28664 + 0.00243X_C \text{ nm} \tag{11-1-1}$$

$$c = 0.28664 - 0.00017X_N \text{ et } a = 0.28664 + 0.00242X_N \text{ nm} \tag{11-1-2}$$

where X_C and X_N are the concentrations of carbon and nitrogen respectively, expressed as atomic percentages [Che90a], [Che91]. *The tetragonality thus increases with carbon and nitrogen content*, and is accompanied by an increase in the hardness of the martensite.

Bain's 1924 model and crystallographic aspects

Bain proposed a mechanism for the transformation, based on the experimentally determined lattice parameters of the austenite and martensite [Pax72]. The model assumes a homogeneous deformation, the Bain strain, involving a 12 % expansion along two of the crystal axes and a contraction of 20 % along the third. Growth should occur in the plane of minimum strain.

Bain's model is not fully satisfactory, since it does not predict an invariant plane, whose existence, associated with surface relief effects, is revealed by experimental observations. Furthermore, the change in structure must comply with interfacial relationships between the martensite and the parent austenite. This requires additional strains, which are achieved by slip, twinning and stacking faults, producing an invariant habit plane where the mean deformation is zero [Por92].

In the majority of ferrous alloys, the martensite/austenite interface is semi-coherent. Slight lattice mismatch must be relaxed periodically. In the most commonly encountered configurations, the orientation relationships are such that both the close-packed planes and close-packed directions are parallel in the two phases. This is the case for the Kurdjumov-Sachs (K-S) relationship reported in Table 11-1-3. Other more complex relationships are fairly close. In particular, the Nishiyama (N) relationship can be derived from the K-S configuration by a 5°15' rotation about the [101] axis. Variations in alloy chemistry modify the lattice parameters and can therefore change the orientation relationships. K-S type behaviour is observed in steels with low to medium carbon contents. The situation is much more complex in alloy steels, where the interface planes have high Miller indices. This is also true for the habit plane, defined as the average plane of a martensite plate (Table 11-1-3).

Table 11-1-3: Orientation relationships between martensite and austenite in steels.

	Orientation relationship	Habit plane
Kurdjumov and Sachs (K.S.)	$(111)A//(011)M$, $[0\bar{1}\bar{1}]A//[1\bar{1}\bar{1}]M$	Close to {111}
Nishiyama (N)	$(111)A//(101)M$; $[1\bar{2}1]A//[10\bar{1}]M$	Close to {225}
Greninger and Troiano	$(111)A//(011)M$; $[\bar{5},\overline{12},17]A//[7,\overline{17},17]M$	Close to {259}

11-2 Characteristics of the martensite transformation

Thermodynamic aspects of the martensite transformation

Since there is no change in composition, the transformation can be considered as a phase change in a single component system. Martensite can form at and below a temperature *Te* corresponding to a metastable equilibrium. However, at *Te*, the change in free energy that provides the driving force is not sufficient to create an interface and induce the necessary elastic and even plastic strain in the austenite. The reaction therefore begins at a temperature Ms (martensite start) significantly lower than *Te*. Similarly, during reheating, the austenite start temperature As at which the martensite begins to revert to austenite is higher than *Te*. The martensite transformation is not reversible in the thermodynamic sense, since it is not an equilibrium phase. However, it can be reversible crystallographically. Thus, when the change in volume is small, the reverse transformation on heating can occur by shear in the opposite direction. However, in steels, martensite formation involves plastic strain that is too large to be eliminated reversibly.

> *Some alloys, for example in the Fe-Ni system, are known to undergo a reversible martensitic transformation that is accompanied by the so-called "shape-memory" effect. In this case, the free energy change is small and is insufficient to induce plastic strain. Growth of the martensite plates therefore stops before the yield strength of the austenite has been attained. The martensite is said to be in thermo-elastic equilibrium. When the temperature is lowered, the platelets start to grow again, but shrink if the temperature is raised, leading to spectacular shape-change effects relatively close to ambient temperature.*

Martensite nucleation

The overall kinetics of martensite transformation are theoretically determined by both the nucleation and growth stages, but in fact, the transformation is so rapid that they are difficult to distinguish. It can therefore be assumed that the activation energy for growth is negligible and that the kinetics are entirely controlled by nucleation. Nucleation is considered to be the formation of an *embryo* that can become stable under certain conditions. The application of classical nucleation models to martensite predicts excessively large dimensions for an embryo to be stable. It must therefore be assumed that other factors facilitate nucleation, such as thick layers of stacking faults, lattice defect combinations, or the pre-existence of preferred sites in the austenite. Since the number of such defects is probably limited, various processes are envisaged, all based on the fact that martensite formation is accompanied by an increase in volume and induces severe elastic and plastic strain in the austenite. Detailed treatments of various mechanisms, such as sympathetic nucleation [Bha92] and autocatalytic nucleation [Ols81], together with an analysis of the driving forces [Gho94], can be found in the literature.

For heterogeneous nucleation to be possible, it appears that the embryo must initially be a flat platelet that is either semi-coherent with the austenite matrix, or fully coherent, as in the case of GP zones in aluminium alloys. The lowest interface energy corresponds to a twinned ellipsoid. The free energy of nucleation ΔG_N is provided by the difference in bulk chemical free energy between the austenite and martensite, and must be sufficient to create the interface and overcome dynamic friction effects as well as the strain due to the increase in volume. It could possibly be assisted by the elimination of dislocations and defects already present in the austenite before transformation. In the model developed by Ghosh [Gho94], the critical driving force is considered to involve a strain energy contribution, a defect-size dependent interfacial energy term and a composition-dependent interfacial work term.

Effect of stresses and magnetic fields

The presence of stresses generally facilitates transformation, so that a smaller amount of undercooling is required for nucleation. In practice, this has led to the definition of a temperature Md, which is the Ms temperature for a given stress or degree of cold work. It is higher than Ms and therefore closer to Te. The origin of the stress field can be a static or dynamic load, isostatic pressure [Kak99], a chemical transformation (*e.g.* surface treatments) or surface impacts (*e.g.* peening) (see Figures 11-3-4 B and 21-5-3).

The application of a magnetic field can also raise the Ms temperature. This has been observed in Fe-Ni-C steels in which the martensite has a lenticular or plate morphology. The effect is anisotropic, since the first plates to form tend to adopt a preferred orientation with respect to the magnetic field [Kak99].

Epsilon martensite in alloy steels

Because of their large concentrations in alloying elements, austenitic stainless steels have a very low Ms temperature and therefore do not generally form martensite. However, martensite can sometimes be obtained by prolonged holding at very low temperatures, below Ms. The process can be aided by plastic strain. The martensite formed below Md can be different, with a close-packed hexagonal structure, a form called epsilon martensite (ε) (see [Bla73], [Pec77], [Bro79], [Osh76], [Lac93]). Thus, both bcc α' and cph ε martensites can be formed. Several mechanisms are possible. In particular, epsilon martensite may represent an intermediate step in the formation of α' martensite : $\gamma \rightarrow \varepsilon \rightarrow \alpha'$.

In Cr-Ni austenitic stainless steels with about 18 % Cr and low interstitial contents (<0.1 %), nickel modifies both the spacing of the close-packed planes and the stacking fault energy in the austenite. Stacking faults represent local regions of cph structure. The

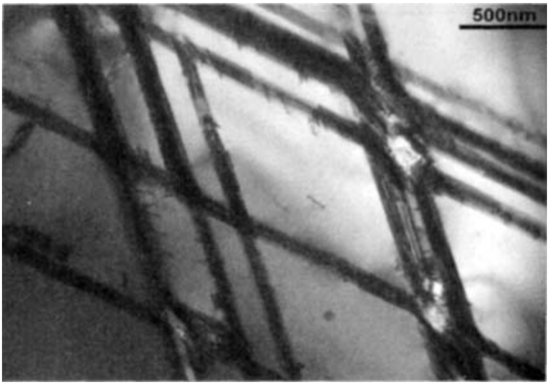

Figure 11-2-1:
Transmission electron micrograph of a type 304L stainless steel deformed 10 % at 77 K, showing the formation of both ε martensite (long thin plates in dark contrast) and α' martensite (small light zones at the intersections of dark plates).
Courtesy Hamilton University, Canada (see also [Ver01]).

important parameter with regard to ε martensite is the c lattice parameter of the cph phase. The lower c compared to its theoretical value of 0.415 nm, the greater the tendency for ε martensite to act as an intermediate step in the formation of α' martensite (c can fall to a minimum of 0.408 nm). The spacing of the close-packed planes in the ε phase is then close to that of the closest-packed planes in α' martensite, and the ε → α' transformation can take place without the creation of new dislocations.

In the case of a type 304 stainless steel deformed at 77 K (Fig. 11-2-1), ε martensite forms from superimposed stacking faults and twins in the austenite. The intersection of two slip systems causes the formation of α' martensite. The α' martensite induced in this way by plastic strain does not have the same orientation relationships with austenite as thermal martensite produced by quenching.

Influence of alloying elements

The temperature at which the martensite transformation starts is designated Ms, while that at which it finishes is called Mf. Contrary to the pearlite transformation, these temperatures are generally independent of the cooling rate, so that the beginning and end of transformation are represented by horizontal straight lines in CCT diagrams. The difference between Ms and Mf is or the order of 200 °C, some authors suggesting a value of 215 °C (*cf.* Appendix 22-6). When quenching is interrupted between Ms and Mf, the transformation is incomplete and a certain amount of austenite is retained. The proportion of martensite increases in a non-linear manner with the degree of cooling below Ms. However, the transformation is not always complete on reaching Mf, due to high stresses induced by the associated volume expansion of up to 5 %. A small amount of retained austenite can therefore remain even below Mf.

Interstitial alloying elements, such as carbon and nitrogen, strongly suppress Ms. In practice, it is therefore not possible to obtain complete transformation at ambient temperature for steels containing more than about 0.7 % C (Figure 11-2-2). Except for aluminium and cobalt, all substitutional solute elements lower Ms to a certain extent. Numerous empirical

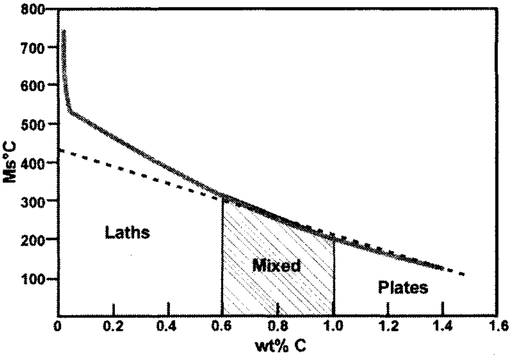

Figure 11-2-2:
Influence of carbon content on the Ms temperature in plain carbon steels (the Mf temperature is about 200 °C lower). The schematic curve in grey is the result of a compilation by Marder and Krauss, while the dashed line is that due to Mirzayev *et al.* (cited in [Zha95]).

formulae expressing Ms as a function of alloy chemistry have been developed since the 1940s [Kra80].

Each is valid for homogeneous austenite with a particular range of composition (*cf.* Appendix 22-6). Corrections must be made for elements tied up in other stable phases (*e.g.* nitrogen in nitrides), taking into account only the part dissolved in the austenite. A recent relation has been established based on a vast compilation of data, including all the iron binary systems concerned [Zha92]. It is the only one which distinguishes between the types of product formed, either lath martensite (LM) or twinned martensite (TM). However, the contributions of a number of elements often present in steels (V, W, Ti, Si and Al) are omitted.

Attempts have been made to predict martensite transformation behaviour using models based on the metastable thermodynamic equilibrium temperature *Te* and the sum of the strain and interface friction contributions to the energy balance. *Te* can be calculated using data banks such as Thermocalc. The prediction determines the degree of undercooling with respect to Te necessary to overcome obstacles to nucleation and growth. The error is estimated to be less than 40 °C. Although this approach appears promising, it is currently limited by the lack of accurate thermodynamic data concerning alloyed martensites [Gho94].

Although the hardness of martensite increases linearly with its carbon content, a maximum value is attained for the steel as a whole, due to the effect on Ms, since above a certain carbon level, transformation is no longer complete, and the volume fraction of retained austenite increases.

The martensite transformation is anisothermal. Below Ms, the temperature must be lowered further for transformation to continue. It stops when the temperature is held constant. However, when cooling is resumed after isothermal holding, the transformation does not restart immediately, due to a so-called "thermal stabilisation" phenomenon.

Furthermore, the martensite transformation in plain carbon steels is not thermally activated, and is said to be athermal. This is not quite true for alloy steels, such as Fe-Ni-Mn and Fe-Ni-Cr materials, where only the growth stage is athermal, nucleation being thermally activated.

Growth is extremely rapid, the extension velocity of certain individual martensite plates having been evaluated to be around 105 cm/s, while the speed of propagation of the overall transformation front has been estimated to be about a third of that for elastic waves, corresponding to 1015 cm/s. There is insufficient time for thermal activation and the transformation occurs without diffusion. Indeed, the transformation velocity is so high that it was long considered that nothing could inhibit it. However, recent work has revealed that the transformation can be prevented by ultra-rapid quenching, with a critical cooling rate for a given steel [Zha95].

11-3 The morphology of martensite

Lath martensite

Lath martensite is observed in plain carbon and low alloyed hypoeutectoid steels. Groups of roughly parallel laths (sheaves, bundles or blocks) are generally visible in the optical microscope. The laths are long and narrow, with a typical width of the order of 0.5 μm (Figure 11-3-1). The angles between adjacent laths are relatively small. The orientation relationship with respect to the parent austenite is of the K-S type, with a {111} habit plane (Table 11-1-3). Four families of equivalent orientations can therefore exist within a given prior austenite grain. Twin orientation relationships between laths are rare in plain carbon steels, but frequent in nickel-rich grades. The growth of lath bundles is stopped when they meet a prior austenite grain boundary. A large austenite grain size leads to large lath bundles (Figure 11-3-2).

When the austenite contains precipitates, bundle growth is impeded, and a fine structure

Figure 11-3-1:
Optical micrograph of an air-cooled X46Cr13 (1.4034) steel, showing lath martensite. The structure is divided into blocks, consisting of bundles of more or less parallel laths. The white arrow indicates the boundary between two lath bundles in the same grain. Lath growth is stopped by prior austenite grain boundaries, the black arrow indicating a triple junction.
Courtesy CRU, Ugine-Savoie-Imphy,

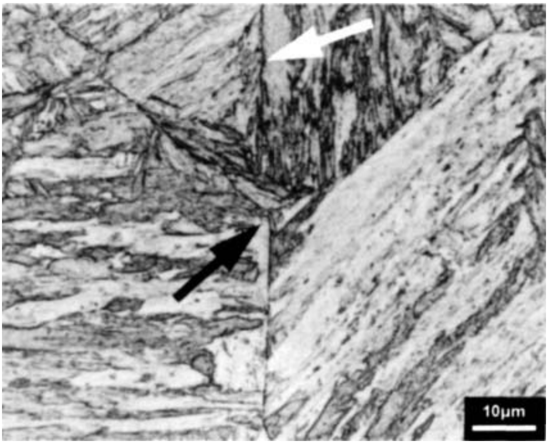

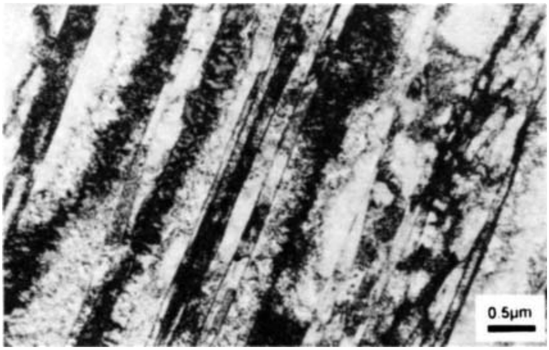

Figure 11-3-2:
Transmission electron micrograph of an X12Cr13 (1.4006) steel treated for 1 hour at 985°C then oil quenched and tempered for 4 hours at 400°C. The laths are long and thin, with a thickness of only 0.1 to 0.2 µm, much smaller than the other two dimensions. The laths contain a high density of dislocations.
Courtesy CRY, Imphy Ugine Précision, Arcelor Group.

is obtained. This effect is often sought deliberately to improve the mechanical properties. Examples of lath martensite can also be found in other chapters (Figs. 7-1-5, 8-3-3, 18-1-3, 18-2-1). When the transformation is incomplete, due to the excessive stresses generated, the retained austenite is in the form of narrow bands between the martensite laths, and cannot generally be distinguished by optical microscopy.

Plate martensite

Plate martensite occurs in medium and high carbon steels. In hypoeutectoid steels, it can form provided that the degree of undercooling is sufficient (*cf.* Fig. 9-2-1). The individual plates interfere with one another, leading to an apparently tangled microstructure, but where the orientations are in fact well defined. The commonly used term "acicular martensite" (*i.e.* needle-like) is not really appropriate, since the plates are more lenticular in shape when seen in three dimensions, similar to deformation twins. Transmission electron microscopy reveals them to have an internal substructure consisting of very fine parallel twins, and for this reason, a better name is twinned martensite (TM), Figures 11-3-3 and 11-3-4.

The martensite plates grow along high index habit planes in the austenite ({225}, {259}), leading to a large number of possible orientations within a same grain. The first plates to form are stopped only by the austenite grain boundaries, but create obstacles for subsequent plates with different orientations, leading to successively shorter lengths. The strain associated with the increase in volume impedes plate growth but also helps to nucleate new plates of different orientation. This autocatalytic nucleation process can lead to "zig-zag" chains of small plates rebounding across the space between larger ones (Fig. 11-3-4 C).

Plate martensite is also observed in high alloy steels, which often have low Ms points and large amounts of retained austenite. In the two steels with sub-ambient Ms points corresponding to the structures illustrated in Figure 11-3-4, the proportion of martensite obtained by quenching to –196 °C is larger in the alloy with an Ms point of –10 °C (C) than in the one where transformation begins at –150 °C (A) [Gau95], [Li-98a]. Comparison of micrographs (A) and (B) reveals that the application of a 500 MPa stress during transformation in sample (B) has caused thickening of the plates. The austenite in Fe-Ni

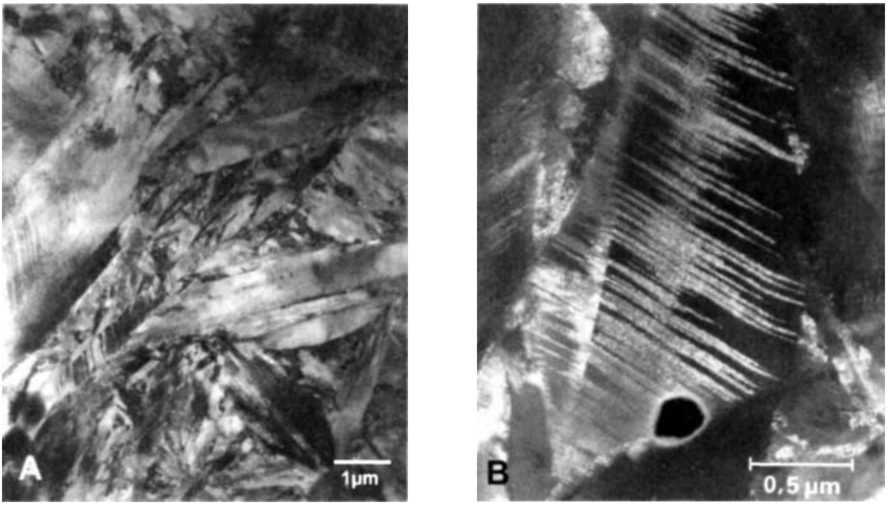

Figure 11-3-3:
Transmission electron micrographs of a 100Cr6 steel austenitised at 1050 °C then water quenched. (A) Overall view, showing the large martensite plates and darker retained austenite, containing a high density of dislocations. (B) Higher magnification image showing the finely twinned structure of the martensite plates.
Courtesy Ecole des Mines de Nancy and IWT Bremen. Adapted from [Sch99].

alloys is often heavily twinned, and it can be seen in micrograph (A) that the martensite plates grow across the twin boundaries, changing their orientation accordingly. Close examination of certain wide plates in micrograph (C) reveals the presence of a central "midrib", which is in fact a twin boundary. In the martensite with a $\{225\}\gamma$ habit plane in low carbon or low nickel steels, the central twinned region generally forms first and the rest of the plate grows out from it. In contrast, the martensite with a $\{225\}\gamma$ habit plane in high carbon or high nickel steels is heavily twinned throughout.

In as-cast alloy steels, the Ms temperature varies with local composition, following the outlines of dendritic segregation. A typical example is shown in Figure 11-3-5 for a tool steel, where the martensite plate distribution reveals the dendrite cores, while the tungsten-enriched interdendritic spaces (lighter back-scattered electron contrast) have generally not transformed. The plate orientations are the same in adjacent dendrite arms, which belong to the same grain, and some plates can be seen to cross from one arm to another. Figure 11-3-6 illustrates another example, corresponding to a high carbon, high chromium steel, whose composition is almost equivalent to an alloy cast iron. The martensite morphology is mixed, with both large plates and laths, confined to the grain (or dendrite arm) centres. The phase marking the grain/dendrite arm contours is M_7C_3 carbide formed by the γ/M_7C_3 eutectic reaction. The dendrite edges are richer in alloying elements than the cores, the measured difference being 2 % for chromium and 0.76 % for

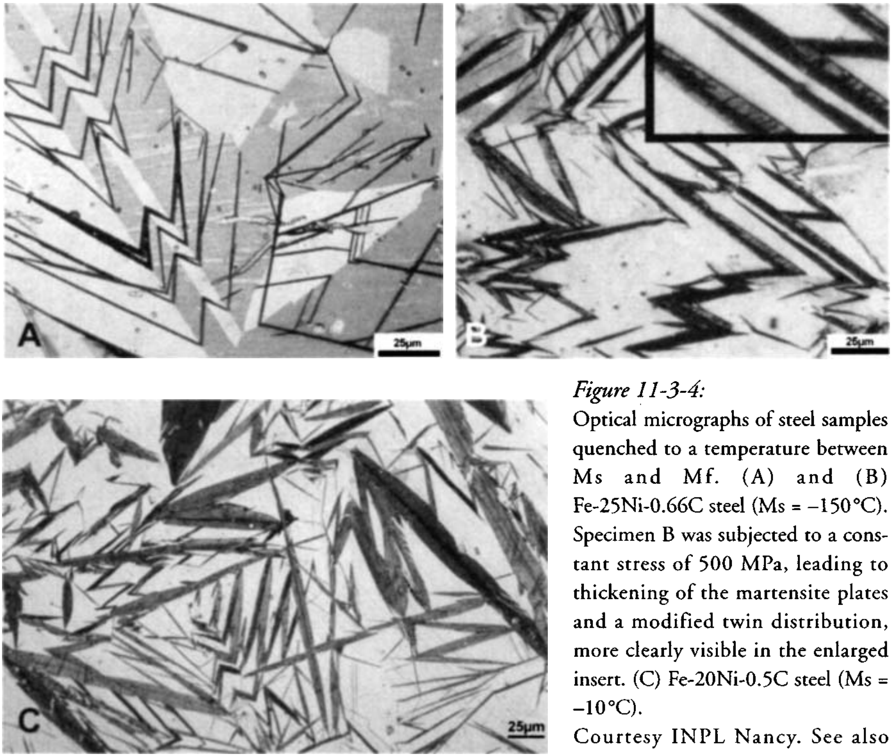

Figure 11-3-4:
Optical micrographs of steel samples quenched to a temperature between Ms and Mf. (A) and (B) Fe-25Ni-0.66C steel (Ms = –150 °C). Specimen B was subjected to a constant stress of 500 MPa, leading to thickening of the martensite plates and a modified twin distribution, more clearly visible in the enlarged insert. (C) Fe-20Ni-0.5C steel (Ms = –10 °C).
Courtesy INPL Nancy. See also [Li-98a], [Gau95].

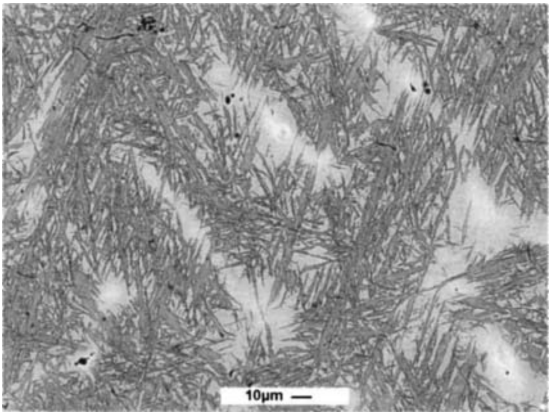

Figure 11-3-5:
Scanning electron micrograph of an as-cast Fe-0.8C-0.34Si-0.1Mn-1.2Cr-1W steel. The tungsten-enriched interdendritic spaces (light contrast) are essentially free from martensite plates.
Courtesy INPG, Grenoble.

molybdenum, corresponding to an Ms point approximately 60 °C lower. This is sufficient to bring the local Ms below the quenching temperature. Quenching in liquid nitrogen would have caused complete transformation of the austenite.

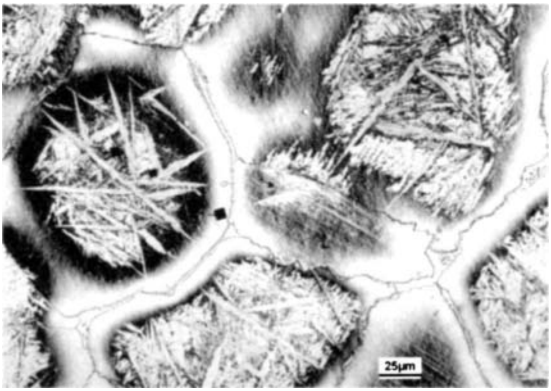

Figure 11-3-6:
Optical micrograph of an Fe-12Cr-3Mo-0.7Mn-0.3Si-1C alloy DTA sample cooled at 60 °C/h from the liquid and water quenched at the end of the cycle. The grain/dendrite arm centres have transformed to martensite, while the edges have remained austenitic (uniform light contrast). γ/M_7C_3 eutectic has formed in the grain boundaries/interdendritic spaces. The small black squares are Vickers microhardness indentations, corresponding to hardness values of 920 in the martensite and 376 in the austenite. Courtesy INPG, Grenoble (see also [De-83]).

11-4 Softening and tempering of martensite

Precursor stages and softening in the range 200–450 °C

Martensite is a *metastable* phase which tends to revert to the stable state by diffusion of carbon, a thermally activated process whose extent depends on temperature and time. Indeed, carbon diffusion can occur slowly even at room temperature. The carbon atoms, initially regularly distributed in interstitial sites in the martensite crystal lattice, move in different ways, tending to segregate to various types of defect. For example, the occupation of octahedral and tetrahedral sites does not create the same distortion (*cf.* § 3-1). Consequently, the transfer of carbon atoms from one type of site to another will change the overall lattice distortion. In fact, the carbon atoms tend to group together, and eventually form local clusters [Che91]. In the second stage of rearrangement, the population of isolated carbon atoms decreases and the clusters grow, forming embryos for carbide precipitation.

In the pre-precipitation phase, it has been observed that the carbon atoms tend to preferentially occupy octahedral sites along the c axis of the martensite, leading to the development of a "tweed" structure, modulated on a nanometre scale, which is probably responsible for the brittle behaviour of non-softened martensite [Ols83].

Between 50 and 160 °C, the first carbides precipitate, in coherency with the matrix. At around 250 °C, several types of metastable carbide can form in Fe-C alloys. They include the monoclinic Hägg's carbide (ξ), Fe_5C_2, and the hexagonal ε carbide, Fe_2C, in the presence of silicon. These carbides grow on particular crystal planes (*cf.* Fig. 13-1-3). The tetragonality of the carbon-depleted martensite, and hence its hardness, decreases. The process stops when the residual carbon content reaches a particular value, for which the phase can be termed α". The occurrence of precipitation can be detected by chemical etching, where only softened martensite reacts. The carbide particles themselves can be seen in the transmission electron microscope.

Although the process described above is typical of continuous precipitation reactions, with the formation of precursor clusters, followed by coherent metastable particles, in the case of martensite, it is accompanied by softening rather than hardening, due to the dominant influence of the relaxation of lattice distortion. Moreover, an indirect consequence is the relaxation of stresses on neighbouring retained austenite, which may then undergo transformation in accordance with its composition and temperature, forming either martensite or bainite. For temperatures below 250 °C, this stage gives a good combination of mechanical properties, due to a uniform distribution of softened martensite and bainite.

The initial structure of the martensite is increasingly modified as the temperature is raised above 250 °C. Between 250 and 400 °C, the changes have detrimental effects on the mechanical properties. At around 350 °C, orthorhombic cementite, Fe_3C, is formed alongside the carbides already mentioned [Ma83], [Sch75]. The carbon-depleted martensite converts to ferrite, while cementite plates grow parallel to {110}α planes and coalesce to rods oriented in the <111>α direction. There is always a precise orientation relationship between the carbides and the martensite, corresponding to epitaxy on close-packed planes. The resulting microstructures are brittle and the phenomenon is often called 500 °F embrittlement.

The case of Fe-N martensite

Martensite formed in Fe-N alloys undergoes softening at room temperature, where the nitrogen atoms rearrange in three ways : 1 - segregation to lattice defects ; 2 - transfer from interstitial sites on the a and b axes to octahedral sites on the c axis ; 3 - local ordering of the majority of nitrogen atoms, eventually forming coherent $Fe_{16}N_2$ particles [Che90a]. At longer times, the precipitates lose their coherency. In order to understand the difference in behaviour between martensites containing either carbon or nitrogen, it is necessary to consider two components of the interactions between interstitial solutes. There is thus a repulsive elastic component for both carbon and nitrogen, whereas the electronic component is repulsive for nitrogen and attractive for carbon. The double repulsive interaction for nitrogen causes long range ordering, whereas the electronic attraction predominates in the case of carbon and induces clustering [Böt99]. In the presence of alloying elements such as chromium and nickel, modification of the bonding forces between interstitial atoms and their neighbours in regular lattice positions can either enhance or inhibit one or other of these phenomena.

Tempering of martensite

Tempering is the name usually given to treatments performed between about 500 and 700 °C (below A1), during which martensite converts to the thermodynamically stable phases, namely ferrite and carbides (cementite in plain carbon steels, although strictly

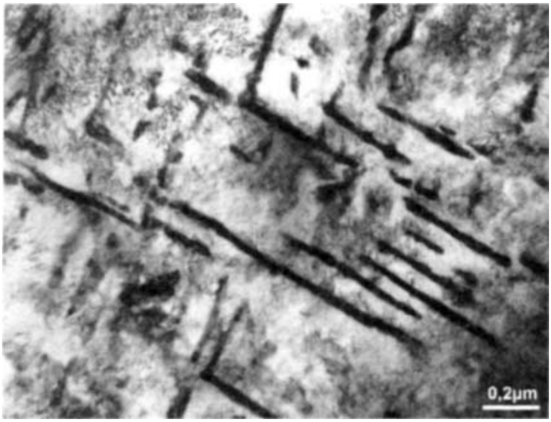

Figure 11-4-1:
Transmission electron micrograph of a 100Cr6 steel specimen austenitised for 20 mn at 1050 °C then held for 1 h at 355 °C and quenched into oil at 60 °C, showing relatively coarse carbides precipitated on preferred crystal planes. These carbides are in zones that have transformed to martensite, alongside regions of upper bainite formed during holding at 355 °C. Courtesy Ecole des Mines de Nancy and IWT Bremen. Adapted from [Sch99].

speaking this phase is still only metastable with respect to graphite). In carbon steels, the phases are the same as in pearlite, but their distribution is different, since the carbides are formed by a continuous precipitation reaction. In the early days of metallography, the resulting structure was referred to as *sorbite*. The ferrite matrix is continuous and highly ductile, while the cementite particles are very fine, but not sufficiently to induce significant hardening.

In the very earliest stages of tempering, either cementite or Hägg's carbide are the first to precipitate (Figs. 11-4-1 and 11-4-2), even in alloy steels where other carbides are thermodynamically more stable [Gho99]. Their compositions are close to those of the matrix, with the same proportion of metallic elements. This is observed for particle sizes between about 50 and 150 nm and suggests that their formation occurs under para-equilibrium conditions, in spite of the retarding effect of the alloying additions. The system subsequently evolves slowly with time, tending towards the true equilibrium. The equilibrium carbides probably nucleate independently, on dislocations, and grow at the expense of the metastable phases. In this respect, cobalt has an indirect beneficial effect, since it retards dislocation recovery, preserving potential nucleation sites.

In highly alloyed steels containing ferrite-stabilising elements, the A1 temperature is raised and tempering can be performed at higher temperatures. Carbide transformations can become complex, involving several steps, depending on the diffusivities and on the relative stabilities of the different phases [Sht97]. For example, in an Fe-4Mo-0.2C steel, the sequence is $Fe_3C \rightarrow Mo_2C \rightarrow M_6C$. The replacement of cementite by an alloy carbide can occur in two ways :

- by in situ transformation, the alloy carbide nucleating at several sites on the cementite/ferrite interface, eventually producing a finer dispersion of carbides;
- by independant nucleation and growth, the new carbides forming at dislocations, lath boundaries, or prior austenite grain boundaries. Growth then involves transfer of the carbon from the cementite [Por92].

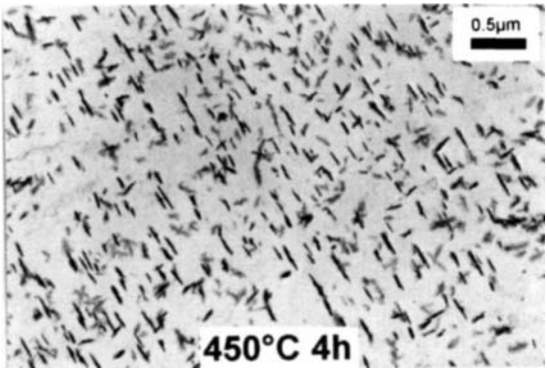

Figure 11-4-2:
Transmission electron micrograph of an extraction replica taken from an X12Cr13 steel treated for 4 hours at 450 °C then water quenched. The precipitates are cementite.
Courtesy CRY, Imphy Ugine Précision, Arcelor Group.

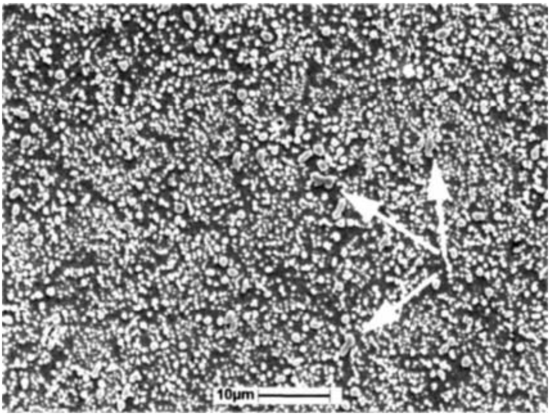

Figure 11-4-3:
Scanning electron micrograph of a quenched and tempered 100Cr6 steel, showing fine spheroidal chromium carbides in a ferrite matrix. The arrows indicate coarser secondary carbides at grain boundaries, which were already present in the austenite before quenching. The original hardness of the martensite (800–900 H_V) has been reduced to about 200 H_V and the ductility has become excellent.
Courtesy INPG, Grenoble.

Secondary hardening

Numerous carbides can precipitate in alloy steels tempered between 500 and 600 °C. The initial Fe_3C particles are partially dissolved and the carbon released combines with other elements whose carbides are more stable. Common "secondary" carbides include M_7C_3, $M_{23}C_6$, Mo_2C, TiC, V_4C_3, $(MoCr)_2C$ and W_2C [Spe72], [Pic78], [Kra80]. The precipitates formed at these relatively low temperatures are fine, abundant and uniformly distributed, and are often coherent with the matrix, with well established orientation relationships [Por92]. Carbides with complex crystal structures and low heats of formation, such as M_7C_3, M_6C and $M_{23}C_6$, generally tend to form somewhat coarser distributions (Figure 11-4-3). On prolonged high temperature exposure, the particles coarsen and lose there coherency. However, the resistance to coarsening, or high temperature stability, varies from one phase to another. Thus, the maximum temperature for satisfactory coarsening resistance decreases in the order : V_4C_3 (600/625 °C), $(Mo,Cr)_2C$ (575 °C), M_7C_3 (500 °C). Provided that the carbides remain fine and coherent, the softening caused by the loss of carbon from the martensite is compensated by secondary precipitation hardening.

12

The bainite transformation

«The mechanism of bainite formation has been the subject of numerous original research papers and reviews for almost a century but without any signs of controversies being resolved. For beginners and even for experts in related fields this wealth of information has been very confusing...» M. Hillert in "Preface to the Viewpoint Set on: Bainite" [Hil02]
The confusion unfortunately persists today and it has been chosen in the present chapter to let the microstructures speak for themselves.

12-1 Bainite structures

The nature of bainite

The common feature of the different bainite structures is that they all contain dislocation-rich ferrite which frequently has a more or less acicular morphology. Two microstructures are generally distinguished, corresponding to upper bainite, which forms in a temperature range immediately below that for pearlite, and lower bainite, whose range of formation extends down to that for martensite. Upper bainite is comprised of lath bundles or sheaves, while lower bainite is in the form of individual plates. The ferrite in bainite structures is harder than normal ferrite due to its high dislocation content, with densities that range from about 10^{15} to 10^{14} m^{-2} as the transformation temperature rises between 400 and 700 °C. The microhardness of bainite varies between 300 and 500 H_V.

It is now accepted that the bainite transformation occurs without redistribution of substitutional solute elements, the conditions of equilibrium at the interface corresponding to either the para-equilibrium (PE) or the no partitioning local equilibrium (NPLE) modes. For example, in a steel containing copper, no precipitates can be detected by conventional transmission electron microscopy in either the ferrite or cementite constituents of bainite formed at 350 °C. In contrast, copper particles appear during tempering treatments of several hours at and above 500 °C [Fou96]. This shows that there is no partitioning of copper during the upper bainite transformation itself.

From a kinetic standpoint, the bainite transformation is not as rapid as that involving martensite. The rates of both nucleation and growth are controlled by carbon diffusion [Qui02]. In the temperature range concerned, growth can only occur at *mobile* incoherent interfaces and not at ones that are semi-coherent with the austenite and pinned by misfit dislocations (*cf.* § 9-3). It involves a terrace and ledge mechanism. Two alternative interpretations are possible concerning the rearrangement of the iron and substitutional solute atoms, which may occur either reconstructively, by diffusional exchanges restricted to the incoherent terrace edges, or displacively, as in the martensite transformation. What is clear is that *it is the iron and slowly diffusing solutes that govern the change in crystal structure* [Aar90], [Bha92], [Qui01].

The controversy

The term bainite was first coined in 1934, in honour of Bain who reported this particular microstructure in 1933. The subject of the bainite transformation has remained a lively topic for debate ever since. The basic principles of the underlying mechanisms were announced by Zener as early as in 1946 [Zen46]. The idea that growth is controlled by the diffusion of carbon was developed in the 1960s [Zac62], but was not totally accepted at the time.

Numerous studies revealed the extreme complexity of the bainite transformation. The subsequent use of more sophisticated experimental techniques, such as in situ transmission electron microscopy, lent support to certain interpretations [Pur78]. However, several mechanisms remain in the running today and are still hotly debated. There are two major schools of thought, corresponding respectively to displacive and diffusive reconstruction processes [Pur84], [Aar90], [Ohm91], [Bha90], [Rey91], [Bha92], [Hil95]. Several of the articles and books cited are reviews including hundreds of references, where detailed arguments are developed, generally founded on experimental observations.

The displacive interpretation considers that the ferrite in bainite is formed by a military transformation, as for martensite. Indeed, the morphology is similar to that of martensite. The arguments advanced are the fact that the bainite transformation causes a relief effect, and the existence of specific orientation relationships. Because these considerations represent the fundamental basis for the displacive mechanism, they have been strongly contested. The Phenomenological Theory of Martensite Crystallography (PTMC) considers the relief to be evidence for the existence of an Invariant Plane Strain (IPS) induced by the transformation. However, similar relief effects have been observed to accompany plate-type precipitation in many other systems, without meeting all the requirements of a martensite transformation. These crystallographic arguments do not imply the complete absence of diffusion. In a fully displacive mechanism, the ferrite inherits the composition of the austenite at the moment of formation, but since the temperature concerned in the case of bainite is higher than for the martensite transformation, carbon diffusion is no longer negligible. Depending on the temperature, carbon diffusion can occur to a certain extent after the transformation, leading to the formation of carbides within or between laths in upper and lower bainite.

The diffusive interpretation states that short range diffusion in the vicinity of the transformation front is necessary to induce the change in crystal structure. Diffusion of substitu-

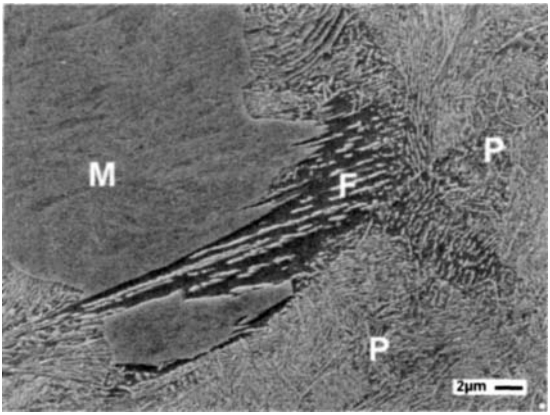

Figure 12-2-1:
Scanning electron micrograph of an Fe-5Ni-0.5C steel held for 1 hour at 450°C after austenitising. The matrix consists of fine pearlite (P) and martensite (M). The darker constituent is a bundle of bainitic ferrite laths (F). Courtesy INPG, Grenoble and IRSID, Arcelor Group (see also [Qui02]).

tional solutes is considered to occur by random thermally activated atomic jumps with little coordination. The interface is rebuilt by a process of *reconstructive diffusion*. This mechanism does not exclude the possibility of substitutional solute partitioning by longer range diffusion.

> *It is not the purpose of the present book to take part in the controversy, but merely to describe the most fundamental aspects of the transformations in a simplified manner. Nevertheless, it is important to use the right vocabulary in order avoid ambiguity. Consequently, it has been chosen to employ Hillert's definitions, which emphasize physical-chemical criteria [Hil00]. Bainite is defined as a eutectoid structure, with two phases formed together at the transformation front.*

12-2 Upper bainite

Upper bainite in hypoeutectoid steels

The laths of upper bainite nucleate at austenite grain boundaries and grow in groups, called sheaves or bundles, of about ten units (Figure 12-2-1). On a planar section they appear as plates, but in three dimensions they are in fact irregular ribbons. Contrary to pearlite colonies, growing bainite laths never cross austenite grain boundaries, revealing a greater dependence on grain orientation.

Each lath appears to be a small columnar grain, irregular in thickness and limited in length. Observations suggest that competitive growth leads certain laths to stop growing while new ones take their place. The need to respect a certain degree of coherency with the austenite induces a distortion which increases as the lath becomes longer, eventually stopping growth. The stress induced in the austenite at the tip of the lath helps to nucleate a new one. Some authors consider that the individual laths in a sheaf grow sequentially [Bha92]. Whatever the case, the mean growth velocity is much lower than for martensite,

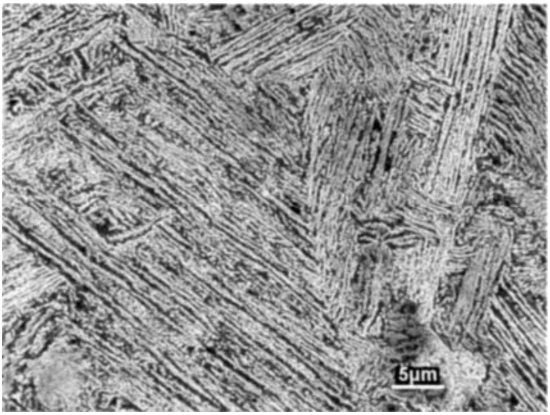

Figure 12-2-2:
Scanning electron micrograph of an Fe-0.5C-0.7Mn steel held for 1 hour at 500 °C after austenitising (nital etch). Upper bainite forms at 525 °C. The phase in light contrast is cementite.
Courtesy INPG, Grenoble and IRSID, Arcelor Group.

lending support for the diffusive interpretation. After a sufficient length of time, the transformation becomes total (Fig. 12-2-2). The final microstructure consists of intermingled lath bundles with different preferred orientations, as in the case of martensite.

The growth mode of upper bainite has sometimes been compared to that of pearlite, but the difference is that only the ferrite forms directly from the austenite, with the independent nucleation of carbides. By analogy with solidification processes, pearlite formation can be likened to a eutectic mechanism, whereas that of bainite is closer to dendritic growth (or more precisely, peritectic growth, with the pro-peritectic phase ahead of the front). Indeed, similar models exist for both bainite and dendrites [Tri70]. Moreover, the micrograph in Figure 12-2-1 shows that pearlite has a finer structure than bainite for the same formation temperature. Since the transformation occurs entirely in the solid state, crystallographic factors are important, and in this respect there are similarities with martensite. For example, the orientation relationships between the ferrite and austenite are of the K-S type commonly observed for martensite. The macroscopic habit plane of a lath bundle is $\{110\}\alpha$ close to $\{111\}\gamma$.

One of the principal characteristics of upper bainite is that no precipitation occurs within the laths. The supersaturation of carbon leads to cementite precipitation in the lath boundaries. The ferrite and cementite thus grow in a synchronised manner, and in this respect, the transformation resembles a eutectoid process. The lath thickness appears to increase with isothermal holding temperature, varying from about 0.2 to 2 µm over the range 425 to 570 °C. A similar tendency has been observed for martensite laths. When transformation is not isothermal, the lath thickness decreases with increasing cooling rate (Figure 12-2-3 A and B).

Upper bainite in silicon-rich steels

Silicon has two effects. Firstly, like nickel, it strongly retards bainite formation. Secondly, *it inhibits carbide formation* at lath boundaries. High carbon supersaturation then prevents

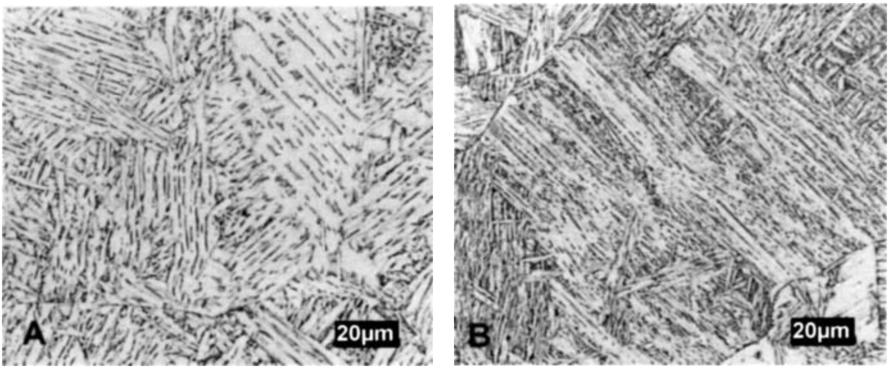

Figure 12-2-3:
Optical micrographs of an Fe-0.07C-1.5Mn-0.3Si-0.04Al-0.04V-0.04Nb steel austenitised for 15 mn at 1 100 °C then cooled at either 25 °C/s (A) or 95 °C/s (B), producing upper bainite structures.
Courtesy IRSID, Maizières-les-Metz, Arcelor Group.

Figure 12-2-4:
Scanning electron micrograph of an Fe-0.5C-1.5Mn-1.5Si steel isothermally treated at 450 °C after austenitising (nital etch). The structure resembles upper bainite, but does not contain cementite. The light coloured phase is austenite, which has partially transformed to martensite in some of the largest regions.
Courtesy INPG, Grenoble and IRSID, Arcelor Group.

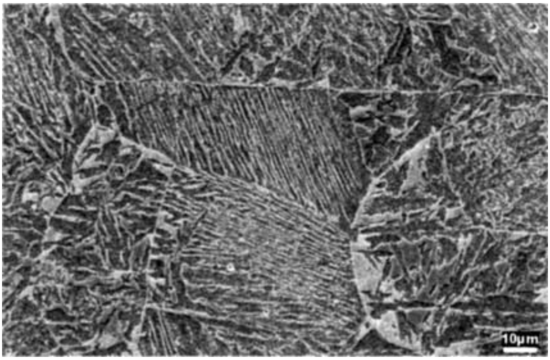

the austenite from transforming to either ferrite or martensite. Steels containing more than 1.5 % silicon form a carbide-free constituent and a large proportion of retained austenite. Aluminium appears to have a similar effect, but has been less extensively studied. If bainite is considered to involve a particular form of eutectoid decomposition, with the formation of both ferrite and carbides, then the carbide-free constituent formed in silicon-rich alloys should be considered rather as Widmanstätten ferrite. In the example shown in Figure 12-2-4, it could be described as a *compact Widmanstätten structure,* to reflect the fact that the transformation consumes the whole of the austenite grains. The retarding effect of silicon is used in certain TRIP (transformation-induced plasticity) steels (see § 17-3).

The example illustrated in Figure 12-2-5 is a silicon-rich steel also containing nickel, which has been subjected to a two-step isothermal holding sequence after austenitising, at

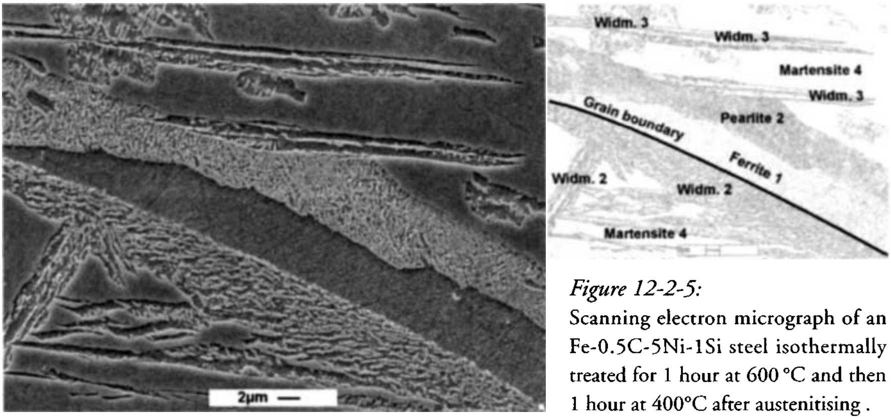

Figure 12-2-5:
Scanning electron micrograph of an Fe-0.5C-5Ni-1Si steel isothermally treated for 1 hour at 600 °C and then 1 hour at 400°C after austenitising . (Villela's reagent etch). A schematic explanation is given on the right. Courtesy INPG, Grenoble and IRSID, Arcelor Group

600 °C then 400 °C, followed by final quenching. Four constituents can be seen in the micrograph, corresponding to the four following stages :
1 primary ferrite has nucleated at a grain boundary at 600 °C, in epitaxy with one austenite grain and growing into the other ;
2 bainite has nucleated on grain boundary ferrite at 400 °C and has grown in coherency with the austenite. On the opposite side of the boundary, pearlite has formed in the region enriched in carbon next to the primary ferrite ;
3 bainite has nucleated on the pearlitic ferrite at the edge of the carbon-enriched zone ;
4 remaining austenite has transformed to martensite during final quenching.

Neither martensite nor ferrite are attacked by the etchant employed. However, the hard martensite appears smooth, whereas the softer ferrite is slightly grooved by polishing. The pearlite has a finer structure than that of the “bainite” (Widmanstätten ferrite). The most noteworthy feature is that the presence of ferrite facilitates the nucleation of bainite, which forms in epitaxy with either pro-eutectoid ferrite or pearlitic ferrite. The complexity of the microstructures resulting from continuous cooling can be readily imagined !

Upper bainite in high carbon steels

The carbon supersaturation in the bainitic ferrite increases with the initial concentration in the steel. A continuous carbide film is then formed at lath boundaries rather than a necklace of individual particles. The orientation relationships between adjacent ferrite laths then tend to be masked and the structure closely resembles pearlite. The fact that the terms bainitic pearlite or pearlitic bainite are sometimes employed reflects the perplexity of observers. Indeed, genuine pearlite with an extremely fine structure can sometimes form below Bs under conditions of marked undercooling. *The essential characteristic of bainite is the presence of a high density of dislocations in the ferrite,* giving it moderate hardness. Typical

Figure 12-2-6:
Transmission electron micrograph of a 100Cr6 steel sample austenitised for 20 mn at 1050 °C then held for 1 hour at 355 °C and finally quenched in oil at 60 °C. The microstructure corresponds to upper bainite. The carbides form more or less continuous lamellae at the ferrite lath boundaries. Courtesy Ecole des Mines de Nancy and IWT Bremen. Adapted from [Sch99].

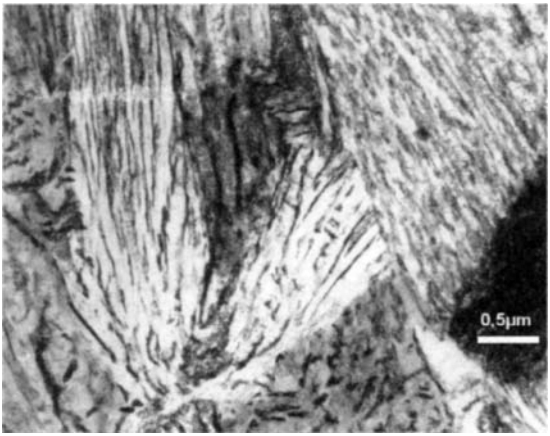

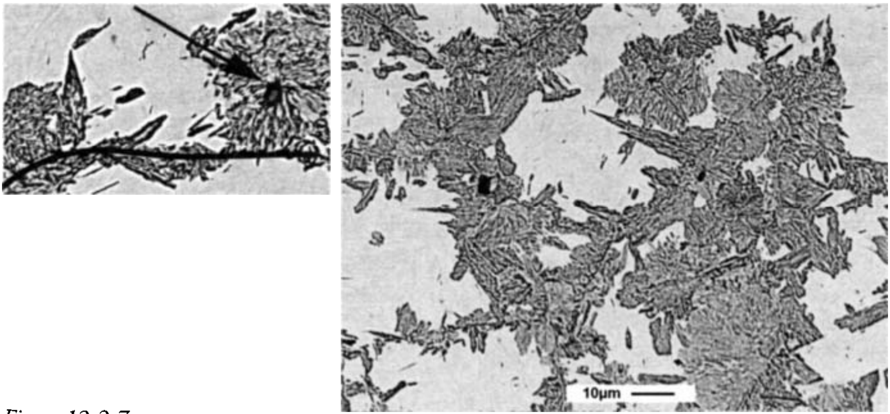

Figure 12-2-7:
Scanning electron micrograph of an as-forged Fe-0.9C-0.3Cr-0.1V steel (nital etch). The enlargement above shows bainite nucleation at a grain boundary (black line) and at an oxide inclusion (arrow). Courtesy INPG, Grenoble.

microhardness levels are 70–190 H_V for ferrite, 190–350 H_V for austenite, 300–550 H_V for bainite, and 700–950 H_V for martensite (excepting very low carbon varieties).

Figure 12-2-6 shows upper bainite in a 100Cr6 bearing steel. Another type of microstructure, observed when large amounts of austenite are retained, is called granular bainite, since it contains large austenite islands partially transformed to martensite [Bha92]. When the bainite transformation is limited, the transformed regions appear as cells that have nucleated preferentially at grain boundaries, precipitate particles or oxide inclusions (Figure 12-2-7). The bainite cells have a much more dishevelled morphology compared to pearlite colonies (*cf.* Fig. 10-1-2).

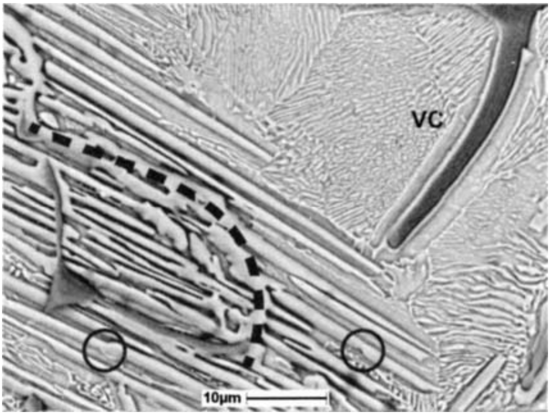

Figure 12-2-8:
Scanning electron micrograph of a deeply etched Fe-3.3C-9.2V-2Si steel cooled from the liquid at 300 °C/h. The grain boundary is indicated by the dashed line. The light-coloured rods growing from the boundary are cementite surrounded by ferrite. Some of these cementite laths are irregular in places (*e.g.* circled regions). The remainder of the austenite has transformed to pearlite. The dark carbides are eutectic VC and are surrounded by an envelope of secondary cementite, which they have helped to nucleate (*cf.* also Figure 6-3-4).
Courtesy INPG, Grenoble.

Inverse bainite

Another type of bainite observed in hypereutectoid steels is called inverse bainite, due to the fact that the cementite nucleates and grows in the austenite ahead of the interface and becomes surrounded by ferrite as the front advances, contrary to what happens in hypoeutectoid steels. An example observed in an alloy steel is shown in Figure 12-2-8. Nucleation has begun principally in the vicinity of interdendritic cementite at grain boundaries. The bainitic cementite grows in the form of laths. The irregular thickness of certain laths could indicate that nucleation has occurred repetitively by the so-called *sympathetic* mechanism proposed for ferrite [Bha92]. The remainder of the structure has transformed to pearlite.

Atypical microstructures

A very particular morphology is observed in alloys rich in both carbon and molybdenum [De-83]. In the two examples illustrated in Figures 11-2-9 A and B, the structure appears to be composed of a dispersion of needles of different sizes, with certain preferred orientations, although the needles are in fact strings of fine carbide particles. This structure is observed in as-cast alloys, near eutectic carbides formed in the molybdenum-enriched spaces between austenite dendrites. For the chromium-rich steel in Figure 12-2-9 A, the accompanying transmission electron micrograph AZ reveals that the irregular needles are composed of strings of very fine cuboidal Mo_2C precipitates oriented at 45° to the needle axis. The Mo_2C particles are surrounded by ferrite, with $(001)Mo_2C//(001)\alpha$ and $[120]Mo_2C//[111]\alpha$ orientation relationships. This is similar to the situation for ε carbides in martensite. Indeed, ε-carbide has the same structure as Mo_2C.

In the lower chromium grade shown in Figure 12-2-9 B, the needles indicated by the left hand side arrow are also M_2C carbides, of the $(Mo,Cr)_2C$ type. Both these structures could be assimilated to inverse bainite, since the carbides have been shown to be

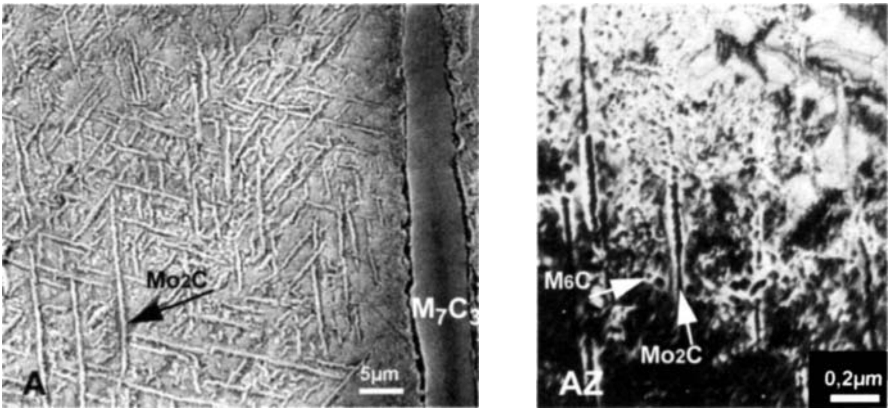

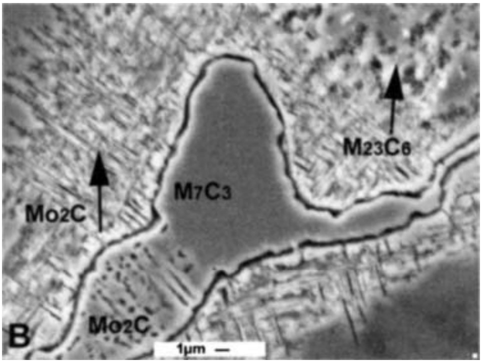

Figure 12-2-9:
A) Scanning electron micrograph of an Fe-0.9C-11.3Cr-0.7Mn-2.95Mo-0.3Si steel cooled from the liquid at 150 °C/h, showing Mo_2C needles. A coarse eutectic M_7C_3 carbide can be seen on the right.
AZ) Transmission electron micrograph of the same sample showing that the needles are composed of strings of cuboidal Mo_2C carbides (dark) oriented at 45 ° to the needle axis, surrounded by an envelope of ferrite (light).
B) Scanning electron micrograph of an Fe-1.33C-6.8Cr-2.4Mo-0.2Si steel quenched during unidirectional solidification (Villela's reagent etch). The image shows a transformed interdendritic region next to a coarse eutectic M_7C_3 carbid and a fine eutectic constituent containing Mo_2C (bottom left). Needle-like Mo_2C is indicated by the lef hand side arrow.
Courtesy INPG, Grenoble (see also [De-83], [De-85]).

surrounded by a ferrite envelope. In Figure 12-2-9 AZ, the matrix surrounding the composite carbide/ferrite needles is austenite containing a high density of coherent M_6C particles with an orientation relationship close to the cube/cube type. The matrix of the lower chromium alloy (Figure 12-2-9 B) contains $M_{23}C_6$ precipitates, which are also coherent. In this case, the composition and cooling conditions have probably affected the morphology of the M_2C carbides, which are sometimes facetted and sometimes more rounded, but always aligned in strings. Microstructures of this type have also been observed near grain boundaries in Fe-Cr-C alloys [Jun96], [Kay98].

Many different epithets have been employed to describe such atypical microstructures, including feathery, starlike and spiky. This tends to cause confusion and reflects the

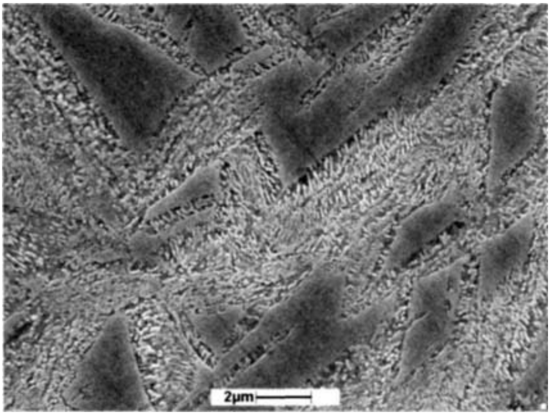

Figure 12-3-1: (
Scanning electron micrograph of an Fe-0.5C-0.7Mn steel isothermally treated at 325 °C after austenitising, showing lower bainite (nital etch). The dark phase is untransformed austenite. The carbide particles are aligned at a fixed angle of about 60° to the bainite plate axis.
Courtesy INPG, Grenoble and IRSID, Arcelor Group.

problem of interpreting certain microstructures, since it is sometimes difficult even to distinguish pearlite from upper bainite.

12-3 Lower bainite

Lower bainite in hypoeutectoid steels

There are several features that clearly distinguish lower bainite from other constituents [Pic67], [Ohm71], [Bha92]. Contrary to martensite, it does not contain twins and its habit planes are irrational. Above all, *the carbon in the parent austenite is not integrally transferred to the bainitic ferrite.* This experimentally established fact is confirmed by the presence of carbon-enriched retained austenite. Lower bainite forms at temperatures around 350 °C, where carbon diffusion is limited. The role of shear during the transformation remains a major question.

As regards the morphology, lower bainite occurs as bundles of adjacent laths with the same orientation, which together form a sort of plate. The lath bundles are distinct and often separated by retained austenite, as for plate martensite. This is illustrated for a medium carbon steel in Figure 12-3-1. The separation between individual laths is made visible only by the apparent change in orientation of the rod or platelet shaped carbide particles precipitated inside them.

There is an abundant literature concerning the transition between upper and lower bainite, particularly the temperature at which it occurs. The results analysed by Zhao and Notis [Zha95] and by Bhadeshia [Bha92] reveal considerable complexity. For example, the Bs point for the same alloy is defined in a different manner for isothermal treatments and continuous cooling, leading to static and dynamic Bs temperatures. A third value, the microstructural Bs temperature, has been defined by Aaronson as the highest temperature at which bainite is detected. Because of the disparity between the experimental techniques employed and the alloy compositions studied, it is difficult to discern the influence of particular parameters, including the initial carbon content. However, there appears to be a tendency for the formation of upper bainite to be facilitated in low carbon steels and that of lower bainite at high carbon levels. It appears as though the carbon supersaturation at the interface cannot be resorbed by the austenite beyond a certain threshold, since the diffusivity of carbon decreases with rise in concentration.

Lower bainite in high carbon steels

The first example to be described is an as-cast high carbon chromium-rich steel in which the heterogeneous composition has led to the formation of several constituents. Figure 12-3-2 shows the structures of samples cooled from the liquid at different rates [Dur80b]. In all cases, the coarse carbides are interdendritic eutectic M_7C_3 and the matrix is untransformed austenite. A depleted zone has formed in contact with the eutectic carbides, with carbon and chromium concentration gradients (see explanation in § 8-2). The width of the depleted zone depends on the time at temperature and is narrower in the more rapidly cooled sample (Figures 12-3-2 B and C). The Bs temperatures for upper and lower bainite depend on the local composition, so that the constituents formed vary according to the position. Thus, the dark border at the grain edges, in contact with the eutectic carbides, has been identified as upper bainite, while the small light-coloured acicular grains between the upper bainite and the austenite were shown to be lower bainite.

The second example is a high carbon alloy steel and again shows the formation of several different transformation constituents (Figure 12-3-3). The specimen has been quenched during unidirectional solidification. The austenite dendrites are coarse and the first lower bainite plates have been able to grow to a long length. They have the form of staggered laths, corresponding to the so-called sympathetic nucleation model. The stresses induced by the transformation have two effects. They limit plate growth, but at the same time help to nucleate new ones by generating elastic and plastic strain. This process is called *auto-catalytic nucleation* (Fig.12-3-3 A). Furthermore, the formation of lower bainite involves partial rejection of carbon into the austenite, lowering its Bs temperature and eventually inhibiting continuation of the transformation. The carbide precipitation observed inside the laths is characteristic of lower bainite, but in the alloy considered here, carbides also form at the lath boundaries, revealing partial segregation of carbon (Figures 12-3-3 B and C). The carbides at lath boundaries are observed mainly in the smaller laths formed at a later stage, in carbon-enriched austenite.

Another microstructure was observed in a different zone of the same unidirectionally solidified bar (Figures 12-3-3 D and E), corresponding to bainite plates with a central ferrite *midrib.* A similar structure was observed after isothermal treatments on plain carbon hypereutectoid steels by Okamoto and Oka [Oka86]. These authors suggest a two step transformation process. Between 200 and 150 °C, isothermal martensite appears first of all, in the form of very narrow plates (martensite of this type can form only in high carbon or alloy steels). These plates comprise the midrib from which the bainite develops laterally

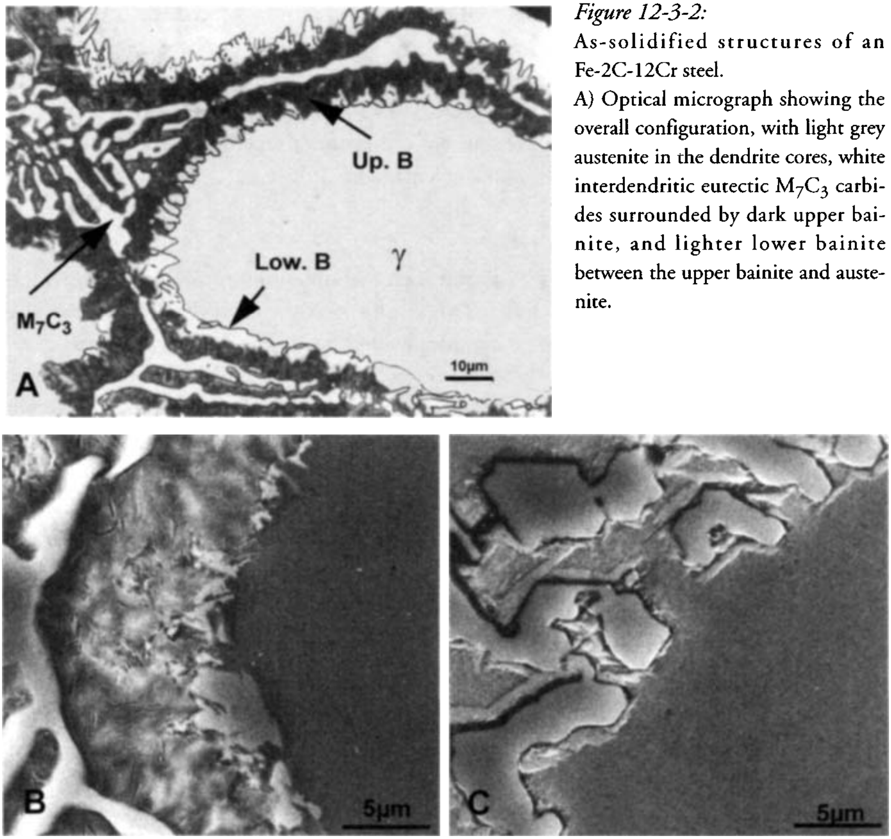

Figure 12-3-2:
As-solidified structures of an Fe-2C-12Cr steel.
A) Optical micrograph showing the overall configuration, with light grey austenite in the dendrite cores, white interdendritic eutectic M_7C_3 carbides surrounded by dark upper bainite, and lighter lower bainite between the upper bainite and austenite.

B) Scanning electron micrograph of a unidirectionally solidified sample of the same alloy cooled from the liquid at a withdrawal rate of 7 cm/h, showing a close-up of the bainite zone.
C) As in B, but with a withdrawal rate of 60 cm/h, leading to a narrower bainite zone [Dur80b].
Courtesy INPG, Grenoble

during the second step. Structures comprising a midrib with twinned regions on either side of a non-twinned zone have been observed in nickel and cobalt containing steels, and have been qualified as martensite, but their mode of formation remains unclear [Shi72].

Lower bainite or self-tempered martensite ?

In plain carbon steels, the carbides in lower bainite are extremely fine, corresponding either to cementite, or in the presence of silicon, to ε carbide. In alloy steels, particularly those containing chromium and/or molybdenum, numerous other carbides can occur. Although fresh martensite never contains precipitates, softening treatments or slow cooling can cause their subsequent formation. The question arises as to how to distinguish *a postiori* between lower bainite and self-tempered martensite ? In other words, do the carbides in the bainite

Figure 12-3-3:
Optical and electron micrographs of an Fe-1.33C-6.8Cr-2.4Mo-0.2Si steel quenched during unidirectional solidification (Villela's reagent etch). The alloy is the same as in Figure 12-2-9 C, but it is the region in the dendrite centres that is observed here.
A) Low magnification optical micrograph.
B) Scanning electron micrograph and BZ enlargement of the same region.
C) Scanning electron micrograph of a region cooled more slowly than in B and CZ enlargement of region C.
D) Transmission electron micrograph revealing the bainitic carbides.
Courtesy INPG, Grenoble (see also [De-83]).

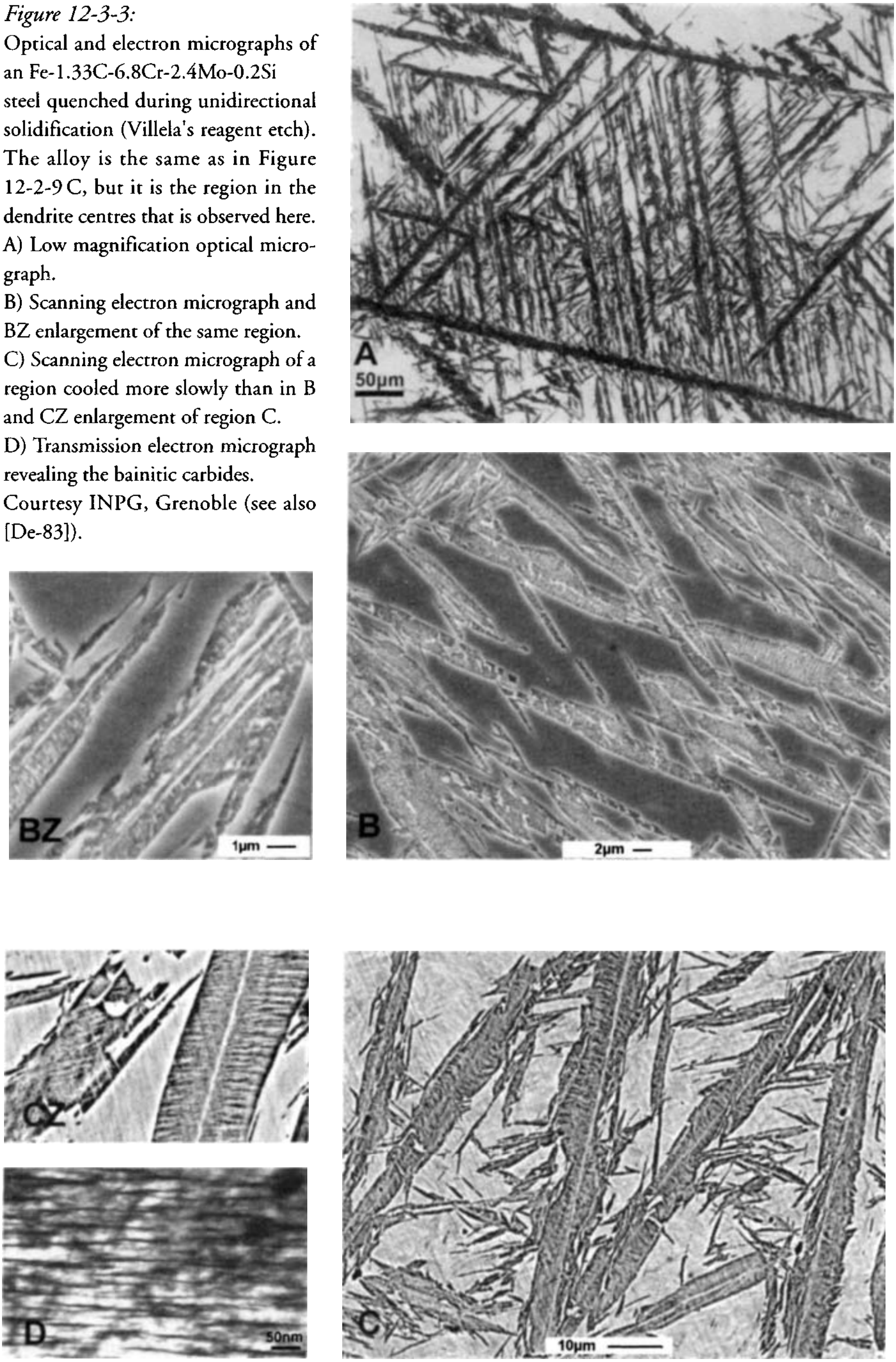

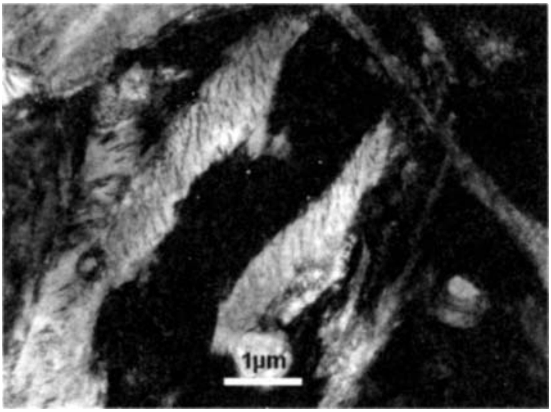

Figure 12-3-4:
Transmission electron micrograph of a 100Cr6 steel austenitised for 15 mn at 860 °C then held two hours at 220 °C, followed by air cooling. The microstructure corresponds to lower bainite. The carbides are inclined at an angle of 50-60 ° with respect to the plate axis.
Courtesy Ecole des Mines de Nancy and IWT Bremen. Adapted from [Sch99].

form behind the transformation front, so that the term bainite is then a misnomer, or do they form cooperatively during reconstruction of the interface? The balance of evidence appears to favour their formation at the transformation front. Thus, in particular, their rapidity of formation would tend to indicate a cooperative reconstruction process. The carbide particles are aligned in a well defined direction in the ferrite constituent, making an angle of about 57 ° to the plate axis (Fig. 12-3-4). Bhadeshia [Bha92] states that "the striking feature of lower bainite is that the internal carbides within the bainitic ferrite in general form in a single crystallographic variant, whereas the tempering of martensite leads to the precipitation of many variants of cementite".

Widmanstätten ferrite in silicon-rich cast irons

When treated in the bainite transformation range, spheroidal graphite cast irons form a structure consisting of wide feather-like lenticular plates similar in appearance to lower bainite (Figure 12-3-5). These cast irons are sometimes called bainitic, although the term *austempered* is probably more appropriate. The plates are composed of ferrite slightly enriched in carbon, with a high density of dislocations. During the transformation, only a small proportion of carbon is conserved in the ferrite, the rest remaining in the retained austenite, which can contain up to 2 %. The presence of large amounts of silicon, which is a graphitising element, inhibits carbide formation in both the austenite and ferrite, but carbides eventually precipitate in both phases after long holding times. Several carbides and silico-carbides have been identified in the ferrite, different to those in the austenite [Sch75], [Bha92].

The tempering of bainite

The effect of tempering on bainite structures is less marked than for martensite, the main reason being that the ferrite constituent is less supersaturated in carbon. Both upper and lower bainites already contain cementite and other carbides, whose growth can remove the excess carbon. In certain alloy steels, the initial cementite is not the equilibrium phase and

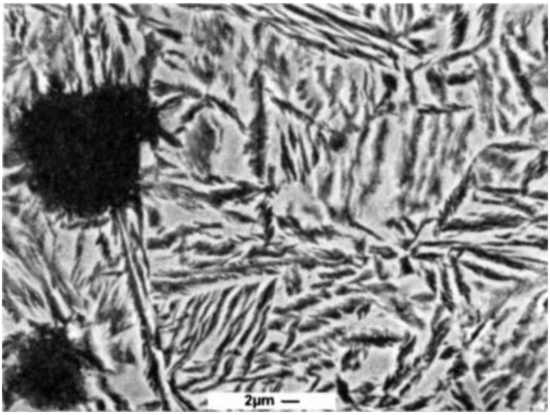

Figure 12-3-5:
Scanning electron micrograph of a "bainitic" spheroidal graphite Fe-C-Si-Mn cast iron given a step quenching treatment at about 350 to 400 °C. The austenitising treatment has homogenised the austenite without affecting the graphite nodules (left). The austenite has partially transformed to a feathery constituent during the isothermal step. The lighter regions are retained austenite. Sample prototype Renault.
Courtesy INPG, Grenoble.

therefore tends to be replaced by more stable carbides. This can happen extremely slowly, sometimes taking several years, and may involve the formation of transient phases (see § 20-1).

13
Precipitation

The phenomena described in the three previous chapters are related to the decomposition of austenite and apart from steels, the mechanisms involved are encountered in only a limited number of alloy systems. For example, martensitic transformations also exist in titanium alloys. In contrast, precipitation is extremely common in many binary or multicomponent materials. It is a process whereby an additional phase is formed from a supersaturated solution. Indeed, the term precipitation is familiar even to non specialists, being used among other things to describe rain, which can be promoted by the use of nucleants, as in metallurgy. Although the examples given are chosen among iron-base materials, the principles outlined in the present chapter can be applied to most alloy systems, including those based on lead, nickel, copper, aluminium, etc.

13-1 Continuous precipitation

Nucleation and growth of precipitates

Precipitation is the formation of local regions of a new phase B within a parent phase A', usually a supersaturated solid solution. The reaction can then be written A' → A + B. A is the same phase as A', but with a composition closer to that corresponding to thermodynamic equilibrium. In the general case of both homogeneous and heterogeneous precipitation, the transformation is controlled by long range diffusion. Short range diffusion can be the dominant parameter in particular cases, such as disorder-order transformations or allotropic transformations in pure elements, although the latter case does not concern a supersaturated solid solution.

Precipitation is said to be continuous when the new phase nucleates randomly within the parent phase, with no localised transformation front, each particle growing independently by diffusional transport of solute [Hon76]. Homogeneous precipitation refers to situations where there is no preferred nucleation site, such as vacancy clusters, dislocations, stacking faults, etc. Precipitation confined to such energetically favourable sites is termed heterogeneous. The energy balance associated with embryo formation can be written :

$$\Delta G_N = v\Delta G_V + s\gamma + E \qquad (13\text{-}1\text{-}1)$$

where ΔG_N is the overall change in free energy accompanying nucleation, ΔG_V is the change in chemical free energy per unit volume, γ is the interfacial energy per unit area and E is the strain energy due to the change in volume. v is the volume of the embryo and s its surface area. ΔG_V is negative, while γ and E are usually positive. However, the term E may be reduced, and even become negative, if pre-existing defects are eliminated. For an embryo to be stable, $\Delta G_N \leq 0$. Since the volume increases with embryo size faster than the surface area, for a given temperature (*i.e.* a given value of ΔG_V), there is a critical embryo size beyond which a nucleus becomes stable. The subject of precipitate nucleation has been extensively treated in numerous physical metallurgy textbooks [Cah83], [Por92].

It is energetically favourable for nucleation to occur at a grain boundary or on lattice defects, *such as dislocations* (see Figure 13-3-3 below), which represent local regions of excess energy, and it is well known that both *grain refinement and cold work facilitate precipitation* by increasing the number of preferred nucleation sites.

A high concentration of vacancies retained by quenching from elevated temperature can help to absorb a volume increase, for example, during the precipitation of carbides, particularly in austenitic steels. Vacancy clusters tend to collapse, forming small dislocation loops on which nucleation can occur. This process can be aided by the presence of small amounts of boron or phosphorus. These elements have intermediate sized atoms that fit with difficulty into either interstitial or substitutional sites and therefore tend to interact with vacancies, retarding return to the equilibrium vacancy concentration at the precipitation temperature [Dav73], [Row72].

The interfacial energy term γ is also reduced when the nucleus is coherent with the matrix. The presence of other precipitate phases and inclusions may provide interfaces on which the nuclei can form in a coherent manner. The formation of a thermodynamically metastable phase whose crystal lattice includes planes that provide close matching with the matrix, inducing lower γ or E values, may lead to a smaller critical embryo size, in spite of a less favourable ΔG_V term. In fact, the initial nucleation of metastable phases is extremely frequent and many examples occur in iron-base alloys, a typical case being the ε carbide that forms during the tempering of martensite (§ 11-4). These metastable phases are only transient, and after a certain time, which depends on the temperature, are eventually replaced by the thermodynamically stable phase. Because the latter is less coherent and therefore has a higher interfacial energy, it tends to coarsen rapidly. For this reason, fine dispersions of metastable phases are often deliberately sought, since they provide more efficient strengthening.

Certain precipitate phases that are semi-coherent with the matrix may become oriented along particular planes which are not necessarily those of lattice coincidence, in order to minimise the overall strain field caused by the mismatch [Dah84]. Short or long range stress fields can cause precipitates to become aligned, the strain generated around a particle influencing subsequent nucleation of other particles in its vicinity [Joh99].

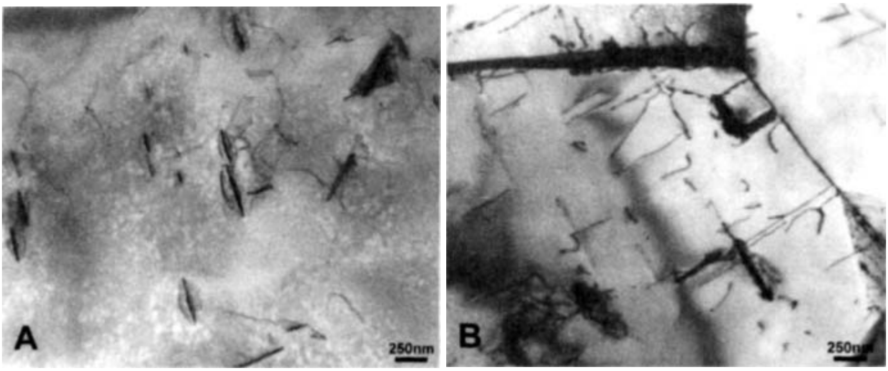

Figure 13-1-2:
Transmission electron micrographs of thin foils taken from a steel containing 56 ppm C, 300 ppm Mn and 12 ppm N, quenched after annealing at 670 °C, then held at 250 °C for either 30 mn (A) or 24 h (B).
A) A majority of fine ε carbide platelets co-exist with cementite.
B) Cementite is now the majority phase and the particles have coarsened.
Courtesy IRSID, Arcelor Group (see also [Mau01]).

The example illustrated in Figure 13-1-2 corresponds to the precipitation of ε carbide in a mild steel annealed at 670 °C and then aged for either 30 minutes or 24 hours at 250 °C. Two types of particle can be seen. In figure 13-1-2 A, after 30 mn, the carbides identified as the hexagonal ε phase can be distinguished from cementite by their preferred orientation and their finer elongated shape. The orientation relationships with the parent ferrite are:
<100>ferrite//<100>ε ; and <100>ferrite//<110>ccementite

After 24 h (Figure 13-1-2 B), cementite, Fe_3C, is now the majority phase and the platelets have thickened, while many ε particles have redissolved. However, the number of cementite particles appears to have increased, suggesting that nucleation has continued between 30 minutes and 24 hours.

Another interesting example of precipitation is that of copper in Fe-Cu alloys, which has been extensively studied due to its importance in certain precipitation hardening stainless steels, which find applications in nuclear engineering [Goo73], [Lle95], [Des01], [Hab02]. Copper is much less soluble in ferrite than in austenite and its solubility decreases to very low values when the temperature falls (*cf.* Fe-Cu phase diagram in Fig. 4-10-1). If copper-rich ferrite is quenched from a temperature where the copper is in solution and then held at about 500 °C, virtually pure copper precipitates out.

Hardening is observed from the earliest stages of holding at 500 °C, even before precipitates have become visible by conventional transmission electron microscopy. More powerful techniques, such as FIM atom probe analysis or diffuse low angle scattering of X-rays or neutrons, are needed to reveal that the precursor stage consists of coherent bcc

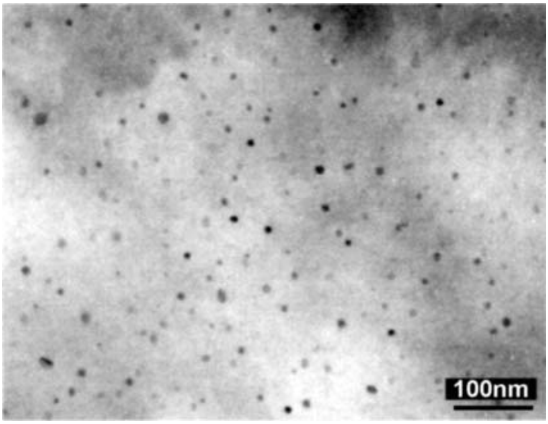

Figure 13-1-3:
Thin foil transmission electron micrograph of an Fe-1.4 at% Cu alloy sample aged for 100 hours at 500°C, showing very fine rounded precipitates of fcc copper.
Courtesy INPG, Grenoble (see also [Des01]).

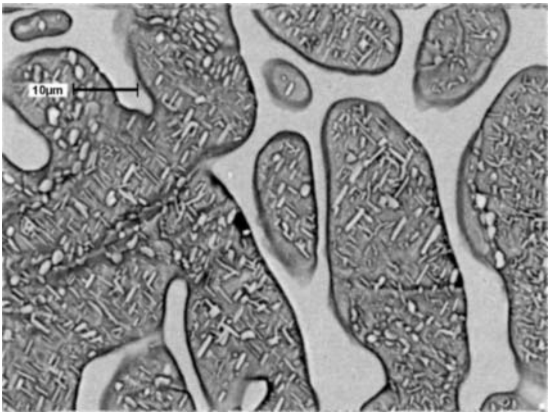

Figure 13-1-4:
Precipitation in a rapidly solidified Fe-Cu-Co alloy annealed for 10 days at 800 °C. The copper phase is in light contrast and includes massive regions formed at higher temperatures during solidification and Widmanstätten platelets precipitated from the darker ferrite phase at 800 °C (*cf.* Fe-Cu-Co phase diagram in figure 4-10-4).
Courtesy INPG, Grenoble.

clusters of copper atoms. At longer holding times, the clusters grow and transform to precipitates of the equilibrium fcc γ-Cu phase. In an Fe-1.4 at.% Cu alloy, the hardness reaches a maximum after about one hour at 500 °C, with a large density of particles whose size does not exceed 2.4 nm. After 100 hours at the same temperature, the precipitates are still fine and have all attained a stable fcc structure (Figure 13-1-3).

Another Fe-Co-Cu alloy was prepared by rapid solidification from the melt, during which two separate liquid phases solidified independently (*cf.* Fig. 6-3-12). The copper-rich part was then treated for ten days at 800°C and quenched. Figure 13-1-4 shows the resulting microstructure consisting of a ferrite matrix with copper in the form of both a massive interdenritic phase and relatively coarse Widmanstätten precipitates with preferred orientations.

Spinodal decomposition

When precipitation is represented by the reaction A' ⟶ A + B, in conventional processes, it is normally assumed that random diffusion-induced fluctuations in A' create an embryo which has the composition and structure of a stable or metastable phase B, and that nucleation is then a question of attaining a certain critical size. *The boundary between the parent phase and the precipitate is a sharp interface* A/B, marking a change in both chemistry and crystallography. Thermodynamic equilibrium is *immediately* established at the interface and the precipitate grows by the diffusive transport of atoms to maintain the local equilibrium (Figure 13-1-5 A). However, as the system moves from A' to A + B, the local compositions go through intermediate configurations, for which the change in chemical free energy ΔG_V is initially unfavourable, becoming negative only on approaching the final situation. There is therefore a chemical activation barrier to be overcome before attaining the status of a physical embryo with its associated physical activation barrier related to the interface and elastic distortion terms.

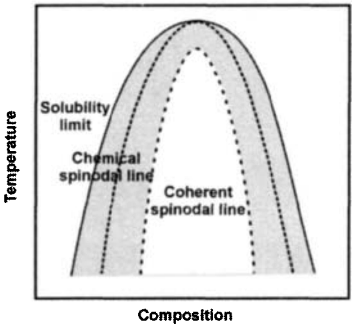

Figure 13-1-6:
Schematic representation of the solvus, chemical spinodal and coherent spinodal lines (adapted from [Phi02]).

This situation arises due to the variation in free energy with composition for the A and B phases. In certain cases, the variation is such that there is no chemical activation barrier, any fluctuation in composition between A' and A+B being accompanied by a local reduction in free energy. Furthermore, if A and B are also very similar in crystal structure, the physical activation terms may also virtually disappear. Precipitation can then occur by what is known as spinodal decomposition [Por92], [Phi02]. In fact, in the range of composition and temperature where the phenomenon occurs, there can be considered to be a single free energy- composition curve for the two phases at a given temperature, with two minima and inflexions at the spinodal points or spinodal compositions. The locus of the spinodal points as a function of temperature represents the chemical spinodal line, whose position with respect to the normal solubility limit or solvus is shown schematically in Figure 13-1-6. For matrix compositions and temperatures along this line, *any small fluctuation in composition induced by thermal agitation will locally reduce the overall chemical free energy and will spontaneously tend to become accentuated,* with diffusion up concentration gradients (but down chemical potential gradients !). *Phase separation then occurs continuously, with no clearly materialised interface,* producing a modulated structure (*cf.* Figure 13-1-5 A). There is no critical embryo size. Subsequent growth to sharply defined precipitates can be quite slow.

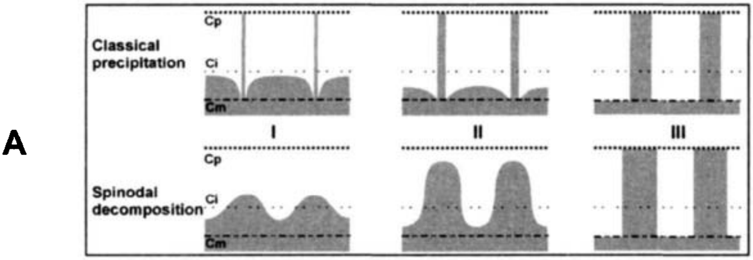

Figure 13-1-5:

A) Schematic concentration profiles at different stages (I = start, II = well advanced, III = end) during classical precipitation and spinodal decomposition. Ci, Cp and Cm are the solute concentrations in the initial alloy, the precipitates and the matrix respectively.

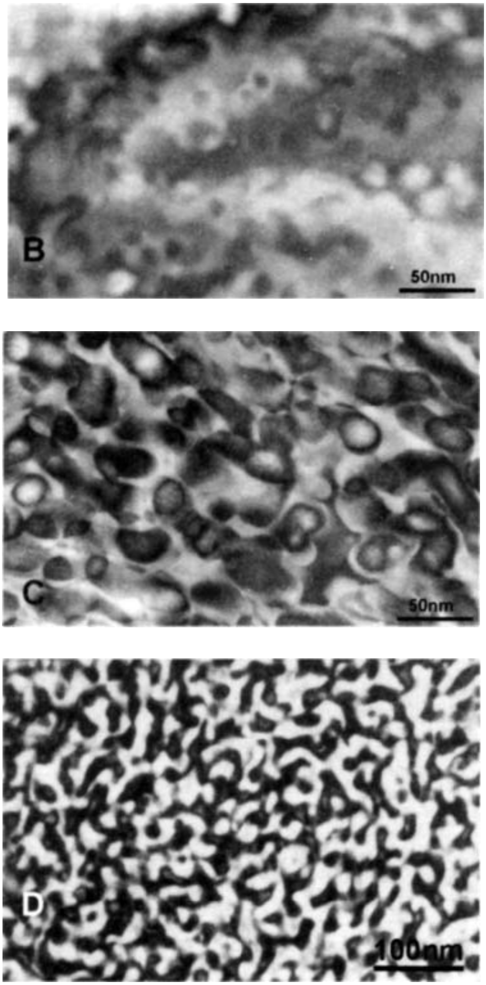

B) Transmission electron micrograph of an experimental Fe-28Cr-10Co alloy (weight %) treated for 1 hour at 980°C followed by two 80 minute annealing steps at 680 then 615 °C. The decomposition is revealed by fuzzy clusters

C) As in B, with slow cooling from 615°C to 525 °C in 12 hours. The nodules of chromium-rich α2 are the majority phase and now appear quite sharp. The matrix is iron-rich α1. The experimentally measured compositions and volume fractions F_V are given in the table below, where a is the initial alloy composition analysed in the same conditionst.

Courtesy Imphy Ugine Précision, Arcelor Group .

Compositions (at.%) and volume fractions Fv

	Fv	Fe	Cr	Co
α	100	60.7	29.7	9.5
α1	68	76	11.3	12.7
α2	32	28.6	68.8	2.6

D) Transmission electron micrograph of an Fe-29.5Cr-12.5Co alloy (weight %) held for 132 hours at 566°C. The foil is oriented normal to [100]. Different thinning between the two phases clearly reveals the interwoven structure.Courtesy INPG, Grenoble (see also [Sim89]).

However, the variations in composition may induce elastic stresses to maintain lattice coherency, in which case a modified coherent spinodal line must be considered (dashed curve in Figure 13-1-6). Although the mechanism of spinodal decomposition and the resulting microstructure are quite specific, the final phase compositions are still represented by the normal equilibrium solvus curves. It can be seen in Figure 13-1-6 that, during a continuous cooling process, precipitation can theoretically begin in a normal manner below the solvus and proceed by spinodal decomposition on crossing the spinodal line.

A typical example of spinodal decomposition is observed in the Fe-Cr system (Figure 4-4-2), in which the ferrite separates into two distinct bcc phases at low temperature, one rich in iron (α) and the other in chromium (α'), with closely similar lattice parameters. In the early stages of the process, stable fluctuations in composition have been observed with sizes of only about 0.7 nm, corresponding to groups of about ten atoms.

The micrographs in Figures 13-1-5 B and C show the modulated structure observed in an experimental Fe-28Cr-10Co alloy at two stages of decomposition, while Figure 13-1-5 D illustrates that in a closely similar alloy after a much longer aging time. The two phases are highly interwoven in three dimensions, with long continuous paths in each phase. Although these structures coarsen during long time exposure, they do so more slowly than classical precipitate distributions [Mil95], [Sim89]. The occurrence of spinodal decomposition in Fe-Cr alloys depends principally on the chromium content and the temperature. In high chromium ferritic stainless steels, conventional precipitation occurs above about 500 °C, where sigma phase is formed (*cf.* Figure 4-4-2), whereas spinodal decomposition is observed below 500 °C [Sol78]. It can be accompanied by significant hardening and loss of ductility. Indeed, it is the cause of the so-called 475 °C embrittlement phenomenon between 400 and 500 °C, for which the maximum kinetics are situated at about 475 °C. In Fe-Cr-Co alloys, it modifies the magnetic properties.

13-2 Discontinuous precipitation

Discontinuous precipitation with a pearlite-type morphology

Discontinuous or cellular precipitation occurs locally. It divides the material into two distinct regions, one in which the supersaturated parent phase A' persists, and another consisting of cells or colonies where the transformation to the equilibrium phases A and B has occurred at a moving interface, starting at grain boundaries. The grain boundary acts as a mobile heterogeneous nucleation site and facilitates diffusive exchanges.

The phenomenon is generally observed when the nucleation of continuous precipitation is difficult, such as at small supersaturations, for example, on slow cooling through the equilibrium precipitation temperature, or when the interfacial energy between A and B is high. It can be suppressed by heavy cold work, which facilitates continuous precipitation. Numerous examples are encountered in high alloy steels. The morphology generated is

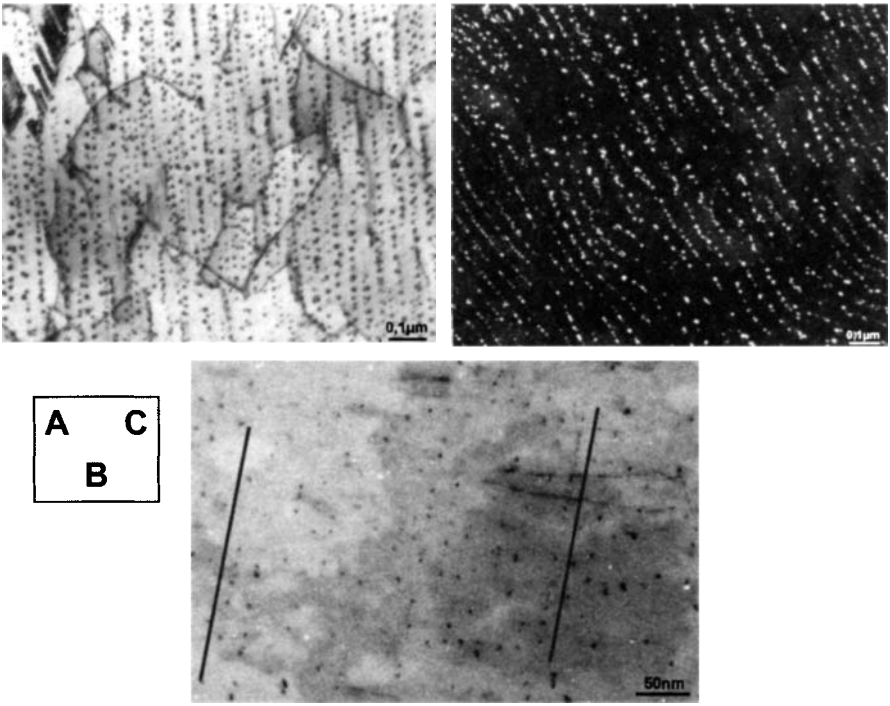

Figure 13-2-1:
Interphase precipitation of MC carbides in three different steels.
A) Transmission electron micrograph of VC precipitates in an Fe-0.049C-0.3Mn-0.126V steel hot rolled then treated for 2 hours at 700 °C.
B) Transmission electron micrograph of VC precipitates in an Fe-0.38C-1.5Mn-0.5Si-0.1V steel cooled to ambient temperature at 18 °C/mn after hot forging. The two black lines outline a region where the precipitates are aligned in rows. Sample supplied by Ascométal-CREAS, Amnéville, France.
C) Dark field transmission electron micrograph of curved rows of TiC carbides formed by an interphase precipitation mechanism in an Fe-0.052C-0.18Mn-0.12Ti steel hot rolled then treated for 2 hours at 700°C.
Courtesy IRSID, Maizières-les-Metz, Arcelor Group

very similar to that of pearlite, although the reactions are different (*cf.* Figures 19-7-4 and 19-7-4) :
A' → A+B for precipitation ; and A → B+C for eutectoid transformation

Interphase precipitation

So-called interphase precipitation is discontinuous, since it involves transformation at a moving front rather than random nucleation, even though the result may resemble that of a continuous precipitation process. The reaction involved is similar to that given above for a eutectoid transformation, since two new phases are formed. The characteristic feature is the distribution of the precipitates in regularly spaced parallel rows (Figure 13-2-1). The individual particles are generally very fine and close together, so that when their volume fraction is large they can give the impression of an irregular plate. It is now acknowledged that this precipitation mode is related to growth of the matrix (A) phase by a terrace-and-ledge mechanism. It is frequently observed during austenite decomposition processes in steels. Austenite is replaced by ferrite at the moving step noses. Under conditions of para-equilibrium, the excess carbon diffuses away from the displacement front and the local supersaturation leads to carbide nucleation on the immobile terrace regions of the α/γ interface, which represent low energy planes (Fig. 13-2-1 A, B and C).). The fact that it does not occur preferentially on the high energy incoherent steps is due to their excessively large lateral displacement speed [Por92]. The carbides become integrated within the ferrite when they are covered by additional layers as successive ledges move laterally across the front. The ledges must therefore be sufficiently high for their movement not to be impeded by the presence of the carbides. For example, it has been shown that $M_{23}C_6$ carbides formed by this mechanism have an orientation relationship with both the austenite and the ferrite. Furthermore, the ferrite constituent conserves a K-S type orientation relationship with the austenite [Hon80]. The spacing between rows is smaller the lower the temperature [Lag01]. The sample illustrated by the micrograph in Figure 13-2-1 B was cooled immediately after hot forging and precipitation must have occurred at a lower temperature and for a shorter time than in the case illustrated in Figure 13-2-1 A for a fairly similar steel, since the VC precipitates are much finer and closer (note the large difference in scale).

Interphase precipitation can also occur at non planar high energy interfaces whose growth does not necessarily involve the terrace-and-ledge mechanism. The precipitates can then be aligned in curved rows (Figure 13-2-1 C). This configuration is more common at temperatures above about 700 °C, where the mobility of such high energy interfaces is greater. Indeed, both planar and curved arrangements can be observed in the same sample [Sak84]. Numerous examples of both types, involving carbides and carbonitrides, are found in steels, particularly in the presence of strong carbide and nitride forming elements such as niobium, titanium and vanadium, for which the solubility products are very low, even in austenite. However, somewhat less stable carbides, such as Mo_2C, Cr_7C_3, $Cr_{23}C_6$, W_2C, and M_6C can also form by this mechanism during cooling. Interphase precipitation is accompanied by a certain degree of hardening and is the principal strengthening process in microalloyed (HSLA) steels [Gla97], [Sak84]. Aligned precipitates of copper have also been observed in both ferrite [Fou95a] and cementite [Kha93].

Fibrous precipitation

Fibrous precipitation is another process that occurs during the decomposition of austenite in alloy steels, in competition with interphase precipitation, under conditions of temperature and composition where ferrite growth is inhibited. It has been studied principally in molybdenum-containing grades, where Mo_2C fibres are formed, but has also been

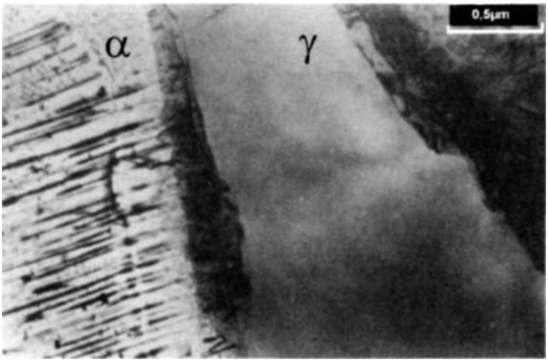

Figure 13-2-2:
Transmission electron micrograph of an Fe-0.35C-0.9Mo steel thin foil heated in the microscope then slowly cooledfrom 950 to 550 °C. The image taken 15 minutes after the start of cooling shows fibrous Mo_2C formed at the growing α/γ interface. Courtesy McMaster University, Hamilton, Canada (see also [Pur78]).

encountered for W_2C, VC, Cr_7C_3 and TiC carbides. The fibres are very fine, with average diameters of 10 to 50 nm, and can be either regularly distributed or completely disorganised. Both fibrous and interphase precipitation can be observed together in a same grain, depending on the orientation of the transformation interface and the temperature range concerned [Ain79], [Hon80], [Pur78]. The micrograph shown in Figure 13-2-2 is a still image made during in situ observations of a moving α/γ interface. The fibrous Mo_2C carbides appear to form at the interface.

13-3 Precipitate growth

Isothermal growth

In conventional precipitation processes, at a constant temperature, the different phases eventually reach their equilibrium compositions and their volume fractions subsequently remain constant. However, the structure continues to evolve, in the endeavour to reduce the excess energy represented by the particle/matrix interfaces [Ven82], [Voo84]. Larger particles tend to grow at the expense of smaller ones, in a process termed *Ostwald ripening*, which has been extensively studied and is described by a well established general model developed by Lifshitz, Slyozov and Wagner. The LSW model assumes a small constant precipitate volume fraction and a distance between particles much larger than their radius. Local equilibrium imposes the equality of chemical potentials on either side of the interfaces. According to the Gibbs-Thompson equation, the local potential at the interface is a function of the radius of curvature. Smaller radii correspond to higher energies, so that the interface equilibria vary with particle size. In order to minimise the total energy of the system, there is a gradual transfer of matter from smaller, less stable, particles to larger, more stable, ones. The presence of alloying elements can accelerate or inhibit growth depending on whether or not they are directly involved in the precipitate growth process [Bjö72].

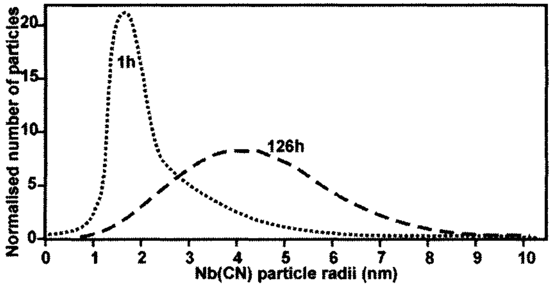

Figure 13-3-1:
Variation of the size distribution of Nb(C,N) precipitates in a HSLA steel containing 699 ppm C, 66 ppm N and 843 ppm Nb during holding for 1 hour and 126 hours at 650 °C. The curves are smoothed histograms. After 126 hours, the mean particle radius has doubled and their number has been halved compared to the situation after 1 hour.
Courtesy IRSID, Arcelor Group.

Holding time	Number density (μm^{-3})	Mean radius (nm)
1h	9800	2.3
126h	4700	4.5

Figure 13-3-1 shows an example of niobium carbonitride particle sizes measured in a microalloyed (HSLA) steel after 1 hour and 126 hours exposure at 650°C. The curves show that the number of particles decreases while their sizes increase. Local analyses reveal that the average composition of the particles also changes, showing that the chemistry is different for the small and large particles. The effect of composition on the interface and strain energy during nucleation can impose a local chemistry for which these terms are reduced (for example, smaller lattice mismatch). The situation evolves as the particle grows and as the residual matrix composition changes with increasing precipitate volume fraction. Gradients in composition can arise within the particles for the same reason.

Anisothermal precipitation

When the volume fraction of precipitates continues to increase, nucleation and coarsening occur simultaneously. This is particularly true during cooling, since the solubility of the precipitate phase usually decreases with temperature. This is particularly true during cooling, since the solubility of the precipitate phase usually decreases with temperature, the effect being markedly enhanced when the matrix transforms from austenite to ferrite (*e.g.* precipitation of Nb, Ti and V carbides and nitrides). The equilibrium compositions change and also the lattice parameters, and hence the mismatch. If precipitation occurs during thermomechanical processing, dislocations create preferred nucleation sites and thus modify the precipitate distribution. The final microstructure can then consist of several particle populations, with different sizes, shapes and locations depending on their history.

The HSLA steel illustrated in Figure 13-3-2 contains three populations of niobium carbides. The coarsest particles are situated in the grain boundaries and were formed first at high temperature. They have depleted the surrounding metal of niobium, leading to a precipitate-free zone on either side of the boundaries (according to the mechanism

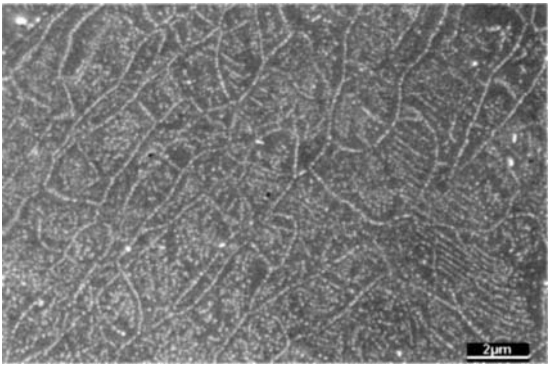

Figure 13-3-2:
Scanning electron micrograph of a HSLA steel containing 3000 ppm Nb and 300 ppm C. Three different NbC populations can be seen, corresponding to necklaces at ferrite and prior austenite grain boundaries and at sub-boundaries, aligned rows formed by an interphase type mechanism, and randomly distributed particles produced by classical nucleation.
Courtesy IRSID, Arcelor Group.

explained in § 8-2). The precipitates within the grains vary from one region to another, their distribution corresponding either to classical random precipitation or to an aligned interphase type configuration (the latter form often becomes more clearly visible on changing the angle of observation). Another case of anisothermal precipitation, involving inter- and intragranular $M_{23}C_6$ carbides in a martensitic stainless steel, is illustrated in Chapter 19, Figure 19-1-4.

Another example, also involving a HSLA steel, is shown in Figure 13-3-3, in which (Nb,Ti)C particles can be seen in the ferrite. The interpretation of another similar micrograph representing the same specimen aroused lively debate, summarised in [Cha01]. The question was whether the carbides had formed in the austenite, in the ferrite, or at the growing interface, by an interphase precipitation mechanism. The authors believed that they had formed in the ferrite. They are very fine and aligned in rows, while particles nucleated in the austenite are more massive. In fact, they are located on dislocations and have a Baker-Nutting type orientation relationship with the ferrite : $(100)p//(100)\alpha$ and $[011]p//[010]\alpha$.

Numerous parameters affect the morphology and distribution of precipitates, including the nature of the matrix (orientation relationships) and the possible presence of defects, the initial composition (degree of supersaturation), and the cooling rate. The different arguments advanced by the opposing parties emphasize the difficulty in interpreting transformations that have occurred over a range of temperatures. The discussions demonstrated that the precipitation process was highly sensitive to the conditions prevailing during hot rolling and hot coiling, and especially the rate of cooling between these two steps. Indeed, it is the cooling rate which has a decisive influence in the case of interphase precipitation. Moreover, because of the very low solubility of carbon and nitrogen in ferrite, a small variation in composition can significantly change the precipitation temperature [Ver98a].

Carbides, nitrides and carbonitrides are frequently observed in both HSLA and interstitial-free (IF) steels. They often have a well defined cuboidal morphology, particularly in the case of TiN, indicating precipitation in the liquid phase, probably in the solute

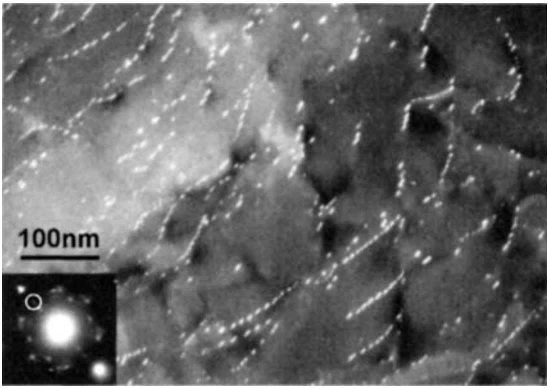

Figure 13-3-3:
Dark field transmission electron micrograph of an Fe-0.07C-1.35Mn-0.047Ti-0.086Nb HSLA steel, examined in the hot rolled then hot coiled condition, made using a reflection from the (Nb,Ti)C particles (*cf.* circled spot in the diffraction pattern shown in the insert). The precipitates are in the form of short rods and the grain size is about 3 µm.
Courtesy, University of British Columbia, Canada and INPG, Grenoble (see also [Cha01]).

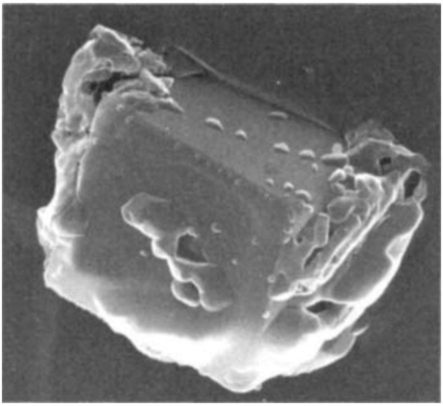

Figure 13-3-4:
Scanning electron micrograph of a TiN particle on an extraction replica taken from an Fe-1.35Ti-0.025C-0.035N interstitial-free type steel annealed at 765 °C. The cubic precipitate measures about 200 µm. Titanium sulphides can be seen adhering to the nitride.
Courtesy IRSID, Arcelor Group.

enriched interdendritic grooves towards the end of solidification (Figure 13-3-4). Other deliberate minor additions and impurity elements can also segregate to the same regions, explaining the presence of sulphides or carbosulphides (TiS or $Ti_4C_2S_2$) adhering to the nitride. The partition coefficients between the liquid and solid are very small for both titanium and sulphur, leading to a strong tendency for segregation in the liquid. In this case, the mixed precipitate probably grew entirely in the liquid phase, although similar associations can form in the solid, due to favourable epitaxial relationships.

Part 3

Steels and cast irons

«It is now truer than ever that steels are the most important group of engineering materials, for they are continually evolving to meet new needs and challenges, and this is really the main justification for doing research in this field.»
R.F.K. Honeycombe 29th Hatfield memorial lecture 6 December 1979 [Hon80]

«Steel, the most versatile of the structural materials is present in practically all the sectors - buildings and public works, transport (automobiles, marine engineering), packaging, furniture, tools, mechanical engineering, industrial and consumer goods,...

Moreover, due to its intrinsic low cost and ease of recovery, steel is particularly suited to the development of multiple-use cycles, and this is already reflected by the highest effective recycling rate of all materials.»
M Giget "Functional properties and choice of materials", Chapter 2 of "The book of steel" [Bér96a].

14

Steel Design

The most modern quality of steel is undoubtedly its great versatility. In spite of the fact that world steel consumption is no longer increasing, the range of available grades has risen significantly in response to ever more stringent and precise market demands. For the potential user, the first step in the steel selection process is to compare the technical properties of the different grades with the characteristics required for the intended application [Ash92], [Ash99], [Ash02]. For the steel designer, property combinations can be improved and optimised only by a detailed scientific analysis of the metallurgical mechanisms involved. A clear understanding of the underlying phenomena provides the flexibility needed to tailor properties to meet particular needs in a reliable and reproducible manner. However, it is not only the final functional properties of a component that must be considered, but also the ease and cheapness of manufacture, including the cost of raw materials. Recyclability and environmental considerations are also becoming increasingly important. The best material is the one that meets all these requirements at the lowest total life cost.

14-1 Mechanical properties

Strengthening mechanisms

Mechanical strength is often the major property requirement, usually expressed in terms of the yield and ultimate tensile stress in a uniaxial tensile test. There are four basic strengthening mechanisms that can be used in different ways to improve the mechanical properties of steels (and alloys in general), corresponding to strain hardening, grain refinement, solid solution strengthening, and precipitation hardening. The first two can also be employed in pure metals, while the last two depend on the physical-chemical equilibria in alloy systems. In order to evaluate the effect of the various parameters involved in the different mechanisms, a number of empirical formulae have been established, usually based on the observed increase in 0.2 % yield stress (the flow stress at 0.2 % permanent or plastic strain, often also called the 0.2 % proof stress). The formulae contain proportionality coefficients which provide an indication of the comparative efficiency of different contributions to strengthening [Pic78].

Strengthening by grain refinement

Grain boundaries usually represent obstacles to dislocation motion, due to the difference in orientation of the two crystals that they separate. The propagation of a strain vector across the interface generally requires the activation of new slip systems, with an associated increase in flow stress. The smaller the grain size, the larger the number of obstacles and the greater the degree of strengthening. However, since grain boundaries are local regions of excess energy, there is a natural tendency for their total area to decrease by grain growth during high temperature processing and heat treatment cycles. To achieve a fine grain size it is necessary to promote recrystallisation with a high nucleation density, generally by controlled thermomechanical processing, and to prevent subsequent grain growth. The mobility of grain boundaries can be impeded by the presence of precipitate particles and certain elements in solid solution. A fine primary solidification grain size can often exert a beneficial influence, even after several subsequent solid state phase transformations.

Strain hardening

The stiffening produced when metals are cold worked and the subsequent softening that can be achieved by appropriate heating are phenomena that have long been known and exploited by smiths, even though their origins have become understood only in more modern times. Strain hardening, or work hardening, occurs in all cold forming processes, including forging, rolling, wire-drawing, sheet drawing, etc. We now know that plastic deformation involves the generation and movement of crystal dislocations. The distorted dislocation core structures and their associated longer range elastic stress fields interact with one another and their motion is impeded. New dislocations must be created for deformation to continue and this requires a higher stress. The number of dislocations, and therefore the number of obstacles and the resulting flow stress, thus increase with strain. Dislocation density is measured as the total length of dislocations per unit volume and is usually expressed in units of cm^{-2}. For example, in an annealed single crystal, a typical value would be of the order of $10^7 cm^{-2}$, whereas levels of 10^{10} to $10^{12} cm^{-2}$ are observed after common cold working operations. The strengthening that accompanies strain hardening is associated with a loss of residual ductility. It is therefore usually necessary to limit the amount of cold work in order to achieve an acceptable balance between strength and ductility.

Figure 14-1-1 shows the microstructure of a low alloy steel that has been heavily cold rolled, the individual grains being flattened to a so-called pancake shape. The high dislocation density represents a large amount of stored mechanical energy, so that such structures are unstable when the material is subsequently heated. The dislocation density decreases during heat treatment, and depending on the time and temperature, three thermally activated softening processes can occur, corresponding to recovery, recrystallisation and grain growth.

Recovery is the process with the lowest activation energy and corresponds to a reduction in the density of dislocations and their rearrangement into lower energy configurations. It

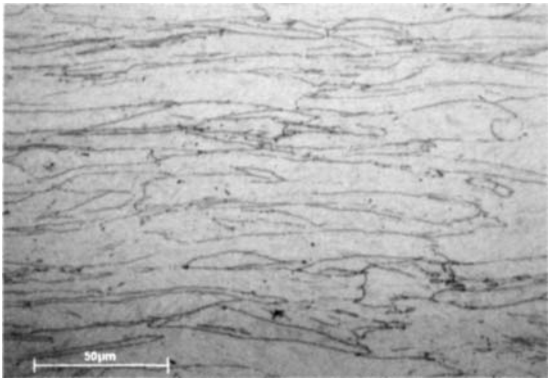

Figure 14-1-1:
Optical micrograph of a low alloy steel hot rolled in the austenite field at a temperature sufficiently low to prevent recrystallisation. The individual grains have been flattened to a "pancake" morphology. Etching in 4 % picric acid reagent has revealed the prior austenite grain boundaries.
Document Arcelor Recherche, Fr

involves diffusion-dependent processes such as climb and cross-slip and enables the mutual annihilation of dislocations of opposite sign. The extent of softening depends on the temperature and time, and eventually leads to a network of more-or-less two-dimensional dislocation sub-boundaries surrounding regions of perfect crystal. The latter process is sometimes called polygonisation. The sub-boundaries still represent obstacles to dislocation motion, while *the deformed grain morphology remains unchanged*, so that the associated softening is relatively limited. To achieve maximum softening, it is necessary to raise the temperature to a level where recrystallisation becomes possible. The minimum temperature necessary depends on the alloy and the degree of cold work, but is generally around 0.5 *Tm*, where *Tm* is the absolute melting temperature (solidus for an alloy). New grains with low dislocation density and a relatively equiaxed morphology *nucleate and grow* in the deformed matrix, leading to a fully recrystallised structure when the process is complete, that is, when the cold worked regions have been totally consumed. The density of recrystallisation nuclei is greater the larger the amount of prior strain, while extended holding times and higher annealing temperatures lead to a reduction in the number of grains, and therefore the total grain boundary area, by the grain growth phenomenon. Certain grains grow at the expense of others by boundary migration. The increase in grain size is accompanied by additional softening. Grain refinement is possible when these parameters are appropriately controlled.

Table 14-1-2: :
The different stages of softening during static annealing, Tm is the melting point in Kelvins

I: Cold working	II: Recovery, T<0.5 Tm	III: Recrystallisation T ≈ 0.5 Tm	IV: Grain growth, T>0.5 Tm
High dislocation density.	Decrease in dislocation density, polygonisation	**Nucleation and growth** of new grains with low dislocation density.	Reduction in the number of grains.
High hardness, low ductility.	Slight softening.	Marked softening, depending on the final grain size.	Marked softening, depending on the final grain size.

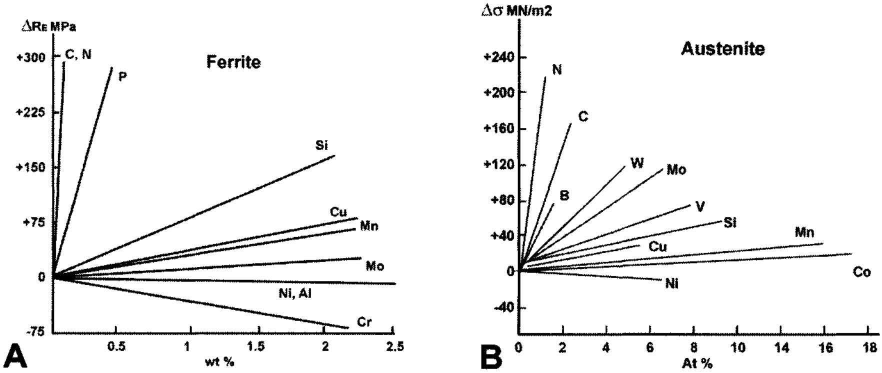

Figure 14-1-3:
A) Solid solution strengthening in HSLA type ferrite-pearlite steels.
B) Solid solution strengthening in austenite. [Pic78].

A similar result can be obtained when the initial dislocation-rich structure is produced by warm or hot working, and in practice, grain refinement is usually achieved by controlled thermomechanical processing cycles, often by the hot rolling of materials under conditions where concomitant precipitation prevents grain growth. In this case, the recrystallisation process can be either *dynamic* (during deformation) or *static* (after deformation or between passes).

Solid solution strengthening

The presence of alloying elements in interstitial or substitutional solid solution can cause strengthening. Substitutional alloying elements whose atomic size is different to that of the solvent metal locally distort the crystal lattice. The resultant elastic stress fields interact with those around dislocations, requiring a higher applied stress for glide to continue. In the case of interstitial solutes, the local lattice distortion depends on the size and shape of the interstices and the type of atom concerned. A carbon atom in an octahedral interstice in fcc iron induces a symmetrical stress field, whereas the same atom in a tetrahedral site in bcc iron generates a non-symmetrical stress field. The non-symmetrical distortion due to interstitial atoms in the body-centred tetragonal lattice of martensite produces a strengthening effect much larger than that for normal solid solution strengthening.

It can be energetically more favourable for certain alloying elements to position themselves at dislocations. For example, this is the case for interstitial elements such as carbon and nitrogen, whose mobility allows them to diffuse to dislocations, where they form a so-called Cottrell atmosphere, which tends to pin the dislocation, impeding its movement, since if it breaks away, the overall energy of the system is increased. This is the cause of the strain-aging phenomenon observed in extra mild steels. Nitrogen can diffuse to dislocations at ambient temperature, while carbon diffusion becomes significant above about 100 °C. A higher stress is required to move the dislocations, but once they have torn free from their atmosphere they can glide under a lower stress, leading to a yield drop. This effect is used in the bake-hardening steels, whose name derives from the fact that the atmospheres form during the baking treatment used to cure paint coatings. At medium temperatures, from 200 to 400 °C, the interstitial atoms are sufficiently mobile to catch up with the dislocations again when they are held up by obstacles. Under these conditions, a repeated series of yield drops can be observed during a tensile test. The phenomenon is described as dynamic strain aging and is also known as the Portevin-Le Chatelier effect [Cah83].

The solid solution strengthening effects of common alloying elements in ferrite are well established (Fig. 14-1-3 A). Unfortunately, the elements with the greatest strengthening effects (C, N and P) have very low solubilities, so that their practical interest is small, except when trapped in supersaturated solid solution, as in the case of martensite. The situation for austenite is illustrated in Figure 14-1-3 B. The most efficient strengtheners are again the interstitial elements, whose solubilities remain relatively low and which can form unwanted precipitate phases. The most potent substitutional elements (W, Mo, V) are ferrite stabilisers, so that their concentrations must often be limited for this reason.

Precipitation hardening

Particles of a second phase generally act as obstacles to dislocation motion. The nature of the interaction depends on the mechanical properties of the precipitate phase, together with the crystal structure and orientation. Matrix dislocations may shear precipitates that are coherent if their size and shear stress are sufficiently small. A large lattice mismatch may induce coherency stresses that interact with dislocations, providing a contribution to strength. In the case of incoherent particles, since the slip planes are not continuous, dislocations must loop round the precipitates, by the classical Orowan mechanism, or climb over them at high temperatures. The stress necessary for looping is inversely proportional to the particle spacing. For coherent precipitates that are stronger than the matrix, the stress necessary for shear increases with particle size, so that above a critical dimension looping becomes easier, since for a constant volume fraction the distance between particles is greater the larger the precipitate diameter.

The yield stress of the material therefore depends on the size, strength, volume fraction and coherency of the precipitate phase. For example, in martensitic steels, heat treatment in the range 500–600 °C can cause the continuous precipitation of coherent carbides, provided that the temperature-time combination is not excessive. The process is often referred to as *secondary hardening*, since it occurs after the primary hardening due to the martensite transformation and offsets the softening associated with the reduction in interstitial solution hardening. The maximum hardness is obtained when the carbide particle size is about 10 nm. Further particle coarsening (overaging) leads to a rapid loss in strength. The high strength resulting from precipitation hardening is often difficult to maintain at high temperatures, since the precipitates coarsen rapidly and lose coherency, and may even begin to redissolve. An exception concerning phases whose size remains stable due to high coherency is described in § 20-3.

Even at low temperatures, coarse second phase particles have only a limited strengthening effect, particularly when they are intrinsically weak. This is true for pearlite, for ferrite islands in duplex stainless steels, and for secondary carbides in austenitic materials.

Toughness

At ordinary temperatures, there are two basic ways in which a crystalline material can react under heavy loading ; by shear, generally involving the movement of dislocations, or by decohesive failure, often termed cleavage, particularly when it occurs along clearly defined crystal planes. Pure shear is associated with high ductility, with necking down to a fine point in a tensile test. In contrast, pure cleavage gives zero reduction in area, that is, brittle behaviour. Fortunately, the stress necessary for cleavage is usually higher than that for shear in most defect-free metallic materials, but in non-compact crystal structures (other than fcc and cph), this may no longer be true at low temperatures. However, cleavage can be promoted in conditions where dislocation movement is inhibited, such as under very high strain rates or strongly triaxial loading. The latter situation exists at the tip of a notch or microcrack (for example, caused by the fracture or disbonding of a hard brittle particle, by fatigue, by gas evolution, etc.). The increase in stress associated with strain hardening can eventually lead to local decohesive failure at such defects, so that many metals show at least a small amount of brittle fracture. Ductile fracture absorbs a large amount of energy, whereas pure brittle failure, once initiated, can be self propagating.

The tendency of a material to fail in a more-or-less ductile or brittle manner is called its toughness. An indication is given by the reduction in area at failure in a tensile test, but it is usually measured under conditions where cleavage fracture is promoted by the presence of a machined notch or fatigue crack. The most common test is the Charpy V-notch impact test, in which the standard specimen is struck opposite the notch by a heavy falling pendulum. The toughness is expressed in terms of the kinetic energy absorbed by the fracture. A more rigorous technique is fracture toughness testing, in which a sharp crack is produced in fatigue and then extended under monotonic loading until the appearance of an instability in the load-displacement curve. The fracture toughness is expressed in terms of the stress σ and crack length a at the onset of unstable propagation. The stress intensity factor K ($= \sigma\sqrt{a}$) is given in units of $\mathrm{MPa}.\sqrt{\mathrm{m}}$. The fracture toughness is generally inversely proportional to the yield strength (*cf.* Figure 17-2-4) and the higher its value, the larger the specimen required for a valid measurement, different criteria being used depending on the type of behaviour observed.

In a brittle material, there is no plastic deformation at the crack tip, which remains sharp. The increasing elastic stress concentration induces cleavage, generally along preferred crystal planes, or possibly along grain boundaries. The resulting fracture surface is strongly facetted (Figures 7-1-6, 14-1-5 B and 21-4-7 A). The absence of plastic work leads to a low overall energy dissipation.

In a ductile material, the stress concentration at the crack tip causes the emission of dislocations, leading to blunting and reduction of the local stress concentration. The load must

Figure 14-1-4:
Schematic Charpy impact-temperature curves for different types of stainless steel.
Adapted from a Ugine document, Arcelor Group.

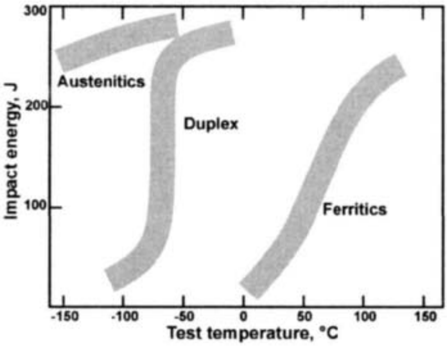

be increased to produce further propagation. Some cleavage fracture usually occurs at locally brittle points such as inclusions or hard precipitate particles. However, the ductile metal in between stretches plastically and thins down to form narrow necks. The resulting fracture surface consists of ductile dimples, with the brittle particles situated in their centres. A large amount of energy is dissipated during fracture due to the extensive plastic work.

The mobility of dislocations depends on the crystal structure and is highly temperature sensitive in bcc structures, where cross-slip plays an important role. Large differences in fracture energy can be observed depending on the temperature, with a transition from ductile to brittle behaviour as the temperature decreases. The transition is often close to ambient temperature for carbon steels (*cf.* Figure 17-2-2 for the effect of carbon), the fracture mode being mixed over a certain range of temperature. This is illustrated in Figure 14-1-4, where the energies at 20°C range from 20 to 70 J. The relative proportions of ductile and brittle fracture areas vary in the transition zone. Figure 14-1-5 shows schematic impact strength-temperature curves for austenitic, duplex and ferritic stainless steels. Face-centred-cubic austenitic structures do not show a ductile/brittle transition, remaining ductile at all temperatures.

In order to improve toughness, brittle precipitate particles should be avoided, particularly at grain boundaries, while the facility of cross-slip depends on the composition and is enhanced by the presence of nickel.

> *Spectacular examples of brittle fracture occurred in certain of the Liberty ships built with all-welded hulls during the second world war. Fractures initiated at low temperatures in the North Atlantic were able to propagate right through the structure, the vessel breaking in two.*
>
> *The tragic case of the Titanic, which sank on its maiden voyage in 1912, is another illustration. The steel employed, which represented a standard quality for the time, tore in a brittle manner in 2 °C water when the ship hit an iceberg. The sister ship Olympic remained in service for 20 years [Fel98]. The development of steels with*

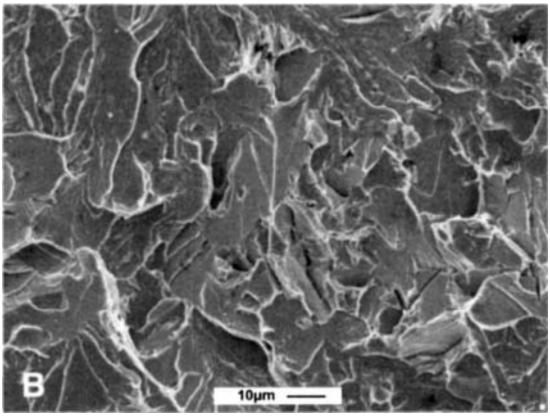

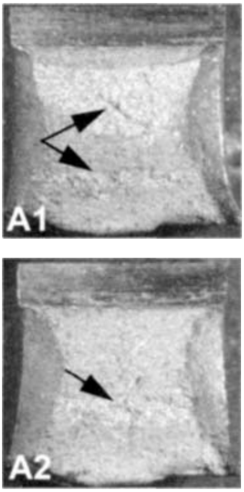

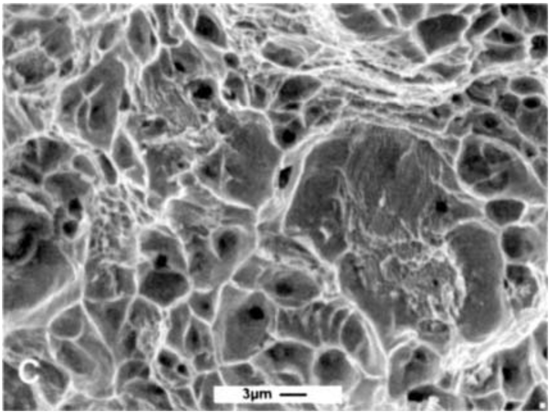

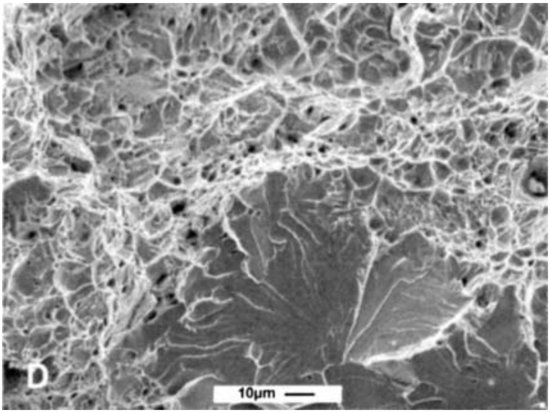

Figure 14-1-5:
Charpy fracture surfaces for a 1035 (C35E4) ferrite-pearlite steel.
A1, A2) Standard 1 cm^2 cross-section specimens broken at 20 °C, showing bright brittle zones (arrows) and dark ductile zones.
B) Scanning electron micrograph of the brittle zone, showing flat areas of cleavage radiating from a central point and forming a so-called river pattern. The deep grooves correspond to grain boundary fracture.
C) Scanning electron micrograph of the ductile zone, showing dimples in many of which a precipitate particle is clearly visible. One large dimple contains a region of pearlite.
D) Scanning electron micrograph of the transition between the ductile and brittle zones, revealing the difference in size of the two fracture morphologies.
Courtesy INPG, Grenoble, Fr.

improved toughness in the second half of the 20th century enabled their safe use in severe low temperature applications such as ice-breakers and arctic pipelines.

Formability

Formability is the ability of a material to be shaped by processes such as deep drawing, bending or rolling. It is greater the lower the yield strength and the greater the capacity to undergo plastic strain without fracture. Strain hardening is generally an advantage provided that it is not excessive, since it prevents local thinning (necking). Indeed, this is the principle of the so-called TRIP steels (TRansformation Induced Plasticity), in which strain-induced martensite formation maintains a high work hardening coefficient. While the intrinsic ductility of the material is of prime importance, forming behaviour can be impaired by the presence of inclusions that are either brittle or have weak interfaces. Ductile inclusions that can deform with the matrix are generally harmless, whereas hard and brittle phases, such as carbides, should be avoided. The inclusion population (cleanness) is determined essentially by the melting and refining practice, which must be carefully controlled (*cf.* § 15-4) [Phi02].

Hardness

The macroscopic hardness of a material provides a measure of its flow stress for a fixed amount of strain determined by the indenter geometry. The indenter is generally either a pyramidal diamond or a hard steel sphere, which is pressed into the specimen under a predetermined load. For a valid measurement of overall hardness, the volume beneath the indenter must contain a representative distribution of the different microstructural constituents present. The hardness of individual constituents can be evaluated in the same way with the aid of a microhardness indenter. Many phases commonly found in steels are very hard (Appendix 22-8). Indeed, their hardness is often used to advantage by embedding them in a relatively softer matrix (*e.g.* cast irons) or in a binder (*e.g.* tool steels) (*cf.* § 21-2). The behaviour of the material as a whole is determined by the properties of the particles and matrix and by the cohesion between them. High hardness generally confers good resistance to abrasive wear.

14-2 The effects of alloying elements

"Residual" elements

Commercial steels generally contain small amounts of many different elements, often considered as impurities or "tramp" elements. Some are introduced by contact with the atmosphere during melting and hot processing. They include oxygen, nitrogen and hydrogen, and can be present in solution or as compounds. Others, such as manganese, silicon, aluminium, magnesium and calcium, are deliberately used during refining of the liquid metal to remove oxygen and/or sulphur. The oxides and sulphides formed are mainly transferred to the slag, but small excess amounts of these additions can remain in the metal. Manganese is often present in the raw materials and acts as a mild deoxidant, producing discontinuous MnO inclusions (and also sulphides). It prevents the formation of more harmful FeO at grain boundaries, but not the generation of CO. The evolution of CO bubbles during solidification causes frothing of the liquid and steels produced in this way are known as *rimming* grades. This can be prevented by the use of a more powerful deoxidant, such as silicon or aluminium. The steels are then said to be *killed*. Residual oxides containing these elements can be retained in the steels and represent a potential source of micro-cracks. Killed steels are more homogeneous, but the presence of higher carbon and silicon contents makes them harder and more difficult to process, and they are also more expensive.

Many residual elements are contained in the raw materials (*e.g.* Si, Al, P, As, S) and scrap (*e.g.* Ni, Cr, Cu, Sn) used to produce the steel. Lead, tin, antimony and arsenic are known to have deleterious effects, embrittling grain boundaries after welding or tempering [Gut77].

Deliberate micro-additions

A number of elements are added deliberately to steels in small amounts, from a few tens of ppm to the order of 1 %. Except for the interstitials, they have little influence on the distribution of the major phases. They can have numerous different effects, which are often interactive. Most of the mechanisms involved have already been discussed and are recalled briefly below to facilitate the interpretation of the summary table given in Appendix 22-7.

- Precipitation in the liquid phase (*e.g.* during solidification). Elements such as titanium and niobium have very low solubilities in the presence of carbon and nitrogen and are often used to tie up these species in a relatively harmless form. Manganese is often employed in a similar manner to scavenge sulphur. The formation of stable phases in the liquid can modify the solidification process by acting as nucleants.
- Precipitation due to interdendritic segregation, with the formation of minor phases at the end of solidification. Sulphur and phosphorus tend to segregate markedly in the interdendritic regions, leading to low incipient melting points and the risk of hot-shortness during processing. The presence of sufficient manganese will prevent sulphur segregation by forming MnS.
- Segregation to grain boundaries in the solid state of insoluble elements such as phosphorus, boron and sulphur, sometimes leading to precipitation by interaction with rapidly diffusing species, such as nitrogen (*e.g.* BN formation). Boron is believed to enhance grain boundary cohesion and sulphur to reduce it, while particles can provide strengthening by acting as pinning points, but when present in excessive quantities, may cause embrittlement.
- Precipitation during the tempering of martensite. Secondary hardening is produced by the precipitation of a fine dispersion of alloy carbides. The major carbide forming elements, in the order of increasing affinity for carbon (*i.e.* carbide stability), are Mn, Cr, W, Mo, V, Ti, Zr, Ta and Nb.

- Age hardening reactions. Apart from carbides, the addition of small amounts of insoluble elements can lead to precipitation strengthening, for example by copper particles (additions up to 3 % Cu) or intermetallic compounds (*e.g.* Ni_3Ti in maraging steels).
- Effects on quench hardenability. The aptitude of a steel to transform to martensite depends essentially on the Ms temperature and the rapidity of the pearlite and bainite transformations. Except for cobalt and aluminium, limited additions of all alloying elements increase hardenability. Strong carbide forming elements act indirectly, raising Ms due to removal of carbon from the austenite.

14-3 The common alloying additions

Stabilisation of ferrite or austenite

Elements that are liable to significantly modify the phase equilibria in the Fe-C system are considered as major alloying additions. Elements which extend the range of existence of the austenite field are said to be austenite or gamma stabilisers. The typical example, which is used as a reference, is nickel. Elements which decrease the austenite field and extend the range of the δ and α fields are called ferrite or alpha stabilisers. Chromium is considered as the reference in this case. The Fe-Ni and Fe-Cr phase diagrams are given in Figures 3-3-3 and 4-4-2 respectively. Figure 14-3-1 shows the effects of manganese, a gamma stabiliser, and silicon, a ferrite stabiliser, on the Fe-C diagram. The binary phase diagrams between iron and austenite stabilisers show two configurations. The elements Ni, Mn, Co, Pt, Pd, Ru, Rh, Os and Ir form a continuous range of solid solutions with austenite at high temperature, while the gamma field is limited in the systems with C, N, Cu, Au and Zn.

Two general types of binary diagram are also found for alpha stabilizing elements. The gamma loop is completely surrounded by ferrite in the systems with Cr, W, Mo, V, Ti, Si, Al, P, Be, As, Sn and Sb. In the case of S, B, Zr, Ta, Nb and Ce, the extent of the γ field is reduced without extending that of ferrite, being replaced by a two-phase equilibrium between austenite and an iron compound. The effect of the different alloying elements when associated with iron can be understood in terms of their crystal structures. Thus, most elements with fcc structures similar to that of austenite are gamma stabilisers. All the alpha stabilisers either themselves have bcc structures or form bcc compounds.

Nickel and chromium equivalents

In multi-component steels, it is useful to be able to evaluate the tendency to form ferrite or austenite by reference to the influence of chromium and nickel. Empirical formulae have been derived in which the ferrite or austenite stabilising effects of the different elements are expressed by a weighting coefficient referred to chromium or nickel. The sum of the ferrite-stabilising terms is called the chromium equivalent and that of the austenite stabilising terms the nickel equivalent. It is then possible to plot a two-dimensional diagram Ni_{eq} versus Cr_{eq} showing the ranges of existence of the different phases at ambient temperature

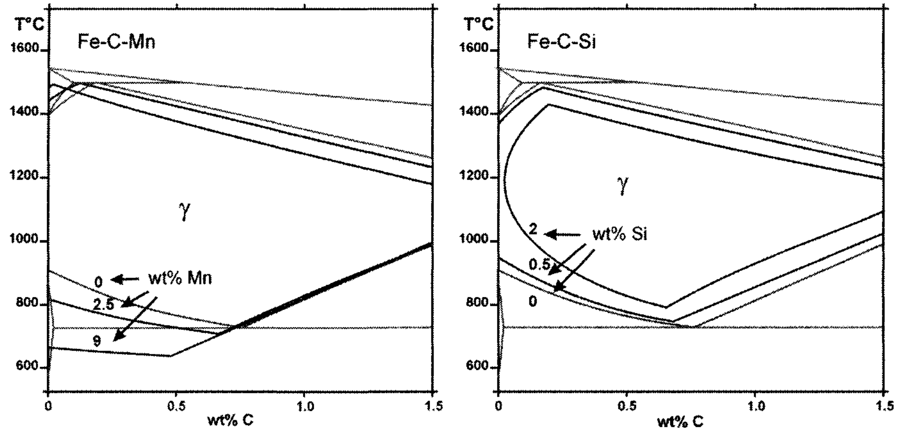

Figure 14-3-1:
Calculated isopleths showing the effect of manganese and silicon additions on the austenite phase field in the Fe-cementite-Mn and Fe-graphite-Si systems. The reference system (0% addition, grey) is Fe-cementite. Silicon is a ferrite stabiliser and reduces the extent of the austenite field. Manganese is a gamma stabiliser and extends the austenite field. The effects are quite significant even at low concentrations.

(Figure 14-3-2). The corresponding phase fields are shown by the black lines, which are valid for a particular austenitising temperature. Another important factor in practice is the tendency to form martensite on quenching, which depends on the Ms and Mf temperatures. This is represented in the diagram by the grey lines.

Diagrams of this type were originally designed to predict the structures of welds. The first one was that of Schaeffler in 1949 [Sch49], subsequently modified by Delong in 1960 [Del60] and then in 1973 [Lon73]. Figure 14-3-2 is a frequently used version of the Schaeffler diagram [Lac93]. The various diagrams differ chiefly by the number of elements included in the formulae for the equivalents and the values of their corresponding coefficients (*cf.* Appendix 22-3). Special equivalent formulae have been adapted for cast microstructures and for different types of alloys, for example, 12 % Cr steels and duplex stainless grades [Kra80], [Cam00]. A recent comparison between the predictions of these formulae and thermodynamic calculations showed excellent agreement for ferrite stabilizing elements, but relatively poor concordance for austenite stabilisers, particularly manganese [Ind02].

Another effect of chromium is to promote the formation of embrittling σ phase in the temperature range from 500–820°C (*cf.* Fe-Cr phase diagram, Figure 4-4-2). Other elements, such as silicon and molybdenum, stabilise sigma phase, extending its range of existence. Several elements stabilise both ferrite and sigma and there is a certain tendency to confuse the two effects. In fact, σ phase is an electron compound, whose existence is extremely sensitive to the average number and configuration of shared electrons. At lower temperatures, below about 500 °C, high chromium contents lead to the decomposition of

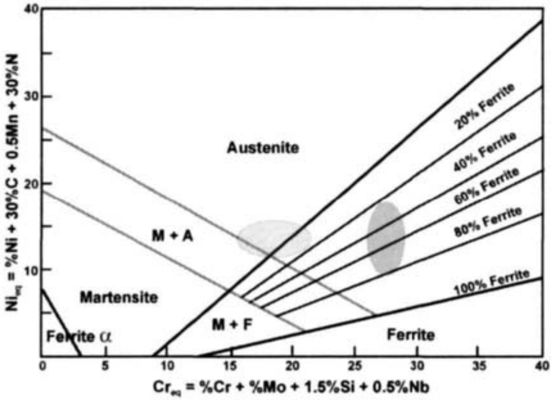

Figure 14-3-2:
Schaeffler diagram. The black lines represent the phase field boundaries, while the grey lines indicate the region where either the Mf point (lower line) or both the Mf and Ms points (upper line) lie above ambient temperature. Between them, transformation to martensite is only partial.

ferrite into two bcc phases, α and α' (or α-Cr), by either a classical or spinodal mechanism, depending on the composition. This latter tendency is not a general characteristic of the ferrite stabilising elements.

The classification of steels

There are many different types of steels and their classification is not simple. In keeping with the general theme of the present work, the criterion chosen here is that of a common room temperature microstructure within each category. In this respect, the empirical Schaeffler and Delong diagrams provide excellent guides.

- *Mild steels and micro-alloyed* (HSLA) steels have ferritic structures close to that of pure iron. They are very ductile and have good corrosion resistance. They are situated in the a ferrite region in the Schaeffler and Delong diagrams. They are widely employed for sheet forming operations and are often used in the coated condition. The HSLA grades combine high strength and toughness and are also manufactured in the form of long products for structural applications.
- *Hardenable steels* include low alloy grades that can be transformed to martensite, bainite or pearlite by controlled cooling from the austenite field. They are situated in the region labelled Martensite in the Schaeffler and Delong diagrams. The matrix of high carbon and alloy grades such as the high speed and tool steels also depends on heat treatment, but contains additional primary and secondary carbides. These materials are manufactured in the form of long products, for abrasion-resistant applications, such as cutting tools and bearings.
- *The martensitic stainless steels* have a chromium content sufficient to ensure good corrosion resistance (typically 12–17 %) while remaining within the gamma loop at high temperatures. They are situated in the M+F or martensite regions of Figure 14-3-2 depending on the carbon (and sometimes nickel) contents. They are used for applications requiring a combination of high strength, hardness and corrosion resistance, such

as engineering components, high temperature bolting, tooling, cutlery, etc. The precipitation hardened (PH) martensitic stainless steels are strengthened by fine particles of copper or intermetallic compounds. They are in fact stainless maraging grades.

- *The austenitic stainless steels* contain sufficient chromium to ensure good corrosion resistance, together with gamma stabilising elements, especially nickel, to promote an austenitic structure. Their compositions lie mainly within the light grey oval shown in Figure 14-3-2. They find many applications for equipment in the food and pharmaceutical industries, for domestic appliances, cooking utensils, sinks, etc.
- *The ferritic stainless steels* contain essentially alpha stabilising elements, particularly chromium, with compositions such that they lie outside the gamma loop in the phase diagram. They are situated in the ferrite field in the Schaeffler and Delong diagrams.
- *The duplex stainless steels* are high chromium, nickel-containing grades whose structure typically contains roughly equal proportions of ferrite and austenite. They are represented by the dark grey oval in Figure 14-3-2. They are employed for parts demanding a combination of high strength and excellent corrosion resistance for severe petroleum, chemical and nuclear engineering applications.
- *The heat-resisting alloys* and iron-containing superalloys are austenitic materials that maintain good strength and corrosion resistance at high temperatures. They find a wide range of applications in the fields of high temperature processing, heat treatment, power generation, aircraft and automobile engines, etc. This category is often at the limit of what can be reasonably termed steels and covers a variety of alloys and structures, each optimised for a particular high performance utilisation.

The roles of the different alloying elements are summarised in Appendix 22-7).

15

Solidification macrostructures

The term macrostructure is used to designate a structure on a scale visible to the naked eye. Macrography is extensively used, in particular, to study the distribution of the solidification zones in as-cast metals. For example, many ingots show two major solidification zones, corresponding to either columnar crystals or equiaxed grains. Indeed, this distribution is often observed, whatever the volume of solidified material, from large forging ingots to narrow weld seams.

15-1 Solidification of steels

Most steel products begin life in the liquid state, during the melting and refining processes, where their composition is adjusted and unwanted elements and inclusions are removed. In the case of castings, the liquid is solidified in a shaped mould to produce a part with a geometry very close to that of the final component. Castings are used to obtain complex parts that would be difficult or expensive to produce by forming and machining, such as pump and valve housings, turbine wheels and blades, propellers, etc. With the exception of powder metallurgy materials, other products are solidified in the form of ingots or continuously cast billet, bloom or slab, for subsequent processing by forging and/or rolling. Ingot casting is employed for very large forgings and for special materials which cannot be produced by continuous casting, for either technical or economic reasons. Continuously cast slab, for processing to flat products, can range from 5 to 40 cm in thickness, with widths up to 2.5 m. Square bloom varies from 15 to 45 cm, while smaller sections (typically 10 to 20 cm) are usually referred to as billet. The direct casting of 3–5 mm thick strip, completely eliminating the need for hot rolling, is currently in the pre-industrialisation stage [Bir98].

For certain special applications, a primary ingot is produced in the form of an electrode and is then remelted by either the vacuum arc remelting (VAR) or electro-slag remelting (ESR) process. These processes produce further refining, either by exposing liquid droplets to vacuum or by passing them through a carefully chosen molten slag. However, their main purpose is to allow solidification under closely controlled conditions, leading to a finer structure with more uniform composition.

The solidification macrostructure is composed of different types of grains, with their residual segregation patterns, together with various defects, such as porosity, microshrinkage cavities, pipes, etc. In castings, which are used without further processing, other than perhaps a simple stress-relieving treatment, the as-cast structure strongly influences the service properties.

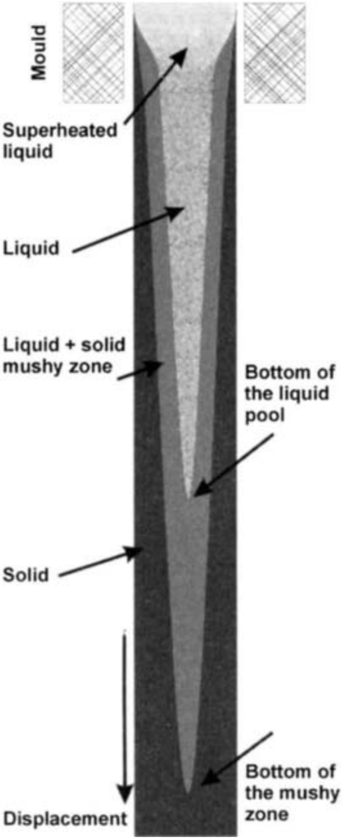

Figure 15-1-1:
Schematic axial section through a continuously cast ingot.

Although ingots and continuously cast materials undergo hot and cold processing, solidification defects, and particularly chemical segregation, are not always completely effaced [Bér97], and can often still be identified in the final product. Careful control of the entire sequence of hot and cold processing and heat treatment cycles is necessary to optimise the final quality.

15-2 Solidification structure of a continuously cast steel

Continuous casting

The idea of continuous or semi-continuous casting of metals dates back almost a hundred years, but the application of the process to steels was developed essentially in the second half of the 20th century [Wol92], and is today employed for nearly 98 % of all steel.

The liquid metal is teemed onto a starting block in a water-cooled bottomless mould, generally made of copper. In contact with the mould and starting block, the steel forms a solid skin which serves as a container for the liquid. The starting block and solidifying ingot are withdrawn from the mould at a controlled rate. In the early stages of solidification, the thin skin is supported by a series of rollers and is rapidly cooled by water sprays. Typical withdrawal rates are of the order of a metre per minute. The depth of the liquid pool at the centre can attain 14 metres [Sta82], [Gat95], [Bér96a].

The schematic axial section in Figure 15-1-1 shows the shape of the liquid and solid + liquid *mushy* zones. The latter region, shown in dark grey, consists of a cohesive dendritic skeleton impregnated with liquid. The liquid pool contains suspended solid crystals, except in the superheated top zone.

Figure 15-2-1:
Transverse section of a 205 mm square continuously cast stainless steel bloom. The separation between the outer columnar zone and the central equiaxed region is extremely sharp. This is due to the use of electromagnetic stirring during the casting process.
Courtesy CRU, Ugine Savoie Imphy, Arcelor Group.

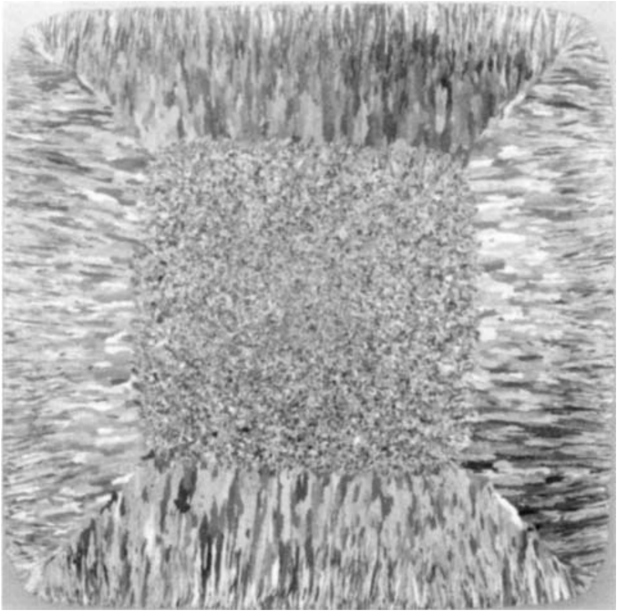

The different solidification zones

Figure 15-2-1 shows the macrostructure of a continuously cast stainless steel bloom. The size, shape and orientation of the grains reveal two distinct zones :

- a central region of fine randomly oriented equiaxed grains
- an outer region of columnar grains, elongated normal to the ingot surface. Careful examination shows that their width increases from the surface to the centre.

A third zone, corresponding to very fine chill crystals, is present at the extreme skin, but cannot be clearly distinguished on the photograph.

In order to understand the formation of this structure, it is necessary to consider various thermal, hydrodynamic and physical-chemical phenomena. Ingot solidification during continuous casting can be analysed as a steady state process in which a given slice evolves as it moves downwards through a temperature field that is fixed with respect to the mould. The first solid crystals form in contact with the mould wall (possibly separated by a thin film of slag). The sudden cooling produces a very thin layer of extremely fine grains, no more than a few millimetres thick, called the chill zone. Slight ripples formed on the surface of the chill zone are caused by oscillation of the mould, which aids the withdrawal process [Bér00]. Figure 15-2-2 shows the dendrite structure in the chill zone, with a dendrite arm spacing that increases with distance from the surface, within a same grain. An oscillation ripple has left a visible mark, due to changes in grain orientations and associated segregation effects.

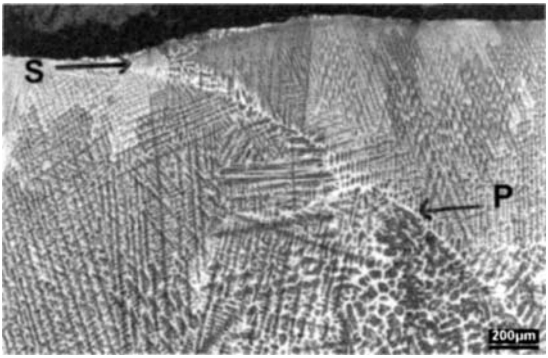

Figure 15-2-2:
Cross section of the chill zone at the surface of a type 304 stainless steel slab, etched with the Lichtenegger-Bloesch reagent. A few millimetres below the surface, the dendrites are four to five times coarser than in the extreme skin. The defect labelled P is the trace of an oscillation ripple, while S is an associated segregation zone.
Courtesy CRU, Ugine Savoie Imphy, Arcelor Group.

The columnar zone is composed of grains that nucleate on those in the chill layer and which grow perpendicular to the solidification front. Grains with certain preferred orientations prevail over others, gradually becoming broader. Even in metals with relatively isotropic crystal structures, particular orientations grow more rapidly and eventually predominate. The solidification front closely follows the liquidus isotherm. Since heat is evacuated from the liquid principally by conduction in the solid phase, the columnar grains grow inwards, leading to an elongated morphology.

The columnar zone is composed of grains that nucleate on those in the chill layer and which grow perpendicular to the solidification front. Grains with certain preferred orientations prevail over others, gradually becoming broader. Even in metals with relatively isotropic crystal structures, particular orientations grow more rapidly and eventually predominate. The solidification front closely follows the liquidus isotherm. Since heat is evacuated from the liquid principally by conduction in the solid phase, the columnar grains grow inwards, leading to an elongated morphology.

> *The anisotropy of the columnar zone may lead to poor ductility during forming, although it can sometimes also be used to advantage, as in the case of the Alnico hard magnetic alloys, where the intensity of magnetisation can be enhanced.*

Relative sizes of the columnar and equiaxed regions

Equiaxed crystals form in suspension in the liquid, with random orientations and no preferred macroscopic growth direction. This implies that the liquid becomes undercooled, due to heat conduction through the columnar layer. Since the liquid also becomes enriched by solute rejection from the solid, the undercooling refers to the local composition. Growth of the equiaxed grains eventually stops the extension of the columnar zone. The origin of the nuclei that give rise to equiaxed grains is still the subject of debate. Many authors believe that they can be formed either spontaneously in the liquid or by fragmentation of dendrites in the columnar zone. Thus, the broken ends of columnar dendrites can be entrained in the liquid by convection currents, and can remain relatively stable if the temperature is not too high. The fragments may partially remelt in the solute enriched liquid or coalesce. As the temperature of the liquid continues to fall, solidification ends by massive heterogeneous nucleation.

The respective proportions of the columnar and equiaxed zones depend on numerous factors. In particular, the temperature range between the liquidus and solidus is important, and is determined by the alloy composition. The degree of superheating of the liquid and the efficiency of cooling also have a strong influence, together with the hydrodynamic conditions, involving either natural convection or stirring. The columnar zone is thicker the greater the amount of superheating above the liquidus [Bér96a].

Since the columnar zone is usually not desirable, its extent can be reduced by lowering and homogenising the temperature in the liquid pool. This is commonly achieved by the use of *electromagnetic stirring*, associated with efficient water spray cooling of the ingot surface. The stirring also leads to greater chemical uniformity in the liquid, limiting segregation effects.

15-3 Solidification structures in large conventional ingots

Grain structure

The solidification structures observed in conventional ingots are more complicated than in continuously cast products, due to the absence of a steady state regime. The time necessary for complete solidification depends on the ingot size and can vary from one hour to several days. The local solidification time (*i.e.* the time taken for a given point to cool from the liquidus temperature to the solidus) can be several tens of hours, for example 35 hours at the centre of a 180 tonne ingot [Van98]. As in continuous casting, three characteristic zones can be distinguished in terms of the size, shape and orientation of the grains, corresponding to the chill layer, columnar growth and equiaxed regions, although the latter can be subdivided, as shown in Figure 15-3-1 [Les89].

The columnar layer, perpendicular to the surface immediately beneath the chill zone, varies in thickness from the top to the bottom of the ingot. The extensive equiaxed zone shows a variety of grain sizes and morphologies, different regions being distinguished in the simplified schematic representations.

The difference in density between the liquid and solid causes the equiaxed grains to slowly settle. They accumulate at the bottom of the ingot, forming a sedimentation cone. This process is believed to occur at a relatively early stage of solidification. The oldest dendrites have become *spheroidised* and have lost their characteristic dendritic structure (zone SZ in Figure 15-3-1). As cooling continues, the grains coarsen and eventually come totally in contact with one another when the last liquid is exhausted (zones CEZ and H in Figure 15-3-1).

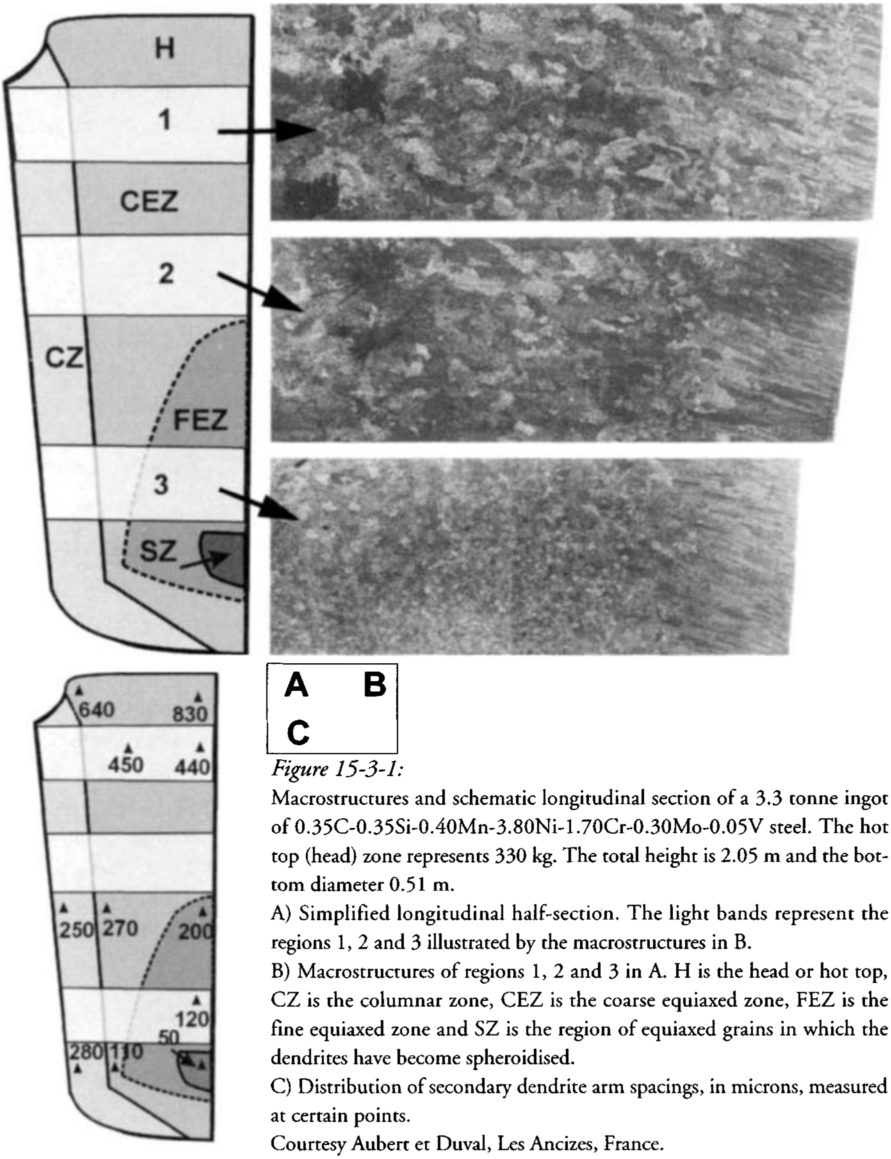

Figure 15-3-1:
Macrostructures and schematic longitudinal section of a 3.3 tonne ingot of 0.35C-0.35Si-0.40Mn-3.80Ni-1.70Cr-0.30Mo-0.05V steel. The hot top (head) zone represents 330 kg. The total height is 2.05 m and the bottom diameter 0.51 m.
A) Simplified longitudinal half-section. The light bands represent the regions 1, 2 and 3 illustrated by the macrostructures in B.
B) Macrostructures of regions 1, 2 and 3 in A. H is the head or hot top, CZ is the columnar zone, CEZ is the coarse equiaxed zone, FEZ is the fine equiaxed zone and SZ is the region of equiaxed grains in which the dendrites have become spheroidised.
C) Distribution of secondary dendrite arm spacings, in microns, measured at certain points.
Courtesy Aubert et Duval, Les Ancizes, France.

Segregation on the scale of the ingot

The dendrite skeleton forms at a temperature where solute exchanges are highly active. Extremely mobile species such as carbon, nitrogen and oxygen diffuse readily in the solid already formed and the conditions are far from those corresponding to the Scheil-Gulliver (S-G) model (*cf.* Chapter 5). However, thermodynamic equilibrium is not attained.

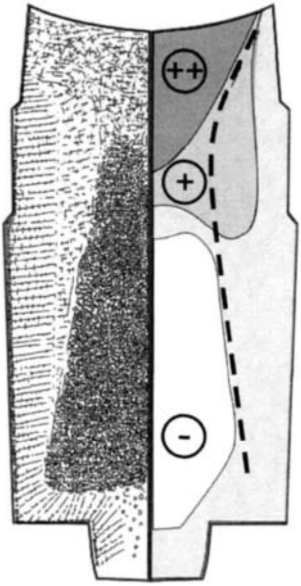

Figure 15-3-2:
Carbon macrosegregation in a 65 tonne, 3.5 m high and 1.8 m in diameter, Fe-0.22C-0.18Si-0.25Mn-1.14Ni-1.6Cr-0.19Mo steel ingot, in which solidification lasted 20 hours.
The left hand side of the diagram is a sketch of the grain structure, showing the columnar zone, a globular equiaxed sedimentation cone and a dendritic equiaxed region at the top of the ingot. An intermediate zone between the columnar and equiaxed regions can also be seen at mid-height, where the grains are neither oriented nor equiaxed.
The right hand side of the diagram is divided into regions where the carbon content is approximately uniform, the signs "–", "+" and "++" indicating negative and positive differences compared to the nominal composition. The maximum difference is of the order of 20% of the nominal value.
Additional carbon fluctuations associated with V-type segregations (*cf.* § 15-4) are not indicated.
Drawing adapted from [Maz95], INPL, Nancy.

Certain substitutional alloying elements, such as manganese, chromium and nickel, have lower diffusivities, but since their equilibrium concentrations are similar in the liquid and solid, they show little tendency to segregate. Silicon, sulphur and phosphorus have low partition coefficients and tend to concentrate in the liquid. At the end of solidification, the final liquid can often attain eutectic compositions, with incipient melting temperatures below 900°C.

Dendritic segregation thus produces a diffusion layer in the liquid extending several microns ahead of the solidification front. Solute redistribution in the liquid occurs on a macroscopic scale by convection, due to temperature and composition gradients, and leads to macrosegregation effects. In the case of solutes whose partition coefficients are less than one (*i.e.* which segregate to the liquid), such as sulphur and carbon, their concentrations in the dendrites formed at the beginning of solidification are lower than in the alloy as a whole. The schematic diagram in Figure 15-3-2 shows the ingot regions where the concentration of carbon is less than and greater than that in the initial liquid. It can be seen that the sedimentation cone, where the first equiaxed dendrites have settled, contains less carbon than the nominal composition, the carbon segregation being said to be negative [Fle76], [Ols86], [Maz95].

Such segregation on the scale of the ingot is called major segregation. It is considered as a defect only if it affects the subsequent response to heat treatments. For example, a large difference in composition between two regions could lead to local changes in thermal contraction behaviour, enhancing stresses due to temperature gradients, and might even cause cracking in severe cases.

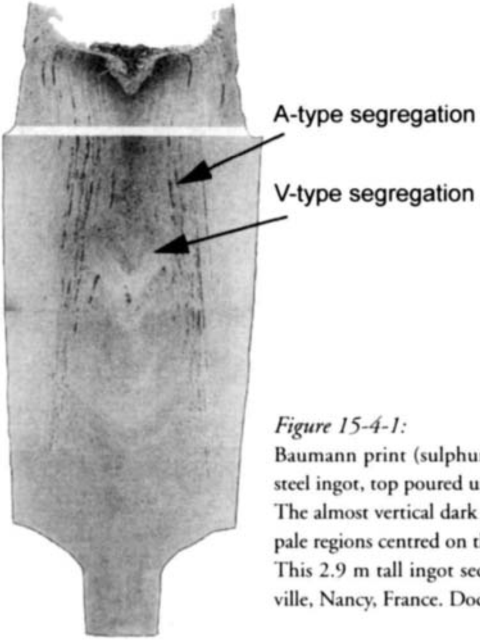

Figure 15-4-1:
Baumann print (sulphur image) of a 35 tonne, killed semi-hard alloy steel ingot, top poured under vacuum.
The almost vertical dark lines are traces of A-type segregation, while the pale regions centred on the ingot axis are V-type segregations.
This 2.9 m tall ingot section is on display in the Musée du Fer at Jarville, Nancy, France. Document reproduced from [Pok67].

15-4 Quality of solidification structures

Mesosegregation

All ingots, including those produced by the ESR and VAR processes, together with continuously cast products, can show segregation on a scale intermediate between the dendrites and the structure as a whole, provided that their dimensions are sufficiently large (at least 100 mm). This is sometimes termed mesosegregation [Hul73], [Jac83], [Les89]. The segregated regions have an elongated shape, with a narrow dimension of the order of 10 mm, in which the composition changes abruptly. Three types of mesosegregation can be distinguished. The most clearly visible are *A-type segregations*, sometimes called dark veins, due to their appearance in a longitudinal section. They occur beyond the columnar zones, forming rings in a horizontal section, starting at the top of the ingot (Figure 15-4-1). *V-type segregations* are localised in the central equiaxed zone (Figure 15-4-1). *Channel type segregation* is a density-driven phenomenon. The filamentary segregated regions appear as round spots in a horizontal section, and for this reason are often referred to as freckles. A common feature of the segregated zones is a local population of abnormal dendrite sizes, often associated with an exceptionally high volume fraction of secondary eutectic phase and micropores. Finally, *axial segregation* occurs along the symmetry axis of the cast product, and is also associated with a sudden change in composition and an abnormally high proportion of eutectic-type minor phase.

Both macrosegregation and mesosegregation involve solute transport over relatively long distances, by various mechanisms. The transport speeds remain small, similar to the rate of advance of the isotherms, typically of the order of a few microns per second.

The segregation resulting from the sedimentation of equiaxed grains (*cf.* Figures 15-3-1 and 15-3-2) is a special case. The solid crystals are heavier than the liquid and fall slowly downwards. Their solute content is generally lower the earlier their formation in the solidification process

Another type of transport is associated with currents of interdendritic liquid in the mushy or pasty zone. These currents can have several driving forces :

- the change in volume associated with solidification is the principal origin of inverse segregation;
- gravitational forces due to temperature- or composition-based density gradients;
- deformation of the skeletton formed by the partially solidified dendrites, which can act like a sponge. Interdendritic liquid can be either absorbed or expelled, depending on external stresses. For example, thermal stresses can arise due to differences in cooling rate between the outside and centre of the ingot. The partially solidified dendrite structure remains mechanically unstable until the fraction of solid exceeds about two thirds. The deformation may occur suddenly, by shear propagation, and this is one of the explanations proposed for V segregation in ingots and continuous castings [Fle76]. In both static ingots and continuously cast products, the tendency for V segregation increases with the carbon content of the steel [Eng83], [Bir85].

Macro- and mesosegregation can have serious consequences [Jac83], [Wei79]. Their scale makes subsequent homogenisation difficult. These defects occur principally in high carbon steels and in grades with large amounts of heavy elements (Mo, W, etc.), particularly when the ingot dimensions lead to very slow solidification (*e.g.* large forging ingots or rolling mill rolls) [Sha86]. Mesosegregation phenomena prevent the use of continuous casting for the production of carbon-rich bearing steels [Bir85]. Numerical models have been developed for simulating the combined effects of thermal, hydrodynamic and physical-chemical phenomena on segregation [Van98], [Com98].

Inclusions

The term inclusion is used to describe an undesired non-metallic particle in a solidified product. Exogenous inclusions are ones which are simply entrained in the liquid, originating from refractory linings or slag layers. They are usually avoided by appropriate measures during casting (special pouring configurations, dams, skimmers, filters, etc.). Endogenous inclusions are ones formed by precipitation from the liquid, due to the presence of impurities, particularly oxygen, but also sulphur, phosphorus and nitrogen [Gat95]. Large inclusions can have an extremely detrimental influence on fatigue strength [Met86]. Inclusion contents can be controlled by good melting practice to reduce impurity levels.

Low inclusion contents, corresponding to high cleanness, are particularly important in very thin products, such as foil or fine wire (dimensions of the order of ten microns can be achieved, about ten times smaller than the diameter of a typical hair).

Most inclusion phases form in the liquid and are usually less dense than the metal and can be floated off into a slag layer before teeming. The teeming configuration is extremely important in this respect. For continuous casting, a vertical mould is preferable, and many modern machines are of the curved type, with a vertical mould and horizontal product removal, which is more convenient, for both space saving and subsequent handling and processing operations.

The majority of inclusions are oxides and the oxygen content in the liquid is a critical factor. The oxygen level is reduced by the addition of strong reducing agents, such as aluminium and silicon, to form their respective oxides, most of which are removed in the slag. Subsequent oxide formation then depends on the affinity of the different alloying and residual elements for the remaining oxygen. Sulphur is also an important impurity and can be controlled by the addition of elements such as manganese, calcium and magnesium. Several categories of inclusion can be distinguished, depending on the liquid metal treatments employed. In particular, the ductility of the inclusions is important, since it determines their behaviour during working, forming and machining operations. Some sulphide inclusions are quite malleable and can often be tolerated. Sulphides frequently have a particular formation mode during solidification (*cf.* § 6-5 and 19-6). In cast irons, inclusions can act as inoculants for spheroidal graphite formation [Ska93].

Porosity

Pores are holes or cavities in the metal. A major cause is the decrease in volume, typically of the order of 10 %, when liquid transforms to solid. Holes are formed when pockets of liquid are isolated inside the solid, for example, in the interdendritic spaces. The size of the pores, or shrinkage cavities, is proportional to that of the original liquid pocket. Small pores, less than about a micron in size, are generally harmless. Larger ones may subsequently be closed during hot working of the cast product. It is interesting to note that pores can sometimes also be a sign of incipient melting, since local liquid formation during excess heating causes an increase in volume, with plastic deformation of the surrounding solid. On subsequent cooling, the difference in volume remains in the form of a cavity.

Many pores are gas bubbles formed by the rejection of certain solute elements from the liquid during solidification. The gases most commonly involved are *carbon monoxide, nitrogen and hydrogen*. The presence of these gases depends on the melting and refining route followed. Blast furnace iron is processed in a basic oxygen converter and initially has a high oxygen content before secondary ladle refining. Even scrap recycled in the electric arc furnace contains some oxygen, due to reaction with air. In both cases, the final oxygen content depends principally on the additions made during the final refining steps (*e.g.* Si, Al). Nitrogen is introduced into steel mainly by reaction with air and its content can be controlled to a certain extent by liquid refining steps such as gas scavenging, vacuum treatments, etc. However, nitrogen is sometimes a deliberate alloying addition in a number of special steel grades. Hydrogen generally has a low solubility in steels, but can be introduced into the liquid at high temperature from moisture. The general hygrometry of the charge materials, refractories and atmosphere is therefore an important factor.

All these elements have much lower solubility in the solid than in the liquid, corresponding to a partition coefficient significantly less than one, so that they are rejected into the liquid during solidification. Their concentration in the liquid rises, and if the saturation point is reached, gas bubbles are formed. In fact, a certain degree of supersaturation is required for bubble nucleation. The bubble formation and release process can affect the morphology of the columnar solidification front. The bubbles may coalesce, and most of them eventually rise to the liquid surface. However, some may become trapped in the mushy zone, or in places where two solidification fronts meet, especially in complex castings, leading to cavities in the solid.

Typical gas concentrations in liquid carbon steel are of the order of 2 to 4 ppm of hydrogen and 10 to 80 ppm of nitrogen, depending on the process used. Since the solid/liquid partition coefficients for oxygen, hydrogen and nitrogen are much lower for ferrite than for austenite, gas bubble formation is more critical in alloys that solidify chiefly to ferrite. Saturation is reached before the end of solidification, as the gases become concentrated in the remaining interdendritic liquid. At this stage, the dendrite structure can be sufficiently complete to trap the bubbles, which then remain in the solid as micropores.

In the partially solidified structure of the mushy zone, differences in thermal contraction between the solid and liquid can lead to local cracking, or even collapse. The liquid usually fills in the cavities, but cracks can sometimes remain. In continuous casting, the position of the bending and straightening rolls and the pressure they exert can repair this type of defect by high temperature welding.

Inclusion and gas control by secondary refining

Refining

In modern steelmaking practice, the oxygen converter and electric arc furnace perform only rough refining. In the case of the arc furnace, the principal purpose is to achieve rapid melting of the charge. Fine trimming of the composition, including carbon, and control of impurities (oxygen, sulphur, phosporus, nitrogen) are carried out in a separate vessel, often a transfer ladle, in special installations. There are numerous different processes and only the major features will be described here. A more detailed discussion can be found elsewhere [Bér96a].

These processes use various combinations of stirring, slag, gas injection or vacuum treatments, sometimes with additional heating. Carbon can be removed by injecting oxygen, the resulting carbon monoxide being eliminated by stirring, vacuum treatment and dilution. The injection of neutral gas, particularly argon, causes stirring and entrains gas bubbles, helping them to reach the surface (CO and nitrogen). It also enhances the oxidation of carbon by reducing the partial pressure of CO (dilution). Sulphur is removed by metal/slag reaction under highly reducing conditions. Hydrogen removal requires vacuum treatment. Two common processes, almost invariably associated with stainless steel manufacture, are Argon Oxygen Decarburising (AOD) and Vacuum Oxygen Decarburising (VOD).

Remelting

Certain special alloys are often produced by remelting a charge produced by the electric arc and ladle refining route, in a vacuum induction furnace. This can often be considered as an additional secondary refining stage, since volatile impurities and gases can be removed and reactive alloying additions can be made without risk of oxidation (*e.g.* Ti, Al, etc.). Induction furnaces are also commonly used in foundries, where they provide a rapid and compact melting process, generally without refining.

For many special alloys, the metal from the vacuum induction melting (VIM) furnace is cast into an electrode for further processing by consumable electrode remelting. In these processes, the tip of the electrode is gradually melted into a water cooled copper crucible, producing a new ingot in which the solidification conditions can be closely controlled. The principal purpose of remelting is to obtain a sound ingot, with reduced segregation, porosity and other solidification defects. Depending on the type of process, additional refining is also possible. Thus, in vacuum arc remelting (VAR), an electric arc is maintained between the tip of the electrode and the molten pool at the top of the remelted ingot. The arc moves randomly over the electrode tip, which is melted in the form of fine droplets, facilitating the removal of gases by exposure to the vacuum. In electroslag remelting (ESR), melting is caused by resistance heating of a slag layer between the electrode and the ingot. The slag composition is chosen to be in equilibrium with the alloy, while at the same time serving as a refining medium. The liquid metal droplets from the electrode must pass through the molten slag layer before joining the melt pool at the top of the ingot, enabling chemical exchanges to occur. For example, sulphur removal is possible in this way. In some special cases, double remelting may be employed, for example, VAR + VAR, or ESR + VAR. The choice of route depends on considerations outside the scope of the present work. However, it is possible by these means to obtain complex alloys with very low impurity contents and high cleanness, together with uniform chemical composition, for particularly demanding applications (*e.g.* high temperature alloys, *cf.* § 20).

16

Macro- and microstructures of sintered powder products

Sintering is a technique that was used in ancient times to obtain compact iron products after reduction of the ore.

16-1 Sintering

The process

The sintering process came back into the limelight in the twentieth century when technological progress made it possible to use it for the manufacture of cheap near-net shape parts. The range of alloys and composite materials to which it can be applied is growing constantly. A particular advantage is the ability to produce compositions impossible to achieve by conventional melting and working routes, either because the melting point of one of the constituents is too high or due to inappropriate microstructures.

Sintering essentially involves two operations, which can be performed either separately or simultaneously, depending on the case concerned. The first step is to agglomerate the powders to a "green" compact, with sufficient strength to allow subsequent handling. The powders are mixed with a wax-type binder, later eliminated by heating, and hot or cold pressed in a mould to obtain a shape close to the final component geometry. The second step is hot consolidation of the green compact to allow diffusion bonding between the powder particles, leading to an increase in strength and density. The two steps are performed simultaneously when the powders are hot compacted under high pressure. A more sophisticated technique is hot isostatic pressing (HIP), in which the powders are placed in a sealed container which is exposed to a gas pressure of the order of 100 MPa in a high temperature autoclave. The container deforms as the powder contracts, making it possible to achieve 100 % theoretical density.

Various mechanisms can be involved in sintering, depending on the type of powder employed. They include self-welding, welding via a chemically inert constituent, and welding due to a constituent that reacts with the base powder. The temperature and holding time must be suitably adapted to achieve adequate densification, without excessive grain coarsening (*cf.* § 5-4).

Sintering is an extremely flexible process, since many metals and alloys can be obtained in the form of powders. It is used chiefly for the economic manufacture of near-net shape parts, with considerable savings on raw materials and machining costs, particularly in the case of components with complicated geometry, such as gear wheels. The process can also be employed to produce composite or porous materials impossible to obtain otherwise, and even materials with built-in composition gradients. The following discussion is illustrated by commercial examples concerning steels and iron-base alloys.

The powders

The principal characteristic of a powder is that it consists of small particles with a high surface area to volume ratio, and therefore a large total surface energy. At sufficiently high temperatures, the system will tend to reduce this surface energy by welding together of the individual particles. This provides the major driving force for sintering. The energy involved is fairly small and depends on the type of powders and their surface condition. The powder characteristics impose the choice of sintering technique and determine the mechanical properties of the compact. A number of common powder types are as follows :

- *Carbonyl iron* (Fig. 16-1-1 A) is obtained in the form of very fine roughly spherical particles, a few millimetres in diameter, by the decomposition of gaseous $Fe(CO)_5$. The same method is used to produce nickel and cobalt powders.
- *Sponge iron powder* consisting of coarse, irregular and porous particles, is obtained by the direct reduction of iron ore. The average particle size of powder screened to below 212 μm is about 80 μm.
- *Atomised elemental or prealloyed powder* can be obtained by breaking up a stream of liquid metal with high pressure jets of water, steam or inert gas. The liquid metal is broken up into fine droplets which solidify rapidly. The solidification structure of the powder grains can vary greatly, depending on the atomising conditions and the initial composition. A typical average particle size is about 80 μm (Fig. 16-1-1 B). In the case of alloy steels, the powders obtained are often coarse and porous. The high solidification speed leads to a fine, generally dendritic, solidification structure and causes the formation of martensite. The powder must be softened by heat treatment before cold pressing.
- *Pre-diffused powder* consists of very pure iron powder to which finely divided alloying elements have been *diffusion bonded.* In this way the extremely high compressibility of the iron powder is maintained, and the risk of segregation minimised (Fig. 16-1-1 C). The mixture is subjected to a continuous heat treatment in a reducing atmosphere at a temperature somewhat below the lowest melting temperature of the constituent elements, forming coarse agglomerate particles.

Figure 16-1-1:
A) Pure carbonyl iron powders obtained by thermal decomposition of gaseous iron carbonyl, $Fe(CO)_5$. The mean particle size is about 4 µm. Nickel and cobalt powders can be produced in the same way
Courtesy Eurotungstène Poudres, Grenoble.

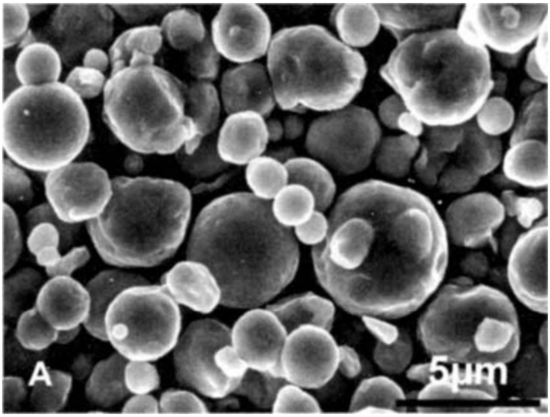

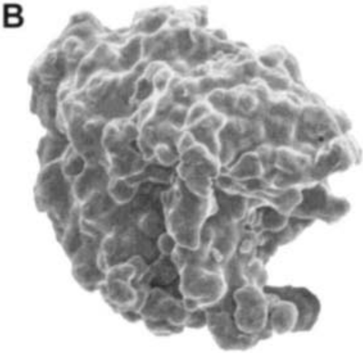

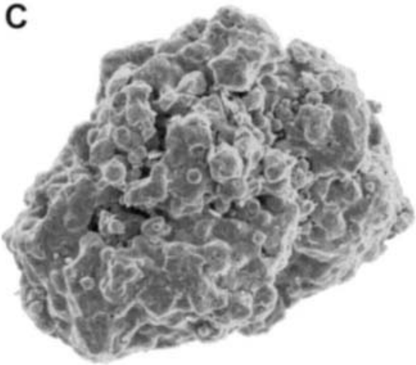

B) Atomised high purity ASC100.029 iron powder with an average particle size of about 80 µm.
C) Distaloy AE alloy consisting of iron powder with fine satellite particles of nickel, copper and molybdenum welded together by pre-diffusion treatment.
Courtesy Höganas

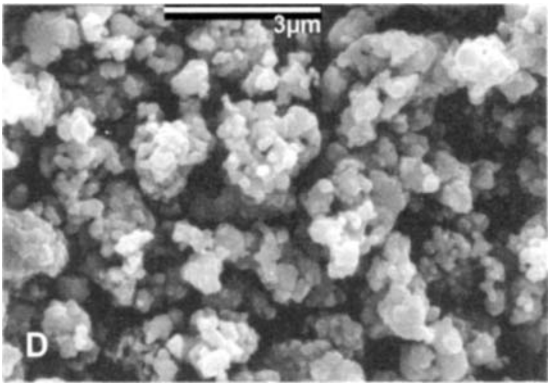

D) Scanning electron micrograph of a powder produced by co-precipitation of Cu, Fe and Co. The agglomerate particles have a mean size of 7 to 10 µm, with constituent grains of about 0.4 µm.
Courtesy Eurotungstène Poudres, Grenoble.

- *Precipitated powders* are produced by drying and reducing hydroxides or other water-insoluble salts deposited from aqueous solutions. The method can be applied only to certain metals, including iron, nickel, cobalt and copper, and is sometimes used to prepare "co-precipitated" powder mixtures. The powders obtained are relatively coarse, but the particles consist of an agglomerate of sub-micron size grains (Fig. 16-1-1 D). Tungsten powders are obtained by a similar process, involving the reduction of chemically produced salt particles.
- *Crushed powders* can be produced from brittle metals and alloys, such as chromium and manganese.

16-2 Steels produced by solid state sintering

Sintering of "pre-diffused" Fe-Ni-Cu-Mo-C alloy

Alloys are often produced by mixing elemental powders in appropriate proportions. For the Distaloy AE alloy in this example (typically sponge iron plus 1.75% Ni-4% Cu-0.5% Mo), coarse iron powders are blended with very fine nickel, molybdenum and copper powders. This coarse prealloyed powder is mixed with appropriate quantities of graphite and binder and cold pressed to form a compact, which is then sintered for 25 minutes at 1 120 °C and cooled at a rate of about 1 °C/s. For a carbon content of 0.6 % and a densification pressure of 500 MPa, the density obtained is typically about 7 g/cm^3, compared to a theoretical value of 7.8, while the residual pores have an average size of about 10 µm. The Vickers hardness obtained is of the order of 200 (H_{V10}).

During sintering, diffusional exchanges occur between the satellite particles and the iron grains. Nickel diffuses only slowly in the solid state and significant gradients in composition persist, with residual concentrations as high as 30 % at the sites of the former nickel particles, which therefore remain as austenite islands. Even after holding for 4 hours at 1 120 °C, they are not eliminated. Since pure copper is molten at 1 120 °C, it flows between the grains by capillary action and diffuses more rapidly, leading to a more uniform distribution (*cf.* Fig. 7-2-5). The maximum concentrations at the former copper particles are therefore only of the order of 5 to 7 %. Paradoxically, molybdenum also diffuses fairly readily, since it locally converts the austenitic iron to ferrite, in which diffusion rates are much higher (see characteristic diffusion lengths Table 22-5).

The differences in local composition lead to a variable quenching response, with two types of zones. Close to the pores, the alloying elements stabilise austenite, which transforms to martensite or bainite on cooling, leading to high hardness. Away from the pores, at points where nickel, copper and molybdenum have not had time to reach significant levels, the essentially iron-rich material transforms to ferrite and pearlite (Fig. 16-2-1). The high ductility of the latter regions facilitates subsequent consolidation by compression [Hög99].

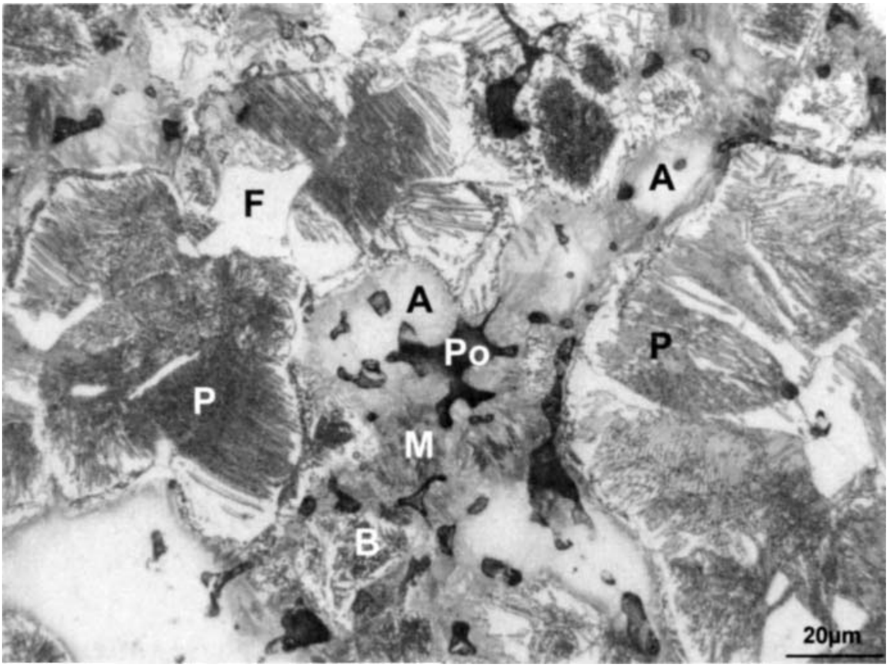

Figure 16-2-1:
Optical micrograph of a sintered material produced from "pre-diffused" Fe-0.6C-4Ni-1.5Cu-0.5Mo steel powder. The complex microstructure contains light islands of ferrite F, lamellar pearlite P, retained austenite A (light grey), martensite M and bainite B (dark grey). Residual pores Po mark the positions of prior powder particle boundaries.
Sample supplied by Federal Mogul, Le Pont de Claix, France

"Prealloyed" Fe-Mo-C steel powders

These materials are produced from Fe-Mo alloy powders prepared by atomisation and carbon in the form of graphite. The major advantage of this route is the ability to achieve a homogeneous composition after sintering. The alloys retain good compressibility, enabling a high density, that is low porosity, to be obtained by compaction. The process is used for the manufacture of components intended for subsequent thermochemical surface hardening. For a carbon concentration of 0.2 %, the as-sintered hardness is typically of the order of 135 H_{V10}, with a density of about 7 g/cm^3.

The microstructure, consisting of ferrite, pearlite and pores, is illustrated in Figure 16-2-2. The pores have a wide range of sizes. Some of them decorate the prior powder particle boundaries, while many of the smaller ones are shrinkage cavities situated in the interdendritic spaces within powder grains. Sintering is performed at 1 120 °C and is theoretically a solid state process. However, transient melting probably occurs during the early stages,

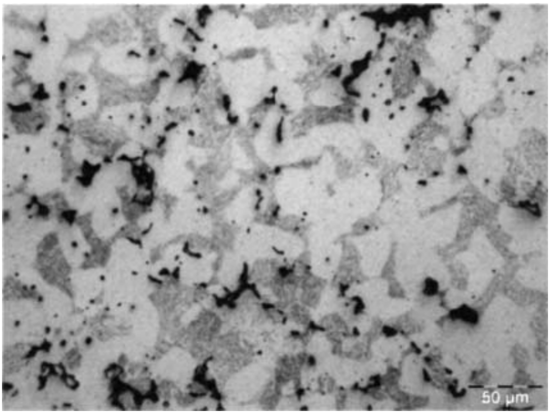

Figure 16-2-2:
Optical micrograph of an Fe-0.2C-1.5Mo steel powder sample sintered for 25 minutes at 1 120°C. Ferrite appears white, pearlite grey and pores black. The pearlite does not have a regular lamellar structure, due to the presence of molybdenum. Sample courtesy Federal Mogul, Le Pont de Claix, France.

since a ternary eutectic with a melting point of 1 065 °C exists in the Fe-Mo-C system (*cf.* Fig. 6-5-1), and could form in contact with carbon in regions of local molybdenum segregation.

16-3 Steels produced by transient liquid phase sintering

Fe-Cu and Fe-Cu-C alloys produced from elemental powders

Transient liquid phase sintering is frequently performed using elemental powder mixtures of iron and 1.5 to 4 % of copper. Sintering is carried out above the melting point of copper (1 083 °C). The liquid copper has good wettability and flows readily between the iron particles, then it infiltrates the structure along the grain boundaries during sintering, leading to rapid disappearance of the liquid. That explains why grain boundaries are hard to separate from particle to particle contacts. (*cf.* § 7-2). However, copper contents greater than 2.5 % cause swelling due to phase changes associated with sintering [Dub02]. This effect is reduced by carbon. The final microstructure illustrated in Figure 16-3-1 is a mixture of ferrite and pearlite. The solubility of copper in iron is relatively high (7 to 9 %) in the temperature range used for sintering, but is very low at ambient temperature. Copper particles therefore tend to precipitate from the ferrite during cooling, causing significant hardening (*cf.* Fig. 13-1-3).

It is not essential for one of the elemental powders to have a melting point below the sintering temperature for a transient liquid phase to form. For example, two elements may combine to form a eutectic with a lower melting point. In this case, the process is described as activated sintering.

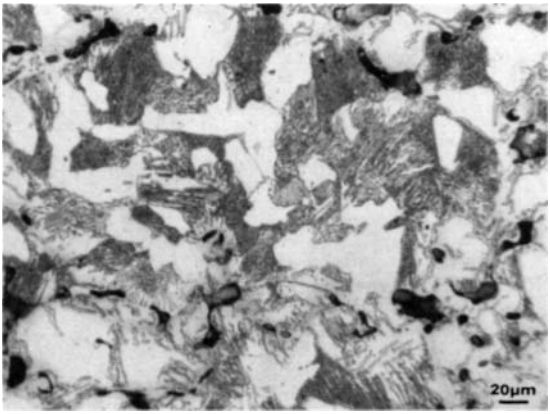

Figure 16-3-1:
Optical micrograph of a sintered Fe-0.5C-2.2Cu steel powder sample. The microstructure consists of ferrite and pearlite. The sample has a Vickers hardness of 180 and a density of 7 g/cm^3.
Sample courtesy Federal Mogul, Le Pont de Claix, France.

16-4 Sintered Fe-Cu-Co composite alloys

Solid state sintering

The Fe-Cu-Co system involves two immiscible liquids, making it impossible to produce certain alloy compositions by conventional melting and casting processes. This problem can be overcome by sintering elemental or co-precipitated powders. Sintering is typically performed by holding the powder mixture under a pressure of about 35 MPa for a relatively short time (3 to 7 minutes) usually between 750 and 850°C. All the phases concerned remain solid under these conditions.

The materials are referred to here as composite alloys to emphasize the fact that the original constituents remain relatively unchanged. Indeed, in the range of sintering temperatures employed (700–900°C), three phases can form, αFe, γCo and γCu. Copper accepts very little iron or cobalt in solution, while α-(Fe,Co) and γ-(Co,Fe) have very low solubility for copper (*cf.* § 4-10). Due to the very fine particle size and intimate mixing, equilibrium is rapidly attained. However, the resulting microstructures differ significantly depending on whether the powders employed are elemental or co-precipitated (Figure 16-4-1 A, B and C). The microstructure is an order of magnitude finer in the case of co-precipitated powders and the hardness values are correspondingly higher (see figure caption). Moreover, the individual particles undergo hardening reactions during cooling, due to precipitation in the case of α-Fe and γ-Cu and ordering for α-(Fe,Co). Since these materials are used principally as a binder phase for diamond tools, hardness and cohesion are the two essential properties required.

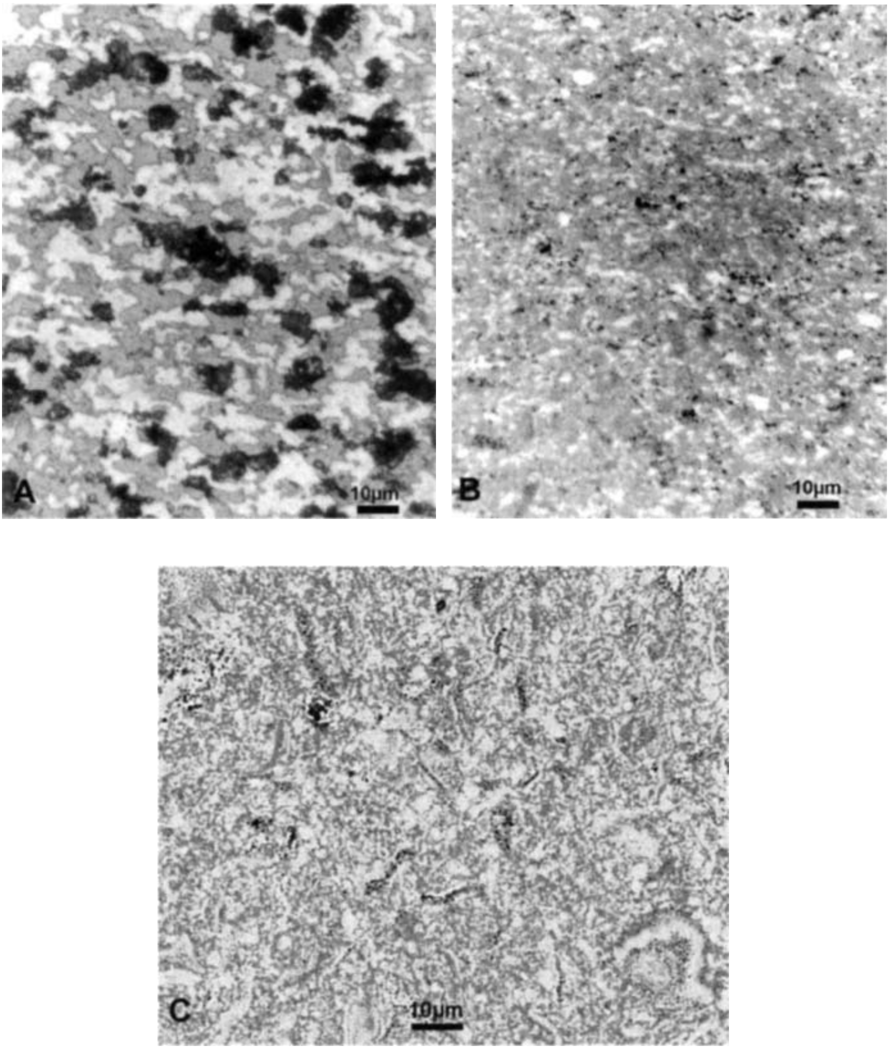

Figure 16-4-1:
Fe-23Co-50Cu alloy sintered for 3–5 minutes at around 800°C under a pressure of 35 MPa.
A) Optical micrograph of an alloy prepared from elemental powders. Electrochemical etch.
Hardness = 220 H_V.
B) Optical micrograph of an alloy prepared from co-precipitated powders. Electrochemical etch.
Hardness = 320 HV_V.
C) Scanning electron micrograph of the material shown in B. Copper appears in light contrast, while the Fe-Co solid solution is darker. A few iron oxide particles (FeO) appear black.
Courtesy Eurotungstène, Grenoble, France.

17

Plain carbon and low alloy steels

Modern artists have produced paintings representing beverage cans. They presumably felt that these objects were representative of our age, both by their decoration and as a symbol of contemporary society. They probably did not realise that their manufacture can also be considered as a metallurgical milestone, since it has required a significant advance in the quality and cleanness of the metal employed (steel or aluminium) to achieve such reliable containers, whose weight has been reduced by 30 % in twenty years, by the use of ever thinner sheet.

For the general public, a more noticeable advance has been the improvement in corrosion resistance of car bodywork. In both cases, the starting materials are in the form of strip or sheet. For steel, "flat" products represent by far the largest tonnage, for many different grades, including the plain carbon and so-called low alloy steels.

17-1 Mild steels for deep drawing

Interstitial-free (IF) or ultra low carbon (ULC) steels

High purity iron is used essentially for its physical properties, particularly its ferromagnetism. It has high ductility and excellent corrosion resistance. Very low carbon steels are close to pure iron and their high ductility enables them to be employed for components of complex geometry involving severe sheet forming processes. The good ductility is a consequence of a low yield stress. The grain size must therefore not be too fine. However, an excessive grain size must also be avoided in order to ensure a smooth surface finish after drawing, particularly when the component is to be coated.

Extra deep drawing quality (EDDQ) steels must be able to withstand severe forming operations without tearing, and this is achieved by ensuring low concentrations of the interstitial elements carbon and nitrogen, typically of the order of 20 to 30 ppm (Table 17-1-1). These low concentrations are achieved by vacuum degassing of the liquid metal, which also removes hydrogen. The residual carbon and nitrogen is tied up by adding small amounts of titanium and/or niobium, which form fine precipitates of TiN, Nb(C,N) and $Ti_4C_2S_2$ (H phase). The latter compound forms in the presence of sulphur, by transformation of titanium sulphide TiS [Hua97].

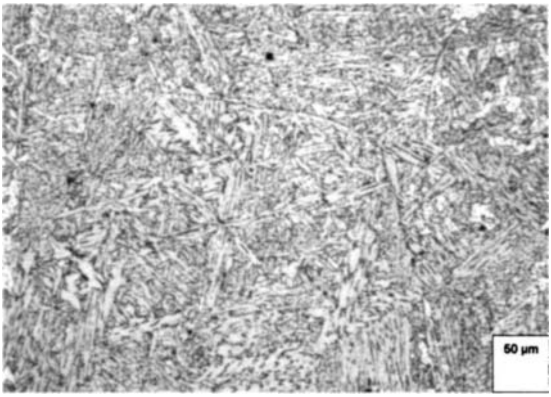

Figure 17-1-2:
Optical micrograph of an S460 titanium and niobium micro-alloyed construction steel. Acicular ferrite is visible in the coarse grained zone of a weld. The small dark spots are titanium oxide inclusions, which sometimes act as nucleation sites for the ferrite.
Courtesy Arcelor Recherche

Oxide inclusions are also detrimental, to an extent which depends on their nature and size. They can be kept very fine and sparse by the use of strong deoxidants such as calcium, cerium or zirconium, during refining. The first generation of EDDQ steels had yield strengths of the order of 150 MPa. This was later increased to around 200–300 MPa, without loss of formability, by the addition of phosphorus or the use of subsequent heat treatments [DeA98].

Table 17-1-1: Typical composition of an IF steel

Alloy	C	Si	S	P	N	Al	Mn	Ti
Typical	0.003	0.007	0.007	0.007	0.003	0.020		0.060
Maximum	0.08		0.03	0.025			0.45	

High strength low alloy (HSLA) or micro-alloyed steels .

Many applications involve less severe forming but require higher strength levels. The steels used in this case belong to the family of high strength low alloy (HSLA) or micro-alloyed (MA) grades, which are similar to the IF materials. However, slightly higher carbon levels are tolerated, being balanced by appropriate titanium and/or niobium levels. The hot rolling process is closely controlled and represents a veritable sequence of thermomechanical treatments below 1000 °C, involving precipitation of carbides and/or cabonitrides and recrystallisation (*cf.* Table 14-1-2). The strengthening mechanisms are complex and are summarised for the case of niobium in Table 17-1-3, adapted from [Thi98]. The insoluble particles mentioned in this table are niobium carbides or carbonitrides formed either in the liquid or during solidification. They contribute to strengthening by restricting grain growth. Precipitation continues in the solid as the temperature decreases. The particles formed in the austenite field and the upper part of the ferrite range act essentially on the grain size (see § 13-1 and Figure 13-3-2). They inhibit recrystallisation of the austenite and help to conserve a high dislocation density, leading to a large number of potential nucleation sites during transformation to ferrite. The last hot rolling pass must be performed at as low a temperature as possible, just before the $\gamma \rightarrow \alpha$ transformation, in order to optimise this effect.

Direct cooling from the austenite field then produces a particular structure containing *acicular ferrite* (Figure 17-1-2), which should not be confused with soft martensite. This structure has high ductility and excellent toughness. Precipitation continues during cooling of the ferrite, which contains numerous dislocations, leading to a distribution of very fine particles that promote considerable strengthening [Kes97].

Table 17-1-3:
Effects of niobium as the temperature decreases during hot rolling and subsequent cooling [Thi98].

	Mechanism	Role	Consequences
Austenite	Insoluble particles	Pin grain boundaries and prevent grain growth	Grain refinement
	Solid phase precipitation	Inhibits recrystallisation and maintains a high dislocation density	Nucleation of finer ferrite
	Niobium atoms in substitutional solid solution	Inhibit recovery and recrystallisation and maintain a high dislocation density	Nucleation of finer ferrite
		Retard transformation to ferrite and generate an acicular structure	Dislocation strengthening
Ferrite	Solid phase precipitation	Pins grain boundaries and prevents grain growth	Grain refinement
		Fine dispersion in ferrite grains	Precipitation hardening
	Niobium atoms in substitutional solid solution	Available for precipitation during subsequent heat treatment	Solution strengthening and possible further precipitation hardening

17-2 Low alloy structural steels

Historical development

The use of steel was greatly diversified in the 19th century, with the discovery of reinforced concrete, and military applications, such as armour plating for ships. Steel consumption for both civil and military uses grew tremendously in the early 20th century. Iron and steel were employed for many spectacular architectural and engineering achievements, including bridges, ships, railways, stations, etc. A famous example is the Eiffel tower, which was built from puddled iron in 1887–1889.

The quality of steels made great progress in the second half of the 20th century, due to improved understanding of the underlying metallurgy, thanks to powerful new experimental techniques, such as electron microscopy. Because of the increased strength levels attained, together with competition from other materials, world tonnage steel consumption has ceased to increase in more recent times. However, the quality and diversity of the products available continue to rise, and modern steels can be used under increasingly severe conditions.

In earlier times, steels were chosen mainly on the basis of tensile strength, without considering weldability or toughness. Steel structures were assembled by riveting. Typical carbon contents were around 0.3 %. Pickering [Pic78] has pointed out that the sheets used to build the Mauritania in 1907 were almost identical in composition to the steel employed for the Sydney Harbour Bridge in 1932. Carbon was long considered as the cheapest and most efficient strengthening mechanism. The structural steels used at this time typically had a total alloying element concentration less than 1 %. Towards the middle of the 20th century, rivets tended to be replaced by welding. Welds involve locally degraded structures and therefore require high intrinsic toughness, particularly considering the metal continuity across the joint. Higher performance steels were therefore developed, with emphasis on weldability, toughness and formability, enabling welded structures to be employed even in cold climates, for applications such as arctic pipelines, ice-breakers, etc. All this had to be achieved at minimum cost, considering the large quantities involved. Table 17-2-1 compares the composition of a modern structural steel with materials used in the first half of the 20th century. The principal difference is a tighter control of the embrittling elements, sulphur and phosphorus. In this respect, a high Mn/S ratio is an important factor.

Table 17-2-1: Evolution of structural steel compositions [Pic78], [Fel98].

Steel	C	Si	S	P	N	Cu	Mn	O	Mn/S
1907 Mauritania	0.27	1.2					0.7		
1912 Titanic	0.21	0.017	0.069	0.045	0.0035	0.024	0.47	0.013	6.8/1
1932 Harbour Bridge Sydney	0.30	0.15					1.2		
ASTM A36 (modern structural steel)	0.20	0.007	0.037	0.012	0.0032	0.01	0.55	0.079	14.9/1

The compromise between strength and toughness

The need to combine both high strength and good toughness is a difficult metallurgical problem. All strengthening mechanisms inhibit slip and therefore have a natural tendency to impair toughness (*cf.* Chapter 14). One marked exception is grain refinement, which restricts the extension of incipient microcracks. Any strengthening mechanism which also reduces the grain size will therefore help to improve the strength/toughness compromise. As described above, carbonitrides that remain undissolved in the austenite retard grain growth during heat treatment and act as nucleation sites for the transformation to ferrite, but have little effect on strength (Table 17-1-3). Precipitation at grain boundaries can help to maintain a fine grain size, but must not be sufficient to significantly reduce local cohesion. Nitrogen induces marked solid solution strengthening in ferrite, but its solubility is limited. It tends to migrate to dislocations, even at ambient temperature, and can cause strain aging, with deleterious consequences for the toughness. Forming operations should therefore be carried out rapidly, with little time between passes [Cah83]. Nitrogen

Figure 17-2-2:
Effect of carbon content on the Charpy V-notch ductile/brittle transition for normalised steels. The rectangles represent the specimens B (20 J) and C (70 J) shown in Figure 14-1-5.
From [Bur64], cited in [Pic78].

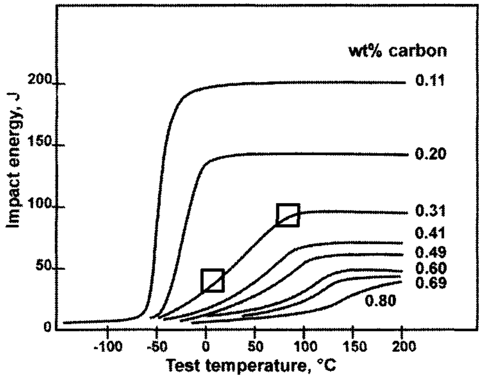

diffusion can be prevented by tying it up with small additions of aluminium or vanadium, which form AlN or VN respectively. Other harmful factors with regard to toughness are substitutional solid solution elements, pearlite, and high carbon contents in general (*cf.* Figure 17-2-2). However, carbon is less soluble in ferrite than nitrogen and diffuses more slowly. Strain aging effects due to carbon are not observed below about 100°C. Copper can also be used to produce significant precipitation hardening in ferrite, but again tends to reduce toughness.

The structural steels include many different grades designed for particular applications [Ash92], [Gla97], [Man99c]. One of the principal difficulties is the behaviour of welds. Microsegregation in the fusion zone can cause embrittlement, particularly when it leads to the formation of eutectic phases or shrinkage cavities. In the heat affected zone (HAZ), rapid cooling can cause martensite formation and associated stresses. It is therefore necessary to reduce the carbon level, together with the concentrations of elements with a marked segregation tendency, such as sulphur, phosphorus, and even niobium. Empirical formulae based on the steel composition have been derived to define the tendency for weld cracking in terms of a carbon equivalent. Equation 17-2-3 is an example. If the carbon equivalent is below a threshold value of about 0.14 %, cracking will not occur and welds will remain sound.

$$C_E = C + Mn/6 + Si/24 + (Ni+Cu)/15 + (Cr+Mo)/10 \quad \text{[Pic78]} \qquad (17\text{-}2\text{-}3)$$

Since grain refinement is the only factor that is favourable for both strength and toughness, the optimisation of hot rolling sequences is extremely important.

Effect of alloying elements

The principal alloying elements used in structural steels are carbon, manganese, niobium, vanadium, nitrogen and aluminium. Their effects on the strength-toughness trade-off in different steel categories is illustrated graphically in Figure 17-2-4. However, a number of other alloying elements are also employed (Cr, Cu, Si, Ti, Mo, Zr, Ni).

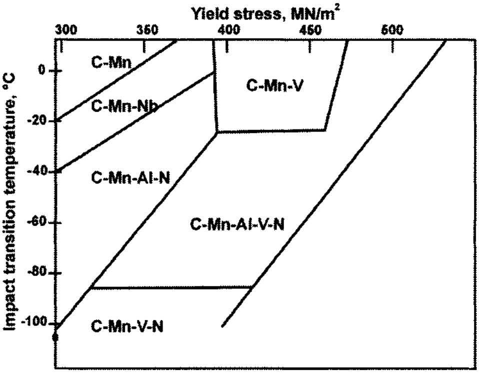

Figure 17-2-4:
Effect of steel composition on the compromise between yield strength and toughness. From [Pic78].

Compound	A	B	[M].[X] at 900 °C
TiC	5.33	10475	$2.5\ 10^{-4}$
NbC	3.42	7900	$4.8\ 10^{-4}$
VC	6.72	9500	$4.2\ 10^{-2}$
TiN	0.322	8000	$3.2\ 10^{-7}$
NbN	2.8	8500	$3.6\ 10^{-5}$
VN	3.02	7840	$2.2\ 10^{-4}$

Table 17-2-5:
Some solubility products in ferrite at 900 °C, calculated using the relation

$$[M]\cdot[X] = 10^{A-\frac{B}{T}}$$

where *T* is the temperature in Kelvins and A and B are experimentally determined constants.
From [Li_98b] and [Ino01].

Several alloying elements can combine with carbon and nitrogen to form carbide and nitride precipitates, in amounts that depend on the corresponding solubility products. Thus, in the order of decreasing solubility in austenite, the ranking is as follows : VC, TiC, NbC, VN, TiN. In ferrite, it is again VC and TiC which have the highest solubilities, followed by NbC and NbN (*cf.* Table 17-2-5). The solubility of vanadium carbide is an order of magnitude lower in ferrite than in austenite at the transformation temperature, so that vanadium in solution can precipitate out during the transformation and refine the ferrite grain size. All the nitrides have lower solubilities than the corresponding carbides. Strictly speaking, the nature of the phases which form depends not only on the solubility products, but also on the relative activities of the various solute elements. Furthermore, carbides and nitrides often have significant mutual solubilities, so that the effects of carbon and nitrogen tend to combine [Gla97], [Li_98b], [Ino01]. The concentrations typically employed are of the order of 0.03 % Nb and 0.10 % V. Aluminium is often used to tie up nitrogen as insoluble AlN, rather than VN (Fig. 17-2-4). The solubility product of niobium carbonitride is given by :

$$\log_{10}[Nb].[C + 12/14N] = -6770/T + 2.26 \qquad (17\text{-}2\text{-}6)$$

where T is the temperature in Kelvins. Although the volume fraction precipitated is very small, the effect is large, due to the very fine size of the particles, which are often coherent with the matrix (*cf.* § 13-3 and Figure 13-3-3).

17-3 The TRIP steels

The TRIP (Transformation Induced Plasticity) steels

The so-called TRIP steels offer a much better combination of strength and ductility than the conventional low alloy grades. It is possible to obtain yield strengths of more than 750 MPa together with a uniform elongation greater than 20 %, conserving the possibility of cold forming. The initial structure in the blank used for component forming is composed of a mixture of ferrite (50–75 %), bainite (20–45 %) and retained austenite (5–20 %). The retained austenite is transformed to martensite during cold forming, due to the plastic strain. The strength of the martensite is such that the transformation is associated with high strain hardening, retarding the onset of necking, since the load is transferred to weaker, less deformed zones. This is the so-called transformation-induced plasticity phenomenon. Furthermore, the thermomechanical processing cycle used to produce the initial sheet leads to a fine ferrite grain size, contributing to the high ductility.

The TRIP grades are essentially carbon-manganese steels containing additions of silicon or aluminium to retard and control cementite formation. Typical compositions are 0.1–0.4 % C, 0.5–1.5 % Si (or Al) and 0.5–2 % Mn. During transformation in the bainite temperature range, ferrite laths form without carbide precipitation [Ble98]. The microstructure (Figure 17-3-1) is similar to those observed in experimental alloys in which nickel is used as a cementite retardant (*cf.* Figures 12-2-1 and 12-2-2).

The austenite trapped between the ferrite laths tends to become enriched in carbon during transformation, and therefore remains (meta)stable at ambient temperature. Nevertheless, the application of plastic strain is sufficient to cause it to transform to martensite, with the result described above. An initial microstructure consisting of a mixture of austenite and bainitic ferrite is thus considered to be ideal. However, the martensite produced during forming is hard and represents a potential crack initiation site.

The high silicon content of these steels is a limiting factor, since it can have several harmful effects. For example, it can cause thickening and loss of ductility in galvanised coatings, while in other cases, silicon-rich oxides can impair surface quality. Recent studies have shown that it is possible to obtain a TRIP effect in low silicon steels, by appropriate carefully controlled heat treatments. Up to 10 % of metastable austenite can be retained in this way.

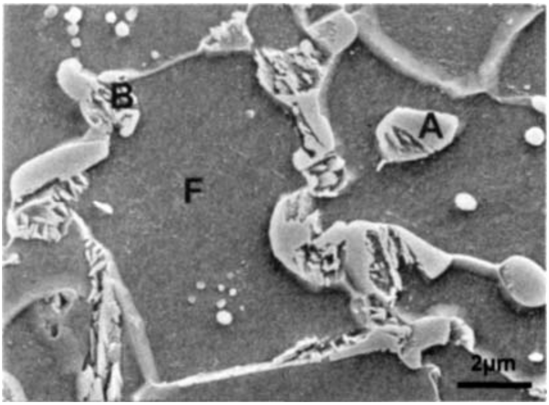

Figure 17-3-1:
Scanning electron micrograph of a low silicon ($Fe\text{-}0.18C\text{-}1.33Mn\text{-}0.39Si\text{-}0.029Al$) TRIP steel heat treated 6 minutes at 730°C then 5 minutes at 370°C, showing austenite (A), bainite (B) and ferrite (F). Note the very fine grain size.
Courtesy Catholic University of Louvain, Belgium. See also [Jac98].

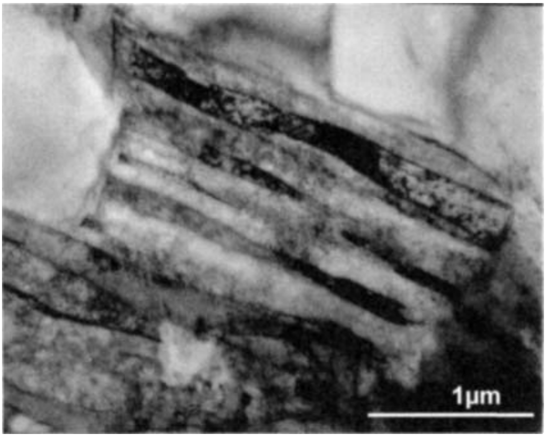

Figure 17-3-2:
Transmission electron micrograph of a “bainitic” zone of the same steel as in Figure 17-3-1. Because the parent austenite grains are very small, the laths cross them completely.
Courtesy Catholic University of Louvain, Belgium. See also [Jac98] and [Jac01].

An example is shown in Figures 17-3-1 and 17-3-2. During subsequent deformation, the austenite transforms to bainite and martensite, dispersed among fine ferrite grains [Jac98], [Jac01]. Cementite is observed between the bainite laths in these low silicon alloys..

18

Quench hardening steels

One of the most characteristic features of steels is their flexibility. This quality is particularly marked in the quench hardening grades, where small modifications in composition can significantly change the heat treatment response.

18-1 Hypoeutectoid steels

Hardenability

It has been seen that the austenite decomposition in carbon and low alloy steels can give rise to various products, including pearlite, bainite and martensite, depending on the composition and heat treatment. It is possible in this way to adjust the properties of a wide variety of cast, forged or machined components by an appropriate final heat treatment. In particular, the microstructural constituents formed during cooling from the austenite field depend on the rapidity of the pearlite and bainite transformations, which can be retarded by suitable control of the steel chemistry (*cf.* § 10-3 and Figure 10-3-1). This enables the formation of martensite, for maximum hardness. However, for a given steel, there is a minimum cooling rate in order to avoid the pearlite and bainite regions in the continuous cooling transformation (CCT) diagram. The slower this minimum rate, the easier it is to obtain a fully martensitic structure, even in the centre of thick components. The hardenability of a steel is defined on this basis and is measured in terms of the distance to which maximum hardening can be obtained in a bar specimen water quenched at one end (*e.g.* Jominy end-quench test). In practice, TTT and CCT diagrams are available in atlases [Atlas] and standards and can be used to determine critical cooling rates. More detailed analyses of steel heat treatments can be found elsewhere [Kra80], [Con92].

Isothermal treatments

While the austenite transformation during cooling is the essential step in steel heat treatment, other isothermal stages are also important. The first of these is a*ustenitising*, whose aim is to convert the initial structure as completely and uniformly as possible to austenite. This is fairly easy in hypoeutectoid steels, where the carbides can be rapidly taken into solution. Holding times of about 30 minutes are usually sufficient at a temperature

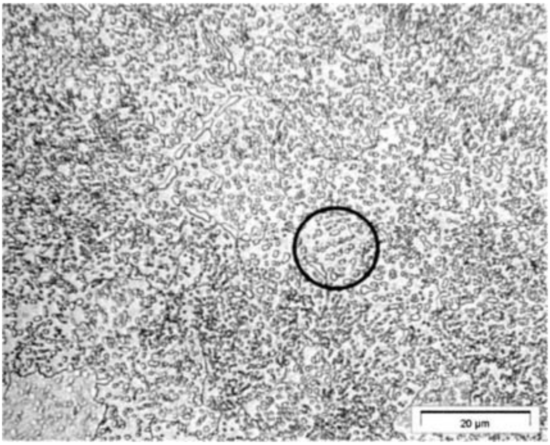

Figure 18-1-1:
Optical micrograph of a 100Cr6 steel austenitised at 810 °C, followed by slow cooling at 5–10 °C/h between 750 and 650 °C. The structure consists of a ferrite matrix containing micron-size globular cementite particles. The alignment of certain cementite particles (circle) corresponds to pearlite lamellae.
Courtesy SNR Roulements, Nancy, France

between 825 and 950 °C, depending on the grade. An excessive temperature leads to a coarse austenite grain size which impairs the final mechanical properties.

After quenching, *stress relieving* in the range 100–200 °C attenuates internal stresses generated by the phase transformation and by steep temperature gradients, and improves toughness. The treatment allows some rearrangement of dislocations and lattice defects. The formation of carbon clusters in the martensite (*cf.* § 11-4) is accompanied by a slight drop in hardness, but the essential characteristics of the martensite are retained.

Tempering is generally performed in the range from 500 to 600 °C. Carbon atoms trapped in the martensite are able to precipitate out as cementite or other carbides, depending on the steel composition (Figure 18-1-1). In the case of cementite, although the particles are fairly fine (about a micron), they are too coarse to compensate for the loss of hardness due to removal of carbon from the martensite. Indeed, tempering is often performed to enhance ductility before machining or final shaping, a new heat treatment then being performed on the finished part. In alloy steels, finer and more stable carbides, such as VC, NbC, etc., are formed during tempering and can provide genuine secondary hardening, at temperatures up to about 550 °C (*cf.* § 11-4). This process leads to a good combination of strength and toughness.

Quenching/cooling

Cooling from the austenitising temperature is usually continuous. For example, in 36NiCrMo16 (EN 1.6773) steel, the pearlite and bainite transformations are significantly retarded by the presence of nickel, chromium and molybdenum, and fully martensitic structures can be readily obtained in the centre of heavy section components. The CCT diagram is shown in Figure 18-1-2 A. Another possibility, which requires more complex equipment, is the use of step quenching, where cooling is interrupted by holding at a temperature above Ms, before rapidly continuing to ambient temperature (grey dotted

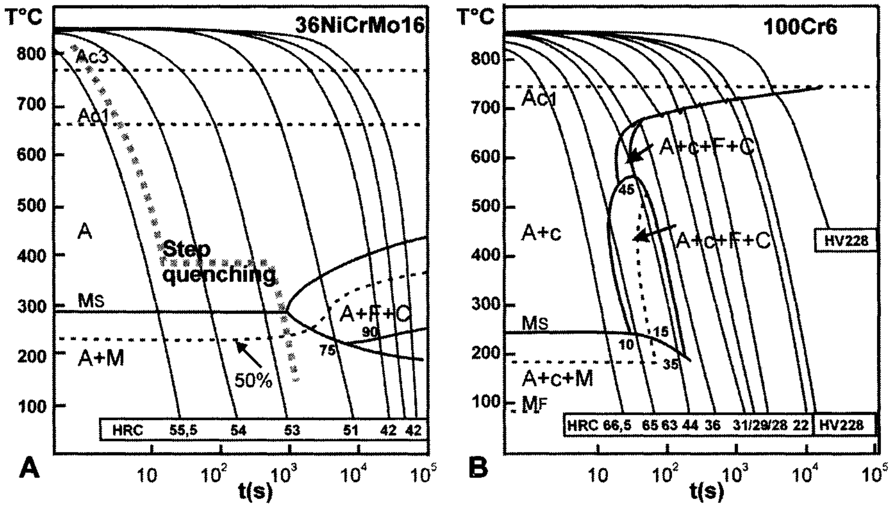

Figure 18-1-2:
CCT diagrams for two common martensitic steels, both austenitised 30 minutes at 850°C. The microstructural constituents are designated A for austenite, F for ferrite, C for cementite associated with ferrite, c for secondary cementite and M for martensite. F+C indicates either pearlite or bainite. The lower dotted lines represent the locus of points where 50% of the austenite has transformed. The small numbers near a transformation field boundary indicate the percentage of austenite transformed in the immediately preceding field. The final hardness is given as a function of cooling rate in the rectangles at the bottom of the diagrams, expressed either in Rockwell units, or in Vickers units for the lowest values.

A) Hypoeutectoid 36NiCrMo16 / EN 1.6773 steel (0.34C-4Ni-1.54Cr-0.31Mo-0.35Mn-0.26Si).
The hardness values were measured after final quenching and holding for 2 minutes in liquid nitrogen.
B) Hypereutectoid 100Cr6 / L3 / 52100 / A573Gr70 steel (1C-1.71Cr-0.3Mn-0.14Cu-0.04Mo).
Adapted from the IRSID Atlas [Atlas].

path in Figure 18-1-2 A). This procedure homogenises the temperature before final transformation to martensite and reduces internal stresses in the final product.

Case hardening treatments

Fully martensitic structures are often hard but brittle. In many applications, high hardness is required only at and near the surface, for example, for wear resistance, while good toughness is needed in the substrate. This can be achieved by heating only the surface, usually by induction, although laser treatments are also possible in small local areas. This operation is often termed case hardening. The resulting graded microstructure is illustrated in Figure 18-1-3 A for 100Cr6 steel (*cf.* CCT diagram in Figure 18-1-2 B). Figures 18-1-3 B and C show higher magnification views of the ductile core and hard surface structures, in positions separated by a distance of only 1 mm. Numerous different treatments of this type are performed on components such as gearwheels and shafts [Bro92].

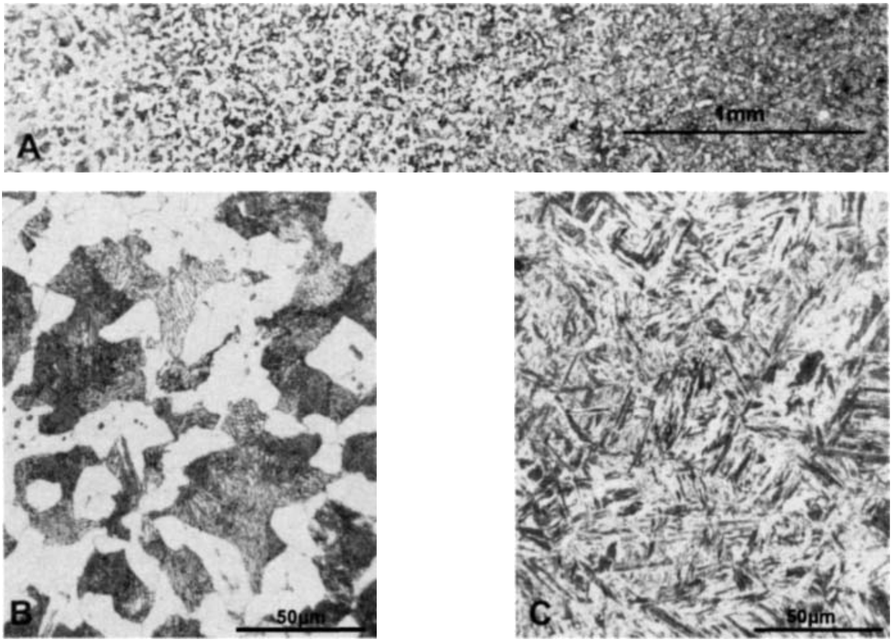

Figure 18-1-3:
Optical micrographs of an Fe-0.4C-0.7Mn-0.03P-0.04S-0.2Si-0.002B steel sample surface hardened by induction heating. Nital etch. A) Transition zone. B) Ferrite-pearlite core structure. C) Martensite surface structure. In the transition zone, the amounts of the three constituents, ferrite, pearlite and martensite vary continuously.
Courtesy INPG, Grenoble

Another approach to this problem is to modify the surface chemistry of the steels, for example, by case carburising or nitriding, followed by uniform heat treatment of the complete component. During quenching, only the carbon- or nitrogen-rich surface layer forms hard martensite (see § 8-3).

18-2 Hypereutectoid steels

Bearing steels (about 1 % carbon)

Among the most common examples of hypereutectoid steels are the bearing grades, with about 1 % carbon. They contain secondary cementite particles that are significantly coarser than eutectoid cementite and therefore more difficult to take into solution. Austenitising temperatures and times must therefore be suitably adapted. In some cases, full solutioning is not possible, due to narrowing of the austenite field temperature window by alloying elements. Moreover, complete dissolution gives a carbon-rich austenite with a low Ms

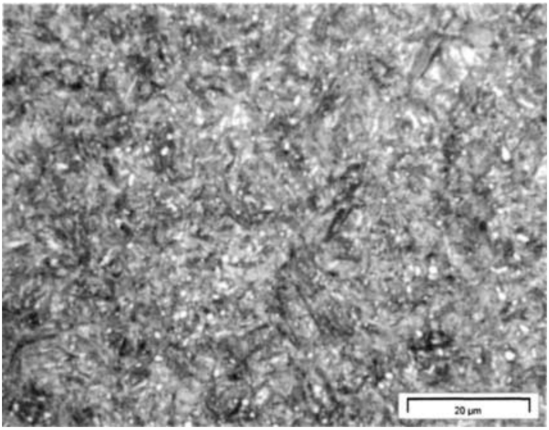

Figure 18-2-1:
Optical micrograph of a 100Cr6 steel sample quenched after austenitising at 850°C.
Courtesy SNR Roulements, Annecy, France.

point, so that a fully martensitic structure cannot be obtained by quenching to room temperature. It is therefore often preferred to use a lower austenitising temperature and to tolerate the presence of coarse undissolved carbides. The presence of such carbides is indicated on the CCT curve by the indication *A+c* (Figure 18-1-2 B). The as-quenched microstructure then consists of a dispersion of coarse carbides in a martensite matrix (Figure 18-2-1). The martensite laths remain relatively fine, since their growth is limited by the carbides. The overall hardness is very high, with the carbides contributing significantly to the abrasion resistance. Like in cast irons and certain alloy steels, in high carbon steels, a partial high temperature dissolution treatment is sometimes followed by a lower temperature hold to precipitate finer carbides and lower the carbon content of the austenite to the point where it is able to fully transform to martensite on subsequent cooling to ambient temperature. The second hold is then called an austenite *destabilisation treatment.*

The internal stresses generated by martensite transformation from high carbon austenite can be colossal. Castings with coarse solidification structures can be extremely brittle. Large high carbon steel castings such as rolling mill rolls even present the risk of explosive stress relaxation. Stress relieving treatment at about 200 °C is then essential. The softening and precipitation processes during stress relieving and tempering treatments are the same as those described in § 11-4.

Ultra high carbon steels

The so-called Ultra High Carbon (UHC) steels, containing from 1 to 2.1 % carbon, have been extensively studied in recent years. They have been shown to demonstrate superplastic behaviour at medium temperatures, around 800 °C, making possible their thermomechanical processing, for example, by hot rolling. The final microstructure consists of a high density of finely distributed spheroidal carbides in a ferrite matrix, with excellent toughness [She85b].

18-3 Tool steels and high speed steels

Tool steels are designed to work other metallic materials, including steels. They must be hard, tough and abrasion resistant. The so-called high speed steels include two categories, designated M-type and T-type, depending on whether the principal strengthening element is molybdenum or tungsten. They conserve their hardness (up to 1000 H_V) to high temperatures (up to 600 °C) and were originally designed to withstand heating in high speed cutting applications, but are also employed for other purposes, such as dies, punches, etc. All the tool steels have microstructures consisting of fine, hard and stable carbides embedded in a strong and tough matrix, produced by quenching and tempering [Hoy88], (Appendix 22-8). Various alloying elements are chosen to promote :

- the formation of stable alloy carbides of different sorts,
- in variable amounts,
- with morphologies that do not induce excessive brittleness,
- while at the same time providing a hard and tough matrix.

The carbides in high speed tool steels are principally of the MC, M_6C and M_2C types, which are both hard and very stable. The cubic MC carbides (*e.g.* VC) are the most stable. The three most frequently used alloying elements are molybdenum, tungsten and vanadium (Table 18-3-1). The addition of about 4 % Cr is commonly employed to prevent the formation of cementite, which tends to corrode at high temperatures. The volume fraction of carbides is determined by the carbon content, which varies according to the category of tool steels concerned. In the high speed steels it is generally limited to 0.8 to 1 % to enable almost complete dissolution during austenitising. The total concentration of carbide forming elements (*W+Mo+V*) is limited to about 15 at.%. Beyond these limits, primary carbides with extremely coarse morphologies are formed. Within the above composition range, the primary carbides obtained are eutectic VC, M_6C or M_2C (Mo_2C), as illustrated in Figures 5-6-12, 5-6-14, 6-3-6, 6-3-7 and 6-5-9.

Table 18-3-1: :
Nominal compositions (in weight %) of three high speed steels and a tool steel produced by powder metallurgy (ASP60). T_F is the forging temperature and $T\gamma$ the austenitising temperature. From [Hoy88].

Steel type	C %	W %	Mo %	Cr %	V %	T_F °C	$T\gamma$ °C
T1	0.75	18		4	1	954–1177	1260–1302
M1	0.8	2	8	4	1	927–1149	1177–1218
M2	0.85	6	5	4	2	927–1149	1191–1232
ASP60	2.3	6.5	7	4	6.5		

When tool steels are used in the form of large castings, some primary carbides can have a facetted morphology that impairs toughness, while others induce poor high temperature oxidation resistance [Hwa98]. The carbon level and the concentrations of carbide forming elements must be closely controlled to optimise the solidification path in order to prevent such deleterious morphologies [Kuo55], [Bar72], [Gal74], [Fre79b], [Fis89]. Indeed, eutectic carbides practically always have a detrimental effect on mechanical properties, and *must be broken down during hot working*. This is generally achieved by forging below the solidus, at around 1050°C (*cf.* Table 18-3-1). A reduction in section of about 97 % is required to obtain a fully uniform carbide distribution. A reduction of only 80 % leaves a deformed network of eutectic cells.

For the carbides to provide effective abrasion resistance, they must be embedded in a hard and tough matrix. This is the principal reason why the MC forming elements titanium, niobium and tantalum are not used. In fact, their carbides are too stable and lead to an excessively low residual carbon content in the matrix, which transforms to a relatively soft martensite. With molybdenum, tungsten and vanadium, when most of the alloy carbides are taken into solution by austenitising at a high temperature, sufficient carbon remains in solution during quenching to ensure a hard martensite. Generally, only a small quantity of carbides remain undissolved and these are relatively fine due to the forging sequence. The transformation to martensite is often achieved by a complex multi-stage treatment [Hoy88]. A first quenching step leads to only partial transformation, with significant amounts of retained austenite, since the Ms temperature is lowered due to the high carbon and alloy contents. Subsequent tempering at around 55°C softens the martensite and causes a fine precipitation of secondary carbides. At the same time, carbon diffuses from the austenite towards the carbides already formed. On cooling, some of the austenite is sufficiently depleted to transform to martensite. Up to five successive tempering and cooling cycles are often performed to achieve maximum transformation. The heating and cooling rates must be carefully controlled to limit thermal stresses, since these materials are relatively brittle, and step sequences are often employed. The final microstructure contains two populations of carbide sizes. The particles not dissolved during austenitising typically have dimensions of a few microns and play an essential role in abrasion resistance. The secondary carbides formed during tempering provide the main source of strength and hardness and their size should not exceed about 10 nm to be effective.

The use of powder metallurgy techniques enables the achievement of very fine and uniform carbide distributions. Although these processes are expensive and not necessarily applicable to all types of component, they enable the use of higher carbon and alloying element contents (Table 18-3-1) allowing the attainment of enhanced high temperature performance.

Hard facing materials

Hard facing involves the application of a hard surface layer on a component by welding or by the projection of powders. It is used to provide wear resistance just where it is needed, and also for repair work, restoring the initial geometry by replacing worn-off material. Typical applications include dies, bearings and hydraulic turbine blades. There are many different hard facing processes. In the order of decreasing size of the concentrated energy source, they include flame spraying, plasma spraying, arc welding, electron beam and laser beam techniques. The hard facing material can be deposited in the form of sprayed powder or from a welding electrode, and may be spread over the surface with a binder.

Depending on the combination of properties required, principally hardness, wear, impact and corrosion resistance, various families of materials can be employed. They include iron-base materials with total alloy contents ranging from 2 to 50 %, nickel- and cobalt-base alloys and carbides in a metal binder. Like in tool steels, the hardness and wear resistance are conferred essentially by stable alloy carbides, and carbon contents can be up to 2 % or more. The cobalt-base alloys are the most versatile. They retain their strength to higher temperatures, with excellent hot corrosion resistance, and are also biocompatible (Stellites in massive form have been used for surgical implants). They typically contain up to 12 % tungsten and form M_7C_3 and M_6C type carbides, with a microstructure similar to that of chromium-containing cast irons.

Boron-rich nickel base alloys have been developed principally for applications requiring excellent abrasion resistance. Boron combines with chromium to form hard chromium borides. However, several other precipitate phases involving iron, carbon and silicon are also observed in these complex materials [Leb88], [Chr01].

19

Stainless steels

Three millenia elapsed between the discovery of iron and the development of a means for preventing its corrosion, the first stainless steels being introduced only in the early 20th century. These materials are protected by the spontaneous formation of a so-called passive layer. Baroux [Lac93] pointed out the apparently paradoxical fact that passivity is achieved most readily in highly oxidizable materials. In particular, chromium, which oxidizes more easily than iron, is the major additive in stainless steels.

19-1 Martensitic stainless steels

As their name implies, martensitic stainless steels are designed to combine the strength of martensite with the corrosion resistance conferred by chromium, while limiting additions of expensive alloying elements. By forming a thin stable surface layer of chromium oxide, chromium protects the underlying metal from further corrosion. The minimum concentration of chromium necessary to obtain an effective passive layer is about 10.5 to 11 %, although corrosion resistance increases with chromium content beyond this level. The composition must therefore be adjusted to enable heat treatment within the austenite loop. The most common grades contain between 12 and 15 % chromium and 0.1 to 0.5 % carbon, although concentrations up to 1 % C are sometimes employed.

The composition is chosen depending on the combination of strength, toughness and corrosion resistance required. High carbon grades contain carbides that cannot be taken into solution during austenitising and are subsequently dispersed in the martensite matrix. Lower carbon grades are generally tempered. Figure 19-1-1 schematically shows the effects of modifications in composition on the trade-off between strength and corrosion resistance, starting from a 13 % Cr base.

- An increase in carbon raises the strength and hardness, but decreases corrosion resistance due to removal of chromium from the matrix.
- Additions of nickel improve the toughness and enable the use of higher chromium contents to further enhance corrosion resistance, while maintaining the possibility of obtaining a martensitic structure.
- In the precipitation hardening (PH) grades (see next section), additions of copper,

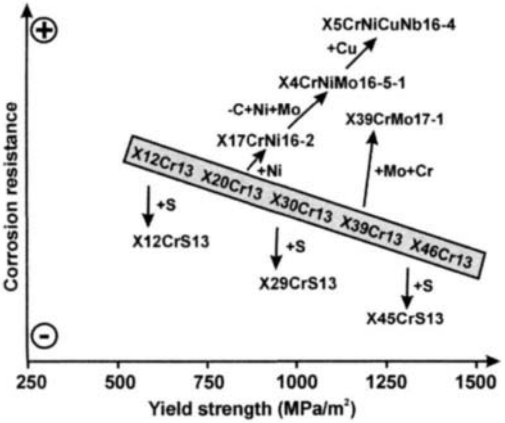

Figure 19-1-1:
Schematic representation of the effect of alloying additions on the combination of strength and corrosion resistance, starting from a 13% Cr base (grey rectangle showing the effect of carbon).
The X12Cr13 grade corresponds to DIN 1.4006 and AISI 410, and X46Cr13 to DIN 1.4034 and AISI 420.
Adapted from a document from Ugine Savoie Imphy, Arcelor Group.

titanium, niobium or aluminium enable the achievement of excellent combinations of strength and corrosion resistance.

Finally, a special series of free-machining martensitic stainless steels has been designed with additions of sulphur and selenium and careful control of or oxide inclusions. The morphology and distribution of the sulphides is described in § 19-5. Typical sulphur contents are in the range from 0.15 to 0.35 % (*e.g.* X12CrS13 or DIN 1.4005, or AISI 416).

Austenitising

In order to obtain a martensitic structure, it is necessary to be able to heat the material into the austenite field. Compared to the Fe-C binary system, the extent of the latter is significantly reduced, in terms of both temperature and composition, by the presence of chromium and other ferrite stabilising elements. For example, molybdenum, which enhances both hardness and corrosion resistance, and vanadium and niobium which improve strength, are all ferrite stabilisers. Their use must therefore be compensated by the addition of austenite stabilising elements, such as nickel, manganese and copper (*cf.* Appendix 22-3). However, the total quantity of alloying elements must be limited to ensure that the Ms temperature remains sufficiently high to prevent the retention of austenite.

The effect of molybdenum is illustrated in Figure 19-1-2 by isopleths and isotherms from the Fe-Cr-C phase diagram. The reduction of the austenite field by molybenum is greater the higher the chromium content (see also Figure 4-7-4). Furthermore, molybdenum stabilises $M_{23}C_6$ carbides rather than M_7C_3 (Fig. 19-1-2 B). The solubility of carbon in the austenite depends on the chromium content and the temperature (Fig. 19-1-2 C). *The austenitising temperatures necessary to completely dissolve carbides are significantly higher* than in low alloy steels. Tungsten has an almost identical effect to molybdenum when added in equivalent atomic concentrations. However, tungsten is both more expensive and heavier.

Figure 19-1-2:
A) Superimposed 14.5% Cr isopleths for the Fe-C (continuous lines) and Fe-0.9Mo-C (dashed lines and shaded γ field) systems. Chromium limits the austenite field. Molybdenum accentuates this effect and shifts the M_7C_3 stability field to higher temperatures.

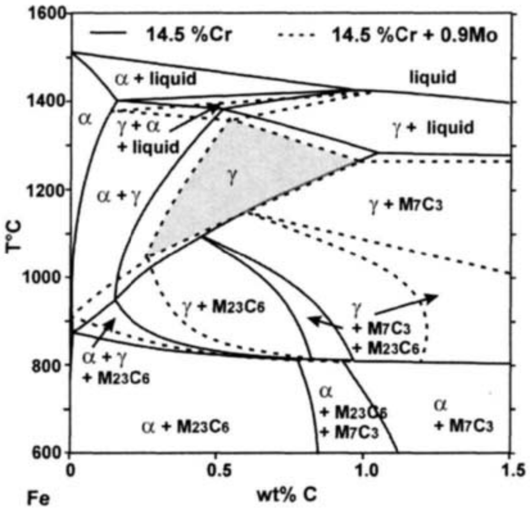

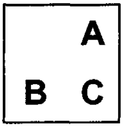

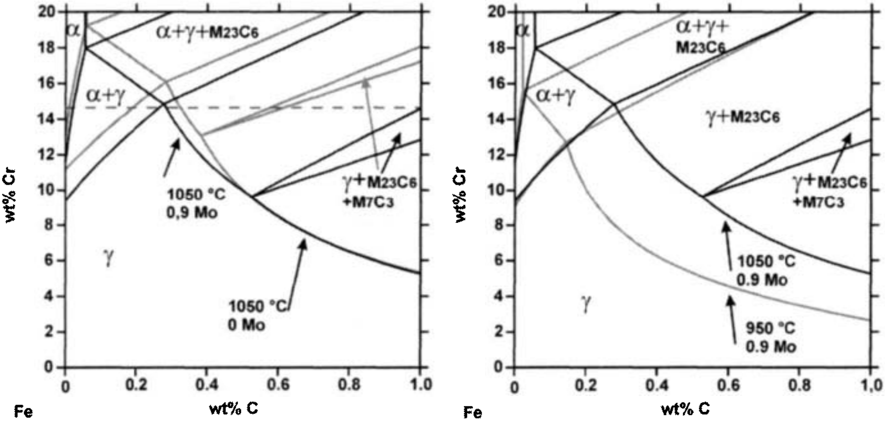

B) Superimposed 1050°C isothermal sections for the Fe-14.5Cr-C (grey lines) and Fe-14.5Cr-0.9Mo-C (black lines) systems.

C) Superimposed 950°C and 1050°C isothermal sections for the same Fe-14.5Cr-0.9Mo-C alloy. No tie-lines are shown, since the system contains more than three elements. The effect of temperature is significantly greater than that of molybdenum.

When the total concentration of alloying elements is too high, the Ms temperature becomes too low and a certain amount of austenite is retained on cooling (*cf.* Appendix 22-6). The austenite must then be destabilised, either by heat treatment in the range 600–700 °C or by mechanical work (*cf.* § 18-2). Details concerning the heat treatment of stainless steels can be found in the following references : [Pec77] [Lac93], [Dav94], [Fin96], [Sas97], [Sou01]. However, in this respect, chromium has a beneficial

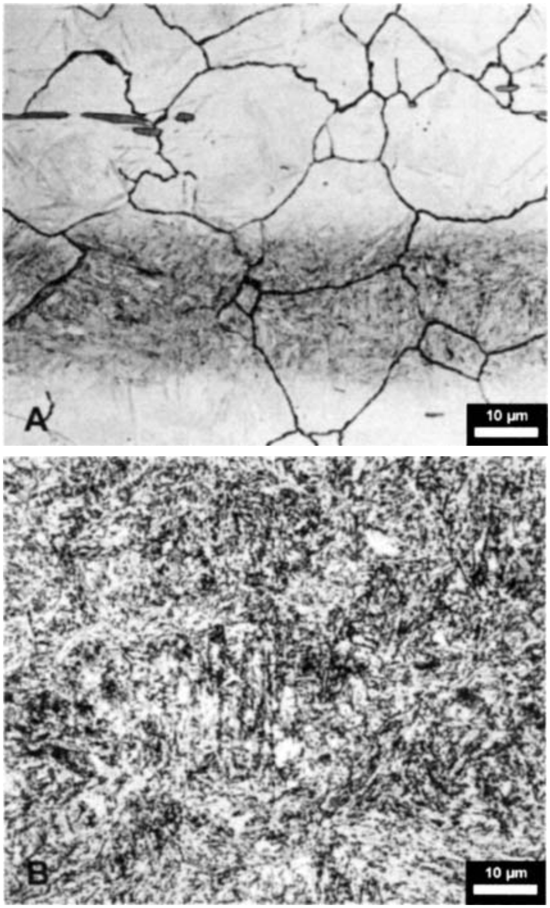

Figure 19-1-3:)

A) Optical micrograph of an as-hot rolled X46Cr13 steel, showing a banded structure due to differential etching (the lighter regions contain a larger amount of retained austenite). The dark grey elongated particles are MnS.

B) Optical micrograph of the same steel after tempering for 4 hours at 680 °C followed by air cooling. Courtesy Ugine Savoie Imphy, Arcelor Group.

effect, since it retards the transformation of austenite to ferrite, pearlite or bainite, making it possible to obtain martensite by simple air cooling. Figure 19-1-3 A shows martensite formed in an X46Cr13 steel in the as hot-rolled condition. A more regular structure is obtained in the same alloy by destabilising the retained austenite at 680°C (Figure 19-1-3 B).

Cutlery steels

The martensitic stainless steels used for cutlery are high carbon grades and are generally employed in the as-quenched and stress-relieved condition. They combine high hardness with good resistance to corrosion. Knife blades are usually hot forged, then quenched and stress-relieved at 200 to 220 °C. Typical carbon contents are between 0.3 and 0.6 %, but can be as high as 0.7 to 0.9 % in high quality professional tools requiring an excellent cutting edge. Figure 19-1-4 shows the microstructure of an Fe-0.7C-14.5Cr-0.9Mo steel

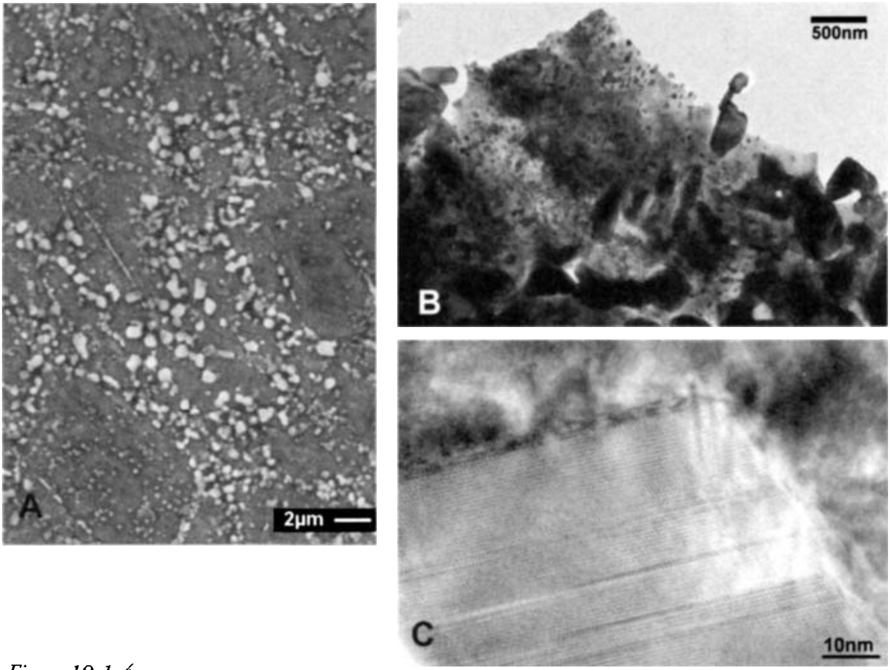

Figure 19-1-4:

A) Scanning electron micrograph of an etched Fe-0.7C-14.5Cr-0.9Mo steel sample, showing coarse intergranular $M_{23}C_6$ particles and finer intragranular ones.

B) Thin foil transmission electron micrograph of the same sample, showing additional fine $M_{23}C_6$ particles formed during stress relieving of the martensite.

C) High resolution transmission electron micrograph showing the coherency of these fine particles, which have a cube/cube orientation relationship with the matrix, the lattice parameter of the carbide being three times that of the martensite.

Courtesy INPG, Grenoble, and McMaster University, Hamilton, Canada.

sample that has been subjected to thermal cycles simulating the manufacture of a knife blade. The steel contains $M_{23}C_6$ carbide particles, in various sizes illustrated at different magnifications. In Figure 19-1-4 A, the coarsest ones (about 0.5 µm) are located at and near grain boundaries and have precipitated in austenite during cooling, while the finer intragranular ones have precipitated at lower temperature. Very fine coherent precipitates, a few nm in size, have formed during the stress relieving treatment (Figure 19-1-4 B and C).

> *Knife handles and other fine cutlery items are often made from austenitic stainless steels, which have a more attractive silvery colour and can be given a brighter polish. They can be readily distinguished by the fact that they are not ferromagnetic, contrary to the martensitic grades.*

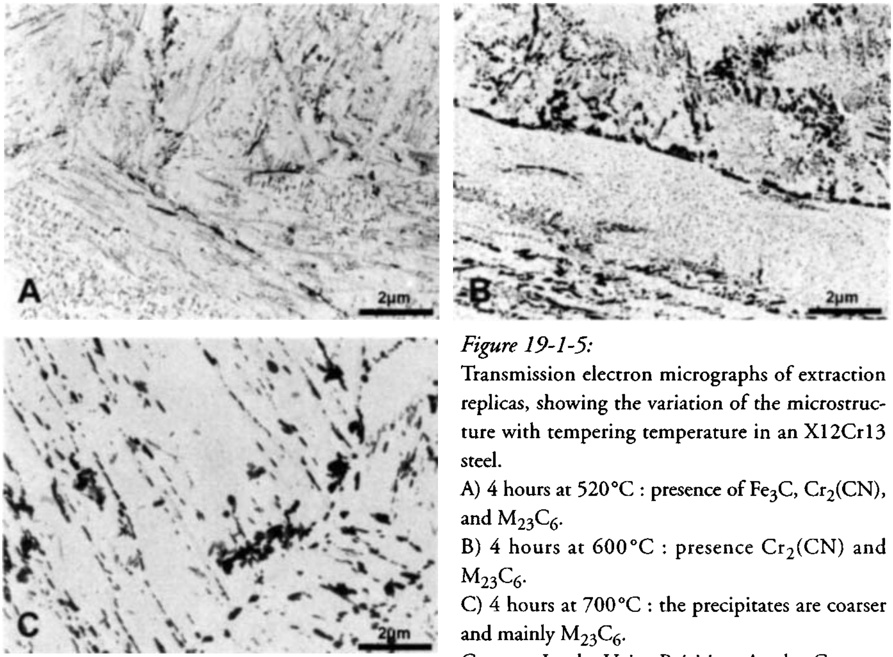

Figure 19-1-5:
Transmission electron micrographs of extraction replicas, showing the variation of the microstructure with tempering temperature in an X12Cr13 steel.
A) 4 hours at 520 °C : presence of Fe_3C, $Cr_2(CN)$, and $M_{23}C_6$.
B) 4 hours at 600 °C : presence $Cr_2(CN)$ and $M_{23}C_6$.
C) 4 hours at 700 °C : the precipitates are coarser and mainly $M_{23}C_6$.
Courtesy Imphy Ugine Précision, Arcelor Group.

Tempered microstructures

The presence of chromium raises the *Ac1* point and enables the use of higher tempering temperatures. This is important, since the morphology, distribution and possibly the nature of the tempering products vary significantly with temperature. The microstructures obtained in an X46Cr13 (DIN 1.4034) steel after tempering for 4 hours at 450, 520, 600 and 700 °C are shown respectively in Figures 11-4-2 and 19-1-5 A, B and C.

- At 450 °C, only cementite forms, as fine particles along preferred matrix planes (Fig. 11-4-2).
- At 500 °C and above, coherent $Cr_2(N,C)$ forms within the laths, with coarser $M_{23}C_6$ at the lath boundaries (Fig. 19-1-5 A, B).
- At 700 °C, only coarse $M_{23}C_6$ subsists. The configuration of the martensite laths is still visible after four hours at this temperature, due to the precipitate alignment at the lath boundaries (Fig. 19-1-5 C), but disappears at longer times.

The consideration of phase equilibria suggests that common alloying additions such as molybdenum, tungsten, vanadium and boron are incorporated in $M_{23}C_6$, which they stabilise. However, the precipitates coarsen readily, limiting their hardening effect, which cannot compensate for the loss of strength due to removal of these elements from solid solution.

Maraging steels

The martensitic stainless steels described so far derive their strength from carbon-rich martensite and carbide precipitates. Another approach is that employed in the so-called maraging steels. In these alloys, a very low carbon content leads to a fairly soft martensite, with a hardness typically around 300 H_V, which is subsequently strengthened by aging to induce the precipitation of an extremely fine dispersion of copper or intermetallic compounds. Contrary to high carbon martensites, the unaged material is sufficiently ductile to be readily worked.

The maraging steels, whose name derives from the fact that they are aged in the martensitic condition, were initially developed without chromium. They are basically low carbon Fe-Ni alloys containing cobalt, molybdenum and a small amount of titanium. The composition must be balanced to adjust the Ms and Mf temperatures and ensure negligible amounts of retained austenite. The yield strength after aging depends on the amount of hardening elements employed and can be as high as 2000 MPa, or even greater. The maraging steels can be produced with a very fine grain size and enable the achievement of toughness/yield strength combinations unattainable with other materials.

Their high nickel content, between 17 and 26 %, together with a very low carbon level (<0.03%) gives them excellent ductility and toughness. Unfortunately, the standard maraging steels have two weaknesses, corresponding to their *poor corrosion resistance* and the *high cost* associated with their chemical composition.

The nature of the very fine precipitate phases (<10 nm) depends on the composition. In the standard series of maraging grades, starting from the composition Fe-18Ni-9Co-3Mo-0.10Al-0.20Ti, hardening is due principally to the precipitation of Ni_3Mo and Ni_3Ti, while the Laves phase Fe_2Mo can form in heavily overaged structures. In higher nickel alloys, such as Fe-25Ni-1.5Ti-0.25Al (and/or 0.5Nb), molybdenum and cobalt are replaced by an increase in titanium, aluminium or niobium. In this case, hardening is due to $Ni_3(Al,Ti)$ and Ni_3Nb.

Because of the high nickel content, the Ms temperature is low. The austenite must therefore be destabilised before quenching by heat treatment at about 700 °C. This "ausaging" treatment depletes the austenite by precipitation, raising Ms sufficiently to allow subsequent transformation to martensite [Pic78].

Precipitation hardened martensitic stainless steels

The same principle has been applied to low carbon stainless maraging steels, usually designated as precipitation hardening (PH) stainless steels. The need to conciliate a high chromium content for corrosion resistance with an Mf temperature sufficient to ensure the absence of retained austenite leads to limited nickel levels. The strengthening phases are therefore different, typical examples being copper (Figure 19-1-6) and β-NiAl (Figure 19-1-7). The aging treatments correspond typically to holding for a few hours at around 600°C. Overaging occurs at longer times and these steels are generally not

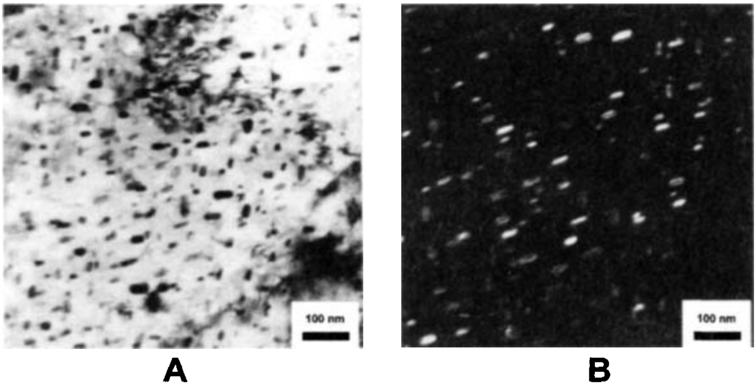

Figure 19-1-6:
Transmission electron micrographs showing the precipitation of ε copper in martensite in an X5CrNiCuNb17-4 (PH 17-4) steel treated 1 h 1040°C C oil quench + 4 h 620°C, air cooled.
A) Bright field image.
B) Dark field image using an ε-Cu reflection, showing the oriented copper platelets.
Courtesy Imphy Ugine Precision, Arcelor Group.

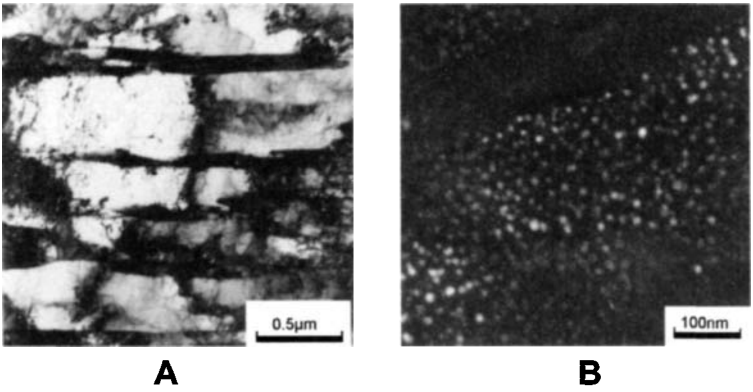

Figure 19-1-7:
Transmission electron micrographs of an X3CrNiMoAl13-8-2 (PH 13-8 Mo) steel treated 1 h 1010°C oil quench + 4 h 590°C, air cooled.
A) Bright field image showing martensite laths and retained austenite.
B) Dark field image showing β-NiAl precipitation in the martensite, but not in the austenite.
Courtesy Imphy Ugine Precision, Arcelor Group

intended for use at high temperatures. Indeed, spinodal decomposition α/α' has been reported in a PH 17-4 type steel after only 100 hours at 400°C [Mur99].

19-2 Austenitic stainless steels

The austenitic stainless steels, which in addition to at least 17 % chromium also contain nickel, have generally better corrosion resistance than the cheaper ferritic grades, together with greater formability and better high temperature strength.

The austenitic grades represent 70 to 80 % of total stainless steel production, and world consumption continues to grow steadily. They are employed in many areas, including the food and pharmaceuticals industries, domestic appliances, transport, power engineering, decorative architectural applications and hospital equipment. Their major advantages are their ease of forming and welding, their mechanical strength and toughness, and of course, their corrosion resistance. These properties, together with their ability to be given a bright polish, make them ideal for decorative purposes and for all applications where hygiene is essential, since they do not contaminate the products with which they come in contact, and can be readily cleaned. A drawback of austenitic stainless steels is their high thermal expansion coefficient. When excellent machinability is required, as for example for components produced automatically at very high speeds, like for the martensitic grades, this can be achieved by the use of specially designed grades with sulphur and selenium additions and carefully controlled oxide inclusions.

Table 19-2-1: Examples of standard austenitic stainless steels.
In the 200 series, shaded in grey, nickel is partially replaced by manganese.

Grade	EN	AISI/UNS	Comments
X12CrNi18-8	1.4300	302	
X8CrNiS18-9	1.4305	303	S=0.3
X2CrNi18-9	1.4307	304L	
X8CrNi25-21	1.4845	310	
X1NiCrMo25-20-5	1.4539	904L	Ni>Cr
X2CrNiMoN18-14-3	1.4439	317LNM	
X2CrNiMo17-12-2	1.4404	316L	
X6CrNiTi18-10	1.4541	321	
X6CrNiNb18-10	1.4550	347	
X12CrMnNi18-7-5	1.4372	201	
X12CrMnNi18-9-5	1.4373	202	

The most important factor in aggressive environments is the resistance to localised corrosion. This is characterised by the pitting index or Pitting Resistance Equivalent Number (PREN), defined by the alloy composition, expressed in weight % :

$$\text{PREN} = [\text{Cr}\,\%] + 3.3\,[\text{Mo}\,\%] + 16[\text{N}\,\%] \qquad (19\text{-}2\text{-}2)$$

Another important factor is the resistance to intergranular corrosion, which is related to the precipitation of chromium carbides at grain boundaries. If the chromium concentration in depleted zones around carbides falls below the critical level for passivation, these regions are selectively attacked. Care must be taken to avoid this phenomenon during heat treatment or welding cycles. The problem can be overcome by the use of very low carbon contents and/or by tying up carbon in a more stable form, by the addition of strong carbide forming elements, such as titanium, niobium or zirconium. All these aspects are covered in more detail in a number of general works [Pec77], [Pic78], [Ash92], [Lac93], [Dav94].

Nickel is not included in the above formula since it plays little direct role in the resistance to localised corrosion. However, nickel is essential for ensuring a fully austenitic structure, without α or δ ferrite or deleterious phases such as σ (*cf.* § 4-8). Higher chromium contents must be compensated by a larger quantity of nickel. The Cr/Ni ratio is therefore an essential parameter, and is often used to designate the type of alloy (*e.g.* 18/8 for the 302 and 304 grades, 25/20 for 310 grade, Table 19-2-1). The heat resisting 310 grade is in fact not completely stable, since it is prone to the formation of σ phase (see § 20-2). The composition can be expressed in terms of a chromium equivalent and a nickel equivalent in order to control the tendency to form phases other than austenite (*cf.* § 14-3 and Appendix 22-3).

The stability of the austenite is also determined by the Ms temperature, which is generally very low in these materials (Appendix 22-6). However, in certain lower nickel grades, such as 301, 304 and 307, the austenite is only metastable at normal ambient temperatures and can be partially *transformed to martensite by deformation*, at a temperature situated above Ms. It is possible to define a temperature Md_{30}, for which a 50 % martensite structure will be obtained with the aid of a true strain of 30 % [Pic78]. The transformation to martensite is accompanied by an increase in strain hardening, which can have a favourable influence in certain types of forming process. It also produces considerable strengthening, which is used to advantage in grades such as AISI 301 (17Cr-7Ni). Finally, in exceptional circumstances, high chromium and nickel austenite containing hydrogen can transform to martensite, inducing embrittlement.

Strengthening mechanisms

The basic austenitic stainless steels have relatively low yield and tensile strengths, typically less than 300 and 650 MPa repectively. These values can be improved by various strengthening mechanisms.

Solid solution strengthening by interstitial elements, particularly nitrogen, is quite marked. In contrast, the effect of substitutional solid solution elements is only moderate, and is very small for austenite stabilisers. *Grain refinement* is also an effective means of strengthening, increasing both the yield and UTS (Ultimate Tensile Strength) values. Alloys with low stacking fault energies contain numerous twins, and in this case, the UTS level is more dependent on the twin spacing than on the grain size. However, the twin spacing does not affect the yield stress. The stacking fault energy is lowered by chromium, molybdenum, silicon, cobalt, nitrogen and carbon and is raised by nickel and copper. The presence of residual ferrite δ also contributes to strengthening, but the effect is only slight.

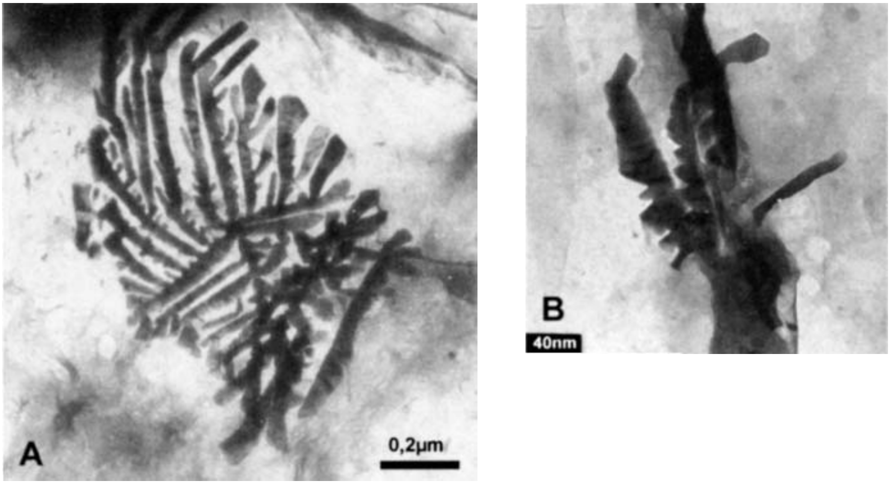

Figure 19-2-3:
Transmission electron micrograph of an extraction replica showing an arborescent $M_{23}C_6$ carbide in an Fe-0.4C-25Cr-20Ni stainless steel sample cooled from the liquid at 5°C/minute.
Courtesy INPG, Grenoble.

Precipitation hardening of austenitic stainless steels is employed only in the heat resisting grades or iron-base superalloys, which are treated in Chapter 20.

Finally, probably the most effective strengthening mechanism in these materials is strain hardening, particularly when the austenite is only metastable and can transform to martensite during deformation. However, the ability to use strain hardening in practice depends on the type of component and the manufacturing process involved.

$M_{23}C_6$ carbides

The principal carbide formed in the basic austenitic grades is chromium-rich $M_{23}C_6$. In simple alloys such as 304 grade, it is the only one observed. Precipitation is relatively rapid in the range 600–900°C, the kinetics following a typical C-shaped curve. At the highest temperatures (lowest supersaturation), nucleation tends to be limited to grain boundaries and lattice defects. Intergranular particles show a $\{111\}$carbide//$\{111\}\gamma$ orientation relationship with one of the two grains. $M_{23}C_6$ has a cubic structure with a lattice parameter of 1.062 nm, representing a ratio of 3 compared to that of the austenite (typically around 0.358). Semi-coherency is therefore often possible, depending on the alloy composition, which determines the exact lattice parameters.

Between 500 and 600 °C, the precipitates also form on dislocations and twin boundaries, while flat, arborescent morphologies are often observed (Fig. 19-2-3 A) in grain boundaries. The particles tend to form triangular or hexagonal platelets in coherent twin boundaries, but adopt a lath shape in incoherent regions. Close examination of the dendritic structure illustrated in Figure 19-3-3 A reveals alignments of small triangular particles (Figure 19-2-3 B). It has been suggested that each precipitate creates a stress field which promotes nucleation of a new one, either ahead of it, or sideways, along dislocation loops.

The precipitation of $M_{23}C_6$ carbides locally depletes the surrounding metal in chromium. If diffusion from the matrix is not sufficiently rapid to attenuate the loss, the local concentration can fall to levels below the critical amount needed to prevent corrosion. This is the so-called sensitization phenomenon, which occurs particularly at grain boundaries. The resulting corrosion network provides easy paths for crack propagation. This problem is generally overcome by reducing the carbon to very low levels and/or by adding more stable carbide formers, such as titanium and niobium, to preferentially tie up the carbon as TiC or NbC. Titanium-stabilised grades are cheaper and therefore more common (*e.g.* AISI 316Ti, 321) than those containing niobium (*e.g.* AISI 347), *cf.* Table 19-2-1. When these solutions are not possible, the heat treatment temperature and time must be sufficient to allow chromium homogenisation in the matrix after precipitation of chromium carbides (see § 8-2 and Figure 8-2-1).

Another possibility is to adjust the alloy composition, for example by adding molybdenum, so as to conserve a small amount of ferrite in the form of scattered islands. The ferrite tends to concentrate the α-stabilising elements, while carbon partitions preferentially to the austenite, and precipitation then occurs at the phase interfaces, where its effect is less harmful than at grain boundaries.

Sigma phase

The presence of manganese and limited amounts of nickel in iron-chromium alloys stabilises the σ phase to higher temperatures. Sigma phase is intrinsically brittle and, depending on its morphology and distribution, can lead to a marked loss in ductility. The precipitate morphology is determined chiefly by the alloy composition and temperature. Grain boundary particles sometimes adopt a massive form or may grow by a discontinuous cellular mechanism. However, they often spread through the grains as long semi-coherent needles or plates. Cellular precipitation is observed at high temperatures in the presence of ferrite stabilising elements, particularly in the duplex stainless steels (see § 19-8). Massive grain boundary precipitates are more common in fully austenitic grades. Intragranular plate-type sigma phase generally occurs below about 800–900 °C, after fairly long exposure times [Bar83], and it is this form which has the most severe embrittling effect.

Figure 19-2-4 shows sigma phase in the form of massive and smaller particles at grain boundaries in an Fe-0.05C-20Cr-12Ni-Si alloy (1.4828 grade) exposed at 700 °C for 1 700 hours. Scattered intragranular plates are also visible. In the case of AISI 316 Ti alloy (Fe-0.06C-0.06C-17Cr-12Ni-2Mo-Ti) treated in the same conditions, sigma phase precipitation was less marked and limited to the grain boundaries.

The mechanism of sigma phase nucleation appears to depend markedly on alloy composition and is the subject of considerable debate. In austenitic steels, it is generally preceded

Figure 19-2-4:
Optical micrograph of an X15CrNiSi20-12 (1.4828) grade steel exposed for 1700 hours at 700°C. Electrolytic etch in KOH solution. Massive and finer particles of sigma phase can be seen at grain boundaries, together with a few plates within the grains.
Courtesy Ugine Savoie Imphy, Arcelor Group.

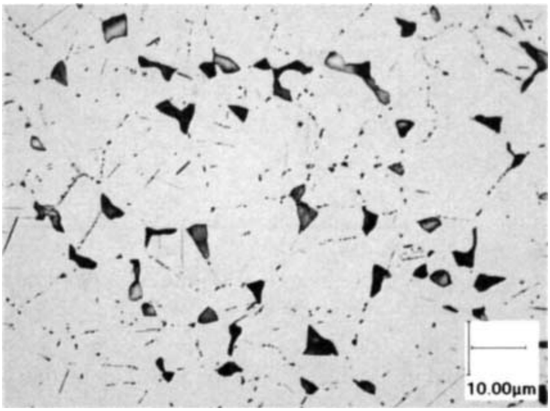

Figure 19-2-5:
Scanning electron micrograph of an Fe-0.4C-25Cr-21Ni alloy slowly cooled from the liquid phase. The specimen surface (top) has been decarburised and the regions of $M_{23}C_6/\gamma$ eutectic have been transformed to sigma phase. The circular insert shows a close-up of the transition region.
Courtesy INPG, Grenoble.

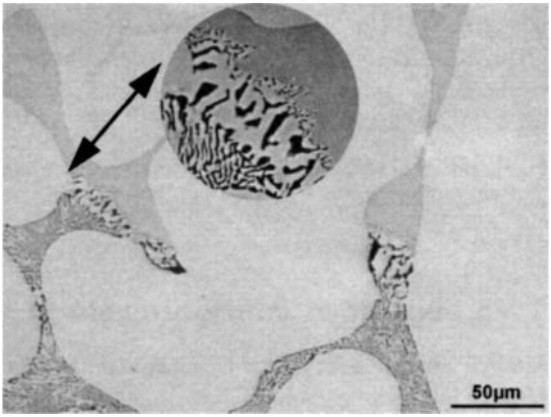

by the formation of $M_{23}C_6$ carbide, except for chromium contents greater than 18 % and very low carbon levels. The critical carbon level has been estimated to be about 0.006 % in 25Cr-20Ni steel [Bar88]. The partial transformation of $\gamma/M_{23}C_6$ eutectic to σ in an alloy of this type is shown in Figure 19-3-5. The surface zone has been decarburised during slow cooling in an insufficiently protective atmosphere, leading to decomposition of the carbide and its replacement by sigma phase, a well established phenomenon in stainless steels [Str99]. Indeed, the ferrite-stabilising metallic elements in $M_{23}C_6$ are present in concentrations similar to those in σ phase or ferrite. However, in the example in Figure 19-2-5, the sigma phase appears to have replaced both the austenite and carbide constituents of the eutectic. It is not known whether ferrite formation is a necessary intermediate step in the transformation to sigma. When ferrite is already present, the fact that it concentrates sigma-forming elements and facilitates diffusion, particularly at grain boundaries, clearly accelerates sigma formation [Bar83]. High carbon contents react preferentially with chromium and inhibit sigma formation.

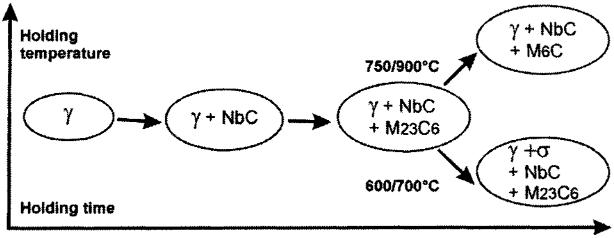

Figurel9-2-6:
:Schematic sequence of events in the formation of sigma phase precursors, $M_{23}C_6$ and M_6C, in niobium-containing austenitic stainless steels [Bar88].

In stabilised steels where the carbon is tied up by titanium or niobium, the mechanisms of sigma formation appear more complicated. The rapid precipitation of MC carbides initially prevents that of $M_{23}C_6$. However, after extended holding times between 600 and 900 °C, $M_{23}C_6$, or M_6C in the presence of molybdenum, can eventually form, as indicated schematically in Figure 19-2-6, and act as precursors for sigma phase. The exact mechanism appears to depend on composition and can be assisted by the application of a stress [Min86], [Bar88], [Lac93], [Sou01].

Sigma phase can be taken back into solution by annealing at high temperatures, in the range 1000–1050°C.

19-3 Nitrogen-containing stainless steels

Most stainless steels contain small amounts of nitrogen due to pick-up from the atmosphere during melting. More recently, nitrogen has been deliberately introduced, because of its beneficial influence on both strength and corrosion resistance (*cf.* equation 19-3-1) and its powerful austenite stabilising effect (*cf.* duplex grades, Figure 19-7-3). Furthermore, nitrogen is cheap and readily available. Although these favourable actions have been known for some time, their commercial exploitation was limited by the difficulty of introducing large amounts of nitrogen in solid solution. For this reason, the development of nitrogen-alloyed stainless steels began only in the latter half of the 20th century [Lil99]. Because of their many advantages, their use is growing steadily.

One method of increasing the relatively low solubility is to use a high pressure nitrogen atmosphere, either during melting or during sintering of powders. An easier means is to take advantage of the effects of other alloying elements. Thus, Figure 19-3-1 shows that the solubility of nitrogen in pure iron is very low, but that it is significantly raised by the addition of chromium. Furthermore, it should be noted that the solubility is much higher in austenite than in δ ferrite. The sharp decrease on solidification can cause problems due to gas bubbles, particularly in castings and welds [Fei99] (*cf.* § 15-3). A remarkable feature is the fact that, particularly in the presence of chromium, the solubility increases with

Figure 19-3-1:
A) Effect of chromium and temperature on the solubility of nitrogen in iron under 1 bar of nitrogen.
B) Magnification for pure iron.
Thermocalc calculation (see also [Fri99]).

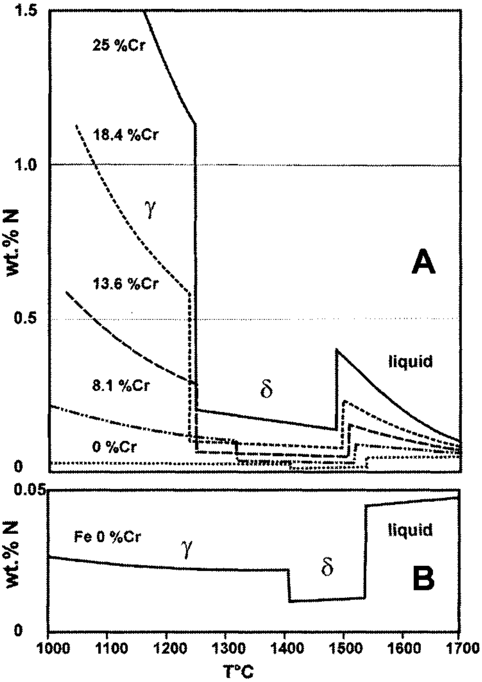

decrease in temperature. More generally, nitrogen has a strong affinity for the elements in groups IVB, VB, VIB and VIIB of the periodic table. When these elements (*e.g.* V, Zr, Ti, Ta) are employed, they initially increase the solubility of nitrogen in liquid iron, but since they also form stable nitrides and carbonitrides, the solubility products fall rapidly with temperature and little nitrogen effectively remains in solid solution. The two most useful elements for raising the solubility of nitrogen are manganese and especially chromium. Nitrogen interacts more strongly with chromium than with any other element, without necessarily forming nitride precipitates [Sum99]. Indeed, at high temperatures, nitrogen is trapped in chromium clusters within the austenite lattice. This increases the flow stress and reduces the diffusivities of both chromium and nitrogen. The existence of these clusters raises the stability of the austenite and retards the precipitation of chromium carbides and chromium-rich intermetallic phases such as sigma. The austenite-stabilising effect of nitrogen is illustrated in Figure 19-3-2, which shows an isopleth for an Fe-0.4C-15.5Cr-1.8Mo-0.3V steel as a function of nitrogen content.

Nitrogen-alloyed stainless steels include a wide range of compositions, with up to 33 % Cr and 30 % Ni [Por99]. Depending on the alloy chemistry, Cr_2N chromium nitride particles may form coherently within the grains, with a beneficial effect on mechanical properties [Kob01], or conversely, at high chromium and nitrogen contents, by a detrimental discontinuous grain boundary reactione $\gamma' \rightarrow \gamma + Cr_2N$ [Van95].

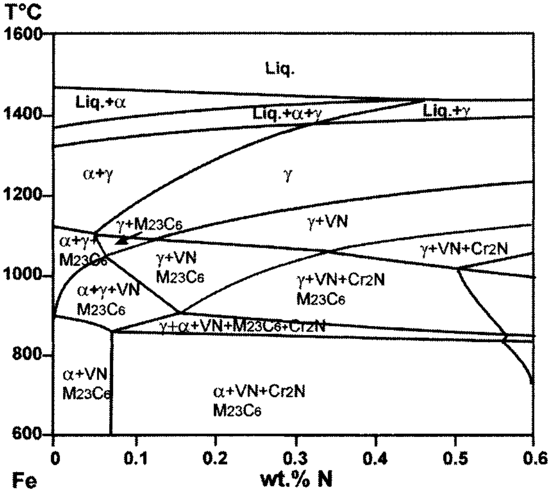

Figure 19-3-2:
Isopleth for an Fe-0.4C-15.5Cr-1.8Mo-0.3V steel as a function of nitrogen content. Courtesy Aubert et Duval, Les Ancizes, France

19-4 Manganese-containing austenitic steels

The first manganese-containing austenitic steel was invented by Sir Robert Hadfield in 1882 and compositions close to his 1.2 % C–12 % Mn alloy are still used today, for applications requiring high toughness and wear resistance, such as ore crushing equipment, heavy duty railway wheels, etc. Manganese stabilises austenite by retarding transformation [Tak87], which can nevertheless be induced by strain, leading to high but gradual work hardening. However, manganese does not enhance corrosion resistance. It is used in stainless steels principally as a cheap alternative to nickel. At the carbon levels typically employed in stainless steels, concentrations of 15 to 18 % manganese are usually sufficient to stabilise austenite, although amounts up to 25 % are sometimes employed. Moderate chromium contents of 13 to 16 % ensure adequate corrosion resistance, while additions of 0.15 to 0.35 % nitrogen help to stabilise the austenite and improve strength. These alloys have a relatively low coefficient of thermal expansion, similar to that of carbon steels. This combination of properties has led to their use for railway rails.

Manganese-rich stainless steels are also non-magnetic, and their combination of low susceptibility and low thermal expansion has been exploited in certain special cryogenic applications. One particular low temperature use is for liquid natural gas pipelines. In order to increase the ductility at very low temperatures, chromium has sometimes been replaced by aluminium, which when present in sufficient quantity can form a corrosion-resistant surface oxide layer.

Another suggested advantage of replacing nickel by manganese is avoidance of allergic effects in contact with the skin. However, allergic response to nickel requires release of this element from the alloy. This does not occur in the case of standard austenitic stainless steels, which are widely used in applications involving food compatibility and hygiene requirements.

Table 19-4-1:
Some examples of manganese-containing austenitic steels

Alloy	C	Cr	Ni	Mn	Mo	Cu	Si	N	Applications
204Cu	<0.15	16/18	1.5 3.5	6.5/9	<1	2/4	<1	0.05/ 0.25	
X2CrMnNiMoN19-12-11-1 P506 Böhler, Austria	0.012	19.2	10.9	12	0.86		0.23	0.33	cryogenics
X8MnCrNi28-7-1 KHMN30L, Kawasaki, Japan	0.1	6.7	0.82	28			0.6	0.1	cryogenics
1.4565 UNS34565		24	18	6	4.5			0.4	

Table 19-4-1 gives a few typical examples of manganese-containing austenitic steels. Manganese contents greater than 30 % and prolonged exposures at around 550 °C must be avoided, since they can induce the formation of the embrittling ß-Mn phase. It can be seen that nitrogen additions are commonplace in these grades. Indeed, manganese enhances the solubility of nitrogen in austenite and inhibits the formation of Cr_2N at high chromium levels.

19-5 Resulphurised stainless steels

Sulphur has low solubility in both ferrite and austenite and segregates strongly during solidification. It is generally considered as an impurity and excessive amounts cause the formation of low melting point eutectics. The detrimental effects on ductility and corrosion resistance are such that sulphur levels are generally reduced by calcium treatment during liquid metal processing. However, sulphur is sometimes deliberately added to improve machinability, in so-called *free-machining grades*. The presence of sulphides enhances chip fragmentation during machining, reducing power consumption and preventing build-up and entanglement on the cutting tools. This effect can also be achieved by adding small amounts of lead and by ensuring the presence of low melting point oxide inclusions, based on the Al_2O_3-SiO_2-CaO system. Although the sulphide particles and oxide inclusions break readily during machining, they are sufficiently ductile at high temperatures not to excessively impair the hot rolling behaviour. These principles can be applied to numerous standard martensitic, ferritic and austenitic stainless steels, for which many free-machining versions are commercially available.

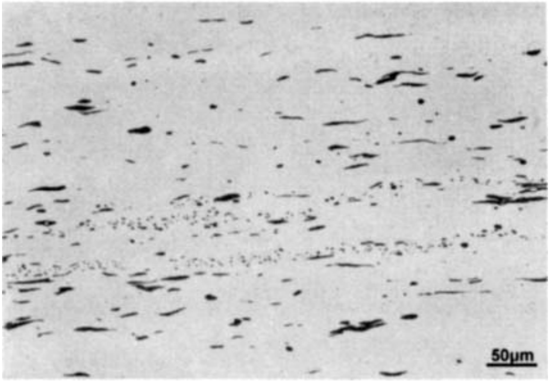

Figure 19-5-1:
Optical micrograph of a longitudinal section of a hot rolled type 303 stainless steel bar, showing mixed chromium-manganese sulphide particles. Courtesy Ugine Savoie Imphy, Arcelor Group.

Sulphide formation processes and morphologies

Because of their marked influence on properties, sulphides in steels were extensively studied during the early 20th century and in the 1930s were classified by Sims in three categories, designated types I, II and III. This basic classification has subsequently been discussed and improved by many different authors [Fre71], [Bak72], [Bak73], [Fre73], [Big75], [Fre75], [Fre77], [Stj80], [Oik99]. Type I sulphides are coarse and are associated with oxide inclusions. This could indicate that the oxides have acted as a nucleus, but may simply be due to joint precipitation in the last liquid of a sulphur-rich droplet. Type II sulphides are generally elongated, with various sizes, and are often assumed to be formed as rod-like eutectic particles. Type III sulphides have a coarse angular morphology considered to be deleterious. The diversity of sulphide morphologies is essentially related to differences in alloy composition, including both major additions, such as chromium and nickel, and minor elements, such as carbon, oxygen, aluminium and titanium, and of course, the sulphur content. These factors can affect segregation behaviour and sulphide nucleation. The common feature of sulphur-rich free-machining steels is the formation of two immiscible liquids during the solidification process. Dissociated liquid droplets have a much greater tendency to float, grow and coarsen than solid particles. The cooling rate therefore has a marked influence on the final morphology.

The hot-rolled 303 grade resulphurised austenitic stainless steel illustrated in Figure 19-5-1 shows elongated type II sulphides, with two size ranges. This observation suggests a solidification sequence such as that described in § 6-5 (*cf.* Figures 6-5-6 and 6-5-7). The interpretation is based on consideration of the Fe-Mn-S ternary phase diagram (§ 4-9), which shows that an iron-rich alloy will follow a whole series of transformations during cooling from the liquid. Thus, peritectic, metatectic, monotectic and eutectic reactions occur successively within a short temperature interval. In these circumstances, it is hardly surprising that small variations in composition change the phase equilibria and modify the solidification sequence, and hence the sulphide morphology. In particular, for stainless steels, it is not the Fe-Mn-S diagram that should be considered, but rather the multi-component system including chromium, nickel and oxygen. Indeed, Figure 19-6-1 shows that the sulphides correspond in fact to a mixed (Mn,Cr)S phase. However, knowledge of these complex systems is insufficiently precise for them to provide a useful basis for interpreting the observed structures.

19-6 Ferritic stainless steels

Most ferritic stainless steels have a structure consisting entirely of ferrite at all temperatures. However, the category also includes alloys in which small amounts of high temperature austenite can be removed by annealing below about 800 °C. Ferrite is promoted by a high chromium content and low concentrations of austenite stabilising elements, such as nickel and manganese. Carbon and nitrogen, which are also strong austenite stabilisers, have very low solubilities in ferrite. Since the precipitation of chromium carbide can cause sensitisation of grain boundaries, particularly in weld zones, carbon levels are usually kept as low as possible, by the use of secondary refining processes such as AOD and VOD (*cf.* § 15-3). Residual carbon and nitrogen can be tied up by the addition of strong carbide and nitride formers, such as titanium, niobium and zirconium. For enhanced corrosion resistance, very high chromium contents (28–29 %) are combined with molybdenum additions, in the so-called super-ferritic stainless steels [Lac93]. Examples of standard ferritic stainless steels are given in Table 19-6-2.

According to the Fe-Cr phase diagram (*cf.* Fig. 4-4-2), the minimum chromium content needed to avoid the δ/γ two-phase region bounding the γ loop and thus ensure a fully ferritic structure at all temperatures is about 12 %. However, in the presence of about 300 ppm carbon, the value is raised to 17 %. At greater carbon levels, austenite can form at high temperatures. This is illustrated in Figure 19-6-1, corresponding to a specimen of 17 % Cr steel quenched during directional solidification, where the primary ferrite dendrites have decomposed to a mixture of ferrite and austenite on cooling. However, annealing below 800–900 °C is sufficient to transform the austenite to ferrite. The basic ferritic stainless steel thus typically contains 17 % Cr and about 0.08 % C, but various carbon levels are in fact employed.

When the matrix is fully ferritic, the principal microstructural features are the minor phases, particularly $M_{23}C_6$ carbides in unstabilised alloys. In stabilised grades containing titanium, niobium or zirconium, the carbides, nitrides or carbonitrides tend to precipitate at high temperatures and may even form in the liquid. In order to avoid excessively coarse particles, which can impair ductility, it is always preferable to minimise the interstitial levels at the melting stage. Facetted titanium and zirconium nitrides (MN) nucleated in the liquid can have sizes of several microns and often appear with an outer envelope of the corresponding MC carbide, probably formed in the solid (see Figure 13-3-4). In niobium-stabilised alloys, mixed Nb(C,N) carbonitrides are formed, generally with a

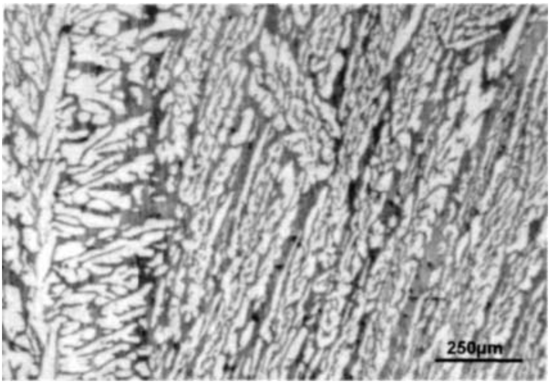

Figure 19-6-1: Optical micrograph of an X17U4 steel specimen quenched during directional solidification. The primary δ ferrite dendrites formed at 1460 °C have transformed to a mixture of ferrite and austenite (light contrast) on cooling through the two-phase region bounding the γ loop. The region shown was at 1260 °C at the moment of quenching. Courtesy Aubert et Duval, Les Ancizes, France

plate-like morphology. Other phases formed at the end of solidification include Laves phases, such as $(Fe,Cr)_2Nb$, and phosphides such as $(Fe,Ti)_2P$ [Lac93]. Carbide and carbonitride precipitates formed in the solid phase at lower temperatures are generally much finer (< 500 nm). Very high chromium ferritic grades can undergo decomposition to a mixture of α-Fe and α'-Cr when exposed in the temperature range 400-500 °C, resulting in severe embrittlement. The presence of fine MC carbides and M(C,N) carbonitrides provides an increase in strength. For example, although ferritic materials have generally poor creep strength, the 436, 441 and 444 grades (*cf.* Table 19-6-2) can support their own weight for high temperature applications up to 700–950 °C, where their oxidation resistance is perfectly adequate [Ant02].

Table 19-6-2: Examples of ferritic, martensitic and duplex stainless steels.

Alloy type	Grade	EN	USA	Comments
Ferritics	X6Cr17	1.4016	430	
	X3CrTi17	1.4510	430Ti	
	X6CrMoNb17-1	1.4526	436	
	X2CrTiNb18	1.4509	441	
	X2CrMoTi18.2	1.4521	444	
	X2CrMoTi29.4	1.4592	447	Super-ferritic
	X6CrS13	1.400	410	0.015<S<0.035
Martensitic	X6Cr13	1.400	403	
	X6CrS13	1.400	410	0.015<S<0.035
Duplex	X2CrNi23-4	1.4362	32304	
	X3CrNiCuN 27-5-2	1.4460	329	0.05<N<0.20
	X2CrNiMoN22-5-3	1.4462	31803/32205	0.08<N<0.20
	X2CrNiMoCuN25-6-3	1.4507	32550/32520	0.20<N<0.35

19-7 Duplex stainless steels

The matrix of duplex stainless steels consists of a mixture of ferrite and austenite, but each of these major phases can undergo transformations, sometimes leading to quite complex microstructures. The earliest studies date back to 1927, while the first patents were filed in the 1930s [Gun97], [Joh00]. However, their industrial development was for a long time inhibited due to difficulties in processing, heat treatment and welding. This is now no longer the case and these problems have been largely overcome by a better understanding of the metallurgy and behaviour of these materials. Commercial alloys contain roughly equal proportions of austenite and ferrite, requiring carefully balanced compositions (*cf.* Table 19-6-2).

The various processing problems encountered include the following factors :

- The solidification structure consists of primary δ dendrites surrounded by γ. Since austenite and ferrite have different thermal expansion coefficients, differential shrinkage during cooling gives rise to stresses that can induce micro-cracking.
- Local stress concentrations can also arise during hot working, due to the marked difference in flow stress between the two phases. The generation of a finely divided microstructure comprising similar volume fractions of the two phases greatly helps to mitigate these two problems.
- The partitioning of nitrogen to the liquid during solidification can generate gas bubbles in castings and welds (*cf.* § 15-4).
- The high concentrations of chromium, together with molybdenum additions, cause significant segregation and can lead to the precipitation of harmful intermetallic compounds in the enriched regions. Homogenising treatments must therefore be performed in the range 1050 to 1300 °C. Homogenisation is more difficult in duplex steels than in ferritic grades, due to the low diffusivities in austenite. It is therefore preferable to use temperatures above 1200 °C. Modern high nitrogen grades do not become fully ferritic even at 1300 °C.
- The interstitial elements, carbon and nitrogen, have a detrimental effect on toughness and weldability, due to the formation of embrittling precipitate phases. Carbon in particular is kept to very low levels, generally less than 200–300 ppm. However, nitrogen alloying is deliberately used in so-called super duplex grades, both to enhance the resistance to localised corrosion and to help to balance the distribution of ferrite and austenite.

Due to their fine grain size and the difference in crystal structure between the two phases, the duplex stainless steels have higher strength than the individual constituent phases. For example, it is possible to reduce component cross sections by about 30 % compared to an austenitic grade of equivalent corrosion resistance. Indeed, their corrosion resistance is often better than that of austenitic alloys, while their relatively low nickel content makes them economical. Furthermore, their thermal conductivity is 50 % higher than that of austenitic grades and their expansion coefficients are closer to those of carbon steels. For example, in Table 19-7-1 comparison between the austenitic grade 1.4435 (AISI 316 L) and the super duplex alloy 1.4507 (data for Uranus® 52N+) shows the following values [Cha93], [Cha94], [Cha95] :

Table 19-7-1: Properties of typical austenitic and duplex stainless steels

	1.4435	1.4507
0.2% Proof Stress MPa	220	550
Pitting Resistance Equivalent Number	23	40
Coefficient Thermal Expansion at 20 °C (10^{-6}/K)	16.5	13.5

Typical applications for duplex stainless steels include components such as tanks, tubing, valves and pumps for contact with aggressive media such as sulphuric and phosphoric acids, papermaking liquors and sour oil-country media containing CO_2 and H_2S. Their weight-saving potential makes them attractive for off-shore engineering and even for architectural uses [Gun97], [Cha00]. The progress made in recent years suggests an even more promising future for these exceptional materials.

Optimisation of the α/γ ratio

Optimum design of duplex alloys is based on the fact that *the overall behaviour is better than those of the separate phases.* The best combination of strength and ductility is obtained when the volume fractions of ferrite and austenite are approximately equal, because high stresses are necessary to transmit strain across phase interfaces. Alloy development then involves improving the properties of each phase, taking into account their mechanical and chemical interactions. In particular, the optimisation of fatigue strength and corrosion-fatigue resistance has often been a major consideration [Cou00], [Sto00]. Figure 19-7-2 shows the dislocation structure in two 1.4460 (AISI 329) alloy strain-controlled fatigue specimens, cycled at 300 and 200 °C. The strain is concentrated in the ferrite grains, which contain a high density of dislocations distributed in tangled cells. The austenite, in which the nitrogen and carbon are concentrated, has a higher yield strength and shows only a low dislocation density. However, austenite volume fractions greater than 50 % lead to a loss in fatigue strength [Her00a]. This is probably because excessive strain concentration in the ferrite then promotes cracking. However, other phenomena can also be involved. The ductility of ferrite can be reduced by the excessive precipitation of intermetallic phases, due to high chromium and molybdenum contents. In corrosion fatigue, local depassivation can occur in austenite where slip lines emerge at the surface, followed by corrosion-induced crack initiation and propagation.

The optimum proportions of the two phases are obtained principally by closely controlling the balance of austenite and ferrite stabilising elements (Cr, Mo and W, and Ni, Cu, C and N respectively) [Cam00], [Par01]. The effect of nitrogen in an Fe-23Cr-6Ni alloy is illustrated in Figure 19-8-2 by corresponding isopleths from the ternary and quaternary phase diagrams. .

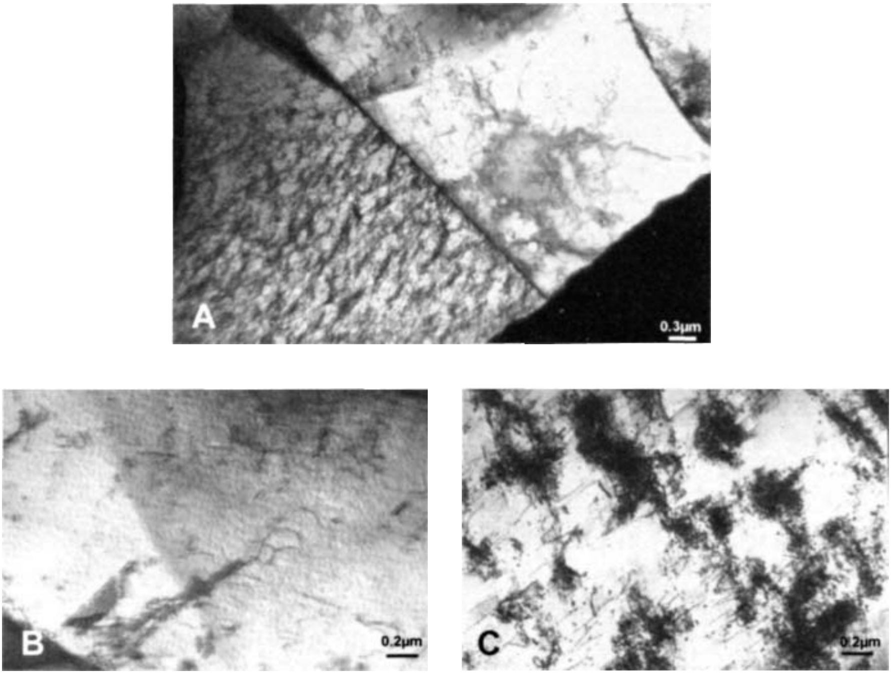

Figure 19-7-2:
Thin foil transmission electron micrographs showing the dislocation structure induced in 1.4460 (AISI 329) alloy by strain controlled fatigue ($\Delta\varepsilon t = 0.57\%$).
A) Cycling at 300 °C. The darker ferrite grain on the left contains a much higher dislocation density than the lighter austenite grain on the right.
B) and C) Cycling at 200 °C. The austenite (B) again contains a low dislocation density, while the ferrite (C) contains a high density of dislocations in the form of a tangled cell structure.
Courtesy CONICET Rosario, Argentina (see also [Her00a] and [Her01]).

The optimum proportions of the two phases are obtained principally by closely controlling the balance of austenite and ferrite stabilising elements (Cr, Mo and W, and Ni, Cu, C and N respectively) [Cam00], [Par01]. The effect of nitrogen in an Fe-23Cr-6Ni alloy is illustrated in Figure 19-7-3 by corresponding isopleths from the ternary and quaternary phase diagrams. .

For a given composition, the proportions and distribution of ferrite and austenite can also be adjusted by heat treatment. Thus, the precipitation of austenite from ferrite on cooling often leads to a coarse structure containing an excessive amount of irregular γ plates (*cf.* Figure 7-1-2). This can be improved by heat treatment at around 1050 °C, followed by quenching.

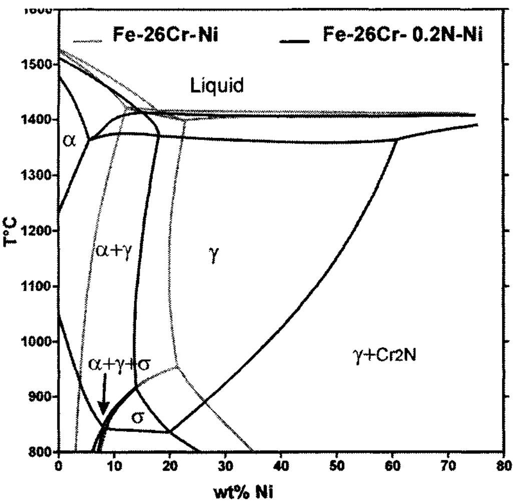

Figure 19-7-3:
Calculated Fe-23Cr-6Ni isopleths for 0 and 0.2 % N. Nitrogen shifts the γ and α+γ fields towards lower nickel contents and reduces the extent of the σ phase field.

Minor phases formed between 1000 and 600°C

Since exposure below 1000 °C can lead to the formation of numerous undesirable minor phases, the duplex stainless steels are generally not deliberately heat treated in this range. However, cooling from higher temperatures during processing can lead to a certain risk, depending on the sensitivity of the particular alloy.

First of all, in materials containing carbon, carbide precipitation tends to occur at α/γ interfaces, with cellular colonies growing out into the ferrite grain. It probably involves a eutectoid type transformation, for example $\alpha \rightarrow \gamma_2 + M_6C$, in the case of Cr, Mo and W rich carbides. Indeed, the constituent formed is termed *delta pearlite*, since it is preferred to refer to the high temperature ferrite as δ rather than α. In the carbon and chromium supersaturated austenite, continuous precipitation of fine secondary $M_{23}C_6$ carbides occurs at around 800 °C [Ama00].

In fact, modern duplex grades have very low carbon contents (Table 19-6-2), but contain deliberate additions of nitrogen. Nitrogen has low solubility in chromium carbides (*cf.* Figure 4-13-3) and tends to form either Cr_2N, or possibly π-($Fe_7Mo_{13}N_4$) after several hours exposure at 600 °C. The π nitrides precipitate at grain boundaries and are often mistaken for σ phase.

Chromium and molybdenum combine with iron to form the intermetallic compounds σ, χ, π and R (*cf.* phase diagrams in § 4-11) [Her00b], [Dup00], [Gun97]. Figure 19-7-4 shows σ and χ phases in a super duplex grade and gives the analyses of the different constituents present. The intermetallic phases have nucleated principally at α/γ interfaces and grown into the ferrite, with a cellular morphology in the case of σ. As in the Fe-Cr-Mo reference system, the σ and χ phases have very similar compositions. Both the ferrite and austenite grains show slightly varying contrast in the scanning electron micrograph, suggesting small variations in composition from one grain to another, which were

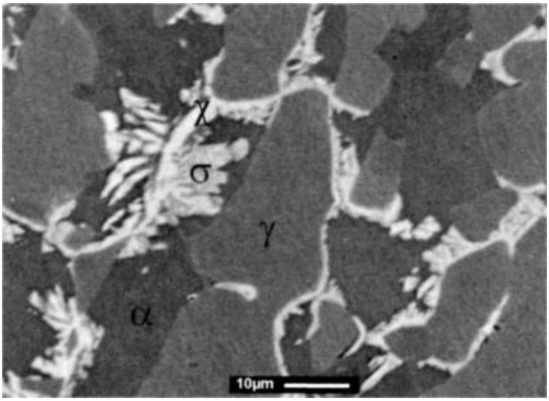

Figure 19-7-4:
Scanning electron micrograph of the super duplex grade Uranus 52N+. The sample was rapidly heated at 20°C/s to 1200°C, held for 10 s and then cooled at 500°C/h. The structure consists of darker ferrite and lighter austenite grains. The intermetallic phases appear medium grey (σ) and light grey (χ). The chemical compositions of all four phases, given in the table below, were found to be quite close. Consequently, the electron contrast was only small and has been strongly enhanced in the micrograph.
Sample courtesy Industeel, Le Creusot, Arcelor Group.

α	Fe60-Cr29-Ni4-Mo5-Si0.6-Cu1.4
γ	Fe62-Cr24-Ni8.5-Mo3.3-Si0.5-Cu1.7
χ	Fe54.8-Cr31.3-Ni4.2-Mo8-Si0.8-Cu0.9
σ	Fe61.1-Cr28-Ni4.6-Mo4.5-Si0.5-Cu1.3

effectively revealed by local analyses. This is not really surprising, since the sample has not been given a homogenising treatment.

Like in austenitic stainless steels, the precipitation kinetics for these compounds are generally fairly slow in ordinary duplex grades. Rapid cooling at about 70 °C/minute usually leads to negligible amounts of intermetallic phases [Nil00]. However, the σ phase is stabilised at high temperatures by chromium and molybdenum and several other elements (*e.g.* Si, Ta, V, Nb, W, *etc.).* Precipitation is significantly faster in ferrite than in austenite, due to the higher diffusivities, as well as the tendency for these elements to partition more strongly to this phase. Thus, sigma phase can form after only two minutes at 900°C in the super duplex grade S32520 (Figure 19-7-5). Although σ phase is intrinsically hard and brittle, its effect on ductility is probably less detrimental when it is in the fine cellular form often observed at high temperatures (Fig. 19-7-4) than when present as long plates. In common with Cr_2N nitride, σ phase also has a deleterious effect on corrosion resistance. Both phases can be associated with local chromium depletion. However, this occurs only in the austenite and not in the ferrite, since diffusion in the latter case is sufficiently fast to ensure homogenisation. Tungsten can replace molybdenum in duplex alloys, where it tends to promote σ phase and other intermetallic compounds in a similar manner, but its effects on properties are not clearly established [Her00b], [Lee00].

An experimental relationship has been shown to exist between impact strength and the volume fraction of intermetallic phases. The minimum acceptable value of about 27 J/cm2 corresponds to a proportion of about 5 % [Nil00].

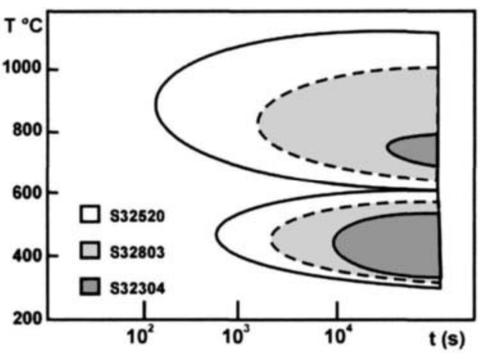

Figure 19-7-5:
TTT diagrams for three duplex stainless steels (see Table 19-6-2). The curves in the range 600–1050 °C are based on micrographic observations of precipitation, without firm identification of the phases concerned. Those in the range 300–600 °C are based on hardness measurements, again without identification of the underlying mechanisms. At high temperatures, the chromium and molybdenum rich alloy S32520 forms what is probably σ phase after only about two minutes at around 900 °C. Adapted from [Cha93].

Minor phases formed between 600 and 300°C

Ferrite decomposition to α-Fe and α-Cr can occur below about 500 °C (*cf.* Figures 4-4-2 and 13-1-5), with the formation of a very fine two-phase structure [Sol78), [Lac93]. The αCr phase may subsequently promote the formation of needle-line Cr_2N particles, while G phase may develop from α-Fe/α-Cr interfaces after long exposures in the range 300–400 °C, due to local enrichment in silicon and nickel. In the presence of copper, additional hardening may occur due to precipitation of ε-Cu in the ferrite. Indeed, this reaction is sometimes used for strengthening. Figure 19-7-5 shows the kinetics of hardening due to low temperature precipitation in three different duplex stainless steels.

20

Heat resisting steels and iron-containing superalloys

The typical operating life of a modern automobile is 2 000 to 3 000 hours. That of a civilian aircraft engine is ten times longer, while certain thermal power station components are expected to last more than 300 000 hours (1 year = 8 760 hours), often with a maximum tolerated strain of only 1 %. Materials to be used in such applications must be extremely stable with excellent creep resistance. Although alloy optimisation is based on similar principles to those applied in the case of other steels, special attention must be paid to the possibility of very slow transformations, and it is necessary to reconsider what can be reasonably defined as a state of equilibrium. High temperature strength and stability tends to be expensive. In particular, austenitic structures are intrinsically stronger at high temperatures than ferritic materials, but require large proportions of costly alloying elements. Depending on the operating conditions, a whole series of materials have therefore been developed, ranging from low alloy steels to nickel base superalloys. For this reason, a brief mention is given to alloys that can no longer be considered as steels, but which provide a comparative framework.

20-1 Ferritic heat resisting steels

The "ferritic" heat resisting steels in fact have martensitic or bainitic structures, strengthened by precipitation, mainly of secondary carbides. They are extensively employed in thermal power stations, for many different components, including boiler vessels, tubing, disks, rotors and bolting. A wide range of different materials has been developed as plant efficiency has increased. Extensive efforts have been made in the USA, Japan and Europe to enhance the thermal yield of the steam turbine cycle, reducing fuel consumption and the associated CO_2 emissions. Since it is a well-established thermodynamic principle that efficiency increases with operating temperature, this has led to increasingly severe demands on materials performance. Thus, *supercritical* plants operate with steam temperatures of 580–600 °C and pressures of around 250 bars, while *ultrasupercritical* processes involve temperatures up to 650°C and pressures of 300–350 bars. Such conditions are extremely demanding in terms of structural stability, creep strength and corrosion resistance, particularly

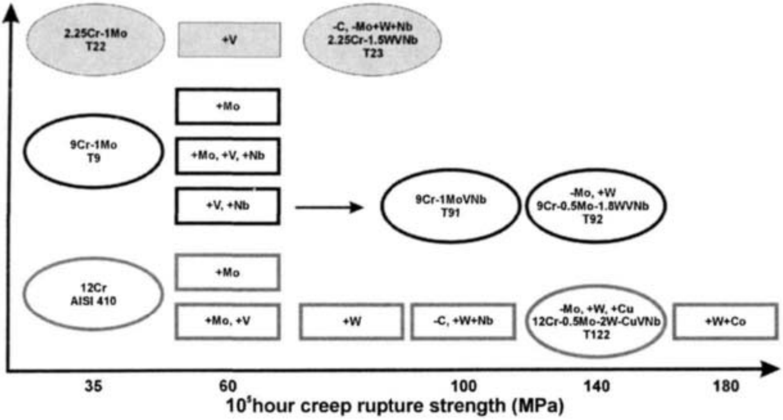

Figure 20-1-1:
Schematic evolution of the three major families of ferritic creep resistant steels, containing respectively 2.25, 9 and 12 % Cr. Standard grades are represented by ovals, while the rectangles indicate development steps. Adapted from [Mas00].

since these properties must generally be associated with good weldability and toughness. A temperature of 650 °C almost certainly represents an upper limit for ferritic materials.

There are three main classes of ferritic heat resisting steels, which have each undergone successive improvements (Figure 20-1-1). The first group, corresponding to 2.25Cr-1Mo steels, includes the T22 grade developed in the 1950s, which is still used for certain components. A modified version developed by Sumitomo in Japan was included in the ASME standard as T23 grade in 1995. Its properties have been improved by controlled additions of tungsten, vanadium, niobium, nitrogen and boron (*cf.* Table 20-1-2). Apart from enhanced creep strength, the new alloy can be readily welded, without the need for pre- or post-weld heat treatment. The second family represents the 9Cr-1Mo steels, initially developed in the USA in the 1970s, with various designations (G91, P91, T91). Significant progress was made in Japan in the 1990s, particularly by the use of tungsten and nitrogen additions to precipitate highly stable carbonitrides. These steels are now known under the standard designations P92 and T92. The third category corresponds to the 12 % Cr steels, whose chromium content is sufficient to be genuinely stainless. Similar improvements to these grades, also made initially in Japan, have led to the recent P122 and T122 standard denominations (*cf.* Figure 20-1-1 and Table 20-1-2).

Alloy development is made difficult by the long design lives required, since the creep properties must be evaluated up to about 100 000 hours (> 10 years) to preclude the risk of loss in strength due to very slow structural transformations. The addition of molybdenum, and later tungsten, induces both solid solution strengthening and precipitation hardening. The quantities employed, in weight %, are roughly such that W + 2Mo = 2. Larger amounts lead to an excessive loss in toughness. However, the basic strengthening mechanism in these materials is precipitation hardening of a martensitic or bainitic matrix. The presence of δ ferrite must be avoided in order to preserve the possibility of obtaining a fully austenitic structure before transformation. This places a limit on the concentrations of strong ferrite forming elements that can be used. Residual δ ferrite impairs both the creep strength and the ductility. This is especially important in the case of large rotors and high chromium contents, since segregation is enhanced by slow solidification rates and cannot be fully removed in the forgings, even after long homogenising and austenitising treatments. In order to avoid δ ferrite, the chromium equivalent must either be maintained < 11 %, or compensated by austenite stabilising elements such as nickel, copper (in limited amounts) or cobalt. However, these elements reduce the creep strength and lower the Ms temperature, leading to a risk of retained austenite. The low corrosion resistance of the 2.25 % Cr grades is improved slightly by the addition of 0.3 to 0.6 % Si. Higher silicon contents enhance the tendency for the formation of embrittling Laves phase.

Table 20-1-2: Compositions of ferritic creep resistant steels, containing respectively 2.25, 9 and 12 % Cr.

Grade	C	Cr	Si	Mn	Ni	Mo	W	P	V	Nb	N	B	Cu
G 22 (ASTM), 10CD9.10 (AFNOR), X22CrMo(W)V	0.15	2.25	0.5	0.60		1.13		0.03		8			
G 23	0.10	2.25	0.5	0.60		0.3	1.75	0.03	0.3	0.08	0.03	0.006	
G 92	0.13	8.5-9.5	0.15	0.60	0.25	0.60	2	0.002	0.25	0.09	0.07	0.006	
GP122	0.11	10-12.5	0.02	0.56	0.32	0.42	1.94	0.013	0.19	0.05	0.05	0.001	0.87

A recent trend has been to add small amounts of boron, which has been clearly shown to have a beneficial influence on creep strength at long lifetimes. Boron segregates to dislocations and grain boundaries and interacts with vacancies, slowing diffusion. It has been found to retard particle coarsening and to segregate preferentially at the precipitate/matrix interfaces. However, the presence of excessive concentrations of nitrogen can neutralise the effect of boron due to the formation of highly stable boron nitride.

On the contrary, combined additions of nitrogen and vanadium cause the formation of stable vanadium nitride, VN, which can significantly enhance the creep strength. When sufficient quantities of these two elements are present in solution during austenitising at about 1 050 °C, vanadium nitrides can be precipitated by subsequent tempering below 700 °C.

Structural stability at very long holding times

An extensive literature is available concerning the creep behaviour and structural stability of 9–12 % Cr steels. The latter aspect is particularly considered in the following references: [Enn97], [Str97], [Jak98], [Hal98], [Abe98], [Kub98], [Str98], [Kad98], [Spi98], [Hof98], [Vod00]. Creep behaviour has been studied for times up to 100 000 hours at temperatures between 500 and 650 °C. In virtually all cases, the initial alloy structure consists of a bainite or lath martensite matrix, with $M_{23}C_6$ carbides at prior austenite and lath boundaries and M_2X particles inside the laths, where X is carbon and/or nitrogen.

Vanadium nitrides, VN, can also be present in alloys containing vanadium and nitrogen. The evolution of these and certain other phases during long exposure times at 600 °C is described below

Matrix

The matrix initially contains a high density of dislocations, which becomes low after 10 000 hours, when the sub-boundaries coincide with the lath boundaries. After 30 000 hours, dislocations become rare and the structure is almost fully recovered.

$M_{23}C_6$ carbides

Carbides or carboborides of the type $(Fe,Cr,Mo)_{23}(C,B)_6$ can form during austenitising, either at austenite grain boundaries or in segregated interdendritic zones containing locally high concentrations of ferrite-stabilising elements. During tempering, they form preferentially at the lath boundaries, by transformation of metastable bainitic cementite. During holding, the average size of these particles increases from a few tens of nanometers initially to about 200 nm after 40 000 hours. The growth kinetics appear to indicate both an increase in volume fraction and a ripening phenomenon. The particle composition also changes, with a gradual increase in chromium content.

Nb(CN) carbonitrides

The M(C,N) carbonitrides (where M = Nb, Ti or V) are primary phases formed in the liquid and trapped during solidification. They refine the as-solidified grain size by acting as nucleants and subsequently impede grain growth. Although such carbonitrides are thermodynamically stable, they tend to gradually transform to a mixture of carbides (NbC) and nitrides (VN) after long holding times. Their stability has been shown to be related to the difference between the lattice parameters of the terminal compounds (*e.g.* NbC and NbN, [Ino01]).

M_2X and MX carbides and nitrides (Cr_2N, Mo_2C, VN)

The Cr_2N phase is not very stable. It tends to dissolve and be replaced by M(C,N) carbonitrides. The latter form inside the laths, with particular orientations, the initially particle sizes being of the order of 30–60 nm. They grow only slowly, elongating in a preferred direction, reaching sizes of 50–100 nm after 40 000 hours. Their growth law and the fact that they are always found to be associated with dislocations suggests that they grow along the latter [Kad98]. The *exceptional long time stability* of these phases makes them extremely efficient strengthening agents.

Laves phases $(Fe,Cr)_2(W,Mo)$

Laves phases are not usually observed in the initial microstructure, but form after relatively short exposure times, increasing in volume fraction up to about 30 000 hours, beyond which the particles coarsen by a ripening process. The initial precipitate sizes are of the order of 70 to 130 nm and can reach 300 to 500 nm after 100 000 hours. The growth rate is highly temperature dependent. It is rapid at 600 °C, but redissolution occurs above 650 °C.

Z phase Cr(V,Nb)N

The Z phase has been observed to form close to $M_{23}C_6$ carbides or Nb(C,N) carbonitrides, which redissolve at long times [Str96]. The Z particles grow rapidly, but a wide range of sizes persist even after very long times, suggesting continued nucleation. Precipitation of the Laves and Z phases tends to absorb a significant proportion of the heavy elements that are the chief contributors to strengthening. The consequence is a loss in creep strength, since the particle sizes are fairly coarse and are unable to compensate for the weakening of the matrix.

η ou M_6Ccarbides , $(Fe,Cr)_3(W,Mo)_3$

The η carbides appear either after long exposure times, or after tempering when the molybdenum content is greater than 1.6 %. Their formation at the detriment of other phases tends to decrease both solid solution and precipitation hardening.

Several authors have used thermodynamic calculations to determine the γ/δ equilibrium at high temperature, in order to appropriately adjust the concentrations of ferrite stabilising elements and predict the proportion of precipitate phases. Relatively good agreement was found with experimental observations [Sch98], [Lun97], [Kad98]. However, the data bases do not contain information concerning all possible phases (*e.g.* Z phase) and comprise inevitable simplifications for the intermetallic compounds (*cf.* § 4-11).

The long time behaviour of the T22 grade is well established, due to its early introduction. It differs from the above description due to its low chromium content. The initial microstructure consists of tempered martensite containing M_3C, M_2C and $M_{23}C_6$ carbides. After 18 000 hours at 540 or 580 °C, the cementite disappears and a few small M_6C particles are observed. The M_2C carbides, in the form of aligned platelets initially 50 nm thick, coarsen and become less numerous. The $M_{23}C_6$ carbides are initially coarser, of the order of 600 nm, but grow very little [Gop93]. This is because the driving force for growth is low, due to the small amount of chromium in the matrix [Str97].

20-2 Austenitic heat resisting steels

The common feature of this family of alloys is their high creep strength at elevated temperatures. One of the chief reasons is the fact that the diffusivity of all elements is considerably lower in the face-centred cubic austenite structure than in body-centred cubic ferrite. This effect is enhanced by the presence of large amounts of major alloying elements, such as nickel and chromium, together with other more minor additions, in particular the heavy elements, molybdenum and tungsten. These alloys are a natural extension of the austenitic stainless steels. Three groups can be distinguished:

- alloys strengthened by solid solution ;
- alloys containing carbides ;
- alloys strengthened by intermetallic compounds, formed during a deliberate precipitation treatment.

Solid solution strengthening

Table 20-2-1:
Compositions of some typical austenitic heat resisting alloys and iron-containing superalloys.

Alloy	Fe	C	Mn	Si	Cr	Ni	Co	Mo	W	Ti	Nb	B	Al	V
Discaloy	54.2	0.04	0.9	0.8	13.5	26		2.75		1.75			0.1	
A286	53.2	0.05	1.4	0.4	15	26		1.25		2.15		0.03	0,2	0.3
1.4859, Manaurite 900 (Cast Incoloy 800)	45	0.1	1	1.5	19	33					<1			
1.4852, Manaurite XM, A297	36	0.5	1.2	1.5	25	35				<1	<1			
Hastelloy X	18.5	0.15			22	48	1.5	9	0.6					
In 718	18.5	0.04			19	52.5		3		0.9	5.1	0.02	0.5	
In 909 (Pyromet CTX-909	42	0.01		0.4	0	38	13			1.5	4.8	0.005	0.1	

The most efficient solid solution strengthening elements are molybdenum and tungsten, while chromium confers high temperature corrosion resistance. A large concentration of nickel is necessary to stabilise the austenite in the presence of these ferrite-promoting elements. Hastelloy X (Table 20-2-1), which is one of the oldest superalloys, is a representative example, although situated at the high alloy end. It can be readily welded, and is used in sheet form for components such as combustion chambers. Because of its relatively low carbon content (0.15 %), $M_{23}C_6$ and M_6C carbides form mainly only after fairly long exposures at high temperature, together with the compact intermetallic phases σ and μ. The presence of molybdenum and nickel stabilises σ phase to higher temperatures than in the Fe-Cr system (see the Fe-Mo-Cr and Fe-Ni-Cr phase diagrams, § 4-8 and 4-11). However, the kinetics of σ phase precipitation in Hastelloy X are fairly slow, as shown by the TTT diagram in Figure 20-2-2, where they are compared to those for μ phase and $M_{23}C_6$ [Zha00].

Sigma phase is also a problem in the 25Cr-20Ni grades (*e.g.* AISI 310, 314) which are widely used for many high temperature applications. These alloys should not be exposed for long periods at temperatures between 600 and 850 °C, where they can become seriously embrittled. However, in the event of accidental exposure in this range, the sigma

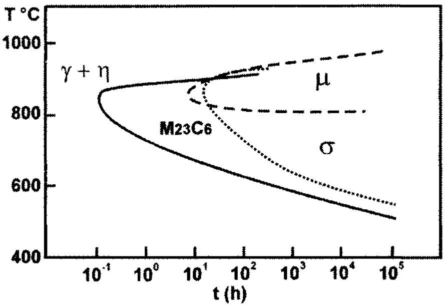

Figure 20-2-2:
TTT diagram for Hastelloy X (*cf.* Table 20-2-1), based on transmission electron microscopy and X-ray diffraction studies. The μ phase and the η carbides (M_6C and $M_{12}C$) have similar proportions of heavy elements, and the same is true for σ phase and $M_{23}C_6$. Simple chemical analysis is therefore not sufficient to distinguish them. Adapted from [Zha00].

phase can be taken back into solution by heat treatment above 900 °C. The tendency for σ phase precipitation is reduced at higher carbon contents, for which the solubility of chromium is significantly lowered. In this case, sigma phase can be avoided by a carbon content of 0.35 % or more (*cf.* Figure 4-8-3). However, σ phase can appear locally in decarburised areas.

Carbide strengthening

Carbon is a cheap and effective strengthening element in these materials. Its influence is due to both solid solution and precipitation hardening, although deliberate carbide precipitation treatments are generally not employed. However, at levels beyond about 0.35 %, the materials become difficult to work and the alloys are produced mainly in the form of castings. Typical carbon levels employed in this case are around 0.4 %, which is generally sufficient to induce the formation of primary carbides. For example, a 25Cr–20Ni steel with 0.4 % C forms a $\gamma/M_{23}C_6$ eutectic at the end of solidification. A slight decrease in the Cr/Ni ratio is sufficient to replace this by a γ/M_7C_3 eutectic. The latter has a more facetted and more highly interconnected morphology, leading to lower toughness and easier penetration of corrosion along the carbide network [Gri83].

An important application for heat resisting alloys is the manufacture of tubing for high temperature, high pressure, petrochemical processes, such as reforming and cracking. The tubes are generally produced by casting into rotating moulds (centrifugal casting). The requirements are good creep strength and good resistance to oxidation and carburisation. The Manaurite XM grade (DIN 1.4852) is used up to 1 100 °C. It has a 35Ni–25Cr base composition with 0.5 % C and additions of niobium and titanium. The high chromium and nickel contents, together with 1.5 % Si, confer excellent resistance to the carburising environments encountered in many petrochemical processes. For comparison, the temperature capability of cast Manaurite 900 or Incoloy 800 (DIN 1.4859) is only 1000 °C (*cf.* Table 20-2-1). Other more sophisticated alloys with still higher nickel contents have been developed for even more demanding applications, but fall outside the scope of the present book. However, it is interesting to point out that many cast cobalt-base superalloys employ similar strengthening mechanisms.

The microstructures of the Manaurite 900 and XM alloys after exposure for 1 000 hours at their maximum design temperatures (respectively 1000 and 1 100 °C) are illustrated in Figure 20-2-3. In the as-cast condition, the structures of these alloys are composed of primary austenite dendrites with various eutectic constituents in the interdendritic regions. In the order of formation, these are $\gamma/M_{23}C_6$, γ/NbC and a small amount of a three-phase constituent. Although the eutectic carbides can be either $M_{23}C_6$ or M_7C_3, as in the 25 Cr–20Ni composition, the secondary carbides which form during high temperature exposure are $M_{23}C_6$. The presence of 1.5 % Si also leads to the formation of a few precipitates of G phase ($Ni_{16}Si_7Ti_6$). In Figure 20-2-3 aging has caused the eutectic carbides to coalesce and secondary carbides have precipitated within the dendrites. The dendrites are much coarser in the Manaurite 900 sample, indicating a significantly longer local

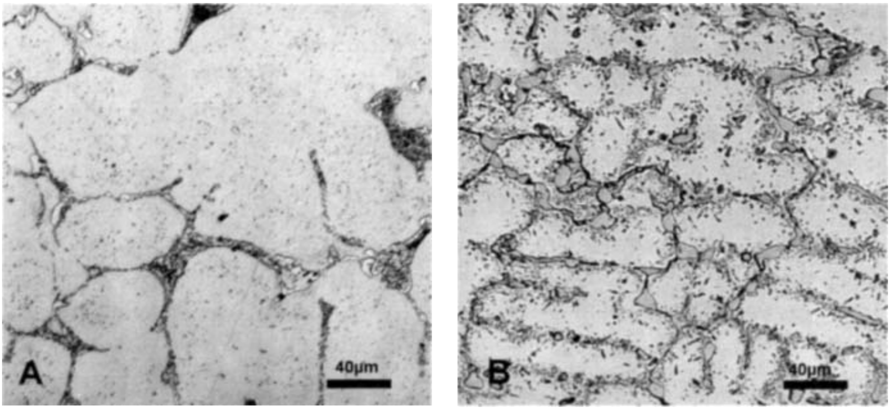

Figure 20-2-3:
Scanning electron micrographs of samples aged for 1000 hours after casting :
A) Manaurite 900 exposed at 1000°C. The as-cast carbide network remains relatively little changed, but secondary carbides have been precipitated inside the dendrites.
B) Manaurite XM exposed at 1100°C. Significant carbide coalescence can be seen.
Courtesy Manoir Industries, Pitres, France.

solidification time. One of the causes is the lower carbon content, which increases the solidification range. However, the main reason is the casting process employed. The Manaurite 900 sample in Figure 20-2-3 A was cast in a static mould, whereas Figure 20-2-3 B represents a 60 mm thick centrifugally cast Manaurite XM tube, for which the cooling rate is much faster.

20-3 Precipitation hardened alloys

The high temperature strength of nickel-base alloys, and to a certain extent austenitic iron-base materials, can be markedly enhanced by the addition of aluminium and titanium. This effect was first observed in 1929, by Chevenard in France, in 36Ni-11Cr heat resisting steels used for steam turbine blades, and simultaneously by Bedford, Pelling and Merica in the USA, in a Ni-20Cr alloy employed for electrical heater elements (cited by [Dur97b]). The strengthening mechanism, which was understood only much later, involves the formation of the so-called gamma prime (γ') phase, $Ni_3(Al,Ti)$. The crystal structure of this phase, designated $L1_2$, can be considered as an ordered face-centred cubic. It has the quite exceptional property that its flow stress increases with temperature, reaching a maximum around 700 °C. Furthermore, shear by single dislocations introduces local disorder, requiring extra energy. Since the order is restored by a second dislocation, particle cutting tends to involve dislocation pairs, with disordered stacking faults between them. The increase in strength with temperature is believed to be due to complex non-planar dislocation dissociation behaviour.

Since the crystal structures and lattice parameters of the γ' and γ phases are very similar, preferred habit planes exist for which coherency is excellent. Precipitation therefore occurs easily and particle coarsening is very slow. However, variations in lattice mismatch can have secondary effects and depend largely on the compositions of the matrix and precipitate phases. In particular, they determine the morphology adopted by the precipitate particles, which are generally either spherical or cubic. The volume fraction of precipitates is also important in this respect. In fact, the volume fraction of γ' can vary over an extremely wide range, from about 8 % in the iron-base Alloy 286 to around 70 % in modern single crystal nickel-base superalloys.

Phase equilibria

The model system for interpreting equilibria between γ and γ' is the Ni-Al-Ti ternary. At 1 000 °C, the γ+γ' two phase region in the Ni-Al binary extends to high titanium contents, corresponding to Ti/Al ratios close to one [Dur97]. In fact, both γ and γ' are stable up to the melting point. In the ternary system, the γ' phase is represented by the formula $Ni_3(Al,Ti)$, but more generally, if its composition is written A_3B, then various other elements can be present on one or both of the sub-lattices A and B. Thus, nickel, cobalt and iron partition preferentially to the A sites, while aluminium, titanium, niobium and tantalum occupy the B sites. The γ' phase has a limited solubility for chromium (3 to 4 %), and chromium therefore partitions preferentially to the matrix. The small amount which is included in γ' can occupy either A or B sites. Gamma prime can accept fairly large amounts of, niobium and tantalum.

In the presence of iron, the γ' field is displaced progressively to lower temperatures with increase in iron content and the range of possible compositions becomes much narrower, and is difficult to define accurately in multi-component alloys. The use of thermodynamic calculations to predict the phases present in these iron-rich alloys remains less reliable than for nickel-base materials [Mil02]. The experimental diagram illustrated in Figure 20-3-1 was determined in 1965 [Hug65]. It shows the intermetallic phases in equilibrium at 800 °C in an Fe-25Ni-15 Cr austenitic matrix as a function of aluminium and titanium contents. For a given titanium content, the phases formed with increasing aluminium are η-Ni_3Ti, γ'-$Ni_3(Ti,Al)$[6], the Heussler phase Ni_2AlTi and β-Ni(Al,Ti). Only γ'-$Ni_3(Al,Ti)$ has the exceptional high temperature strengthening properties described above. Furthermore, the other intermetallic phases tend to have coarse platelet morphologies and overage rapidly.

However, in the range where hexagonal η-Ni_3Ti is theoretically stable *in titanium-rich alloys,* it tends to be replaced by a metastable $L1_2$ structure, γ'-Ni_3Ti. In the Ni-Ti binary system, its composition is close to Ni_6Ti, but in complex alloys it is assimilated to a phase

---

[6] When titanium is present in larger amounts than aluminium, the phase is designated γ'-$Ni_3(\underline{Ti},Al)$ to distinguish it from the identical phase γ'-$Ni_3(\underline{Al},Ti)$ in which aluminium is the majority B element.

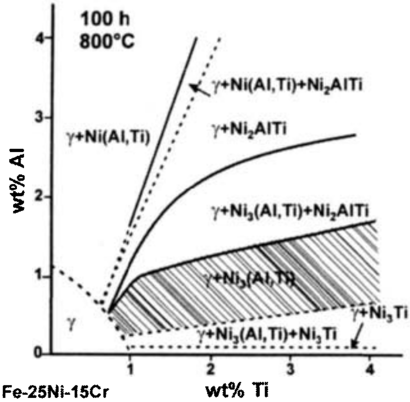

Figure 20-3-1:
Experimental diagram showing the phases present after exposure for 100 hours at 800°C in Fe-25Ni-15Cr alloys containing different amounts of titanium and aluminium. From [Pic78].

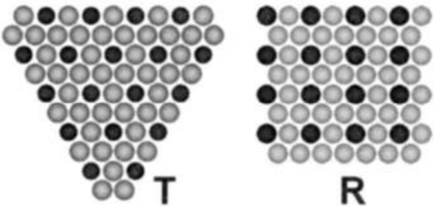

Figure 20-3-2:
Triangular (T) and rectangular (R) arrangements of B atoms in close-packed planes of A_3B structures. The light atoms represent nickel and the dark ones respectively Al in T planes and Nb in R planes, their dimensions being proportional to their atomic size.

Table 20-3-3: Precipitate phases formed on addition of different strengthening elements S in various matrices M. The shaded cells correspond to the alloy in Figure 20-3-1.

M	S	Phase and morphology up to 650–700 °C	Phase and morphology above 650 °C
Fe-25Ni-15Cr	Al, Ti		η-Ni$_3$Ti : hexagonal, D0$_{24}$; γ'-Ni$_3$(Al,Ti) : fcc, L1$_2$; Heusler phase Ni$_2$AlTi : cubic; β-Ni(Al,Ti) : cubic; Except for γ', all precipitates coarsen rapidly
(Ni,Fe)	Ti	γ'-Ni$_3$(Ti, Al) : L1$_2$, fcc T type compact planes Very fine, coherent precipitates Precipitate volume fraction limited to about 10%	η-Ni$_3$Ti hexagonal, D0$_{24}$ T type compact planes Long plates : either intragranular or grain boundary cells
	Nb	γ"-Ni$_3$Nb : body-centred tetragonal, D0$_{22}$ R type compact planes Very fine, coherent precipitates Precipitate volume fraction limited to about 20%	δ-Ni$_3$Nb : orthorhombic, D0$_a$ R type compact planes Long plates, either intragranular or grain boundary cells
Ni	Al, Ti	γ'-Ni$_3$(Al, Ti) : fcc, L1$_2$; fine, coherent, stable precipitates ; T type compact planes precipitate volume fraction up to 70%	

of the type A_3B and it is often considered as a metastable form of Ni_3Ti. The metastable structure provides considerable strengthening, but prolonged exposure above about 650 °C leads to partial replacement by the stable hexagonal form, accompanied by a loss in strength.

An alternative to titanium for precipitation hardening in iron-containing alloys is niobium, which forms another A_3B phase, called *gamma double prime* γ''-Ni_3Nb, at moderate temperatures, where the very fine coherent precipitates provide efficient strengthening. Gamma double prime, with a body-centred tetragonal structure, is believed to be only metastable and transforms to orthorhombic δ-Ni_3Nb during prolonged exposure above about 650 °C. Like η-Ni_3Ti, δ-Ni_3Nb tends to form coarse platelets, associated with only very limited strengthening. When titanium and aluminium are also present, these Ni_3Nb phases are formed beyond a certain Nb/(Al+Ti) ratio.

There are numerous different A_3B phases, whose common feature is the existence of geometrically compact crystal planes consisting of alternate rows of A atoms and ordered A and B atoms. The B atoms on successive A-B rows are located so as to form either a rectangular (R) or triangular (T) pattern (*cf.* § 3-4, Figure 20-3-2 and Table 20-3-3). Variations in the stacking sequence of R or T type planes create different crystal structures [Tom02]. The compact planes are also the slip planes and *tend to form preferred interfaces between the precipitate and the matrix.*

Alloy 286

The matrix of Alloy 286 is very close to that of the experimental alloys in Figure 20-3-1. For example, in Alloy 286 (*cf.* Table 20-2-1), both γ' and η can form, but the η phase usually appears only after long exposure times at temperatures above about 650-700 °C. The transformation tends to occur by a cellular mechanism, initiated at grain boundaries. Since the coarse η platelets are much less effective obstacles to dislocations, the transformation is accompanied by a loss in strength. The exclusive precipitation of γ' could be ensured by choosing an Al/Ti ratio in the hatched zone in Figure 20-3-1 [Pic78]. However, the strength of the γ' phase is also dependent on the Al/Ti ratio, so that the avoidance of all risk of η formation is not necessarily the optimum approach.

Figures 20-3-4 A, B and C shows the gradual replacement of γ'-Ni_3(Ti,Al) by coarse η-Ni_3Ti platelets in hot-rolled Alloy 286 bar solution treated then exposed for long times at 750 and 800 °C.

Figure 20-3-3 D shows the microstructure of a sample from an Alloy 286 disk forging in the standard solution treated and aged condition, and reveals some of the secondary phases that can be observed. It is a transmission electron micrograph made on an extraction replica. The principal hardening phase, γ'-Ni_3(Ti, Al), is present in the form of coherent spherical particles about 10 nm in size, which are too small to have been extracted. Platelets of η-Ni_3Ti are visible at and near the grain boundaries, together with some sulphide and carbosulphide platelets (Ti_2S and $Ti_4C_2S_2$). A secondary network appears to decorate former grain boundaries and consists of particles of M_3B_2 boride (where M is mainly Cr

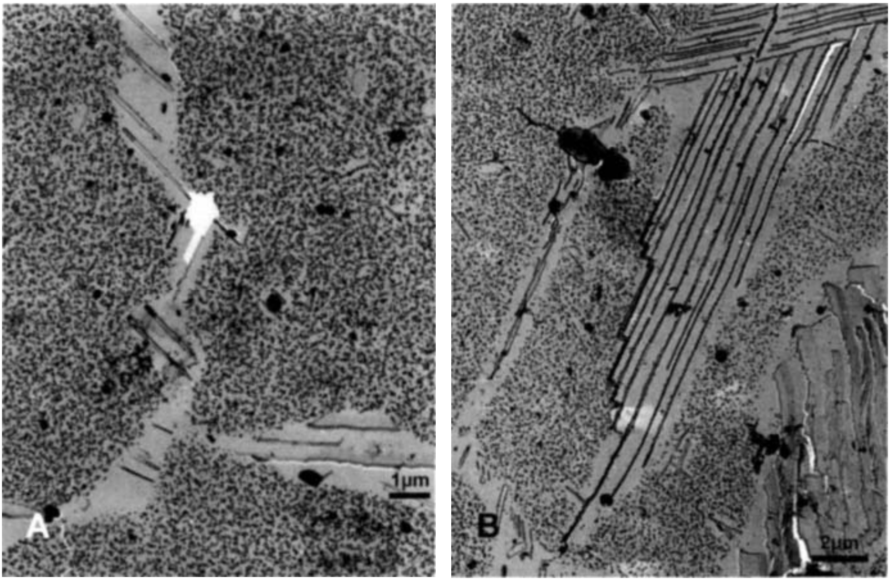

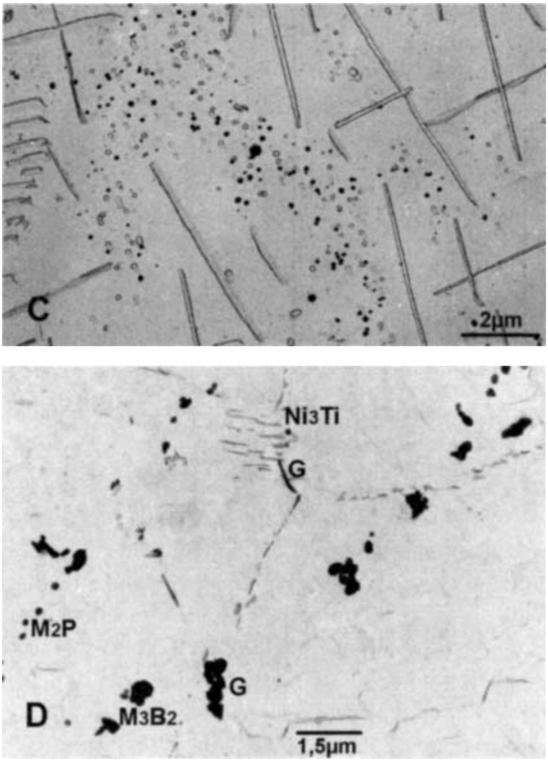

Figure 20-3-4:
Transmission electron micrographs of extraction replicas :
A, B and C) Hot-rolled Alloy 286 bar, solution treated 1 hour at 1000 °C, followed by water quenching and aging for
A) 300 hours at 750°C,
B) 100 hours at 800°C,
C) 1000 hours at 800°C, showing the gradual replacement of γ' by coarse η platelets, initially in the form of cellular colonies at grain boundaries.
D) Alloy 286 disk forging sample in the standard heat treated condition (1 h 900°C oil quench + 16 h 725°C air cool). Platelets of η phase and sulphides are visible at grain boundaries, together with a secondary network consisting of borides, phosphides and G phase, presumably formed at grain boundaries during an earlier stage of processing.
Courtesy Imphy Ugine-Précision, Arcelor Group, Fr

and Mo), M_2P phosphide (where M is mainly Fe and Ti), and the complex silicide known as G phase ($Ni_{16}Si_7Ti_6$). Other secondary phases not visible in the micrograph are TiC and TiN.

Iron-containing superalloys

The definition of a superalloy is somewhat vague. The term is most commonly employed to describe materials which can be used in applications involving both high temperatures and high stresses. Apart from most cobalt-base superalloys, the majority of the materials concerned are strengthened by the precipitation of an intermetallic phase. In the case of nickel-base alloys, the latter is γ', with the $L1_2$ crystal structure (Table 20-3-3). Typical volume fractions range from about 15 to 70 %. The precipitation hardened iron-base alloys described above, such as Alloy 286 or Discaloy, can be included in this category, although the volume fractions of γ' are much smaller. The reason for this is that, as already mentioned, iron favours other intermetallic phases and γ' is stable up to significantly lower temperatures. The optimum ratio between titanium and aluminium tends to be higher. Furthermore, the electronic structure of iron promotes the formation of detrimental topologically compact phases, such as σ and μ. Iron is often simply tolerated, its principal interest being its cheapness.

Alloy 718 and derivatives

A particularly important example of an iron-containing superalloy is Alloy 718 and its derivatives (*e.g.* Alloy 706). It contains 18.5 % of iron and is strengthened essentially by precipitation of the Ni_3Nb phase called γ''. Although in this respect it is exceptional, it in fact represents more than half the total tonnage of superalloys produced, being extensively used for the manufacture of aero-engine turbine disks. It was originally developed by the International Nickel Company and was patented in 1958. A special series of four-yearly conferences is now devoted to these materials. Their microstructural aspects have been described in numerous papers, including [Coz73], [Coz91], [Ora91], [Gar92], and [Wlo94].

Alloy 718 contains 5 %Nb, 0.9 %Ti and 0.5 %Al (Table 20-2-1). The main strengthening phase is γ'', although a small amount of γ' is also formed. The total volume fraction of precipitates is about 18–20 %. The strength level attained is significantly higher than in many nickel base superalloys containing much higher volume fractions of γ'. Unfortunately, the γ'' phase is unstable at high temperatures, so that the service temperature of Alloy 718 is limited to about 650 °C.

The heat treatment comprises solution annealing at between 930 and 1 000 °C, after which the structure contains primary niobium carbides and generally a small amount of intergranular δ phase platelets, which are often deliberately sought to refine the grain size. The standard two-step aging sequence involves holding at 720 °C and then 620 °C, for a total of about 18 hours. The sizes of the γ' and γ'' particles are of the order of 10 nm. The γ' phase forms more rapidly than γ'' and the overall hardening kinetics are slower than in superalloys strengthened solely by γ'. After 1 hour at 760 °C, Collier [Col88] reported

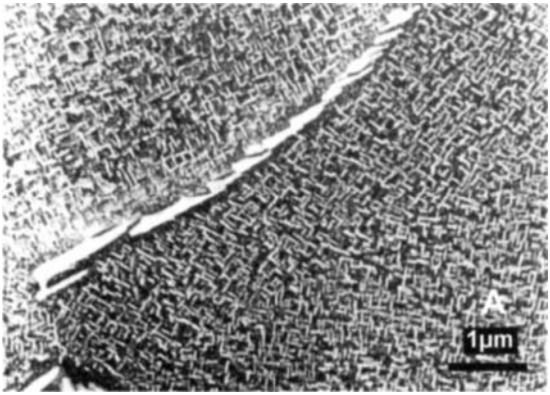

Figure 20-3-5:
Transmission electron micrograph of an extraction replica of an Alloy 718 sample exposed for 10 000 hours at :

(A) 650°C;

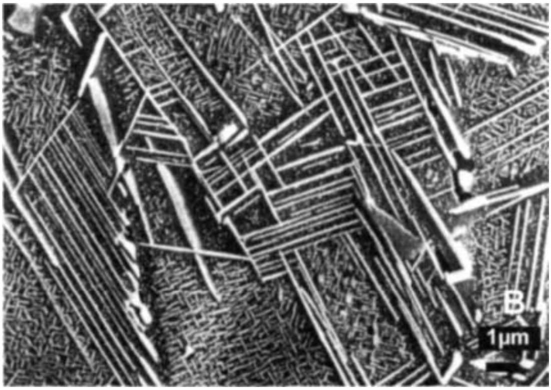

(B) 700°C.
Courtesy Ecole des Mines de Paris [And94].

3.5 % of γ' and 10.1 % of γ". Both phases are coherent with the matrix. The coherency is maintained even after long exposures in service. For example, Figure 20-3-5 A shows the microstructure after 10 000 hours at 650°C [And94]. The γ" platelets have remained fine, with a mean size of 26 nm, while a small amount of δ phase can be seen at the grain boundaries. After the same time at 700°C, the δ phase has spread through the grains in the form of long plates (Figure 20-3-5 B). It can form either by separate nucleation in the matrix or by transformation of γ" particles. The coarse morphology of the δ phase leads to a sharp drop in strength.

The limited temperature capability of 718 type alloys (in common with other iron-rich superalloys) has led to attempts to improve the high temperature stability of the γ" phase. Cozar [Coz73] originally noticed that the γ" precipitates often tend to nucleate on γ' particles which form more rapidly. He found that, when the Nb/Al/Ti contents and aging treatments are appropriately chosen,it is possible to obtain cubes of γ' which become coated on all six faces with γ" platelets, forming what he called a *compact structure.* Interaction of the γ" platelets along the cube edges then prevents growth beyond the dimensions of the cube

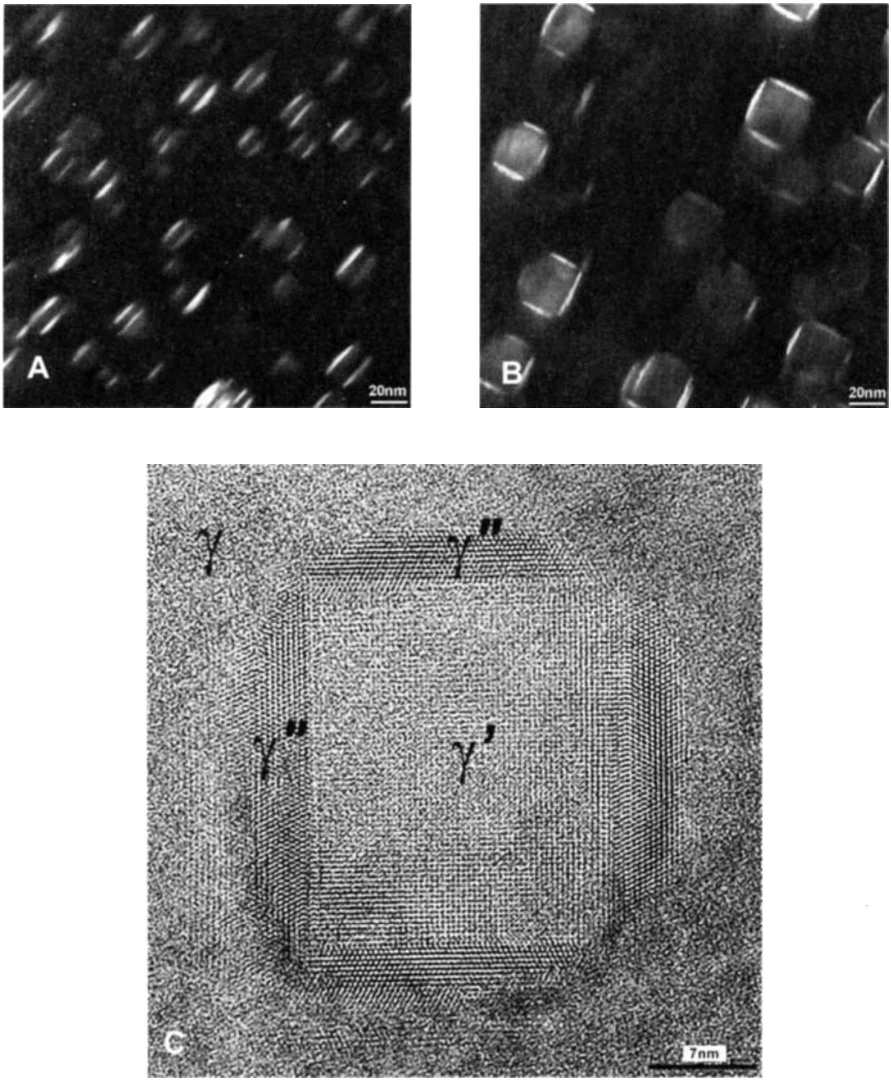

Figure 20-3-6:
Transmission electron micrographs of thin foil specimens of a 718 type derivative alloy showing γ" platelets coating cubic γ' particles :

A) *Sandwich* precipitates after aging for 200 hours at 700°C (dark field image using a γ" reflection).

B) *Compact* precipitates after aging for 16 hours at 750°C (dark field image using a γ" reflection).

C) High resolution image of a compact precipitate.

Courtesy Chogoku National Industrial Research Institute, Hiroshima. See also [He98].

(*cf.* Figures 20-3-6 A et B), leading to enhanced thermal stability [Col88], [Shi96], [He-98]. The γ''/γ and γ'/γ interfaces are fully coherent, with a cube/cube orientation relationship. The absence of a transition region is clearly visible in the high resolution image shown in Figure 20-3-6 C. Unfortunately, the need to precisely synchronise the precipitation of the γ' cubes and γ'' platelets in suitable proportions involves extremely tight control of both the alloy composition and the aging sequence, which so far has proved incompatible with industrial practice. Nevertheless, the subject continuous to arouse appreciable interest.

Low expansion superalloys

There is a demand for materials capable of combining high strength at temperatures up to about 600 °C with low thermal expansion, particularly for aero-engine casing components. Attempts have therefore been made to combine the Invar effect with intermetallic strengthening. The *Invar effect* is an exceptionally low thermal expansion due to the contraction associated with the loss of ferromagnetism on heating. The optimum composition to obtain minimum expansion in the range from 20 to 600 °C corresponds to the Fe-29Ni-17Co alloy, which is therefore used as the matrix. Various alloys have been developed in which strengthening is obtained by the precipitation of γ'-(Ni_3Ti) or γ''-(Ni_3Nb) [Wan91], (*cf.* IN 909, Table 20-2-1, the overall alloy chemistry being calculated to give the required matrix composition after precipitation. The major problem is the need to strictly limit the chromium content, since this element strongly depresses the Curie point, with the consequence that the alloys are prone to embrittlement by intergranular corrosion (Stress Assisted Grain Boundary Oxidation = SAGBO). A recently developed grade compensates the lack of chromium by a large addition of aluminium. Hardening is then obtained partly by the β-NiAl phase.

21

Cast irons

The term cast irons covers a wide range of iron-base materials, whose principal common feature is a relatively low melting point compared to steels.

21-1 Phases and microstructural constituents in cast irons

The cast irons are carbon-rich iron-base alloys with compositions close to the cementite or graphite eutectic in the corresponding Fe-C or multi-component phase diagram. As their name implies, they are used essentially in the form of castings, and are generally too brittle to be hot worked. Although heat treatments are sometimes employed to optimise the microstructure, components are frequently used in the as-cast condition, making the solidification structure particularly important. Depending on the alloy chemistry and the solidification conditions, especially the degree of undercooling attained (*cf.* § 5-6), the carbon-rich eutectic constituent is either a carbide or graphite. The corresponding materials are known as either white or grey cast irons respectively. Rapid cooling rates lead to greater undercooling and generally promote carbide eutectic. The difference in solidification temperature between the white and grey eutectics is determined by the alloy composition (see Figure 21-3-4 below), but the ease of nucleation also depends on the presence of other minor phases that can act as nucleants. In *white cast irons,* the carbon-rich eutectic constituent is either cementite or an alloy carbide, particularly a chromium carbide. In *grey cast irons,* carbon is in the form of graphite, with either a flake or a nodular (spheroidal) morphology. Some cast irons have mixed (*mottled*) structures, with both carbides and graphite. Typical compositions of different types of cast iron are given in Table 21-1-1.

21-2 White cast irons

In low alloy white cast irons, the eutectic is composed of γ-Fe and cementite and has a typical morphology known as *ledeburite* (see Figure 5-6-10). The cementite confers high hardness and excellent abrasion and erosion resistance. It forms a *stiff network* of interconnected carbides, within which the austenite is not continuous. The ductility and toughness are consequently low. Most common white cast irons are hypo-eutectic in order

Table 21-1-1: Typical compositions of different types of cast iron. For the chromium cast irons, the chromium values in brackets represent the approximate concentration remaining in the as-cast matrix. From [Mar70].

Type	C	Si	Cu	Ni	Mn	Mo	Cr	P	Ce	Mg	S
White	1	1		0.2-1	0.5-1	1.5	5-12				
Grey	3.2-3.5	1.8-2.3	0.15-0.4	0.05-0.2	0.6-0.9	0.05-0.1	0.05-0.2	0.12			0.15
SG	3.5-3.9	2.2-3	0-0.5	1	0.3-1	0-0.05	0.10	0.015	0.05-0.2	0.03-0.05	0.02
Cr	2.1					1.4	11.3 (6)				
	2.4					3	20 (12.4)				
	2.7					2.5	25 (15.5)				
Ni	2.3-3	1-6		18-37	0.7-1		1-2.3	0.08			

to compensate for the stiffness of the cementite by a larger volume fraction of austenite. The corrosion resistance of ordinary cast irons is poor and numerous alloy grades have been developed. Only a few of these will be described, chosen to illustrate the overall design philosophy (*cf.* Table 21-1-1).

One group of medium alloy white cast irons contains 3–5 % nickel to retard the pearlite transformation, together with 1–4 % chromium to ensure the formation of carbides by countering the graphite-promoting effects of nickel and silicon. Another family contains 5–7 % nickel and 7–11 % chromium, with M_3C being replaced by M_7C_3 as the eutectic carbide. M_7C_3 is very hard (*cf.* Appendix 22-8) and has a lanceolate morphology that tends to impair toughness. However, the stiff interconnected cementite network is avoided and the volume fraction of carbide in the eutectic is lower. The presence of nickel in these different materials leads to a martensitic matrix and they are often designated as *Ni-hard* cast irons.

The so-called *chromium cast irons* contain from 11 to 23 % chromium, together with up to 3.5 % molybdenum. Their chromium contents ensure good corrosion and high temperature oxidation resistance. High abrasion and erosion resistance is associated with slightly improved ductility compared to ordinary white cast irons. A martensitic or austenitic matrix can be obtained by appropriate heat treatment. These materials are widely used for cast components exposed to corrosive environments, such as hot rolling mill rolls [Dog97], [Par99]. Molybdenum and other alloying elements, such as tungsten, vanadium and niobium, participate in the M_7C_3, $M_{23}C_6$ and M_6C eutectic carbides and also form specific carbides (*e.g.* Mo_2C, VC). Furthermore, molybdenum and tungsten strengthen the matrix by solid solution hardening. Several typical microstructures have been shown in previous chapters (Figures 6-3-6, 6-3-7, 11-3-6 and 12-3-2). Large castings have coarse dendritic structures, with marked segregation that cannot be removed by heat treatment, so that they remain heterogeneous.

The intrinsic characteristics of the eutectic carbides have an essential influence on the mechanical properties of the alloy as a whole. For example, brittle carbides will be fragmented during rubbing between two surfaces and will enhance abrasion. The best behaviour is obtained with alloy compositions close to the eutectic, for which the carbides are most uniformly distributed [De_86], [Yu_02]. Secondary carbides often make a significant contribution to abrasion resistance [Bar72], [De_84]. However, as in the case of tool steels (*cf.* § 18-3), they are efficient only if they are embedded in a hard and tough matrix. The austenite must therefore maintain good hardenability after precipitation, with a carbon content that is sufficiently low to prevent retained austenite, but high enough to ensure adequate hardness in the martensite. A good compromise can be achieved in vanadium-containing chromium cast irons (Figure 6-3-7). A *destabilisation treatment* at about 800 °C is used to precipitate secondary carbides and enable the austenite to fully transform to martensite on subsequent cooling.

Cast irons with very high chromium contents, between 25 and 28 %, together with 1.5 % molybdenum, were developed in the first half of the 20th century. They have excellent abrasion resistance, but are expensive. Finally, cast irons with more than 30 % chromium have a relatively soft ferritic matrix and combine high corrosion resistance with good ductility. Their high carbon contents preclude the formation of σ phase, in spite of the chromium level, but the risk of decarburisation prevents their use in oxidising environments above about 500 °C.

21-3 Grey cast irons

Flake graphite cast irons

Fe-C cast irons containing 2 to 3 % silicon form eutectic graphite on slow cooling, in the form of *twisted flakes* (Figure 21-3-1). Depending on the alloy composition and the cooling rate, the matrix may be austenite, ferrite, or a mixture of ferrite and pearlite. This aspect is treated in detail in the next section concerning spheroidal graphite cast irons. The principal weakness of grey cast irons is their *lack of toughness* associated with the brittleness and morphology of the graphite flakes, which promote the initiation and propagation of microcracks. However, there are various means of modifying the graphite morphology to improve toughness. For example, by the use of appropriate liquid inoculants (see below), it is possible to replace the coarse flakes by a finer, *vermicular* graphite (Figure 21-3-2). In order to conserve a high fluidity for the production of intricate castings, it is preferable not to approach the eutectic composition (4.2 % C) too closely, so that the carbon content is generally limited to the range 2.9–3.8 %.

The crystal structure of graphite consists of sheets of hexagonally arranged atoms stacked perpendicular to the *c* axis. Each atom within these planes is linked to its three neighbours by strong covalent bonds. The fourth valency electron is delocalised and ensures cohesion with the adjacent planes, and at the same confers a high electrical conductivity. However, the strength of the bonds between sheets is only moderate [AES93]. The associated anisotropy explains the facetted growth observed. Thus, the sheets normal to the c [0001] axis grow laterally in the $[10\bar{1}0]$ direction. Steps on the atomic scale are responsible for the apparent curvature of the flakes. Certain elements can inhibit growth in these preferred

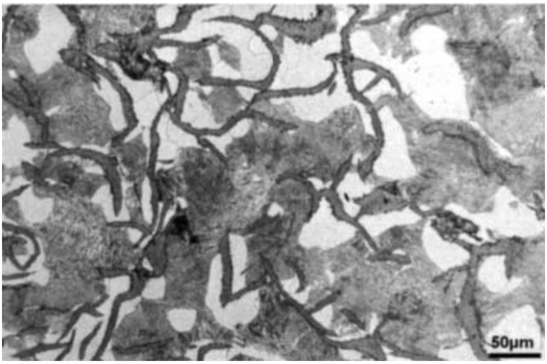

Figure 21-3-1:
Optical micrograph of a nital-etched sample of grey cast iron showing flake graphite. The austenite matrix has transformed during slow cooling to ferrite (light) and pearlite (grey).

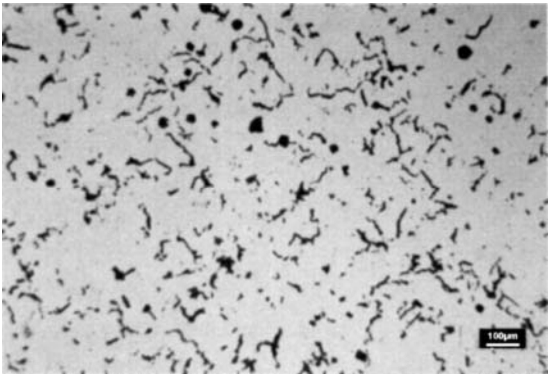

Figure 21-3-2:
Optical micrograph of a hypo-eutectoid grey cast iron showing a vermicular graphite morphology.
Courtesy CTIF, Paris.

directions, leading to nodular or vermicular morphologies. Several minor additions can modify the graphite morphology in this way, including aluminium, antimony, arsenic, bismuth, magnesium, calcium and cerium. The case of spheroidal or nodular graphite is considered in more detail in § 21-4

Malleable grey cast irons – graphitisation of white cast irons

White cast irons can be made ductile by prolonged annealing. The process is termed malleablising. Two phenomena can be concerned. One consists in surface decarburising to decrease the amount of cementite. The product is then termed *whiteheart malleable cast iron* because of the steely white appearance of the core fracture surface. The second involves transformation of the cementite to nodular graphite and leads to *blackheart malleable cast iron.* This is achieved by treatment for several hours at about 1 000°C. The technique has been known for a very long time and the conditions were first described publicly by Réaumur at the end of the 18th century. The cementite decomposes and the carbon liberated forms rosette-shaped graphite nodules, sometimes called *temper carbon.* They have a ragged, non-compact morphology, unlike the nodules in SG irons (Figure 21-3-3). The matrix has become ferritic and the white cast iron has been converted to a perfectly

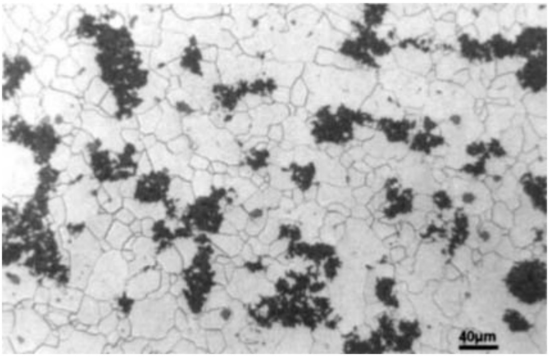

Figure 21-3-3:
Optical micrograph of a white cast iron after a malleablising treatment. The light matrix is entirely ferritic and the graphite nodules appear black.
Courtesy CTIF, Paris.

ductile grey cast iron. The rate controlling mechanism appears to be the diffusion of iron [Sel73]. *Long treatment times are necessary* and the process is therefore costly. It has been virtually abandoned since the discovery of the technique for producing spheroidal graphite cast iron directly from the melt (*cf.* § 21-4).

Graphitisation can also occur during the hot working of high carbon steels. Accelerated graphitisation has been observed recently in products obtained by the direct casting of strip. The fine solidification structure enhances diffusion, while hot rolling breaks up the primary carbides, forming cracks which act as graphite nucleation sites [Son00].

The transition between grey and white cast irons

Low alloy cast irons, without strong carbide forming elements, can form either cementite or graphite eutectic, depending on the degree of supercooling required for growth of each eutectic, that is, on the difference between the effective temperature at the liquid/solid interface and the equilibrium temperature of the eutectic concerned (*cf.* § 5-6). The eutectic considered as the stable one is that whose growth temperature is highest. The presence of alloying elements modifies the respective equilibrium and growth temperatures of the cementite and graphite eutectics and can thus promote one type or the other. However, whatever the kinetic conditions, the equilibrium temperatures defined by the phase diagrams indicate a reliable tendency, since the probability of effective formation of the stable eutectic is greater the larger the difference in equilibrium temperature with respect to that for the metastable eutectic.

Two elements commonly present in commercial cast irons, namely silicon and manganese, have opposite effects. Silicon is a strong graphite stabiliser and its influence can be best analysed by considering the calculated liquidus surfaces in the *stable* Fe-Si-graphite and *metastable* Fe-Si-cementite systems (Figures 21-3-4 A and B) [Lac91], [Mie98a]. The monovariant eutectic lines starting from the points Es and Em on the Fe-C side of the stable and metastable diagrams both end at a ternary eutectic, respectively Ets and Ems. The line EsEts goes through a maximum at about 5 % Si, which is greater than the silicon content generally encountered in cast irons. In contrast, the line EmEtm in the metastable

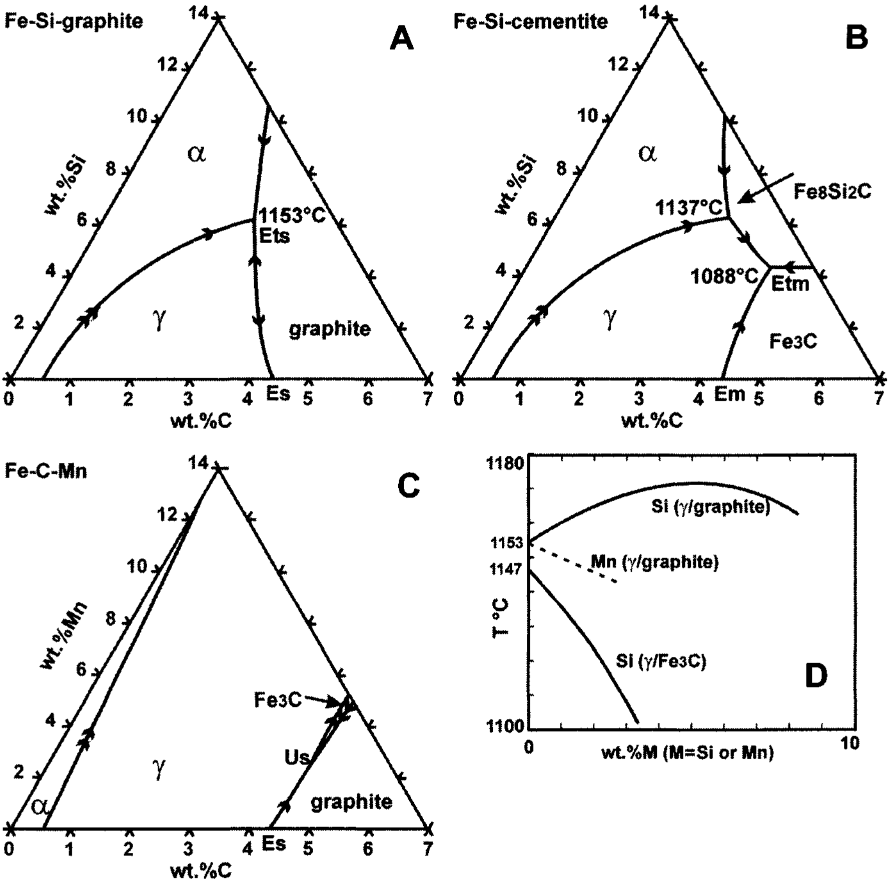

Figure 21-3-4:
Calculated liquidus surface projections
A) Fe-Si-graphite system.
B) Fe-Si-cementite system.
C) Fe-C-Mn system calculated for the presence of both graphite and cementite. The point Us corresponds to a pseudo-peritectic reaction L+graphite=M_3C+γFe whose calculated coordinates are 1141°C, 4.39 % C and 1.9 % Mn. >From the compilation of experimental data [Riv84], the corresponding values are 1139°C, 4.32 % C and 3.0 % Mn.
D) Effects of Si and Mn on the profiles of the eutectic lines (EsEts in A, EmEtm in B and EsUs in D), plotted using values from [Lac91] and [Mie98a] for silicon and [Riv84] for manganese.

diagram falls continuously. The addition of silicon therefore increases the γ/graphite eutectic temperature and decreases that for γ/cementite. The temperature profiles along the two monovariant eutectic lines are illustrated as a function of silicon content in Figure 21-3-4 D. It can be seen that the difference between the two eutectic temperatures increases rapidly with silicon content. The graphite eutectic is stabilised and becomes much less dependent on the solidification conditions. Manganese additions decrease the liquidus temperature for both the graphite and cementite eutectics and promote the formation of cementite. The calculated liquidus surface projection for the Fe-C-Mn diagram is shown in Figure 21-3-4 C and the profile of the γ/graphite eutectic line as a function of manganese content is indicated in Figure 21-3-4 D. The slope is relatively small, but nevertheless decreases the effect of silicon.

Aluminium increases the temperature of the graphite eutectic even more than silicon and is therefore also a strong graphite stabiliser. Nickel, copper and tin are also known to promote graphite formation.

Apart from considerations concerning the equilibrium or growth temperatures, for each type of eutectic, there is a specific degree of supercooling necessary for nucleation. In particular, the nucleation of cementite is difficult. Moreover, even when cementite embryos manage to form, their growth is made difficult by segregation, since this phase cannot accept either silicon or nickel, although it can dissolve a large proportion of manganese. Solute rejection into the liquid generates a boundary layer which inhibits growth. Formation of the cementite eutectic thus requires a large degree of supercooling and a high cooling rate.

A Carbon Equivalent concept is frequently employed to determine whether a cast iron will be hypo- or hyper-eutectic. Empirical relations have been established indicating the carbon equivalent of the graphite eutectic as a function of the carbon, silicon, phosphorus, manganese and sulphur contents. A typical example is :

$$C_{equi} = C - 0.3\ Si + 0.33\ P - 0.027\ Mn + 0.4\ S \qquad (21\text{-}3\text{-}5)$$

where the concentrations are in weight %. The composition of the graphite eutectic in the Fe-C binary system is 4.25 % C.

Transitions between grey and white structures due to cooling rate

During casting, the sudden contact between the liquid metal and the cold mould walls induces very high cooling rates, which can produce a cementite eutectic in compositions that would normally be graphitic. The equilibrium graphite structure is re-established when the cooling rate becomes sufficiently slow (§ 5-6) [Hil68]. Although the degree of undercooling is an essential factor, it will be shown below that *segregation effects are also important.*

Mixed or "mottled" structures

Three examples are described to illustrate transitions for different solidification conditions. The first corresponds to an experimental camshaft casting (Figure 21-3-6 A), whose structure consists of a white outer ring and a grey core, with a mixed region in between. This effect is often deliberately used to obtain components with high abrasion resistance at the surface and good toughness in the centre. In the present case, the alloy is slightly hypo-eutectic and primary austenite dendrites are visible throughout the section. It was

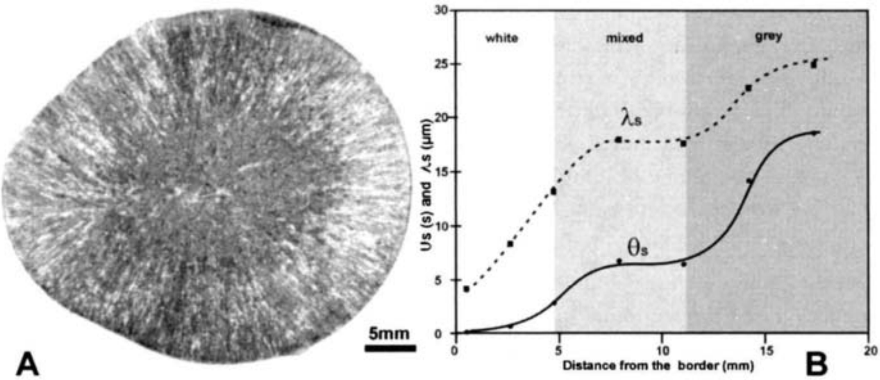

Figure 21-3-6:

A) Macrostructure of an Fe-3.4 C-2 Si-1 Mn-0.003 Ni-0.16 P-0.08 S cast iron camshaft. The columnar surface region is composed of white cast iron, while the centre has a flake graphite structure, with a mixed region in between.

B) Secondary dendrite arm spacing λs and local solidification time θ_S as a function of radial position. The values for θ_S were determined from relation 5-5-3 in which the constant B was evaluated with the aid of unidirectional solidification experiments [Tas01].

Courtesy INPG, Grenoble, and Renault

thus possible to measure the secondary dendrite arm spacing as a function of the radial position (Figure 21-3-6 B). Based on laboratory unidirectional solidification experiments, in which the secondary dendrite arm spacing λs was correlated to the local solidification time θ_S (the time taken to cool from the liquidus to the solidus), it was also possible to plot θ_S as a function of distance from the surface. The experimental relationship between λs in µm and θ_S in seconds is :

$$\lambda s = 8.3^*(\theta_S)^{0.33} \qquad (21\text{-}3\text{-}8)$$

> *In modern cast iron foundry practice, several parameters are controlled. Calculation codes are available for determining local temperature distributions and cooling rates. The local solidification time is an important parameter and can be used to validate heat transfer models describing the propagation of the solidification front in a mould. It can be measured directly during experimental casting runs, with the aid of thermocouples. This is preferred to the evaluation of secondary dendrite arm spacings, which is indirect and more tedious. However, as demonstrated by Figure 21-3-6 B, the microstructure can provide valuable indications concerning the thermal history of a sample.*

The second example corresponds to an Fe-3.8C-3Si hypo-eutectic cast iron, rapidly solidified from the melt by sucking liquid into a thin quartz tube, a quarter section of the rod obtained being illustrated in Figure 21-3-7 A. The high solidification rate at the surface has led to a very fine white structure (Figure 21-3-7 B). The secondary arm spacing of the austenite dendrites is of the order of a micron and the eutectic is in the form of fine plates

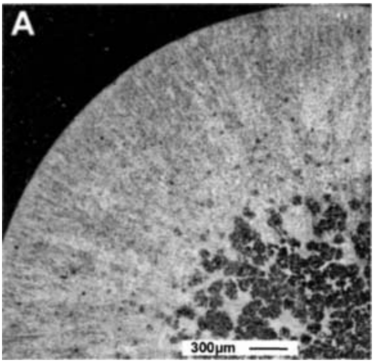

Figure 21-3-7:
Scanning electron micrographs of an Fe-3.8C-3Si hypo-eutectic cast iron.
A) General view showing a columnar grained white surface region and a mixed core structure.
B) Close-up of the surface region showing the fine austenite dendrites and plate-like cementite eutectic.
C) Close-up of the core region showing the mixed structure, with both cementite and graphite eutectic. A few branches of the primary austenite dendrites have been outlined in black (arrow).
Courtesy INPG, Grenoble

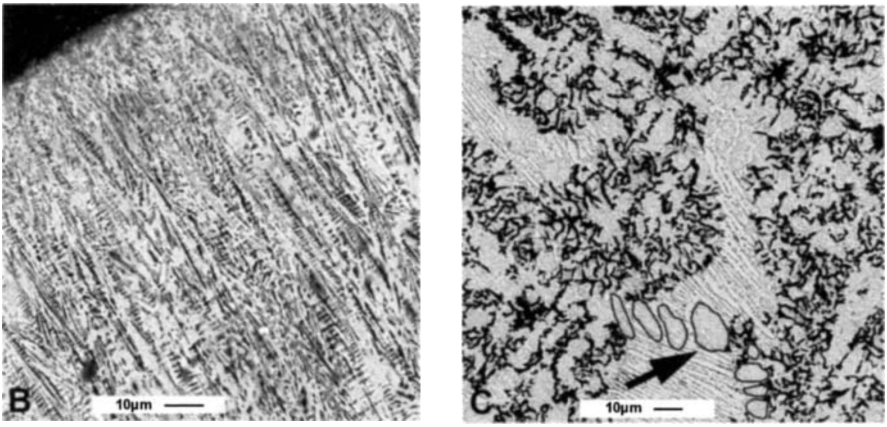

without lateral branches. The core structure consists of coarse primary austenite dendrites that have transformed to pearlite, together with both grey and white eutectics, the latter being the last to solidify (Figure 21-3-7 C). The graphite eutectic has a degenerate vermicular morphology, probably due to the presence of unidentified impurities. The amount of grey eutectic increases towards the centre. The dendrite dimensions show that the growth rate decreased from the surface to the centre. As in the previous example, the transition between white and grey structures occurs between the surface and core, as a function of cooling rate, while that between the grey and white eutectics takes place in the mixed central region, due to segregation effects in the course of the solidification sequence. This will be discussed in the next example.

The third example is a several centuries old cannon ball recovered from a sunken ship in the Mediterranean Sea. The micrographs in Figure 21-3-9 show the structure in an internal region of the cannon ball revealed by slow attack in the seawater, which has preferentially dissolved away the ferrite, leaving the cementite, graphite and Fe_3P phases intact. The microstructure in this part of the cannon ball is mixed (Figure 21-3-9 A), with cells of grey eutectic composed of curved graphite flakes radiating outwards from a central

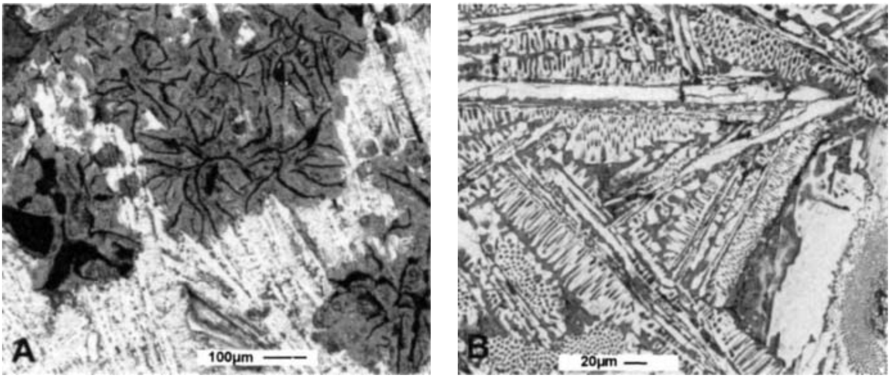

Figure 21-3-9:
Scanning electron micrographs of an ancient cannon ball.
A) Mixed region showing grey eutectic cells surrounded by white eutectic.
B) Close-up of the intercellular white eutectic. The differences in orientation of the eutectic colonies with respect to the plane of section reveal that the cementite is in the form of either wide plates or rods. The grey regions between the colonies are $\gamma/\mathrm{Fe_3C/Fe_3P}$ ternary eutectic.
Specimen courtesy Monaco Oceanographic Museum.

nucleus. These cells clearly formed first, freely growing into the liquid, and were then followed by white eutectic. The latter (*ledeburite*), also consists of relatively coarse colonies, the centre of which comprises a large cementite plate surrounded by a fibrous austenite/cementite mixture. The grey zones between the ledeburite cells are $\gamma/\mathrm{Fe_3C/Fe_3P}$ ternary eutectic, indicating that the alloy contains a fairly large amount of phosphorous.

The coarse grey eutectic cells suggest a slow solidification rate, typical of a large sand-cast part. The alloying elements detected by micro-analysis were silicon, manganese and phosphorus. During solidification of the grey eutectic, the liquid is depleted in silicon and enriched in manganese and phosphorus, leading to a composition more conducive to the formation of white $\gamma/\mathrm{Fe_3C}$ eutectic and finally, at the end of solidification, the $\gamma/\mathrm{Fe_3C/Fe_3P}$ ternary eutectic (*cf.* § 5-6 and § 21-4). Since the partition coefficient for silicon between the grey eutectic and the liquid is greater than one, *silicon is removed from the liquid and its graphite stabilising effect is eventually lost.*

21-4 Spheroidal graphite (SG) cast irons

> *Ductile spheroidal graphite (SG) cast iron was discovered in the 1950s. However, «If coke (which is high in sulfur) had not been used for melting iron and if high purity ores had been used, then ductile iron would have been accepted as the normal form of iron, with flake graphite iron only being discovered much later as an accident of adding S and O. This seems to have been close to the situation in China*

where spheroidal graphite irons were produced over 2 000 years ago [Han91].» in *[Har97].*

Microstructure and mechanical properties

The spheroidal graphite (SG) cast irons illustrated in Figure 21-4-1 have compositions very similar to the flake graphite grades described previously (Table 21-1-1). The change in graphite morphology is obtained by means of a special liquid metal treatment. The graphite is in the form of roughly spherical nodules, which give these materials their name. Because their ductility is significantly improved, an alternative designation is ductile cast irons. The castability, corrosion resistance, machinability and abrasion resistance are similar to those of flake graphite (FG) grades. However, in addition, the tensile elongation can be as high as 17 % [AES93].

The introduction of SG grades has considerably extended the range of application of grey cast irons. Indeed, since 1955, their production has become a hundred times greater than for FG materials. They are used for a wide variety of components, in the automotive industry, civil and hydraulic engineering, etc. Their good toughness in the as-cast condition has led to the fabrication of pipes by the centrifugal casting process, in which the liquid metal is poured into a rapidly rotating mould and is projected against the walls, where it solidifies.

Several mechanisms have been proposed to explain the growth of graphite nodules, according to different observed morphologies [Mur86]. One of these considers them to consist of a compact bundle of cones radiating outwards from a common nucleus (Figures 21-4-1 A and a). Each cone is built up by helical growth around a dislocation. A second mechanism involves layered lateral growth to form a cabbage-like structure (Figure 21-4-1 B). The nodular morphology degenerates in the presence of excessive quantities of strong carbide-forming elements, or when the effects of graphite-stabilising elements are exhausted (Figure 21-4-1 C). The spheres then develop branches that can sometimes evolve into tangled filaments, closer to a vermicular morphology. However, the branches conserve a layered structure, which is clearly visible in the broken section shown in Figure 21-4-1 c. The growth process is not clearly understood on the atomic scale. The observation of regions of amorphous carbon has led to the suggestion that the latter represent the first step in a two-stage mechanism involving subsequent crystallisation to graphite [Pur85].

Process used to produce SG cast irons

SG cast irons are produced directly by the solidification of a melt containing sufficient silicon to ensure graphite formation, after careful removal of sulphur and oxygen [AES93]. Magnesium additions to the bath tie up sulphur and oxygen and radically change the graphite growth morphology. Magnesium reacts with oxygen to form highly stable MgO, which floats to the surface and can be skimmed off. The oxygen content is reduced from typical levels of 90–135 ppm to about 15–35 ppm. Magnesium also reacts with sulphur to

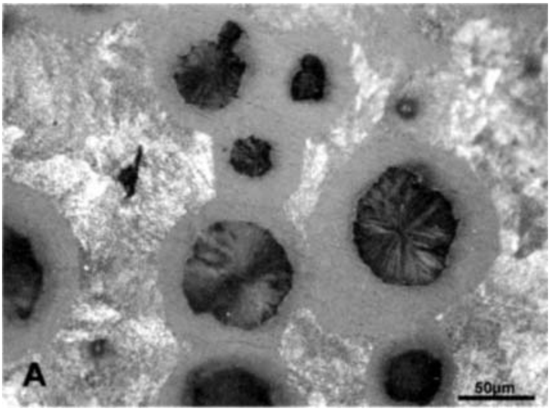

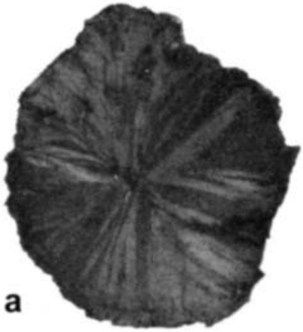

Figure 21-4-1:
Scanning electron micrographs of graphite nodules.
A) SG cast iron in which the matrix has partially transformed to ferrite around the nodules, the remainder being pearlite. Photo a shows a close-up of the radiating nodule structure. Courtesy INPG, Grenoble.

B) Nodule observed on the fracture surface of a ferritic SG cast iron tensile specimen.
Courtesy Ecole Centrale, Paris [Don97].

C) Degenerate graphite nodule exposed by deep etching in an alloy cast iron which also contains cementite (visible at top left). The close-up in c shows a broken branch of a nodule, revealing the stratified graphite structure.
Courtesy INPG, Grenoble

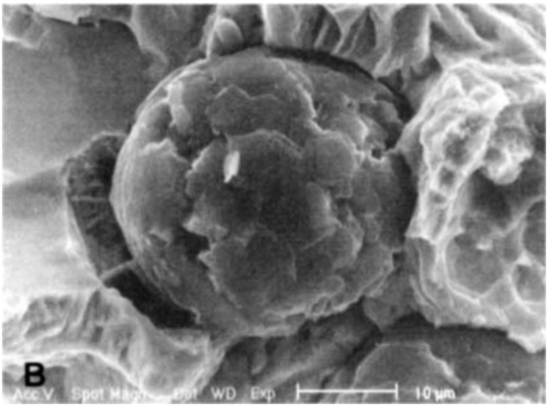

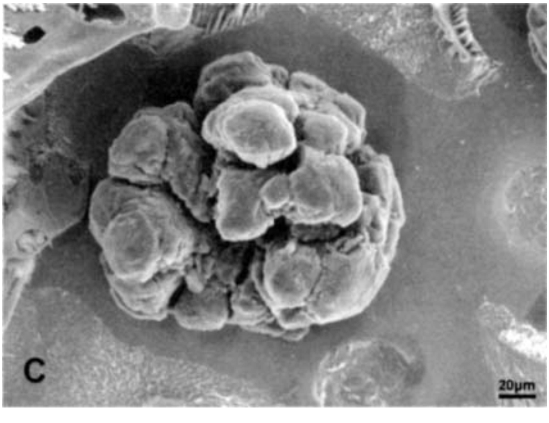

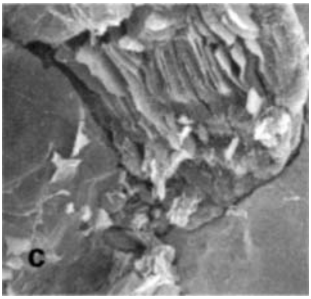

produce MgS, which again floats to the bath surface, but is less stable than the oxide. Since magnesium has low solubility in the metal and is volatile, the reactions can become reversible if losses are too great. Silicon in the form of ferro-silicon is generally added to provide additional deoxidation. Other elements from groups IA, IIA and IIIB can also be employed to tie up oxygen and sulphur. In particular, cerium forms highly stable oxides and sulphides and is less volatile than magnesium, with which it is often used in combination. Some of the inclusions formed by the inoculants act as nuclei for the graphite and are found at the centre of the nodules [Ska93].

The simplest explanation of the spheroidising effect of inoculants such as magnesium is that oxygen and sulphur are adsorbed preferentially on the hexagonal planes of graphite, inhibiting growth parallel to the c axis, leading to a lamellar morphology. The removal of sulphur and oxygen by the inoculant allows more isotropic growth. A careful choice of alloying additions is used to appropriately adjust *the deoxidation, graphitising and nucleation effects.*

The elements present in conventional low alloy SG cast irons are C, Si, S, P and Mn. The carbon equivalent is higher than in ordinary grey cast irons and the sulphur content much lower. In these materials, the final microstructure is essentially determined by the heat treatment employed. The silicon content can range from 1.8 to as high as 6 % when good oxidation resistance is sought. However, high silicon and carbon contents promote flotation of the graphite nodules, while low carbon enhances solidification shrinkage and low silicon leads to carbide formation instead of graphite. Because of the very low sulphur level, manganese is not converted to MnS and is free to strengthen the matrix and stabilise pearlite. However, beyond about 0.7 %, its carbide-stabilising influence becomes significant. Finally, the effects of the alloying elements on solid state transformations will be discussed later in the section on heat treatments.

Alloy SG irons form a second group. They often contain high silicon contents (up to 7 %) to ensure graphite formation and up to 23 % nickel, together with small amounts of chromium (Table 21-1-1). The strong ferrite-forming tendency of silicon is counteracted

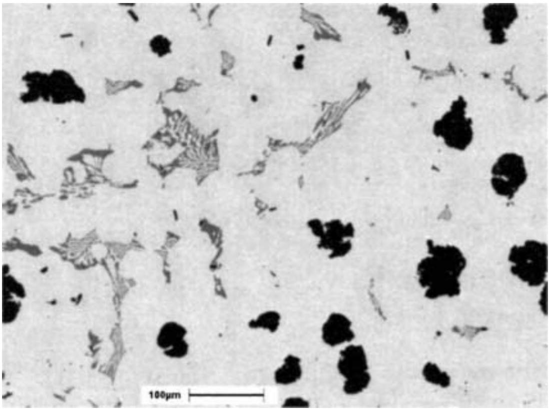

Figure 21-4-2:
Scanning electron micrograph of an as-solidified cast iron : Fe-2.38C-2.6Si-0.9Mn-20Ni-2Cr. The irregular spheroidal graphite appears black and the eutectic M_7C_3 carbides dark grey.
Courtesy INPG, Grenoble.

by nickel, which stabilises an austenitic matrix. The microstructure is not fully spheroidal, and irregular graphite nodules co-exist with regions of interdendritic γ/M_7C_3 eutectic (Figure 21-4-2). Nickel-rich ductile irons have excellent corrosion, oxidation and erosion resistance, together with good castability and machinability, and are non-magnetic. They are used for components designed to withstand high pressures over a wide range of temperature (–196 to +500°C) [AES93].

Solidification of SG cast irons

The solidification of graphite nodules from the liquid is always associated with pronounced undercooling. The graphite sphere grows from a nucleant particle and then becomes surrounded by austenite. At the eutectic composition, the combination of austenite and graphite corresponds to the eutectic. As the austenite cools, it becomes supersaturated in carbon and the new equilibrium is established principally at the graphite/austenite interface, the excess carbon diffusing towards the graphite nodule, where it precipitates out.

The transfer mechanism is explained schematically in Figure 21-4-3, based on the Fe-C binary diagram, taking into account the interfacial equilibria. The reaction involves an increase in volume, which is responsible for the swelling phenomenon observed during the cooling of SG irons. The effect can lead to distortion of castings, requiring corrective machining.

Formation of ferrite halos around graphite nodules

Three stages can be distinguished during the formation of an SG structure. The first is solidification, which is governed essentially by the nucleation process. The second is growth of the graphite spheroids and their austenite envelopes. The third step is the formation of a ferrite halo around the graphite nodules when the temperature falls below that of the eutectoid transformation. Numerous models have been proposed to explain some or all of these stages [Cha92], [Ska93], [Nas97], [Zha97], [Wes97], [Les98], [Lac98], [Lac99a], [Ons99], [Ger00].

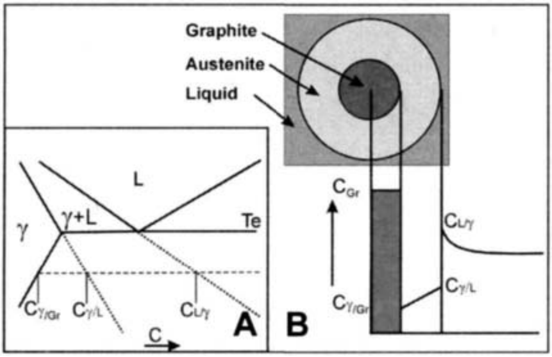

Figure 21-4-3:
Schematic mechanism of graphite nodule formation.
A) Schematic phase diagram. For a given degree of supercooling, the interface concentrations are read from the metastable extensions of the phase boundaries (dotted).
B) Carbon concentration profile at a nodule.

Figure 21-4-4:
Formation of ferrite halos around graphite nodules below the eutectoid temperature.
A) Schematic phase diagram. For a given temperature, the interface concentrations are read from the metastable extensions of the phase boundaries (dotted).
B) Carbon concentration profile at a nodule.

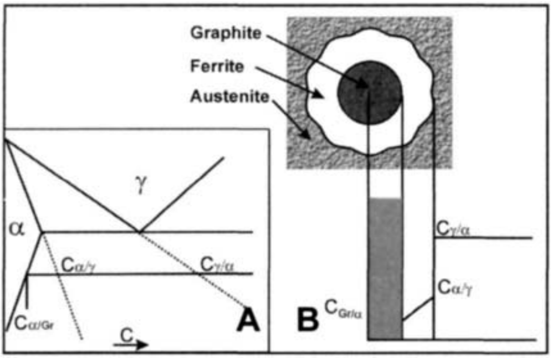

Thus, below the eutectic temperature, new metastable equilibria tend to be established at the interfaces. Figures 21-4-3 and 21-4-4 show schematically how the graphite nodules tend to drain the carbon from the surrounding matrix until it attains the equilibrium composition at the temperature concerned. Assuming that the attainment of equilibrium principally involves the carbon content, the transformation path during cooling can be described more rigorously with the aid of the 4 % Si isopleth shown in Figure 21-4-5. On cooling, the composition and temperature will eventually be situated in the α/γ/graphite three phase region, where ferrite begins to form. It nucleates on the graphite nodules, which become surrounded by a halo of ferrite. A typical example is illustrated in Figure 21-4-6.

The diffusional exchanges are then complicated by the fact that the excess carbon from the austenite must diffuse through the ferrite to the graphite. However, the diffusivity of carbon in ferrite is several orders of magnitude faster than in austenite. The ferrite halo grows to a certain extent, depending on the cooling rate (Fig. 21-4-4). Two cases can arise. If cooling is sufficiently slow, the whole of the matrix transforms to ferrite and the austenite disappears when the temperature and composition are in the α/graphite two phase field. When cooling is rapid, the matrix remains supersaturated in carbon and metastable austenite is retained on entering the two phase field, and subsequently transforms to pearlite. This reasoning demonstrates the importance of the limiting temperature between the α/γ/graphite and α/graphite phase fields. There is a critical heat treatment temperature above which pearlite cannot be formed. In the example shown in Figure 21-4-6, the cooling rate was sufficiently rapid for the matrix to transform completely to pearlite. It should be noted that ferrite halos can also form around flake graphite, as can be seen in Figure 21-3-1.

Fracture behaviour of spheroidal graphite cast irons

Although all forms of graphite remain brittle, the dispersion and limited dimensions of the nodules in SG irons allow the ductility of the matrix to exert a significant influence during deformation. Fracture or disbonding of the graphite nodules occurs only after an

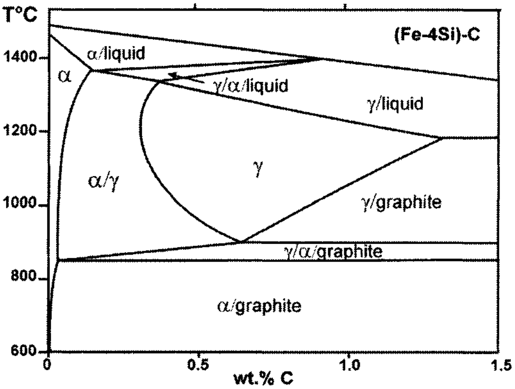

Figure 21-4-5:
4% Si isopleth of the Fe-Si-C phase diagram.

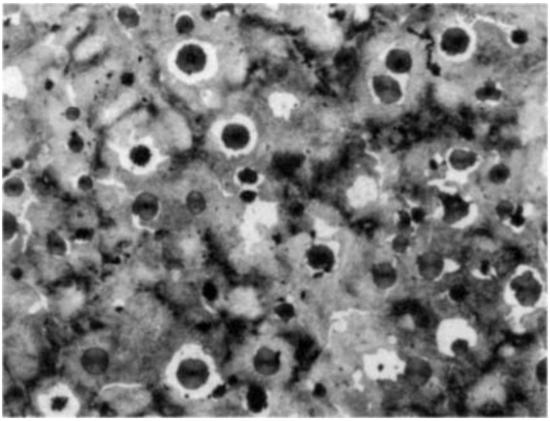

Figure 21-4-6:
Optical micrograph of an Fe-3.7C-2.5Si-0.5Mn-1Cu SG cast iron etched in nital. The sample has undergone a DTA cycle, with cooling at 10 °C/minute between 950 °C and room temperature. Because of the relatively rapid cooling rate, the ferrite halos around the graphite nodules have remained narrow and the austenite has transformed to pearlite. Courtesy INPT, Toulouse

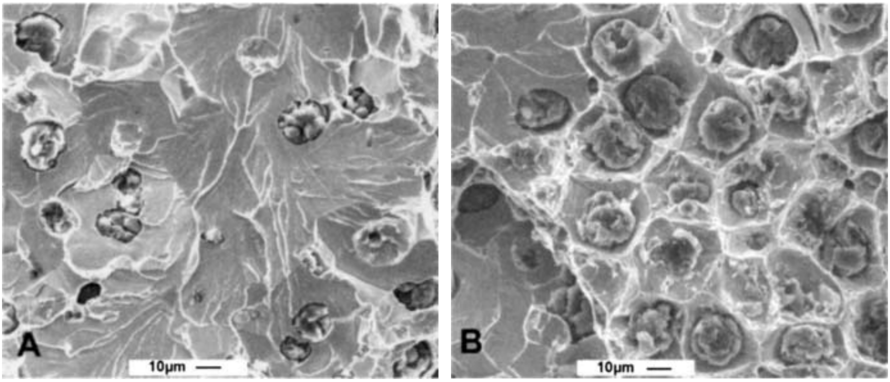

Figure 21-4-7:
Scanning electron micrographs showing the fracture surface of a ferritic SG iron Charpy impact specimen. A) Area near the peened surface. B) Central region.
Courtesy INPG, Grenoble and Renault.

appreciable amount of plastic strain, Figures 21-4-1 [Don97] and 21-4-7. Figure 21-4-7 shows the fracture surface of a Charpy impact specimen taken from the surface region of a ferritic SG iron casting which had been heavily shot peened. The area near the peened surface (A) shows brittle cleavage features, which appear to be independent of the graphite nodules. In the region further from the surface (B), more ductile behaviour is observed, with dimples centred on the graphite spheroids.

21-5 The heat treatment of grey (SG) cast irons

A wide range of mechanical properties can be obtained with SG irons, for fairly limited variations in composition [AES93]. For example, a ferritic iron containing 70–80 % ferrite has a yield strength of around 350 MPa, whereas a similar material given a step quenching treatment can show values between 550 and 1250 MPa.

The recently developed Austempered Ductile Iron (ADI) grades are obtained by step quenching [El197]. They combine good abrasion resistance with excellent ductility and toughness, and also have a high acoustic damping capacity. They can offer a cheaper alternative to certain wrought steel components, requiring shorter overall heat treatments and little or no machining. They are employed for numerous engineering applications, including components such as gearwheels and crankshafts.

In nearly all cases, the first stage in heat treatment is a relatively long homogenising step, generally 2 to 4 hours at 900–930 °C, which also graphitises any carbides that may be present. Higher temperatures are avoided to prevent grain coarsening. Austenitising is then performed for about 4 hours between 820 and 900 °C, the choice of temperature determining the amount of carbon retained in the matrix. These two stages have recently been combined by employing controlled cooling sequences, aided by modelling of the solid state transformation processes concerned [Yoo99], [Bay99].

Ferritic grey (SG) cast irons

In this case, austenitising is performed without homogenising, at a temperature sufficiently low to ensure the subsequent formation of a fine-grained ferritic structure with high toughness. However, it is necessary to dissolve any residual carbides produced during solidification, and this may require times up to about 20 hours. A compromise is to use a short pre-treatment at a higher temperature, to dissolve carbides without excessive grain growth. Various factors must be considered, including the solidification structure and the silicon content. Figure 21-5-1 illustrates the different standard heat treatments employed for SG irons with reference to a TTT diagram. The path required to obtain a ferritic structure is that indicated G+F. When grain size is not a limiting factor, it is possible to employ a direct austenitising treatment consisting in holding for about 12 hours at 930 °C, followed by slow cooling, during which the matrix transforms completely to ferrite.

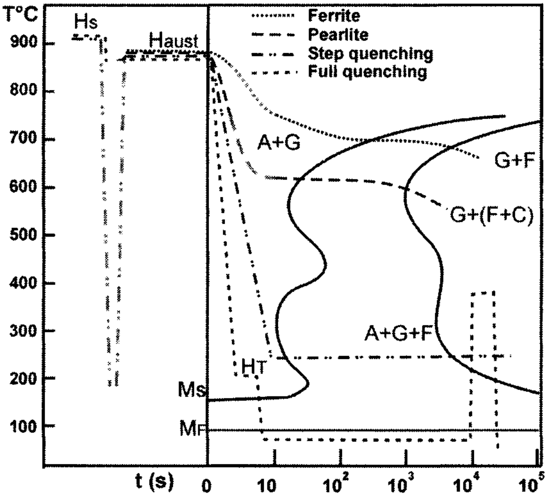

Figure 21-5-1:
Conventional heat treatments for grey (SG) cast irons referred to a schematic TTT diagram.
Hs is the homogenising treatment and Haust the austenitising treatment.
HT represents a low temperature hold to homogenise the temperature before quenching.

Pearlitic grey (SG) cast irons

Pearlitic structures are obtained either after relatively slow cooling or by isothermal holding in the range 450–650 °C (path G+F+C in Figure 21-5-1). Copper, nickel and manganese lower the A1 temperature and enable a finer pearlite structure to be achieved (*cf.* Figure 21-4-6). For equivalent concentrations, the effect of silicon on the TTT diagrams is the same in both cast irons and steels [Lac99b]. The pearlite transformation is promoted by manganese additions [Lac97] (see also § 10-3).

Acicular or "bainitic" cast irons

Step quenching treatments involving a hold in the range 330–420 °C lead to partial transformation of the matrix to ferrite with a lath-type or lenticular morphology. The preferred orientations of the ferrite laths lead to a Widmanstätten type structure (*cf.* Figure 12-3-5 and § 12-3). Due to its appearance, this structure is often referred to as "bainitic". However, because of the silicon content, contrary to the situation in bainite, the ferrite does not contain carbides [Sch75], [Bha92], [AES93]. The manganese content is limited to about 0.5 % to avoid the formation of pearlite. The effect of other elements, particularly copper, nickel and molybdenum, is mainly to modify the transformation kinetics [Cis99].

The choice of austenitising temperature and holding time determines the amount of carbon dissolved in the matrix before transformation. A higher carbon content in the austenite leads to lenticular ferrite with a high dislocation density, similar to lower bainite, in which the carbon partitions between the remaining austenite and the ferrite, while lower carbon contents promote a Widmanstätten ferrite morphology, like that of upper bainite. Excessive carbon contents due to high temperature austenitising lead to the presence of

Figure 21-5-2:
Scanning electron micrograph of an SG cast iron sample that has been step quenched, showing partial transformation of retained austenite to martensite.
Courtesy Ecole des Mines, Nancy, France and IWT, Bremen, Germany. Adapted from [Sch99], [Liu97].

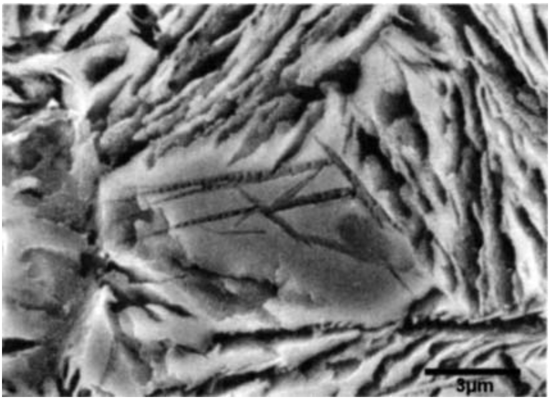

retained austenite, both between the ferrite laths and in the form of massive blocks. The latter subsequently transform to martensite, causing embrittlement (Figure 21-5-2) [Liu97]. When austenitising is performed at very high temperatures, above 1050 °C, phosphorus, which normally appears to be associated with magnesium, possibly in the form of Mg_3P_2, is released into solution and spreads along the boundaries, leading to a marked loss in toughness.

Martensitic cast irons

Martensitic cast irons are used in the quenched and tempered condition. In order to ensure effective martensite formation, the austenitising temperature must be sufficiently low to limit the amount of carbon in solution in the austenite, ensuring a high Ms temperature. Figure 21-5-1 shows an SG cast iron that has been step quenched, leading to retained austenite, which has partially transformed to martensite on subsequent cooling to room temperature

Martensite can be induced mechanically in SG irons given a step quenching treatment (path A+G+F in Figure 21-5-2), by intense peening, which transforms the retained austenite in the surface region. Shot peening, in which a component is exposed to a high velocity stream of metal or glass particles, is often employed to produce compressive residual stresses in the surface when good fatigue strength or resistance to stress corrosion cracking is required. Peening is similar to the shot and sand blasting processes used for cleaning castings, but the deformation produced is much more intense. Figure 21-5-3 shows the strain-induced martensite in the surface of a peened SG cast iron component that has been step quenched and peened.

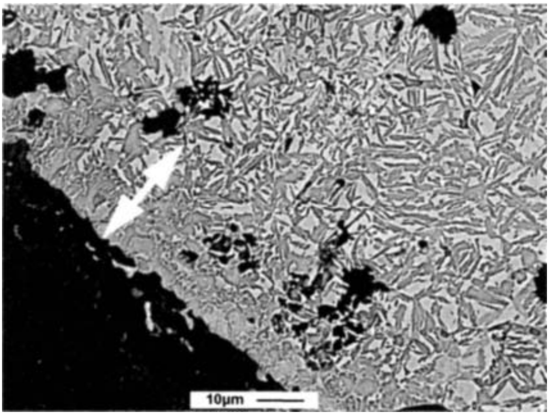

Figure 21-5-3:
Scanning electron micrograph of an Fe-C-Si-Mn SG cast iron sample that has been step quenched and then peened. The peening has affected a surface layer about 100 µm deep (arrow). The lighter coloured retained austenite between the darker ferrite laths has been transformed to martensite in this region.Courtesy INPG, Grenoble and Renault.

22

Appendices

22-1 General comments

Concentration units

In practice, metallurgical phase diagrams are usually represented in terms of weight percentages

Phase diagram calculations

The majority of calculations were made using either the Thermocalc or Pandat softwares, together with data from the SGTE base as available in 2002-2003.

22-2 Interface energies

Interface energies at 1 100 °C reported by [Eus83], [Rot75]# and [Van51]

Fe/Liquid metal	Fe/Fe	Fe/Cu	Fe/Cu/Cu_2S	Fe/Pb	Fe/Ag	Fe/Na
σ in mJ/m^2	254 (estimated)	430	850#	1080	1370	2000

22-3 Chromium and nickel equivalents

Empirical relationships for determining chromium and nickel equivalents in stainless steels, with concentrations in wt. %.

* In stabilised grades containing titanium and/or niobium, allowance must be taken for the fact that these elements are partly tied up in the form of carbides, nitrides or carbonitrides.

Delong [Lon73]	Eq.Cr = Cr% + 1.5 Si% + Mo% + 0.5 Nb% Eq.Ni = Ni% + 0.5 Mn% + 30 C% + 30% N
12Cr steels [Pic78]	*Eq. Cr = Cr + 2 Si + 1.5 Mo + 5 V + 5.5 Al + 1.75 Nb + 1.5 Ti + 0.75 W Eq. Ni = Ni + Co + 0.5 Mn + 0.3 Cu + 30 C + 25 N

22-4 Etching reagents

Alcaline etchings are distinguish by a grey color

	Procedure	Use
1) Nital	1 to 5 ml nitric acid (*s.g.* 1.4), 100 ml ethyl (or methyl) alcohol from a few seconds to 1 minute, and even longer for alloy steels	Iron, grey iron, low alloyed steels. The intensity of attack increases and the selectivity decreases with increasing acid content of the reagent.
2) Nital	5 ml nitric acid (*s.g.* 1.4), 100 ml amyl alcohol. Use cold, or between 50 and 60°C	Gives a more uniform etch on pearlitic steels.
3) Picral	4 g picric acid, 100 ml ethyl alcohol Etching time from a few seconds to 1 minute	Can be used for revealing fine structures in iron, steels, cast irons and martensitic or bainitic steels.
4) Picral (acid)	0.3 g picric acid, 0.2 nitric acid, (*s.g.* 1.4), 100 ml ethyl alcohol	To reveal fine structure
5) Villella	1 g picric acid, 5 ml hydrochoric acid, (*s.g.* 1.19), 100 ml ethyl (or methyl) alcohol	General structure. Can etch iron-chromium and iron chromium-nickel steels.
6) Alkaline sodium picrate	2 g picric acid, 25 g sodium hydroxide, 100ml distilled water Use fresh; leave in water bath for about 1/2 h. Etching time from 5 to 10 minutes at 50°C. Remove the deposit formed on the surface of the specimen.	Colours cementite and carbides, except the chromium-rich carbides containing more than 10% chromium. Attacks the sulfides and reveals the iron phosphides.
7)	5 ml nitric acid (*s.g.* 1.4), 1 ml hydrofluoric acid (40%), 44 ml distilled water, etching time of about 5 mn	To show up the general structure of austenitic stainless steels
8)	45 ml lactic acid, 10 ml hydrochloric acid (*s.g.* 1.19), 45 ml ethyl alcohol Etch electrolytically for 10 to 30 sec at 6 volts	For chromium stainless steels or for the δ-ferrite in austenitic stainless steels.
9) Kalling's reagent	5g $CuCl_2$,100 ml hydrochloric acid (*s.g.* 1.19), 100 ml ethyl alcohol, 100 ml distilled water	To reveal the structure of austenitic and ferritic stainless steels; δ-ferrite is readily attacked while carbides and σ-phase are not attacked at all.
10)	10 g ferric chloride, 30 ml hydrochloric acid (*s.g.* 1.19), 120 ml distilled water. Etching time: no more than 30 seconds, apply with a cotton swab	For stainless steels

22-4 Etching reagents

Alcaline etchings are distinguish by a grey color

	Procedure	Use
11) Murakami's reagent	10g K_2FeCN_6; 10 g potassium hydroxide; 100 ml distilled water; use fresh solution either cold or boiling, for 10 à 15 mn	The chromium-containing carbides and tungstides take on a dark color. Cementite is hardly coloured.
12) Murakami's reagent	30 g K_2FeCN_6; 30 g potassium hydroxide; 60 ml distilled water; use fresh solution at boiling point, for 10 à 15 mn	Distinguishes the σ-phase from ferrite. The σ-phase turns blue after 20 to 40 sec. the austenite is not affected and the ferrite becomes yellow-brown, $M_{23}C_6$ are also coloured
13) Lichtenegger and Bloech's reagent	20 g NH_4HF_2, 0.5 g $K_2S_2O_5$ and 100 ml distilled water, cold solution, a few seconds, cold.	Used for welds, reveals δ-ferrite, σ-phase and carbides in austenitic stainless steels
14) Perchloric/ acetic acid mixture	10% perchloric acid in acetic acid. Electrochemical attack under 6 V.	Deep etches the matrix leaving the carbides unattacked

22-5 Characteristic diffusion lengths

The following characteristic diffusion lengths $l = \sqrt{Dt}$ were calculated at 910 °C for diffusion in iron, using the formula D = Do.exp(–Q/RT). For N, C, Mn and Ni, the data are from reference [Les89], those for Cr, Mo and W are from [Alb74], and those for Co from [Hon95]. For the diffusion of Cu in ferrite, the reference [Wri60] enables comparison in a slightly lower temperature range.

Solute	Frequency factor D_0 (m^2s^{-1})		Activation energy Q (kJ/mol^{-1})		Diffusion length (μm) for 1 hour at 910°°C	
	in α	in γ	in α	in γ	in α	in γ
C	$1.27*10^{-6}$	$1.00*10^{-6}$	81.4	113	1080	192
N	$3.73*10^{-7}$	$2.26*10^{-5}$	76.9	152	735	125
Mn	$7.60*10^{-5}$	$4.90*10^{-5}$	225	276.54	5.6	0.33
Ni	$9.70*10^{-4}$	$3.44*10^{-5}$	262	283	3	0.2
Co	$2*10^{-5}$		226		2.7	
Cr	$2.4*10^{-4}$	$6.27*10^{-6}$	239.8	252.3	4.7	0.40
Mo	$7.85*10^{-5}$	$3.6*10^{-5}$	225.5	239.8	5.6	0.58
W	$1.57*10^{-4}$	$1.3*10^{-5}$	243.5	267.4	3.16	0.27

22-6 Empirical formulae for determining the Ms and Mf temperatures

Ms and Mf are in °C and all concentrations are in weight %. # The contribution of these elements is indirect, since they tie up nitrogen by forming stable nitrides.

Stevens and Haynes (1956)	$Ms = 561 - 474\,C - 33\,Mn - 17\,Cr - 17\,Ni - 21\,Mo$ $Mf = Ms - 215$
Andrews (1965).	$Ms = 539 - 423\,C - 30{,}4\,Mn - 12{,}1Cr - 17{,}7Ni - 7.5\,Mo$ or, more precisely $Ms\,(°C) = 512 - 453\,C + 15Cr - 16{,}9\,Ni - 9{,}5\,Mo + 217\,(C)^2 - 71.5(C)(Mn) - 67.6\,(C)(Cr)$ *The field of application is limited to* $<0.6\,C$, $< 4.9\,Mn$, $< 5\,Cr$, $< 5\,Ni$, $< 5.4\,Mo$.
Finkler and Schirra (1996) [Fin96]	$Ms = 635 - 474[C+0{,}86\{N - 0{,}15(Nb+Zr)\# - 0{,}066(Ta+Hf)\}]-[17Cr + 33Mn + 21Mo + 17Ni + 39V + 11W]$ *Applicable for 8-14% Cr*
Pickering [Pic78]	$Ms = 502 - 810C - 1230N - 13Mn - 30Ni - 12Cr - 54Cu - 46Mo$ *For austenitic stainless steels*
Quoted by [Lac93]	$Ms = 1302 - 42Cr - 61N - 33Mn - 28Si - 1667(C + N)$ Valid in the range 10-18% Cr, 6-12% Ni, 0.6-5% Mn, 0.3-2.69% Si, 0.004-0.12% C, 0.01-0.06% N

22-7 Effects of alloying elements in steels

When the cell is shaded grey, the element concerned is an austenite stabiliser, otherwise it is a ferrite stabiliser. SS signifies solid solution. L indicates limited solubility. The other symbols refer to the strengthening effect : VS = very strong, S = strong, M = medium, W = weak, VW = very weak.

Element	SS	Comments
Cu	L	Reduces the rate of wet corrosion of austenite in non-oxidising media. Very low solubility at low temperature. Forms precipitates of virtually pure copper, leading to pronounced age hardening.
Mn	W	One of the cheapest and most effective strengthening elements. Lowers the pearlite transformation temperature (A1), enabling treatment in the austenite field at lower temperature. Although an austenite stabiliser, Mn also has a slight tendency to promote sigma phase. Forms carbides, including Mn_3C, fully miscible with Fe_3C. Forms manganese sulphide, MnS. Retards and slows the pearlite transformation.
N	VS	Like carbon, strongly lowers the Ms temperature. Forms nitrides, including CrN and Cr_2N. Forms hard and highly stable nitrides and carbonitrides. Enhances resistance to pitting corrosion.
Co	V W	Participates in certain mixed carbides and intermetallic phases (*e.g.* in maraging steels). Retards recovery

22-7 Effects of alloying elements in steels

When the cell is shaded grey, the element concerned is an austenite stabiliser, otherwise it is a ferrite stabiliser. SS signifies solid solution. L indicates limited solubility. The other symbols refer to the strengthening effect : VS = very strong, S = strong, M = medium, W = weak, VW = very weak.

Element	SS	Comments
Ni	W	Lowers the minimum austenitising temperature. Increases corrosion resistance in sulphuric acid media. Forms Ni_3X phases with Mo, Ti and Al, leading to pronounced precipitation hardening. Retards the pearlite transformation and thereby increases hardenability. Lowers the ductile/brittle transition temperature. Promotes graphite formation in cast irons.
Al	L	Increases high temperature oxidation and corrosion resistance (contents >2%). Very limited solubility, even at high temperatures. Forms AlN precipitates at grain boundaries. Forms intermetallic compounds. Promotes graphite formation in cast irons.
Cr	W	Improves resistance to both wet and high temperature corrosion, especially for contents >10-11%. Raises the liquidus temperature in the presence of carbon. Forms nitrides and carbides, including M_7C_3 and $M_{23}C_6$, although its affinity for carbon is less than those of Mo, V, Ti, Nb, Ta, and Zr. Forms intermetallic compounds, including the detrimental sigma phase. Forms embrittling αCr phase by decomposition of chromium-rich ferrites at low temperature. Improves hardenability.
Mo	VS	Enhances resistance to pitting corrosion. Forms carbides, including Mo_2C, Mo_3Fe_3C and Fe_2MoC. Forms intermetallic compounds and stabilises sigma phase. Highly efficient addition for improving hardenability, even at low concentrations. Generates secondary hardening due to carbide precipitation during tempering.
P	VS	The very low solubility limits effective strengthening. Segregates strongly, and in high carbon steels, forms low melting point eutectics, leading to a risk of hot shortness. Segregates to grain boundaries, causing embrittlement in low carbon steels.
S	L	Very low solubility, even at high temperatures. Segregates and forms low melting point eutectics, except in the presence of manganese. Segregates to grain boundaries, causing embrittlement during hot working. Improves machinability. Impairs resistance to pitting corrosion.
Sn, Sb, As	L	Segregate to grain boundaries, causing temper embrittlement. Embrittle welds.

22-7 Effects of alloying elements in steels

When the cell is shaded grey, the element concerned is an austenite stabiliser, otherwise it is a ferrite stabiliser. SS signifies solid solution. L indicates limited solubility. The other symbols refer to the strengthening effect : VS = very strong, S = strong, M = medium, W = weak, VW = very weak.

Element	SS	Comments
B	L	Produces marked strengthening, even at low concentrations (0.001-0.003%). Segregates strongly to grain boundaries. Inhibits ferrite precipitation at austenite grain boundaries. Markedly improves hardenability. Retards recovery. Improves creep strength and ductility. Can cause intergranular embrittlement and impair weldability when present in excessive amounts.
Si	S	Frequently present in steels at levels up to 0.2-0.35%, for which its effects are small. In larger amounts (0.5-3%), improves oxidation and corrosion resistance at high temperatures. Forms intermetallic compounds and stabilises sigma phase. Decreases ductility during hot working. Impairs weldability. Prevents the formation of bainitic carbides. Promotes graphite formation in cast irons. Improves hardenability.
V	M	Forms highly stable carbides, nitrides and carbonitrides of the MX type (X = C or N). Forms intermetallic compounds and stabilises sigma phase. Higher austenitising treatments are required to dissolve secondary carbides. Improves hardenability and generates secondary hardening during tempering. Strengthens ferrite by carbide precipitation at low temperatures.
W	VS	Forms carbides, including W_3Fe_3C and WC. Forms intermetallic compounds and stabilises sigma phase. Improves hardenability. Retards recovery. Generates secondary hardening during tempering.
Ti Nb Ta Zr	L	Form highly stable carbides, nitrides and carbonitrides of the MX type (X = C or N). Tie up carbon and nitrogen to leave very little free in solid solution (interstitial-free steels and stabilised stainless steels). Improve the resistance to grain boundary corrosion (sensitisation) in stainless steels. The carbides refine as-cast grain size but can cause brittleness under certain conditions. Higher austenitising temperatures are required.Raise the Ms temperature by removing carbon from solution. Generate secondary hardening during tempering. Retard recovery. Strengthen ferrite by interphase precipitation at low temperatures.

22-7 Effects of alloying elements in steels

When the cell is shaded grey, the element concerned is an austenite stabiliser, otherwise it is a ferrite stabiliser. SS signifies solid solution. L indicates limited solubility. The other symbols refer to the strengthening effect : VS = very strong, S = strong, M = medium, W = weak, VW = very weak.

Element	SS	Comments
Y Ce La	L	Improve high temperature oxidation resistance, and in particular, reduce the tendency for scale spallation under cyclic temperature conditions. Improve hot workability by tying up sulphur and oxygen, but can cause hot shortness when present in excessive amounts. Sometimes used for oxide dispersion strengthening (ODS) in materials produced from mechanically alloyed powders (*e.g.* Y_2O_3).

22-8 Typical hardness values of various constituents found in steels

The following table gives *indicative* Vickers microhardness values for various homogeneous phases. For carbides, the hardness range depends on two effects, including sometimes wide stoechiometry variations (VC, NbC) and strong anisotropy (Fe_3C, diamond). In the case of martensite, the hardness increases markedly with carbon content. For austenite and ferrite, the highest value corresponds to extensive solid solution strengthening.

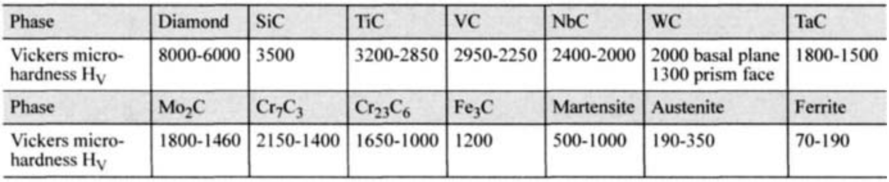

Phase	Diamond	SiC	TiC	VC	NbC	WC	TaC
Vickers micro-hardness H_V	8000-6000	3500	3200-2850	2950-2250	2400-2000	2000 basal plane 1300 prism face	1800-1500
Phase	Mo_2C	Cr_7C_3	$Cr_{23}C_6$	Fe_3C	Martensite	Austenite	Ferrite
Vickers micro-hardness H_V	1800-1460	2150-1400	1650-1000	1200	500-1000	190-350	70-190

23

References

Classification of books

Because of the importance of the subject and its age, the literature concerning steels and cast irons is colossal. In addition to articles in scientific journals, there are many specialised textbooks of either a fundamental or applied nature, together with works of a more encyclopaedic character, such as the handbooks. Many recent scientific papers are published in the form of conference proceedings devoted to a particular subject. In the following list, certain more general works are indicated by a code to the left of the reference, as follows :

- GM = General metallurgy text book
- SpF = Specialised book of fundamental nature
- SpA = Specialised book of applied nature
- E = Work of encyclopaedic nature
- DB = Data base

[Aar90], H.I. Aaronson, T. Furuhara, J.M. Rigsbee, W.T. Reynolds Jr and J.M. Howe, "Crystallographic and Mechanistic Aspects of Growth by Shear and by Diffusional Processes" *Metall. Trans.* **21A** (Sept. 90), 2369-2409.

[Abe98], F. Abe, M Igarashi, N. Fujitsuna, K. Kimura and S. Muneki, "Research and development of advanced ferritic steels for 650°C USC boilers", *Materials for Advanced Power Engineering 1998*, **5**, Ed J. Lecomte-Becker, F. Schubert and P.J. Ennis, Pub Forschungszentrum Jülich GmbH Germany, 259-268.

[Adn92], L. Adnane, R. Kesri, S. Hamar-Thibault, "Vanadium carbides formed from the melt by solidification in Fe-V-X-C alloys (X=Cr, Mo, Nb)", *J. of Alloys and Compounds* **178** (1992) 71-84.

SpA [AES93], *Ductile Iron Handbook*, Ed. Pub. American Foundrymen's Society (1992, revised 1993) USA.

[Ag92], J. Ägren, "Computer Simulations of Diffusional Reactions in Complex Steels", *ISIJ International* **32**, No3 (1992), 291-296.

[Ain79], M.H. Ainsley, G.J. Cocks and D.R. Miller, "Influence of grain boundary structure on discontinuous precipitation in austenitic steel", *Metal Science,* **13** (1979), 20-24.

[Alb74], P.J. Alberry and C.W. Haworth, "Interdiffusion of Cr, Mo, and W in Iron", *Metal Science,* **8** (1974), 407-412.

[Ama00], T. Amadou, A. Ben Rhouma, H. Sidhom, C. Braham, and J. Ledion, "Influence of Thermal Ageing on the Reactivity of Duplex Stainless Steel Surfaces", *Metall. and Mater. Trans.* **31A** (Aug. 2000), 2015-2024.

[And88], J.O. Andersson, "A Thermodynamic Evaluation of the Fe-Cr-C System", *Metall. Trans.* **19A** (March 1988), 627-636.

SpA [And91], J.Y. Andrieux, *Les travailleurs du fer*, Découvertes Gallimard, Sciences et Techniques Ed. Gallimard 1991.

[And94], E. Andrieu, N. Wang, R. Molins and A. Pineau, "Influence of compositional modifications on thermal stability of alloy 718", *Superalloys 718, 625, 706 and Various Derivatives*, Ed. E.A. Loria, The Minerals, Metals and Materials Society, (1994) USA, 695-710.

[Ans93], I. Ansara and Å. Jansen, "Assessement of the copper-iron system", *TRITA-MAC-0533* Dec 1993, Materials Research Center, The Royal Institute of Technology, Stockholm, Sweden.

SpA [Ans96], I. Ansara, "Phase diagrams and thermodynamics", *The Iron-Nickel Alloys*, G. Béranger *et al.* Eds., Lavoisier Tech. & Doc. (1996), 141-156.

[Ans97], I. Ansara *et al.* "Thermodynamic Modelling of Solutions and Alloys : Thermodynamic Modelling of Selected Topologically Close-Packed Intermetallic Compounds", *Calphad* **21** No 2 (1997), 171-218.

[Ant01], A. Antoni-Zdziobeck and C. Colinet, "CVM calculations of phase equilibria in the Fe-Cu-Co systel including both chemical and magnetic interactions", *Scand. J. of Metallurgy,* **30** No4 (2001), 265-272.

[Ant02], L. Antoni, B. Baroux, "Tenue des aciers inoxydables à l'oxydation cyclique. Application à l'échappement automobile", *Rev. Mét.* Feb. 2002, 177-188.

E [Ash92], M. F. Ashby, *Materials Selection in Mechanical Design*, Ed. Pergamon Books Ltd, (1992).

E [Ash99], M.F. Ashby, *Materials Selection in Mechanical Design*, Ed. Butterworth Heineman, (1999).

[Ash02], M.F. Ashby, Y.J.M. Bréchet, D. Cebon, L. Salvo, "Selection strategies for materials and processes", *Materials and Design*, **25/1** (2003), 51-67.

DB [ASM92], *Alloy Phase Diagrams*, ASM Handbook, **3**, The Materials Information Society USA,(1992).

DB [Atlas], *Atlas des courbes de transformation des aciers de fabrication française*, IRSID.

[Bai62], E.C. Bain, "Nippon-tô, an introduction to old swords of Japan", *J.I.S.I.* April 1962, 265-282.

[Bak72], T.J. Baker and J.A. Charles, "Morphology of Manganese Sulphides in Steel", *J.I.S.I.* Sept. 1972, 702-706.

[Bak73], T.J. Baker and J.A. Charles, "Type II Manganese Sulphides : their Deformation and Effect on Steel Fracture", *J.I.S.I.* March. 1973, 187-192.

SpA [Bal92], R.N. Balsiger, E.J. Kläy, *Bei Schah Emir und Khan,* (1992), Meier Verlag, Schaffhausen.

[Bar72], R.H. Barkalow, R.W. Kraft, and J.I. Goldstein, "Solidification of M2 High Speed Steel", *Metall. Trans.* **3** (April 1972), 919-926.

[Bar83], J. Barcik, "The Kinetics of σ-Phase Precipitation in AISI 310 and AISI 316 Steels", *Metall. Trans.* **14A** (April 1983), 635-641.

[Bar88], J. Barcik, "Mechanism of σ-phase precipitation in Cr-Ni austenitic steels", *Mater. Sci. and Tech.,* **4** (Jan. 1988), 5-15.

GM [Bar91], J. Barralis et G. Maeder, *Précis de Métallurgie*, 6th edition (1991), Ed. Nathan Paris, France.

[Bay99], H. Bayati and R. Elliott, "The Concept of a Heat Treatment Processing Window", *Int. J. Cast Metals Res.* **11** (1999), 413-417.

[Bei00], S. Bein, C. Colinet, M Durand-Charre, "CVM calculation of the ternary system Co-Cu-Fe", *J. of Alloys and Compounds*, **313** (2000), 133-143

SpA [Bér96a], *The Book of Steel*, G. Béranger *et al.* Eds., Lavoisier, Tech. & Doc., Paris (1996).

SpA [Bér96b], *The Iron-Nickel Alloys*, G. Béranger *et al.* Eds., Lavoisier Tech. & Doc., Paris (1996).

SpA [Bér97], *Les aciers spéciaux*, G. Béranger *et al.* Eds., Lavoisier Tech. & Doc. Paris, (1997).

[Ber00], R Berthod, G. Lesoult, "Study of the formation of the skin in the meniscus free continuous casting. I- Surface features on continuous casting products", *Rev. Mét.* Déc. 2000, 1441-1450.

[Bha90], H.K.D.H. Bhadeshia and J.W. Christian, "Bainite in steels", *Metall. Trans.* **21** (April 1990), 767-797.

SpF [Bha92], H.K.D.H. Bhadeshia, *Bainite in steels*, The Institute of Materials (1992), London U.K.

[Big75], L.K. Bigelow, M.C. Flemings, "Sulfide Inclusions in Steel", *Metall. Trans.* **6B** (June 1975), 275-783.

[Bil72], J. Billingham, P.S. Bell and M.H. Lewis, "Vacancy Short-Range Order in Substoichiometric Transition Metal Carbides and Nitrides with NaCl Structure. I Electron Diffraction Study of Short-Range Ordered Compounds", *Acta Cryst.* **A 28** (1972), 602-606.

[Bir85], J.P. Birat, M. Bobadilla, J.L. Jacquot, M. Martinot, J. Ruer, L. Backer, J.M. Bastian, "Continuous casting and electromagnetic stirring of steels with large solidification interval", Proc. Int. Conf. on *Continuous Casting 85*, London, U.K. (1985), paper 18, 1-12.

[Bir98], J.P. Birat, "Recent advances in near-net shape flat steel manufacturing", *Rev. Mét.* Nov. 1998, 1387-1406 (296 ref.)

[Bjö72], S. Björklund, L.F. Donnaghey, and M. Hillert, "The Effect of Alloying Element on the Rate of Ostwald Ripening of Cementite in Steel", *Acta Met.* **20** (1972), 867-874.

[Bla73], G. Blanc, R. Tricot and R. Castro, "Transformations martensitiques dans les aciers inoxydables austénitiques Fe-Cr-Ni", *Mém. Sci. Rev. Mét.* **LXX, 7-8** (1973), 527-541.

[Ble98], W. Bleck, K. Hulka, and K. Papamentellos, "Effect of Niobium on the Mechanical Properties of TRIP Steels", *Microalloying in Steels*, Ed. J.M. Rodriguez-Ibade *et al.*, Pub. Trans. Tech. (1998), 327-334.

[Bob88], M. Bobadilla, J. Lacaze and G. Lesoult, "Influence des conditions de solidification sur le déroulement de la solidification des aciers inoxydables austénitiques", *J. of Crystal Growth,* **89** (1988), 531-544.

[Boe00], W.J. Boettinger, S.R. Coriell, A.L. Greer, A. Karma, W. Kurz, M. Rappaz and R. Trivedi, "Solidification Microstructures : Recent developments, future directions", *Acta Mater.* **48** (2000), 43-70.

[Bon94], R. Bonnet and M. Loubradou, "Atomic positions around misfit dislocations on a planar hetero interface", *Phys. Rev. B* **49** No20 (1994), 14397-14402.

[Bor00], A. Borgenstam, A. Engström, L. Höglund, and J. Ågren, "DICTRA, a Tool for Simulation of Diffusional Transformations in Alloys", *J. of Phase Equilibria,* **21** No 3 (2000), 269-280.

[Böt99], A. Böttger and E.J. Mittemeijer, "Phase Transformations in Iron-Nitrogen Martensites; Role of Elastic Strain Energy", in *High Nitrogen Steels*, Ed. H. Hänninen *et al.* (1999), Trans. Tech. Pub. Switzerland, 61-70.

[Bow66], T.F. Bower, H.D. Brody, M.C. Flemings, "Measurements of Solute Redistribution in Dendritic Solidification", *Trans. AIME,* **236** (May 1966), 624-634.

[Bro66], H.D. Brody, M.C. Flemings, "Solute Redistribution in Dendritic Solidification", *Trans. AIME* **236**, (May 1966), 615-624.

[Bro79], J.W. Brooks, M.H. Loretto and R.E. Smallman, "Direct observations of martensite nuclei in stainless steels", *Acta Metall.* **27** (1979), 1839-1847.

SpA [Bro92], C.R. Brooks, *Principles of the surface treatment of steels*, Pub. Technomic, (1992), Lancaster (Pennsylvania) USA.

[Buc75] V.F. Buchwald, *Handbook of iron meteorites*, University of California Press, Los Angeles CA, USA (1975).

[Bud88], P. Z. Budka, "Meteorites as Specimens for Microgravity Research", *Metall. Trans.* **19A** (1988), 1919-23.

[Bun58], K. Bungardt, E. Kunze and E. Horne, "Untersuchungen über den Aufbau des Systems Eisen-Chrom-Kohlenstoff", *Archiv. Eisenhüttenwesen* **29** No**3** (1958), 193-203.

[Bur64], K.W. Burns and F.B. Pickering, "Deformation and fracture of ferrite-pearlite structures", *J. Iron Steel Inst.* **202** (1964), 899-906.

[Cah62], J.W. Cahn and W.C. Hagel, "Theory of the pearlite reaction", in *Decomposition of austenite by diffusional processes*, Ed. V.F. Zakay and H.I. Aaronson, Interscience Pub. N.Y. (1962), 131-192.

GM [Cah83], R.W. Cahn and P. Haasen, *Physical metallurgy*, (1983), North-Holland Physics Publishing, Amsterdam

[Cam00], C. Del Campo, R. Sanchez, J. Botella, "Non-Standard Low-Ni High-Mn-N Duplex Stainless Steel. Microstructural Balance through Thermal History", *6th World Duplex 2000*, Pub. Associazione italiana di metallurgia, Milan, Italy, (2000), 41-48.

[Cha93], J. Charles, M. Verneau, B. Bonnefois, "Beneficial effects of nitrogen additions on the microstructure stability and corrosion properties of welded UR 52N+ superduplex stainless steels" *XIIth NACE Congress*, NACE International, Houston, (1993).

[Cha94], J. Charles, "Structure and mechanical properties of duplex stainless steels", in *DSS'94*, Ed. T.G. Gooch , Abington Pub., Cambridge, U.K.**1**, paper KI.

[Cha95], J. Charles, "Composition and properties of duplex stainless steels", in *Welding in the world 1995*, **35**, 43-45, Proceedings of IIW, Welding of Stainless Steel International Conference, Stockholm 06/12-13/1995.

[Cha00], J. Charles, "10 years later, obviously duplex grades in industrial applications look like a success story", *6th World Duplex 2000*, Pub. Associazione italiana di metallurgia, Milan, Italy, (2000), 1-12.

[Cha01], M. Charleux, W.J. Poole, M. Militzer and A. Deschamps, "Precipitation Behavior and its Effect on Strengthening of an HSLA-Nb/Ti Steel", *Metall. Mater. Trans.* **32A** (July 2001), 1635-1647
H.J. Kestenbach, S.S. Campos, J. Gallego and E.V. Morales, Discussion of "Precipitation behavior...", *Metall. Mater. Trans.* **34A** (4) (2003), 1013-1017.
Authors' Reply, *Metall. Mater. Trans.* **34A** (4) (2003), 1017-1019

[Che90a], L. Cheng, N.M. van der Pers, A. Böttger, Th.H. de Keuser and E.J. Mittemeijer, "Lattice Changes of Iron-Nitrogen Martensite Aging at Room Temperature", *Metall. Trans.* **21A** (Nov. 1990), 2857-2867.

[Che90b], Z.W. Chen, R.M. Sharp, J.T. Gregory, "Fe-Al-Zn ternary phase diagram at 450°C", *Mater. Sci. and Tech.* **6** (Dec. 1990), 1173-1176.

[Che91], L. Cheng, N.M. van der Pers, A. Böttger, Th.H. de Keuser and E.J. Mittemeijer, "Lattice Changes of Iron-Carbon Martensite Aging at Room Temperature", *Metall. Trans.* **22A** (Sep. 1991), 1957-1967

[Chr65], W. Christian, "Military transformations : an introductory survey", *Physical Properties of Martensite and Bainite*, The Iron and Steel Inst. Special Report **93** (1965), 1-25.

[Chr01], P. Christodoulou, N. Calos, "A step toward designing Fe-Cr-B-C cast alloys" *Mater. Sci. and Eng.* **A301** (2001), 103-117.

[Cis99], M.M. Cisneros G., M.J. Pérez L., R.E. Campos C., and E. Valdès C., "The role of Cu, Mo and Ni on the kinetics of the bainitic reaction during the austempering of ductile irons", *Int. J. Cast Metals Res.* **11** (1999), 425-430.

[Col88], J.P. Collier, A.O. Selius and J.K Tien, "On developing a microstructurally and thermally stable iron-nickel base superalloy", *Superalloys 88*, Ed. S. Reichman *et al.*, The Metallurgical Society, (1988), USA 43-52.

SpA [Col65], L Colombier and J Hochmann, *Aciers inoxydables et aciers réfractaires*, Dunod (1965).

[Col00], C. Colinet and A. Antoni-Zdziobek, "Alpha/Gamma Equilibria in the Fe-Co Phase Diagram" *JOM,* July 2000, 26-28.

[Col01], C. Colinet, "Phase Diagrams Calculations : Contribution of ab initio and Cluster Variation Methods", *Calphad and Alloy Thermodynamics*, TMS Ed. P.E.A. Turchi, A. Gonis and R.D. Schuller.

[Col02], C. Colinet, "Applications of the Cluster Variation Method to Empirical Phase Diagram Calculation", *Calphad*, **25**, No4 (2001), 607-623.

[Com98], H. Combeau, B. Appolaire, G. Lesoult, "Recent progress in understanding and prediction of macro and mesosegregation", in *Modeling of Casting, Welding and Advanced Solidification Processes VIII,* Ed. B.C. Thomas and C. Beckermann, The Minerals, Metals and Materials Society, (1998), 245-256.

SpA [Con92], A. Constant, G. Henry, *Les principes de base du traitement thermique des aciers*, PYC-Edition, (1992), Ivry, France.

SpF [Cot76], P Cotterill and P.R Mould, *Recrystallization and Grain Growth in Metals*, Ed Surrey University Press, London (1976)

[Cou00], L. Coudreuse, J. Charles, "Fatigue and corrosion-fatigue behaviour of duplex stainless steels", *6th World Duplex 2000,* Pub. Associazione italiana di metallurgia, Milan, Italy, (2000), 629-638.

[Cow87], S.A. Cowley and D.V. Edmonds, "Proeutectoid cementite transformation in a 12Mn-0.8C steel" Proc. *1987 Solid-Solid Phase Transformation*, Ed. G. Lorimer, Pub. Inst. of Metals London, 459-461.

[Cow98], J.R. Cowan, H.E. Evans, R.B. Jones and P. Bowen, "The grain-boundary segregation of phosphorus and carbon in an Fe-C-P alloy during cooling", *Acta Mater.* **46** No 18 (1998), 6565-6574.

[Coz73], R. Cozar and A. Pineau, "Morphology of γ' and γ" Precipitates and Thermal Stability of Inconel 718 Type Alloys", *Metall. Trans.* **4** (1973), 47-59.

[Coz91], R. Cozar, M. Rouby, B. Mayonobé, C. Morizot, "Mechanical Properties, Corrosion Resistance and Microstructure of Both Regular and Titanium Hardened 625 Alloys", *Superalloys 718, 625 and Various Derivatives,* Ed. E. A. Loria, Pub TMS-AIME, Warrendale, PA (1991)

[Dah84], U. Dahmen, P. Ferguson anf K.H. Westmacott, "Invariant line strain and needle-precipitate growth directions in Fe-Cu", *Acta Metall.* **32** No 5 (1984), 803-810.

[Dan00], J.A. Dantzig, "Solidification Modeling Status and Outlook", Overview, *JOM,* Dec. 2000, 18-21.

[Dav73] J. Davidson, P. Balladon, Y. Honnorat et X. Wache, "Influence du bore sur la précipitation de carbures dans des matrices austénitiques Fe-Ni-Cr", *Mém. Scien. Rev. Mét.* **LXX 7-8** (1973), 543-558.

D [Dav94], *Stainless steels,* ASM Specialty Handbook, Ed. J.R. Davis, ASM International, Materials Park OH USA.

[De_83], J.D.B. De Mello, S. Hamar-Thibault, M. Durand-Charre, "Solidification and Solid-State Transformations of Chromium-Molybdenum White Cast Irons", *Metall. Trans.* **14A** (Sept. 1983), 1793-1801.

[De_84], J.D.B. De Mello, M. Durand-Charre, "Phase Equilibria and Solidification Sequences of White Cast Irons Containing Vanadium and Chromium", *Materials Sci. and Engineering,* **67** (1984), 109-117.

[De_85], J.D.B. De Mello, S. Hamar-Thibault, M. Durand-Charre, "Eutectoid transformations and precipitation in high carbon tool steels", *J. of Mater. Sci.* **20** (1985), 3453-3461.

[De_86], J.D.B. De Mello, M. Durand-Charre and T. Mathia, "Abrasion Mechanisms of White Cast-Irons : Part I : Influence of Metallurgical Structure of Molybdenum White-Cast Irons; Part II : Influence of Metallurgical Structure of Vanadium White Cast-Irons", *Materials Sci. and Engineering,* (1986), Part I **73**, 203-213, Part II **78** 127-134.

[DeA98], A.J. DeArdo, "Microalloyed Strip Steels for the 21st Century" *Microalloying in Steels*, Ed. J.M. Rodriguez-Ibade *et al.*, Pub. Trans. Tech. (1998), 15-26.

[DeL60], W.T. DeLong, "A Modified Phase Diagram for Stainless Steels", *Metal Progress,* 77 (1960), 98-100.

[Des01], A. Deschamps, M. Militzer, W.J. Poole, "Precipitation Kinetics and Strengthening of a Fe-0,8wt% Cu Alloy", *ISIJ International,* **41** No2 (2001), 196-205.

[Don97], M.J. Dong, C. Prioul, and D. François, "Damage Effect on the Fracture Toughness of Nodular Cast Iron : Part I Damage Characterization and Plastic Flow Stress Modeling, Part II : Damage Characterization ahead of a Crack Tip", *Metall. and Mater. Trans.* **28A** (Nov. 1997), 2245-2254 and 2255-2262.

[Du_00], H. Du, M.A.J. Somers, and J. Ägren, "Microstructural and Compositional Evolution of Compound Layers during Gaseous Nitrocarburizing", *Metals and Mater. Trans.* **31A** (Jan. 2000), 195-211.

[Dub00], D. Dubief, F. Hodaj, C.H. Allibert, D. Rezel, "Dilatometric study of the swelling effects in compacted powder mixtures Fe-Cu", *2000 Powder Metallurgy World Congress*, Ed. K. Kosuge and H. Nagai, Pub. Japan Society of Powder Metallurgy (2000), 643-646.

[Dub02], D. Dubief, F. Hodaj, D. Rezel, C. H. Allibert, "Phenomena producing dimensional variations during the sintering of Fe-3Cu-0.6C", 3rd International Powder Metallurgy Conference, Ankara (Turkey) 3-6 sep 2002.

[Dup00], L. Duprez, B.C. De Cooman, N. Akdut, "Microstructural Changes in Duplex Stainless Steel during Isothermal Annealing", *6th World Duplex 2000*, Pub. Associazione italiana di metallurgia, Milan, Italy, (2000), 355-365.

[Dur80a], M. Durand-Charre, B. Chovelon, N. Valignat and J.J. Rameau, "Ségrégations interdendritiques dans les aciers 25-20 : influence de la teneur en carbone, des conditions de solidification et comportement en corrosion", *Mém. Scien. Rev. Mét.* June 1980, 717-727.

[Dur80b], M. Durand-Charre, S. Hamar-Thibault and F. Durand, "Influence of microsegregations on the formation of bainite during the solidification of Fe-2C-12Cr steel", *Zeitschrift für Metallkde*, Dec. 1980, 802-808.

[Dur97a], M. Durand-Charre, JM Chaix and P.H. Yang, "The Effect of Grain Growth upon Eutectic Carbide Particles in H.S.S.", *Physical Metallurgy of Cast Irons V,* Ed. G. Lesoult and J. Lacaze *Advanced Materials Research* **4-5** (1997), Scitec Pub. Switzerland 355-360.

SpA [Dur97b], M. Durand-Charre, *The Microstructure of Superalloys*, Ed. Gordon and Breach, (1997), London.

[Ehr88], M. Ehretsmann, "L'épée carolingienne de Strasbourg", Cahiers Alsaciens, *Art et Histoire*, **31**, (1988) 85-94.

SpA [Eli77], M. Eliade, *Forgerons et alchimistes*, Champs Flammarion (1977), Paris, France.

[Ell97], R. Elliot, "Current Status of Austempered Cast Irons" , in *Physical Metallurgy of Cast Irons V,* Ed. G. Lesoult and J. Lacaze, *Advanced Materials Research* **4-5**, Scitec Pub. (1997) Switzerland, 1-16.

[Eng83], G. Engström, H. Fredriksson, B. Rogberg, "On the mechanism of macrosegregation formation in continuously cast steels", *Scand. J. Metallurgy,* **12** (1983), 3-12.

[Enn97], P.J. Ennis, A. Zielinska-Lipiec, O. Wachter and A.Czyrska-Filemonowicz, "Microstructural stability and creep rupture strength of the martensitic steel P92 for advanced power plant", *Acta Mater.* **45** No12 (1997), 4901-4907.

[Esa85], H. Esaka and W Kurz, "Columnar dendrite growth : Experiments on tip growth", *J of Crystal Growth*, **72** (1985), 578-584.

[Eus83], N. Eustathopoulos, "Energetics of solid/liquid interfaces of metals and alloys", Intern. Metals Review, **28** No4, (1983) 189-210.

[Fei99], H.K. Feichtinger and G. Stein, "Melting of High Nitrogen Steels", *High Nitrogen Steels*, Ed.H. Hänninen *et al.* (1999), Trans. Tech. Pub. Switzerland, 261-270.

[Fel98], K. Felkins, H.P. Leighly Jr, and A. Jankovic, "The Royal Mail Ship Titanic : Did a Metallurgical Failure Cause a Night to Remember?", *J.O.M.* **50** No1 (1998), 12-18.

[Fer76], A. Ferrier, F. Galdon, "Influence de tiers éléments sur la constitution des couches formées par des couples de diffusion Fe/Zn", *C. R. Acad. Sci.* Paris (1976), 283.

SpA [Fig91], L.S. Fiegiel, *On the Damascus Steel*, Atlanta Arts Press, Atlanta, USA (1991).

[Fin96], H. Finkler and M. Schirra, "Transformation behaviour of high temperature martensitic steels with 8-14% chromium", *Materials Technology, Steel Research* **67** No8 (1996), 328-342.

[Fis80], D. J. Fisher ans W. Kurz, "A Theory of Branching Limited Growth of Irregular Eutectics", *Acta Metall.*, **28** (1980), 777-794.

[Fis89], H.F. Fischmeister, R. Riedl and S. Karagoz, "Solidification of High-Speed Tool Steels", *Metall. Trans.* **20A** (Oct. 1989), 2133-2148.

[Fle76], M. Flemings, "Principles of Control of Soundness and Homogeneity of Large Ingots", *Scand. J. Metallurgy,* **5** (1976), 1-15.

[Flu83] P. Fluzin et L. Uran, G. Béranger, C. Coddet, "Structures et mise en forme d'armes gauloises", *Rev. archéologique de Picardie*, **1**, (1983), 181-194

SpA [For64], R.J. Forbes, *Studies in Ancient Technology* **IX**, (1964), Ed. E.J. Brill, Leiden.

DB [For73], W.D. Forgeng and W.D. Forgeng Jr, "Metallography, Structure and Phase Diagrams", *Metals Handbook*, 8th edition, A.S.M., Metals Park, Ohio (1973)

[Fou95a], G. Fourlaris, A.J. Baker and G.D. Papadimitriou, "A microscopic investigation of ε-Cu interphase precipitation in hypereutectoid Fe-C-Cu alloys" *Acta Metall. Mater.* **43** No7 (1995), 2589-2604.

[Fou95b], G. Fourlaris, A.J. Baker and G.D. Papadimitriou, "A microscopic investigation of the precipitation phenomena observed during the pearlite reaction in vanadium alloyed steels", *Acta Metall. Mater.* **43** No10 (1995), 3733-3742.

[Fou96], G. Fourlaris, A.J. Baker and G.D. Papadimitriou, "Effect of copper additions on the isothermal bainitic transformation in hypereutectoid copper and copper-nickel steels" *Acta Mater.* **14** No12 (1996), 4791-4805.

[Fra52], A. France-Lanord, "Les techniques métallurgiques appliquées à l'archéologie", *Rev. Mét.* **XLIX** No6 (1952), 411-422.

[Fre71], H. Fredriksson, M. Hillert, "Eutectic and Monotectic Formation of MnS in Cast Irons", *ISIJ* Feb. 1971, 109-113.

[Fre72], H. Fredriksson, "The Solidification Sequence in an 18-8 Stainless Steel, Investigated by Directional Solidification" *Metall. Trans.* **3** (Nov. 1972), 2989-2997.

[Fre73], H. Fredriksson, M. Hillert, "On the Formation of Manganese Sulphide Inclusions in Steels", *Scan. J. of Metallurgy* **2** (1973), 125-145.

[Fre75], H. Fredriksson and J. Stjerndahl, "On the Formation of a Liquid Phase During Cooling of Steel", *Metall. Trans.* **6B** (Dec. 1975), 661-664.

[Fre76], H. FREDRICKSSON, "The mechanism of the peritectic reaction in iron-base alloys", *Metal Science,* **10** (March 1976), 77-86.

[Fre77], H. FREDRIKSSON and J. STJERNDHAHL, "The Influence of the Ferrite to Austenite Transformation on the Formation of Sulfides", *Metall. Trans.* **8A** (July 1977), 1107-1115.

[Fre79a], H. FREDRICKSSON and B. ROGBERG, "Thermal analysis for interpretation of solidification cycles" *Metal Science,* Dec. 1979, 685-691.

[Fre79b], H. FREDRICKSSON and M NICA, "The influence of vanadium, silicon and carbon on the eutectic reaction in M2 high speed steels", *Scand. J. Metallurgy,* **8** (1979), 243-253.

[Fri77], J. FRIDBERG and M. HILLERT, "On the eutectoid transformation of δ-ferrite in Fe-Mo-C alloys", *Acta Metall.* **25** (1977),19-24.

[Fri99], K. FRISK, "Nitriding of Steel Powder : Thermodynamic Calculations and Experiments", *Materials Science Forum* **318-320** (1999), 95-102.

[Gal74], E.J. GALDA and R.W. KRAFT, "The Effect of Mo and W on Solidification of High Speed Steels", *Metall. Trans.* **5** (Aug. 1974), 1727-1733.

[Gar92], C. I. GARCIA, A. K. LIS, E. A. LORIA and A. J. DEARDO, "Thermomechanical processing and continuous cooling transformation behavior of IN-718", *Superalloys 1992,* Ed. S. D. Antolovitch *et al.*, Pub. The Minerals, Metals and Materials Society, Warrendale, (USA) (1992), 527-536.

[Gat95], C. GATELLIER, H. GAYE, J. LEHMANN, "Origine des inclusions dans les aciers peu alliés", *Rev. Mét. CIT,* April 1995, 541-553.

[Gau95], E. GAUTIER, J.S. ZHANG and X.M. ZHANG, "Martensitic Transformation under Stress in Ferrous Alloys, Mechanical Behaviour and Resulting Morphologies", *Journal de Physique IV,* Colloque C8 **5** (Dec. 1995), C41-C50.

[Gav99], V.G. GAVRILJUK, "Atomic Scale Mechanisms of Strengthening of Nitrogen Steels 98", *High Nitrogen Steels,* Ed. H. Hänninen *et al.* (1999), Trans. Tech. Pub. Switzerland, 3-11.

SpA [Ger85], R. M. GERMAN, *Liquid Phase Sintering,* (1985), Plenum Publishing Corporation N.Y. USA.

SpA [Ger98], R. M. GERMAN, *Powder Metallurgy of Iron and Steel,* (1998), Wiley Interscience Publication, N.Y. USA.

[Ger00], V. GERVAL, J. LACAZE, "Critical temperatures of spheroidal graphite cast irons : a review of literature data", *ISIJ International* **40** (2000), 827-836.

[Gho94], G. GHOSH and G.B. OLSON, "Kinetics of fcc->bcc heteregeneous martensitic nucleation- I. The critical driving force for athermal nucleation; II. Thermal activation" *Acta Metall. Mater.* **42** (1994), 3361-3370 and 3371-3379.

[Gho99], G. GHOSH, C.E. CAMPBELL, and G.B. OLSON, "An Analytical Electron Microscopy Study of Paraequilibrium Cementite Precipitation in Ultra High Strength Steel" *Metall. and Mater. Trans* **30A** (March 1999), 501-512.

[Gir95], G. GIRON and M. DURAND-CHARRE, "High Temperature Phase Equilibria in the System Fe-Mo-C", *Z. Metallkd.* **86** (1995), 15-21.

SpA [Gla97], T. GLADMAN *The Physical Metallurgy of Microalloyed Steels,* (1997), The Institute of Materials, London 1997 U.K.

[Goo73], S.R. GOODMAN, S.S. BRENNER and J.R. LOW Jr. "An FIM-Atom Probe Study of the Precipitation of Copper from Iron-1.4 At. Pct Copper. Part I : Field-Ion Microscopy", *Metall. Trans.* **4** Oct. 1973, 2363-2369.

[Gop93], N. GOPE, A. CHATTERJEE, T. MUKHERJEE, and D.S. SARMA, "Influence of the Long-Term Aging and Superimposed Creep Stress on the Microstructure of 2.25Cr-1Mo", *Metall. Trans.* **24A**, Feb. 1993, 315-326.

[Gra80], M.J. GRAHAM, P.E. BEAUBIEN, G.I. SPROULE, "A Mössbauer study of Fe-Zn phases on galvanized steel", *J. of Materials Sci.* **15** (1980), 626-630.

[Gré88], D. GRÉBÉNART, "Reassessment of the Evidence for Early Metallurgy in Niger, West-Africa", *J of Archæological Science,* USA **V15** (1988), 367-394

[Gri62], N.R.GRIFFING, W.D. FORGENG and G.W. HEALY, "C-Cr-Fe Liquidus Surface", *Metall. Trans.* **224**, (Feb. 1962), 148-159

[Gri83], L.M. GRIBAUDO, F. DURAND, M. DURAND-CHARRE, "Changements structuraux des aciers 25Cr -20Ni en fonction des teneurs en Cr, Si et W", *Mém. Scien. Rev. Mét.* April 1983, 211-220.

SpA [Gun97], R.N. GUNN, *Duplex stainless steels : Microstructure, properties and applications,* Abington Pub., (1997), Cambridge U.K.

[Gut77] M. GUTTMANN, Ph. DUMOULIN, M. PAMIER, P. LE BLANC, M. BISCONDI, "Fragilité de revenu et ségrégations intergranulaires dans les aciers de type 20 CND 10-10; I- Influence des impuretés fragilisantes P, Sn, Sb, As" *Mém. Scien. Rev. Mét.* June 1977, 377-392.

[Gut82], M. GUTTMANN, Ph. DUMOULIN, and M. WAYMAN, "The Thermodynamics of Interactive Co-Segregation of Phosphorus and Alloying Elements in Iron and Temper-Brittle Steels", *Metall. Trans.* **13A** (Oct. 1982), 1693-1711.

[Gut95], M. GUTTMANN, Y. LEPRÊTRE, A. AUBRY, M.J. ROCH, T. MOREAU, P. DRILLET, J.M. MATAIGNE, H. BAUDIN, "Mechanisms of the galvanazing reaction, Influence of Ti and P contents in steel and of its surface microstructure after annealing", in *Galvatech 95,* Iron and Steel Society, Warrendale P.A. (1995), 295-307.

E [Hab66], L. HABRAKEN et J.-L. DE BROUWER, *De ferri metallographia,* **Vol. I** (1966), Ed. CNRM, Pub Presses Académiques Européennes, Brussels.

[Hab02], H.R. HABIBI BAJGUIRANI, "The effect of ageing upon the microstructure and mechanical properties of type 15-5 PH stainless steel", *Materials Scienc. and Eng.* **A00** (2002), 1-18.

[Hac87a], S.A. HACKNEY and G.J. SHIFLET, "The Pearlite-Austenite Growth Interface in an Fe-0.8C-12Mn Alloy", *Acta Metall.* **35** No5 (1987), 1007-1017.

[Hac87b], S.A. HACKNEY and G.J. SHIFLET, "Pearlite Growth Mechanism" *Acta Metall.* **35** No5 (1987), 1019-1028.

[Hal98], J. HALD, S. STRAUB, "Microstructural Stability of 9-12 CrMo(W)VNbN-Steels", in *Materials for Advanced Power Engineering 1998,* Ed J. Lecomte-Becker, F. Schubert and P.J. Ennis Pub Forschungszentrum Jülich GmbH Germany, **5**, 155-169.

DB [Han58], M. HANSEN, *Binary alloy phase diagrams,* (1958), Mc Graw Hill.

[Han91], Q. HANCHENG, and P. XIAODONG, "Study of the Formation of Spheroidal Graphite in Ancient Cast Iron in China" *AFS Transactions,* **99** (1991), 415-420.

[Har97], R.A. HARDING, J. CAMPBELL and N.J. SAUNDERS, "The Inoculation of Ductile Iron : A Review of Current Understanding", in *Solidification Processing,* Ed. J. Beech and H. Jones, Pub. University of Sheffield U.K. (1997), 489-493.

[He_98], J. HE, G. HAN, S. FUKUYAMA and K. YOKOGAWA, "Interfaces in a modified Inconel 718 with compact precipitates" *Acta Mater.* **46** No 1 (1998), 215-223.

[Her00a], S. HEREÑÚ, I. ALVAREZ-ARMAS and F. ARMAS, "Role of the ferritic phase during cyclic loading in a duplex stainless steel" *6th World Duplex 2000,* Pub. Associazione italiana di metallurgia, Milan, Italy, (2000), 681-689.

[Her00b], S. HERTZMAN, R. PATTERSSON, K. FRISK, T. JERWIN, "The relation between alloy composition and kinetics of intermetallic phase formation", *6th World Duplex 2000,* Pub. Associazione italiana di metallurgia, Milan, Italy, (2000), 347-354.

[Her01], S. HEREÑÚ, I. ALVAREZ-ARMAS and F. ARMAS, "The influence of dynamic strain aging on the low cycle fatigue of duplex stainless steel", *Scripta Materiala* **45** (2001), 739-745.

[Heh72], R.F. Hehemann, K.R. Kinsman and H.I. Aaronson, "A Debate on the Bainite Reaction", *Metall. Trans.* **3** (May 1972), 1077-1094.

[Hil68], M. Hillert and V.V. Subba Rao, "Grey and white solidification of cast iron", *J. of the Iron and steel Inst.* **110** (1968), 204-212.

[Hil71], M. Hillert, "Diffusion controlled growth of lamellar eutectics and eutectoids in binary and ternary systems", *Acta Metall.* **19** Aug. 1971, 769-778.

[Hil79], M. Hillert, "Keynote Address : Eutectic and peritectic solidification", *Solidification and castings in metals*, Metals Society (1979), London, U.K. 81-87.

[Hil81], M. Hillert, "An analysis of the effect of alloying elements on the pearlite reaction", in *Solid/solid phase transformations*, *TMS* 1981, 789-806.

[Hil95], M. Hillert, "The Nature of Bainite", *ISIJ International*, **35** No 9 (1995), 1134-1140.

SpF [Hil98], M. Hillert, *Phase Equilibria, Phase Diagrams and Phase Transitions. Their Thermodynamic Basis*, Cambridge University Press, (1998) Cambridge U.K.

[Hil99a], M. Hillert, L. Höglund, and M. Schalin, "Role of Back-Diffusion Studied by Computer Simulation", *Metall. and Materials Trans.* **30A** (June 1999), 1635-1641.

[Hil99b], M. Hillert, "Overview No 135 : Solute drag, solute trapping and diffusional dissipation of Gibbs energy" *Acta Mater.* **47** No 18 (1999), 4481-4505.

[Hil00], M. Hillert and G. R. Purdy, "On the misuse of the term bainite", *Scripta Materiala* **43** N°9, (2000), 831-833

[Hof98], P. Hofer, H. Cerjak, "Quantitative evaluation of precipitates in the martensitic cast steel G-X12CrMoWVNb10-1-1", in *Materials for Advanced Power Engineering 1998*, Ed J. Lecomte-Becker, F. Schubert and P.J. Ennis, Pub Forschungszentrum Jülich GmbH, Germany, **5**, 549-557.

SpA [Hög98], *Höganäs iron and steels powders for sintered components.* (1998), Höganäs

SpA [Hög99], *Metallography, Höganäs handbook for sintered components.* (1999), Höganäs

DB [Hol84], H. Holleck, *Binäre und ternäre Carbid- und Nitridsysteme der Übergangsmetalle* Ed. G. Petzow, Pub. Gebrüder Borntraeger (1984), Berlin

[Hon72], R.W.K. Honeycombe and F.B. Pickering, "Ferrite and Bainite in Alloy Steels", *Metall. Trans. 3* (May 1972), 1099-1112.

[Hon76], R.W.K. Honeycombe, "Transformation from Austenite in Alloy Steeels", *Metall. Trans.* **7A** (July 1976), 915-936.

[Hon80], R.W.K. Honeycombe, "Ferrite", *Metal Science*, June 1980, 201-214

[Hon83], G. Hongye and H. Jueming "Research on Han Wei Spheroidal-Graphite Cast Iron", *Foundry Trade Journal Intern.* March 1983, 89-94.

SpF [Hon95], R.W.K. Honeycombe and H.K.D.H. Bhadeshia, *Steels, Microstructure and Properties,* second edition, Edward Arnold London U.K. (1995)

SpA [Hoy88], G Hoyle, *High Speed Steels,* Butterworths & Co publishers (1988).

[Hua97], M. Hua, C.I. Garcia and A.J. DeArdo, "Precipitation Behavior in Ultra-Low-Carbon Steels Containing Titanium and Niobium", *Metall. and Materials Trans.* **28A** (Sept. 1997), 1769-1780.

[Hub81], C.R. Hubbard and L.D. Calvert, "The Pearson Symbol", *Bull. of Alloy Phase Diagrams*, **2** No2, (1981), 153-157

[Hug65], H. Hughes, "Precipitation in alloyed steels containing chromium, nickel and titanium", *J. Iron Steel Inst.* **203** (1965), 1019-1023.

[Hul73], A. Hultgren, "A and V segregation in killed steel ingots", *Scand. J. Metallurgy,* **2** (1973), 217-227.

[Hum01], F.J. HUMPHREYS, "Review : Grain and subgrain characterisation by electron backscatter diffraction", *J. of Materials Sci.* **36**, (2001), 3833-3854.

[Hun94], J.D. HUNT, "Cellular and Primary Dendrite Spacing", in *Solidification Processing*, Iron Steel Inst. Pub. (1977), 3-9.

[Hun96], J.D. HUNT and S.-Z. LU, "Numerical Modeling of Cellular/Dendritic Array Growth : Spacing and Structure Predictions", *Metall. and Materials Trans.* **27A** (1996), 611-623.

[Hun97a], J.D. HUNT and THOMAS, "Microscopical Modelling of Binary/Multicomponent Alloys" in *Solidification Processing* Ed. J. Beech and H. Jones, Pub. University of Sheffield (1997) U.K. 350-353.

[Hun98], O. HUNZIKER, M. VANDYOUSSEFI, W. KURZ, "Phase and Microstructure Selection in Peritectic Alloys Close to the Limit of Constitutional Supercooling", *Acta Mater.* **46** No18 (1998), 6325-6336

[Hut01], C. HUTCHISON, "The Formation of Partitioned Pearlite in Fe-Mn-C Steels", Ph. D. Thesis, University of Virginia, USA, May, 2001.

[Hwa98], K.C. HWANG, S. LEE, H.C. LEE, "Effects of alloying elements on microstructure and fracture properties of cast high speed rolls Part I Microstructural analysis; Part II Fracture behavior", *Mater. Sci. and Engineering,* **A254** (1998), 282-295 and 296-304.

[Ind97], G. INDEN, "Cinétique de transformation de phases dans des systèmes polyconstitués", *Entropie,* **202/203**, (1997) 6-14.

[Ind02], G. INDEN, "Computational Thermodynamics and Simulation of Phase Transformations", *Calphad and Alloy Thermodynamics*, Ed. P.E.A. Turchi, A. Gonis, R. Schull (2002), Pub. TMS (The Minerals, Metals and Materials Society), 107-129.

[Ino97], TATSUO INOUE, "Japanese sword", *Materials Science Research International,* **2** No4 (1997), 193-203.

[Ino99], TATSUO INOUE, "Japanese swords in comparison with others", in *Progress in Mechanical Behaviour of Materials* Proceedings ICM8 **II** *Materials Properties* Ed. F. Ellyin, J.M. Provan (1999),

[Ino01], K. INOUE, N. ISHIKAWA, I. OHNUMA, H. OHTANI and K. ISHIDA, "Calculation of Phase Equilibria Between Austenite and (Nb, Ti, V)(C, N) in Microalloyed Steels", *ISIJ Int.* **41** No2 (2001), 175-182.

[Jac66], K.A. JACKSON and J.D. HUNT, "Lamellar and Rod Eutectic Growth", *Trans AIME,* **236** (Aug. 1966), 1129-1142.

[Jac70], R.S. JACKSON, "The Austenite Liquidus Surface and Constitutional Diagram for the Fe-Cr-C Metastable System", *J. Iron and Steel Inst.* Feb.1970, 163-167.

[Jac76], H. JACOBI and K. SCHWERDTFEGER, "Dendrite Morphology of Steady State Unidirectionnally Solidified Steel", *Metall. Trans.* **7A** June 1976, 811-820.

[Jac83], W.J. JACKSON, "Ghost bands in steel castings" , in *Solidification technology in the foundry and casthouse, The Metals Soc., Book* **273** (1983) 426-431.

[Jac98], P.J. JACQUES, X. CORNET, Ph. HARLET, J. LADRIÈRE and F. DELANNAY, "Enhancement of the Mechanical Properties of a Low-Carbon, Low-Silicon Steel by Formation of Multiphased Microstructure Containing Retained Austenite", *Metall. and Materials Trans.* **29A** (Sep. 1998), 2383-2393.

[Jac01], P.J. JACQUES, E. GIRAULT, Ph. HARLET and F. DELANNAY, "The Developments of Cold-rolled TRIP-Assisted Multiphase Steels. Low Silicon TRIP-Assisted Multiphase Steels", *ISIJ International,* **41** No9 (2001), 1061-1067.

[Jak98], A. Jakobová, V. Vodárek, K. Hennhfer, V. Voldyna, "Microstructure and creep properties of P91 steel and weldments", in *Materials for Advanced Power Engineering 1998*, Ed J. Lecomte-Becker, F. Schubert and P.J. Ennis, Pub Forschungszentrum Jülich GmbH, Germany, **5**, 373-382.

[Jay92], P. Jay and M. Durand-Charre, "Structural and Morphological Investigation of Vanadium White Cast Irons", *Cast Metals*, **5** No 3 (1992), 169-174.

[Jel36], W. Jellinghaus, "Das System Eisen-Kobalt-Kupfer", *Archiv für Eisenhüttenwesen*, **10 (4)**, (1936), 1-4.

DB [Jer77], *A Guide to the Solidification of Steels*, Jerkontoret (1977) Stockholm, Sweden.

SpF [Joh99], W.C. Johnson, "Influence of Elastic Stress on Phase Transformations", *Lectures on the Theory of Phase Transformatons,* Ed. H.I. Aaronson, 2nd Ed., Pub. TMS (1999), USA, 35-134.

[Joh00], K. Johansson, "Duplex stainless steels; past, present and future", in *6th World Duplex 2000*, Pub. Associazione italiana di metallurgia, Milan, Italy, (2000), 13-28.

[Jon80], H. Jones and W. Kurz, "Growth Temperatures and the Limits of Coupled Growth in Unidirectional Solidification of Fe-C Eutectic Alloys", *Metall. Trans.* **11A** (Aug. 1980), 1265-1273.

[Jon81], H. Jones and W. Kurz, "Relation of Interphase Spacing and Growth Temperature to Growth Velocity in Fe-C and Fe-Fe_3C Eutectic Alloys", *Z. Metallkde.* **72** (1981) H. 11, 792-797.

[Jor97], C.E. Jordan, R. Zuhr and A.R. Marder, "Effect of Phosphorus Surface Segregation on Iron-Zinc Reaction Kinetics During Hot-Dip Galvanizing", *Metall. Trans.* **28A**, (Dec. 199), 2695-2703.

[Jun96], Y.C. Jung, H. Ohtsubo, K. Nakai and Y. Ohmori, "Isothermal Decomposition Processes of Austenite in Fe-Cr-C Alloy Steels", *Materials Trans. JIM*, **37** No 4 (1996), 676-683.

[Kad98], Y. Kadoya, B.F. Dyson, and M. McLean, "Microstructural stability during creep of Mo and/or W-bearing 12Cr steels", in *Materials for Advanced Power Engineering 1998*, Ed J. Lecomte-Becker, F. Schubert and P.J. Ennis, Pub Forschungszentrum Jülich GmbH, Germany, **5**, 593-602.

[Kag80], A. Kagawa and T. Okamoto, "Partition of silicon during eutectic solidification of iron-carbon-silicon alloy", *Metal Science*, Nov. 1980, 519-524.

[Kak99], T Kakeshita, T. Saburi, K. Kindo and S. Endo, "Martensitic transformations in some ferrous and non-ferrous alloys under magnetic field and hydrostatic pressure", *Phase Transitions*, **70** (1999), 65-113.

[Kal98], W.J. Kaluba, R. Taillard and J. Foct, "The bainitic mechanism of austenite formation during rapid heating" *Acta Mater.* **46** No16 (1998). 5917-5927.

SpA [Kap87], L. Kapp, H. Kapp and Y. Yoshihara, *The Craft of the Japanese Sword,* Ed. Kodansha Int. (1987), Tokyo, Japan.

[Kat97], U.R. Kattner, "The Thermodynamic Modelling of Multicomponent Phase Equilibria", *JOM* Dec. 1997, 14-19.

DB [Kau89], I. Kaur and W. Gust, *Handbook of Grain and Interphase Boundary Diffusion Data,* Ziegler Press Stuggart, 1989.

[Kay98], A.A. Kaya and D.V. Edmonds, "Non-classical Decomposition Products of Austenite in Fe-C-Cr Alloys", *Metall. Trans.* **29A** (Dec. 1998), 2913-2924.

[Kei98], A. Von Keitz, G. Sauthoff and P. Neumann, "Laves Phases for High Temperatures -Structure, Stability and Constitution", *Z. Metallkd.* **89** No12 (1998), 803-809.

[Ker96], H. W. Kerr and W. Kurz, "Solidification of peritectic alloys", *International Materials Reviews*, **41** No4 (1996), 129-164.

[Kes87], R. KESRI and M. DURAND-CHARRE, "Phase equilibria, solidification and solid state transformations of white cast irons containing niobium", *J. of Mater. Sci.* **22** (1987), 2959-2964.

[Kes88a], R. KESRI and M. DURAND-CHARRE, "Metallurgical structure and phase diagram of the Fe-V-C system : comparison with other systems forming MC carbides", *Mater. Sci. and Tech.* **4** (Aug. 1988), 692-700.

[Kes88b], R. KESRI et S. HAMAR-THIBAULT, "Structures ordonnées à longue distance dans les carbures MC des fontes", *Acta Metall.* **36** No1 (1988), 149-166.

[Kes97], H.J. KESTENBACH, "Dispersion hardening by niobium carbonitride precipitation in ferrite", *Mater. Sci. and Tech.*, Sept. 1997, 731-739.

[Kha93], F.A. KHALID and D.V. EDMONDS, "A Transmission Electron Microscopy Study of Copper Precipitation in the Cementite Phase of Hypereutectoïd Alloy Steels", *Metall. Trans.* **24A** (April 1993), 781-793.

[Kik90], M. KIKUCHI, T. URABE, G. CLIFF, and G.W. LORIMER, "The loss of driving force due to volume diffusion ahead of a migrating boundary in a cellular precipitation reaction", *Acta Metall. Mater.* **38** No6 (1990), 1115-1120.

[Kim00], D.I. KIM and R. ABBASCHIAN, "The Metastable Liquid Miscibility Gap in Cu-Co-Fe Alloys", *J. Phase Equilibria*, **21** No1 (2000), 25-31.

[Kob01], S. KOBAYASHI, K. NAKAI and Y. OHMORI, "Isothermal decomposition of δ-ferrite in a 25Cr-7Ni-0.4N stainless steel", *Acta Mater.* **49**, (2001), 1891-1902.

SpA [Kra80], G. KRAUSS, *Principles of heat treatments of steels* , Ed. ASM USA, (1980).

[Kra97], T. KRAFT and Y.A. CHANG, "Predicting Microstructure and Microsegregation in Multicomponent Alloys", *JOM*, Dec. 1997, 20-28.

[Kud72], G.V. KURDJUMOV and A.G. KHACHATURYAN, "Phenomena of Carbon Atom Redistribution in Martensite", *Metall. Trans.* **3** (May 1972), 1069-1076.

[Kuo54], K. KUO, "Metallography of Delta Ferrite Part I-Eutectoid decomposition of delta ferrite", *J. Iron and Steel Inst*, April 1954, 433-441.

[Kuo55], K. KUO, "Metallography of Delta Ferrite Part I-Eutectoid decomposition of delta ferrite; Part II-Formation of delta-eutectoid in 18-4-1-type high-speed steels", *J. Iron and Steel Inst*, Oct. 1955, 128-134.

[Kur90], W. KURZ and R. TRIVEDI, "Solidification microstructure : Recent developments and future directions" Overview No **87**, *Acta Metall. Mater.* **38**, No1 (1990), 1-17.

SpF [Kur98], W. KURZ and D. J. FISHER, *Fundamentals of solidification*, Trans. Tech. Publ. Switzerland, 4th edition, (1998).

[Lac89], J. LACAZE, M CASTRO, N. AICHOUN, G LESOULT, "Influence de la vitesse de refroidissement sur la microstructure et la cinétique de solidification de fontes GS ; expériences et simulation numérique de solidification dirigéee", *Mém. Scien. Rev. Mét.* Feb. 1989, 85-97.

[Lac91], J. LACAZE and B. SUNDMAN, "Assessment of the Fe-C-Si System", *Metall. Trans.* **22A** (Oct. 1991), 2211-2223.

SpA [Lac93], *Stainless steels*, Ed. P. Lacombe, B. Baroux and G. Béranger, Les Editions de Physique, (1993), Les Ulis, France.

[Lac97], J. LACAZE, A. BOUDOT, V. GERVAL, D. OQUAB, and H. SANTOS, "The Role of Manganese and Copper In the Eutectoid Transformation of Spheroidal Graphite Cast irons", *Metall. and Mater. Trans.* **28A** (Oct. 1997), 2015-2025.

[Lac98], J. LACAZE, M. CASTRO and G. LESOULT, "Solidification of Spheroidal Graphite Cast Irons-II. Numerical Simulation", *Acta Mater.* **46** No3 (1998), 997-1010.

[Lac99a], J. LACAZE, "Solidification of Spheroidal Graphite Cast Irons-III. Microsegregation Related Effects", *Acta Mater.* **47** No14 (1999), 3779-3792

[Lac99b], J. LACAZE, “Pearlite growth in cast irons : a review of literature data”, *Int. J. Cast Metals Res.* **11**, (1999), 431-436.

[Lac03] S. Lacroix, Y. Bréchet, M. Véron, D. Quidort, M. Kandel, T. Iung, “Influence od deformation on austenite to ferrite transformation in low carbon steels : experimental approach and modelling”, *Austenite Formation and Decomposition,* MS&T (2003), Ed. TMS, 367-379.

[Lag01], R. LAGNEBORG and S. ZAJAC, “A Model for Interphase Precipitation in V-Microalloyed Structural Steels”, *Metall. and Mater. Trans.* **32A** (Jan. 2001), 39-50.

[Lai90], G. LAIRD II, R.L. NIELSEN, and N.H. MACMILLAN, “On the Nature of Eutectic Carbides in Cr-Ni White Cast Irons” *Metall. Trans.* **22A** (Aug. 1991), 1709-1720.

[Le_00], J. LE COZE, “Purification of Iron and Steels a Continuous Effort from 2000BC to 2000AD”, *Materials Transactions, JIM,* **41** No1 (2000), 219-232.

[Le_03], J. LE COZE, “About the Signification of Wootz and Other Names Given to Steel”, *Indian J. of History of Science, JIM,* **38** No2 (2003), 117-127.

[Leb88], S. LEBAILI, M. DURAND-CHARRE and S. HAMAR-THIBAULT, “Metallurgical structure of as-solidified hardfacing Ni-Cr-B-Si-C alloys”, *Journal of Materials Science,* **23** (1988), 3603-3611.

[Lee00], C.S. LEE, J.S. AHN, K.A LEE, K.T. KIM, C.G. PARK and K.Y. KIM, “Effect of χ-Phase Precipitation on the Mechanical Properties of Duplex Stainless Steels”, *6th World Duplex 2000,* Pub. Associazione italiana di metallurgia, Milan, Italy, (2000), 785-794.

[Lep98a], Y. LEPRÊTRE, J.M. MATAIGNE, M. GUTTMANN, J. PHILIBERT, “Reactive interdiffusion in the Fe-Al-Zn system : Reaction mechanisms during hot-dip galvanizing” *Zinc-Based Steels Coatings Systems: Production and Performance* Ed. F.E. Goodwin, The Minerals, Metals, Materials Society, (1998), USA 95-10.

[Lep98b], Y. LEPRÊTRE, J.M. MATAIGNE, “A new interpretation of the Sandelin effect” in *Zinc-Based Steels Coatings Systems: Production and Performance* Ed. F.E. Goodwin, The Minerals, Metals, Materials Society, (1998), USA 303-312.

[Les89], G. LESOULT, “Solidification, cristallisation et microstructure; Solidification: macrostructures et qualité des produits”, *Techniques de l'ingénieur,* **M58** (26 pp) and **M59** (24 pp), (1989).

[Les98], G. LESOULT, M. CASTRO and J. LACAZE, “Solidification of Spheroidal Graphite Cast Irons-I. Physical Modelling”, *Acta Mater.* **46** No3 (1998), 983-995.

[Li_98a], D.F. LI, X.M. ZHANG, E. GAUTIER and J.S. ZHANG, “Morphology Transitions of Deformation,-Induced Thin-Plate Martensite in Fe-Ni-C Alloys”, *Acta Mater.* **46**, No 13 (1998) 4827-4834 in *Microalloying in Steels, Materials Science Forum,* **284-286**, (1998), Trans Tech. Pub. Switzerland.

[Li_98b], P.H. LI, A.K. IBRAHEEM and R. PRIESTNER, “Eutectic Precipitation of (TiNbV)(CN) in Cast, Microalloyed, Low-C Austenite and Effects of Reheating”, *Microalloying in Steels, Materials Science Forum,* **284-286**, (1998), Trans Tech. Pub. Switzerland 517-524.

[Lil99], M. LILJAS and J.-O. NILSSON, “Development of Commercial Nitrogen-Rich Stainless Steels”, *High Nitrogen Steels,* Ed.H. Hänninen *et al.* (1999), Trans. Tech. Pub. Switzerland, 189-200

[Liu97], Y.C. LIU, J.M. SCHISSLER, J.P. CHOBAUT and H. VETTERS, “Structural Evolution of Austempered Ductile Irons (ADI) During Tempering”, in *Physical Metallurgy of Cast Irons V,* Ed. G. Lesoult and J. Lacaze, *Advanced Materials Research* **4-5**, Scitec Pub. (1997), Switzerland 407-414.

[Lle95], D.T. LLEWELLYN, “Copper in steels”, *Iron making and steel making,* **22** No1 (1995), 25-34.

[Lo_01], T.S. LO, A. KARMA, and M. FLAPP, “Phase-field modelling of microstructural pattern formation during directional solidification of peritectic alloys without morphological instability”, *Physical Review E,* **63** 031504, 1-15.

[Lon73], C.J. LONG and W.T. DELONG, “The Ferrite Content of Austenitic Stainless Steel Weld Metal”, *Welding Research, supplement to the Welding J.* July 1973, 281s-297s.

[Lun97], L. LUNDIN, M. NORELL, H.-O. ANDRÉN and L. NYBORG, "Remanent life assessment of creep-resistent modified 12% chromium steels : microstructural analysis development models", *Scand. J. of Metallurgy,* **26** (1997), 27-40.

[Ma_83], C-B. MA, T. ANDO, D.L. WILLIAMSON and G. KRAUSS, "Chi-Carbides in Tempered High Carbon Martensite", *Metall. Trans.* **14A** (June 1983), 1033-1045.

SpA [Maî96], *Les maîtres de l'acier,* Ed. Musée dauphinois (1996), Grenoble France.

[Mag87], P. MAGNIN and W. KURZ, "An analytical model of irregular eutectic growth and its application to Fe-C", *Acta Metall.* **35** No5 (1987), 1119-1128.

[Mag88], P. MAGNIN and W. KURZ, "Competitive Growth of Stable and Metastable Fe-C-X Eutectics : Part I. Experiments; Part II. Mechanisms", *Metall. Trans.* **19A** (Aug. 1988), 1955-1964 and 1965-1971.

[Mal99], S. MALET and M. DURAND-CHARRE, unpublished work.

[Man99a],M.A. MANGAN, N.V. KRAL and G. SPANOS, "Correlation between the crystallography and morphology of proeutectoid cementite precipitates" *Acta Mater.* **47** No17 (1999), 4263-4274.

[Man99b] M.A. MANGAN and G.J. SHIFLET, "The Pitsch-Petch Orientation Relationship in Ferrous Pearlite at Small Undercooling", *Metall. Trans.* **30A** (Nov. 1999), 2767-2781.

SpA [Man99c],PAT. L. MANGONON, *The Principles of Materials Selection for Engineering Design,* (1999), Ed. Prentice Hall, New Jersey, USA.

[Mar58], J. MARÉCHAL, "La nitruration du fer était utilisée par les anciens", *Métaux,* **391** (March 1958), 133-137.

DB [Mar70] F MARATRAY and R USSEGLIO-NANOT, *Atlas, courbes de transformation de fontes blanches au chrome et au chrome-molybdène,* Ed. Climax Molybdenum, Paris (1970).

[Mar93], B. MARTINELLI, "Fonderies ouest-africaines. Classement comparatif et tendances", *Techniques et culture,* **21** (1993), 195-221.

[Mar96], S.P. MARSH and M.E. GLICKSMAN, "Overview of Geometric Effects on Coarsening of Mushy Zones", *Metall. and Mater. Trans.* **27A** (March 1996), 557-567.

DB [Mas90], T. B. MASSALSKY, *Binary Alloy Phase Diagrams* Ed. H. Okamoto, P.R. Subramanian, L. Kacprzak, 2nd edition (1990), ASM International, USA.

[Mas00], F. MASUYAMA, "Materials Design of Ferritic Heat Resistant Steels" *CAMP-ISIJ,* **13** (2000), 566 (in Japanese).

[Mau01], P. MAUGIS, D. GENDT, S. LANTERI, P. BARGES, "Modelling of niobium carbide precipitation in steel" *Defect and diffusion forum,* Ed.Y. Limoge and J.L. Bocquet, Pub SCITEC Swizerland, **194-199** (2001), 1767-1772

[Maz95], T. MAZET, "Etude des structures de solidification et des ségrégations dans les lingots d'acier", INPL Doctorate Thesis submitted 20 September 1995.

E [Met85], Metals Handbook, *Metallography and Microstructures,* **9**, 9th edition, ASM (1986), USA.

E [Met86], Metals Handbook, *Failure Analysis and Prevention,* **11**, 9th edition, ASM (1986), USA.

E [Met90], Metals Handbook, *Properties and Selection : Irons, Steels and High Performance Alloys,* **1**, 10th edition, ASM (1990), USA.

E [Met96], Metals Handbook, *Fatigue and Fracture,* **19**, ASM (1996), USA.

[Mie98a], J. MIETTINEN, "Reassessed Thermodynamic Solution Phase Data for the Ternary Fe-Si-C System", *Calphad,* **22** No 2 (1998), 231-256.

[Mie98b], J. MIETTINEN, "Thermodynamic Assessment of the Fe-FeS-MnS-Mn System", *Calphad,* **22** N°2 (1998), 257-273.

[Mie98c], J. MIETTINEN, "Approximate Thermodynamic Solution Phase Data for Steels", *Calphad,* **22** No2 (1998), 275-300.

SpA [Mil84], F. Millet, *La mesure des températures de l'ambiante à 2500K*, PYC (1984), Paris, France.

[Mil95], M.K. Miller, J.M. Hyde, M.G. Hetherington, G.D.W. Smith and C.M. Elliott, "Spinodal decomposition in Fe-Cr alloys: experimental study at the atomic level and comparison with computer models -Introduction and methodology" *Acta Metall. Mater.* **43** No 9 (1995), 3385-3401.

[Mil02], M.K. Miller, S.S. Babu, M.G. Burke, "Comparison of the phase compositions in Alloy 718 measured by atom probe tomography and predicted by thermodynamic calculations", *Materials Science and Engineering*, **A327** (2002), 84-88.

[Min86], Y. Minami, H. Kimura, Y. Ihara, "Microstructural changes in austenitic stainless steels during long-term aging", *Mater. Sci. and Tech.*, **2** (Aug. 1986), 795-806.

SpA [Moh90], J.P. Mohen, *Métallurgie préhistorique. Introduction à la paléométallurgie*, Masson (1990), Paris.

[Mur86], V.S.R Murthy, Kishore, S. Seshan, "Morphology of Flake, Ductile and Compacted Graphite", *JOM*, Dec. 1986, 24-28.

[Mur99], M. Murayama, Y. Katayama, and K. Hono, "Microstructural Evolution in a 17-4 PH Stainless Steel after Aging at 400°C", *Metall. and Materials Trans.* **30A** (Feb. 1999), 345-353.

[Nas97], L. Nastac and D.M. Stefanescu, "Modelling of the Stable-to-Metastable Structural Transition in Cast Iron" , in *Physical Metallurgy of Cast Irons V*, Ed. G. Lesoult and J. Lacaze, *Advanced Materials Research* **4-5** (1990), Scitec Pub. 1997 Switzerland, 469-478.

[Nag91], S.V. Nagender Naidu, A.M. Sriramanamurthy and P. Rama Rao, "Fe-W (Iron-Tungsten)", in *Phase Diagrams of Binary Tungsten Alloys* 89-101.

[Nil00], J.O. Nilsson, P. Kangas, T. Karlsson, and A. Wilson, "Mechanical Properties, Microstructural Stability and Kinetics of σ-Phase Formation in 29Cr-6Ni-2Mo-0.38N Superduplex Stainless Steel", *Metall. and Mater. Trans.* **31A** (Jan. 2000), 35-45.

[Ohm71], Y. Ohmori, "The Crystallography of the Lower Bainite Transformation in Plain Carbon Steel", *Transactions ISIJ*, **11** (1971), 96-101.

[Ohm91], Y. Ohmori and T. Maki, "Bainitic Transformation in View of Displacive Mechanism", *Mater. Tran. JIM*, **32** No 8 (1991), 631-641.

[Oik99], K. Oikawa, S. Sumi and K. Ishida, "Morphology Control of MnS Inclusions in Steel During Solidification by Addition of Ti and Al", *Z. Metallkd.* **90** (1999), 13-18.

[Oka78], T. Okamoto, S. Matsuo and K. Kishitake, "Dendrite Arm Spacings in Iron-Chromium-Carbon Alloys", *Trans ISIJ*, **5** (1978), 289-294.

[Oka86], H. Okamoto and M. Oka, "Lower Bainite with Midrib in Hypereutectoid Steels", *Metall. Trans.* **17A** (1986), 1113-1120.

[Old62], W. Oldfield, "The chill-reducing mechanism of silicon in cast iron", *BCIRA J.* **10** (1962), 17-27.

[Ols81], G.B. Olson and M. Cohen, *Ann. Rev. Mat. Sci.* Ed. R.A. Huggins *et al.*, Annual Reviews Inc, CA (1981), 1-30.

[Ols83], G.B. Olson and M. Cohen, "Early Stages of Aging and Tempering of Ferrous Martensites" *Metall. Trans.* **14A** (June 1983), 1057-1065.

[Ols86], A. Olsson, R. West, H. Fredriksson, "Macrosegregation in ingots", *Scand. J. Metallurgy*, **15** (1986), 104-112.

[Ons99], M.I. Onsoien, Ø Grong, Ø. Gundersen and T. Skaland, "A Process Model for the Microstructure Evolution in Ductile Cast Iron : Part I. The Model; Part II Applications of the Model", *Metall. and Mater. Trans.* **30A** (1999), 1053-1068 and 1069-1079.

[Ora91], A. ORADEI-BASILE and J. F. BASILE, "A Current T.T.T. Diagram for Wrought Alloy 718" in *Superalloys 718, 625 and Various Derivatives,* Ed. E. A. Loria, Pub. TMS-AIME, Warrendale (1991), 325-335.

[Osh76], R. OSHIMA, H. AZUMA and F.E. FUJITA, "The formation of intermediate phase in martensite transformation of Fe-Mn-C and Fe-Mn-Cr-C steel", *Scripta Met.* **10** (1976), 1011-1014.

[Par99], J.W. PARK, H.C. LEE, and S. LEE, "Composition, Microstructure, Hardness, and Wear Properties of High-Speed Steel Rolls", *Metall. and Mater. Trans.* **30A** (Feb. 1999), 399-409.

[Par01], Y-H. PARK, Z-H. LEE, "The effect of nitrogen and heat treatment on the microstructure and tensile properties of 25Cr-7Ni-1,5Mo-3W-xN duplex stainless steel castings" *Mater. Sci. and Eng.* **A297** (2001), 78-84.

[Pat98], Billgren *et al.* United States Patent; Patent Number 5,815,790 ; Date Sept. 29, 1998.

[Pax72], H.W. PAXTON and J.B. AUSTIN, "Historical Account of the Contribution of E.C. Bain", *Metall. Trans.* **3** (May 1972), 1035-1042.

DB [Pea91], W.B PEARSON, *Handbook of Crystallographic Data for Intermetallic Phases,* Ed P. Villars and B. Calvert, 2nd edition (USA) (1991).

E [Pec77], D. PECKNER, I.M. BERNSTEIN, *Handbook of Stainless Steels* (1977), Mc Graw Hill USA.

[Pen89], J.M. PÉNISSON and G REGHEERE, "Characterization of Internal Interfaces in Metal and Alloys by High Resolution Microscopy" *Mater. Science and Engineering,* **A107** (1989), 199-205.

[Per92], P. PERROT, J.C. TISSIER, J.Y. DAUPHIN, "Stable and metastable equilibria in the Fe-Zn-Al system at 450°C", *Z. Metallkde,* **11** (1992), 786-790.

[Per94], P. PERROT and G. REUMONT, "Thermodynamic Description of Dross Formation when Galvanizing Silicon Steels in Zinc-Nickel Baths" *J. of Phase Equilibria,* **15** No 5 (1994), 479-482.

[Per95a], P. PERROT and G. REUMONT, Reply to "An Alternative Description of Dross Formation when Galvanizing Silicon Steels in Zinc-Nickel Baths" *J. of Phase Equilibria,* **16** No 3 (1995), 207.

[Per95b], P. PERROT, G. REUMONT, J.C. TISSIER and J. FOCT, "Dross Formation by Reaction Between the Tank Surface and the Zn-Al Bath" in *Galvatech 95,* Iron and Steel Society, Warrendale P.A. (1995), 763-767.

SpF [Phi91], J. PHILIBERT, *Atom Movements, Diffusion and Mass Transport in Solids,* Les Editions de Physique (1991).

GM [Phi02], J. PHILIBERT, A. VIGNES, Y. BRÉCHET, P. COMBRADE, *Métallurgie, Du minerai au matériau,* Dunod, 2nd edition, Paris (2002).

[Pic67], F.B. PICKERING, "The Structure and Properties of Bainite in Steels" , Symposium *Transformation and Hardenability in Steels,* Feb. 27-28 1967, Climax Moly. Ann Arbor, MI USA, 109-132.

SpA [Pic78], F.B. PICKERING, *Physical Metallurgy and the Design of Steels,* Applied Science Publishers (1978), Barking, U.K.

[Ple88], R. PLEINER, "Les débuts de la métallurgie du fer chez les Celtes", *Les Princes Celtes et la Méditérranée,* La documentation française, (1988), Paris 179-185

E [Pok67], A. POKORNY and J. POKORNY, *De Ferri Metallographia,* **III**, Berger-Levrault, (1967), Nancy, France.

[Pol70], C. B. POLLOCK and H. H. STADELMAIER, "The Eta Carbides in the Fe-W-C and Co-W-C Systems" *Metall. Trans.* **1** (1970), 767-770.

GM [Por92], D.A. PORTER and K.E. EASTERLING, *Phase Transformations in Metals and Alloys,* second ed. (1992), Chapman and Hall, London, U.K.

[Por99], P.D. Portella, M. Köhler and M. Renner, "Investigation of Microstructure and Properties of a Chromium-Rich Austenitic Material with High Nitrogen Content", *High Nitrogen Steels*, Ed.H. Hänninen *et al.* (1999), Trans. Tech. Pub. Switzerland, 201-208.

[Pra95], B. Prakash, "Some Aspects of Process Control of Ancient Iron making", *Paléométallurgie du fer et cultures*, Ed. P. Benoit and P. Fluzin, Pub. Vulcain Belfort, France, (1995), 33-40

SpF [Pri66], A. Prince, *Alloy Phase Equilibria*, Ed. Elsevier, Amsterdam, London, New York (1966)

[Pur78], G.R. Purdy, "The Dynamics of Transformation Interfaces in Steels- I. The Ferrite-Austenite Interfaces in Fe-C-Mo Alloys, II. Transformation in Fe-C-Mo Alloys at Intermediate Temperatures", *Acta Metall.* **26** (1978), 477-486 and 487-498.

[Pur84], G.R. Purdy and M. Hillert, "Overview No. **38**, On the nature of the bainite transformation in steels", *Acta Metall.* **32** No6 (1984), 823-828.

[Pur85], G.R. Purdy and M. Audier, "Electron Microscopical Observations of Graphite in Cast Irons", *Mat. Res. Soc. Symp. Proc.* **34** (1985), 13-23.

[Qui01], D. Quidort and Y.J.M. Bréchet, "Isothermal Growth Kinetics of Bainite in 0.5%C Steels", *Acta Mater.* **49** (2001), 4161-4170

[Qui02], D. Quidort and Y.J.M. Bréchet, "The role of carbon on the kinetics of bainite transformation in steels", *Scripta Mater.* **47** No9 (2002), 151-156.

[Rag84], V. Raghavan, "The C-Fe-V (Carbon-Iron-Vanadium) System", *Bull. of Alloy Phase Diagrams*, **5** No 3 (1984), 293-322.

DB [Rag88a], V. Raghavan, "The C-Fe-P (Carbon-Iron-Phosphorus) System" *Phase Diagrams of Ternary Iron Alloys: Part 3- Ternary Systems Containing Iron and Phosphorus*, The Indian Institute of Metals, Calcutta (1988), 33-44.

DB [Rag88b], V. Raghavan, "The Fe-S (Iron-Sulphur) System" and "The Fe-Mn-S (Iron-Manganese-Sulphur) System", *Phase Diagrams of Ternary Iron Alloys: Part 2- Ternary Systems Containing Iron and Sulphur*, The Indian Inst. of Metals, Calcutta (1989), 5-9 and 154-173 respectively.

DB [Rag92a], V. Raghavan, "The Cu-Fe-O (Copper-Iron-Oxygen) System", *Phase Diagrams of Ternary Iron Alloys: Part 5, Ternary Systems containing Iron and Oxygen*, The Indian Institute of Metals Calcutta (1989), 105-121.

DB [Rag92b], V. Raghavan, *Phase Diagrams in Ternary Iron Alloys* Part 6A, The Indian Institute of Metals Calcutta (1992).

DB [Ray88], G.V. Raynor and V.G. Rivlin, *Phase Equilibria in Iron Ternary Alloys*, Part 4, The Institute of Metals, Calcutta (1988).

[Raz76], N.A. Razik, G.W. Lorimer, and N. Ridley, "Chromium Partitioning During the Austenite-Pearlite Transformation", *Metall. Trans.* **7A** (Feb. 1976), 209-214.

[Rie90], R. Riedl and H.F. Fischmeister, "Dendrite Arm Climb by Temperature Gradient Zone Melting during Solidification of a High Speed Tool Steel", *Metall. Trans.* **21A** (Jan. 1990), 264-266.

[Riv84], V.G. Rivlin, "Critical review of constitution of carbon-chromium-iron and carbon-iron-manganese systems", *International Metals Reviews*, **29** No4 (1984), 299-327.

[Reh92], J.E. Rehder, "Iron versus Bronze for Edged Tools and Weapons. A Metallurgical View" *JOM*, Aug. 1992, 42-46.

[Reu98], G. Reumont, P. Perrot, J. Foct, "Thermodynamic study of the galvanizing process in a Zn-0.1Ni bath", *J. of Mater. Science*, **33** (1998), 4759-4768.

[Rey91], W.T. Reynolds, Jr. , H.I. Aaronson and G. Spanos, "A Summary of the Present Diffusionist Views on Bainite" *Mater. Trans. JIM*, **32** No 8 (1991), 737-746.

DB [Rog98], P. Rogl, *Phase Diagrams of Ternary Metal-Boron-Carbon Systems*, Ed. G. Effenberg Pub ASM The Materials International Society (1998), OH U.S.A.

[Rot75], T.A. ROTH, "The Surface and Grain Boundary Energies of Iron, Cobalt and Nickel", *Mater. Science and Eng.* **18** (1975), 183-192.

[Row72] A.F. ROWCLIFFE and R.B. NICHOLSON, "Quenching defects and precipitation in a phosphorus-containing austenitic stainless steel", *Acta Metall.* **20** Jan. 1972, 143-155.

[Rub95], HAN RUBIN, T. KO "Ancient Iron and Steel Technology in China", *Paléométallurgie du fer et cultures*, Ed. P. Benoit and P Fluzin, Pub. Vulcain Belfort, France, (1995), 111-117.

[Rus90], K.C. RUSSEL, "Effects of solid-state diffusion on the incubation time for nucleation of solids", in *Fundamentals and applications of ternary diffusion* Ed. Purdy G.R. Pergamon Press, (1990), 59-65.

SpA [Sac94], M. SACHSE, *Damascus Steel*, Ed. Stahleisen, Düsseldorf, Germany (1994).

[Sak84], T. SAKUMA and R.W. HONEYCOMBE, "Microstructures of isothermally transformed Fe-Nb-C alloys", *Metal Science*, **18** Sept. 1984, 449-454.

[Sal57], E. SALIN, "La civilisation mérovingienne" Part 3 : *Les techniques,* Published with the aid of the CNRS (1957), Picard, Paris.

[Sal78], G. SALJE and M. FELLER-KNIEPMEIER, "Das Kupfer-Eisen Zustandsdiagramm im Bereich von 650 bis 1050°C", *Z. Metall.* **63** No 3 (1978), 167.

E [Sas97], H. SASSOULAS, "Guide de choix des traitements thermiques des aciers inoxydables", *Techniques de l'Ingénieur*, **M 1 160**, traité Matériaux métalliques (1997).

SpF [Sau98], N. SAUNDERS and A.P. MIODOWNIK, *CALPHAD Calculation of Phase Diagrams. A Comprehensive Guide*, Pergamon Materials Series Ed. R.W. Cahn, Elsevier Science Ltd, Oxford U.K (1998).

[Sch49], A.L. SCHAEFFLER, "Constitution Diagram for Stainless Steel Weld Metal", *Met. Prog.* **56** Nov. 1949, 680 and 680B.

[Sch75], J.M. SCHISSLER, J. ARNOULD, G. METAUER, "Etude de la décomposition de l'austénite post-bainitique d'alliages fer-carbone-silicium à 1%C-4%Si au cours d'un maintien isotherme à 420°C. Influence d'une addition de 1% de manganèse" *Mém. Sci. Rev. Mét.* Nov. 1975, 779-793.

SpA [Sch78], P.R. SCHMIDT, *Historical Archaeology, A Structural Approach in an African Culture*, Greenwood Press, (1978), Westport, Conn. USA.

[Sch98], B. SCHAFFERNAK, P. HOFER, H. CERJAK, "Description of the precipitation behavior of advanced 9-12 Cr steels for power plants applications", *Materials for Advanced Power Engineering 1998*, Ed J. Lecomte-Becker, F. Schubert and P.J. Ennis, Pub Forschungszentrum Jülich GmbH Germany, **5**, 519-527.

[Sch99], J.M. SCHISSLER, H. VETTERS, "Etudes des transformations bainitiques et martensitiques d'alliages Fer-Chrome-Carbone et Fer-Carbone-Silicium", *ATT-AWT,* **319** Nov. 1999, 15-21.

[Sel73], E. SELÇUK, "Kinetics of Graphitization Reaction in White Cast Iron", *Heat Treatment 73,* Ed. Iron and Steel Institute, London 1973, 33-38.

[SGTE], SCIENTIFIC GROUP THERMODATA EUROPE, Domaine Universitaire de Grenoble, St Martin d'Hères, France.

[Sha86], L.H. SHAW, J. BEECH, R.H. HICKLEY, "Channel segregates in cast steel rolls", *Ironmaking and Steelmaking*, **13** (1986), 154-160.

[She85a], O.D. SHERBY and J. WADSWORTH, "Damascus Steel" *Scientific American*, **252** (1985), 112-120

[She85b], O.D. SHERBY, T OYAMA, D.W. KULM, B. WALSER and J. WADSWORTH, "Ultrahigh Carbon Steels" *JOM*, June 1985, 50-56.

[She92a], O.D. SHERBY and J. WADSWORTH, "Comments on Damascus Steel, Part III : The Wadsworth-Sherby Mechanism by Verhoeven *et al.*", *Mater. Char.* **28** (1992), 165-172.

[She92b], J.Y. Shen, G. Giron, P. Jay and M Durand-Charre, "Etude des équilibres liquide-solide dans les systèmes Fe-Mo-C et Fe-W-C", $18^{\text{èmes}}$ *Journées d'Etudes des Equilibres entre Phases*, University PARIS XI Chatenay-Malabry 2-3 April 1992.

[Shi72], K. Shimizu and Z. Nishiyama, "Electron Microscopic Studies of Martensitic Transformations in Iron Alloys and Steels", *Metall. Trans.* (May 1972), 1055-1068

[Shi96], T. Shibata, Y. Shudo and Y. Yoshono, "Precipitates in Wrought Ni-Fe Base Superalloy 706" *J. Inst. Metals*, **60** No9 (1996), 802-808.

[Sht97], D.V.Shtansky and G. Inden, "Phase transformation in Fe-Mo-C and Fe-W-C steels - I The structural evolution during tempering at 700°C; - II Eutectoid reaction of $M_{23}C_6$ carbide decomposition during austenitization" *Acta Mater.* **45** No7 (1997), 2861-2878 et 2879-2895.

[Sht99a], D.V Shtansky, K. Nakai and I. Ohmori, "Formation of Austenite and Dissolution of Carbides in Fe-8.2Cr-C Alloys", *Z. Metallkd.* **90** (1999), 25-37.

[Sht99b], D.V Shtansky, K. Nakai and I. Ohmori, "Pearlite to austenite transformation in an Fe-2.6Cr-1C alloy" *Acta Mater.* **47** No 9 (1999), 2619-2632.

SpA [Sie77], C. A. Siebert, D. V. Doane and D.H Breen, *The Hardenability of Steels*, Ed. ASM USA (1977).

[Sim89], J.P. Simon and O. Lyon, "Phase separation in a Fe-Cr-Co alloy studied by anomalous small angle X-ray scattering", *Acta Metall.* **37** No7 (1989), 1727-1733.

SpF [Sin72], A.K. Sinha, "Topologically Close-Packed Structures of Transition Metal Alloys", Pergamon Press, (1972), Oxford, U.K.

[Ska93], T. Skaland, Ø. Grong, and T. Grong, "A Model for the Graphite Formation in Ductile Cast Iron: Part I: Inoculation Mechanisms; Part II: Solid State Transformation Reactions", *Metall. Trans.* **24A** (Oct. 1993), 2321-2345 and 2347-2353.

[Smi48], C.S. Smith, "Grains, Phases, and Interphases : An Interpretation of Microstructure", *Trans. AIME,* **175** (1948), 15-51.

SpA [Smi65], C.S. Smith, *A History of Metallography*, The Univ. of Chicago Press (1965), Chicago & London

[Sol78], H.D. Solomon and L.M. Levinson, "Mössbauer effect study of 475°C embrittlement of duplex and ferritic stainless steels", *Acta Metall.* **26** (1978), 429-442.

[Son00], J.M. Song, B.C. Kuo, T.S. Lui, and L.H. Chen, "The Effect of Rolling on Graphitization Characteristics of Strip Cast Fe-C-Si White Cast Iron", *Metall. and Mater. Trans.* **31A** Jan. 2000, 275-281.

[Sou01], T. Sourmail, "Precipitation in creep resistant austenitic stainless steels", *Mater. Sci. and Tech.*, **17** Jan. 2001, 1-14.

[Spa90], G. Spanos and H.I. Aaronson, "The interfacial structure and habit plane of pro-eutectoid cementite plates" *Acta Metall. Mater.* **38** No12 (1990), 2721-2732

[Spe72], G.R. Speich and W.C. Leslie, "Tempering of Steel", *Metall. Trans.* **3** (May 1972), 1043-1054.

[Spe02] J.G. Speer and D.K. Matlock, "Recent Developments in Low-Carbon Steels", *JOM,* July 2002,19-24

[Spe03], K. Spencer, J.D. Embury and M. Véron, "The Formation of Strain-Induced Martensite in Stainless Steels", Proceedings of *COM 2003*, August 24-27 2003, Vancouver.

[Spi98], S. Spiragelli, E. Cerri, E. Evangelista and P. Bianchi, "Effect of microstructural evolution of a T91 steel during creep", in *Materials for Advanced Power Engineering 1998*, Ed J. Lecomte-Becker, F. Schubert and P.J. Ennis Pub Forschungszentrum Jülich GmbH, Germany, **5**, (1998), 539-548

[Sta69], C. Stawström and M. Hillert, "An improved depleted zone theory of intergranular corrosion of 18-8 stainless steel" *J. of Iron and Steel Inst.* Jan. 1969, 77-85.

[Sta82], P. STADLER, K. HAGEN, K. SCHWERTFEGER, "Untersuchung zur Erstarrungsstruktur und Makroseigerung von stranggegossenen Stahlbrammen", *Stahl und Eisen,* **102** (1982), 451-459.

[Stj80], J. STJERNDAHL and C.A. DÄCKER, "Sulphide formation in Stainless Steel", *Scand. J. Metallurgy,* **9** (1980), 217-224

[Sto00], J. STILARZ and J. FOCT, "Microstructural barriers to fatigue crack propagation in duplex stainless steels- The influence of ageing and nitrogen additions", *6th World Duplex 2000*, Pub. Associazione italiana di metallurgia, Milan, Italy, (2000), 639-660.

[Str96], A. STRANG and V. VODAREK, "Z phase formation in martensitic 12CrMoVNb steel", *Mater. Sci. and Tech.* **12** (July 1996), 552-556

SpA [Str97], *Advances in Turbine Materials, Design and Manufacturing*, Ed. A. Strang, W.M. Banks, R.D. Conroy and M.J. Goulette (1997), Pub. The Institute of Materials London (UK).

[Str98], A. STRANG and V. VODAREK, "Microstructure degradation of martensitic 12%Cr power plant steels during prolonged high temperature creep exposure", *Materials for Advanced Power Engineering 1998*, Ed J. Lecomte-Becker, F. Schubert and P.J. Ennis, Pub Forschungszentrum Jülich GmbH Germany, **5**, 603-614.

[Str99], A.J. STRUTT and K.S. VECCHIO, "Simultaneous Oxidation and Sigma-Phase Formation in Stainless Steel", *Metall. and Materials Trans.* **30A** (Feb. 1999), 355-362.

[Sum99], V.V. SUMIN, G. CHIMID, Ts RASHEV and L. SARYIVANOV, "The Neutron-Spectroscopy Proof of the Strong Cr-N Interactions in Nitrogen Stainless Steels", *High Nitrogen Steels*, Ed.H. Hänninen *et al.* (1999), Trans. Tech. Pub. Switzerland, 31-40.

[Sut96], A.P. SUTTON and R.W. BALUFFI, *Interfaces in Crystalline Materials*, Ed. Oxford Science Publications, Clarendon Press Oxford (1996), U.K.

[Tah82], M.A. TAHA, H. JACOBI, M. IMAGUMBAI, K. SCHWERDTFEGER, "Dendrite Morphology of Several Steady State Unidirectionally Solidified Iron Base Alloys", *Metall. Trans.* **13A** (Dec. 1982), 2131-2141.

[Tak57], S. TAKEDA and N. YUKAWA, "Studies on Cr-Mo-Fe Super-Heat-Resistant Alloys. Equilibrium Diagram of the Cr-Mo-Fe System", *J. Japan Inst. Met.* **21** (1957), 275-279.

[Tak87], T. TAKEMOTO, Y. MURATA, and T. TANAKA, "Effect of manganese on phase stability of chromium-nickel non magnetic stainless steel", *High Manganese Austenitic Steels*, Ed. R.A. Lula, Pub. ASM, (1987), 23-32.

[Tan80], H. TANIMURA, "Development of the Japanese Sword", *JOM,* Feb 1980, 63-73.

[Tan95a], NAI-YONG TANG, "Refined 450°C isotherm of Zn-Al-Fe phase diagram", *Mater. Sci. and Tech.* **11** (Sept. 1995), 870-873.

[Tan95b], NAI-YONG TANG, "An Alternative Description of Dross Formation when Galvanizing Silicon Steels in Zinc-Nickel Baths", *J. of Phase Equilibria,* **16** No 2 (1995), 110-112.

[Tas02] C. TASSIN, M. DURAND-CHARRE, C. ANTION, "Genesis of intradendritic sulfides in the AISI 303 resulfurized stainless steels", Communication *Thermodynamics of Alloys*, 9-13 Sep. 2002, Rome.

[Ted71], C.S. TEDMON Jr, D.A. VERMILYEA, and J.H. ROSOLOWSKI, "Intergranular Corrosion in Austenitic Stainless Steel", *J. Electrochem. Soc.* Feb. 1971, 192-202.

[Tew85], S.K. TEWARI and ROMESH C. SHARMA, "The effect of Alloying Elements on Pearlite Growth", *Metall. Trans.* **16A** (April 1985), 597-603.

[Tia98], J. TIADEN, B. NESTLER, H.J. DIEPERS, I. STEINBACH, "The multiphase-field model with an integrated concept for modelling solute diffusion" *Physica D,* **115** (1998), 73-86.

[Thi98], V. THILLOU, M. HUA, C.I. GARCIA, C. PERDRIX and A.J. DEARDO, "Precipitation of NbC and Effect of Mn on the Strength Properties of Hot Strip HSLA Low Carbon Steels" *Microalloying in Steels,* Ed. J.M. Rodriguez-Ibade *et al.* , Pub. Trans. Tech. (1998), 311-318.

[Tho83], T. THORVALDSSON, G.L. DUNLOP, "Grain boundary Cr-depleted zones in Ti and Nb stabilized austenitic stainless steels", *J. of Materials Sci.* **18** (1983), 793-803.

[Tho85], W.R. THORPE, B. CHICCO, "The Fe-Rich Corner of the Metastable C-Cr-Fe Liquidus Surface", *Metall. Trans.* **16A** (Sept. 1985), 1541-1549.

[Til53], W.A. TILLER, K.A. JACKSON, J.W. RUTTER, B. CHALMERS, "The redistribution of solute atoms during the solidification of metals" *Acta Met.* **1** (1953), 1663-1670.

[Tom02] K. TOMIHISA, Y. KANENO, T. TAKASUGI, "Phase relation and microstructure in Ni_3Al-Ni_3Ti-Ni_3Nb pseudo-ternary alloy system", *Intermetallics*, **10** (2002), 247-254.

[Tri70], R. TRIVEDI, "The Role of Interfacial Free Energy and Interface Kinetics During the Growth of Precipitate Plates and Needles" *Metall. Trans.* **1** (1970), 921-927.

[Tri94], R. TRIVEDI and W. KURZ, "Dendritic growth" *International Materials Reviews*, **39** No 2 (1994), 49-74.

[Tri95], R. TRIVEDI, "Theory of Layered-Structures Formation in Peritectic Systems", *Metall. and Materials Trans.* **A 26** (1995), 1583-1590.

SpA [Tyl87], R.F. TYLECOTE, *The early history of metallurgy in Europe*, Longman archeology series, Pub. Longman INC. New York USA.

[Uhr80], B. UHRENIUS, "Calculation of phase equilibria in the Fe-W-C system", *Caphad* **4** No 3 (1980), 173-191.

[Ure73], M. UREDNICEK and J.S. KIRKALDY, "Mechanism of Iron Attack Inhibition Arising from Additions of Aluminium to Liquid Zn(Fe) During Galvanizing at 450°C", *Z. Metallkde*, **64** (1973), 899-910.

[Van51], L. H. VAN VLACK, "Intergranular Energy of Iron and Some Iron Alloys", *Trans. AIME,* March 1951, 251-259.

[Van89], G.F. VANDER VOORT, "Applied Metallography : The Metallography of Stainless Steels", *JOM,* March 1989, 6-11.

[Van95], F. VANDERSCHAEVE, R. TAILLARD, J. FOCT, "Discontinuous precipitation of Cr_2N in a high nitrogen, chromium-manganese austenitic stainless steel", *J. of Materials Sci.* **30** (1995), 6035-6046.

[Van97] M. VANDYOUSSEFI, *Microstructure selection during directional solidification and solid-state transformation in Fe-Ni alloys*, EPFL Thesis Lausanne, Swizerland (1997)

[Van98], I. VANNIER, C. DAVID, H. COMBEAU, G. LESOULT, "A comparison between experiments and empirical criteria predicting A-Type segregation and microporosity", *Modeling of Casting, Welding and Advanced Solidification Processes VIII*, Ed. B.C. Thomas and C. Beckermann, The Minerals, Metals and Materials Society (1998), 337-344.

SpA [Van99], G.F. VANDER VOORT, *Metallography. Principles and Practice*, Ed. ASM International, 1999, USA

[Ven82], R.D. VENGRENOVITCH, "On the Ostwald Ripening Theory", *Acta Met.* **30** (1982), 1079-1086.

[Ven87], M. VENKATRAMAN and J.P. NEUMANN, "The Cr-Mo (Chromium-Molybdenum) System", *Bull. of Alloy Phase Diagrams,* **8** No3 (1987), 216-220.

GM [Ver75], J.D. VERHOEVEN, *Fundamentals of Physical Metallurgy*, (1975), J Wiley & Sons.

[Ver93], J.D. VERHOEVEN, A.H. PENDRAY, "Studies of Damascus Steel Blades : Part I-Experiments on Reconstructed Blades, Part II-Destruction and Reformation of the Pattern ", *Mater. Char.* **30** (1993), 175-186 and 187-200.

[Ver96], J.D. VERHOEVEN, A.H. PENDRAY, and E.D. GIBSON, "Wootz Damascus Steel Blades", *Mater. Char.* **37** (1996), 9-22.

[Ver97], B. VERHAEGHE, F. LOUCHET, B. DOISNEAU-COTTIGNIES, Y. BRÉCHET, "Micromechanisms of deformation of an austenoferritic duplex stainless steel", *Phil. Mag. A.***76** No5 (1997), 1079-1091.

[Ver98a], J.D. VERHOEVEN, A.H. PENDRAY, and W.E. DAUKSCH, "The Key Role of Impurities in Ancient Damascus Steel Blades" *JOM,* Sept. 1998, 58-64.

[Ver98b], J.D. VERHOEVEN, and E.D. GIBSON, "The Divorced Eutectoid Transformation in Steel", (1998) *Metall. and Mater. Trans.* **29A** (1998), 1181-1189.

[Ver98c], J.D. VERHOEVEN, and H.F CLARK, "Carbon Diffusion Berween the Layers in Modern Pattern-Welded Damascus Blades", *Mater. Char.* **41** (1998), 183-191.

[Vod00], V. VODAREK and A. STRANG, "Compositional changes in minor phases present in 12CrMoVNb steels during thermal exposure at 550°C and 600°C", *Mater. Sci. and Tech.,* **16** Oct. 2000, 1207-1213.

[Vol99], V.R. VOLLER and C. BEKERMANN, "A Unified Model of Microsegregation and Coarsening", *Metall. and Materials Trans.* **30A** (Aug. 1999), 2183-2189.

[Voo84], P.W. VOORHEES and M.E. GLICKSMAN, "Ostwald Ripening During Liquid Phase Sintering -Effect of Volume Fraction on Coarsening Kinetics", *Met. Trans.* **15A** (1984), 1081-1088.

[Wad80], J. WADSWORTH and O. SHERBY, "On the Bulat-Damascus Steels Revisited" *Progress Materials Science,* (1980), **25**, 35-68.

[Wad02] J. WADSWORTH, "Ancient and Modern Steels and Laminated Composite Containing Steels", *MRS Bulletin,* Dec. 2002, 980-987.

[Wag74], SIGURD WAGNER and D. A. RIGNEY, "Binary Systems Involving the "Catatectic" Reaction Solid1⇔Solid2+Liquid" *Metall. Trans.* **5** (Oct. 1974), 2155-2160.

[Wan91], E. A. WANNER, D. A. DEANTONIO, D. F. SMITH and J. S. SMITH, "The Current Status of Controlled Thermal Expansion Superalloys" , *JOM* March 1991, 38-43.

[Wan97b],X. WAN, Q. HAN and J.D. HUNT, "The Existence of Two Growth Regimes During Directional Dendritic Growth" *Solidification Processing,* Ed. J. Beech and H. Jones, Pub. University of Sheffield (1997), U.K., 397-400.

E [Wat91], N.A. WATERMAN and M. ASHBY, *Materials Selector,* Elsevier Applied Science, (1991), Barking England.

[Wat01], A. WATSON, F. H. HAYNES, "Some experiences in the modelling of the sigma phase in the Ni-V system", *J. of Alloys and Compounds,* **320** No2 (2001), 199-206.

[Wei79], F. WEINBERG, J. LAIT, R. PUGH, "Solidification of high carbon steel ingots", *Solidification and Casting of Metals,* The Metals Soc. Book **102** (1979), 334-339.

SpA [Wen64], WESLEY WM. WENDLANDT, *Thermal Methods of Analysis,* Ed. P.J. Elving, I.M. Kolthoff, Interscience Publishers, J. Wiley & sons (1964), NewYork, USA.

SpF [Wes82], D.R.E. WEST, *Ternary Equilibrium Diagrams,* Chapman and Hall, London (1982).

[Wes97], M. WESSÉN and I.L. SVENSSON, "Modelling and Simulation of Ferrite Growth in Nodular Cast Irons" in *Physical Metallurgy of Cast Irons V,* Ed. G. Lesoult and J. Lacaze, *Advanced Materials Research* **4-5**, Scitec Pub. (1997), Switzerland 479-484.

[Wlo94], S. T. WLODEK and R. D. FIELD, "The effects of long time exposure on alloy 718", *Superalloys 718, 625, 706 and Various Derivatives,* Ed. E. A. Loria, Pub. TMS-AIME, Warrendale (USA) (1994), 659-670.

[Wol85], G. WOLF, E. FLENDER, P.R. SAHM, "Solidification Behavior of Technical Metastable Near-Eutectic Iron-Carbon Alloys (Experimental and Numerical Simulation)" *Mat. Res. Soc. Symp. Proc.* **34** (1985), 241-249.

[Wol92], M.M. WOLF, "History of continuous casting", in *Proceedings of the 75th Steelmaking Conference,* Toronto, April 5-6 1992, Iron and Steel Society, 83-137
also published in French "L'histoire de la coulée continue", *Rev. Mét.* **I** (Jan. 1994), 75-98; **II** (March 1994), 445-463; **III** (April 1994) United States Patent , 589-608.

[Wri60], H.A. WRIEDT and L.S. DARKEN, "The solubility of Copper in Ferrite", *Trans. AIME,* **218** (1960), 30-36.

[Yak85], H.L. YAKEL, "Crystal structure of stable and metastable iron-containing carbides", Intern. *Metals Reviews,* **30** No1 (1985), 17-40.

[Yan96], C.W. YANG and D.B. WILLIAMS and J.I. GOLDSTEIN, "A Revision of the Fe-Ni Phase Diagram at Low Temperatures (<400°C)" *J. of Phase Equilibria,* **17** N° 6 (1996), 522-531.

[Yoo99], S.M. YOO, K. MOELNIPOUR, A. LUDWIG and P.R. SAHM, "Numerical Simulation and Experimental Results of in situ Heat Treated Austempered Ductile Iron", *Int. J. Cast Metals Research,* **11** (1999), 483-488.

[Ype81], J. YPEY, "Au sujet des armes avec damas soudé en europe", *Archéologie médiévale,* Tome **XI** (1981), Centre de Recherches Archéologiques Médiévales, Caen France, 147-165.

[Yu_02] S-K. YU and Y MATSUBARA, "Effects of Carbide Morphology and Heat Treatment on Abrasion Wear Resistance of Chromium White Cast Irons", *Abrasion Wear Resistant Alloyed White Cast Iron for Rolling and Pulverizing Mills,* Ed. Y. Matsubara, H-K Wu and N. Sasaguri, Pub. Japan Foundry Engineering Society-Kyushu Branch, (2002), 119-126.

SpA [Zac62], *Decomposition of austenite by diffusional processes,* Ed. V.F. Zackay and H.I. Aaronson (1962), Interscience Pub., J. Wiley & Sons N.Y. USA.

[Zen46], C. ZENER, "Kinetics of the Decomposition of Austenite", *Trans. AIME,* **167** (1946), 550-583.

[Zer02], Z. ZERMOUT, D. QUANTIN, J.M. MATAIGNE, "Les produits galvanisés en continu pour application automobile", *Rev. Mét.* June 2002, 569-580.

[Zha92], J-C. ZHAO, "Continuous cooling transformations in steels" and *Isothermal decomposition of supercooled austenite in steels, Mater. Sci. and Tech.* **8** Nov. 1992, respectively 997-1003, and 1004-1010.

[Zha93], J-C ZHAO, M.R. NOTIS, "Phase Transformation Kinetics and the Assessement of Equilibrium and Metastable States", *J. of Phase Equilibria,* **14** No 3 (1993), 303-315.

[Zha95], J-C. ZHAO, M.R. NOTIS, "Continuous cooling transformation kinetics versus isothermal transformation kinetics of steels : a phenomenological rationalization of experimental observations", *Mater. Science and Engineering,* R15, **4-5** (Nov. 1995), 135-208.

[Zha97], Y. ZHANG, S.V. SUBRAMANIAN and G.R. PURDY, "Graphite Growth In S.G. Cast Irons : Simulation vs. Experiments", *Physical Metallurgy of Cast Irons V,* Ed. G. Lesoult and J. Lacaze, *Advanced Materials Research* **4-5**, Scitec Pub. (1997), Switzerland 461-468.

[Zha00], J.C. ZHAO, M. LARSEN, V. RAVIKUMAR, "Phase Precipitation and time-temperature transformation diagram of Hastelloy X", *Mater. Sci. and Engineering,* **A293** (2000), 112-119.

[Zho91], D.S. ZHOU and GJ. SHIFLET, "Interfacial Steps and Growth Mechanism in Ferrous Pearlite", *Metall. Trans.* **22A** (June 1991), 1349-1365.

[Zho92], D.S. ZHOU and G.J. SHIFLET, "Ferrite:Cementite Crystallography in Pearlite", *Metall. Trans.* **23A** (April 1992), 1259-1269.

[Zsc24] B. ZSCHOKKE, "Du Damassé et des lames de damas", *Rev. Mét.* Part I, **21**, (1924), 635-669.

Index

Index terms Links

A

- antiphase boundaries 41
- AOD, VOD, VIM, see refining processes 323
- austenite
  - crystallographic structure 37
  - regression austenite 118 143
  - retained 171 213 218
  - stabilizer, former, see stabilizers
- austenitising 206 300 306

B

- back-diffusion 127
- Bain 210 224
- bainite
  - “midrib” 235
  - debate 224
  - in hypereutectoid steels 228 233
  - in molybdenum steels 230
  - in silicon-rich cast irons 236 364
  - in silicon-rich steels 226
  - inverse bainite 230
  - lower bainite 232
  - tempering 236
  - upper bainite 225

This page has been reformatted by Knovel to provide easier navigation.

blooms, billets, slabs 269
boron
  carboborides 334
  effect of boron 203 333
Bridgman 121

C

carbides
  (V,Ta)C 131
  carbonitrides, see nitrides 334
  cementite 132 193 198 222 298
  crystallographic structures 44
  dissolution 136 208 221
  general 42
  $M_{23}C_6$ 205 309 315 334
  M_2C 230 248 302 334
  M_6C 302 335
  M_7C_3 133 136 205
  NbC 86 133 155 251
  phase diagrams for mixed carbides 86
  secondary hardening 222
  TiC 246
  VC 86 133 134 246 302
case hardening
  carburising 7 168
  nitriding 170
  treatments 299
cast irons (grey)
  general 349
  grey/white transition 351

This page has been reformatted by Knovel to provide easier navigation.

Index terms	Links		
cast irons (grey) *(Continued)*			
micrographs	112	350	
mixed structure micrographs	353		
nickel-rich	360		
cast irons (nodular or SG)			
ferrite halos	360		
general	356		
heat treatments	363		
micrographs	237	358	
cast irons (white)			
general	347		
micrographs	113	219	234
cells			
eutectic	110	134	356
pearlitic	146	196	
Charpy impact-temperatures	261	293	
chill casting	124		
chill zone	271		
coalescence, secondary dendrite arm	103		
coarsening			
discontinuous pearlite coarsening	199		
grain coarsening	104		
LSW law	248		
solid state grain coarsening	248		
columnar zone	272		
continuous castings	270		
copper, see precipitates, precipitation hardening			
corrosion			
localized	168		
see PREN	168		

Index terms	Links				
creep strength	332				
crystallographic structures	37				
damascene structures					
contemporary forge welded	31				
produced by powder metallurgy techniques	32				

D

damassé	21				
dendrites					
morphology	102	108	123	135	144
	156				
ripening, arm coalescence	101	123			
see growth					
depleted zone	165	234			
diffusion					
back-diffusion	127				
coefficients	164				
couples	172				
general aspects	163				
length	165	369			
paths	175				
dislocations					
in duplex steels	327				
nucleation sites	240	251			
work hardening, recovery	256				
dissolution					
re-dissolution of pearlite	206				
solid state dissolution of carbides	136	208			
divorced eutectoid	199				

Index terms	Links		
DTA, see thermal analysis	125		
ductile/brittle transition	261		
duplex, see steels	325		
E			
effects of alloying elements			
general	263		
see pearlite, martensite (Ms)			
see stabilizers, curves			
summary	370		
electronic compounds	44		
equiaxed zone	271		
equivalents			
carbon	293	353	
nickel and chromium equivalents	265	327	367
see PREN			
etching reagents	368		
eutectic			
morphology	114	127	140
see solidification paths			
ternary/three-phase	51		
white/grey	351		
eutectoid see pearlite transformation			
F			
facetted growth	104	155	
ferrite			
acicular	290		
allotriomorph	191		

Index terms	Links			
ferrite *(Continued)*				
crystallographic structure	38			
nucleation	192			
stabilizer, former, see stabilizers				
Widmanstätten ferrite	180	191	226	236
forging				
early ironmaking process	7			
tool steels	303			
fracture	156	262	362	
free energy (excess)	53			

G

galvanizing	173			
gamma loop	57	70	265	323
grains				
case of multi-phase constituents	155			
grain boundaries	151			
grain boundary diffusion	157			
grain boundary energy	152	159	367	
grain growth	104	257	298	
grain observation technics	159			
intergranular fracture	156			
orientation	160			
single crystals	122	156		
size	159	256		
structure	151			
graphite				
lamellar	112	350	355	
see cast irons				
vermicular	350			

Index terms	Links		
growth			
cells	96		
dendrites	96	98	
LSW law	103		
planar front/dendritic transition	96		
see grain growth			
supercooling	98		
H			
Hadfield	320		
Hallstatt	9		
hamon	30		
hard facing	303		
hardenability	265	297	
hardening			
case hardening	299		
precipitation	240	312	
secondary hardening	222		
hardness			
bainite	229		
CCT curves	183	299	
effect of tempering	222		
microhardness in a white cast iron	219		
heat treatments			
grey cast irons	363		
steels	297		
superalloys	343		
tool steels	303		
very long holding times	333		
high resolution TEM	152	309	345

Index terms	Links			
I				
inclusions	251	277		
ingots	273			
interfaces				
coherent	153	345		
energies	367			
liquid/solid equilibrium	91	159		
local equilibrium, para-equilibrium	187			
mobility of solid/solid interfaces	184			
see grain boundary				
see high resolution TEM				
structure of solid/solid interface	185			
intermetallic compounds				
crystallographic structure	45			
hardening effect	312	338		
thermal stability of superalloys	344			
interphase boundaries	153			
interstices (tetrahedral and octahedral)	38			
invariant equilibrium	48	57	61	66
invariant habit plane	210			
iron smelting	6			
isopleth (definition)	60			
J				
Johnson-Mehl-Avrami law	199			
L				
La Tène	9			
Laves phases	44	334		
ledeburite	113			

Index terms	Links
ledges	
growth ledges	185 198
structural ledges	185
liquidus	
perspective view	59 65 69 74 78
projection	81 85 130 142 147 352
projection, surface	60
local equilibrium (see interface equilibrium)	
loop, gamma loop	57 70 265 323

M

Index terms	Links
malleablising	351
manganese, see manganese-containing	
steels	320
martensite	
effect of stress	218 314
epsilon	213
Fe-N	220
laths	133 146 156 171 192 215 225 300 301 308 312 366
laths or plates	180 214
lattice parameters	210
mixed	219
plates	128 216 365
see temperature	
shape memory effect	211
softening	219 309
strain-induced	212 366

This page has been reformatted by Knovel to provide easier navigation.

Index terms	Links		
martensite *(Continued)*			
tempering	219	298	310
twinning	217		
melting			
AOD, VOD, VIM	280		
see also remelting, refining			
metatectic transformation	147		
meteoritic kon	4		
microporosity	104		
monotectic	138		
monovariant line	52		
Ms see temperature			

N

Index terms	Links	
nitrides		
carbonitrides	334	
Cr_2N	334	
VN	333	
Z phase	335	
nodules, see spheroidal graphite cast irons		
nucleation		
autocatalytic	216	
free energy	239	
strain effect	192	

O

Index terms	Links	
ordering	40	
orientation relationships		
$M_{23}C_6$/austenite	309	315
martensite/austenite	211	

Index terms	Links	
orientation relationships *(Continued)*		
pearlite	197	
outburst (arborescences)	176	
P		
paths, see solidification, diffusion		
pearlite		
delta pearlite	146	205
divergent pearlite	204	
effect of alloying elements	200	
globular pearlite	198	298
interlamellar spacing	197	
orientation relationships	197	
see dissolution		
see transformations		
peening, shot peening, sand blasting	365	
peritectic		
growth competition	99	
marking of the transformation	143	
origin of microstructure	116	
ternary peritectic, pseudo-peritectic	51	
Phacomp	46	
phase diagrams		
ab initio calculations	54	
calculated	53	
calculation	83	
calculation softwares	54	
Co-Cu	75	
Cr-C	58	
Cr-C-Mo	88	

Index terms	Links		
phase diagrams *(Continued)*			
Cr-C-N	89		
Cr-Mo	78	79	
Cr-Ni	92		
Fe-C	19	56	
Fe-C-Mn	87	266	352
Fe-C-Mo	142		
Fe-Co	41	75	
Fe-Co-Cu	76		
Fe-C-P	19		
Fe-Cr	58		
Fe-Cr-C	58	88	130
Fe-Cr-C-Mo	307		
Fe-Cr-Mo	78		
Fe-Cr-Mo-V-C-N	320		
Fe-Cr-N	319		
Fe-Cr-Ni	69	147	
Fe-Cr-Ni-Mo	83		
Fe-Cr-Ni-N	328		
Fe-C-Si	266	352	362
Fe-Cu	75		
Fe-C-V	85		
Fe-Mn	71		
Fe-Mn-S	71		
Fe-MnS	74		
Fe-Mo	79		
Fe-Ni	42		
Fe-Ni-Cr-Al-Ti	340		
Fe-S	71		
Fe-V	84		
Fe-W	80		

Index terms	Links		
phase diagrams *(Continued)*			
Fe-W-C	88	141	
Fe-Zn	174		
general	47		
Mn-MnS	74		
V-C	84		
VC-TaC	86		
phase field modeling	108	120	
planes			
close-packed planes	46	153	341
habit plane	185		
slip plane	154		
stacking sequence	38	46	340
porosity	278		
powders (characteristics of metallic powders)	281		
precipitates			
carbides, see carbides	230		
chi phase	328		
copper	242	312	
G phase	330		
gamma double prime	343		
gamma prime	343		
Laves phases	334		
MnS	308	322	
NiAl	312		
nitrides (see nitrides)			
pi phase	328		
R phase	329		
see thermal stability	331		
sigma phase	316	328	

This page has been reformatted by Knovel to provide easier navigation.

Index terms	Links		
precipitates *(Continued)*			
Z phase	335		
precipitation			
continuous	239		
discontinuous (cellular)	206	245	
fibrous	247		
interphase	246		
spinodal	243	330	
PREN	313		

Q

quasi-binary	64	73	85
quasi-peritectic, pseudo-peritectic	51		
quenching			
cooling fluids	183		
during directional solidification	123		
during thermal analysis	126	148	
during unidirectional solidification	128	134	
step quenching	363		

R

reactions		
metatectic	51	72
monotectic	51	73
peritectic	51	
syntectic	51	
ternary peritectic and quasi-peritectic	51	
recovery	257	
recrystallisation	257	

This page has been reformatted by Knovel to provide easier navigation.

refining processes
  AOD, VOD, VIM 279 323
remelting
  (VAR, ESR) 269 280
  segregation-induced 149
retrodiffusion, see back-diffusion
ripening, dendrite ripening 103 123
rules
  barycentre (and lever rule) 49 91
  for adjacent phase fields 50
  Hillert's criterion 51
  tangent 51
  variance 48

S

Scheil-Gulliver law 93
segregation
  dendrite 98 127 217
  in carbides 130
  major segregation 274
  mesosegregation 276
sensitization to corrosion 167
separation between two liquids 138
settling, flotation 126 138
sigma stabilizers, see stabilizers
sintered alloys, micrographs 285
sintering 281
softening of martensite 219
solid solutions 39

Index terms — Links

solidification
  directional solidification 121 134
  origin of the microstructure 91
  paths 62 127
  quench interrupted during thermal analysis 126 144 148
  see continuous castings, ingots
  solidification time 106 354
solidus 64
solubility product 294
spacings
  eutectic interlamellar spacing 108
  interlamellar spacing of pearlite 197
  primary dendrite arm spacing 99 100
  secondary dendrite arm spacing 106 354
spinodal decomposition 243
stabilizers
  austenite stabilizers 265 314 326 370
  ferrite stabilizers 265 307 314 326 370
  sigma stabilizers 80 318 370
steels
  austenitic heat resisting steels 335
  duplex steels 154 325
  ferritic heat resisting steels 331
  ferritic steels 323
  low alloy steels 289
  low alloy structural steels 291
  manganese-containing steels 320
  maraging steels 311
  martensitic stainless steels 305
  nitrogen-containing steels 318

This page has been reformatted by Knovel to provide easier navigation.

steels *(Continued)*
  quench hardening steels 297
  resulphurised stainless steels 321
  sintered powder steels 284
  tool steels and high speed steels 302
  TRIP steels 295
  wootz steel 21
strengthening
  grain size 256
  mechanisms 255
  solid solution strengthening 258
sub-lattices 55 83
sulphides 114 147 322
superalloys 343
supercooling
  associated with DTA measurements 125
  constitutional supercooling 95
  theoretical approach 125
surface treatments
  galvanizing 173
  see also hard facing, shot peening, case hardening
swords
  Celtic 14
  Damascus steel swords 20 27
  general aspects 13
  Japanese 28
  Malaysian kris 30
  Merovingian and Carolingian 16
  pattern welded 20

This page has been reformatted by Knovel to provide easier navigation.

Index terms	Links			
T				
temperature				
A1, A2	184			
ductile/brittle transition	261	293		
liquidus temperature determination	125			
Ms	214			
tempering, see martensite				
thermal analysis	124			
DTA curves	125	142		
TA curves	124			
thermal stability	331			
tie-lines	48			
Titanic	263	292		
topologically close packed phases	44			
toughness	260	294		
transformation curves				
CCT	183	299		
TTT	182	199	330	336
transformations				
bainite	223			
classes	179			
martensite	211			
ordering	40			
pearlite	195			
representation	180	200		
TRIP steels	295			
TTT, CCT, see transformation curves				
twinning	152	217	218	

Index terms	Links	
W		
Widmanstätten, see meteoritic iron, ferrite		
wootz	9	21
Z		
Z phase	335	